Advances in FLUID MECHANICS VI

Editors: M. Rahman
and C.A. Brebbia

WIT PRESS

Advances in Fluid Mechanics VI

WIT PRESS

WIT Press publishes leading books in Science and Technology.
Visit our website for the current list of titles.
www.witpress.com

WIT eLibrary

Home of the Transactions of the Wessex Institute.
Papers presented at Advances in Fluid Mechanics VI
are archived in the
WIT eLibrary in volume 52 of WIT Transactions on
Engineering Sciences (ISSN 1743-3533).

The WIT eLibrary provides the international scientific community with immediate and
permanent access to individual papers presented at WIT conferences.
http://library.witpress.com

Transactions Editor

Carlos Brebbia
Wessex Institute of Technology
Ashurst Lodge, Ashurst
Southampton SO40 7AA, UK

Email: carlos@wessex.ac.uk

WIT Transactions on Engineering Sciences

Editorial Board

B. Abersek
University of Maribor
Slovenia

B Alzahabi
Kettering University
USA

K S Al Jabri
Sultan Qaboos University
Oman

A G Atkins
University of Reading
UK

J A C Ambrosio
IDMEC
Portugal

A F M Azevedo
University of Porto
Portugal

H Azegami
Toyohashi University of Technology
Japan

R Belmans
Katholieke Universiteit Leuven
Belgium

G Belingardi
Politecnico di Torino
Italy

E Blums
Latvian Academy of Sciences
Latvia

S K Bhattacharyya
Indian Institute of Technology
India

F-G Buchholz
Universitat Gesanthochschule Paderborn
Germany

A R Bretones
University of Granada
Spain

W Cantwell
Liverpool University
UK

J Byrne
University of Portsmouth
UK

S K Chakrabarti
Offshore Structure Analysis
USA

D J Cartwright
Bucknell University
USA

H Choi
Kangnung National University
Korea

A Chakrabarti
Indian Institute of Science
India

L De Biase
University of Milan
Italy

J J Connor
Massachusetts Institute of Technology
USA

R de Borst
Delft University of Technology
Netherlands

L Debnath
University of Texas-Pan American
USA

G De Mey
Ghent State University
Belgium

S del Giudice
University of Udine
Italy

M Domaszewski
Universite de Technologie de Belfort-Montbeliard
France

I Doltsinis
University of Stuttgart
Germany

W Dover
University College London
UK

J Dominguez
University of Seville
Spain

K M Elawadly
Alexandria University
Egypt

J P du Plessis
University of Stellenbosch
South Africa

F Erdogan
Lehigh University
USA

M E M El-Sayed
Kettering University
USA

H J S Fernando
Arizona State University
USA

M Faghri
University of Rhodes
Island
USA

E E Gdoutos
Democritus University of
Thrace
Greece

C J Gantes
National Technical
University of Athens
Greece

D Goulias
University of Maryland
USA

R Gomez Martin
University of Granada
Spain

D Gross
Technische Hochschule
Darmstadt
Germany

R H J Grimshaw
Loughborough University
UK

R C Gupta
National University of
Singapore

R Grundmann
Technische Universitat
Dresden
Germany

K Hameyer
Katholieke Universiteit
Leuven
Belgium

J M Hale
University of Newcastle
UK

P J Heggs
UMIST
UK

L Haydock
Newage International
Limited
UK

D A Hills
University of Oxford
UK

C Herman
John Hopkins University
USA

T H Hyde
University of Nottingham
UK

M Y Hussaini
Florida State University
USA

N Ishikawa
National Defence Academy
Japan

D B Ingham
The University of Leeds
UK

N Jones
The University of Liverpool
UK

Y Jaluria
Rutgers University
USA

T Katayama
Doshisha University
Japan

D R H Jones
University of Cambridge
UK

E Kita
Nagoya University
Japan

S Kim
University of Wisconsin-Madison
USA

A Konrad
University of Toronto
Canada

A S Kobayashi
University of Washington
USA

T Krauthammer
Penn State University
USA

S Kotake
University of Tokyo
Japan

F Lattarulo
Politecnico di Bari
Italy

M Langseth
Norwegian University of Science and Technology
Norway

Y-W Mai
University of Sydney
Australia

S Lomov
Katholieke Universiteit Leuven
Belgium

B N Mandal
Indian Statistical Institute
India

G Manara
University of Pisa
Italy

T Matsui
Nagoya University
Japan

H A Mang
Technische Universitat Wien
Austria

R A W Mines
The University of Liverpool
UK

A C Mendes
Univ. de Beira Interior
Portugal

T Miyoshi
Kobe University
Japan

A Miyamoto
Yamaguchi University
Japan

T B Moodie
University of Alberta
Canada

G Molinari
University of Genoa
Italy

D Necsulescu
University of Ottawa
Canada

D B Murray
Trinity College Dublin
Ireland

H Nisitani
Kyushu Sangyo University
Japan

S-I Nishida
Saga University
Japan

P O'Donoghue
University College Dublin
Ireland

B Notaros
University of
Massachusetts
USA

K Onishi
Ibaraki University
Japan

M Ohkusu
Kyushu University
Japan

E Outa
Waseda University
Japan

P H Oosthuizen
Queens University
Canada

W Perrie
Bedford Institute of
Oceanography
Canada

G Pelosi
University of Florence
Italy

D Poljak
University of Split
Croatia

H Pina
Instituto Superior Tecnico
Portugal

H Power
University of Nottingham
UK

L P Pook
University College
London
UK

I S Putra
Institute of Technology
Bandung
Indonesia

D Prandle
Proudman Oceanographic
Laboratory
UK

M Rahman
Dalhousie University
Canada

F Rachidi
EMC Group
Switzerland

T Rang
Tallinn Technical University
Estonia

K R Rajagopal
Texas A & M University
USA

B Ribas
Spanish National Centre for
Environmental Health
Spain

D N Riahi
University of Illinios-
Urbana
USA

W Roetzel
Universitaet der Bundeswehr
Hamburg
Germany

K Richter
Graz University of
Technology
Austria

S Russenchuck
Magnet Group
Switzerland

V Roje
University of Split
Croatia

B Sarler
Nova Gorica Polytechnic
Slovenia

H Ryssel
Fraunhofer Institut
Integrierte Schaltungen
Germany

R Schmidt
RWTH Aachen
Germany

A Savini
Universita de Pavia
Italy

A P S Selvadurai
McGill University
Canada

B Scholtes
Universitaet of Kassel
Germany

L C Simoes
University of Coimbra
Portugal

G C Sih
Lehigh University
USA

J Sladek
Slovak Academy of Sciences
Slovakia

P Skerget
University of Maribor
Slovenia

D B Spalding
CHAM
UK

A C M Sousa
University of New
Brunswick
Canada

G E Swaters
University of Alberta
Canada

T S Srivatsan
University of Akron
USA

C-L Tan
Carleton University
Canada

J Szmyd
University of Mining and
Metallurgy
Poland

A Terranova
Politecnico di Milano
Italy

S Tanimura
Aichi University of Technology
Japan

S Tkachenko
Otto-von-Guericke-University
Germany

A G Tijhuis
Technische Universiteit Eindhoven
Netherlands

E Van den Bulck
Katholieke Universiteit Leuven
Belgium

I Tsukrov
University of New Hampshire
USA

R Verhoeven
Ghent University
Belgium

P Vas
University of Aberdeen
UK

B Weiss
University of Vienna
Austria

S Walker
Imperial College
UK

T X Yu
Hong Kong University of Science & Technology
Hong Kong

S Yanniotis
Agricultural University of Athens
Greece

M Zamir
The University of Western Ontario
Canada

K Zakrzewski
Politechnika Lodzka
Poland

SIXTH INTERNATIONAL CONFERENCE ON
ADVANCES IN FLUID MECHANICS

AFM VI

CONFERENCE CHAIRMEN

M. Rahman
Dalhousie University, Canada

C.A. Brebbia
Wessex Institute of Technology, UK

INTERNATIONAL SCIENTIFIC ADVISORY COMMITTEE

E Baddour
SK Bhattacharyya
R Bourisli
A Chakrabarti
G Comini
L Debnath
J P Du Plessis
T B Gatski
R H J Grimshaw
C Gualtieri
R C Gupta
D Hally
W Harris
I G Hassan
M Hribersek
M Y Hussaini
D B Ingham
A K Macpherson
A C Mendes
T B Moodie
M A Noor
W Perrie
H Pina
D N Riahi
L Skerget
G Swaters
K Takahashi
R Verhoeven

Organised by
Wessex Institute of Technology, UK
and
Dalhousie University, Canada

Sponsored by:
WIT Transactions on Engineering Sciences

This page intentionally left blank

Advances in Fluid Mechanics VI

EDITORS:

M. Rahman
Dalhousie University, Canada

C.A. Brebbia
Wessex Institute of Technology, UK

WIT*PRESS* Southampton, Boston



M. Rahman
Dalhousie University, Canada

C.A. Brebbia
Wessex Institute of Technology, UK

Published by

WIT Press
Ashurst Lodge, Ashurst, Southampton, SO40 7AA, UK
Tel: 44 (0) 238 029 3223; Fax: 44 (0) 238 029 2853
E-Mail: witpress@witpress.com
http://www.witpress.com

For USA, Canada and Mexico

Computational Mechanics Inc
25 Bridge Street, Billerica, MA 01821, USA
Tel: 978 667 5841; Fax: 978 667 7582
E-Mail: infousa@witpress.com
http://www.witpress.com

British Library Cataloguing-in-Publication Data

A Catalogue record for this book is available
from the British Library

ISBN: 1-84564-163-9
ISSN: 1746-4471 (print)
ISSN: 1743-3533 (on-line)

The texts of the papers in this volume were set individually by the authors or under their supervision. Only minor corrections to the text may have been carried out by the publisher.

No responsibility is assumed by the Publisher, the Editors and Authors for any injury and/or damage to persons or property as a matter of products liability, negligence or otherwise, or from any use or operation of any methods, products, instructions or ideas contained in the material herein.

© WIT Press 2006

Printed in Great Britain by Athenaeum Press Ltd.

All rights reserved. No part of this publication may be reproduced, stored in a retrieval system, or transmitted in any form or by any means, electronic, mechanical, photocopying, recording, or otherwise, without the prior written permission of the Publisher.

Preface

This book covers a wide range of edited papers in the areas of fluid mechanics presented at the Sixth International Conference on Advances in Fluid Mechanics held on the beautiful island of Skiathos, Greece, 8-10 May 2006. The conference was organized by the Wessex Institute of Technology, UK and Dalhousie University, Canada, and was sponsored by the WIT Transactions on Engineering Sciences.

The conference emphasizes the advancement of knowledge in fluid mechanics problems with novel applications. The basic mathematical formulations and their solutions by analytical and numerical methods are discussed together with physical modelling.

This conference has been reconvened every two years since 1996 and was motivated by the success of previous Meetings and the well-established book series, Advances in Fluid Mechanics. The Scientific Advisory Committee is composed of the experienced and professional Editorial Board Members of the book series.

The conference was first held in New Orleans, USA (1996), then in Udine, Italy (1998); in Montreal, Canada (2000); in Ghent, Belgium (2002), and in Lisbon, Portugal (2004). World renowned Scientists, Engineers and Professionals from around the world participated and presented their latest findings in various topics of Fluid Mechanics.

This book should be of interest to all researchers in fluid mechanics. It contains the following sections:

Computations methods in fluid mechanics; Experimental versus simulation methods; Hydraulics and hydrodynamics; Fluid structure interaction; Convection, heat and mass transfer; Boundary layer flow; Multiphase flow; Non-Newtonian fluids; Wave studies; Industrial applications; Turbulence flow; Biofluids and Permeability problems.

The Editors are very grateful to the contributors as well as to the Board Members for their enthusiastic support and participation in the Meeting. We are also thankful to the staff of the WIT Press for their excellent job in producing such a superb book.

The Editors
Skiathos, 2006

This page intentionally left blank

Contents

Section 1: Computational methods in fluid mechanics

The performance of drag models on flow behaviour in the CFD simulation of a fluidized bed
B. M. Halvorsen, J. P. du Plessis & S. Woudberg 3

Solution of the incompressible Navier-Stokes equations via real-valued evolutionary algorithms
R. I. Bourisli & D. A. Kaminski 13

A parallel computing framework and a modular collaborative cfd workbench in Java
S. Sengupta & K. P. Sinhamahapatra 21

A parallel ILU strategy for solving Navier-Stokes equations on an unstructured 3D mesh
Ø. Staff & S. Ø. Wille 31

On the mathematical solution of 2D Navier Stokes equations for different geometries
M. A. Mehemed Abughalia 39

A computational method for pressure wave machinery to internal combustion engines and gas turbines
A. Fatsis, M. Gr. Vrachopoulos, S. Mavrommatis, A. Panoutsopoulou & F. Layrenti 49

Aerodynamic flow simulation
R. W. Derksen & J. Rimmer 59

Simulations of viscoelastic droplet deformation through a microfluidic contraction
D. J. E. Harvie, M. R. Davidson & J. J. Cooper-White 69

Simulation of single bubble rising in liquid using front tracking method
J. Hua & J. Lou 79

Section 2: Experimental versus simulation methods

Pilot simulation of the temperature field of a continuous casting
J. Stetina, F. Kavicka, B. Sekanina, J. Dobrovska & J. Heger 91

Experimental and computational investigation of kinematic mixing in a periodically driven cavity
S. Santhanagopalan, A. P. Deshpande & S. Pushpavanam 101

Computational Fluid Dynamics (CFD) use in the simulation of the death end ventilation in tunnels and galleries
J. Toraño, R. Rodríguez & I. Diego 113

Prediction of high-speed rigid body manoeuvring in air-water-sediment
P. C. Chu & G. Ray 123

Experimental study and modelling of the kinetics of drying of urban wastewater treatment plant sludge
H. Amadou, J.-B. Poulet, C. Beck & A.-G. Sadowski 133

Experimental investigation of grid-generated turbulence using ultrasonic travel-time technique
W. Durgin & T. Andreeva 143

Aluminized composite solid propellant particle path in the combustion chamber of a solid rocket motor
Y. M. Xiao & R. S. Amano 153

Simulation of unsteady muzzle flow of a small-caliber gun
Y. Dayan & D. Touati 165

Section 3: Hydraulics and hydrodynamics

Hot spots and nonhydraulic effects in surface gravity flows
T. B. Moodie, J. P. Pascal & S. J. D. D'Alessio 175

Finite amplitude evolution of frictionally destabilized abyssal overflows in a stratified ocean
G. E. Swaters 185

Watershed models and their applicability to the simulation of the rainfall-runoff relationship
A. N. Hadadin.....193

Dynamic pressure evaluation near submerged breakwaters
F. T. Pinto & A. C. V. Neves.....203

Mean flow effects in the nearly inviscid Faraday waves
E. Martín & J. M. Vega.....213

High frequency AC electrosprays: mechanisms and applications
L. Y. Yeo & H.-C. Chang.....223

Section 4: Fluid structure interaction

A structured multiblock compressible flow solver SPARTA for planetary entry probes
P. Papadopoulos & P. Subrahmanyam.....235

Eulerian simulations of oscillating airfoils in power extraction regime
G. Dumas & T. Kinsey.....245

Laboratory tests on flow field around bottom vane
M. M. Hossain, Md. Zahidul Islam, Md. Shahidullah, A. de Weerd, P. van Wielink & E. Mosselman.....255

Section 5: Convection, heat and mass transfer

Velocity vorticity-based large eddy simulation with the boundary element method
J. Ravnik, L. Škerget & M. Hriberšek.....267

Flow and heat transfer characteristics of tornado-like vortex flow
Y. Suzuki & T. Inoue.....277

Modeling fluid transport in PEM fuel cells using the lattice-Boltzmann approach
L.-P. Wang & B. Afsharpoya.....287

Painlevé analysis and exact solutions for the coupled Burgers system
P. Barrera & T. Brugarino.....297

Section 6: Boundary layer flow

New scaling parameter for turbulent boundary layer with large roughness
C. S. Subramanian & M. Lebrun 307

Stratified flow over topography:
wave generation and boundary layer separation
B. R. Sutherland & D. A. Aguilar.....317

Group analysis and some exact solutions for the thermal boundary layer
P. Barrera & T. Brugarino 327

Section 7: Multiphase flow

Cavity length and re-entrant jet in 2-D sheet cavitation
I. Castellani.....341

Numerical results for coagulation equation with bounded kernels,
particle source and removal
C. D. Calin, M. Shirvani & H. J. van Roessel.....351

Volume of fluid model applied to curved open channel flows
T. Patel & L. Gill 361

Drag reduction in two-phase annular flow of air and water in an
inclined pipeline
A. Al-Sarkhi, E. Abu-Nada & M. Batayneh.....371

Fluid flow simulation in a double L-bend pipe with small nozzle outlets
A. Rigit, J. Labadin, A. Chai & J. Ho 381

Stability analysis of dredging the flow sediment regiment upstream a dam
G. Akbari.....389

Section 8: Non-Newtonian fluids

Viscous spreading of non-Newtonian gravity currents in radial geometry
V. Di Federico, S. Cintoli & G. Bizzarri.....399

Axisymmetric motion of a second order viscous fluid in a circular
straight tube under pressure gradients varying exponentially with time
F. Carapau & A. Sequeira 409

The flow of power law fluids between parallel plates with shear heating
M. S. Tshehla, T. G. Myers & J. P. F. Charpin.....421

Section 9: Wave studies

Second-order wave loads on offshore structures using the Weber's transform method
M. Rahman & S. H. Mousavizadegan.....435

Rear shock formation in gravity currents
S. J. D. D'Alessio, J. P. Pascal & T. B. Moodie.....445

Nonlinear dynamics of Rossby waves in a western boundary current
L. J. Campbell.....457

Section 10: Industrial applications

Assessment of aerodynamic noise in an industrial ventilation system
A. M. Martins & A. C. Mendes.....469

Airflow modeling analysis of the Athens airport train station
M. Gr. Vrachopoulos, F. K. Dimokritou, A. E. Filios & A. Fatsis.....479

An industrial method for performance map evaluation for a wide range of centrifugal pumps
A. Fatsis, M. Gr. Vrachopoulos, S. Mavrommatis, A. Panoutsopoulou, N. Vlachakis & V. Vlachakis.....489

Large eddy simulation of compressible transitional cascade flows
K. Matsuura & C. Kato.....499

CFD modelling of sludge sedimentation in secondary clarifiers
M. Weiss, B. Gy. Plosz, K. Essemiani & J. Meinhold.....509

Hydro-power plant equipped with Pelton turbines: basic experiments relating to the influence of backpressure on the design
A. Arch & D. Mayr.....519

Section 11: Turbulence flow

CFD modelling of wall-particle interactions under turbulent flow conditions
M. Mollagee.....531

Exact statistical theory of isotropic turbulence
Z. Ran 541

The SGS kinetic energy and the viscous dissipation equations as closure relations in LES
F. Gallerano, L. Melilla & E. Pasero 551

Deforming mesh with unsteady turbulence model for fluid-structure interaction
J.-T. Yeh 561

Dispersion of solid saltating particles in a turbulent boundary layer
H. T. Wang, Z. B. Dong, X. H. Zhang & M. Ayrault 571

Section 12: Biofluids

An exact solution of the Navier-Stokes equations for swirl flow models through porous pipes
N. Vlachakis, A. Fatsis, A. Panoutsopoulou, E. Kioussis, M. Kouskouti & V. Vlachakis 583

Experimental investigation of flow through a bileaflet mechanical heart valve
J. Mejia & P. Oshkai 593

Numerical analysis of blood flow in human abdominal aorta
M. Podyma, I. Zbicinski, J. Walecki, M. L. Nowicki, P. Andziak, P. Makowski & L. Stefanczyk 603

Section 13: Permeability problems

Revising Darcy's law: a necessary step toward progress in fluid mechanics and reservoir engineering
C. Ketata, M. G. Satish & M. R. Islam 615

Hydrodynamic permeability prediction for flow through 2D arrays of rectangles
M. Cloete & J. P. Du Plessis 623

Analytical approach predicting water bidirectional transfers: application to micro and furrow irrigation
D. Crevoisier 633

The meniscus depression of a porous spherical particle at the three phase contact line
P. Basařová, D. Horn & A. Capriotti 643

Author index 653

This page intentionally left blank

Section 1
Computational methods in fluid mechanics

This page intentionally left blank

The performance of drag models on flow behaviour in the CFD simulation of a fluidized bed

B. M. Halvorsen[1], J. P. du Plessis[2] & S. Woudberg[2]
[1]*Department of Process Technology, Telemark University College, Porsgrunn, Norway*
[2]*Department of Applied Mathematics, University of Stellenbosch, South Africa*

Abstract

The aim of this study is to verify the use of a newly developed drag model in the simulation of fluidized beds. The drag model is based on a geometric description of the geometry found in a fluidised bed, treating it as a spatially and temporally variable inhomogeneous, locally isotropic, porous medium. Account is taken of the fact that flow conditions in low porosity parts of a bed can be viewed as flow between particles. At high porosities the bed resembles flow past the particles of a dilute assemblage and for that the current model is complemented with results from other models. The new drag model, as well as other models found in literature, was tested in the numerical simulations. Computational results are compared mutually, as well as to experimental data, and the differences and discrepancies discussed.
Keywords: fluidized bed, numerical simulation, drag model.

1 Introduction

Fluidized beds are widely used in industrial chemical processes. In a fluidized bed gas is passing upwards through a bed of particles and the earliest applications of fluidization were for the purpose of enhancing chemical reactions. Fluidized beds in chemical industry include two main types of reactions, catalytic gas phase reactions and gas-solid reactions. In catalytic gas phase reactions the particles are not undergoing any chemical reaction. This is



WIT Transactions on Engineering Sciences, Vol 52, © 2006 WIT Press
www.witpress.com, ISSN 1743-3533 (on-line)
doi:10.2495/AFM06001

the principal of oil cracking for manufacturing of various chemical substances. In gas-solid reactions the fluidized particles are involved in the reactions and undergo a phase change. An example of this type of process is combustion or gasification of coal. Other application of fluidized beds are drying and coating of solids.

Fluidized beds are applied in industry due to their large contact area between phases, which enhances chemical reactions, heat transfer and mass transfer. The efficiency of fluidized beds is highly dependent of flow behaviour and knowledge about flow behaviour is essentially for scaling, design and optimisation. Computational fluid dynamics (CFD) has during the last decades become a useful tool in predicting flow behaviour in fluidized bed processes. However, further model development and verification of the model and the numerical procedure are still needed.

Gravity and drag are the most predominant terms in the solid phase momentum equation and the application of different drag models has significant impact on the flow of the solid phase by differently influencing the predicted bed expansion and the solid concentration in the dense phase regions of the bed. Yasuna *et al* [1], Halvorsen and Mathiesen [2], Ibsen [3] and Bokkers *et al* [4] showed that the solution of their models is sensitive to the drag coefficient. In general, the performance of most current models depends on the accuracy of the drag formulation.

The Ergun Equation [5], Bird *et al* [6] is frequently used as drag model for calculating pressure gradients during flow in a fluidized beds. An updated value for the first coefficient in the Ergun equation from 150 to 180 was reported by MacDonald *et al* [7] and may also be used as an improved empirical model. Both were, however, derived empirically for Newtonian flow through packed beds in a fairly narrow band of porosities around 40% and their generalization to more general physical situations cannot be performed, but in an approximate and empirical manner. In active fluidized beds the void fraction can change over the full range from zero through unity and the model used in numerical simulations should be equally versatile.

The Ergun equation may be written as follows [5]:

$$\mathrm{FD}^2 = \frac{\mathrm{A}(1-\varepsilon)^2}{\varepsilon^3} + \frac{\mathrm{B}(1-\varepsilon)}{\varepsilon^3}\mathrm{Re} = \frac{150(1-\varepsilon)^2}{\varepsilon^3} + \frac{1.75(1-\varepsilon)}{\varepsilon^3}\mathrm{Re} \tag{1}$$

where ε is the porosity and Re the local Reynolds number expressed by:

$$\mathrm{Re} = \frac{\rho_g \mathrm{qD}}{\mu_g} \tag{2}$$

and q is the superficial velocity:

$$q = \varepsilon\left|U_g - U_s\right| \tag{3}$$

Here U_g and U_s are the local gas and solid velocities respectively.

Gidaspow [8] combined the Ergun equation with the equations of Rowe [9] and Wen and Yu [10] to get a drag model that can cover the whole range of porosities. The following equation of Wen and Yu is used for a voidage above 0.80:

$$FD^2 = \frac{3}{4} C_D \frac{\varepsilon_s \varepsilon \cdot D}{\mu} \rho_g \left| U_g - U_s \right| \varepsilon^{-2.65}, \quad \text{for } \varepsilon > 0.8 \tag{4}$$

Rowe [9] related the friction coefficient, C_D, to Reynolds number by:

$$\begin{aligned} C_D &= \frac{24}{Re_s}\left(1 + 0.15\,Re^{0.687}\right), \quad Re_s \le 1000 \\ C_D &= 0.44, \qquad\qquad\qquad\quad Re_s > 1000 \end{aligned} \tag{5}$$

The particle Reynolds number, Re_s, is expressed by:

$$Re_s = \frac{D\rho_g \left| U_g - U_s \right| \varepsilon_s}{\mu_g} \tag{6}$$

The MacDonald drag model is given, for the entire range of porosities, by:

$$FD^2 = \frac{180(1-\varepsilon)^2}{\varepsilon^3} + \frac{1.8(1-\varepsilon)}{\varepsilon^3} Re \tag{7}$$

Gibilaro *et al* [11] proposed the following drag model:

$$FD^2 = \frac{3}{4} C_D \frac{\varepsilon_s \varepsilon \cdot D}{\mu} \rho_g \left| U_g - U_s \right| \tag{8}$$

where the friction coefficient, C_D, is expressed by:

$$C_D = \frac{4}{3}\left(\frac{17.3}{Re_s} + 0.336\right)\varepsilon^{-2.80} \tag{9}$$

2 The proposed drag model

The deterministic model presented here is based on a fixed simplistic geometrical layout but the voidage can take any value according to the properties found within any part of the bed Du Plessis [12]. Flow conditions are then assumed according to the geometry of the flow passages, the void fraction and the interstitial Reynolds number. In this manner elaboration towards more complex behaviour can be performed in a systematic manner and discrepancies and unexpected behavioural characteristics can be analysed in a scientific manner. The local Reynolds number at any point in the bed is defined as above. The Reynolds number is taken into account when determining the local drag coefficient.

2.1 Creep flow solution at low Reynolds number flow

The low voidage drag model of Du Plessis was improved for creep flow relative to an isotropic granular material, Woudberg *et al* [13]. Since it is impossible to envisage an isotropic geometric arrangement of particles it is assumed that the properties of an isotropic medium are resembled by the average of the properties of flow in three perpendicular directions though an arrangement where the particles are maximally (fully) staggered in one direction and non-staggered in the other two directions. In the one direction the flow thus experiences a fully

staggered configuration with maximal tortuosity of the streamlines. In the other two directions the flow lines are straight and stagnant regions are formed between streamwise adjacent solid particles.

At high voidages creep flow through an assemblage of particles is more appropriately considered as flow past each of the particles than as flow between solid constituents. A model proposed by Hasimoto [14], for flow past a particle that is imbedded in an assemblage of other particles is therefore used in the present work to describe the creep flow situation at high voidage factors. It may also be noted that there is no large difference between the flow conditions in regular or staggered arrays when the voidage is high.

An asymptotic matching technique Churchill and Usagi [15] is used to combine the two asymptotic solutions into one equation, facilitating their use in numerical simulations. This combined equation for all voidage factors is then considered as an asymptotic condition for creep flow situations in the bed.

2.2 Inertial flow solution at intermediate Reynolds number flow

In regions where the Reynolds number is well above unity, local areas of recirculation develop at the lee side of particles, giving rise to inertial effects in the so-called Forchheimer regime. These effects can be modelled as momentum effects resulting in a pressure drop over each particle. This is not yet in the turbulence regime but, since numerous experiments (e.g. MacDonald *et al*) suggest a fairly established asymptotic behaviour, these laminar conditions will be considered as adhering to an asymptotic law at intermediate Reynolds number values of flow locally within in the bed.

2.3 Asymptote matching

The asymptote matching technique is again applied to match two asymptotic solutions, namely that of creep flow and that of inertial but still laminar flow Woudberg [16], resulting in equation (10), where F is the drag factor (inverse of the permeability) and D the average grain diameter. Here the first and last terms respectively reflect the creep solutions at low and high voidage and the middle term the inertial flow conditions when interstitial recirculation occurs.

$$FD^2 = \frac{26.8(1-\varepsilon)^{4/3}}{\left(1-(1-\varepsilon)^{1/3}\right)\left(1-(1-\varepsilon)^{2/3}\right)^2} + \frac{(1-\varepsilon)}{\varepsilon\left(1-(1-\varepsilon)^{2/3}\right)^2}\mathrm{Re} + (162\pi^2)^{1/3}(1-\varepsilon)\left(1+1.79(1-\varepsilon)^{1/3}\right) \tag{10}$$

If the present solution is compared to the existing models, the coefficients A and B of the Ergun equation are functions of the void fraction, respectively as follows:

$$A = \frac{26.8\varepsilon^3}{(1-\varepsilon)^{2/3}\left(1-(1-\varepsilon)^{1/3}\right)\left(1-(1-\varepsilon)^{2/3}\right)^2} \tag{11}$$

and

$$B = \frac{\varepsilon^2}{\left(1-(1-\varepsilon)^{2/3}\right)^2} \tag{12}$$

It is interesting to note that the new model yields an effective B-value that decreases almost linearly from 2.25 at zero voidage to unity at total voidage. Conversely the coefficient A is predicted as 185 at very low voidage, increasing steadily to about 785 at a voidage factor of unity. Differences in magnitudes among the models are thus evident and this should reflect in the drag profiles predicted.

3 Physical description of bed dynamics

Computational and experimental studies have been performed on a 2-D fluidized bed with a central jet. The advantage of using a bed with a jet is that the jet establishes the flow pattern, and this problem is easier to model than uniform fluidization. In the experimental studies a digital video camera was used to measure bubble sizes and bubble velocities.

Spherical glass particles with a mean diameter of 490 μm are used in the experiments and the simulations. For these particles the inter-particle forces are negligible and bubbles are formed as the gas velocity reaches the minimum fluidization velocity, Geldart [17]. The bed expansion is small compared to other types of particles. Small bubbles are formed close to the air distributor and the bubble size increase with distance above the distributor. The bubble size also increases with the excess gas velocity which is defined as the difference between the gas velocity and the minimum fluidization velocity, Geldart [17]. Coalescence is the predominant phenomenon of this group of powders and the bubble size is roughly independent of mean particle size. Most bubbles rise faster than the interstitial gas velocity.

4 Computational procedure

The computational work is performed by using the CFD model (FLOTRACS-MP-3D). The CFD code is based on a multi-fluid Eulerian description of the phases. The kinetic theory for granular flow forms the basis for the turbulence modelling of the solid phase. The CFD code was proposed by Mathiesen *et al* [18] and modified by Halvorsen [19] to improve its use in dense particle systems like bubbling fluidized beds. At high solid volume fraction, sustained contacts between particles occur and the resulting frictional stresses must be accounted for in the description of the solid phase stress.

FLOTRACS-MP-3D is a gas/solid flow model, which is generalized for one gas phase and N number of solid phases. The gas phase turbulence is modelled by a sub-grid scale (SGS) model proposed by Deardorff [20]. The largest scales are simulated directly, whereas the small scales are modelled with the SGS turbulence model. In order to model the fluctuations in the solid phases a



conservation equation for granular temperature is solved for each solid phase. The governing equations given are solved by a finite volume method, where the calculation domain is divided into a finite number of non-overlapping control volumes. The simulations are performed using two-dimensional Cartesian co-ordinates.

The conservation equations are integrated in space and time. This integration is performed using second order upwind differencing in space and is fully implicit in time. The set of algebraic equations is solved by a tri-diagonal matrix algorithm (TDMA), except for the volume fraction where a point iteration method is used. Partial elimination algorithm (PEA) generalized to multiple phases is used to decouple the drag forces. The inter-phase slip algorithm (IPSA) is used to take care of the coupling between the continuity and the velocity equations.

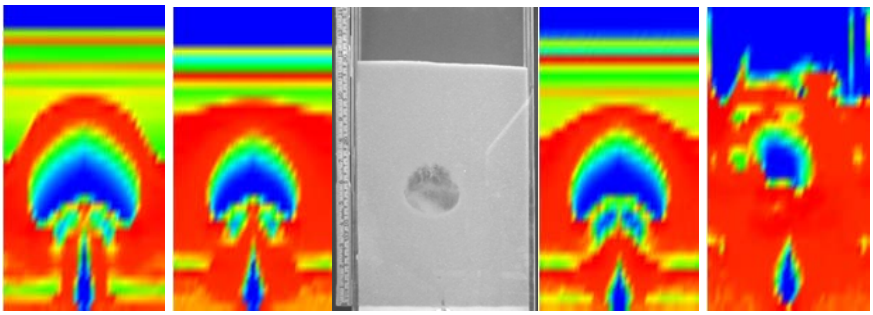
4.1 Computational set-up and results

A two-dimensional Cartesian co-ordinate system is used to describe the geometry. The grid is uniform in both horizontal and vertical direction. Computational set-up for glass particles is given in Table 1. Simulations have been run with one solid phase of identical particles, all of the same size.

Table 1: Computational set-up and conditions, glass particles.

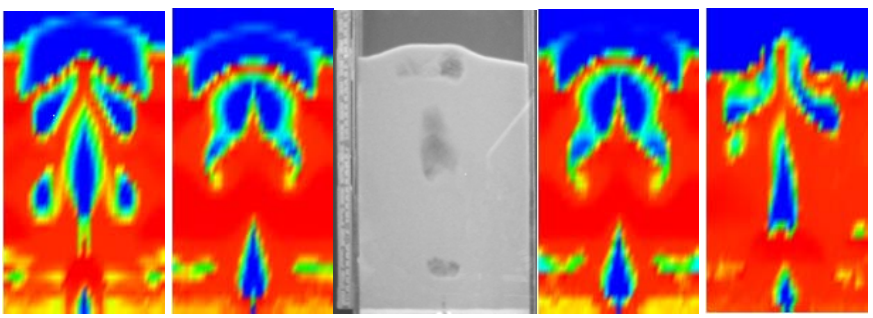
Design:		**Grid:**	
Height	63.0 cm	Horizontal grid size	5.0 mm
Width	19.5 cm	Vertical grid size	10.0 mm
Initial bed height	33.6 cm		
Initial voidage	0.50		
Glass particles		**Flow specifications:**	
Mean diameter	490 μm	Jet velocity	4.90 m/s
		Fluidization velocity	0.29 m/s
		Maximum volume fraction of solids	0.64356

Simulations are performed with the drag models of Du Plessis and Woudberg, Ergun/Wen and Yu, MacDonald *et al* and Gibilaro *et al* as described above. Figure 1 shows a comparison of the experimental and computational bubbles at time 320 ms. It can be seen that the simulations with the models of Du Plessis, Ergun/Wen and Yu and MacDonald give very good agreement with the experiment according to bubble velocity. These models also give a symmetric bubble. Further comparison of these three models with the experimental result show that the Ergun model gives the most realistic bubble size and bed expansion. The Du Plessis model gives a slightly larger bubble and a higher bed expansion than the MacDonald model. The Gibilaro model gives an unsymmetrical first bubble and the bubble velocity differs significantly from the experimental bubble velocity. The bed expansion is too low and unphysical high solid fractions are observed.



t=320 ms (Du Plessis) t=320 ms (Ergun,Wen and Yu) t=320 ms (experimental) t=320 ms (MacDonald) t=320 ms (Gibilaro)

Figure 1: Computational vs. experimental bubble at time 320 ms.



t=620 ms (Du Plessis) t=600 ms (Ergun, Wen and Yu) t=740 ms (experimental) t=620 ms (MacDonald) t=540 ms (Gibilaro)

Figure 2: Computational vs. experimental bubble near the top of the bed.

Figure 2 shows a comparison of the computational and experimental result at the time when the first bubbles erupt. Also at this level the Gibilaro model differ considerably from the others. For all the models the time between bubble creation and bubble eruption is shorter than for the experimental bubble. It can also be seen that all the models give continuous bubble formation. The Ergun and the MacDonald models give about the same shape and velocity for the second bubble. The Du Plessis and the Gibilaro models give the best agreement with the subsequent experimental bubble according to shape and size.

The two figures above show that the computational bubble behaviour is influenced significantly by the particular drag model used. Figures 3 and 4 show the computational drag (FD^2) as a function of radial position in the bed at height 0.2 m and 0.3 m respectively. The drag is averaged over a time lapse of 800 ms. It can be seen from Figure 3 that the drag is low in the centre of the bed where the bubbles are located, and the drag increases towards the walls where the particle concentration is high. At height 0.2 m Du Plessis, Ergun and MacDonald

predict about the same drag in the centre of the bed. There are some discrepancies between the models towards the walls. The Gibilaro model gives a lower drag than the other models in all radial positions at this height.

At a height 0.3 m in the bed, the bubbles erupt or are about to erupt. This can be seen from the drag profile shown in Figure 4. Du Plessis, Ergun and MacDonald predict about the same drag profiles. The drag is rather low in all positions, but some peaks with higher drag are observed in the centre and in a middle core, which indicates a higher particle concentration in these areas. Also at height 0.3 m Gibilaro's model differ significantly from the others. Gibilaro's model gives a drag close to zero which indicates that there are almost no particles at this height.

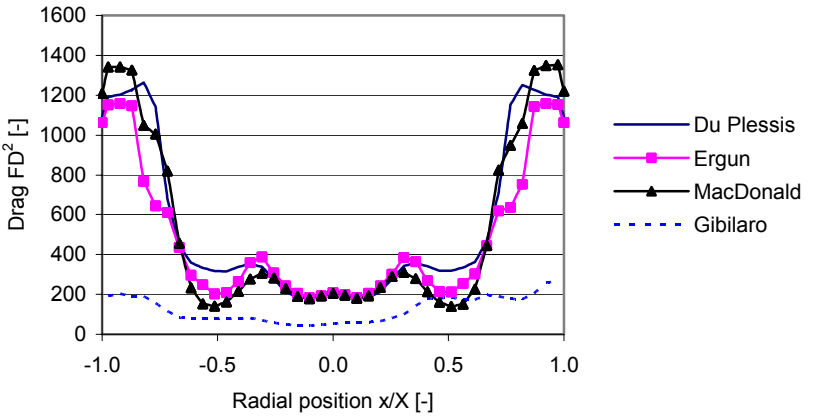


Figure 3: Drag (FD^2) as a function of radial position at height 0.2 m in the bed.

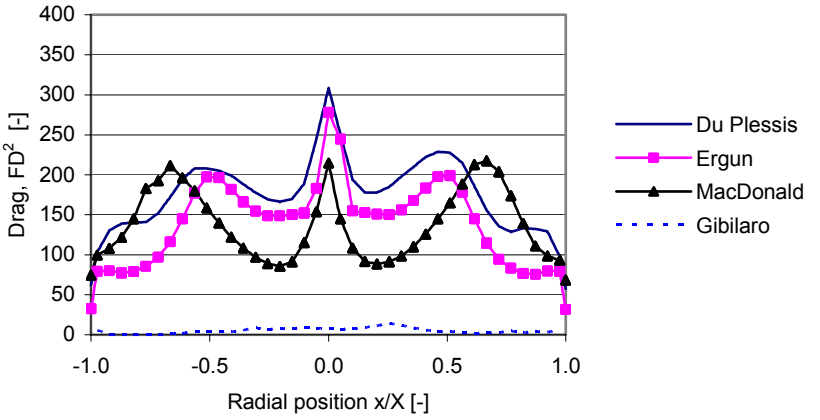


Figure 4: Drag (FD2) as a function of radial position at height 0.3 m in the bed.

5 Discussion

Different drag models were investigated and their predictions for bubble behaviour in a fluidized bed compared with experimental measurements. Although the overall trends are the same there are some particular discrepancies among the models and further careful investigations are needed for conclusive statements. It seems, however, that the model of Du Plessis and Woudberg is the most promising, since it involves no empirical coefficients and, based on the physical conditions in the bed, adaptations towards improvement could be made in a structured manner. Another positive point of this model is that the same model is used over the whole range of voidages and Reynolds numbers found in a bed.

In simulation of dense particle systems it is important to avoid unphysical high packing. It was observed that the Gibilaro drag model gave a too low bed expansion and too high particle concentrations in parts of the bed. The Du Plessis and Woudberg model gave the highest bed expansion and this might give a more symmetric bed and continuous bubble formation over time. This will be studied in further work.

References

[1] Yasuna, J.A., Moyer, H.R., Elliott, S., Sinclair, J.L., Quantitative predictions of gas-particle flow in vertical pipe with particle-particle interactions, *Powder Technology* **84**, pp. 23-34, 1995.

[2] Halvorsen, B., Mathiesen, V., CFD Modelling and simulation of a lab-scale Fluidised Bed, *Modeling, Identification and Control*, **23(2)**, pp. 117-133, 2002.

[3] Ibsen, C.H., An experimental and Computational Study of Gas- Particle Flow in Fluidised Reactors, *Ph.D. Thesis*, Aalborg University, Esbjerg, 2002.

[4] Bokkers, G.A., van Sint Annaland, M., Kuipers, J.A.M., Mixing and segregation in a bidiperse gas-solid fluidised bed: a numerical and experimental study, *Powder Technology,* **140**, pp. 176-186, 2004.

[5] Ergun, S., Fluid flow through packed columns, *Chemical Engineering Progress*, **48(2)**, pp. 89-94, 1952.

[6] Bird, R.B., Stewart, W.E & Lightfoot, E.N., *Transport Phenomena*, John Wiley and Sons, New York, 1960.

[7] MacDonald, I.F., El-Sayed, M.S., Mow, K. & Dullien, F.A.L., Flow through porous media - the Ergun equation revisited, *Ind. Eng. Chem. Fundam*. **18(3)**, 199-208, 1979.

[8] Gidaspow, D., *Muliphase Flow and Fluidization*, Academic Press, Boston, 1994.

[9] Rowe, P.N., Drag Forces in a Hydraulic Model of Fluidized Bed- PartII, *Trans. Instn. Chem*., **39**, pp. 175-180, 1961.

[10] Wen, C.Y. & Yu, Y.H., Mechanics of Fluidization, *Chemical Engineering Progress* **62**, pp. 100-111, 1966.



[11] Gibilaro, L.G., Di Felici, R. & Waldram, S.P., Generalized friction factor and drag coefficient for fluid-particle interaction, *Chemical Engineering Science* **40(10)**, pp. 1817-1823, 1958.
[12] Du Plessis, J.P., Analytical quantification of coefficients in the Ergun equation for fluid friction in a packed bed, *Transport in Porous Media* **16**, pp. 189-207, 1994.
[13] Woudberg, S., Du Plessis, J.P. & Smit, G.J.F., On the hydrodynamic permeability of granular porous media, *Proc. Int. Conf. on Environmental Fluid Mechanics ICEFM'05*, IIT Guwahati, Assam, India, March 2005, pp. 277-283, 2005.
[14] Hasimoto, H., On the Periodic Fundamental Solutions of Fluids Relative to Beds of Spherical Particles, *A.I.Ch.E. Journal* **4(2)**, pp. 197-201, 1958.
[15] Churchill, S.W. & Usagi, R., General expression for the correlation of rates of transfer and other phenomena, *A.I.Ch.E. Journal* **18(6)**, pp. 1121-1128, 1972.
[16] Woudberg, S., *Flow through isotropic granular porous media*, MScEng Thesis, University of Stellenbosch, in progress, 2006.
[17] Geldart, D., *Gas Fluidization Technology*, John Wiley & Sons Ltd, 1986.
[18] Mathiesen, V, Solberg, T, Hjertager, B.H., Prediction of gas/particle flow including a realistic particle size distribution. *Powder Technology* **112**, pp. 34-45, 2000.
[19] Halvorsen, B., An experimental and computational study of flow behaviour in bubbling fluidized beds., Doctoral Thesis at NTNU: 70, 2005.
[20] Deardorff, J.W., On the Magnitude of Subgrid Scale Eddy Coefficient. *Journal of Computational Physics,* Vol. 7, pp. 120-133, 1971.



Solution of the incompressible Navier-Stokes equations via real-valued evolutionary algorithms

R. I. Bourisli[1] & D. A. Kaminski[2]
[1]*Department of Mechanical Engineering, Kuwait University, Kuwait*
[2]*Department of Mechanical, Aerospace and Nuclear Engineering, Rensselaer Polytechnic Institute, USA*

Abstract

The concept of evolutionary algorithms (EAs) is used to solve the 2-D incompressible Navier-Stokes equations. EAs operate on the principle of natural selection, where candidate solutions compete for survival and are given a chance to survive in accordance with their fitness. In an earlier paper the method was described in detail, with particular emphasis on the various evolutionary operators. In this paper, examples are given on applying the evolutionary solver to practical engineering problems such as viscous flow in channels with multiple contractions and expansions. One of the fundamental qualities of this type of solver is its relative indifference to places of high gradients in the flow field. This, in turn, helps circumvent many of the problems related to the stiffness of the system of equations. We believe the method has great value in tackling fluid flow problems where conventional methods fail to achieve timely convergence.
Keywords: evolutionary algorithms, Navier-Stokes, divergence, mutation.

1 Introduction

Many problems in computational fluid dynamics suffer from occasional divergence or slow convergence, depending on the discretization, types of boundary conditions and scale of flow phenomena. This is especially evident when continuum discretization schemes are combined with gradient-based iterative solution techniques. A good example of such convergence problem is the solution of the Navier-Stokes equations. Typical methods such as finite element and finite volume



WIT Transactions on Engineering Sciences, Vol 52, © 2006 WIT Press
www.witpress.com, ISSN 1743-3533 (on-line)
doi:10.2495/AFM06002

can face such difficulties. For example, the methods can progress the solution in an acceptable manner at an acceptable rate until, for example, certain pressure modes of the solution are reached where the solution diverges suddenly, often over a very small number of iterations. There is a need for a non-standard solution technique that can take over the solution process upon incipient divergence or very slow convergence. Evolutionary algorithms are very good candidates to be such rescue techniques.

Evolutionary algorithms are stochastic search and optimization techniques that are based on the principle of natural selection [2]. They have been used extensively and successfully in many optimization problems, especially when the search domain is large and nonconvex. Here, they are used to heuristically optimize the solution to the Navier-Stokes equations by evolving a population of potential solutions and allowing natural selection to promote highly fit members of the population until an acceptable level of fitness is reached.

The use of evolutionary-type optimization algorithms in CFD is not new. However, most applications were focused on optimization of shapes for pressure drop requirements and aerodynamic performance of airfoil and like objects [3–7]. But recently, EAs as fluid flow meta-solvers have seen a promising initiation. In [1], Bourisli and Kaminski introduced a new strategy for adapting an evolutionary algorithm to act as a *go to* solver to be activated when common methods fail to achieve convergence. The method was successfully applied to a sudden expansion problem involving thousands of nodes. Subsequent research in the area followed with more applications [8,9]. In this paper, the method is applied to the full Navier-Stokes equations. The EA solver is designed to be used as a *go to* solver once the basic gradient-based solvers, which can certainly be faster, come close to failure.

2 The evolutionary algorithm

An evolutionary algorithm comprises of four basic operators to mimic the biological evolution process. Similar to biological reproduction steps in haploid organisms, a crossover operator cuts and recombines the series of arrays at a single or more points, not necessarily in the middle as in humans. Randomness is introduced via a mutation operator that changes the value of one allele randomly. To simulate nature, the algorithm requires an objective function that can differentiate between chromosomes based on their fitness. Finally, an appropriate selection scheme is used to select parents for future generations in the volution process.

From our experience, it was clear that the simple, one-size-fits-all evolutionary algorithm is hardly efficient in solving any but the basic combinatorial problems that can be accurately cast in pseudo-binary form. In order to have an efficient search mechanism, knowledge about the problem and the expected nature of the solution must be incorporated into *specially designed* evolutionary operators. Some authors prefer to call the resulting algorithms *evolution programs* because of the specific intended use [10]. Since fluid flow is a new area in evolutionary computations, a number of old, altered and newly conceived operators were used. These include: arithmetical and uniform crossover, uniform, nonuniform,



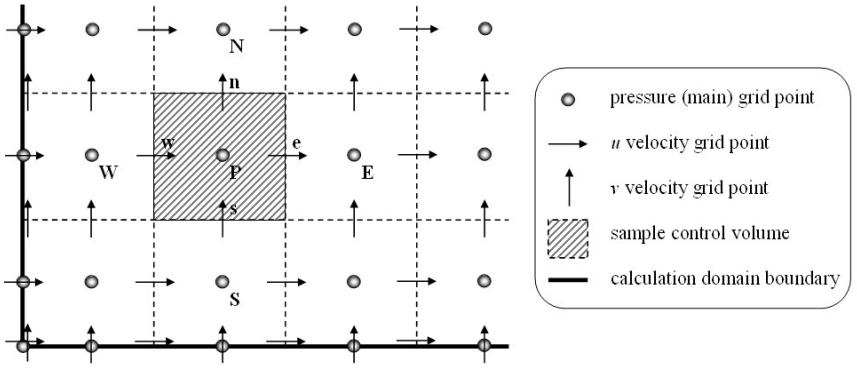


Figure 1: Sample staggered finite volume mesh.

fitness-guided, random-average, and block mutation, population shuffling, gradient-based smoothing, in addition to elitism. The various old and new components are described in detail in [8]. Here, we only discuss the objective function needed to measure relative fitness of the chromosomes.

The objective function used here is based on a staggered finite volume discretization of the flow domain, shown in Figure 1. The flow obeys the steady, incompressible Navier-Stokes equations of motion,

$$\frac{\partial u}{\partial x} + \frac{\partial v}{\partial y} = 0 \qquad \text{(continuity)} \tag{1}$$

$$u\frac{\partial u}{\partial x} + v\frac{\partial u}{\partial y} = -\frac{1}{\rho}\frac{\partial p}{\partial x} + \nu\left[\frac{\partial^2 u}{\partial x^2} + \frac{\partial^2 u}{\partial y^2}\right] \qquad (x\text{-momentum}) \tag{2}$$

$$u\frac{\partial v}{\partial x} + v\frac{\partial v}{\partial y} = -\frac{1}{\rho}\frac{\partial p}{\partial y} + \nu\left[\frac{\partial^2 v}{\partial x^2} + \frac{\partial^2 v}{\partial y^2}\right] \qquad (y\text{-momentum}) \tag{3}$$

The equations are linearized with respect to the convective terms in the momentum equations, resulting in coupled algebraic equations. With Poisson's pressure equation substituted for the continuity equation, the three equations are

$$a_P\, p_P = a_S\, p_S + a_E\, p_E + a_N\, p_N + a_W\, p_W + b \tag{4}$$

$$a_p u_p = a_s u_s + a_e u_e + a_n u_n + a_w u_w + A_p(p_W - p_P) \tag{5}$$

$$a_p v_p = a_s v_s + a_e v_e + a_n v_n + a_w v_w + A_p(p_S - p_P) \tag{6}$$

where the various coefficients are functions of geometry and properties of the fluid. The unknown pressures are defined on non-staggered control volumes such as the one shown in Figure 2. The detailed calculation procedures of the different coefficients are described in detail in [8].

Normally in CFD modeling, these equations are solved iteratively using an appropriate method such as TDMA while using the resulting pressure field to

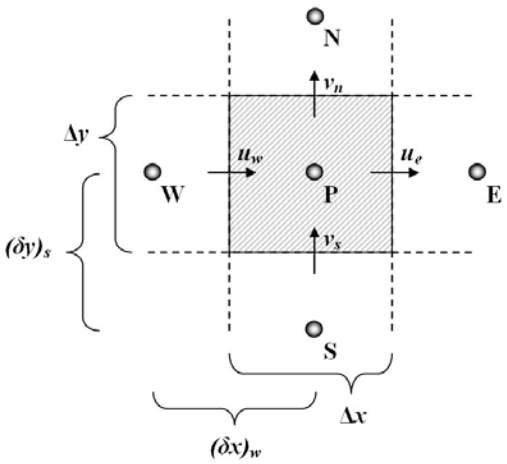


Figure 2: Sample staggered finite volume grid for calculating pressure residuals.

update velocities. The evolutionary algorithm, however, directly uses the residuals of these algebraic equations as an objective measure of the fitness of each chromosome. The resulting form of the objective function is a linear combination of the three residuals for the pressure, x-velocity, and y-velocity equations,

$$r^p = \left| -a_P\, p_P + a_S\, p_S + a_E\, p_E + a_N\, p_N + a_W\, p_W + b \right| \tag{7a}$$

$$r^u = \left| -a_p\, u_p + \Sigma\, a_{nb}\, u_{nb} + A_p\, (p_W - p_P) \right| \tag{7b}$$

$$r^v = \left| -a_p\, v_p + \Sigma\, a_{nb}\, v_{nb} + A_p\, (p_S - p_P) \right| \tag{7c}$$

The actual fitness of a chromosome is defined as the exponential of the maximum residual, r_m, among all interior nodes. This bounds the fitness to be in the interval [0,1] and gives universal assessment of fitness values among different EA runs. In other words,

$$f = e^{-r_m} \qquad \text{where,} \qquad r_m = \max_{\substack{1 \le i \le N_x \\ 1 \le j \le N_y}} r_{i,j} \tag{8}$$

A population is taken to be an initially random set of potential solution to the fluid flow problem. These can be any 2D or 3D structures. For 2D problems a two-dimensional array of random real numbers is sufficient. To save effort on the evolutionary algorithm, a proper starting point is given as a gradient method output after a few iterations just enough to set the fluid in motion and provide a starting scale for the semi-random initialization of the velocities and pressure.

Table 1: EA parameters for the triple contraction/expansion simulation.

nodes	*Popsize*	P_c^a	P_c^u	P_m^r	P_m^u	P_m^a	P_m^b	shuffle
6771	40	0.2	0.4	0.01	0.01	0.001	0.001	20% every 4th

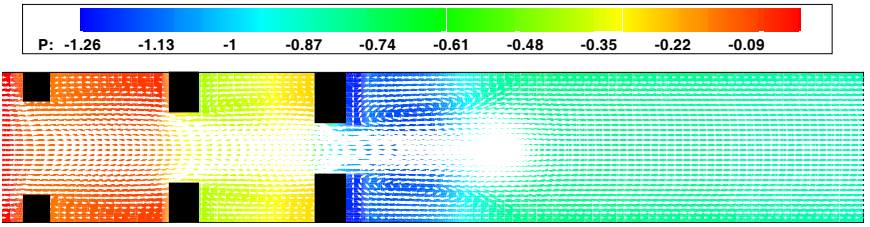


Figure 3: Velocity vectors superimposed on pressure distribution in the flow domain. Actual aspect ratio of the channel is 12-to-1, scaled for appearance.

3 Numerical results and discussion

A channel with a 12-to-1 aspect ratio with three consecutive double steps is modeled. The top and bottom steps simulate 2-to-1, 5-to-2, and 3-to-1 contractions followed by inverse expansions. The flow field is discretized using 6,771 control volumes for a total of about 20,313 unknowns. A population of 40 chromosomes was used, which is slightly higher than what was previously advised but is warranted because of the relative complexity of the present flow situation (cf. [1], where a population size of 18 was determined to be optimum for a potential flow problem.) Other parameters of the simulation are listed in Table 1.

At a Reynolds number of about 55 based on channel width, three different features of the flow are present behind the three different expansions. Specifically, behind the first mild expansion, small eddies develop immediately behind the step and smaller eddies develop in the diagonally opposite corners. As a result, the stagnation point is on the top and bottom surfaces. After the second expansion, the eddies elongate to fill the whole length until the next walls, shifting the stagnation points to the opposite walls (the contractions). After the third and last expansion, the stagnation points are in their usual place at the reattachment points.

The evolutionary algorithm was able to converge to the correct solution, as shown in Figure 3, after 127 sweeps-through, constituting 6,292 generations. The locations of the eddies were found exactly, as validated by two standard finite volume solvers.

The ability to arrive at a valid solution stresses the importance of the evolutionary operators. It is known that the EA does not actually solve any set of equations;

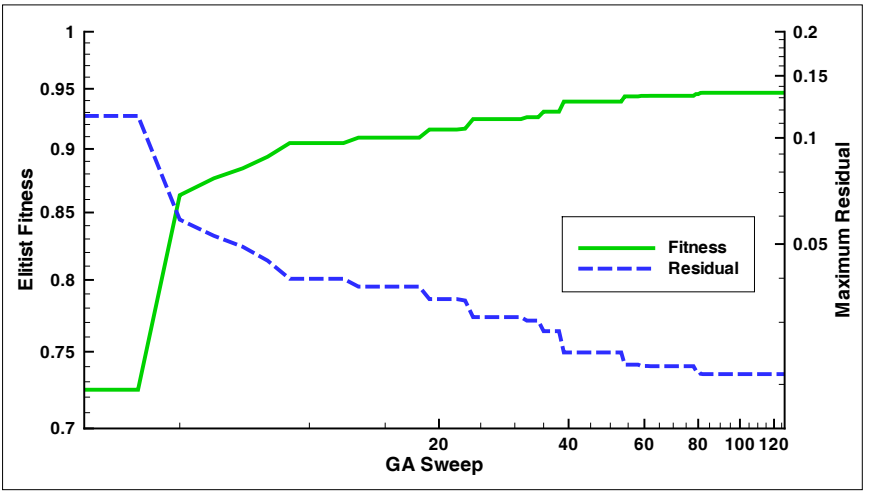


Figure 4: Progress of the fittest individual fitness and the corresponding maximum residual in the domain nodes.

it only looks at their residuals and uses them to assess the fitness of the chromosomes (or potential solutions.) Natural selection then promotes the survival of the more fit chromosomes from one generation to the next. Therefore, all the improvements in the phenotypic (relating to fitness) come from operators work on the genes themselves. This validates past conclusions that operators have to be specially designed with proper knowledge of the search domain.

The nature of the heuristic search has another important quality that can be paramount in a number of other real CFD problems. Namely, the search is indifferent to places of high gradients in the flow field, a source of computational difficulty for most algorithms. The effort needed to solve this problem is closely comparable to that observed for solving a straight channel flow with no obstacles. Many problems involving sharp changes in variables can benefit greatly from such attributes, such as flow with shockwave.

Another test for the EA was its ability to show the expected symmetry in the output solution. At times, the excessive use of one or another operator might cause a drift in the resulting genes. For example, if the block mutation was excessively applied to a subset of the domain where the building blocks were not influential, the chromosome itself would not necessarily realize the damage right away. Suppose that this chromosome has an otherwise very high fitness. Then each time it gets selected for reproduction the area of unrealistically-lowered or -raised blocks will spread to future offspring. The drift noticed in these runs of the algorithm were barely noticeable because of both the design of the operators and the low probabilities of application of most all large-scale operators.

The progress of the evolutionary algorithm is shown in Figure 4. The fitness of the elitist and the corresponding maximum residual in the flow field are plotted against the overall sweep-through number. The convergence of the EA to the acceptable threshold is noticed by the steady rise in fitness and drop in residual. The final solution, when ran through the SIMPLER finite volume algorithm, for example, gives a pressure correction term magnitude of less than 10^{-5}, which is considered convergent by any standard.

It is noted, however, by looking and the figure and from our experience, that the population maximum and average fitness do not improve considerably beyond a certain point in the search. A simple yet not entirely complete explanation is that the random search loses all ability to fine-tune highly fit chromosomes after a given level of fitness is reached. It so happened that the operators were effective enough to carry the population so far such that when convergence was reached the solution was acceptable.

The underlying cause of such loss is the inability of the individual operators to introduce enough randomness to explore the search domain efficiently. This reason has been a fundamental hurdle in the face of past research in this area. The introduction of smart operators such as fitness-guided mutation weighs the amount of randomness supplied to each chromosome in a proportional amount to its fitness. This introduces useful diversity to the population, the backbone of a successful evolution.

4 Conclusions and future work

The current work is another step toward the inclusion of evolutionary techniques in the group of dependable CFD meta-solvers. The problem of viscous flow in a channel with multiple size contractions and expansions was solved using an evolutionary algorithm. The EA optimizer succeeded in arriving at a converged solution to the problem capturing fundamental physical behavior, expected symmetry of solution, and robustness of application.

It should be noted that this problem in particular could be solved using standard gradient-based techniques, albeit with very low relaxation factors. Low relaxation factors were even needed when validation was done using the Fluent segregated solver. This was necessary because it shows that the EA solver is able to negotiate nontrivial CFD problems while we still have the chance to validate its results. The application of the EA solver to nonconvergent problems altogether is discussed in [9].

Regarding the requirement of an operator to scale its randomness up and down depending on the degree of convergence and diversity in the population, the use of a fuzzy logic is an attractive logical next step. The use of a fuzzy controller to perform crossover was explored briefly in [11, 12]. In order to achieve the much needed consistent improvement of evolution over all ranges of diversity and fitness, better control over the operators, mutation in particular, at the genotypic level is still needed.



References

[1] Bourisli, R. & Kaminski, D.A., Solving fluid flow problems using a real-coded genetic algorithm with uniform refinement. *Advances in Fluid Mechanics*, eds. C. Brebbia, A. Mendes & M. Rahman, WIT Press: Southampton, UK, volume V, pp. 63–72, 2004.

[2] Holland, J.H., *Adaptation in Natural and Artificial Systems*. University of Michigan Press, 1975.

[3] Davalos, R.V. & Rubinsky, B., An evolutionary-genetic approach to heat transfer analysis. *Journal of Heat Transfer, Transactions of the ASME*, **118(3)**, pp. 528–532, 1996.

[4] Fabbri, G., A genetic algorithm for fin profile optimization. *International Journal of Heat and Mass Transfer*, **40(9)**, pp. 2165–2172, 1997.

[5] Milano, M. & Koumoutsakos, P., A clustering genetic algorithm for cylinder drag optimization. *Journal of Computational Physics*, **175**, p. 79107, 2002.

[6] Sasikumar, M. & Balaji, C., Optimization of convective fin systems: A holistic approach. *Heat and Mass Transfer*, **39(1)**, pp. 57–68, 2002.

[7] Duvigneau, R. & Visonneau, M., Hybrid genetic algorithms and artificial neural networks for complex design optimization in CFD. *International Journal for Numerical Methods in Fluids*, **44**, pp. 1257–1278, 2004.

[8] Bourisli, R.I., *Computationally intelligent CFD: Solving potential, viscous and non-Newtonian fluid flow problems using real-coded genetic algorithms*. Ph.d. thesis, Rensselaer Polytechnic Institute, 110 8th Street, Troy, New York, 2005.

[9] Bourisli, R.I. & Kaminski, D.A., Evolutionary optimization techniques as versatile solvers for hard-to-converge problems in computational fluid dynamics. *International Journal for Numerical Methods in Fluids*, 2006. In press.

[10] Michalewicz, Z., *Genetic Algorithms + Data Structure = Evolution Programs*. Springer-Verlag: Berlin, 3rd edition, 1997.

[11] Herrera, F. & Lozano, M., Fuzzy connectives based crossover operators to model genetic algorithms population diversity. *Fuzzy Sets and Systems*, **92(1)**, pp. 21–30, 1997.

[12] Herrera, F. & Lozano, M., A taxonomy for the crossover operator for real-coded genetic algorithms: An experimental study. *International Journal of Intelligent Systems*, **18**, pp. 309–338, 2003.



A parallel computing framework and a modular collaborative cfd workbench in Java

S. Sengupta & K. P. Sinhamahapatra
Department of Aerospace Engineering, IIT Kharagpur, India

Abstract

The aim of this study is to give the means for writing parallel programs and to transform sequential/shared memory programs into distributed programs, in an object-oriented environment and also to develop a parallel CFD workbench utilizing the framework. In this approach, the programmer controls the distribution of programs through control and data distribution. The authors have defined and implemented a parallel framework, including the expression of object distributions, and the transformations required to run a parallel program in a distributed environment. The authors provide programmers with a unified way to express parallelism and distribution by the use of collections storing active and passive objects. The distribution of classes/packages leads to the distribution of their elements and therefore to the generation of distributed programs. The authors have developed a full prototype to write parallel programs and to transform those programs into distributed programs with a host of about 12 functions. This prototype has been implemented with the Java language, and does not require any language extensions or modifications to the standard Java environment. The parallel program is utilized by developing a CFD workbench equipped with high end FEM unstructured mesh generation and flow solving tools with an easy-to-use GUI implemented entirely on the parallel framework.
Keywords: Java, framework, parallel programming, program transformation, CFD, mesh.

1 Introduction

The chief aim here is to provide a few tracks in the use and development of an environment or more specifically a programming framework for the development of CFD engineering software with parallel approaches. Many



WIT Transactions on Engineering Sciences, Vol 52, © 2006 WIT Press
www.witpress.com, ISSN 1743-3533 (on-line)
doi:10.2495/AFM06003

authors have shown the strength of the approach in different fields of mechanics, including parallel and/or CFD computations: e.g. a study of a transient model of fluid mechanics fully coupled to an electrochemistry model in [1], some object-oriented techniques dedicated to CFD in [2], a finite element model for modeling heat and mass transfer using the Diffpack library in [3], domain decomposition techniques using pvm [4], [5]. In [6], the problem of the utilization of Java for numerical computation in the industrial real life problems is raised up, and no definitive response is brought probably because of lack of experiments in the domain. One aim of the present work is to give an example of large scale coding in java significantly more complex than sequential programming; the idea of this work is to develop a pure JAVA framework for finite elements or finite volume parallel computations. In this paper, the authors would like to describe some aspects of developing an application in Java for domain decomposition in CFD with examples and proves of data convergence and comparative speedups taking into account another problem of some computational complexity all along using the authors' parallel framework .The paper, however, does not discuss the choices of the algorithms which will be done in a future paper, but to illustrate on complex algorithmic examples the opportunity to move to a new programming paradigm. To begin, the authors show some pure performance comparison tests between JAVA and C/C++ on a classical matrix/vector product and data convergence with a program written for calculating lift and drag over a NACA -0012 aerofoil (using Lifting-Line theory). Programming for multi-processors computers is embedded in the JAVA environment. After a brief description of the basic features of JAVA, the authors introduce a simple way of writing a parallel matrix/vector product in Java implanted for SIMD/MIMD computers for solving large linear systems by the way of an iterative method. At last, the authors show a tentative development for a overlapping domain decomposition method for the Navier-Stokes problem implemented entirely on the framework to illustrate the fast development capabilities in JAVA for object-oriented finite elements and the emerging possibilities of the development of object-oriented distributed computing libraries for lucid programming. The library named JPE includes an easy and intuitive programming model based on distributed threads; object-based, message-passing APIs; and distributable data collection. JPE takes a class library-based approach to providing a distributed parallel programming environment. New classes and interfaces supporting distributed threads, message passing, and distributable data collections are included in this package.

2 Computational problems and the approach

Roughly speaking, we distinguish the Java programming language from the Java Virtual Machine (JVM). The JVM is an interpreter that executes the program compiled to Java byte codes. The main consequence is that a program compiled on a system can be run on all systems. This very attractive aspect could hide a major drawback especially in CFD computation: the efficiency. Most computations in mechanics involve a large number of scalar products (elemental



contributions computation, Crout reduction in direct linear systems solvers, matrix/vector products in iterative linear system solvers). Here, the same code has been tested. (Java has a C++ syntax, only memory allocation) for computation of matrix/vector products, with a direct addressing and with an indirect addressing, i.e. code respectively corresponding to v[j] = A[i][j] * x[j] and v[j] = A[i][j] * x[table[j]], where table[] enables us to address the elements in the array x[]. It is worth noting that the code in C/C++ and JAVA are exactly the same. Various number of matrix/vector products are done, for various size of matrices. Results are shown on Figure 1. Results are similar on different platforms (Windows XP on a Pentium 845, Linux on a single-processor Intel-845, Tru 64 Dec-Unix on a 4 processors EV6 – Version 1.3.0 and 1.4.2 version for JAVA virtual machine and J2SDK1.4.2) and shows roughly speaking that Java is from 72% to 85% within the C compiled code with maximal optimization options for direct memory access, and from 65% to 82% with indirect addressing. It should be noted that with reference to Amdahl's law of speedup in parallel systems, the best results are obtained for large sized matrices. The drawn conclusion is that good performances rate can be achieved for computational tools in Java using threads. This efficiency is acceptable to develop tools for the fast design of numerical algorithms for large application on single processor systems using time-sharing.

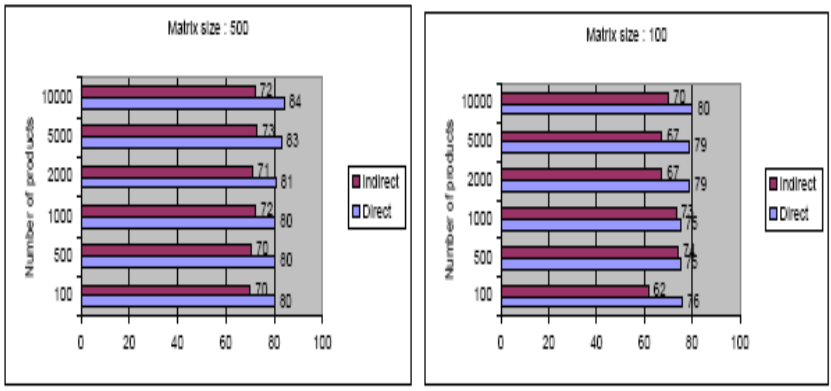


Figure 1: Comparison between C/C++ and Java code for matrix/vector multiplications using threads on single processor systems.

3 Parallel algorithm and approach

3.1 The parallel framework

Looking at MPI which has been accepted as the standard for parallel computing on distributed platforms in C, the library comes with similar functions with almost similar syntax as well as functions. The use of non-blocking communication alleviates the need for buffering since a sending process may

progress after it has posted a send. Therefore the constraints of safe programming can be relaxed. However some amount of storage is consumed by a pending communication. At a minimum the communication subsystem needs to copy the parameters of a posted send or receive before the call returns. If this storage is exhausted then a call that posts a new communication will fail since post send or post receive calls are not allowed to block. A high quality implementation will consume only a fixed amount of storage per posted non-blocking communication thus supporting a large number of pending communications. The failure of a parallel program that exceeds the bounds on the number of pending non-blocking communications like the failure of a sequential program that exceeds the bound on stack size should be seen as a pathological case due either to a pathological program or a pathological JPE implementation.

Table 1: Method specifications.

int JPE_Init(int num_procs,String mother_machine)	The first and foremost of the functions that has to be called to initialize the framework. Return value is 1 if successful else returns error code(0 to 7 except 1).	Is highly dependent on the machine identifier.
int JPE_getID(void)	This method returns the local id of the machine i.e. the integer id of the current processor.	Often used in identifying processors using ids and not machine id.
int JPE_Send(datatype[] data,int size,int hid)	This method can be used to send data to another processor with id hid. (Overloaded)	The hid parameter must be correct to ensure data transfer. Available as both blocking and non-blocking.
nt JPE_Recv(datatype[] data,int size,int hid)	This method can be used to receive data from another processor with id hid.	The hid parameter must be correct to ensure data transfer. Available as both blocking and non-blocking.
int JPE_Bcast(datatype data,int size)	This method can be used to send data to all another processors in the connection. Returns 1 if ok else 0-7 except 1 in case of errors.	Comes in two formats – blocking and non-blocking. Available as both blocking and non-blocking.



Table 1: Continued.

int JPE_iAllReduce(int data,int operation	This method can be used to accumulate the results obtained as a result of certain computations in each processor by the operation parameter and saved in each processor.	Similar implementations exist for short, unsigned short, unsigned int, long, unsigned long, float, unsigned float, double, unsigned double as well as unsigned long double as well as for classes with applicable fields.
int JPE_iReduce(int data,int operation,int hid)	This method can be used to accumulate the results obtained as a result of certain computations in each processor by the operation parameter and saved in the target processor given by the parameter hid-> "host id" to receive final value.	Similar implementations exist for short, unsigned short, unsigned int, long, unsigned long, float, unsigned float, double, unsigned double as well as unsigned long double as well as for classes with applicable fields. Available as both blocking and non-blocking.
int JPE_Finalise()	Returns 1 if ok else returns -1.	Mandatory method.

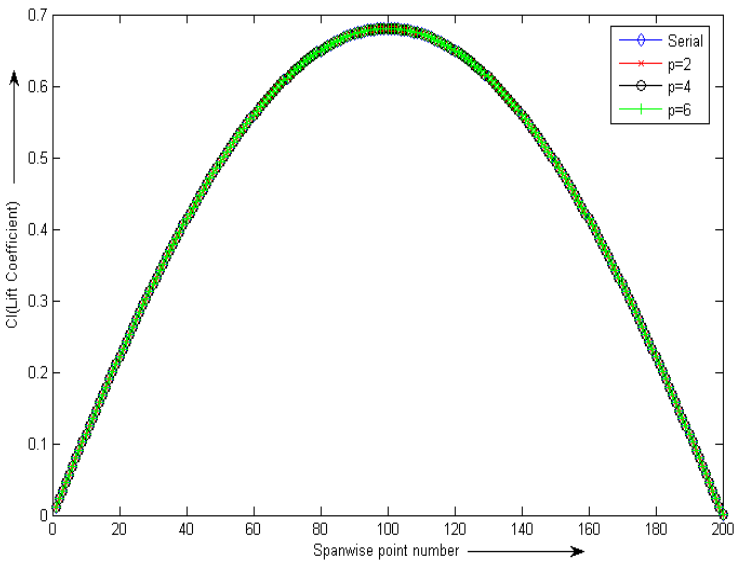


Figure 2: Comparison between data generated between serial and p=2,4 and 6 parallel algorithm.

4 Results

4.1 Data convergence

Here to verify the convergence of the local and global solutions and to yield a satisfactory result that satisfies both advantages of time and space complexity, the authors have considered the computation of drag and lift (along with pressure) distribution on a NACA-0012 aerofoil at a given angle of attack, free-stream conditions etc. making use of the thin aerofoil theory. Figure 2 shows the plot of lift coefficient along a NACA-0012 aerofoil for various numbers of processors against the serial code.

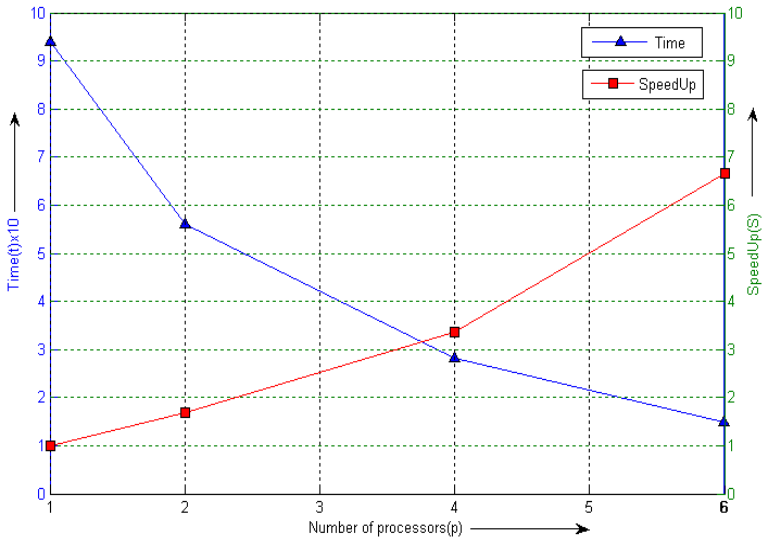


Figure 3: Comparison between speed ups of various processors along with variation in data size.

4.2 Speed up

In Java, parallel programming is embedded into the language. The key point of this kind of programming is the class JDC present in the package JPE. The question is then to check the performance of this class in the context of a CFD code. The test done here is to parallelize an unstructured mesh generation algorithm: the code being tested on Linux systems-Intel-845. Figure 3 shows the speedup achieved over number of processors for a mesh size of 160,000 triangular elements.

4.3 The CFD workbench

The workbench was written in Java and the GUI was implemented using the swing utility. The look and feel is set to platform default look by the Java code piece: 'UIManager.SetLookandFeel(default)'. The workbench provides users

with a canvas to draw arbitrary geometries as well as select certain standard features. The mesh button displays a dialog which prompts the user to select mesh fineness. Solve button displays a dialog prompting the equation to be solved and tolerance factors to be considers. The top-level menus include options to display pressure plots, streamlines and as well as vibration plots along time.

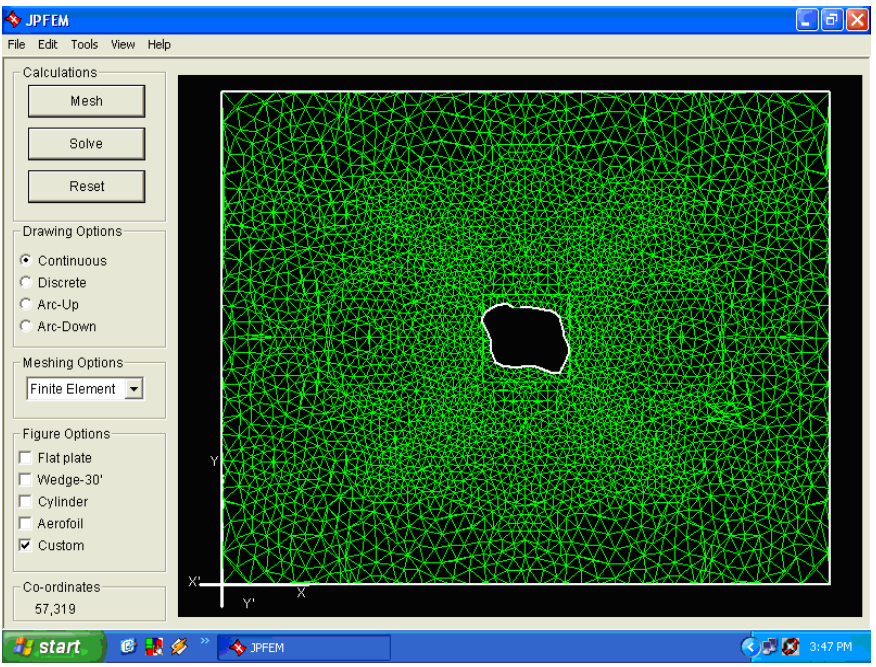


Figure 4: Mesh generated around an arbitrary body. (2-D).

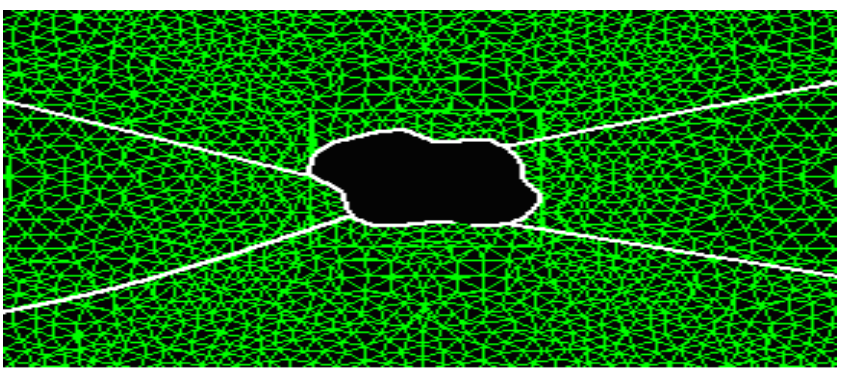


Figure 5: Mesh generated by domain-decomposition around an arbitrary body. (2-D). Boundary lines indicate load-balancing across 4 processors by geometry distribution and inter-zonal boundaries.

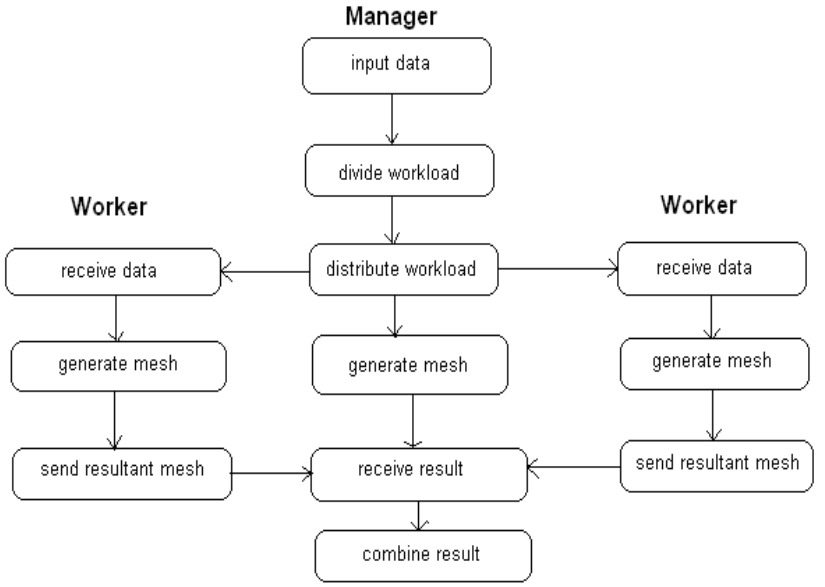


Figure 6: Manager–Worker model to distribute computational load.

The mesh generation is achieved by decomposing the entire flow domain into sub-domains and distributing the computational load across participating processors. The method presented in this paper is geometry-based, in that the geometrical data of the boundary is used to create artificial inter-zonal boundaries. Figure 5 shows the artificial inter-zonal boundaries and figure 6 shows the approach taken to decompose the domain into parts which are separately distributed to the worker processors by the manager.

5 Conclusions

The central point of this project is the development of a parallel framework for developing FEM components, FEM discretisations, adaptive ness and multi-grid solvers and their realisation in a CAD software package as shown, which directly includes tools for parallelism and hardware-adapted high-performance in low level kernel routines; completely platform independent. It is the special goal in this project to realize and to optimize the algorithmic concepts used internally in the environment for specific computers (Sun Solaris, Linux/Unix) and to adapt the mathematical components to complex configurations. In this paper we have presented an expressive parallel programming model implemented by a framework in the Java language. We have not made any extension to the language. The synchronization model is very simple and will be extended in order to enlarge the application domain of our programming model.

References

[1] A. P. Peskin and G. R. Hardin, An object-oriented approach to general purpose fluid dynamics software, Computers & Chemical Engineering, Vol. 20, 1996, pp. 1043-1058.

[2] O. Munthe and H. P. Langtangen, Finite elements and object-oriented implementation techniques in computational fluid dynamics, Computer Methods Applied Mechanics and Engineering, Vol. 190, 2000, pp. 865-888.

[3] S.-H. Sun and T. R. Marrero, An object-oriented programming approach for heat and mass transfer related analyses, Computers & Chemical Engineering, Vol. 22, 1998, pp. 1381-1385.

[4] D. S. Kershaw, M. K. Prasad, M. J. Shaw and J. L. Milovich, 3D element Unstructured mesh ALE hydrodynamics, Computer Methods in Applied Mechanics and Engineering, Vol. 158, 1998, pp. 81-116.

[5] P. Krysl and T. Belytschko, Object-oriented parallelization of explicit structural dynamics with PVM, Computers & Structures, Vol. 66,1998, pp. 259-273.

[6] M. Ginsberg, J. Hauser, J. E. Moreira, R. Morgan, J. C. Parsons and T. J. Wielenga, Panel session: future directions and challenges for Java implementations of numeric-intensive industrial applications, Advances in EngineeringSoftware, Vol.31, 2000,pp.743-751.



This page intentionally left blank

A parallel ILU strategy for solving Navier-Stokes equations on an unstructured 3D mesh

Ø. Staff & S. Ø. Wille
Faculty of Engineering, Oslo University College, Norway

Abstract

An iterative algorithm for solving a mixed finite element formulation of Navier-Stokes equations on a distributed memory computer is presented. The solver is a Krylov subspace method with a parallel preconditioner suitable for high latency clusters. Nodes are pivoted to minimize the number of synchronization points in each solver iteration.

An unstructured mesh is decomposed into non-overlapping subdomains. Each node is given a category depending on which subdomains it is a member of and on the subdomains of its neighboring nodes in the mesh. Based on these categories, an *a priori* pivoting suited for parallel solution is constructed. The solver requires approximately the same number of iterations as good serial solvers with a similar preconditioner.

The incomplete LU (ILU) preconditioning and subsequent solve is performed on a global matrix implicitly formed as a sum of all subdomain matrices. Communication overhead is kept low by generating a schedule to send information to neighboring subdomains as soon as dependencies in the matrix are resolved. Results will be shown to indicate that this is a viable strategy on computer clusters built with cheap off the shelf components.
Keywords: ILU, preconditioning, parallel, unstructured mesh, CFD, Navier-Stokes.

1 Introduction

Simulations on single processors are often limited by CPU speed and available central memory. Even fairly modest three dimensional problems can surpass what



WIT Transactions on Engineering Sciences, Vol 52, © 2006 WIT Press
www.witpress.com, ISSN 1743-3533 (on-line)
doi:10.2495/AFM06004

can be solved on a single processor in a reasonable amount of time. Parallel multiprocessing is a frequently used strategy for overcoming such limits [1, 2, 3].

This work presents a parallel incomplete LU (ILU) factorization strategy developed for solving a stationary and incompressible formulation of the Navier-Stokes equations. The solver utilizes Taylor-Hood elements, *a priori* pivoting and segregation of variables. An unstructured mesh is split into a number of subdomains. Earlier work [4] required the subdomains be slices of the global domain with unconnected interfaces. A more general algorithm discussed her allows for arbitrary domain partitioning. This generalization is only partially motivated by a wish for increased efficiency by reducing the interface areas between subdomains. When scaling beyond a handful of subdomains, it becomes difficult to find a partitioning of an unstructured mesh with unconnected interfaces. Thus, a more robust algorithm is desirable.

2 Navier-Stokes equations

The model problem is the stationary Navier-Stokes system

$$\rho \mathbf{u} \cdot \nabla \mathbf{u} - \mu \nabla^2 \mathbf{u} + \nabla p = \mathbf{f} \qquad \text{in } \Omega \subset \mathbb{R}^3 \tag{1}$$

$$-\nabla \cdot \mathbf{u} = 0 \qquad \text{in } \Omega \tag{2}$$

with homogeneous Dirichlet boundary conditions

$$\mathbf{u} = \mathbf{0} \qquad \text{on } \Gamma = \partial\Omega \tag{3}$$

where $\mathbf{u}$ is the velocity vector, p is the pressure, ρ is the density and μ is the viscosity coefficient.

3 Parallel strategy

An unstructured mesh is decomposed into non-overlapping subdomains matching the number of available processors (figure 3). Each processor then performs an independent ILU on the degrees of freedom internal to the subdomain. A global ILU matrix is then implicitly created by synchronizing the degrees of freedom on interfaces between subdomains. All communication is done through message passing.

Unlike traditional domain decomposition techniques, no special regard is given to solving the interface degrees of freedom (e.g. by constructing a Schur complement). Instead, an implicit global matrix is created through node pivoting and the equivalent of a serial ILU of this matrix is performed (figure 2). The ILU fill-in strategy is to fill in at degrees of freedom connected through an element, and thus the ILU matrix will have the exact same structure as the finite element matrix.

The actual matrix constructed for each subdomain is pivoted to have three parts (figure 1). Velocity and pressure degrees of freedom are separated in each part, and each subdomain is given an arbitrary number. Then internal degrees of freedom



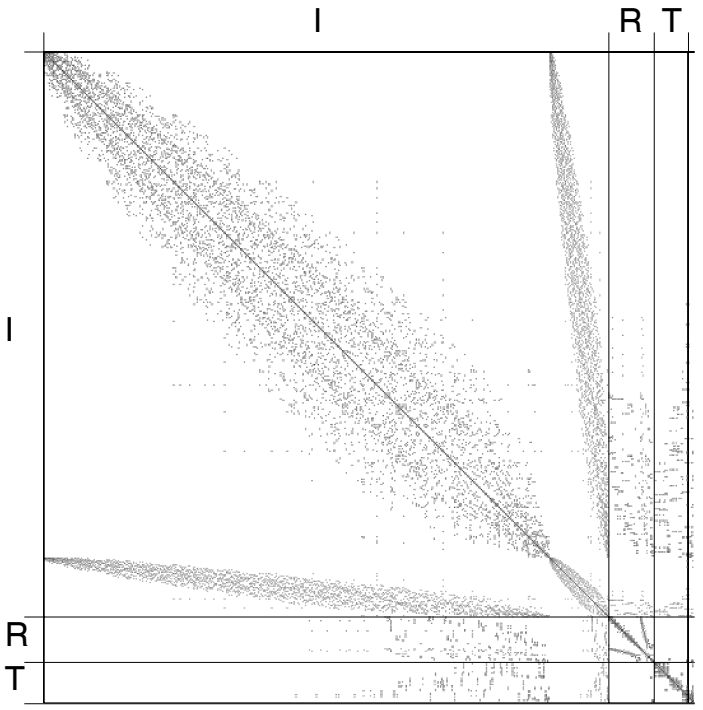


Figure 1: The structure of the solver matrix on a single processor. Each non-zero value in the matrix is marked with a dot. Nodes internal to the submesh are labeled I, those on receive interfaces are labeled R and transmit interfaces are labeled T. The submatrices connecting receive and transmit nodes are almost entirely zero. This allows much of the synchronization between subdomains to happen in parallel.

are pivoted first (I), followed by degrees of freedom on an interface to a lower numbered subdomain (R) and finally those on an interface to a higher numbered subdomain (T). Unless some element connects two interfaces, the submatrices R and T are guaranteed to be independent.

As an example, assume a mesh sliced into subdomains 1, 2 and 3 with subdomains 1 and 3 connected to the center slice 2 (figure 2). Performing a normal serial ILU on the resulting global matrix can then be performed in three steps:

1. Factorize A^1_{II}, A^2_{II} and A^3_{II}.
2. Send A^1_{TT} to subdomain 2 and add it to A^1_{RR}. Do the same with A^2_{TT} and A^3_{RR}.
3. Factorize A^2_{RR} and A^3_{RR}.

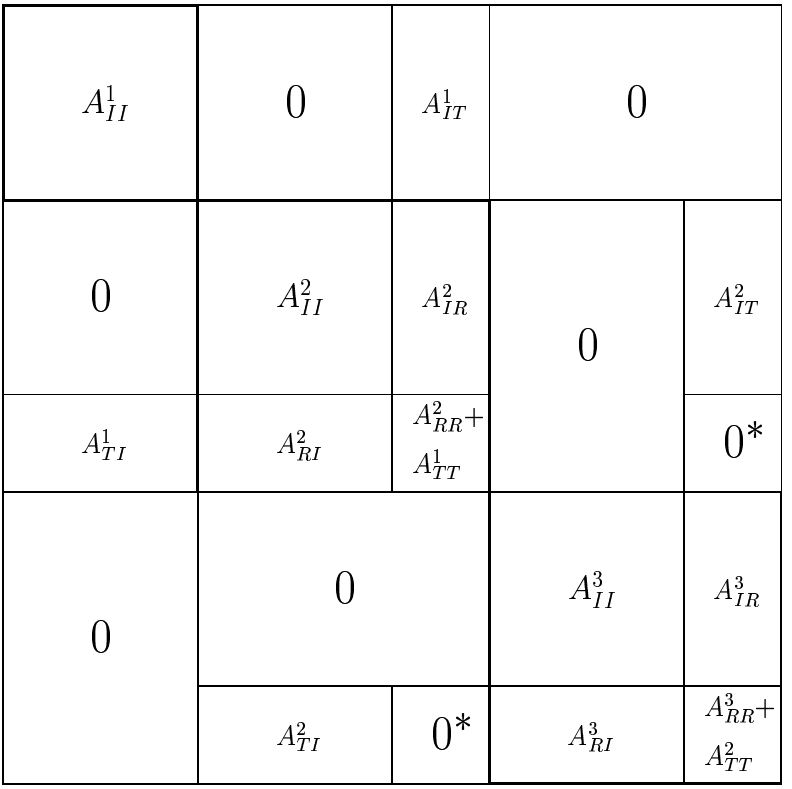


Figure 2: The implicitly generated matrix when running on three processors connected with interfaces between 1 and 2 and between 2 and 3. Running the parallel solver is equivalent to solving this matrix in a standard serial fashion. That is, the parallel solver realizes a serial ILU of this matrix. The starred zeros are zero only under the assumption that the two interfaces are independent and share no single element.

Given independent interfaces between subdomains this parallelization is always possible. However, in the degenerate case there will be no internal degrees of freedom and the parallel potential will be almost nonexistent.

The other complication stems from connected interfaces. Almost any partitioning will have some corners where interfaces meet, and although it will affect relatively few nodes, it is an important situation to handle.

With *a priori* knowledge of the matrix structure for any given node pivoting, lists of all possible dependencies in the ILU factorization are generated. The values of row i depends only on rows $j = [1, \ldots, i-1]$ where $a_{ij} \neq 0$. Consequently, when $k \leq i-1$ rows have been factorized and

$$a_{ij} = 0 \ \forall \ j \in [k, \ldots, i-1] \tag{4}$$

then row i can be factorized. Parallel ILU factorization is possible when $k < i-1$.

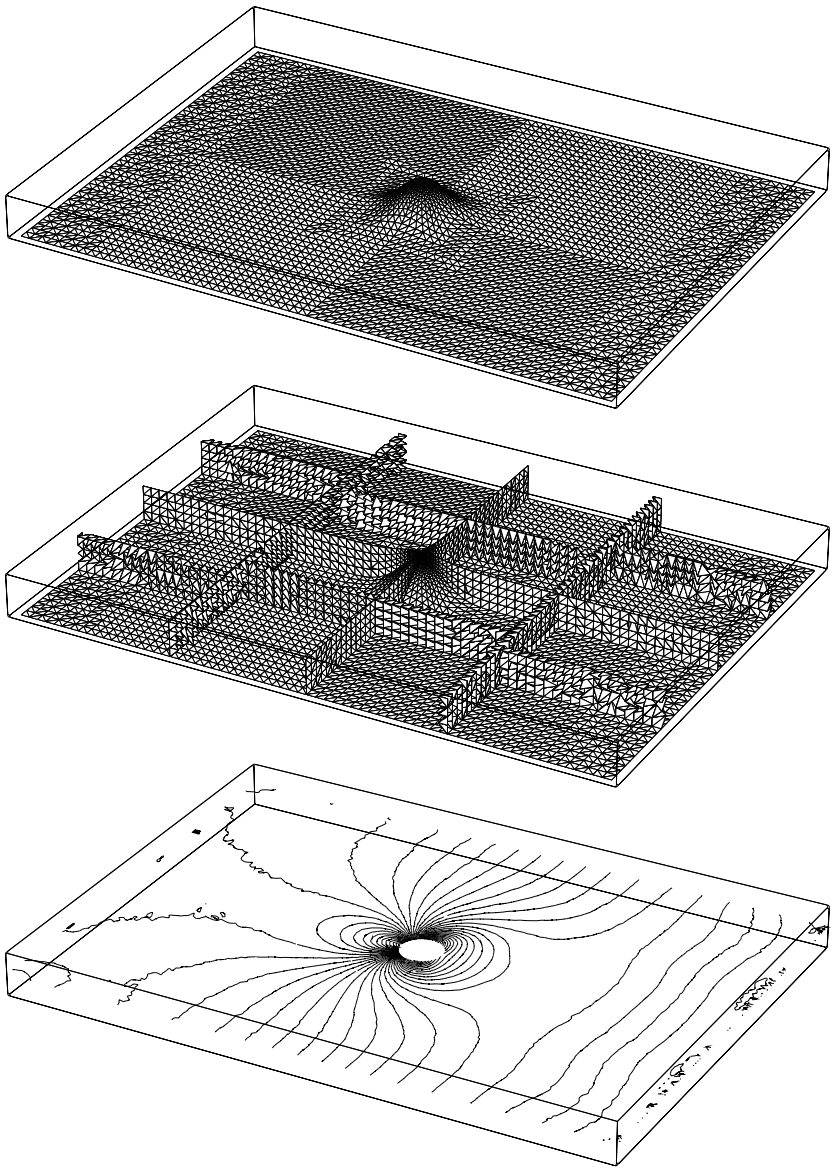


Figure 3: A mesh of a box with an elevated bottom. The middle figure is the mesh divided on 16 processors and the bottom shows pressure isobars of a steady state solution at Reynolds number 400. The flow is driven by a parabolic inflow at the right hand side, the sides and top have slip boundary conditions and the bottom has zero velocity. The walls in the middle mesh are the interface nodes between processors.

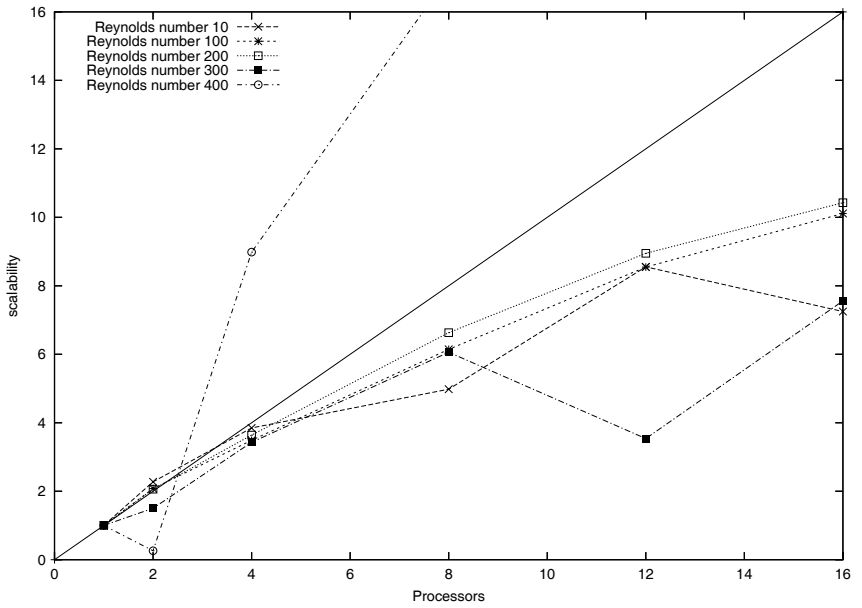


Figure 4: Scalability of the solver running on up to 16 CPUs. Runtime on 16 processors at Reynolds number 300 was 38.9 s.

The following node pivot strategy is designed to maximize the parallel potential between interfaces. For non-connected interfaces, it will produce a pivot identical to previous work [4].

1. For each node, build a list of which subdomains the node is a part of. Order the list in decreasing numerical order.
2. Sort all nodes in increasing order by lexically comparing subdomain lists. When subdomain lists are otherwise identical, the shortest list is considered smaller and ordered first. (The ordering is identical to the sorting of names in a phone book.)
3. For each node, find which other types of subdomain lists it is connected to by traversing the mesh. The node is dependent upon nodes with lexically smaller subdomain lists.
4. Sort nodes with identical subdomain lists in increasing order by their highest dependency.
5. Traverse the nodes in pivoted order. Whenever the node subdomain list changes, find the nodes which now have all their dependencies satisfied. These are guaranteed not to be affected by further factorization. From this construct a schema of transfer events to be used in the actual ILU factorization and CG iterations.



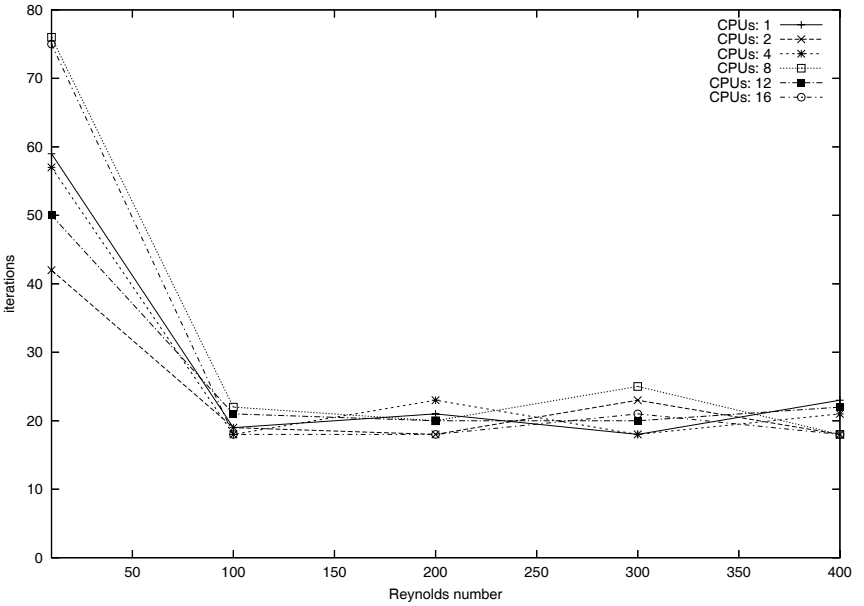


Figure 5: Required number of iterations to achieve $||Ax - b|| < 5.0 \cdot 10^{-6}$. Continuation is performed by scaling the previous solution when the velocity is increased. Each Reynolds number is calculated with five Newton iterations per refinement.

4 Results

Tests were performed on a Linux cluster with 16 3GHz Pentium 4 CPUs. The nodes were connected through a 100Mbit switched Ethernet and communication was performed using TCP/IP sockets.

The problem tested was a box with a bump in the middle (figure 3). The box had dimensions 7x5x1m, and the elevation of the bottom was a normal distribution with $\sigma = 0.5$. Flow at the inlet was set to a parabolic profile, the sides and top had slip boundary conditions, the bottom had no slip and the outlet had free velocity in the flow direction.

The initial mesh had 115,632 elements at Reynolds number 10. Subsequent meshes were adaptively grown to approximately 170,000 elements at Reynolds number 300 and 480,000 elements at Reynolds number 400. Scalability was around 10 for 16 CPUs (figure 4) and shows an increasing trend for the larger problems.

The final problem ran out of real memory on both one and two CPUs with corresponding abysmal single-CPU performance and super-linear scalability. In absolute numbers, the problem still performed well on 16 CPUs. From Reynolds

number 300 to 400, the 16 CPU mesh grew from 173,670 to 481,782 elements (factor 2.8). Runtime only increased from 38.9s to 87.8s (factor 2.3) clearly indicating that the relative parallel overhead decreases as the problem size is increased.

Each run on a given number of CPUs was performed independently. The initial difference this caused in the ILU pivot affected both iteration counts and small differences in the adaptive mesh. However, there is no obvious correlation between iteration count and the number of processors (figure 5). The quality of the preconditioner was not significantly impacted by the parallelization in the tests performed.

5 Conclusion

The presented parallel ILU preconditioner is suitable for implementation on cheap distributed memory, high latency clusters. Scalability is weak in the sense that per processor efficiency decreases as the number of processors is increased on any given problem. On the other hand, the speedup is quite good even on fairly small problems with runtimes less than a minute.

There is reason to believe the algorithm will scale to larger number of processors for constant per-processor element counts. Communication happens only between subdomains with shared nodes. Consequently, adding processors will not significantly impact the parallel overhead of any one processor.

References

[1] Bauer, A.C. & Patra, A.K., Performance of parallel preconditioners for adaptive hp fem discretization of incompressible flows. *Commun Numer Methods Eng*, **18**, pp. 305–313, 2002.

[2] Johnson, A. & Tezduyar, T., Methods for 3D computation of fluid-flow interactions in spatially periodic flows. *Computer Methods in Applied Mechanics and Engineering*, **190**, pp. 3201 – 3221, 2001.

[3] Gropp, W.D., Kaushik, D.K., Keyes, D.E. & Smith, B.F., Analyzing the parallel scalability of an implicit unstructured mesh cfd code. *Lect Note Comput Sci*, **1970**, pp. 395–404, 2001.

[4] Wille, S.Ø., Staff, Ø. & Loula, A., Block and full matrix ILU preconditioners for parallel finite element solvers. *Computer methods in applied mechanics and engineering*, **191(13-14)**, pp. 1381 – 1394, 2002.



On the mathematical solution of 2D Navier Stokes equations for different geometries

M. A. Mehemed Abughalia
Department of Mechanical Engineering, Al-Fateh University, Libya

Abstract

Some analytical solutions of the 1D Navier Stokes equation are introduced in the literature. For 2D flow, the analytical attempts that can solve some of the flow problems sometimes fail to solve more difficult problems or problems of irregular shapes. Many attempts try to simplify the 2D NS equations to ordinary differential equations that are usually solved numerically. The difficulties that are associated with the numerical solution of the Navier Stokes equations are known to the specialists in this field. Some of the problems associated with the numerical solution are; the continuity constraint, pressure–velocity coupling and other problems associated with the mesh generation. This drives the generation of many schemes to simplify and stabilize the 2D Navier Stokes equations. The exact solution of the Navier Stokes equations is difficult and possible only for some cases, mostly when the convective terms vanish in a natural way. This paper is devoted to studying the possibility of finding a mathematical solution of the 2D Navier Stokes equations for both potential and laminar flows. The solutions are a series of functions that satisfy the Navier Stokes equations. The idea behind the solutions is that the complete solution of the 2D equations is a combination of the solutions of any two terms in the equations; diffusion and advection terms. The solution coefficients should be determined through the boundary conditions.
Keywords: Navier Stokes equations, incompressible flow, fluid flow, Newtonian fluids, potential flow, laminar flow, mathematical solution, steady state.

1 Introduction

Since the Navier and Stokes derived the mathematical modeling of the fluid in motion; Navier Stokes equations, the mathematical solution have been



WIT Transactions on Engineering Sciences, Vol 52, © 2006 WIT Press
www.witpress.com, ISSN 1743-3533 (on-line)
doi:10.2495/AFM06005

impossible. The difficult in solving these equations prohibited a theoretical treatment of viscous flows. The boundary layer concept, which breakthrough by Prandtl, linked the theory with practice. Prantl showed that the viscous effect is important in a thin region adjacent to a solid.

The governing equations for steady state incompressible flow are the continuity and momentum equations

Continuity equation

$$\frac{\partial u}{\partial x}+\frac{\partial v}{\partial y}=0 \tag{1}$$

Momentum equations

$$\rho(u\frac{\partial u}{\partial x}+v\frac{\partial u}{\partial y})+\frac{\partial P}{\partial x}=\mu(\frac{\partial^2 u}{\partial x^2}+\frac{\partial^2 u}{\partial y^2}) \tag{2}$$

$$\rho(u\frac{\partial v}{\partial x}+v\frac{\partial v}{\partial y})+\frac{\partial P}{\partial y}=\mu(\frac{\partial^2 v}{\partial x^2}+\frac{\partial^2 v}{\partial y^2}) \tag{3}$$

Analytical solution can be obtained for some simple cases and under some assumptions, these equations simplified to get mathematical solution for the boundary layer thickness, shear stress and some basic definitions. To solve the flow over a flat plate, Blasius defined a dimensionless stream function for a laminar flow over flat plate as; [2]

$$f(\eta)=\frac{\psi}{\sqrt{vxU}} \tag{4}$$

And by applying the according boundary conditions, the boundary layer thickness is

$$\delta=\frac{5.0\,x}{\sqrt{\mathrm{Re}_x}} \tag{5}$$

And shear stress for laminar flow

$$\tau_W=\frac{0.332\,\rho U^2}{\sqrt{\mathrm{Re}_x}} \tag{6}$$

For the turbulent flow, mathematical solution shows these functions for the boundary layer thickness and shear stress; [2]

$$\delta = \frac{0.382\,x}{\mathrm{Re}_x^{\frac{1}{5}}} \tag{7}$$

and shear stress is

$$\tau_W = \frac{0.0594\,\rho U^2}{\mathrm{Re}_x^{\frac{1}{5}}} \tag{8}$$

Some attempts try to convert these equations into ordinary differential equations. The ordinary differential equations usually solved numerically. Usually, the full solution of the NS equations obtained numerically; Finite difference, finite volume or finite element methods. These numerical methods find difficult in solving the NS equations. The difficulties are due to continuity constraint and strong advection term. Numerically, continuity equation usually replaced by pressure Poisson equation or Penalty function. Many schemes developed to overcome the strong advection term. Some other problems associated with the mesh generation such in dividing the domain into elements or cells with graduate size which not easy. Methods such as; Quad Tree or unstructured grid; are powerful but may fail to discretized domain efficiently. All above is the challenge of this time to find a good scheme or powerful grid generation method.

The present study considers mainly the mathematical solution of two-dimensional, steady state laminar flow of Newtonian fluids. The idea that based on is that the full solution of the Navier Stokes equation is a combination of the solution of any two parts. It is known that the solution of the diffusion term is sine and cosine. The advection term solution is exponential.

2 Mathematical solution of 2D laminar flow equations

It is possible to find exact solutions for the Navier Stokes equations in certain cases, mostly in which the quadratic convective terms vanishes in a natural way. [5]. Outside the boundary layer, we can suppose that that the viscosity effect is equal in both direction $\mu_x = \mu_y$ and the diffusion terms are equal in both directions. However, we know the influence of the viscosity confined to the boundary layer.

We can assume a two general function in which one is a solution of the boundary layer and the other is a solution of the free stream potential flow.

We propose that

$$u = U_{PO} + F(y) + H(x) \tag{9}$$

Easily we can obtain the following differentiations

$$\frac{\partial u}{\partial x} = \frac{\partial U_{PO}}{\partial x} + \frac{\partial H(x)}{\partial x} \tag{10}$$



$$\frac{\partial u}{\partial y} = \frac{\partial U_{PO}}{\partial y} + \frac{\partial F(y)}{\partial y} \tag{11}$$

$$\frac{\partial^2 u}{\partial x^2} = \frac{\partial^2 U_{PO}}{\partial x^2} + \frac{\partial^2 H(x)}{\partial x^2} \tag{12}$$

$$\frac{\partial^2 u}{\partial y^2} = \frac{\partial^2 U_{PO}}{\partial y^2} + \frac{\partial^2 F(y)}{\partial y^2} \tag{13}$$

From the continuity constraint;

$$\frac{\partial v}{\partial y} = -\frac{\partial U_{PO}}{\partial x} - \frac{\partial H(x)}{\partial x} \tag{14}$$

$$v = V_{PO} + G(x) - \frac{\partial H(x)}{\partial x} y \tag{15}$$

$$\frac{\partial v}{\partial x} = \frac{\partial V_{PO}}{\partial x} + G'(x) - H''(x) y \tag{16}$$

$$\frac{\partial^2 v}{\partial x^2} = \frac{\partial^2 V_{PO}}{\partial x^2} + G''(x) - H'''(x) y \tag{17}$$

$$\frac{\partial^2 v}{\partial y^2} = \frac{\partial^2 V_{PO}}{\partial y^2} \tag{18}$$

From the first momentum equation, we obtain that;

$$\frac{\partial P}{\partial x} = -\rho(u\frac{\partial u}{\partial x} + v\frac{\partial u}{\partial y}) + \mu(\frac{\partial^2 u}{\partial x^2} + \frac{\partial^2 u}{\partial y^2}) \tag{19}$$

$$\begin{aligned} \frac{\partial P}{\partial x} = & -\rho\left[U_{PO} + F(y) + H(x)\right] \times \left[\frac{\partial U_{PO}}{\partial x} + H'(x)\right] \\ & -\rho\left[V_{PO} + G(x) + H'(x) y\right] \times \left[\frac{\partial U_{PO}}{\partial y} + F'(y)\right] \\ & +\mu\left[\frac{\partial^2 U_{PO}}{\partial x^2} + \frac{\partial^2 U_{PO}}{\partial y^2} + F''(y) + H''(x)\right] \end{aligned} \tag{20}$$

By integrate the pressure gradient from, eqn. (20), with respect to x, we obtain that

$$\begin{aligned} xP = &-\rho\int U_{PO}\times\frac{\partial U_{PO}}{\partial x}dx-\rho\int F(y)\times\frac{\partial U_{PO}}{\partial x}dx-\rho\int H(x)\times\frac{\partial U_{PO}}{\partial x}dx \\ &-\rho\int U_{PO}\times H'(x)\,dx-\rho\int F(y)\times H'(x)\,dx-\rho\int H(x)\times H'(x)\,dx \\ &-\rho\int V_{PO}\times\frac{\partial U_{PO}}{\partial y}dx-\rho\int G(x)\times\frac{\partial U_{PO}}{\partial y}dx-\rho\int -H'(x)y\times\frac{\partial U_{PO}}{\partial y}dx \\ &-\rho\int V_{PO}\times F'(y)\,dx-\rho\int G(x)\times F'(y)\,dx-\rho\int -H'(x)y\times F'(y)\,dx \\ &+\mu\left[F''(y)\,x+H'(x)\right]+M(y) \end{aligned} \tag{21}$$

Thus

$$\begin{aligned} xP = &-\rho U_{PO}{}^2-\rho F(y)\times U_{PO}-\rho H(x)\times U_{PO}+\rho\int U_{PO}\times H'(x)\,dx \\ &-\rho\int U_{PO}\times H'(x)\,dx-\rho F(y)\times H(x)-\rho H(x)^2 \\ &-\rho\int V_{PO}\times\frac{\partial U_{PO}}{\partial y}dx-\rho\int G(x)\times\frac{\partial U_{PO}}{\partial y}dx+\rho\int H'(x)y\times\frac{\partial U_{PO}}{\partial y}dx \\ &-\rho F'(y)\times\int V_{PO}\,dx-\rho F'(y)\times\int G(x)\,dx+\rho\,yF'(y)H(x) \\ &+\mu\left[F''(y)\,x+H'(x)\right]+M(y) \end{aligned} \tag{22}$$

Rearranging the equation eqn.(22)

$$\begin{aligned} xP = &-\rho U_{PO}{}^2-\rho F(y)\times U_{PO}-\rho H(x)\times U_{PO}-\rho F(y)\times H(x) \\ &-\rho H(x)^2-\rho V_{PO}{}^2-\rho G(x)\times V_{PO}+\rho\int G'(x)\times V_{PO}\,dx \\ &+\rho\times H'(x)yV_{PO}-\rho\int H''(x)y\times V_{PO}\,dx \\ &-\rho F'(y)\times\int V_{PO}\,dx-\rho F'(y)\times\int G(x)\,dx+\rho\,yF'(y)H(x) \\ &+\mu\left[F''(y)\,x+H'(x)\right]+M(y) \end{aligned} \tag{23}$$

By applying the expressions for the velocities and their derivatives into the second momentum equation eqn.(3).

$$\frac{\partial P}{\partial y}=-\rho(u\frac{\partial v}{\partial x}+v\frac{\partial v}{\partial y})+\mu(\frac{\partial^2 v}{\partial x^2}+\frac{\partial^2 v}{\partial y^2}) \tag{24}$$

$$\begin{aligned} \frac{\partial P}{\partial y} = &-\rho\left[U_{PO}+F(y)+H(x)\right]\times\left[\frac{\partial V_{PO}}{\partial x}+G'(x)-H''(x)y\right] \\ &-\rho\left[V_{PO}+G(x)-\frac{\partial H(x)}{\partial x}y\right]\times\left[-\frac{\partial U_{PO}}{\partial x}-\frac{\partial H(x)}{\partial x}\right] \\ &+\mu\left[\frac{\partial^2 V_{PO}}{\partial x^2}+G''(x)-H'''(x)y+\frac{\partial^2 V_{PO}}{\partial y^2}\right] \end{aligned} \tag{25}$$

By integrate the pressure gradient from, eqn.(25), with respect to y, we obtain that

$$\begin{aligned} yP = & -\rho\int U_{PO}\times\frac{\partial V_{PO}}{\partial x}dy-\rho\int F(y)\times\frac{\partial V_{PO}}{\partial x}dy-\rho\int H(x)\times\frac{\partial V_{PO}}{\partial x}dy \\ & -\rho\int U_{PO}\times G'(x)\,dy-\rho\int F(y)\times G'(x)\,dy \\ & -\rho\int H(x)\times G'(x)\,dy \\ & -\rho\int U_{PO}\times -H''(x)y\,dy-\rho\int F(y)\times -H''(x)y\,dy \\ & -\rho\int H(x)\times -H''(x)y\,dy \\ & +\rho\int V_{PO}\times\frac{\partial U_{PO}}{\partial x}dy+\rho\int G(x)\times\frac{\partial U_{PO}}{\partial x}dy \\ & +\rho\int -\frac{\partial H(x)}{\partial x}y\times\frac{\partial U_{PO}}{\partial x}dy \\ & +\rho\int V_{PO}\times\frac{\partial H(x)}{\partial x}dy+\rho\int G(x)\times\frac{\partial H(x)}{\partial x}dy \\ & +\rho\int -\frac{\partial H(x)}{\partial x}y\times\frac{\partial H(x)}{\partial x}dy \\ & +\mu\int\left[\frac{\partial^2 V_{PO}}{\partial x^2}+G''(x)-H'''(x)y+\frac{\partial^2 V_{PO}}{\partial y^2}\right]dy \end{aligned} \tag{26}$$

which can be re-expressed as:

$$\begin{aligned} yP = & -\rho U_{PO}{}^2-\rho F(y)\times U_{PO}+\rho\int F'(y)\times U_{PO}\,dy-\rho H(x)\times U_{PO} \\ & -\rho G'(x)\times\int U_{PO}\,dy-\rho G'(x)\times\int F(y)\,dy-\rho G'(x)\times H(x)y \\ & +\rho H''(x)\int U_{PO}\times y\,dy+\rho H''(x)\int F(y)\times y\,dy \\ & +\rho H''(x)H(x)\frac{y^2}{2} \\ & -\rho V_{PO}{}^2-\rho G(x)\times V_{PO}+\rho\times H'(x)yV_{PO} \\ & +\rho G(x)\times H'(x)y+\rho[H'(x)]^2\frac{y^2}{2} \\ & +\mu\left[G''(x)\,y-H'''(x)\frac{y^2}{2}\right]+N(x) \end{aligned} \tag{27}$$

To make the diffusion terms equal in eqn.(23) & eqn.(27);we get;

$$\left\{\begin{matrix} F''(y)=y\ \ or\ \ 0 \\ G''(x)=x\ \ or\ \ 0 \end{matrix}\right\} \tag{28}$$

Therefore, for the advection terms, we get the following conditions:

$$\left\{\begin{array}{l} M(y) = -\rho \;\; G \;\; '(x) \;\; \int F(y) \;\; dy \;\; + \rho \left[H \;\; '(x) \right]^2 \dfrac{Y^2}{2} \\ N(x) = -\rho \left[F \;\; '(y) \right] \iint G(x) \;\; dx - \rho \left[H(x) \right]^2 + \mu \;\; H \;\; '(x) \\ F(y) = YH'(x) \\ G \;\; (x) = H(x) \\ H \;\; ' \;\; (x) = consatnt \end{array}\right\} \tag{29}$$

The solution for the irrotational laminar flow is:

$$u = U_{PO} + H'(x)y + H(x) \tag{30}$$

$$v = V_{PO} + H(x) - \frac{\partial H(x)}{\partial x} y \tag{31}$$

The solution for the rotational laminar flow is:

$$u = U_{PO} + F(y) \tag{32}$$

$$v = V_{PO} + G(x) \tag{33}$$

where

$$H(x) = 0 \,,\; F'(y) = y \;\text{ and }\; G'(x) = x$$

$$U_{PO} = ? \tag{34}$$

$$V_{PO} = ? \tag{35}$$

The pressure distribution for both rotational and irrotational flows is:

$$\begin{aligned} P = & -\rho \left[U_{PO} \right]^2 - \rho \times F(y) U_{PO} + \rho \int F'(y) \times U_{PO} \, dy \\ & - \rho \, H(x) \times U_{PO} - \rho \, G \;\; '(x) \int U_{PO} \;\; dy \\ & - \rho \, G'(x) \int F(y) \;\; dy - \rho \, G'(x) \, H(x) Y \;\; - \rho \left[V_{PO} \right]^2 \\ & - \rho \, G(x) \times V_{PO} \;\; + \rho \, H'(x) \;\; Y \times V_{PO} \\ & + \rho \, H'(x) \, G(x) Y + \rho \left[H'(x) \right]^2 \frac{Y^2}{2} \\ & + N(x) + \mu (G''(x) Y) \end{aligned} \tag{36}$$

The rotation function is defined by [2]

$$\omega = \frac{1}{2}\left(\frac{\partial \mathrm{v}}{\partial \mathrm{x}} - \frac{\partial \mathrm{u}}{\partial \mathrm{y}}\right) \tag{37}$$

$$\omega = \frac{1}{2}\left[\left[\frac{\partial V_{PO}}{\partial x} + G'(x) - H'''(x)y\right] - \left[\frac{\partial U_{PO}}{\partial y} + F'(y)\right]\right] \tag{38}$$

The shear stress;[2]

$$\tau_{xy} = \mu\left(\frac{\partial \mathrm{v}}{\partial \mathrm{x}} + \frac{\partial \mathrm{u}}{\partial \mathrm{y}}\right) \tag{39}$$

$$\tau_{xy} = \mu\left[\frac{\partial V_{PO}}{\partial x} + \frac{\partial U_{PO}}{\partial y} + G'(x) + F'(y)\right] \tag{40}$$

At the walls, the velocity components are equal to zero, so we have that

$$\frac{\partial P}{\partial x} = -\rho\left(u\frac{\partial u}{\partial x} + v\frac{\partial u}{\partial y}\right) + \mu\left(\frac{\partial^2 u}{\partial x^2} + \frac{\partial^2 u}{\partial y^2}\right) = 0 \tag{41}$$

$$\frac{\partial P}{\partial y} = -\rho\left(u\frac{\partial v}{\partial x} + v\frac{\partial v}{\partial y}\right) + \mu\left(\frac{\partial^2 v}{\partial x^2} + \frac{\partial^2 v}{\partial y^2}\right) = 0 \tag{42}$$

3 Conclusion and future work

The mathematical background of the problem will help in the numerical study. In finite element, the element type should be chosen according to the physical problem. The mathematical solution that considered here is a continuous function over the domain; inside and outside the boundary layer; and satisfies continuity and momentum equations. The coefficients included in the solution should be determined through satisfying the boundary conditions for velocity and pressure. But the boundary condition for the pressure at the wall is satisfied already as the boundary condition for the velocity applied. Therefore, the boundary conditions for the velocity just needed to be satisfied.

This solution could be a general solution for potential and laminar flows. The shear between the fluid layers does not vanish outside the boundary layer because the friction between the layers cannot be eliminated. The advantage of the mathematical solution over the numerical solutions is so clear, but can be obtained for simple geometries. A future work will consider the application of the solution for simple cases and a solution for the thermal and turbulent flows will be brought.

References

[1] W. M. Kays, M. E. Crawford, *Convective Heat and Mass Transfer*, McGraw Hill, New York, 1993.
[2] Robert, W. Fox, Alan T. McDonald, *Introduction to Fluid Mechanics*, John Wiley & Sons, 1994.
[3] H. Bateman, Partial Differential Equations of Mathematical Physics, Cambridge University press 1964.
[4] A.J. Baker, Finite element Computational Fluid Mechanics, Hemisphere, 1983.
[5] Hermann Schlichting, *Boundary Layer Theory*, McGraw-Hill, 1968.



This page intentionally left blank

A computational method for pressure wave machinery to internal combustion engines and gas turbines

A. Fatsis[1], M. Gr. Vrachopoulos[1], S. Mavrommatis[1],
A. Panoutsopoulou[2] & F. Layrenti[1]
[1]*Technological University of Chalkis,*
Department of Mechanical Engineering, Greece
[2]*Hellenic Defense Systems S.A., Greece*

Abstract

Pressure wave machinery constitutes promising devices in various engineering propulsion applications such as superchargers in automobile engines and topping devices in gas turbines. This article presents applications of a numerical model for the flow field prediction inside wave rotors. The numerical method used consists of an approximate Roe solver that takes into account viscous and thermal losses inside the rotor as well as leakage losses at the extremities of the rotor. The model is extensively validated and then is applied on configurations suited for automobile engine supercharging and for topping devices for gas turbines. For both cases, satisfactory results are obtained by the comparison of the numerical predictions against experimental data available in the literature. It is concluded that the present method can accurately predict the basic unsteady flow patterns inside the rotor.
Keywords: pressure wave supercharger, wave rotor, internal combustion engine, gas turbine, unsteady flow.

1 Introduction

Pressure wave superchargers or wave rotors or Comprex® are rotating devices in which energy is transferred between two gaseous fluids by short time direct contact of the fluids in slender flow channels. They are composed of two concentric cylinders between which, radial straight planes are arranged giving



WIT Transactions on Engineering Sciences, Vol 52, © 2006 WIT Press
www.witpress.com, ISSN 1743-3533 (on-line)
doi:10.2495/AFM06006

rise to long channels of constant cross section, Berchtold [1]. Lateral non-rotating perforated flanges (stators) are mounted upstream and downstream the rotor. Through the openings of the stators that are commonly called inlet and outlet ports, the air and the hot gases enter and exit the rotor.

Different applications of wave rotors can be obtained depending on the following parameters: (i) the number of ports upstream and downstream the rotor, (ii) the dimensions of the ports, (iii) the aero-thermodynamic quantities specified at the inlet and outlet of the ports and (iv) the direction of the inflow and outflow at each port. Initially wave rotors were designed to supercharge internal combustion engines. In such applications, the ports are connecting the rotor to the fresh air intake, to the exhaust pipe and to the inlet and outlet of the combustion chamber of the engine. Automobile applications of the pressure wave supercharger over a wide range of car and truck diesel engines, showed a fast response to changes in the engine load, resulting in almost instantaneous availability of maximum torque, according to Mayer et al. [2].

Wilson and Fronek [3], present the pressure divider, that is another application of wave rotors. This type of wave rotor is generally equipped with three-ports. It is used to split the inlet flow in two flows; one at a higher pressure and the other at a lower one. Fatsis [4], examined the benefits of wave rotors as topping devices when applied to different types of gas turbines for aeronautical applications.

The flow inside the rotor is unsteady. It is dominated by propagation of compression and expansion waves that interact with each other and reflect on the solid walls of the upstream and downstream stators as well as on the inflow and on the outflow boundaries. One-dimensional methods based on the Euler equations are mainly used including modelling for losses that occur inside the rotor e.g. Fatsis et al. [5], Paxson [6]. Two-dimensional methods such as the one of Welch [7] are rather time-consuming and are mainly suited to study in detail specific regions of interest of the flow field inside the rotor, such as finite opening / closing effects and shock wave – boundary layer interaction.

The present contribution aims to present a general and accurate numerical tool suited for the analysis of unsteady flows encountered inside different types of wave rotors. After a brief description of the numerical method, the model is validated against experimental data for the flow inside a three-port pressure divider. Then the model is implemented to predict the flow inside a reverse flow wave rotor that can be used as a supercharger of internal combustion engines. Comparisons with measurements show that the present method gives accurate results for the cases examined and that it is able to capture the basic unsteady flow phenomena inside the rotor.

2 Numerical method

2.1 Assumptions

In the existing pressure wave superchargers manufactured so far it is observed that the length of each wave rotor channel is much larger than its height and

width, according to Mayer et al. [2]. This justifies the approximation of the flow inside a channel formed by two consecutive blades with the flow inside a shock tube. This consideration simplifies the real three-dimensional and unsteady flow inside the rotor channels with a one-dimensional unsteady flow inside a shock tube. A two-dimensional analysis method, though, could clarify the limits of applicability of one-dimensional methods. As a first approximation, this approach can be considered realistic. Nevertheless pressure losses; viscous phenomena and leakage existing in the flow inside a real wave rotor are taken into account in the present method, Fatsis et al. [5].

2.2 Spatial discretisation

Experience using different numerical schemes showed that upwind schemes are well suited for compressible flows including discontinuities such as shock waves, Hirsch [8]. The second order accurate scheme of Roe [9] was chosen for the space discretisation of the system of the partial differential equations, Fatsis et al. [5].

2.3 Time integration

Since the behaviour of the unsteady flow inside the wave rotor channels is of interest in the present study, the time integration scheme should offer a high accuracy. For this reason, the four-step Runge-Kutta scheme consists of an attractive choice, Fatsis et al. [5]. Studies show that the above scheme is second order accurate for non-linear equations, Hirsch [8].

2.4 Boundary conditions

During the operation of a wave rotor it is possible to have any type of the following boundary conditions: subsonic or supersonic towards the inlet and outlet of the computational domain (rotor channel). According to the theory of characteristics given by Hirsch [8] the numerical model employs different types of boundary conditions depending on the nature of the flow in the extremities of the wave rotor channels.

All boundary conditions implemented use the compatibility equations method described by Fatsis et al. [5]. The boundary conditions are of reflecting type, simulating infinite reservoirs with constant flow conditions connected to the rotor inflow and outflow ports. Under these boundary conditions when moving shock waves reach the rotor extremities, reflect back to the rotor channel interacting with other.

3 Validation

The model has been validated first on shock tube flow by Fatsis et al. [5], where analytical solutions can be found by Kentfield [10]. A second validation test that will be presented here refers to the calculation of the flow inside the three-port through-flow wave rotor or “pressure divider”. This wave rotor was



manufactured and instrumented to validate numerical models aiming to analyse its flow pattern. The experimental data of the unsteady pressure distribution at the following axial positions of the rotor, *x/L=0.025, 0.50, 0.975*, were reported by Wilson and Fronek [3].

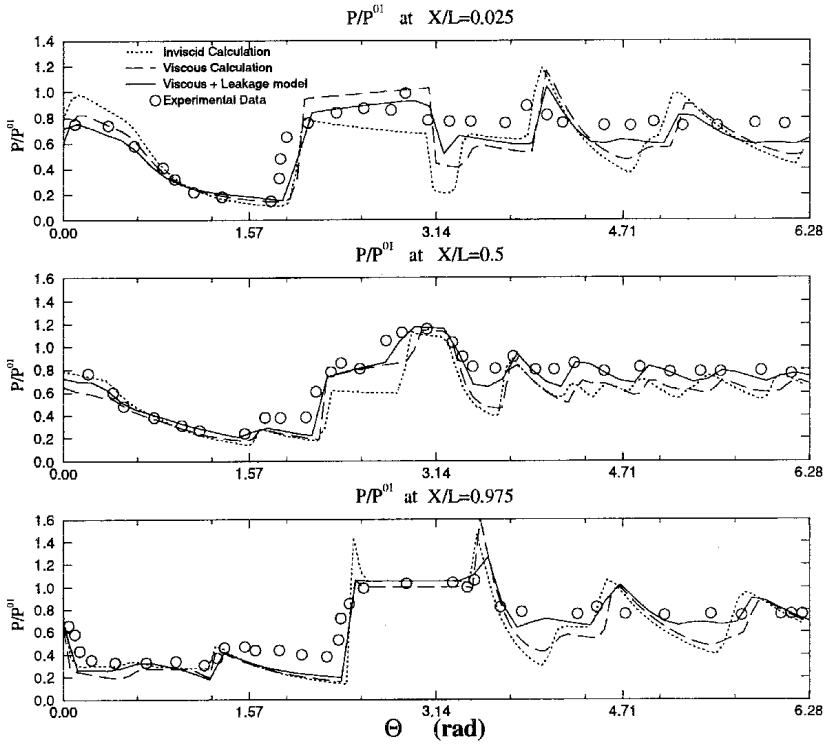


Figure 1: Comparison between numerical predictions and experimental data for the three-port wave rotor.

Figure 1 presents the comparison between the predictions obtained using the present numerical model and experimental data from Wilson and Fronek [3] illustrated by circles. Dotted lines present inviscid flow calculations, long dashed lines present results obtained including viscous and thermal losses and continuous lines present the predictions of the final model which also includes leakage losses at the extremities of the rotor (improved model). Inviscid flow predictions show larger amplitude of oscillation for the three axial locations. This behaviour is expected because upwind schemes (such the one used in this model) include just the minimum numerical damping provided by the numerical flux limiters, Roe [9]. Predictions including viscous and thermal losses give better results than the inviscid flow predictions when compared to the experimental data. The amplitude of pressure oscillations of the model including viscous and thermal losses is reduced due to the dissipation resulting from the

addition of the loss modelling. Ultimately, results obtained adding also leakage source terms, improve further the numerical predictions. Although leakage source terms are included only at the first and last computational cells, they affect the flow field even at x/L=0.5. One can observe that the agreement between the final (improved) model and experimental data is very satisfactory for the three axial locations examined. There are some regions, though, like the one corresponding to the opening of the inflow port at left ($x/L = 0.025$, $\theta \in [2,3]$ rad) where the agreement is not so good. These differences occur due to the fact that the present model supposes that the flow is accelerated instantaneously when a rotor channel arrives in front of an inflow port. In reality there are losses associated to the inflow and outflow phenomena (finite opening time effects), which are not taken into account in the present numerical model.

4 Reverse flow wave rotor

This type of wave rotor is currently used in automobile applications, and experimental data on the subject has been published by Shreeve and Mathur [11] using the same experimental techniques as for the case of the three-port wave rotor described in the previous chapter. Figure 2(a), (b), shows predicted total pressure and total temperature inside the rotor, non-dimensionalised by the total pressure and temperature at the inlet of port (1), during one complete rotation. The rotor is supposed to rotate from the lower to the upper part of figure 2(a), (b). The abscissa is the non-dimensional distance x/L extending from 0 to 1 and the ordinate corresponds to the circumferential coordinate Θ extending from 0 to 2 π. The process in this cycle begins at the lower part of the figure 2(a), (b), when the port (4) towards the exhaust pipe opens and hot gases with a percentage of relatively cold, compressed air exit the rotor. As e result an expansion wave is generated that propagates to the left, hitting the upstream stator walls and then is reflected to the right as a compression wave. At this moment, port (1) opens and due to the large pressure difference, fresh air enters, scavenging the rotor cells and pushing the remaining gases towards the exhaust pipe port (4). As the port (4) closes, the compression wave that was initiated when port (1) was open hits the downstream stator wall and reflects to the left as a shock wave. This shock wave front is progressing faster than the speed of sound before it and it is simultaneously compressing and accelerating the air towards left. At that moment, port (2) opens and hot gases from the combustion chamber of the engine enter the rotor, creating a strong shock wave propagating to the left, compressing and pushing air and remaining gas towards the combustion chamber (port (3)), figure 2(a). When the front between the compressed air and hot gases reaches the port (3), this port closes, preventing the exhaust gases recirculation into the engine. Some of the air that has been contaminated remains in the rotor cells. As the port (3) towards the combustion chamber closes, a compression wave is created, pushing the remaining gas and compressed air towards the exhaust pipe port (4). This remaining air gives the

energy to scavenge the cells, namely to replace the exhaust gas with air. From figure 2(b), one can see that mainly hot gases remain in the right part of the rotor, corresponding to ports (2) and (4), while the air remains in the left part of the rotor, corresponding to ports (1) and (3). Other researchers have made similar observations, e.g. Mayer et al. [2].

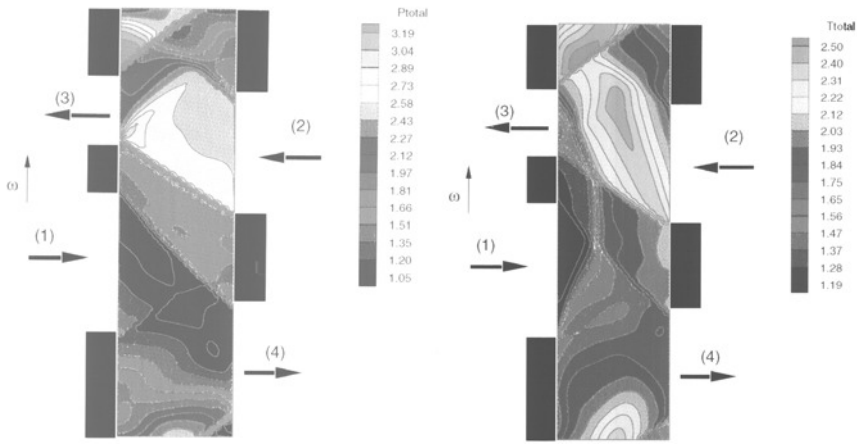


Figure 2: (a) Total pressure non-dimensionalised by the total pressure at port (1), (b) total temperature non-dimensionalised by the total temperature at port (1) field for the reverse flow four-port wave rotor. (1) Air at atmospheric conditions, (2) Compressed air from combustion chamber, (3) Hot gases to combustion chamber, (4) Hot gases and air to the exhaust.

The wave processes as described previously correspond to a "perfectly tuned" pressure wave supercharger according to the engine demands. In reality, a supercharger has to function over a wide engine operating range from very low up to very high rotating speeds. The pressure wave supercharger succeeded this wide range speed operation by using additional stator ports, called "pockets", which, however are not connected to any duct, Berchtold [1].

Detailed comparisons between predicted and measured static pressure distribution at axial locations (a) x/L=0 and (b) x/L=1 respectively are presented in figure 3. At x/L=0 predictions match the experimental data obtained from [19]. The measurement technique applied was similar to the one described in chapter 4. Small discrepancies occur at circumferential locations where $\theta \in [\pi, 3\pi/2]$ rad, corresponding to port (1) and where $\theta \in [7\pi/4, 2\pi]$ rad corresponding to the closing of port (3). At x/L=1 differences between experimental data and predictions occur at circumferential locations where $\theta \in [0, \pi/4]$. rad, corresponding to the opening of port (4) and where $\theta \in [7\pi/4, 2\pi]$ rad corresponding to solid wall area. The comparison can be

considered good taking into account the complexity of the unsteady flow inside the rotor channels and the fact that the experiment was carried on a real engine. Yet, incorporating loss model for the finite closing of ports effect, could improve the accuracy of numerical predictions in the circumferential positions corresponding to the closing of inflow / outflow ports.

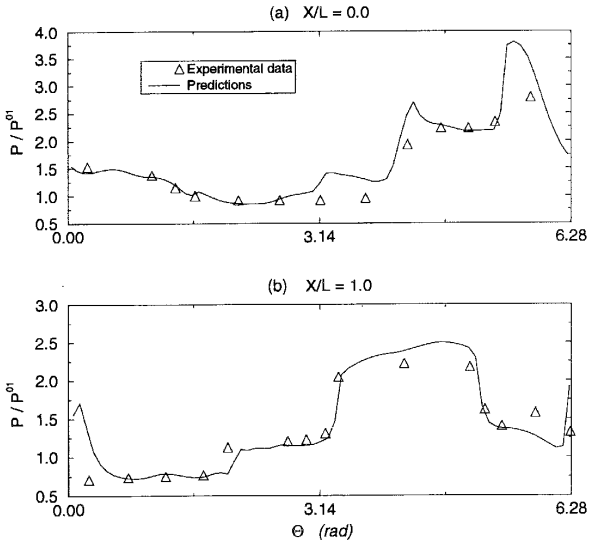


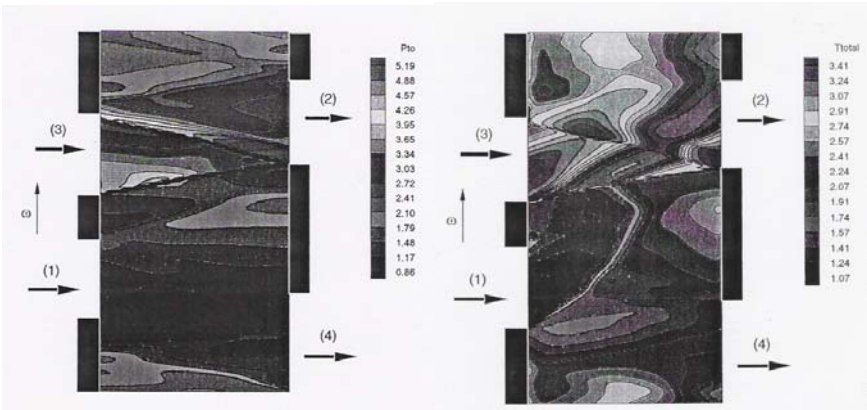
Figure 3: Comparison between computed and measured static pressure distributions for the reverse-flow wave rotor.

5 Through-flow four-port wave rotor

This type of four-port wave rotor is mainly suited for aeronautical applications due to its self-cooling capability, as it will be shown. Input geometrical data are published by Welch [7]. Figures \ref{fig:thru_p} ~and \ref{fig:thru_t} show instantaneous total pressure and total temperature ruster plots for the through-flow wave rotor examined. For both figures, the abscissa is the non-dimensional x/L distance extending from 0 to 1 and the ordinate corresponds to the circumferential coordinate θ extending from 0 to 2π.

The wave rotor is supposed to rotate from the lower to the upper part of the figure. Initially the rotor is filled with hot gases. The operation begins at the lower part where the hot gases expand when the port (4) towards the turbine opens, figure 4(a). The expansion fan which is created hits the left side walls and is reflected to the right. When it reaches the upper part of the port (4) towards the turbine, this port closes. A part of the expansion fan is reflected on the iso-pressure surface (forming thus a coalesced shock) and the rest is reflected on the solid wall. On the other hand, the port (1) from the compressor opens and relatively cold air enters the rotor. The contact interface between cold air and hot

gases can be seen on figure 4(b). When the port (3) from the combustion chamber opens, a strong shock is created which interacts with the interface as it propagates to the right. At that moment, it is probable to anticipate extra losses due to the interaction, but Weber (1995) suggests that they can be neglected at a first approach. When the shock reaches the right end, it reflects on the walls and goes towards left. When the port (2) towards the combustion chamber opens, a part of hot gases (which did not leave the rotor when the port (4) towards the turbine was opened) goes out as well as the most of the compressed air included in the interface, figure 4(b). Then the port closes creating a left-propagating shock which interacts with the expansion fan produced when the port (3) from combustion chamber had been closed.



(a) (b)

Figure 4: Instantaneous (a) total pressure and (b) total temperature contours for the four-port through-flow wave rotor. (1): From Compressor, (2): To Combustion Chamber, (3): From Combustion Chamber, (4): To Turbine.

Similar observations were done by Paxson [6] and Welch [7] on through-flow four-port cycle computations. From figure 4(a) one can see that the upper part (ports (2), (3)) corresponds to the high pressure part of the cycle, while the lower part (ports (1), (4)) corresponds to the low pressure part. The self-cooling aspect of the through-flow configuration can be clearly seen from figure 4(b) where cold air coming from compressor through the port (1) traverses the wave rotor channels and flows out towards the combustion chamber (port (2)). This allows the blade material to be cooled by forced convection and not only by conduction. One can also see the circumferential periodicity at the end of each rotation, as well as the fully unsteady character of the flow inside the rotor. The average total pressure at port (2) towards the combustion chamber is equal to *3.21*, (Welch, [7] found from *2D* computations 3.15) fact which justifies the choice of $PR = 3$ in the cycle analysis done in the beginning of this article. The

wave rotor total pressure ratio of this simulation was $T_4^0 / T_1^0 = 1.943$ and the total pressure ratio $P_4^0 / P_1^0 = 1.145$. Welch [7] reports that $T_4^0 / T_1^0 = 1.91$ and $P_4^0 / P_1^0 = 1.12$ respectively. This means that the existing technology can provide the material for the wave rotor construction. From figures 4(a), (b) one can see that total pressure and temperature are not uniform at the port (4) towards the turbine. This creates extra losses in the ducts which were also taken into account in the cycle analysis.

6 Conclusions

A simple one-dimensional model, able to analyse unsteady flows inside multiple-port wave rotors, was presented. A validation of the model was presented for a three-port wave rotor against experimental data available in the literature. Then the model was applied on a reverse-flow four-port pressure wave supercharger suited for internal combustion engines and for a through-flow wave rotor suited as a topping device for gas turbine performance enhancement. The numerical results obtained showed that the model is able to predict the unsteady flow field features inside the rotor channels, being in agreement with measurements and observations of other researchers. The self-cooling character of the through-flow wave rotor was verified from the fact that the mean blade temperature was found to be less than the turbine inlet temperature. Two-dimensional simulations in [11] can give an insight of the issue and may clarify the applicability limits of one-dimensional prediction methods. Including in the model the effect of pockets in the stator walls can lead to more realistic prediction of the performance map of pressure wave superchargers when integrated in internal combustion engines. That would give the possibility to study the behaviour of the wave processes inside the rotor at off-design conditions.

Acknowledgment

This publication was accomplished in the framework of Archimedes I-Support of Research Programs ΕΠΕΑΕΚ ΙΙ.

References

[1] Berchtold, M. Supercharging with Comprex. VKI Lecture Series 1982-01 entitled “Turbochargers and related problems”, 1982.
[2] Mayer, A., Pauli, E., Gyrax, J. Comprex® Supercharging and Emissions Reduction in Vehicular Diesel Engines SAE Paper No. 900881, 1990.
[3] Wilson, J., Fronek, D. Initial Results from the NASA-Lewis Wave Rotor Experiment. AIAA Paper 93-2521, 1993.

[4] Fatsis, A., Ribaud, Y. Thermodynamic analysis of gas turbines topped with wave rotors, Aerospace Science and Technology, 1999, No. 5, pp. 293-299.
[5] A. Fatsis, A. Lafond, Y. Ribaud, "Preliminary analysis of the flow inside a three-port wave rotor by means of a numerical model". Aerospace, Science and Technology, Vol. 2, No. 5, July 1998, pp. 289-300.
[6] Paxson, D.E. Comparison between Numerically modelled and Experimentally Measured Loss Mechanisms in Wave Rotors. Journal of Propulsion and Power, Vol.11, No.5, pp. 908-914, 1995.
[7] Welch, G.E. Two-Dimensional Computational Model for Wave Rotor Flow Dynamics, ASME Paper No. 96-GT-550, 1996.
[8] Hirsch, C. Numerical Computation of Internal and External Flows, Volumes I & II, John Wiley and Sons, 1991.
[9] Roe, P.L. Characteristic-Based Schemes for the Euler Equations. Annual Review of Fluid Mechanics, Vol. 18, pp.337-365, 1986.
[10] Kentfield, J.A.C. Nonsteady, One-Dimensional, Internal, Compressible Flows. Oxford University Press, 1993.
[11] Shreeve, R.P. and Mathur A. (editors). Proceedings of the 1985 ONR/NAVAIR Wave Rotor Research and Technology Workshop, Naval Postgraduate School, Monterey, California, 1985.



Aerodynamic flow simulation

R. W. Derksen[1] & J. Rimmer[2]
[1]*Department of Mechanical and Manufacturing Engineering, University of Manitoba, Winnipeg, Manitoba, Canada*
[2]*E.H. Price, Winnipeg, Manitoba, Canada*

Abstract

This paper reports our experience of applying a vortex cloud model to simulate the flow over airfoil sections at low-Reynolds numbers. Low-Reynolds number aerodynamics has become increasingly important of late due to interest in the development of unmanned aerial vehicles. The current state-of-the-art consists of a good base of modern experimental data, but relies on simulation methods based on high-Reynolds number experience. Vortex cloud models are numerical flow simulation methods that are based on inviscid flow tools. The method continuously injects many free vortices within the flow field and tracks their convection with time. The convective velocity is determined from the inviscid velocity component due to any bodies within the flow field, all free vortices, and a random component. The random component of the velocity field introduces a viscous effect and its value is scaled to the Reynolds number. Vortex cloud models are believed to be capable of modelling viscous flows and should be able to model separated flow without introducing special methods. We will provide an assessment of the predicted flow for a range of angles of attack for a selected set of airfoils when compared to the very good low-Reynolds number airfoil data compiled by Selig and his co-workers.
Keywords: aerodynamics, vortex cloud models, panel methods.

1 Introduction

The development of aerodynamic flow simulation methods has a substantial history that demonstrates a creative intellectual effort to overcome the difficulties inherent to the governing equations of fluid mechanics. Early efforts at simulating aerodynamic flows were limited by our inability to obtain analytical solutions to the Navier-Stokes equations to all but a few idealized examples.



WIT Transactions on Engineering Sciences, Vol 52, © 2006 WIT Press
www.witpress.com, ISSN 1743-3533 (on-line)
doi:10.2495/AFM06007

This resulted in an overwhelming reliance on experimental methods to obtain aircraft design information that has persisted up until quite recently. Aerodynamicists have developed a rich and interesting set of methods to obtain the approximate behaviour of aerodynamic structures that has evolved and become quite sophisticated. The first methods were based on the observation that inviscid flow methods could be used to model flow over streamline bodies at high Reynolds numbers. This allowed us to obtain reasonably accurate estimates of lift, pitching moments and induced drag using relatively simple analytical or computational methods. These methods cannot be used to estimate the viscous drag and, while very useful, are inadequate. A great deal of effort has been devoted to approximating viscous effects through the use of Prandtl's boundary layer theory. These efforts started by assuming that the airfoil was an equivalent flat plate, which is surprisingly accurate in estimating minimum drag, and were rapidly enhanced to include effect of the velocity distribution on the body. This approach was of very limited use and cannot be used over a sufficiently wide range of angle of attack due to flow separation. It was soon recognized that the flow over an airfoil could be more accurately approximated by iteratively employing an inviscid flow model with a boundary model. This method either creates a set of pseudo-bodies or a surface transpiration distribution that ultimately converges to a limiting state. Most methods are based on some variation of this approach at present. The deficiency of these methods comes from the ad hoc nature of how to deal with separation. The development of modern, high-speed, inexpensive computers has resulted in a number of fast and effective computational fluid dynamics (CFD) methods to solve viscous flows in many complex geometrical configurations, and have been applied to aerodynamic applications. These methods are based on the numerical solution of Navier-Stokes equations and should have no difficulty with flow separation. This approach is very time intensive and expensive and unfortunately has its own concerns.

The objective of this work was to examine a relatively simple, novel, numerical method, the vortex cloud model, as a tool for aerodynamic flow simulation. The developers of this method have suggested that it is suitable to simulate viscous flows in complex geometries and is capable of dealing with flow separation.

2 The Vortex Cloud Model

The Vortex Cloud Model was originally proposed by Chorin [1, 2] as a method to numerically solve viscous flows. It is based on the vorticity equation, derived from the Navier-Stokes equations, and is given by

$$\frac{\partial \bar{\omega}}{\partial t} + \left(\bar{V} \bullet \nabla\right)\bar{\omega} = \left(\bar{\omega} \bullet \nabla\right)\bar{V} + \nu \nabla^2 \bar{\omega}. \tag{1}$$

This approach allows us to set aside the issue of the pressure field until the velocity field has been determined. We should note that many traditional

numerical field solution methods (finite difference methods, etc.) for solving fluid flows have been based on a stream function – vorticity approach. The novelty of the vortex cloud method comes from its approach to solving the vorticity equation.

The vortex cloud method is based on simulating the motion of a cloud of discrete vortices that are continuously released into the flow field. The production of new vorticity is based on the surface vorticity distribution on any bodies within the flow field as obtained from an inviscid flow calculation, and the convection of the vorticity cloud is determined by the inviscid, induced velocities from the bodies and all other vortex elements, and a random component that depends on Reynolds number. The effect of the random component is to introduce a 'diffusivity' that is not present in ideal flows, and is believed to simulate the effect of viscosity. There are several advantages of the cloud model compared to a traditional field method. The first is that the flow field does not need to be discretized, as the location of each vortex is associated with the vortex. Secondly, the core calculations for the vortex cloud model are very simple and rapidly computed. Finally, the vortex cloud model should be able to more naturally deal with any separation regions that develop in the flow field.

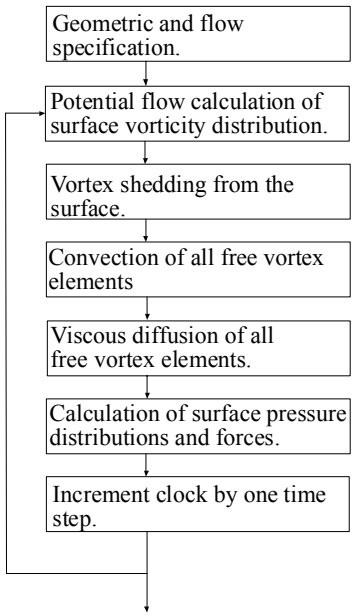


Figure 1: The basic vortex cloud method flow chart.

The basic steps of a vortex cloud model are shown in Figure 1. As to be expected the first step is to define the geometry of the airfoil and the required flow parameters. The initial step is to apply a vortex panel method to obtain the inviscid flow field about an airfoil in the absence of any free vorticity in the flow

field. This gives an initial surface vorticity distribution which is used to shed a finite number of free vortices from the body into the flow. The position of the shed vortices is then advanced one time step using the induced velocities from the inviscid flow field. Viscous diffusion is then simulated by displacing the shed vortices by either randomly displacement of their position or applying a random velocity component. At this point, the instantaneous surface pressure distribution and aerodynamic forces are computed and accumulated for subsequent averaging. This process is repeated from the potential flow step, now including the influence of the shed vortices, till the simulation time or the average values are stable.

The key questions that need answering if the vortex cloud model is to be a successful method are:

1. How many individual vortices must be examined to obtain a sufficiently accurate flow field simulation?
2. How should we determine the production of vorticity, and are the existing methods satisfactory?
3. Can a suitable model for the random velocity components be developed, and if so do the existing models produce satisfactory results?
4. How many time steps are required to obtain stable average values of field variables such as the lift and drag on an object?
5. Is the simulation capable of modelling the unsteady components of the flow?

Several variations of vortex cloud models have been proposed and developed over the last 30 years. We have based our work on the method developed by R.I. Lewis and his co-workers [3].

3 Code development

The first step in coding this simulation was to develop a vortex panel method to compute the ideal flow over a cylindrical profile. The method divided the profile into N linear panels with a uniform vorticity distribution, and results in an $N \times N$ linear system of equations. The panel lengths were adjusted to have a cosine distribution that clusters nodes near the leading and trailing edge of the profile. This reduces the error due to panels being close to each other at the trailing edge and provides greater detail at the leading edge where the flow changes rapidly. This code was then carefully examined by carefully examining its result compared to known analytical solutions. The vortex cloud code was developed from this base by adjusting the right hand side of the panel methods to include the effect of a distribution of free vortices in the flow field. This modification assumed that the location of each free vortex is known and that it has a given strength. Each call returned the surface velocity distribution and allowed us to calculate the induced velocity at any point in the flow field.

This was used by a modified Euler scheme to advance the location of all of the free vortices for a given time step. This process is faster than it may appear as the resulting system of equations does not depend on the location of the free vortices so only one matrix inversion needs to be done, so a velocity calculation

is the result of a simple set of matrix multiplications. This does require a significant computational load over the Euler method but is necessary to minimize the vortex drift error to a tolerable level. We found no need to apply a higher order integration scheme as a time step that resulted in a sufficiently accurate prediction could be based on the free stream velocity and chord length. The performance of this code was compared the theoretical location of a single free vortex with its predicted location and found to be good.

At this point code was developed to insert a number of free vortices into the flow field. Each vortex was shed from the surface at the normal centre of a randomly selected panel a distance $10\sqrt{\nu dt/3}$. The shed vortex strength was set to 25% of the net panel vorticity, and panel vorticity adjusted to 75% of its previous value. The full panel vorticity could not be shed as it would result in instability in the simulation. The number of vortices created each time step was held a constant rate until the total number of vortices equalled a set maximum. Vortices were removed from the analysis for two reasons. First, when a vortex had moved more than four chord lengths behind the cylinder it was removed from the field and a new vortex was inserted. Secondly, vortices are also removed from the simulation if they cross into the body during the intermediate step in the modified Euler method and an additional free vortex was shed.

After the convection step, viscous diffusion was modelled by adding a random, two dimensional displacement to each of the free vortices. The scheme to determine these components was due to Lewis [3]. First two real values, L and K are set to random values and modified to

$$L' = 2\pi L \tag{2}$$

and

$$K' = \sqrt{4\nu dt \ln(1/k)}. \tag{3}$$

Then $K'\cos(L')$ was added to the vortex position's *x*-component and $K'\sin(L')$ to the *y*-component. We should note that this hides the role of Reynolds number as dt is proportional to the product of the cylinder chord length and free stream velocity.

An initial effort was made to compute the lift and drag by integrating the surface pressure distribution over the airfoil. This results in an instantaneous estimate of these quantities that must be averaged over a suitable number of time steps. Unfortunately, this integration has proven to be unstable and alternate means of estimating the lift and drag are being examined.

4 Test cases

The test case chosen was based on the availability of high quality experimental data. This naturally led to the outstanding work done by Selig and his co-workers [4, 5, 6, and 7] in the mid-nineties. This work details the results of a



carefully constructed experimental program to produce a database of modern, low-Reynolds number airfoils. The measurements were exhaustively examined for their accuracy, for example drag was measured by the more accurate wake traverse method. This work filled a gap in previously existing databases by focusing in on low-Reynolds number, and is of great use in the design of R/C aircraft and small unmanned aerial vehicles. We believe that this work sets a new standard on airfoil data.

Our initial work will focus on a single airfoil, the NACA 2414 airfoil shown in figure 2, and was selected for this study as a complete data set could be found in [6]. The data specified the ideal profile shape and the deviation of the experimental model from the ideal. The average difference for this particular airfoil was 0.0044 in.; Surface velocity distributions were given for incidences between -2 and 10° at a Reynolds number of 200,000. Additionally, lift curves and drag polars were given for Reynolds numbers of 60,000, 100,000, 200,000, and 300,000. Future work will examine a larger number of cases from this database.

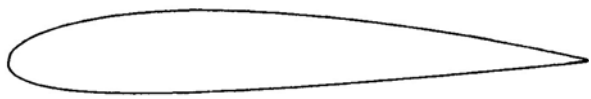


Figure 2: Airfoil profile for a NACA 2412 section.

The data indicated a nearly linear lift curve up to an angle of incidence of roughly 8°. At higher angles the lift curve's slope smoothly decreased until the maximum lift was achieved at approximately 14°, which was followed by a sudden decrease in lift. The maximum lift coefficient increased slightly from 1.15 at a Reynolds number of 60,000 to 1.20 at a Reynolds number of 300,000. The minimum drag, $C_d \approx 0.01$, occurred at $C_l \approx 0.25$ for Reynolds numbers of 200,000 and 300,000. The minimum drag increased to $C_d \approx 0.02$ for $\mathrm{Re} = 100,000$ and was fairly constant for $-0.3 \le C_l \le 0.7$, The minimum drag coefficient at Re=60,000 was approximately 0.22 at a $C_l = -0.2$. The variation in the character of the drag polars indicate that this range of Reynolds numbers contains an interesting change in flow physics.

5 Simulations

A variety of test simulations were run using 120 panels to model the NACA 2414 airfoil, and were equally distributed over the top and bottom surfaces. This number is generally considered to be more than sufficient for an inviscid flow field calculation.

Example flow patterns are shown for 250 free vortices in Figure 3 and 500 free vortices in Figure 4. The simulations were done for airfoil at zero angle of attack and a Reynolds number of approximately 150,000. Both Figures show similar behaviour and as expected the distribution of free vorticity clusters in the

wake of the airfoil. The results show that vortices shed from the lower surface are grouped to the lower half of the wake near the airfoil and diffuse across the wake as we move downstream.



Figure 3: Vortex Cloud Model simulation of flow over a NACA 2414 airfoil at Re = 149,503, with 250 free vortices shed into the flow field.

A time step by time step examination of the motion of the shed vortices demonstrated a nearly uniform motion of the free vorticity in the far wake. One issue that was of concern is the number of vortices that needed to be shed to obtain an accurate representation of the flow field. Our results show similarity of the results for both 250 and 500 shed vortices demonstrates that a large enough number of vortices were being shed to obtain an accurate representation of the flow. All subsequent simulations were done using 500 shed vortices; however we believe that 250 should be sufficient.

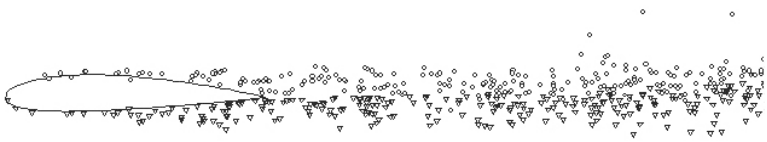


Figure 4: Vortex Cloud Model simulation of flow over a NACA 2414 airfoil at Re = 149,503, with 500 free vortices shed into the flow field.

Simulations of flow over the NACA 2414 airfoil were made for a range of angles of attack, α, and are shown in Figure 5. The airfoil is displayed in its horizontal orientation and the free stream velocity is inclined upward as α is increased. We would expect that the wake would deflect downward for $\alpha = 0°$ as is clearly shown. There was no indication of flow separation over the airfoil at this low angle of attack. When $\alpha = 5°$, the wake deflected slightly upward in the direction of the free stream velocity, and as with the case of $\alpha = 0°$ no separation was evident. These angles of attack are within the linear portion of the lift curve and the flow would not be expected to have significant separation regions. As we move the nonlinear portion of the lift curve, near the maximum lift region of the lift curve, say $\alpha = 10°$, we would expect to see the presence of a significant portion of separated flow on the suction surface near the trailing edge. The simulation represents this situation reasonably well, with a separation zone that is approximately 40% of the chord length. Finally, the flow over the airfoil in the deep stall range, represented by $\alpha = 15°$, clearly shows a separated zone that extends over nearly the entire suction surface, approximately 80 – 90 % of the chord length. In general, the qualitative picture is that the predicted flow appears to give a good qualitative representation of the actual flow.

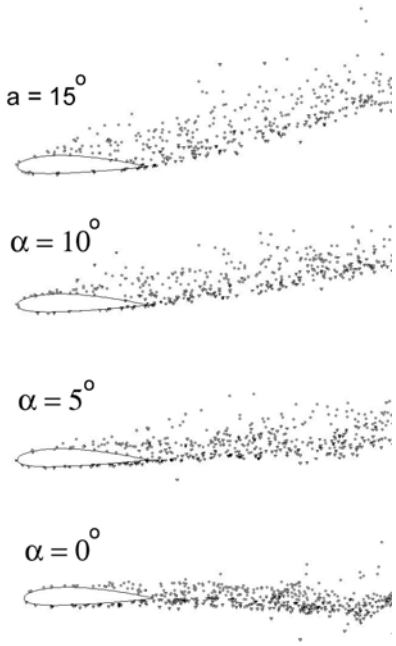


Figure 5: Vortex Cloud Model simulation of flow over a NACA 2414 airfoil at Re = 149,503, 500 vortices shed, for α = 0°, 5°, 10° and 15°.

6 Discussion

Our assessment is that the vortex cloud model is capable of simulating the flow over an airfoil at low-Reynolds number. However we are concerned that a reliable means of estimating the actual forces on the airfoil has not been established. The likely cause of this could come from a number of sources. First, this is a random process that requires averaging and may require a large number of time steps to reach their asymptotic values. Second, the integration method was based on a simple trapezoid rule where a more accurate method may be required. However it should be noted that the method does work for a strictly inviscid estimate. Finally, we have to consider the possibility that the accuracy of the predicted, instantaneous, surface pressure distribution is not sufficiently accurate to allow us to compute these quantities accurately. A better practice may be to use a control volume approach to estimate these forces, such as the Betz and Jones wake traverse methods [8].

Several issues with the Vortex Cloud Model still need to be resolved. The vortex shedding method that was recommended by Lewis did not work as described. In that form the vorticity was wildly flung around the flow field, necessitating a 75% reduction of shed vortex strength for the method to function, indicating that a more formal scientifically based method determination of the shed vorticity needs to be established. As accurate drag measurements were not

available we could not assess the validity of the random vortex displacement model.

Our observation on the application of the Vortex Cloud Model is that it has some significant advantages as a flow simulation tool. First, it is a grid free simulation which saves a lot of work. This is particularly important if it were to be used for the design of optimum shape airfoils. The optimization process typically requires the simulation of a large number of candidate airfoils, and benefits greatly if simulation effort is reduced. We found the method simple to apply and relatively fast, making it quite competitive with other methods.

7 Conclusions

The results of this work show that the vortex cloud method shows promise as a useful tool for airfoil simulation. The method is fairly easy to implement and is relatively fast. However, several issues, such as the calculation of the aerodynamic forces, the vortex shedding process, and suitability of the random displacement model need further consideration.

Acknowledgements

The authors would like to acknowledge the generous support of this work by the Natural Sciences and Engineering Research Council of Canada and E.H. Price. Ltd.

References

[1] Chorin, A.J., Numerical Study of Slightly Viscous Flow, *Journal of Fluid Mechanics*, **57**, pp. 785-96, 1973.

[2] Chorin, A.J., Vortex Sheet Approximation of Boundary Layers, *Journal of Computational Physics*, **27**, pp. 428-442, 1978.

[3] Lewis, R.I., *Vortex Element Methods for Fluid Dynamic Analysis of Engineering Systems*, Cambridge University Press, Cambridge, 1991.

[4] Selig, M.S., Donovan, J.F., and Fraser, D.B., *Airfoils at Low Speeds*, Soartech 8, Soartech Publications, Virginia Beach, U.S.A, 1989.

[5] Selig, M.S., Guglielmo, J.J., Broeren, A.P. and Giguere, P., *Summary of Low Speeds Airfoil Data*, Volume 1, Soartech Publications, Virginia Beach, U.S.A., 1995.

[6] Selig, M.S., Lyon, C.A., Giguere, P., Ninham, C.P. and Guglielmo, J.J., *Summary of Low Speeds Airfoil Data*, Volume 2, Soartech Publications, Virginia Beach, U.S.A., 1996.

[7] Lyon, C.A., Broeren, A.P, Giguere, P., Gopalarathnam, A. and Selig, M.S., Summary *of Low Speeds Airfoil Data*, Volume 3, Soartech Publications, Virginia Beach, U.S.A., 1997.

[8] Schlichting, H., *Boundary-Layer Theory*, McGraw-Hill, New York, pp. 758-777, 1979.



This page intentionally left blank

Simulations of viscoelastic droplet deformation through a microfluidic contraction

D. J. E. Harvie[1], M. R. Davidson[1] & J. J. Cooper-White[2]
[1] *Department of Chemical and Biomolecular Engineering, The University of Melbourne, Australia*
[2] *Division of Chemical Engineering, The University of Queensland, Australia*

Abstract

A modified Volume-of-Fluid numerical method is developed to predict the transient deformation of a viscoelastic drop surrounded by a more viscous Newtonian liquid passing through an axisymmetric microfluidic contraction. Viscoelastic effects are represented using an Oldroyd-B rheological model and can be generated in practice by the addition of small amounts of polymer. The numerical method is tested against experimental observations of viscoelastic drops forming at nozzles. We show that these simulations reliably reproduce flow and drop deformation. Predictions of drop shape and elastic extension are then presented and discussed for drop motion through a microfluidic contraction, and these results are compared against results for an equivalent Newtonian only system.
Keywords: viscoelastic, fluid dynamics, Oldroyd-B, Boger fluid, Volume of Fluid, interfacial, contraction, polymer.

1 Introduction

Microfluidic technology promises to revolutionise chemical and biological processing in the same way that the integrated circuit revolutionised data processing three decades ago [1]. Key to the operation of microfluidic devices will be the manipulation of droplets of viscoelastic fluids, as many biological and biomedical liquids to be processed contain long chain molecules that stretch and rotate in response to local strain fields. As a contraction can induce mixing in droplets, as well as significantly alter their shape, an understanding of how droplets behave when passing through such a geometry will be essential to the operation of future microfluidic devices.


WIT Transactions on Engineering Sciences, Vol 52, © 2006 WIT Press
www.witpress.com, ISSN 1743-3533 (on-line)
doi:10.2495/AFM06008

Previously published studies concerned with viscoelastic fluids passing through contractions deal with single phase systems. As discussed in Boger [2], elastic contraction flows display fluid behaviour that is markedly different to that of their Newtonian counterparts. The non-linearity of elastic fluids, in particular, makes their use in microfluidic scale devices attractive [1]. While numerical studies of single phase viscoelastic fluids are reaching maturity ([3] for example), numerical studies of viscoelastic systems which contain immiscible fluids are few.

The purpose of this study is threefold. Firstly, we describe how a Volume of Fluid computational algorithm has been modified to simulate viscoelastic immiscible fluid systems, with the elastic stresses simulated using an Oldroyd-B rheological model. We then demonstrate the validity of the algorithm by simulating a multiphase problem for which experimental results are available. After establishing confidence in the technique, we present results for a viscoelastic droplet passing through an axisymmetric contraction, and discuss how the behaviour of this droplet differs from an equivalent Newtonian droplet passing through the same geometry.

2 Mathematical model

The system we model consists of two immiscible fluids, one termed the continuous phase and the other the disperse phase. Both phases are viscous and incompressible. Interfacial tension acts at the boundary between the two phases, and the presence of polymers in one or both phases exerts additional elastic stresses on the fluid. We employ the following non-dimensional equations to model the dynamics of this system;

$$\cdot \boldsymbol{u} = 0 \tag{1}$$

$$\frac{\partial \phi}{\partial t} + \quad \cdot \phi \boldsymbol{u} = 0 \tag{2}$$

$$\frac{\partial \rho \boldsymbol{u}}{\partial t} + \quad \cdot \rho \boldsymbol{u}\boldsymbol{u} = - \quad p + \frac{1}{\mathrm{Fr}} \rho \hat{\boldsymbol{g}} + \frac{1}{\mathrm{We}} \kappa \hat{\boldsymbol{n}} \delta(\boldsymbol{x} - \boldsymbol{x}_{\mathrm{s}}) + \frac{1}{\mathrm{Re}} \quad \cdot \tau \tag{3}$$

$$\tau = \mu [\quad \boldsymbol{u} + (\quad \boldsymbol{u})^{\mathsf{T}}] + \frac{\mu_{\mathrm{p}}}{\mathrm{De}} (\mathsf{A} - \mathsf{I}) \tag{4}$$

$$\frac{\partial \mathsf{A}}{\partial t} + \quad \cdot \mathsf{A}\boldsymbol{u} = \mathsf{A} \cdot \quad \boldsymbol{u} + (\quad \boldsymbol{u})^{\mathsf{T}} \cdot \mathsf{A} - \frac{1}{\mathrm{De}} (\mathsf{A} - \mathsf{I}) \tag{5}$$

Equations (1)–(3) are the continuity, disperse phase transport and momentum equations, respectively. These equations are fairly conventional, with the exception of the third term on the right of eqn. (3) which represents the interfacial tension induced stress jump which occurs across the disperse-continuous phase interface. Equation (4) describes the stress within the fluid resulting from both viscous and elastic contributions, while eqn. (5) describes the evolution of the elastic configuration tensor, A.

The above equations are applied in a volume averaged sense when modelling the system. Thus, $\boldsymbol{u}$ represents the fluid velocity, locally volume averaged over

both phases. Other volume averaged variables include ϕ, the disperse phase volume fraction, ρ, the density, μ, the (solvent only) shear viscosity, and $\mu_{\rm p}$, the concentration of polymers present, expressed as the increase in shear viscosity of the solution caused by the addition of polymers. The density is calculated from the disperse phase fraction using $\rho = (1-\phi) + \phi\rho_{\rm d}$ where $\rho_{\rm d}$ is the non-dimensional disperse phase density. Analogous expressions exist for μ and $\mu_{\rm p}$. Note that ρ, μ and $\mu_{\rm p}$ are all uniform away from any interface regions. Other variables in the above equations include $\hat{\boldsymbol{g}}$, a unit vector directed in the direction of gravity, κ, the local curvature of the disperse-continuous phase interface, $\hat{\boldsymbol{n}}$, a unit vector defined along the disperse-continuous phase interface and directed normal to this interface, and $\boldsymbol{x}_{\rm s}$, the location of the disperse-continuous phase interface.

In non-dimensionalising the equations, velocity has been scaled by u^*, length by x^*, density by the continuous phase density $\rho_{\rm c}^*$ and viscosities (including the polymer concentration $\mu_{\rm p}$) by the continuous phase (solvent only) viscosity, $\mu_{\rm c}^*$. These scalings result in three non-dimensional groups describing the ratio between inertial, viscous, gravitational and interfacial forces acting in the system;

$$\mathrm{Re} = \frac{\rho_{\rm c}^* u^* x^*}{\mu_{\rm c}^*},\ \mathrm{We} = \frac{\rho_{\rm c}^* {u^*}^2 x^*}{\sigma^*} \text{ and } \mathrm{Fr} = \frac{{u^*}^2}{g^* x^*}.$$

Note that in our notation an asterisk implies a dimensional quantity, a 'c' subscript a continuous phase property, and a 'd' subscript a disperse phase property.

The Oldroyd-B rheological model has been chosen to represent viscoelastic effects [4]. Oldroyd-B fluids have constant shear viscosities, so are appropriate for modelling Boger fluids such as dilute polymer solutions [2]. In the Oldroyd-B model, polymers are represented as infinitely extensible 'dumbbells', the configuration of which is described by an ensemble averaged tensor $\mathsf{A} = <\boldsymbol{RR}>$, where $\boldsymbol{R}$ represents the orientation and length of individual dumbbells. The length of $\boldsymbol{R}$ is normalised so that in the relaxed state, $|\boldsymbol{R}| = 1$ and $\mathsf{A} = \mathsf{I}$ (the identity matrix). Equation (5) describes the evolution of A. The Deborah number which appears in this equation is the ratio of the relaxation time of the polymer to the timescale of the underlying flow, i.e., $\mathrm{De} = {t_{\rm p}}^* u^*/x^*$ where ${t_{\rm p}}^*$ is the polymer relaxation time. Highly elastic fluids have high Deborah numbers, whereas near Newtonian fluids have Deborah numbers close to zero.

3 Numerical solution technique

The simulations were performed using a finite volume code originally due to Rudman [5], but modified to account for elastic effects. The finite volume code, minus elastic effects, has been previously used to model the formation and subsequent 'pinch-off' of both Newtonian and generalized Newtonian pendant drops [6], the deformation of Newtonian and shear thinning drops that pass through microfluidic sized axisymmetric contractions [7, 8, 9], and the deformation and breakup of a continuous stream of liquid in a microfluidic 'flow focusing' device [10]. The Volume of Fluid (VOF) technique is used to track the disperse-continuous phase

interface with the disperse phase volume fraction (the VOF function) advected using a variation of the Youngs scheme [11]. Surface tension forces are applied using a variation of the Continuum Surface Force (CSF) model [12]. The domain is discretised using a uniform, staggered mesh with pressure and volume fractions stored at cell centres, and velocities stored at cell boundaries.

To include elastic effects, we require a solution for the dumbbell configuration tensor A throughout the flow domain. Rather than solve eqn. (5) directly, we have found that for multiphase problems better accuracy is obtained by solving for $\mu_{\mathrm{p}}\mathsf{A} = \mathsf{B}$ instead. In effect, this is solving for the elastic stress field directly rather than the dumbbell configuration field.

To express eqn. (5) in terms of B, we first note that as

$$\mu_{\mathrm{p}} = (1-\phi)\mu_{\mathrm{p,c}} + \phi\mu_{\mathrm{p,d}} \tag{6}$$

($\mu_{\mathrm{p,c}}$ and $\mu_{\mathrm{p,d}}$ are the polymer concentrations in the continuous and disperse phases, respectively), eqn. (2) implies that

$$\frac{\partial \mu_{\mathrm{p}}}{\partial t} + \quad \cdot \mu_{\mathrm{p}}\boldsymbol{u} = 0. \tag{7}$$

Combining this with eqn. (5) gives the transport equation

$$\frac{\partial \mathsf{B}}{\partial t} + \quad \cdot \mathsf{B}\boldsymbol{u} = \mathsf{B} \cdot \quad \boldsymbol{u} + (\quad \boldsymbol{u})^{\mathsf{T}} \cdot \mathsf{B} - \frac{1}{\mathrm{De}}(\mathsf{B} - \mu_{\mathrm{p}}\mathsf{I}) \tag{8}$$

which is the equation solved for the evolution of B. Elastic stresses are included in the calculation via eqn. (4) once the components of B are known. As the B components are stored at mass cell centres, linear interpolation is used to evaluate any components required at cell vertices.

The main details of the numerical technique used to solve eqn. (8) have been previously described by Davidson and Harrie [13]. For each timestep that the solution is advanced, the technique uses three sequential steps; advection, correction, and the addition of source terms. The correction step ensures that the diagonal components of B in each computational cell are positive, as is required physically. This technique was originally developed by Singh and Leal [3], however here we perform this correction on the components of B rather than on A. The addition of source terms to the evolution of B, that is, the addition of all of the terms on the right hand side of eqn. (8) during each timestep, is accomplished using a first order explicit technique that ensures that the determinant of B is positive to first order (in timestep) given that it was positive at the previous timestep [13]. That the determinant of B remains positive is also required physically [3].

The method used to advect the components of B used in this study is new, and differs from that used in [13]. It is motivated by the need to minimise diffusion of B across fluid phase interfaces, while still providing the high order accuracy necessary to reproduce experimentally observed elastic behaviour.

The advection component of eqn. (8), performed during the advection step, can be represented by

$$\frac{\partial \mathsf{B}}{\partial t} + \quad \cdot \mu_{\mathrm{p}} \boldsymbol{u} \mathsf{A} = 0. \tag{9}$$

The temporal derivative of this equation is discretised using an explicit first order Euler method. In evaluating the spatial derivatives, a value for the flux of B, that is $\mu_{\mathrm{p}} \boldsymbol{u} \mathsf{A}$, must be calculated for each computational cell boundary. As the concentration of polymer contained within a computational cell is just a linear combination of the disperse phase volume fraction contained within that cell (see eqn. (6)), the flux of polymer concentration over each boundary ($\mu_{\mathrm{p}} \boldsymbol{u}$) can be calculated from the disperse phase volume fraction fluxes ($\phi \boldsymbol{u}$) that are already known from the 'VOF' differencing of the disperse phase transport eqn. (2). The flux of B is calculated by multiplying these polymer concentration fluxes ($\mu_{\mathrm{p}} \boldsymbol{u}$) by values of A approximated at each computational cell boundary and averaged over the timestep duration.

The advantage of using the disperse phase volume fluxes in advecting the B components is that the concentration of polymer within a cell and the elastic stress within that cell are always 'synchronised'. This ensures that in regions where there is no polymer, there will be no advection of elastic stress. It also ensures that no diffusion of elastic stress can occur across an interface between a fluid phase that contains polymer and one that does not, as no flux of polymer occurs across such an interface.

Cell boundary values for the components of A are evaluated using a third order spatially accurate method. This method is based on the QUICK scheme [14], however, the upwind gradients used to evaluate each boundary value are limited to ensure that the diagonal components of the A tensor are positive on each boundary, and that the determinant of A calculated from these boundary values is positive, as required physically. Application of these ideas leads to a temporally first order and spatially second order bounded scheme for the advection of B.

4 Validation: viscoelastic pendant drop

To demonstrate the validity of the method, we compared published experimental data [15] against simulation results for the formation of a viscoelastic pendant drop in air. Simulation results for this problem were previously presented in [13]. Although the figures shown here were produced using the present version of the code, the results are almost identical to those in [13].

Figure 1 shows selected experimental and simulation images of the pendant drop evolving. The liquid used in the experiments was a water and glycerol mixture containing $0.1\ \mathrm{wt}\%$ of $1 \times 10^6\ \mathrm{g/mol}$ Polyethylene Oxide (PEO) polymers. The droplet formed on a nozzle of outer radius $2\ \mathrm{mm}$. Using fluid and polymer properties measured by [15], non-dimensional numbers used in the simulations were calculated as $\mathrm{Re} = 2.1$, $\mathrm{We} = 7.5 \times 10^{-4}$, $\mathrm{Fr} = 4.36 \times 10^{-3}$, $\mathrm{De} = 3.1 \times 10^{-2}$ and $\mu_{\mathrm{p,d}} = 7.06 \times 10^{-1}$, where droplet phase properties were used in the non-dimensionalisation. The simulations were performed in axisymmetric coordinates,



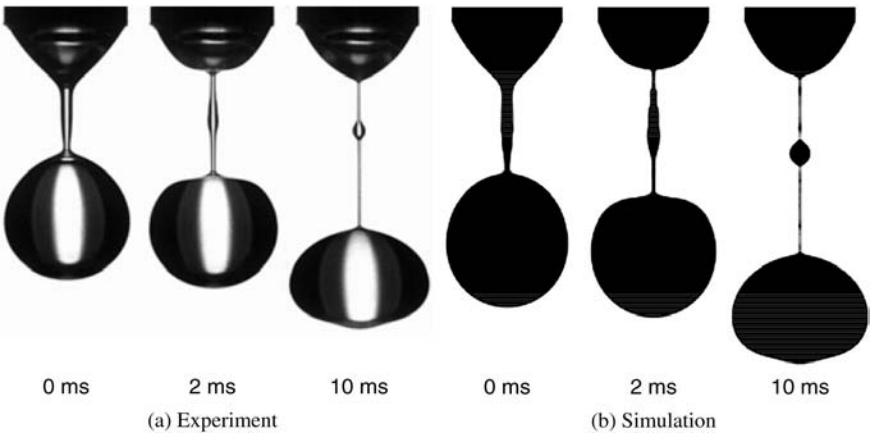


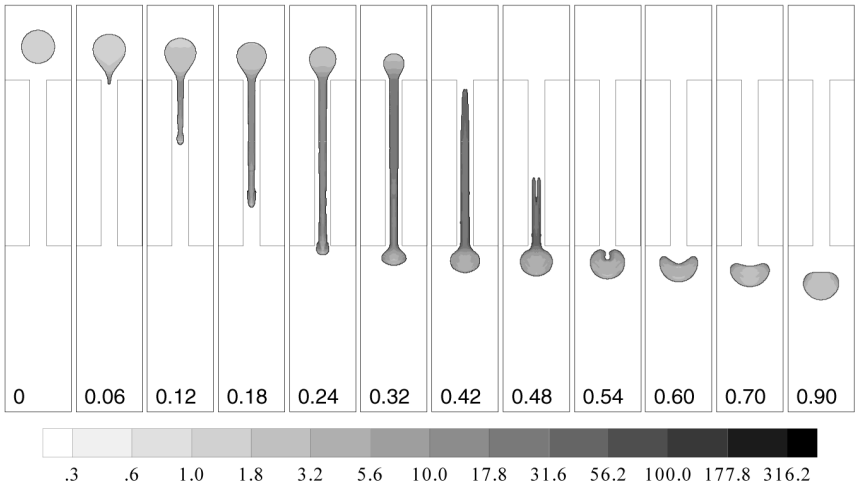
Figure 1: A comparison of experimental and simulation images for the pendant drop experiment. Relative times between the images are indicated.

using a mesh of 64×288 cells. Comparing the images of figure 1 shows that the algorithm captures both qualitative and quantitative features of the experiments well. In particular, the necking of the droplet at two positions, which causes the polymers to locally extend, thus preventing breakage and producing the 'bead-on-a-string' structure, is captured accurately. Experiments conducted using PEO solutions having different molecular weights and concentrations have also been accurately reproduced [13].

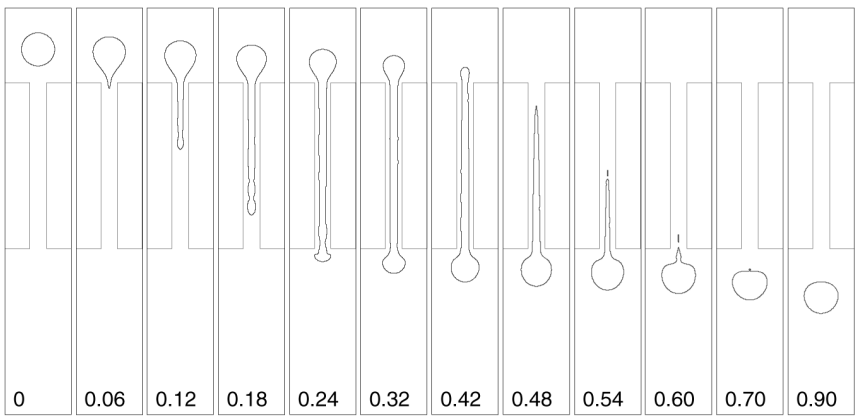
5 Results: axisymmetric contraction

The contraction problem consists of a droplet of viscoelastic fluid, entrained in a more viscous continuous phase, and passing through a $4:1$ axisymmetric contraction. All lengths are non-dimensionalised by the radius of the inlet x^* so that the contraction radius is $1/4$, the contraction length is 5 and the initial droplet diameter is 1. Further details of the geometry can be found in the related Newtonian and shear thinning drop deformation studies [7, 8, 9]. The scaling velocity u^* is taken to be the average inlet velocity, and gravitational effects are ignored. It is assumed that initially the polymers within the droplet are in a relaxed state so that $\mathsf{A} = \mathsf{I}$. A computational mesh of 64×768 cells is used.

Figure 2(a) shows the form of the viscoelastic droplet as it passes through the contraction, as well as the magnitude of the $\sqrt{\mathrm{tr}\mathsf{A}}$ that develops within the droplet: $\sqrt{\mathrm{tr}(\mathsf{A})}$ is a measure of the average length of the polymers. The parameters chosen for the simulation could represent a droplet of water and glycerol based dilute PEO solution, similar to that used in the pendant drop experiments of figure 1, entrained in a low viscosity Silicon oil, and passing through a $x^* = 100\ \mu\mathrm{m}$ contraction with an average continuous phase inlet velocity of $u^* = 3\ \mathrm{cm/s}$. This experimental



(a) Viscoelastic droplet with De = 0 .18 and $\mu_{p,d} = 1$.



(b) Equivalent Newtonian droplet.

Figure 2: Images showing how viscoelastic and Newtonian droplets deform as they pass through the $4 : 1$ axisymmetric contraction. For both cases Re $=$ 0.1, We $= 9.09 \times 10^{-3}$, $\mu_{\mathrm{d}} = 0.1$ and $\rho_{\mathrm{d}} = 1$. Each frame is annotated with its non-dimensional time, and the shading in the viscoelastic case represents $\sqrt{\mathrm{tr}(\mathsf{A})}$, a measure of the average polymer extension.

setup is feasible with current microfluidic technology. Figure 2(b) shows how an identical droplet to that of figure 2(a) would behave in the same system if the droplet contained no polymers.

The first five frames of figures 2(a) and 2(b) show the droplets entering and moving through the contraction. In the Newtonian case, the axial acceleration of

the continuous phase near the entrance to the contraction deforms the drop into an inverted 'tear' shape, with a narrow point at its leading tip. By $t = 0.012$, this tip has rounded, as both interfacial tension and drag from the surrounding continuous phase pull the tip back towards the main body of the droplet. By $t = 0.18$, this tip has become quite bulbous, with secondary interfacial waves propagating back along the extended filament towards the contraction entrance. This process of 'tip bulbing' has been observed in low viscosity Newtonian droplet contraction simulations [9].

The viscoelastic droplet behaves very similarly as it enters the contraction, but the further it progresses into the contraction, the more the polymers extend and alter its behaviour. At the entrance to the contraction, the extensional strain that the polymers experience as the fluid accelerates extends the polymers in the axial direction. This extension causes a small axial stress on the droplet, which 'blunts' the sharpness of the droplet tip at $t = 0.06$. As the droplet continues into the contraction, shear stresses, exerted by the more viscous continuous phase, extend the polymers more significantly, and transport them around the droplet. Polymer extension occurs mainly in two areas; at the leading tip, where the droplet experiences considerable extensional strain rates, and along the sides of the filament, where the droplet experiences large shear strains.

Noticeable effects of polymer extension on droplet deformation do not appear until around $t = 0.18$. At this time, the distribution of $\sqrt{\mathrm{tr}(\mathsf{A})}$ within the leading bulb of the droplet has becomes quite significant and complex, with maximum values of $\sqrt{\mathrm{tr}(\mathsf{A})}$ in this region of 40 and greater. The resulting elastic stresses cause the leading tip bulb to be more 'arrow' shaped than the Newtonian bulb, and also dampen the interfacial waves that were observed on the Newtonian droplet at this time. By $t = 0.24$, maximum $\sqrt{\mathrm{tr}(\mathsf{A})}$ values within the droplet have grown to 50. These extensions are located just behind the leading bulb of the droplet, along its interface.

At times between $t = 0.32$ and $t = 0.6$, the behaviour of the droplets differs mainly in the way in which rear of the each deforms. In the Newtonian case, the rear tip of the droplet forms a fine point, from which a small amount of fluid is shed. Fluid is shed from this tip as drag from the continuous phase, which is directed towards the contraction entrance, has a greater magnitude than interfacial tension, which pulls the tip towards the contraction exit. This behaviour has been observed in previous low viscosity Newtonian droplet deformation simulations [9].

The rear tip of the viscoelastic droplet behaves quite differently, instead forming a distinctive forked tail which leaves the contraction earlier than that of the Newtonian droplet. To understand why, we note that during these later times, the shear stresses that act on the droplet interface affect the polymers in two ways: Firstly, large shear rates caused by the interfacial shear stress extend any polymers that lie close to the interface but within the droplet fluid. These polymers are orientated in a direction that is almost tangential to the interface. A close examination of figure 2(a) at $t = 0.32$ for example shows that near the interface of the droplet, $\sqrt{\mathrm{tr}(\mathsf{A})}$ is higher than in the body of the droplet, and can reach values as large as 70 near the exit to the contraction. Secondly, the interfacial shear stress moves

droplet fluid that is adjacent to the interface backwards relative to the leading tip of the droplet, that is, towards the rear of the droplet. Thus, polymers that are within the droplet and adjacent to the interface are extended and moved towards the rear of the droplet as it progresses through the contraction.

At the rear tip, these extended polymers exert stresses on the fluid, changing the shape of the rear interface. When the rear of the droplet first enters the contraction, its shape is almost pointed. As the tip moves into the contraction however, polymers at the tip become extended and orientated parallel to the droplet interface. At the very end of the droplet, these polymers are directed slightly inwards, as the interface shape here is directed towards a single point. As these polymers are in tension, they exert an elastic stress on the fluid, which pulls the centre of the rear tip forwards, creating the inverted 'dimple' at the rear of the droplet observed at $t = 0.32$. As the flow of polymers along the droplet interface and towards the rear of the droplet continues, the dimple grows, and the forked tail that is shown at $t = 0.48$ in figure 2(a) develops. The growth of this tail is reinforced by the high centreline velocity of the continuous phase that follows the droplet through the contraction. The viscoelastic droplet exits the contraction sooner than the Newtonian droplet simply because its tail is blunt, so is shorter than the narrower Newtonian one.

Beyond the contractions, both droplets shorten and expand radially as the surrounding continuous phase fluid decelerates. The simulations predict that the fluid shed from the rear of the Newtonian droplet coalesces with the rest of the droplet at $t \approx 0.72$. As discussed in Harvie *et al.* [9] however, the timing of this behaviour may or may not be physically realistic as the film drainage that occurs between these two droplets as they coalesce is not captured by the resolution of the computational mesh. At times beyond $t = 0.7$, interfacial tension quickly reforms the Newtonian droplet into an approximately spherical steady state form.

In the viscoelastic case, the forked tail that was present on the droplet while it was within the contraction shortens and expands radially, forming the bulbous 'U' shape observed at $t = 0.54$ in figure 2(a). The droplet then moves towards a more spherical shape under the action of interfacial tension, however, as the polymers take some time to relax, the viscoelastic droplet takes longer to reach a steady state form than the Newtonian droplet does. Even at $t = 0.9$, a time at which the Newtonian droplet is almost spherical, the viscoelastic droplet still has a 'flattened' top, with polymers within it having lengths of up to 9. Simulations show that the viscoelastic droplet does not reach its steady and effectively relaxed elastic state until about $t = 1.6$.

Acknowledgement

This research was supported by the Australian Research Council Grants Scheme.

References

[1] Squires, T.M. & Quake, S.R., Microfluidics: fluid physics at the nanoliter scale. *Reviews of Modern Physics*, **77(3)**, pp. 977–1026, 2005.



[2] Boger, D.V., Viscoelastic flows through contractions. *Annual Review of Fluid Mechanics*, **19**, pp. 157–182, 1987.
[3] Singh, P. & Leal, L.G., Finite-element simulation of the start-up problem for a viscoelastic fluid in an eccentric rotating cylinder geometry using a third-order upwind scheme. *Theoretical and Computational Fluid Dynamics*, **5**, pp. 107–137, 1993.
[4] Oldroyd, J.G., On the formulation of rheological equations of state. *Proceedings of the Royal Society of London, A*, **200(1063)**, pp. 523–541, 1950.
[5] Rudman, M., A volume-tracking method for incompressible multifluid flows with large density variations. *International Journal for Numerical Methods in Fluids*, **28**, pp. 357–378, 1998.
[6] Davidson, M.R. & Cooper-White, J.J., Pendant drop formation of shear-thinning and yield stress fluids. *Applied Mathematical Modelling*, 2005. Accepted.
[7] Harvie, D.J.E., Davidson, M.R. & Cooper-White, J.J., Simulating the deformation of newtonian and non-newtonian drops through a micro-fluidic contraction. *15th Australasian Fluid Mechanics Conference*, University of Sydney: NSW, Australia, 2004.
[8] Harvie, D.J.E., Davidson, M.R., Cooper-White, J.J. & Rudman, M.J., A numerical parametric study of droplet deformation through a microfluidic contraction. *ANZIAM J*, **46(E)**, pp. C150–C166, 2005.
[9] Harvie, D.J.E., Davidson, M.R., Cooper-White, J.J. & Rudman, M.J., A parametric study of droplet deformation through a microfluidic contraction: Low viscosity Newtonian fluids. *Chemical Engineering Science*, 2005. Submitted.
[10] Davidson, M.R., Harvie, D.J.E. & Cooper-White, J.J., Flow focusing in microchannels. *ANZIAM J*, **46(E)**, pp. C47–C58, 2005.
[11] Youngs, D.L., Time-dependent multimaterial flow with large fluid distortion. *Numerical Methods for Fluid Dynamics*, eds. K. Morton & M. Baines, Academic Press, pp. 273–285, 1982.
[12] Brackbill, J.U., Kothe, D.B. & Zemach, C., A continuum method for modelling surface tension. *Journal of Computational Physics*, **100**, pp. 335–354, 1992.
[13] Davidson, M.R. & Harvie, D.J.E., Simulations of pendant drop formation of a viscoelastic liquid. *Korea-Australia Rhoelogy Journal*, 2005. Submitted.
[14] Leonard, B.P., A stable and accurate convective modelling procedure based on quadratic upstream interpolation. *Computer Methods in Applied Mechanics and Engineering*, **19**, pp. 59–98, 1979.
[15] Tirtaatmadja, V., McKinley, G.H. & Cooper-White, J.J., Drop formation and breakup of low viscosity elastic fluids: Effects of molecular weight and concentration. *Journal of Non-Newtonian Fluid Mechanics*, 2005. Accepted.



Simulation of single bubble rising in liquid using front tracking method

J. Hua & J. Lou
Institute of High Performance Computing, #01-01 The Capricorn, Singapore

Abstract

Front tracking method is improved to simulate the rising and deforming of a bubble in quiescent viscous liquid under various flow regimes. The simulation results demonstrate that the current algorithm is more robust in modelling a multi-fluid system with wider ranges of the Reynolds number ($1<Re<200$) and the Bond number ($1<Bo<200$) under a high density ratio ($\rho_l/\rho_b=1000$) and a viscosity ratio ($\mu_l/\mu_b=100$). The new front tracking algorithm is also applied to investigate bubble rising and deforming behaviour in the various flow regimes of the "air bubble-water solution" system under effects of the Reynolds number and the Bond number, which have been explored experimentally in literature. The simulation results are compared with the experiments in aspects of bubble shape, terminal velocity and bubble wake flow pattern. Reasonable agreements are achieved in most flow regimes.
Keywords: bubble rising, front tracking method, numerical simulation, multiphase flow.

1 Introduction

Multi-fluid systems play an important role in many natural and industrial processes such as combustion / chemical reacting, petroleum refining, boiling, etc. The rising of single bubble driven by buoyancy force in viscous liquid is one of such typical multi-fluid systems. A comprehensive understanding of the flow behaviour and mechanism of such multi-fluid systems in full flow regimes has not been well developed so far.

In the present work, front tracking method, a hybrid approach of front capturing and tracking technique proposed by Unverdi and Tryggvason [1] for



WIT Transactions on Engineering Sciences, Vol 52, © 2006 WIT Press
www.witpress.com, ISSN 1743-3533 (on-line)
doi:10.2495/AFM06009

modelling multi-fluid system was examined. In this method, a stationary, fixed grid is used for the fluid flow, and a set of adaptive elements on the front is used to represent the interface. A single set of governing equations (Navier-Stokes equation and continuity equation) for the whole computational domain is solved for the two phases by treating the different phases as one fluid with variable material properties. The fluid properties such as density and viscosity are calculated based on the position of the interface, and updated basing on the motion of the bubble front. Hence, this method could avoid numerical diffusion, and capture sharp interfaces. Interfacial source terms such as surface tension are computed on the front and transferred to the fixed background grid using a δ (dirac-delta) distribution function from the interface between the phases. The front tracking method has been applied to various interfacial flow problems [1]. It has been noted that the capability of conventional algorithm is limited to lower density ratios, lower Reynolds numbers and lower Bond numbers [2]. A further extension of this method is proposed in this paper to make it applicable to wider flow regimes.

As benchmarking tests, the new algorithm is used to model single air bubble rising in viscous liquid, which actually has been treated as typical cases to validate numerical methods for multiphase/interfacial flows. Most of previous validation works are performed under conditions of lower density ratio, the simulation results are validated against experimental observations about bubble shape under some typical flow regimes [3, 4]. In this paper, the front tracking method is used to systematically investigate air bubble rising in water solutions under various flow regimes. The simulation results are compared with experimental results in bubble shape, terminal velocity and wake flow pattern, and good agreement can be obtained in different flow regimes.

2 Mathematical formulation and numerical method

2.1 Governing equations

In this study, we investigate the rise of a bubble in a quiescent liquid. It is normally reasonable to treat both liquid and bubble phases as incompressible fluid. Hence, the mass conservation equation on the whole domain (both fluid phases and the interface) may be expressed as,

$$\nabla \cdot \mathbf{u} = 0 \tag{1}$$

The Navier-Stokes equation, governing the momentum balance in each fluid domain and the interface, may be expressed as,

$$\frac{\partial(\rho \mathbf{u})}{\partial t} + \nabla \cdot \rho \mathbf{u}\mathbf{u} = -\nabla p + \nabla \cdot [\mu(\nabla \mathbf{u} + \nabla^T \mathbf{u})] + \sigma \kappa \, \mathbf{n} \, \delta(\mathbf{x} - \mathbf{x}_f) + (\rho - \rho_l)\mathbf{g} \tag{2}$$

where, p is the pressure in the fluid domain, σ is the surface tension, κ is the curvature of the interface. $\delta(\mathbf{x} - \mathbf{x}_f)$ is a delta function that is zero everywhere except at the interface, i.e., at $\mathbf{x} = \mathbf{x}_f$. $\mathbf{g}$ is the gravitational acceleration, and

subscript f refers the front / interface. ρ refers the density of fluid, and ρ_l the density of liquid phase.

We introduce the following dimensionless characteristic variables,

$$x^* = \frac{x}{D};\ u^* = \frac{u}{(gD)^{1/2}};\ \tau^* = \frac{t}{D^{1/2}g^{-1/2}};\ \rho^* = \frac{\rho}{\rho_l};\ p^* = \frac{p}{\rho_l g D};\ \mu^* = \frac{\mu}{\mu_l};\ \kappa^* = \frac{\kappa}{D^{-1}}.$$

where D is the effective diameter of a bubble and defined as $D = (6V_b/\pi)^{1/3}$ and V_b is the bubble volume. The subscripts l and b stand for the liquid and gas bubble phases, respectively. So, the non-dimensional Navier-Stokes equation may be re-expressed as,

$$\frac{\partial(\rho\,\mathbf{u})}{\partial t} + \nabla\cdot\rho\,\mathbf{u}\,\mathbf{u} = -\nabla p + \frac{1}{\mathrm{Re}}\nabla\cdot[\mu(\nabla\mathbf{u} + \nabla^T\mathbf{u})] + \frac{1}{\mathrm{Bo}}\kappa\,\mathbf{n}\,\delta(\mathbf{x}-\mathbf{x}_f) + (\rho-1)\mathbf{g}, \quad (3)$$

in which the superscript * is omitted for convenience, while the non-dimensional Reynolds number, Bond number (also known as Eotvos number) and Morton number are defined as following,

$$\mathrm{Re}^* = \frac{\rho_l g^{1/2} D^{3/2}}{\mu_l};\ \mathrm{Bo}^* = \frac{\rho_l g D^2}{\sigma};$$

In the experimental work [5], the following dimensionless parameters, Morton (M) and Reynolds numbers (Re), are also used to characterise the fluid flow,

$$\mathrm{Re} = \frac{\rho_l D U_\infty}{\mu_l};\ \mathrm{M} = \frac{g\mu_l^4}{\rho_l\sigma^3} = \frac{\mathrm{Bo}^3}{\mathrm{Re}^4}.$$

2.2 Treatment of the discontinuities across the front

The novelty of the front tacking method proposed by Unverdi and Tryggvason [1] is that the front is considered to have a finite thickness of the order of the mesh size instead of zero thickness. In the transition zone around the interface, the fluid properties change smoothly and continuously from the value on one side of the interface to the value on the other side. The material property fields over whole domain may be reconstructed using an indicator function $I(\mathbf{x},t)$, which has the value of one in the bubble gas phase and zero in the liquid phase at a given time t.

$$b(\mathbf{x},t) = b_l + (b_b - b_l)I(\mathbf{x},t)\ ; \qquad I(\mathbf{x},t) = \int_{\Omega(t)} \delta(\mathbf{x}-\mathbf{x}')d\mathbf{v}' \qquad (4)$$

in which b stands for either fluid density or viscosity. The indicator function can be written in the form of an integral over the whole domain $\Omega(t)$ bounded by the phase interface $\Gamma(t)$. $\delta(\mathbf{x}-\mathbf{x}')$ is a delta function that has a value of one where $\mathbf{x}' = \mathbf{x}$ and zero everywhere else. In this study, the delta function is

approximated by the following distribution function $D(\mathbf{x})$ suggested by Peskin [6] are used for a two-dimensional grid system,

$$D(\mathbf{x}-\mathbf{x}_f)=\begin{cases}(4h)^{-2}\prod_{i=1}^{2}\left(1+\cos\left(\frac{\pi}{2h}\left|\mathbf{x}-\mathbf{x}_f\right|\right)\right), & \text{if}\left|\mathbf{x}-\mathbf{x}_f\right|<2\text{h}\\ 0, & \text{otherwise.}\end{cases} \tag{5}$$

where h is the background mesh grid size. The distribution function defines the fraction of the interface quantity can be distributed to nearby grid point across the artificial thickness of the front.

2.3 Numerical method

Projection method for the integration of the Navier-Stokes equations (3) was used in the previous works of Unverdi and Tryggvason [1]. The difficulties in solving the above pressure equation have been reported. For example, a large density ratio may lead to a problem in convergence [1, 2]. In order to overcome the difficulties in solving the pressure equation, an alternative approach is implemented in the present work. Here, the coupling fluid velocity and pressure is updated by solving the momentum equations and continuity equation using SIMPLE scheme [7], and simulation process is more robust even in case of large density ratio because of the semi-implicit solving approach. In the multi-fluid system, due to density jump over the phase interface, mass flux conservation in the control volume crossing the front interface is not valid. Hence, volume flux conservation is adopted to modify the SIMPLE algorithm. Based on this approach, SIMPLE algorithm is used to calculate the correction value of pressure and velocity after solving the momentum equation.

2.4 Front tracking

Since the fluid velocity is updated on the fixed grid, the node moving velocity on the front should be computed by interpolating from the fixed grid to ensure that the front moves at the same velocity as the surrounding fluids. In section 2.2, the distribution function used to spread the fluid property jump to the fixed points nearby the interface was discussed. Similarly, this function can also be used to interpolate field variables from the fixed background grid to the front using the following equation,

$$\mathbf{u}_f=\sum D(\mathbf{x}_f-\mathbf{x})\mathbf{u}(\mathbf{x}) \tag{6}$$

Then, the front is advected along its normal direction in a Lagrangian fashion,

$$\mathbf{x}_f^{\,n+1}-\mathbf{x}_f^{\,n}=\Delta t\ \mathbf{u}_f\cdot\mathbf{n} \tag{7}$$

After the position of the front is updated, the front elements should be adapted to maintain the element quality.

2.5 Solution procedure

With appropriate initial conditions for the fluid flow and interface shape, the solution algorithm proceeds iteratively through the following steps:

(1) Using the fluid velocity field ($\mathbf{u}^n$) and the interface position ($\mathbf{x}_f{}^n$), the moving velocity of the front marker points ($\mathbf{u}_f{}^n$) is computed using equation (6).
(2) Using the estimated normal interface velocity, the front is advected to the new position ($\mathbf{x}_f{}^{n+1}$). Subsequently, the elements, representing the front, are examined for adaptation and topology change.
(3) At the new interface positions, the redistribution of the interface property is performed with the reconstructed indicator function $I(\mathbf{x}_f{}^{n+1})$. Hence, new fluid property filed such as density (ρ^{n+1}), viscosity (μ^{n+1}), as well as the surface tension ($\mathbf{F}_{st}{}^{n+1}$), are obtained
(4) With appropriate wall boundary conditions, the momentum equation and mass continuity equation can be solved using the modified SIMPLE algorithm. This leads to update fluid velocity ($\mathbf{u}^{n+1}$) and pressure (p^{n+1}).
(5) Repeat the solution steps from (1) to (4) for the next time step calculation.

3 Results and discussion

3.1 Experimental observation of terminal bubble shape and rising velocity

Experimental studies on the rise of single bubble in quiescent liquid have been reported in the literature [5, 8]. The terminal bubble shapes vary greatly in different flow regimes as a function of the non-dimensional parameters such as Eotvos number (Bond number), Reynolds number and Morton number. The terminal shapes of single bubble rising in quiescent liquid under a range of Reynolds and Bound numbers ($\mathrm{Re} < 200, \mathrm{Bo} < 200$) were shown in Figure 1. In general, the rising bubbles have axisymmetric shapes when the Reynolds and Bond numbers are not too higher ($\mathrm{Re} < 200, \mathrm{Bo} < 200$). Hence, the single bubble rising in quiescent liquid under such flow regimes, which produce axisymmetric bubbles, could be simulated using the front tracking method in an axisymmetric co-ordinate system.

3.2 The effect of Reynolds and Bond numbers on the bubble shape

The simulation predicted bubble shapes in a wide range of Reynolds and Bond numbers are summarised in Figure 2. In the regimes of low Reynolds and Bond numbers ($\mathrm{Re}^* < 1$ and $\mathrm{Bo}^* < 5$), the bubbles remain spherical while they are rising in the liquid. With a slight increase in Reynolds number ($\mathrm{Re}^* = 10$), the bubble shape still remains spherical for low Bond number, where surface tension is higher. On the other end of high Bond numbers, the bubble bottom becomes flat or slightly dimpled. With the further increases in Reynolds number ($10 < \mathrm{Re}^* < 20$) and Bond number ($5 < \mathrm{Bo}^* < 20$), bubbles in the shapes of

elliptic/oblate ellipsoid are observed. With further increase in Reynolds number ($100 < \mathrm{Re}^* < 200$) and Bond number ($20 < \mathrm{Bo}^* < 100$), the bubble shapes range from highly deformed elliptical-cap at lower Reynolds number regime to the spherical-cap bubble at higher Reynolds numbers ($50 < \mathrm{Re}^* < 100$). As the bond number increases further ($100 < \mathrm{Bo}^* < 200$), skirt bubbles are formed at higher Reynolds numbers ($20 < \mathrm{Re}^* < 100$). When the Bond number is increased to the range of $100 < \mathrm{Bo}^* < 200$ and Reynolds number to the range $100 < \mathrm{Re}^* < 200$, toroidal bubbles are observed. From the simulation results, presented here, it can be concluded the current modelling method is robust enough to reasonably predict the various bubble shapes under wider flow regimes.

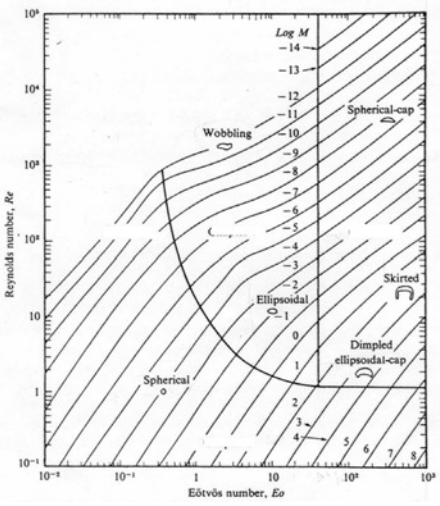


Figure 1: Bubble shapes under difference flow regimes (extracted from [8]).

Parameters		Bo^*					
		5	10	20	50	100	200
Re^*	1						
	10						
	20						
	100						
	200						

Figure 2: The predicted bubble shapes under various Reynolds and Bond numbers.

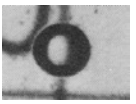
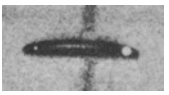
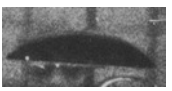
Test Case	Experiments		Simulations	
	Test condition	Observed bubble terminal shape	Predicted bubble Terminal Shape	Modelling conditions
TS1	E = 8.67 M = 711 Re= 0.078			Bo = 8.67 Re*= 0.979 U* = 0.069 Re,c=0.0675
TS2	E = 32.2 M = 8.2×10^{-4} Re= 55.3			Bo = 32.2 Re*= 79.88 U* = 0.663 Re,c=52.96
TS3	E = 243 M = 266 Re= 7.77			Bo = 243 Re*= 15.24 U* = 0.551 Re,c=8.39
TS4	E = 115 M = 4.63×10^{-3} Re= 94.0			Bo = 115 Re*= 134.6 U* = 0.659 Re,c=88.70
TS5	E=641 M=43.1 Re=30.3			Bo = 641 Re*= 49.72 U* = 0.602 Re,c=29.93

Figure 3: Comparison of terminal bubble shapes and rising speeds predicted by simulation and observed experiments.

3.3 Comparison of terminal bubble shapes

Detail comparison of the bubble shapes and terminal velocity is also necessary to understand the accuracy of the numerical predictions. Figure 3 compares the terminal bubble shapes and rising speeds obtained from experiments and simulations under various flow conditions. Typical bubble shapes (spherical, ellipsoid, ellipsoid-cap, spherical-cap and skirt bubbles) formed in different regimes can be predicted accordingly through simulations. The similarity of bubble shapes predicted in the simulations and observed in experiments is quite reasonable. For example, the simulation results on predicted bubble shape presented in Figure 3 shows that the bubble base is dimples or indented at the intermediate Reynolds number ($10 < \mathrm{Re}^* < 100$) and relatively high Bond number ($20 < \mathrm{Bo}^* < 50$). The indentation is also clearly visible in bubble photographs shown in cases TS3 and TS4, where the upper indentation may be seen near the axis of bubbles. At the rim of bubble, the different refractive indices of the gas and the liquid prevent us from seeing how the indentation joins the outer surface of the bubble. If taken this effect into consideration, the simulation predicted terminal bubble shapes agree well with experimental observation for the most study cases.

The terminal bubble velocity is another important indicator to quantitatively evaluate the difference between the experimental and simulations. Based on the parameters given in the experiments, we can derive out the dimensionless parameters ($\mathrm{Re}^*, \mathrm{Bo}^*, \rho_l/\rho_b, \mu_l/\mu_b$) to perform simulations. The simulation can predict the terminal bubble rising velocity (U^*). Actually, based on this dimensionless velocity, the dimensional terminal bubble velocity U_∞ can be calculated as $U^* \cdot gD^{1/2}$, and the dimensional terminal bubble velocity based Reynolds number ($\mathrm{Re,c}$) predicted in simulation can be calculated as $\mathrm{Re,c} = \mathrm{Re}^* \cdot U^*$. The comparison of the Reynolds numbers for the experiment (Re) and simulation cases ($\mathrm{Re,c}$) is also shown in Figure 3. The results from simulation prediction agree with those of experiment with very well within 10% difference.

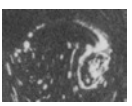
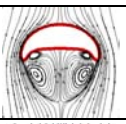
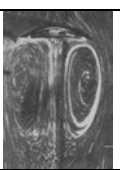
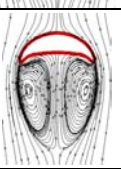
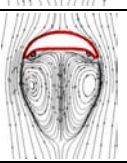
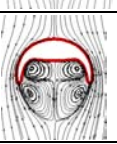
Test Case	Experiments		Simulations	
	Test conditions	Observed terminal bubble wake	Predicted terminal bubble wake	Modelling conditions
TW1	E=96.2 M=0.962 Re=18.2			Bo*=96.2 Re*=31.0
TW2	E=94.3 M=4.85×10^{-3} Re=77.9			Bo*=94.3 Re*=116.3
TW3	E=114 M=4.85×10^{-3} Re=91.6			Bo*=114 Re*=134.11 Re,c=
TW4	E=292 M=26.7 Re=22.1			Bo*=292 Re*=31.07

Figure 4: Comparison of bubble wake predicted by simulation and observed in experiments.

3.4 Comparison of bubble wake flow patterns

The existence of a closed toroidal wake has been observed in experiments [5] through the flow visualisation with the H_2 tracers. Wake flow circulation patterns predicted by the simulation agree well with the observations in experimental as shown in Figure 4. The wake circulation within the bubble base

indentation is clearly shown in the case TW1 by the photograph, where the trace track disappears behind the rim of the bubble. The similar wake circulation pattern is revealed in the simulation. Actually, the simulation show that a second wake circulation occurs just behind the bubble rim. This may be the reason that the bubble photo of TW1 has some bright spots at outside of bubble rim. The second circulation in the skirt bubble wake becomes much clear from the simulation. The photo for the skirt bubble wake (TW4) does have much large bright spot just underneath the bubble. As the bubble size increase (Reynolds number increases), the wake volume increase as well, the wake seems to be torn away from the bubble (TW2 and TW3). In this case, the second bubble wake circulation disappears, and the bubble base indentation becomes smaller.

Compared to the experimental studies [5] on the rising bubble shapes in liquid within different flow regimes, the bubble shapes predicted using the present modelling approach are in reasonable agreement. Most of the previous numerical studies on bubble rising in liquid are limited to certain regimes where the bubble shape deformation is minimal. For example, in the work of [1], the bubble rise was simulated in the regimes of low Reynolds or low Bond numbers. The present work extends the capability to simulate the bubble rise and deformation for a wider flow regime.

4 Conclusions

A front tracking method for modelling two-phase fluid systems has been examined, improved and validated for much wider flow regimes. The new algorithm adopted the treatment of the interface as finite thickness as proposed by Tryggvason et al. The fluid properties (density, viscosity and surface tension) were varied smoothly over the interface, and updated with the new interface position. The interface is advected using the front marker velocities that are interpolated from the velocity field in the fixed grid. The front mesh size is adapted to match the background mesh size due to it variation in front moving and deforming, and the front mesh position is corrected to conserve the front inner volume. The velocity field has been solved implicitly with the finite volume method over the fixed grid using the improved SIMPLE algorithm, which keeps the conservation of volume flux. The newly proposed algorithm is applied to simulate the rise of single bubble in a viscous liquid. The bubble shapes and velocity in a wider flow regime are studied as a function of the non–dimensional parameters such as Reynolds number, Bond number, density ratio and viscosity ratio. The comparison of simulations with the available experiments shows satisfactory agreements in terminal bubble shape, velocity and wake flow pattern.

References

[1] Unverdi, S. O. & Tryggvason, G. A front-tracking method for viscous, incompressible, multi-fluid flows. *J. Comput. Phys.* 100, 25-37, 1992.



[2] Bunner, B. & Tryggvason, G. Dynamics of homogenous bubbly flows. Part 1. Rise velocity and microstructure of the bubbles. *J. Fluid Mech.* 466, 17-52, 2002.
[3] Chen, L., Garimella, S. V., Reizes, J. A. & Leonardi, E., The development of a bubble rising in a viscous liquid. *J. of Fluid Mech*. 387, 61-96, 1999.
[4] Ohta, M., Imura, T., Yoshida, Y. & Sussman M. A computational study of the effect of initial bubble conditions on the motion of a gas bubble rising in viscous liquids. *Intl. J. of Multiphase flow* 31, 223-237, 2005.
[5] Bhaga, D. & Weber, M. E. Bubbles in viscous liquid: shapes, wakes and velocities. *J. Fluid Mech*. 105, 61-85, 1981.
[6] Peskin, C.S. & Printz, B.F. Improved volume conservation in the computation of flows with immersed boundaries, *J. Comput. Phys*. 105, 33-46, 1993.
[7] Patankar, S.V. *Numerical heat transfer and fluid flow*. Hemisphere, 1980.
[8] Clift, R., Grace, J. R. & Weber, M. E. *Bubbles, Drops, and Particles*. Academic Press, 1978.



Section 2
Experimental versus simulation methods

This page intentionally left blank

Pilot simulation of the temperature field of a continuous casting

J. Stetina[1], F. Kavicka[1], B. Sekanina[1], J. Dobrovska[2] & J. Heger[3]
[1]*Faculty of Mechanical Engineering,*
Brno University of Technology, Czech Republic
[2]*VŠB - Technical University of Ostrava, Czech Republic*
[3]*ALSTOM Power Technology Centre, Leicester, U.K.*

Abstract

Solidification and cooling of a continuously cast steel billet is a very complicated problem of transient heat and mass transfer. The solving of such a problem is impossible without a numerical model of the temperature field, not only of the concasting itself while it is being processed through the caster but of the mold as well. This process is described by the Fourier-Kirchhoff equation. An original 3D numerical off-line model of the temperature field of a caster has been developed. It has graphical input and output - automatic generation of the net and plotting of temperature fields in the form of color iso-therms and iso-zones, and temperature-time curves for any point of the system being investigated. This numerical model is capable of simulating the temperature field of a caster as a whole, or any of its parts. Experimental research and data acquisition have to be conducted simultaneously with the numerical computation—not only to confront it with the actual numerical model, but also to make it more accurate throughout the process. After computation, it is possible to obtain the temperatures at each node of the network, and at each time of the process. The utilization of the numerical model of solidification and cooling of a concasting plays an indispensable role in practice. The potential change of technology—on the basis of computation—is constantly guided by the effort to optimize, i.e. to maximize the quality of the process.
Keywords: concasting, solidification, temperature field, numerical model.



WIT Transactions on Engineering Sciences, Vol 52, © 2006 WIT Press
www.witpress.com, ISSN 1743-3533 (on-line)
doi:10.2495/AFM06010

1 A numerical model

Solidification and cooling of a casting and simultaneous heating of the mold is, from the point of view of heat transfer, a case of transient spatial, or 3D, heat and mass transfer in a system comprising the casting, mold and surroundings. This is a case of classical i.e. gravitational pouring. If mass transfer is not taken into account, and conduction is considered as the most important form of heat transfer, then the problem can be reduced to Fourier's partial differential equation.

$$c_v \frac{\partial T}{\partial t} = \frac{\partial}{\partial x}\left(k \frac{\partial T}{\partial x} \right) + \frac{\partial}{\partial y}\left(k \frac{\partial T}{\partial x} \right) + \frac{\partial T}{\partial z}\left(k \frac{\partial T}{\partial z} \right) + Q_{source} \tag{1}$$

In the case of continuous pouring, it is necessary to investigate the solidification and cooling of the concasting and the heating of the crystallizer. The 3D transient temperature field of a concasting, passing through a CCM (through the zones of primary, secondary, and tertiary cooling) in the direction of the z-axis at a shift rate of w_z, is described by the Fourier-Kirchhoff equation.

$$c_v \left(\frac{\partial T}{\partial t} + w_z \frac{\partial T}{\partial z} \right) = \frac{\partial}{\partial x}\left(k \frac{\partial T}{\partial x} \right) + \frac{\partial}{\partial y}\left(k \frac{\partial T}{\partial x} \right) + \frac{\partial T}{\partial z}\left(k \frac{\partial T}{\partial z} \right) + Q_{source} \tag{2}$$

In order to describe the temperature field of a concasting in the liquid phase, in the mushy zone, and in the solid phase, it is necessary to adapt this equation. In this case, it is necessary to introduce the specific volume enthalpy, which is dependent on temperature ($i_v = c_v.T$). The specific volume heat capacity c and conductivity k are also functions of temperature. Equation (2) then transforms to

$$\frac{\partial i_v}{\partial t} + w_z \frac{\partial I}{\partial z} = \frac{\partial}{\partial x}\left(k \frac{\partial T}{\partial x} \right) + \frac{\partial}{\partial y}\left(k \frac{\partial T}{\partial x} \right) + \frac{\partial T}{\partial z}\left(k \frac{\partial T}{\partial z} \right) \tag{3}$$

The 3D transient temperature field of the crystallizer and frame, in which primary cooling takes place, is described by the Fourier equation (1) without the member $w_z(\partial T/\partial z)$. Figure 1 illustrates the thermal balance of an elementary volume (general nodal point i,j,k). The introduced unitary heat conductivities and heat flows in the directions of all main axes are indicated here too. The unitary heat conductivity in the direction of the z-axis is described by

$$VZ_{i,j,k} = k(T)\frac{S_z}{\Delta z} \qquad \text{or} \qquad VZ_{i,j,k-1} = k(T)\frac{S_z}{\Delta z} \tag{4}$$

The heat flows through the general nodal point (i,j,k) in the z-direction are described by the following equations

$$QZ1_{i,j} = VZ_{i,j,k}(T^{(\tau)}_{i,j,k-1} - T^{(\tau)}_{i,j,k}) \tag{5}$$

$$QZ_{i,j} = VZ_{i,j,k+1}(T^{(\tau)}_{i,j,k+1} - T^{(\tau)}_{i,j,k}) \tag{6}$$

The temperature in the general nodal point of the concasting and the frame, in the course of a time step of $\Delta\tau$, is expressed by

$$T_{i,j,k}^{(\tau+\Delta\tau)} = T_{i,j,k}^{(\tau)} + (QZ1_{i,j} + QZ_{i,j} + QY1_i + QY_i + QX1 + QX)\frac{\Delta t}{c_v.\Delta x.\Delta y.\Delta z} \quad (7)$$

The temperature in the general nodal point of the crystallizer in the course of the time step ($\Delta\tau$) is determined from the specific volume enthalpy in time $\tau + \Delta\tau$, expressed

$$i_{v_{i,j,k}}^{(\tau+\Delta\tau)} = i_{v_{i,j,k}}^{(\tau)} + (QZ1_{i,j} + QZ_{i,j} + QY1_i + QY_i + QX1 + QX)\frac{\Delta t}{\Delta x.\Delta y.\Delta z} \quad (8)$$

The heat flow $QZ_{i,j}$ in equation (8) is therefore given by the expression

$$QZ_{i,j} = VZ_{i,j,k}(T_{i,j,k+1}^{(\tau)} - T_{i,j,k}^{(\tau)}) - VZ_{i,j,k}\Delta z.w_z.i_{v_{i,j,k}}^{(\tau)} \quad (9)$$

The accuracy of the presented numerical model depends not only on the spatial and temporal discretization ($\Delta\tau$), but also on the accuracy with which the thermophysical properties of the material of all parts of the system are determined.

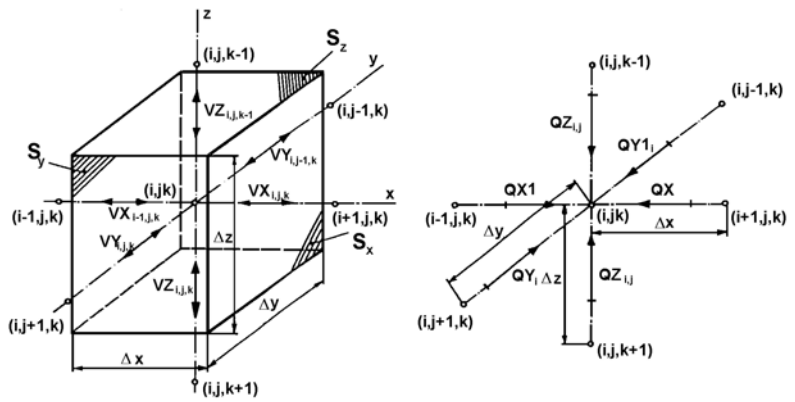


Figure 1: The thermal balance diagram of the general nodal point of the network.

The 3D model, outlined in this paper, is based on the explicit difference method. The numerical simulation of the release of latent heat of phase or structural changes is designed using the thermodynamic enthalpy function. It has a graphical input and output, i.e. automatic generation of the net (for an arbitrary shape of the crystallizer, and any profile of the concasting). The temperature fields are displayed in the form of color iso-therms, iso-zones and temperature-time curves for any point of the system being investigated.

An important part of this investigation is the measurement of the necessary quantities in the course of concasting. Experimental research enables acquisition of data in real time, which is necessary for optimization. This is ensured by the correct process procedure: real process → obtaining of input data → performing of the numerical analysis → optimization → correction of the real process. This procedure is necessary for optimization—especially when reacting to specific needs and conditions in the operation.

The program is designed to trigger the solving of sub-programs, which take over the systems generated by the pre-processing part of the program and, after completing the calculation, send files containing the results to the post-processing part. The system developed is capable of performing all necessary tasks—from the generation of the net, through the determination of the thermophysical properties and the definition of boundary conditions, to the numerical simulation of the temperature field.

2 The preparation for simulation

The thermophysical properties of steels have significant influence on the actual concasting process, and on the accuracy of its numerical simulation and optimization. The determination of these properties often requires more time than the actual numerical calculation of the temperature fields of a continuously cast steel billet. The influence of individual properties should be neither under- nor over-estimated. Therefore, an analysis/parametric study of these thermophysical properties was conducted. The order of importance within the actual process and the accuracy of simulation and optimization were also determined. Individual properties, which, in some cases, were obtained from tables, and in others experimentally, were substituted by an approximation using orthogonal polynomials. The accuracy of each polynomial is dependent on the precision of individual values.

The main properties are heat conductivity λ, density ρ and specific heat capacity c, for the cast material in the liquid and in the solid state. These properties are dependent on temperature. The fourth property is latent heat of the phase change L. Latent heat of the steel phase change is about $2{,}67.10^2$ [kJ.kg^{-1}].

Furthermore, the exactness of the numerical model depends on the derivation of boundary conditions. Therefore the setting of the properties is followed by the setting of the boundary conditions, i.e. the values of the heat transfer coefficient (*HTC*) on all concasting machine (CCM) boundaries. The dependences of these coefficients on temperature and other operation parameters must also be given. The definition of boundary conditions is the most difficult part of the investigation of the thermokinetics of this process.

The boundary conditions of the numerical model of the temperature field of the concasting are defined as the heat transfer by convection (HTC). This *HTC* includes the so-called reduced convection coefficient corresponding to heat transfer by radiation.

The order of the importance of *HTC*s on each boundary has also been settled. In the system comprising the concasting and mould, the order is

1. The *HTC* at the point of contact between the concasting and mould (the influence of a cooling powder has also been included, see Figure 2).
2. The *HTC* on the lower base of the mould.
3. The *HTC* on the level of the melt and the upper base of the mould.
4. The *HTC* on the outside wall of the mould.

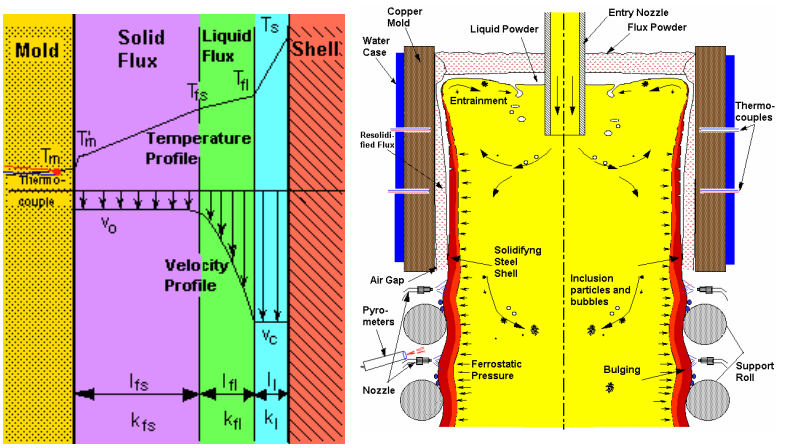


Figure 2: Model of heat transfer between shell and mold and arrangement of measurement sensors.

For example the boundary condition of the billet-mould interface depends on the thermophysical properties and the state of the casting powder, and also on the shape and size of the gap.

The only, but extremely important, coefficient, after leaving the mould, is the *HTC* on the surface of the concasting, and is mainly dependent on the temperature of the surface, the shift rate and the intensity of spraying. This paper therefore continues with a discussion on heat transfer coefficients under cooling jets, which spray the concasting in the so-called secondary-cooling zone.

Regarding the fact that on a real CCM, where there are many types of jets with various settings positioned inside a closed cage, it is practically impossible to conduct measurement of the real boundary conditions. Therefore, a laboratory device was introduced in order to measure the cooling characteristics of the jets. This experimental laboratory device simulates not only the movement, but also the surface of a billet.

This laboratory device enables the measurement of each jet separately. It comprises a steel plate mounted with 18 thermocouples heated by an external electric source. The steel plate is heated to the testing temperature, than it is cooled by a cooling jet. On the return move the jet is covered by a deflector, which enables the movement of the jet without cooling the surface. This device measures the temperatures beneath the surface of the slab–again by means of thermocouples.

The laboratory device allows the setting of:

- The jet type.
- The flow of water.
- The distance between the jet and the investigated surface.
- The surface temperature.
- The shift rate.

Based on the temperatures measured in dependence on time, the *HTC*s are calculated by an inverse task. They are then processed further using an expanded numerical and an identification model and converted to coefficients of the function *HTC(T,y,z)* (Figure 3), which expresses the *HTC* in dependence on the surface temperature, and also the position of the concasting with respect to the jet.

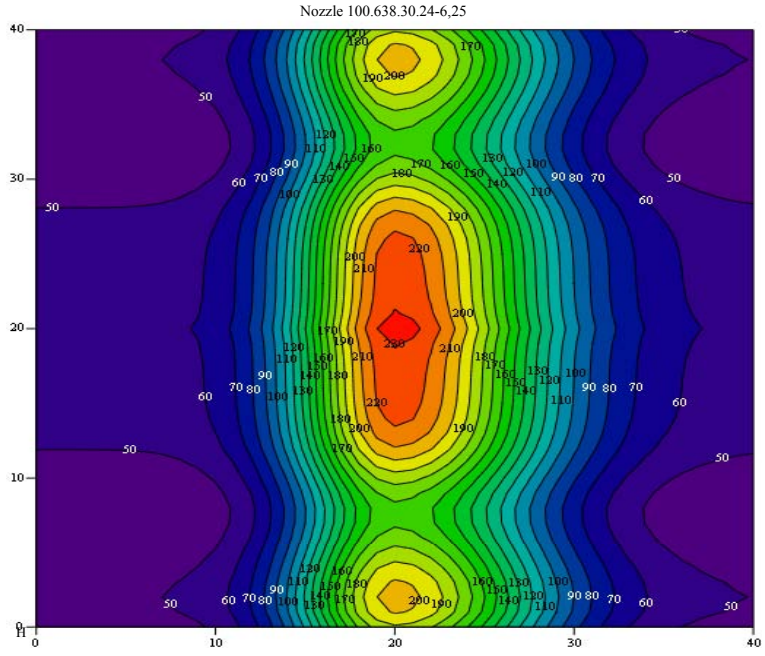


Figure 3: The HTC on the slab surface.

The experimental investigation is conducted also on an actual CCM during production. This investigation was focused mainly on the temperatures of the walls of the mould by means of thermocouples and on the surface temperatures of the slab under the mould by means of several pyrometers (see Figure 2).

3 Application of the numerical model on a concast steel billet

The numerical model described above is applied in order to investigate a concast steel billet with a square profile in any stage of the process. It has been decided

to simulate the temperature field of a 150x150 mm steel billet (30MnVS6). In order to determine the density of the mesh, the billet was analyzed in only one of its symmetrical halves, here on the right half. The selected density for the billet was 15 unit volumes in the x-direction, 30 unit volumes in the y-direction and 1000 unit volumes in the z-direction, which is the direction of a movement of the billet. The time step was selected within the range form 0.1 to 0.5 s and depends on the shift rate. A time step greater than 0.5 s does not guarantee numerically stable results. The temperature field of the billet was simulated for the shift rate 2 and 3 m/min.

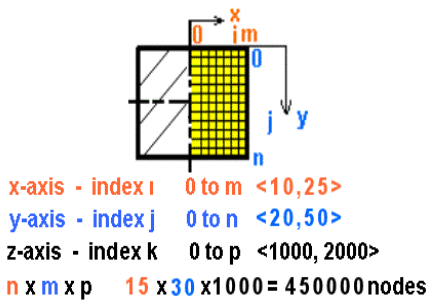


Figure 4: The billet square profile and the numerical mesh.

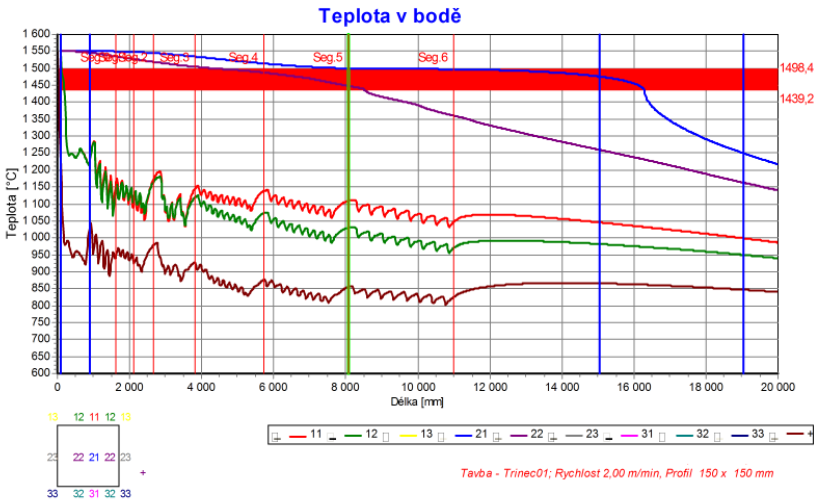


Figure 5: The temperature history in selected points of the cross-section of the billet (shift rate 2 m/min).

4 The results of a pilot calculation

After the computation it is possible to obtain the temperatures at each node of the mesh and at any time of the process. Very useful are the 2D curves. Each curve shows the temperature history at user-defined point of the cross-section of the billet. Figure 5 represents these temperature-distance curves graphically for the shift rate 2 m/min and Figure 6 for the shift rate 3 m/min.

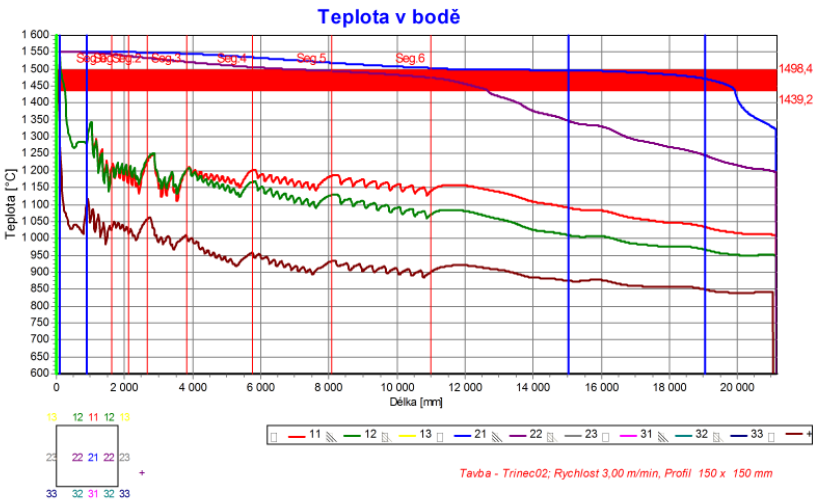


Figure 6: The temperature history in selected points of the cross-section of the billet (shift rate 3 m/min).

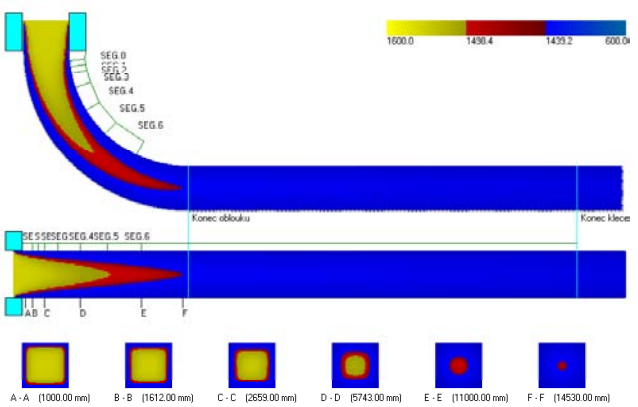


Figure 7: The temperature field of the longitudinal sections and cross sections of the billet (shift rate 2 m/min).

The software allows the user to display or print the temperature field used isotherms or isozones or both whenever necessary. Figure 7 and 8 show the temperature field in the longitudinal sections of the billet 150x150 mm for the shift rate 2 m/min and 3 m/min. by means of isozones. Both figures represent also temperature isozones of the cross sections of the billet at different distances under the level in a mould. It is possible also to see a cone of solidification and its apex, i.e. metallurgical lengths.

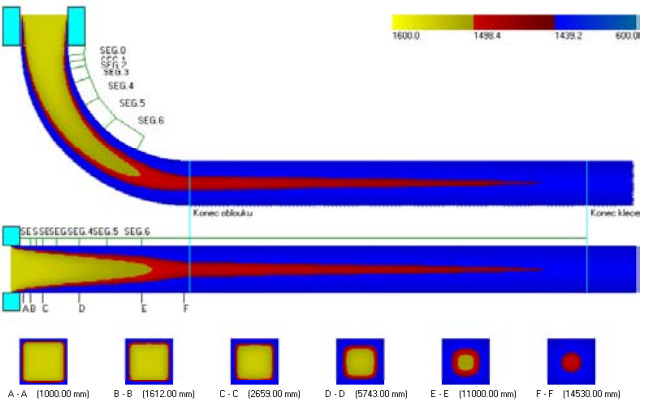


Figure 8: The temperature field of the longitudinal sections and cross sections of the billet (shift rate 3 m/min).

5 Conclusion and outlook

The presented model is a valuable computational tool and accurate simulator for investigating transient phenomena in billet-caster operations, and for developing control methods, the choice of an optimum cooling strategy to meet all quality requirements, and an assessment of the heat-energy content required for direct rolling. It should bring about quality improvement in the case of non-stable casting conditions. The on-line version will automatically set the technological parameters of the casting process in order to achieve the required quality of the cast steel.

Acknowledgement

This analysis was conducted using a program devised within the framework of the GA CR project No. 106/04/1334, 106/06/1210, 106/06/1225, CEZ MSM6198910013 and project MPO CR No. FI-IM/021.

Nomenclature

c	specific heat capacity	$[J.kg^{-1}.K^{-1}]$
c_v	specific volume heat capacity $c_v=c.\rho$	$[J.m^{-3}.K^{-1}]$
h	heat transfer coefficient	$[W.m^{-2}.K^{-1}]$
i	specific enthalpy	$[J.kg^{-1}]$
i_v	specific volume enthalpy $i_v=i.\rho$	$[J.m^{-3}]$
k	heat conductivity	$[W.m^{-1}.K^{-1}]$
w_z	shift rate	$[m.s^{-1}]$
x,y,z	axes in given directions	
Q	heat flow in given direction	[W]
Q_{SOURCE}	latent heat of the phase or structural change	$[W.m^{-3}]$
V	volume	$[m^3]$
VX,VY,VZ	unitary heat conductivity	$[W.K^{-1}]$
T	temperature	[K]
ρ	density	$[kg.m^{-3}]$
τ	time	[s]
$\Delta\tau$	time step	[s]

References

[1] Miettinen J., Louhenkilpi & Laine J., Solidification analysis package IDS. *Proceeding of General COST 512 Workshop on Modelling in Materials Science and Processing,* eds. M. Rappaz & M. Kedro: ECSC-EC-EAEC, Brussels, Luxembourg, 1996.

[2] Thomas B.G., O'Malley R.J. & Stone D.T., Measurement of temperature, solidification, and microstructure in a continuous cast thin slab. *Paper presented at Modeling of Casting, Welding and Advanced Solidification Processes VIII*: San Diego, CA, TMS, 1998.

[3] Brimacombe J. K., The Challenge of Quality in Continuous Casting *Process. Metallurgical and Materials Trans. B*, **Volume 30B**, pp. 553-566, 1999.

[4] Stetina J., Kavicka F., Dobrovska J., Camek L. & Masarik M., Optimization of a concasting technology via a dynamic solidification model of a slab caster. *Proceedings of the 5th Pacific International Conference on Advanced Materials and Processing,* Peking, China, Part 5, p.3831-3834, 2004.

[5] Stetina J., Kavicka F., Dobrovska J., Camek L. & Masarik M., Optimization of a concasting technology via a dynamic solidification model of a slab caster. *Material Science Forum,* **Vol. 475-479**, pp.3831-3834, Switzerland, 2005.

[6] Kavicka F., Stetina J., Stransky K., Sekanina B., Dobrovska J., Dobrovska V. & Heger J., Optimization of a concasting technology by two numerical models. *Proceedings of the ICAMT 2004 Third international conference on advanced manufacturing technology,* Kuala Lumpur, Malaysia, pp. 647-653, 2004.



Experimental and computational investigation of kinematic mixing in a periodically driven cavity

S. Santhanagopalan, A. P. Deshpande & S. Pushpavanam
Department of Chemical Engineering,
Indian Institute of Technology Madras, India

Abstract

Mixing of fluids is important in many industrial processes. In this paper we discuss the process of kinematic mixing in Newtonian fluid and quantify the intensity of mixing. A cavity with a periodically driven lid was chosen for the experimental and numerical analysis. It is shown that the system behavior depends on two dimensionless parameters, the geometric parameter (A_f) and the Stokes number (St). The mixing is quantified by the Planar Laser Induced Fluorescence (PLIF) technique using Rhodamine-B as the dye. Here the emitted fluorescent light intensity was related to the concentration of the dye present in the system. The extent of mixing was determined by calculating the deviation of intensity fluctuations. In addition, numerical analysis using the Particle Separation approach based on the calculation of stretch rates were done and applied to study the effect of two dimensionless parameters on mixing.
Keywords: mixing, periodically-driven cavity, Planar Laser Induced Fluorescence, stretching.

1 Introduction

Mixing is an important feature in many chemical processes. In a chemical reactor a reaction between two or more reactants can occur only when they mix with each other. Chien et al. [1] studied qualitative laminar mixing in a two-dimensional cavity under different configurations based on the motion of the walls. They used material line and blob deformation for their analysis. They found that efficiency of mixing depends strongly on the frequency of oscillation of the walls and reported an optimum value of frequency, which produces best



WIT Transactions on Engineering Sciences, Vol 52, © 2006 WIT Press
www.witpress.com, ISSN 1743-3533 (on-line)
doi:10.2495/AFM06011

mixing in a given time. They also found that the alternate periodic motion of the two walls yields chaotic mixing and demonstrated the existence of Horseshoe functions as an indication of chaotic behavior.

Leang and Ottino [2] carried out flow visualisation experiments on mixing at low Reynolds numbers. The periodic flow was induced in the cavity by means of continuous motion of the wall. They identified periodic points and reported the symmetric occurrence of these points at regular intervals.

Anderson et al. [3] found a method to locate periodic structures in three dimensional time-periodic flows and applied this to mixing in cavity flows. They numerically obtained velocity and stretching fields to identify the periodic points. They tested this method for different mixing protocols.

Chaotic mixing in a bounded three-dimensional flow at moderate Reynolds numbers was investigated by Fountain et al. [4]. The flow structures were captured using a fluorescence dye. They also compared the experimental investigations with numerical simulations and predicted the number of periodic islands.

Roberts and Mackley [5] characterised the kinematic mixing rates quantitatively by computing stretching rates using numerical techniques. The mixing rates were evaluated for two cases i) constant volumetric flow and ii) oscillatory flow in a baffled channel. The mixing rates obtained were based on using a particle separation approach as well as a line element approach. They determined the stretch rate dependency on Reynolds number as well as how the stretch rate varied over the entire flow field.

Classically mixing has been characterised using stretch rates. The repeated stretching and folding is an indication of the amount of mixing. The Lyapunov exponent of a dynamical system is analogous to the stretch rate in a fluid mechanical system. The key to effective mixing lies in producing repetitive stretching and folding.

The mixing that we discuss in this work arises primarily due to convective flow. We neglect, mixing due to diffusion or dispersion. Here we investigate the mixing of Newtonian fluid in periodically driven cavity arrangement. We experimentally quantified mixing by calculating the deviation in the intensity fluctuations. The mixing is also quantified from numerical simulations based on calculation of stretch rates.

2 Quantification of mixing from PLIF measurements

2.1 Experimental details

Fig. 1 shows a front view of the cavity (A) and the working model. The top plate (B) was designed to move to and fro along the x-direction. This was rendered possible with a guide plate (C) arrangement. The periodic motion of the top plate was achieved with a drive wheel (D) and connecting rod (E) assembly. Ball bearings (F1, F2) were used for attaching each end of the connecting rod as well as to support the drive wheel. A permanent magnet DC motor (G) was used to turn the drive wheel. The speed of the motor was controlled by a thyristor drive (H). The plate frequency was varied using the thyristor drive. The amplitude



(maximum displacement) of the top plate motion was set by the radius at which the connecting rod was attached to the drive wheel. For this several holes at different radial positions were provided in the drive wheel (D).

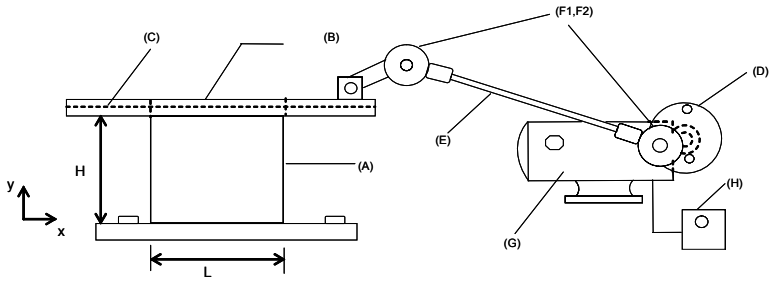


Figure 1: Schematic diagram of the experimental setup.

The dimensionless Reynolds number is defined as $Re = (U_{max}\,\rho H)/\mu$ and the Stokes number is defined as $St = \omega\rho H^2/\mu$. Here the maximum velocity of the plate ($U_{max} = A\omega$) is the velocity scale, ρ is the fluid density and μ is the viscosity of the fluid. The Strouhal number (Str) is defined as $H\omega/U_{max}$. Since in our system $U_{max} = A\omega$, Strouhal number get reduced to the amplitude factor A_f (= H/A). The penetration depth i.e. the distance up to which the momentum penetrates in the cavity in relation to the depth of the cavity is an important parameter. So depth of the cavity (H) is chosen as the length scale for our problem. The choice of Stokes number and the Amplitude factor has the advantage that we can independently study the effects of the amplitude of the plate motion by varying A_f keeping St constant and the frequency of the plate motion by varying St keeping A_f constant.

2.2 Experimental technique

The mixing process was studied by Planar Laser Induced Fluorescence (PLIF), using Rhodamine-B as the fluorescent tracer. The tracer solution of 0.5ml was injected into the cavity after the periodic state is achieved. The central plane of the mixing zone (0.096 m × 0.08 m) was illuminated using 1mm thick Nd: YAG laser sheet, of 120 mJ pulse energy and 532 nm wavelength. The light emitted from the fluorescent molecules was recorded using FlowMaster-3S charge coupled device (CCD) camera (1280 x 1024 pixels, 8 Hz) from La Vision. The acquisition rate was 4 Hz. Two dimensional single frame PLIF images were taken at different time intervals. In order to eliminate the overlapping effect of illumination and emission, a high-pass optical filter (with a cut off wavelength of 550 nm) was placed in front of the camera to obtain the fluorescence signal rejecting the laser light.

2.3 Calibration measurements

The calibrations were done by performing measurements on homogeneous solutions of known concentrations. The amount of emitted light captured on the

CCD camera is a function of the concentration of Rhodamine-B. For each concentration 50 images were taken and the average value of intensity was found. Figure 2 shows the linear relationship between the averaged fluorescent intensity and the Rhodamine-B concentration. For the extreme values of concentration C_{min} and C_{max} the intensity represented as $\overline{I}_{min}(i,j)$ and $\overline{I}_{max}(i,j)$ was calculated. The normalized fluorescence intensity fields were calculated based on,

$$G_i(i,j) = \frac{I_i(i,j) - \mathrm{I}_{\min}(i,j)}{I_{\max}(i,j) - \mathrm{I}_{\min}(i,j)}$$

The dye was injected into the cavity after the initial transients had decayed. The PLIF images were taken at different time intervals for total mixing time of 720 s.

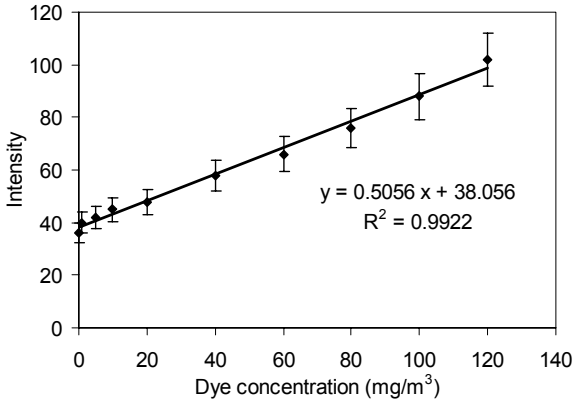


Figure 2: Fluorescence intensity as a function of dye concentration.

The extent of mixing is quantified by calculating the deviation of intensity given by,

$$D_i = \sqrt{\frac{1}{N} \sum_{i=1,\, j=1}^{N} \left(G_i(i,j) - G_{avg} \right)^2}$$

where G_i and G_{avg} denote the normalised intensity at pixel (i,j) and the maximum intensity, respectively.

2.4 Effect of dimensionless parameters on mixing

During a typical mixing run, the dye was injected after the system had an attained periodic state. Instantaneous images were taken at different time intervals and the deviation in the fluorescence intensity as a function of time for different Stokes number is plotted in Fig. 3. The larger values of the standard

deviation in the beginning of the experiments show low degree of mixing. As the time progresses the concentration of the dye decays and as a result we see decrease in the standard deviation (D_i) showing high degree of mixing. Similar trend was observed for different Amplitude factor and plotted in Fig. 4.

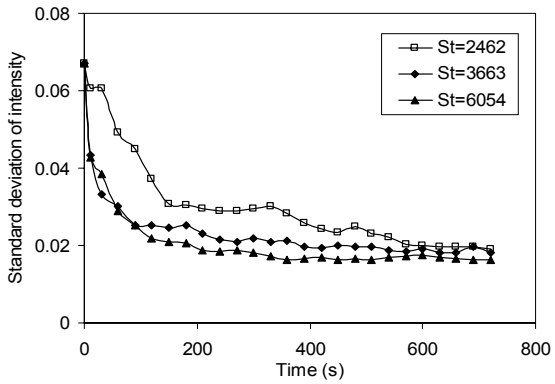


Figure 3: Standard deviation of dye intensity as a function of time for different St.

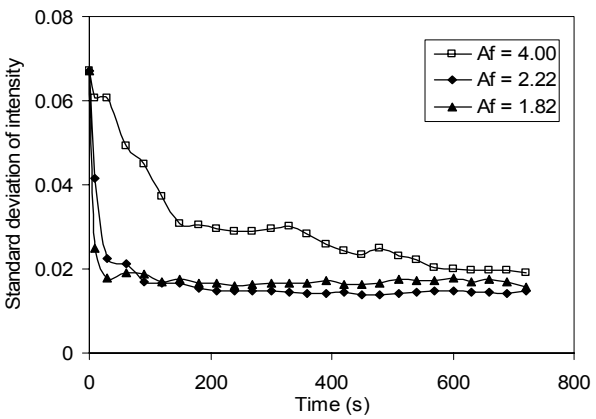


Figure 4: Standard deviation of dye intensity as a function of time for different A_f (μ = 0.00473 Pa.s).

The deviation of the intensities (D_i) after 720 s for different experimental conditions is plotted in Fig 5 and 6. The dependency of Stokes number on D_i i.e. measure of mixing, is shown in Fig. 5. The concentration of the dye decays much more rapidly at high St than at low S_t. As a result we see the increase in degree of mixing with increase in St. The dependency of A_f on D_i is shown in Fig. 6. Here we see that the degree of mixing increases with decrease in A_f.

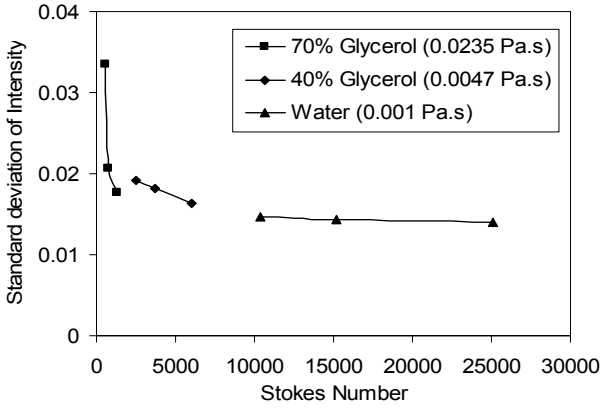


Figure 5: Standard deviation of dye intensity as a function of St.

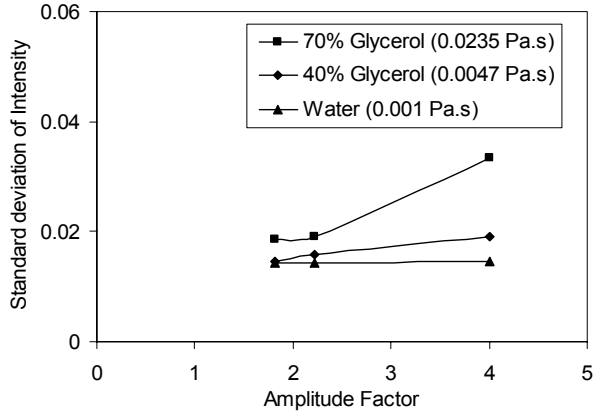


Figure 6: Standard deviation of dye intensity as a function of Af.

3 Quantification of mixing from numerical computations

3.1 Governing equations

The flow is governed by Continuity equation (1) and Navier-Strokes equation (2). The system of equations is made dimensionless so that we can study the effect of various parameters.

$$\nabla \cdot \mathbf{u} = 0 \tag{1}$$

$$\frac{\partial \mathbf{u}}{\partial t} + \frac{1}{Str}\left(\mathbf{u} \cdot \nabla \mathbf{u}\right) = \frac{-1}{Str}\left(\nabla \mathbf{p}\right) + \frac{1}{St}\nabla^2 \mathbf{u} \tag{2}$$

where $\mathbf{u} = (u, v)$ is the non-dimensional velocity and $\mathbf{p}$ the non-dimensional pressure. In the above system of equations the reference scales of the length, time, velocity and pressure were H, ω^{-1}, U_{max}, ρU^2_{max}.

3.2 Computational technique

The fluid motion was tracked by carrying out CFD simulations using Fluent 6.2. The 2-D geometry was made using Gambit 2.1. The grid independency was ensured by meshing the geometry with different spacing between the cells. The quad map type grid with 50000 cells was chosen for detailed studies. A periodic boundary condition on the top plate was imposed using an externally defined macro and the other faces of the cavity were considered as solid stationary walls. The convective terms were discretized using a second order upwind scheme. The coupled implicit time formulation was used with second order accuracy. The particle tracking was done using discrete phase model. Neutrally buoyant tracer particles were injected in the flow domain at different spatial locations, after the system had attained periodic state. The trajectory of a discrete phase particle was obtained as a function of time.

In the present study the particle properties were chosen to be the same as the fluid properties. Therefore the additional forces acting on the particle is zero and the flow is only due to the motion of the plate. The particle was tracked with the fluid flow and time step used was 0.1s. The particles were injected in the flow only after the initial transients have decayed and the flow attains periodic steady state.

3.3 Particle separation approach

A Lagrangian approach is used to characterise the mixing process by calculating the stretch rates of the fluid elements. The stretch rate of a small line between two particles can be estimated form the separation rate of adjacent particles, provided the distance between the two particles is small. We now describe a numerical method which allows us to obtain the stretch rates over the entire flow field using an efficient method. The usual algorithm involves tracking the separation of two particles which are close by initially. Once they are separated we inject a second particle close to the new position of the first particle and continue the procedure.

The particles were initially distributed uniformly in the flow domain as shown in fig. From the location of particles of the particles obtained from the particle tracking at different time instants, the distance between two specific particles is calculated at every time instant. The rate of change of distance between the two particles is assumed to be proportional to the instantaneous distance between them. Under these conditions the separation between two adjacent particles initially at a distance of l_o is given by,

$$s = \frac{1}{t} \ln \left(\frac{l_t}{l_o} \right) \tag{3}$$



where l_t is the distance separating them at a time instant t later, shown in Fig.7. This approach however yields the stretch rate at a particular point or region of the flow field. In order to average the stretch rate over the whole flow field the value of s_p for all adjacent pairs of particles is determined and their average is calculated.

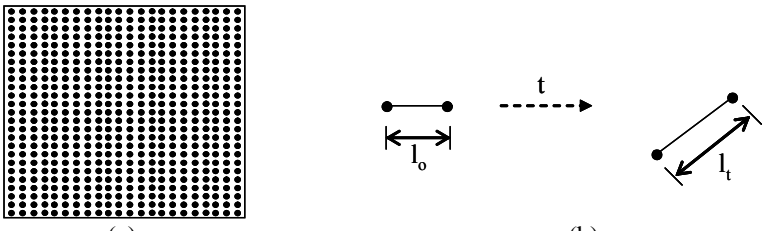


Figure 7: (a) Schematic showing the initial position of the particle array (b) Stretching of a small line between adjacent particles.

To determine the average stretching rate, 2500 particles were injected in the cavity once the initial transients had decayed and the flow attained a periodic state. These particles were initially in an array of uniform spacing i.e., 50 ×50. The motion of individual particles was tracked over a period of time. Using the instantaneous positions of the particles the distance between two particular particles was found and from this the stretch rate was calculated.

The key numerical parameter for the particle separation approach is the number of particles injected as this control the initial separation of the particles, l_o. Taking the value of S_{avg} after three periods of cycle for St = 2024, the effect of the number of particles was studied. The average stretch rate is independent of the number of particles, provided more than 2000 particles were used.

3.3 Influence of dimensionless parameters on average stretch rate

Fig. 8 shows the dependence of S_{avg} on time period for different St. The value at the end of every integral multiple of the time period is shown in the Fig. 8. The initial value is close to zero, reaches a maximum value and after this the average stretch rate begins to decrease. For further calculations of stretch rate are based on the values determined at the time period when the stretch rate is a maximum.

The variation of average stretch rate with Stokes and Amplitude factor are shown in Fig. 9 and 10. We observed that the average stretch rate increases with increase in Stokes number. Here the other parameters, amplitude and viscosity were fixed. On the other hand the average stretch rate decreases with Amplitude factor, in which case the angular frequency and viscosity were fixed. In the range of parameters under study, the amplitude of the plate motion shows strong effect on average stretch rates than the frequency, which can be observed from Fig. 9 and 10.

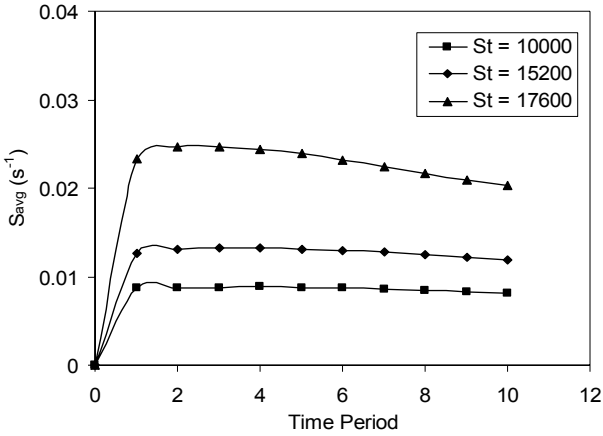


Figure 8: Average stretch rate as a function of time at different St.

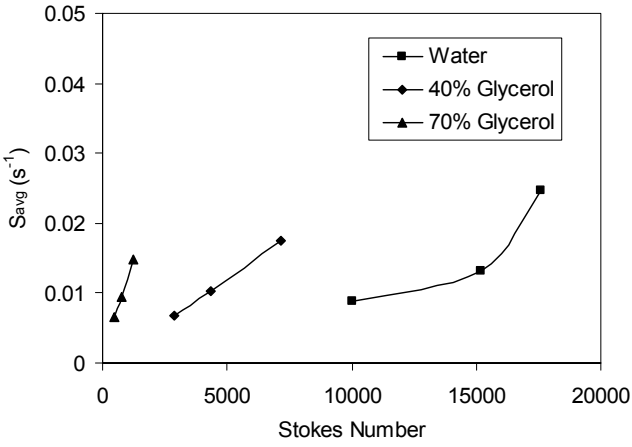


Figure 9: Variation of Average stretch rate on St.

Mixing is efficient when the flow is periodic. In order to compare the order of stretch rates obtained incase of periodic flow, it is compared with flow in a steady lid-driven cavity. To achieve this we define the plate velocity as, $v_p = v_o + A\omega \sin(\omega t)$. Here v_p is the plate velocity and v_o is the maximum plate velocity, which is independent of the frequency as well as the amplitude of plate motion. The equation reduces to $v_p = v_o$, when the amplitude of motion, A = 0 and therefore the flow becomes steady lid driven case.

The simulations were done by varying the amplitudes of motion from 0 – 0.06 m by keeping the other parameters constant. As we see from Fig. 11, the average

stretch rates are higher, when the flow is periodic which goes through a maximum. In case of steady flow the stretch rate is smaller when compared to PDC and are constant, as the particles follows closed circular path and continue to move in same path.

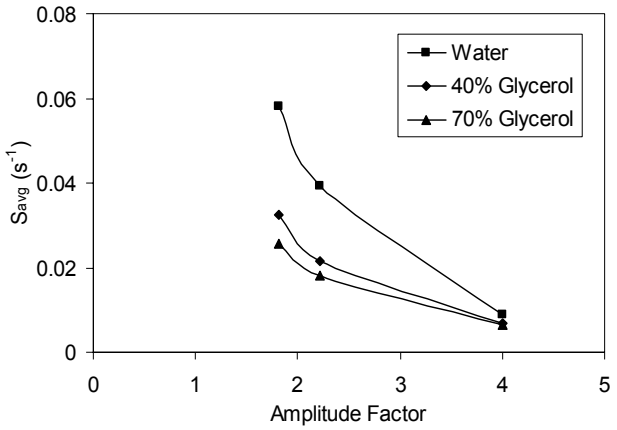


Figure 10: Variation of Average stretch rate on Af.

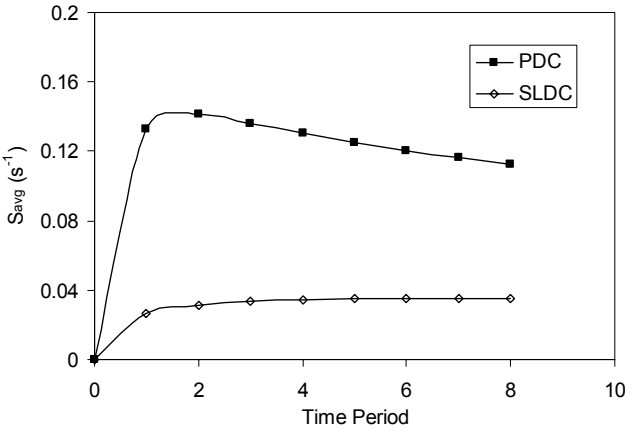


Figure 11: Comparison of average stretch rates for PDC and SLDC.

4 Conclusions

The mixing of Newtonian fluid in a periodically driven cavity has been studied experimentally using PLIF technique. Based on the deviation in intensities at every pixel, the extent of mixing at different experimental conditions was calculated and reported. The dependency of the deviation from mixing on the

dimensionless parameters was studied. The mixing rates were numerically calculated based on stretch rates using particle separation approach. The dependency of the stretch rates on the dimensionless parameters was also studied. It is found that the mixing increases with the Stokes number and decrease with Amplitude factor. The mixing rates observed in periodically-driven cavity were compared with standard lid-driven cavity and found to be more. From experiments as well as CFD simulations it can be observed that the amplitude shows strong effect on mixing than the frequency of plate motion.

References

[1] Chien, W. L., Rising, H., and Ottino, J. M., 1986 "Laminar and chaotic mixing in several cavity flows," Journal of Fluid Mechanics, **170**, pp. 355-377.

[2] C.W. Leong, J.M. Ottino, 1989 "Experiments on mixing due to chaotic advection in a cavity," Journal of Fluid Mechanics, **209**, pp. 463-499.

[3] Anderson, P. D., Galaktionov, O. S., Peters, G. W. M., Van De Vosse, F. N., and Meijer, H. E. H., 1999, " Analysis of mixing in three-dimensional time-periodic cavity flows," Journal of Non-Newtonian Mechanics, **386**, pp.149-169.

[4] Fountain, G. O., Khakhar, D. V., and Ottino. J. M., 1998, "Visualisation of three-dimensional chaos" Science, **281**, pp. 683-686.

[5] Roberts, E. P.L., Mackley, M. R., 1995, "The simulation of stretch rates for the quantitative prediction and mapping of mixing within a channel flow," Chemical Engineering Science, **50**, 3727-3746.



Computational Fluid Dynamics (CFD) use in the simulation of the death end ventilation in tunnels and galleries

J. Toraño, R. Rodríguez & I. Diego
GIMOC, Mining Engineering and Civil Works Research Group, Oviedo School of Mines, University of Oviedo, Oviedo, Spain

Abstract

In the framework of the Research Project CTM2005-00187/TECNO, "Prediction models and prevention systems in the particle atmospheric contamination in an industrial environment" of the Spanish National R+D Plan of the Ministry of Education and Science, 2004-2007 period, a CFD model has been developed to simulate air flows in tunnels and galleries, including its detailed comparison with available experimental data. Taking into account the importance of the air velocity distribution in the tunnels or galleries where there is continuous transport of particulated material by means of conveyor belts, and where PM10 or PM50 particulated material can be easily thrown in suspension, we quickly identify the necessity of studying the air behaviour using CFD software. Several models were developed using the commercial code Ansys CFX 10.0, starting from several 3D meshes of different resolutions generated using ICEM CFD 10.0. Medium complexity turbulence models were selected in order to obtain acceptable resolution times in single processor machines, as well as following advices contained in related bibliography. Zero Equation (constant turbulent eddy viscosity), k-epsilon and Spallart-Allmaras models were used, comparing their results with detailed experimental measurements obtained from the use of hot wire anemometers. Results show good agreement between the simulated data and the experimental measurements depending on the turbulence model: areas close to the tunnel end are best simulated using k-e, but areas far from the tunnel end, in the developed flow area, are best simulated using Spalart-Allmaras. As was expected the constant turbulent eddy viscosity model gave results which were not very approximated.
Keywords: death end ventilation, particulated material, CFD, turbulence.



WIT Transactions on Engineering Sciences, Vol 52, © 2006 WIT Press
www.witpress.com, ISSN 1743-3533 (on-line)
doi:10.2495/AFM06012

1 Introduction

Taking into account the importance of the velocity distribution in the ventilation of the tunnels or galleries where there is continuous transport of particulated material using conveyor belts, from which there can easily appear PM10 and PM50 airborne dust, it was clearly shown the necessity of studying the air flow behaviour through a state of the art tool, CFD or computational Fluid dynamics.

Among the hundreds of data that has to be introduced to start a CFD simulation one of the most important is the selection of the method that is going to perform the turbulence modelling. Generally speaking the model is selected depending on the technician expertise, the help of the CFD software support service, or related bibliography, [2], [3] or [7] in our case. This paper shows the use of three relative simple turbulence models that allow its future use in extensive meshes of complex geometries or multiphase modelling.

The knowledge acquired with these simulations will allow setting the bases for the subsequent simulations that will include dust behaviour. The dust movement will be checked against experimental measurements done using optical dust samplers, as was previously done by the research team that has developed this study, e.g. Toraño et al [5] and [6].

2 Measurements in an disused mine gallery

Measurements have been done in a death end gallery in a disused mine area. It is a gallery supported by a 2UA type roof support, approximately 72 meters ahead from the axis of the main gallery from it is started. Gallery is curved slightly to the right.

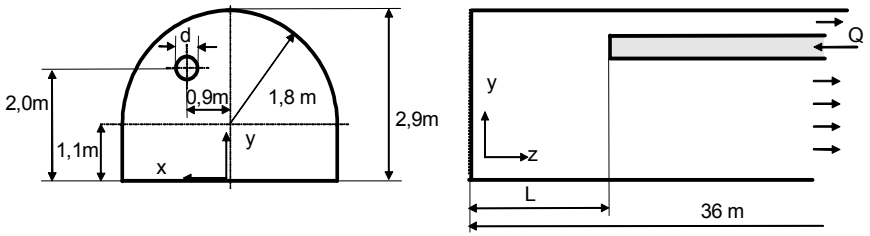


Figure 1: Draft of the disused mine gallery.

During the experiment the air was blown to the gallery end through a ventilation duct, using the power of an electric fan. The duct is flexible in its final part and goes parallel to the gallery wall. Its diameter is 600 mm and finishes its run 6 meters from the gallery end. Environmental conditions during the tests where 22-23ºC and 75-80% of humidity.

Air velocity measurements where done with a hot wire anemometer, TSI IFA 100. Two different probes were used, one omnidirectional (measures the velocity under 0,8 m/s) and a film probe (measures the velocity module within 0 to 20 m/s). There were done around 50 measurements in each one of the gallery

cross sections studied, and a total number of 16 cross sections were studied. This means a number of velocity measurement points as high as 800. Estimated precision in the velocity measurement is around +-5%.

Measured data were shown and empirically treated in the development of a PhD of the University of Oviedo, see [8].

3 CFD simulation

The CFD commercial code Ansys CFX was used to develop a simulation model that allows the comparison of the experimental results and the simulated ones. The model considers a straight gallery and a section approximately semicircular, quite similar to the one that accommodated the experimental measurements.

3.1 Geometry

The simulated gallery has an approximate cross section of 9 m^2 and an overall length of 36 m. In this simulation there has been considered a ventilation pipe of 600 mm of diameter, that guides an airflow of 3,39 m^3/s. The 3D Geometry has been done with the software Solidworks.

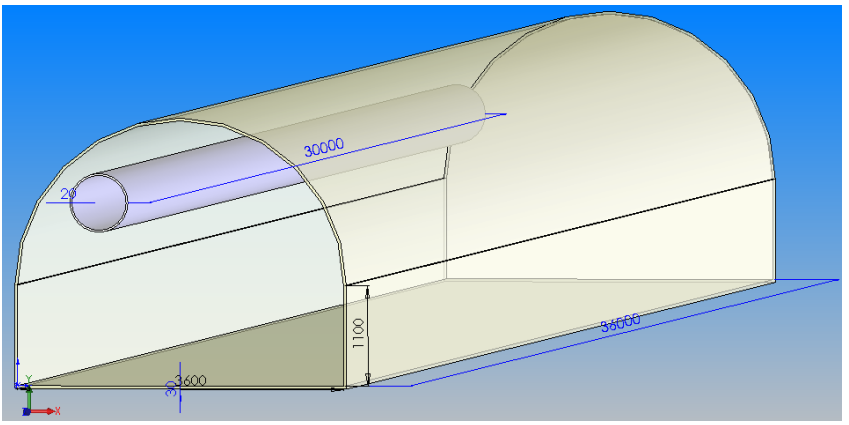


Figure 2: 3D geometry of the model.

On top of the surfaces needed to create the model, other auxiliary surfaces were created for a better subsequent meshing: one in the outlet of the gallery, the input and output covers of the ventilation pipe and an intermediate surface that will serve as divide the air in two regions with different meshing sizes.

3.2 Meshing

The meshing has been done using commercial software ANSYS ICEM CFD 10.0, importing the geometry from Solidworks through IGES format. First a geometry cleaning is done, deleting unnecessary geometry features and checking for physical incongruence.

The mesh was done using tetrahedrical and prismatic cells, and after several tests and initial CFD calculations it was seen that there were not significantly differences in the calculation using meshes over 500k elements.

The mesh was not easy to develop, even using "fool-proof" software as ICEM, due to difficulties selecting appropriate mesh sizes to solve curved surfaces and the space between the pipe and the wall.

The mesh finally used will be different depending on the model area, coarse mesh of 500 mm of tetra size far from the gallery end, a fine mesh of 250 mm of tetra size near the gallery end and three times less in the ventilation tube area.

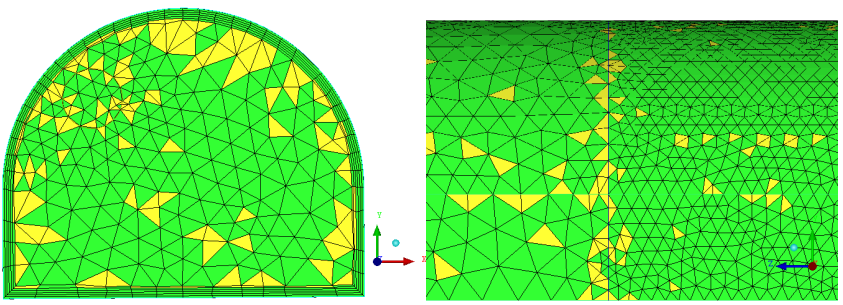


Figure 3: Meshing.

Walls will be meshed using prisms. After finishing the mesh and its optimization we finally get a mesh of 634k elements (shown in figure 3).

3.3 CFD simulation

3.3.1 Introduction

The physical characteristics of the problem are defined in CFX-Pre. Three different simulations will be done, depending on the turbulence model used: Zero equation, K-epsilon and Spallart-Allmaras. CFX offers a wide selection of turbulence models, from the quite simple Zero Equation models to LES and RANS, highly demanding in computing time and hardware requirements. The selection of these 3 more or less complex models is based on related bibliography, e.g. [2], [3] and [4].

3.3.2 Resolution conditions

Problem will be solved as stationary, with three domains separated by "domain interfaces" corresponding to the ventilation pipe, fine mesh and coarse mesh, and isothermal conditions at 23ºC

The boundary conditions used are:

- "Wall", with default characteristics and smooth roughness, located in all walls.
- "Outlet", located in the gallery air outlet, defined by a condition of "Average Static Pressure 0 atm". This air outlet could be also defined as an opening, but convergence behaviour seen with all simulations showed no recirculation presence at this plane.

- "Inlet": characterized by the velocity obtained from the theoretical operating point of the fan installed in the experiment. Turbulence will be considered "medium", intensity=5%.

Convergence is set to reach a 1E-05 level in all governing equations, which is accurate enough as per CFX support documentation.

In case of the "Zero Equation" turbulence model, and after several tests, the Eddy Length Scale is set at 1.25 m.

The Spallart-Allmaras model is experimentally implemented in CFX 10.0, and CCL, CFX Command Language, must to be used to be able to start this model, as it is not available in the CFX-Pre GUI (Graphic User Interface).

4 Results comparison

Each one of the simulations done is compared with the existent experimental data. Comparisons are resumed in two ways: first a general flow comparison and secondly a detailed one in several remarkable sections.

4.1 General view of flow

Figure 4 shows simultaneously cut planes for the velocity flow field, representing velocity contours in following planes: XY at 0.5, 8, 18 and 29 meters from the gallery end, ZX at 0.4 meters from bottom and YZ at 0.5 m from left in the outflow adventional sense. (As seen in the figure, Z is aligned with the gallery axis, Y is the vertical and X is the cross direction axis).

The airflow is mainly characterized by its turn in the middle of the studied domain, as well as its highly turbulent behaviour near the gallery end, with an area of highly separated layers.

The simplest model, the Zero Equation, shows how the air flow gets out of the tube, turns and quickly fits to the down left (as seen in figure 4) corner of the gallery, which will not leave for the complete length of the gallery. The k-epsilon model shows similar behaviour (not considering turbulence effects close to the FRENTE) up to the end of the studied domain (around 25 meters). At that distance the flow turns to the right for 4 meters and then again to the left. The same effect is seen in case of the Spallart-Allmaras model, but this turn is seen closer to the FRENTE, at 16 meters from it.

As we will see later on in the cross sections the Spallart-Allmaras is the best fit, as the experimental data section at 18 meters clearly shows the flow going by the right side of the gallery.

4.2 Detailed comparison

4.2.1 Cross sections

Data available at 200 cm from the gallery end will be compared now (see figure 5). All figures, including the experimental data show a highly negative area (blue), in the output of the tube, and a positive area (red) that indicates output flow towards the beginning of the gallery. The intermediate areas (yellows or white in B/W prints) show the area where there is a change in the sense of the flow, the separated flow.

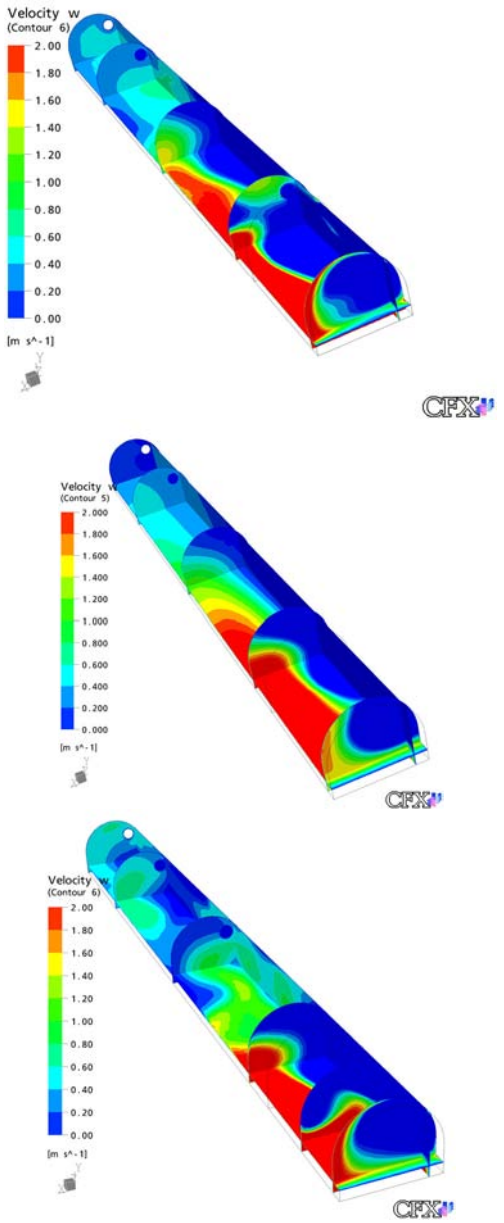


Figure 4: Velocity contours, K-E (up), Zero Equation (middle) and Spalart-Allmaras (down).

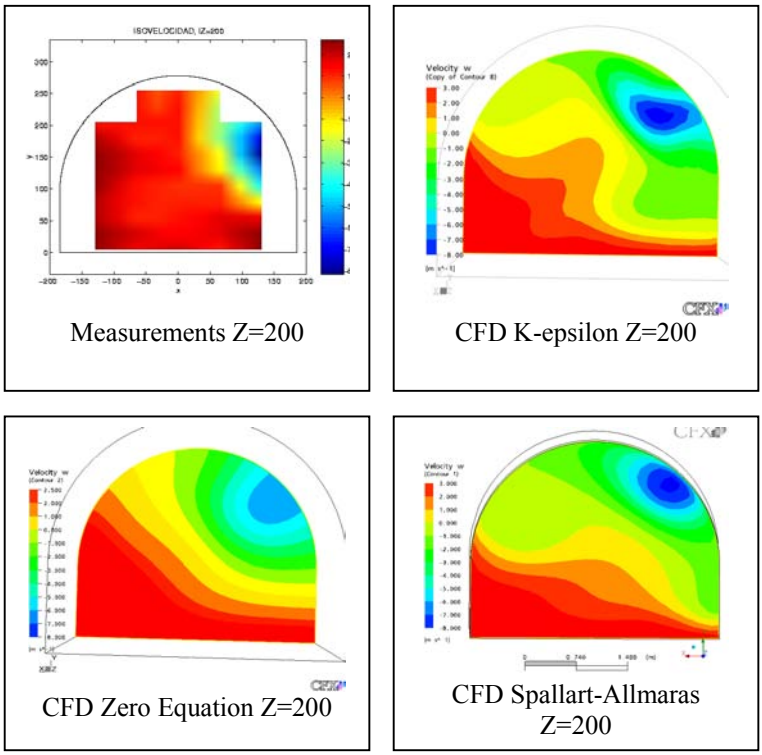


Figure 5: Velocity contours at Z=200 cm.

In all cases the left down area has positive velocities ranging from 0 to 2 m/s, occupying a wide area of the bottom. Experimental data shows this area to be very wide, best reflected by the k-epsilon model.

The area immediately in front of the tube output shows a highly negative velocity, again best simulated by the k-epsilon model.

The middle of the gallery shows an experimental velocity between 0 and 1 m/s. This area is again well predicted by the k-epsilon model.

In any case differences between k-epsilon and Spallart-Allmaras models are not important.

Figure 6 shows equivalent velocity contours in XY planes at 18 meters from gallery end. We can see in the upper left image, the experimental data, that the airflow is now fully developed and velocity values are all below 1 m/s. The output flow has displaced clearly to the right of the gallery, below the ventilation pipe, and at a medium height. Values below zero, flow towards the gallery end, only appears in the upper part of the gallery, over the ventilation tube.

The only model that predicts this effect is the Spallart-Allmaras, with a 1m/s velocity area in the middle of the gallery, clearly displaced to the right of the image, as in the reality. Both k-epsilon and Zero Equation show the flow in the

left, stuck to the wall, although k-epsilon shows a more developed flow with almost no areas with velocity below 0,1 m/s.

This effect can be also clearly seen in figure 4, analysis completed with the fact already commented that the flow turn to the right shown at 18 meters is only seen in case of the k-epsilon model at 25 meters from the gallery end.

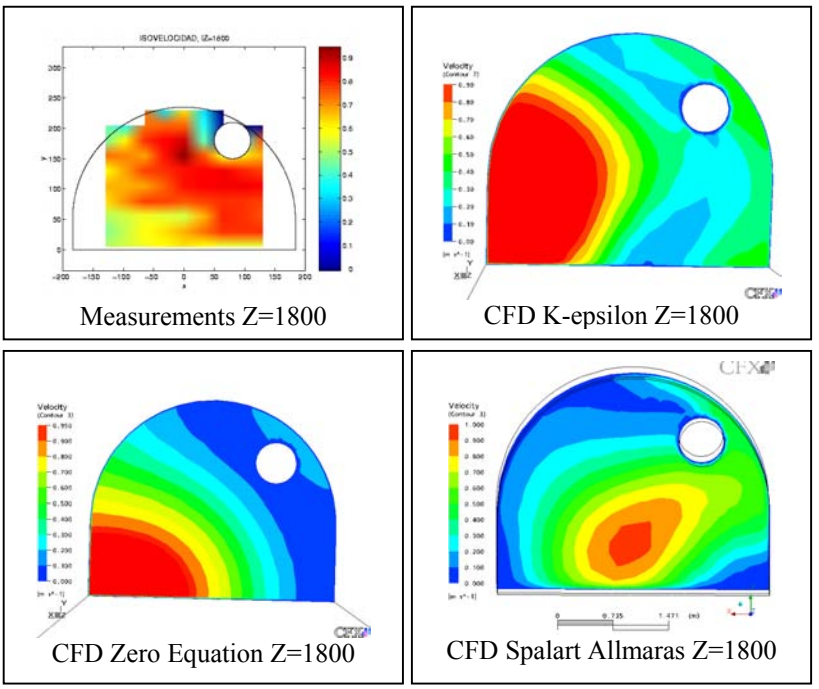


Figure 6: Velocity contours at Z=1800.

5 Conclusions

Air flow in a death end gallery can be adequately calculated using CFD methods, serving as a base to the injection of particles to simulate dust behaviour in this environment.

The comparison of the results shows good agreement between the experimental data and the simulations done using the Spallart-Allmaras model in the majority of the calculation domain. The area close to the gallery end is best simulated using the k-epsilon model.

The flow makes a characteristic turn around 16 meters from the FRENTE and this turn is simulated in that point by the Spallart-Allmaras model. The K-epsilon model also simulates this turn, but at 25 meters of distance. The simplest model, the Zero Equation, or constant turbulent eddy viscosity model, does not simulate this separation at all, as was expected by the advices referring to its limited use contained in the CFX documentation.

After the successful velocity field simulation, currently we are developing the study of the evolution of the particulated material inside this airflow, as well as the subsequent comparison with the experimental data obtained by means of optical particle samplers.

We want to acknowledge the help and advices from the Ansys CFX Technical Support Team in the development of these studies.

References

[1] CFD Help, ANSYS CFX-Solver, Release 10.0: Modelling, pp 98.

[2] K.W. Moloney, I.S. Lowndes and G.K. Hargrave, "Analysis of flow patterns in drivages with auxiliary ventilation", Trans. Instn Min. Metall. 108, pp 17-26 (1999).

[3] A. Wala, J. Jacob, J. Brown and G. Huang, "New approaches to mine-face ventilation", Mining engineering, March 2003, pp 25-30. (2003).

[4] K.W. Moloney and I.S. Lowndes, "Comparison of measured underground air velocities and air flows simulated by computational fluid dynamics", Trans. Instn Min. Metall. 108, pp 105-114 (1999).

[5] J. Toraño, R. Rodriguez, I. Diego and A. Pelegry, "Contamination by particulated material in blasts: analysis, application and adaptation of the existent calculation formulas and software". Environmental Health Risk III, pp. 209-219, (2004).

[6] J. Toraño, R. Rodriguez, J.M. Rivas and A. Pelegry, "Diminishing of the dust quantity during the management of granular material in an underground space", XII International Conference on Modelling Monitoring and management of Air Pollution. (2004).

[7] S.A. Silvester, I.S. Lowndes and S.W. Kingman, "The ventilation of an underground crushing plant", Mining Technology (Trans. Inst. Min. Metall. A), Vol. 113, pp. 201-214 (2004).

[8] López Muñiz, Luis Manuel, PhD. "Explosion retaining through active water barriers", Universidad de Oviedo. 2004.



This page intentionally left blank

Prediction of high-speed rigid body manoeuvring in air-water-sediment

P. C. Chu & G. Ray
Naval Ocean Analysis and Prediction Laboratory,
Naval Postgraduate School, Monterey, USA

Abstract

Falling of rigid body through air, water, and sediment with high speed is investigated experimentally and theoretically. Several experiments were conducted to shoot bomb-like rigid bodies with the density ratio similar to MK-84 into the hydrographical tank. During the experiments, we carefully observe the position and orientation of the bomb-like rigid bodies. The theoretical work includes the development of 3D model for predicting high speed rigid body manoeuvring in air-water-sediment columns (STRIKE35) which contains three components: triple coordinate transform, hydrodynamics of falling rigid object in a single medium (air, water, or sediment) and in multiple media (air-water and water-sediment interfaces). The model predicts the rigid body's trajectory in the water column and burial depth and orientation in the sediment.
Keywords: body-flow interaction, bomb manoeuvring.

1 Introduction

Study on falling rigid body through air, water, and sediment with high water entry speed has wide scientific significance and technical application. The dynamics of a rigid body allows one to set up six nonlinear equations for the most general motion: three momentum equations and three moment-of-momentum equations. The scientific studies of the geotechnical characteristics of a rigid body in water and sediment involve nonlinear dynamics, body and multi-phase fluid interaction, body-sediment interaction, supercavitation, and instability theory.

The technical application of the hydrodynamics of a rigid body with high speed into fluid and non-fluid includes aeronautics, navigation, and civil



WIT Transactions on Engineering Sciences, Vol 52, © 2006 WIT Press
www.witpress.com, ISSN 1743-3533 (on-line)
doi:10.2495/AFM06013

engineering. Recently, the scientific problem about the movement of a rigid body in water column and sediment drew attention to the naval research. This is due to the threat of mine in the naval operations. Prediction of a fast falling rigid body in the water column contributes to the bomb strike for mine clearance in surf zones. In this study, a nonlinear dynamical system is established for the movement of a non-uniform (center of gravity not the same as the center of volume) rigid cylinder through the water-sediment interface. A bomb-strike experiment was conducted. The data collected from the experiment can be used for model development and verification.

2 Triple coordinate systems

Consider an axially symmetric cylinder with the centers of mass (**Mc**) and volume (**Gc**) on the main axis. Let (L, d, χ) represent the cylinder's length, diameter, and the distance between the two points (**Mc**, **Gc**). The positive χ-values refer to nose-down case, i.e., the point **Mc** is lower than the point **Gc**. Three coordinate systems are used to model the falling cylinder through the air, water, and sediment phases: E-, M-, and F-coordinate systems. All the systems are three-dimensional, orthogonal, and right-handed (Chu et al. [1]).

The E-coordinate is represented by F_E(O, **i**, **j**, **k**) with the origin 'O', and three axes: x-, y- axes (horizontal) with the unit vectors (**i**, **j**) and z-axis (vertical) with the unit vector **k** (upward positive). The position of the cylinder is represented by the position of **Mc**,

$$\mathbf{X} = x\mathbf{i} + y\mathbf{j} + z\mathbf{k}, \tag{1}$$

which is translation of the cylinder. The translation velocity is given by

$$\frac{d\mathbf{X}}{dt} = \mathbf{V}, \qquad \mathbf{V} = (u, v, w). \tag{2}$$

Let orientation of the cylinder's main-axis (pointing downward) is given by $\mathbf{i}_M$. The unit vectors of the M-coordinate system are given by (Fig. 1)

$$\mathbf{j}_M = \mathbf{k} \times \mathbf{i}_M, \qquad \mathbf{k}_M = \mathbf{i}_M \times \mathbf{j}_M. \tag{3}$$

Let the cylinder rotate around ($\mathbf{i}_M$, $\mathbf{j}_M$, $\mathbf{k}_M$) with angles ($\varphi_1, \varphi_2, \varphi_3$) (Fig. 1). The angular velocity is calculated by

$$\omega_1 = \frac{d\varphi_1}{dt}, \quad \omega_2 = \frac{d\varphi_2}{dt}, \quad \omega_3 = \frac{d\varphi_3}{dt}. \tag{4}$$

The F-coordinate is represented by F_F(**X**, $\mathbf{i}_F$, $\mathbf{j}_F$, $\mathbf{k}_F$) with the origin **X**, unit vectors ($\mathbf{i}_F$, $\mathbf{j}_F$, $\mathbf{k}_F$), and coordinates (x_F, y_F, z_F). Let $\mathbf{V}_w$ be the fluid velocity. The water-to-cylinder velocity is represented by

$$\mathbf{V}_r = \mathbf{V}_w - \mathbf{V},$$

which can be decomposed into two parts,

$$\mathbf{V}_r = \mathbf{V}_1 + \mathbf{V}_2, \quad \mathbf{V}_1 = (\mathbf{V}_r \cdot \mathbf{i}_F)\mathbf{i}_F, \quad \mathbf{V}_2 = \mathbf{V}_r - (\mathbf{V}_r \cdot \mathbf{i}_F)\mathbf{i}_F, \tag{5}$$

where $\mathbf{V}_1$ is the component paralleling to the cylinder's main-axis (i.e., along $\mathbf{i}_M$), and $\mathbf{V}_2$ is the component perpendicular to the cylinder's main-axial direction. The unit vectors for the F-coordinate are defined by (column vectors)

$$\mathbf{i}_F = \mathbf{i}_M, \qquad \mathbf{j}_F = \mathbf{V}_2/|\mathbf{V}_2|, \qquad \mathbf{k}_F = \mathbf{i}_F \times \mathbf{j}_F. \tag{6}$$

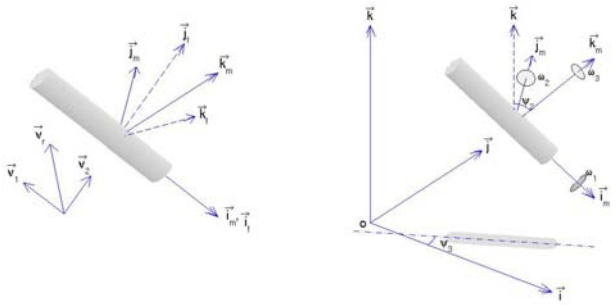


Figure 1: Three coordinate systems.

3 Momentum balance

The translation velocity of the rigid-body ($\mathbf{V}$) is governed by the momentum equation in the E-coordinate system (Maxey and Riley [10])

$$\frac{d}{dt}\begin{bmatrix} u \\ v \\ w \end{bmatrix} = \begin{bmatrix} 0 \\ 0 \\ g(\rho_w/\rho - 1) \end{bmatrix} + \frac{\rho_w}{\rho}\frac{D\mathbf{V}_w}{Dt} + \frac{1}{\rho\Pi}(\mathbf{F}_h + \mathbf{F}_V), \tag{7}$$

where g is the gravitational acceleration; $b = \rho_w g/\rho$, is the buoyancy force; ρ_w is the water density; Π is the cylinder volume; ρ is the rigid body density; $\rho\Pi = m$, is the cylinder mass; $\mathbf{V}_w$ is the fluid velocity in the absence of the rigid-body at the center of volume to the body. $\mathbf{F}_h$ is the hydrodynamic force (including drag, lift, impact forces). The drag and lift forces are calculated using the drag and lift laws with the given water-to-cylinder velocity ($\mathbf{V}_r$). In the F-coordinate, $\mathbf{V}_r$ is decomposed into along-cylinder ($\mathbf{V}_1$) and across-cylinder ($\mathbf{V}_2$) components. $\mathbf{F}_V$ is the force caused by bubble volume variation (bubble force).

4 Moment of momentum equation

It is convenient to write the moment of momentum equation

$$\mathbf{J}\cdot\frac{d\boldsymbol{\omega}}{dt} = \mathbf{M}_w + \mathbf{M}_b + \mathbf{M}_h + \mathbf{M}_v, \tag{8}$$

in the M-coordinate system with the body's angular velocity components ($\omega_1, \omega_2, \omega_3$) defined by (4). Here, $\mathbf{M}_w$ is the torque due to the fluid acceleration

$\rho_w / \rho D\mathbf{V}_w / Dt$. $\mathbf{M}_b$ is the torque due to buoyancy force $\mathbf{F}_b = g(\rho_w / \rho - 1)$. $\mathbf{M}_h$ is the hydrodynamic (drag and lift) torques. $\mathbf{M}_v$ is the torque due to the Basset history force. In the M-coordinate system, the moment of gyration tensor for the axially symmetric cylinder is a diagonal matrix

$$\mathbf{J} = \begin{bmatrix} J_1 & 0 & 0 \\ 0 & J_2 & 0 \\ 0 & 0 & J_3 \end{bmatrix}, \tag{9}$$

where J_1, J_2, and J_3 are the moments of inertia. The gravity force, passing the center of mass, doesn't induce the moment.

5 Supercavitation

As a high-speed rigid body penetrates into the air-water interface, an air cavity will be formed. The shape of cavity is approximately elliptical. A number of scientists have developed formulas to predict the cavity radius such as the Logvinovich [9] formula

$$r_{cav} = r_{\max}\sqrt{1 - \frac{\left(1 - r_1^2 / r_{\max}^2\right)}{\left(1 - t / t_m\right)^{2/\eta}}}, \tag{10}$$

where r_{max} is the maximum cavity radius; t_m is the time for the formation of the cavity midpoint; η (~0.85) is the correction factor; and r_1 is the radius at location x_1; t is the time for the cavity formation at x_1,

$$t = \frac{x_M - x_1}{V_k}, \tag{11}$$

where V_k is the cavitator velocity. Recently, Dare et al. [7] proposed a simpler formula from experimental studies

$$r_{cav} = \frac{d}{2}\sqrt{\frac{kx_M}{d} + 1}, \quad k = 2, \tag{12}$$

where d is the nose diameter. The shock propagation and subsequent bubble formation may be significantly affected by the presence of an air cavity around the rigid-body. Supercavitation often occurs around the body. Cavitating flows are usually described by the cavitation number (σ),

$$\sigma = \frac{p - p_v}{\frac{1}{2}\rho_w V_w^2}, \tag{13}$$

where p is the hydrostatic pressure, p_v is the pressure in the cavity. For supercavitating flow the cavitator is located at the forward most location on the body, and the cavity downstream of the cavitator covers the body. The shape of the cavity is defined by the cavitation number. The aspect ratio (length L versus diameter d_m) is the function of cavitation number

$$\lambda = \frac{L}{d_m} = \frac{\sigma + 0.008}{\sigma(0.066 + 1.7\sigma)}. \tag{14}$$

Several expressions can be used for the drag coefficient. Without considering the geometry of cavity, the cavitator drag coefficient is simply calculated by (Stinebring et al. [12])

$$C_d = 0.82(1+\sigma). \tag{15}$$

With considering the geometry of cavity is considered, the cavitator drag coefficient is expressed by

$$C_d = \left(\frac{2r_{cav}}{d}\right)^2 (\sigma - 0.132\sigma^{8/7}). \tag{16}$$

6 Bubble dynamics

Drag due to bubble volume variation is calculated by (Johnson and Hsieh [8])

$$\mathbf{F}_V = 2\pi r_b^2 \rho_w (\mathbf{V}_w - \mathbf{V}) \frac{dr_b}{dt}, \tag{17}$$

where r_b is the bubble radius. The Rayleigh-Plesset equation (Plesset [11])

$$r_b \frac{d^2 r_b}{dt^2} + \frac{3}{2}\left(\frac{dr_b}{dt}\right)^2 = \frac{1}{\rho_w}(p_v - p_g \frac{\Pi_{b0}}{\Pi_b} - p - \frac{2\tau}{r_b} - \frac{4\mu}{r_b}\frac{dr_b}{dt}), \tag{18}$$

where p_g is the initial partial pressure of the non-condensable gas; Π_{b0} is the initial volume of the bubble; Π_b is the volume of the bubble; τ is the surface tension; and μ is the dynamic viscosity of water.

7 Bomb Manoeuvring Experiments (BOMEX)

To evaluate the high-speed rigid-body manoeuvring model, scaled MK-84 and MK-65 (with and without fins) model experiments with high water entry speed were conducted during September 19-27, 2005.

7.1 Preparation

The overall premise of the bomb strike experiment consists of inserting various bomb-like test shapes into water, and recording their underwater trajectory over the course of the flight path. Data collection was facilitated by a pair of high-speed video cameras mounted below the water surface. Following the data collection phase of the project, all video trajectory data was converted into an array of Cartesian coordinate points which will serve as the initial data set for the development and validation of the bomb-strike prediction model (STRIKE35).

7.2 Bomb-like polyesters

A collection of four bomb-like polyester resin test shapes were used. These shapes consisted of a right-cylinder, right-cylinder with hemispheric nose cone (capsule), scale model of the MK-84 GP munitions (bomb) and a modified version of the model bomb which had no stabilizing fins (shell) (Fig. 2).

The construction of the test shapes consisted of a three-part production process: prototype development, mold construction and test shape casting and finishing. This process was necessary to facilitate more efficient experimentation and to reduce the production cost of the experimental test shapes.

Prototype production began with the development of a 1/12 scale replica of the real-world operational MK-84 GP bomb. This initial prototype was machined from aluminium alloy stock based on known dimensional characteristics. To create the cylinder and capsule prototypes, a polyester resin casting was created by pouring liquid plastic into a 5.08 cm (2") PVC mold. The shapes were allowed to cure, and then were machined to their final dimensions. As these two shapes were not intended to mimic any type of real-world munitions, their dimensions were based solely on similarity to the 1/12 scale model bomb. The final prototype created was the shell shape. Construction of this design consisted of creating a polyester resin casting of the bomb prototype. The shape was then machined and sanded to remove the fins, and produce the final prototype shape. Diagrams of the final prototypes with dimensions can been seen below (Fig. 2).



Figure 2: Various model bombs.

7.3 Pneumatic launching device

To facilitate the high-velocity portion of the experiment, a pneumatic launching device was created to propel the test shapes into the water at a rapid entry speed (Fig. 3). The launcher was primarily constructed of schedule 40 polyvinylchloride piping (PVC). The device consisted of three primary components: air chamber, valve mechanism, breech-load firing barrel. The air chamber was constructed of a single, five foot section of 15.24 cm (6") PVC. The chamber was sealed on the end with a standard 15.24 cm (6") end cap, and then connected to the valve mechanism via a series of PVC reducer bushings. A standard 5.08 cm (2") PVC ball valve was fitted between the air chamber and firing barrel, and served to maintain the chamber in a pressurized state until triggered. When actuated, the valve instantaneously opened releasing the pressurized volume of air into the firing barrel. Because of the high pressures experienced by this valve, a hydraulic actuator was fitted to the device to provide the motive force necessary to open the valve. The final portion of the launcher consisted of a firing barrel. This barrel had a removable cap on the closed end to

facilitate efficient reloading of the test shapes. Small foam sabots with fine wire lanyards which extended through a pinhole in the removable loading cap provided the means by which test shapes were held in the barrel until fired. The launcher was mounted to a steel frame oriented vertically downward with the end of the barrel positioned orthogonal to the water surface at a height of 30.50 cm (12") above the water. The entire apparatus was secured to the tank bridge by lag bolts and ratchet tie down straps. Additional equipment associated with launcher included a pressure indicator, emergency release valve, pneumatic fill and triggering mechanism and a 120 p.s.i. air source.

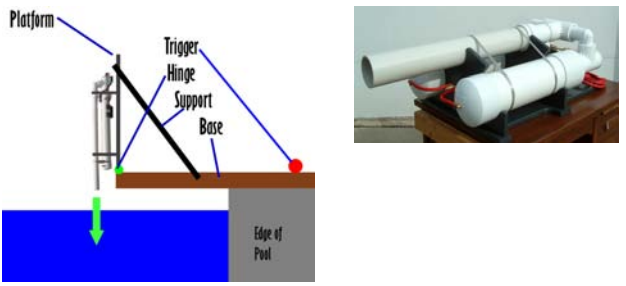


Figure 3: Pneumatic launching device.

7.4 Hydrodynamic test facility

The bomb strike experiment was conducted at the Monterey Bay Aquarium Research Institute (MBARI) Unmanned Underwater Vehicle Test Tank. This tank was used to simulate the near-shore environment frequently experienced in real-world mine countermeasure operations (Fig. 4).

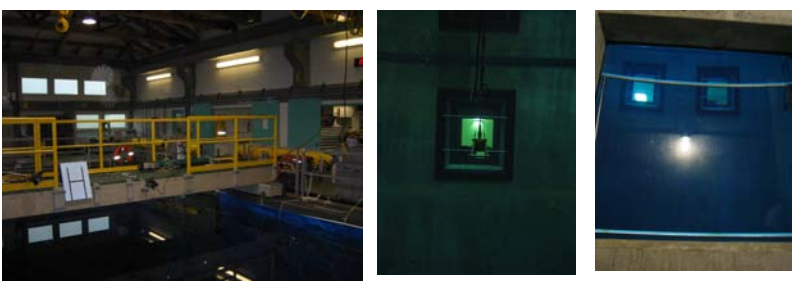


Figure 4: Hydrodynamic test facility.

The facility consists of a 9.14 m × 13.72 m × 9.14 m tank filled with standard sea water, and is contained inside a large building which provided shelter from wind and elements. A sliding bridge spans the width of the tank, and was used as a mounting surface for the pneumatic launcher and lighting equipment. Eight viewing windows located approximately six feet below the water surround the tank, and provided a venue for unimpeded sub-surface data collection to a scaled depth of roughly 36.58 m (120 ft).

In addition to the previously mentioned equipment and facilities, a large test shape recovery device was assembled and installed in the tank prior to testing. This apparatus consisted of a 9.14 m × 13.72 m net attached to a PVC grid-framework constructed of 1.90 cm (¾") piping. The entire apparatus was inserted horizontally across the water, and was used to recover shapes between testing runs using a series of weights and pulleys located in the corners of the tank to raise and lower the device. Lastly, two large blue tarps were placed in the tank against the walls centered in each camera's field of view.

7.5 Motion detection equipment

All data was collected digitally using a network of high-speed and standard video equipment and computers. Surface level information collected included experiment data and the video log. This data was collected using a pair of standard commercially available digital video camera, mounted on tripods, and located at the end of the pool directly in front of the testing zone. Both cameras operated at a 30Hz frame rate. The data camera used a narrow view lens zoomed to focus on the area directly between the launcher and the water surface, and was toggled on and off between test runs. Data from this camera was later used to ascertain the initial velocity of the shapes as they entered the water. The second camera used a wide angle lens, and was employed to record a video log of the experiment. This device ran continuously throughout the experiment (Fig. 5).

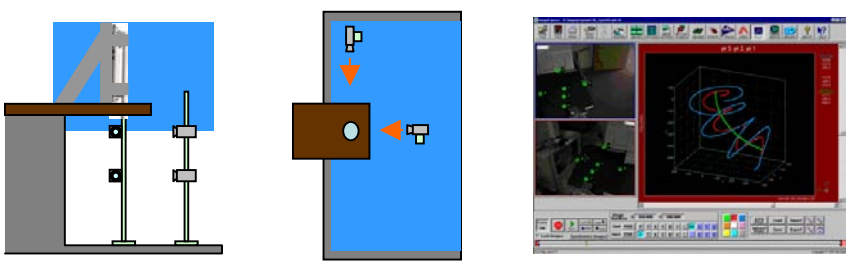


Figure 5: Motion detection equipment.

7.6 Experiments

The bomb-strike experiment consisted of a series of low velocity and high-velocity runs of the four testing shapes which were launched vertically into the water. The entry of each shape into the water was recorded by the two above surface video cameras. This above-surface data was then digitally analyzed using 3D motion analysis software to determine the initial velocity of all shapes. All below-surface data collection was facilitated by the two FASTCAM PCI high-speed cameras. The below-surface digital data was analyzed by 3D motion analysis software to determine the trajectories of each shape. All data from runs which involved malfunctions was discarded. Table 1 shows the number of test shapes which were dropped in the following sequence and repetition.

Table 1: Number of experiments.

	Low Velocity	High Velocity
Cylinder	8	12
Capsule	9	11
Shell	9	13
Bomb	6	8

The overall project was a two-man job conducted via handheld walkie-talkies. One man remained on or near the moveable bridge and was responsible for loading the launcher, toggling the lights and above-surface cameras and performing the launch. The other man was stationed with the high-speed cameras and computer, and served to coordinate the filming and retrieval of the below-surface data. For each individual drop, the experimenter below confirmed the readiness of the high-speed cameras and prepared the computer to save the appropriate film file. When this was confirmed, he signaled the man above, who performed the launch.

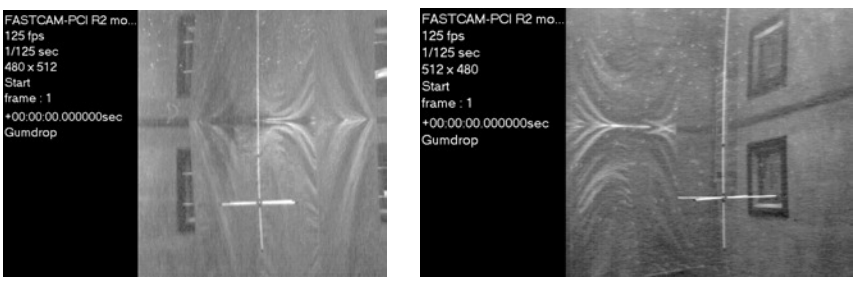


Figure 6: Trajectories of the bomb-like polyesters.

After a coordinated count conducted via the walkie-talkies, the man at the launch position fired the launcher as the man below began filming the test run. When the shape passed through the field of view of both cameras, the camera operator would cease filming, save the appropriately named file, and again signal the man above, who would then turn off the lighting and note the time and shape in the experimental record notebook. The cycle would then repeat itself until all shapes were fired. Recovery of the shapes was as described above. Digital imagery data obtained in the experiment was then analyzed to generate water trajectory data and graphics (Fig. 6).

8 Conclusions

(1) STRIKE35 is developed to predict high speed rigid body manoeuvring in air-water-sediment columns. It contains three components: triple coordinate transform, hydrodynamics of falling rigid object in a single medium (air, water, or sediment) and in multiple media (air-water and water-sediment interfaces). The body and buoyancy forces and their moments in the E-coordinate system, the hydrodynamic forces (such as the drag and lift forces)

and their moments in the F-coordinate, and the cylinder's moments of gyration in the M-coordinate. Supercavitation and bubble dynamics are also included.
(2) The momentum (moment of momentum) equation for predicting the cylinder's translation velocity (orientation) is represented in the E-coordinate (M-coordinate) system. Transformations among the three coordinate systems are used to convert the forcing terms into E-coordinate (M-coordinate) for the momentum (moment of momentum) equation.
(3) Bomb strike experiment was conducted to evaluate the 3D model.

Acknowledgements

The Office of Naval Research Breaching Technology Program (N0001405WR20209) and Naval Oceanographic Office supported this study.

References

[1] Chu, P.C., C.W. Fan, A. D. Evans, and A. Gilles, 2004: Triple coordinate transforms for prediction of falling cylinder through the water column. Journal of Applied Mechanics, 71, 292-298.
[2] Chu, P.C., A. Gilles, and C.W. Fan, 2005: Experiment of falling cylinder through the water column. Experimental and Thermal Fluid Sciences, 29, 555-568.
[3] Chu, P.C., and C.W. Fan, 2005: Pseudo-cylinder parameterization for mine impact burial prediction. Journal of Fluids Engineering, 127, 1515-152.
[4] Chu, P.C., and C.W. Fan, 2006: Prediction of falling cylinder through air-water-sediment columns. Journal of Applied Fluid Mechanics, in press.
[5] Chu, P.C., C.W. Fan, A.D. Eans, A. Gilles, T.B. Smith, and V. Taber, 2006: Development and verification of 3D mine impact burial prediction model. IEEE Journal of Oceanic Engineering, in revision.
[6] Chu, P.C., 2006: Mine impact burial prediction from one to three dimensions. IEEE Journal of Oceanic Engineering, submitted.
[7] Dare, A., A. Landsberg, A. Kee, A. Wardlaw, K. Ruben, 2004: Three-dimensional modeling and simulation of weapons effects for obstacle clearance. HPC Users Group Conference Proceedings, 10 pages.
[8] Johnson, V.E., and T. Hsieh, 1966: The influence of the trajectories of gas nuclei on cavitation inception. Sixth Symposium on Naval Hydrodynamics, 163-179.
[9] Logvinovich, G.V., 1969: Hydrodynamics of Flow with Free Boundaries, Naukova Dumka, Kiev, Ukraine (in Russian).
[10] Maxey, M.R., and J.J. Riley, 1983: Equation of motion for a small rigid sphere in a nonuniform flow, Phys\ics of Fluids, 26, 883-889.
[11] Plesset, M.S., 1948: Dynamics of cavitation bubbles. Journal of Applied Mechanics, 16, 228-231.
[12] Stinebring, D.R., M. L. Billet, J.W. Lindau, and R.F. Kunz, 2001: Developed cavitation–cavity dynamics, 20 pages (personal communication).



Experimental study and modelling of the kinetics of drying of urban wastewater treatment plant sludge

H. Amadou[1], J.-B. Poulet[2], C. Beck[1] & A.-G. Sadowski[1]
[1]*ENGEES UPR SHU, Strasbourg, France*
[2]*INSA, LRIT-ERESA, Strasbourg, France*

Abstract

The treatment of sludge by solar drying under a greenhouse is a technique increasingly used for small and medium sized wastewater treatment plants. In order to contribute to the improvement of dimensioning and the effectiveness of the drying of sludge, we propose using the DVS system (Dynamic System of Vapor Sorption), to determine experimentally the isotherms of desorption at 30 and 50°C. These curves were modelled following a semi-empirical correlation suggested by Oswin. Consequently, experimental results of drying by the forced convection of sludge were obtained, using well controlled thermal conditions of air (30 and 50°C for the temperatures 40 and 60% for relative humidity 1.0 and 2.0 m/s for air velocity). A characteristic curve of drying is built for the different aerothermic conditions. This simplified method makes it possible to simulate the experimental kinetics satisfactorily.
Keywords: modelling, isotherm of sorption, kinetics of drying, sludge, solar drying, wastewater treatment.

1 Introduction

The treatment of domestic wastewater produces large quantities of residual sludge. Nowadays, wide reduction of these waste volumes is necessary to satisfy new environmental regulations [1].

Sun drying whilst covered is a technique increasingly used for small and medium sized wastewater treatment plants. The control of the solar process of drying of sludge is thus essential. Within this context, the present work



WIT Transactions on Engineering Sciences, Vol 52, © 2006 WIT Press
www.witpress.com, ISSN 1743-3533 (on-line)
doi:10.2495/AFM06014

attempted to assess the performances of this type of process in dewatering and reducing the volume of sludge.

The important stage in every drying process of a material consists in evaluating the hygroscopic character of the product, which is materialized by its curve of sorption. The knowledge of this curve makes it possible to draw from useful information, in particular during the drying and during the storage of sludge.

The complexity of the phenomena intervening during drying, the difficulty in determining certain parameters made certain authors [2–4] directs themselves towards an empirical step.

This step consists in starting from the representation of the results of various experiments carried out under various conditions of temperatures of relative humidity and velocity of air, to determine single curve known as characteristic curve of drying. The concept of characteristic curve of drying seems a method adapted to describe the behavior of sludge.

We initially propose to determine the isotherm of sorption in experiments and to choose a semi-empirical model among those existing in the literature. And in the second time to seek, on the basis of the experimental approach, a semi-empirical correlation of the characteristic curve of drying allowing to better simulate the kinetics of drying under various atmospheric conditions.

2 Materials and methods

2.1 Isotherms of desorption

2.1.1 Origin and nature of the sludge

The Studied sludge came from Rosheim urban wastewater treatment plant (11000 population Equivalent) which characteristic was the use of biological treatment process.

The sludge is taken at the end of the mechanical dewatering stage with siccity between 16 and 19%.

2.1.2 Isotherm desorption methodology

This technique allows one to describe the changes of the moisture content within the sample in relation to thermodynamic activity of water, at a fixed temperature [5–8].

Experimentally, samples of sludge are placed in containers. The containers are set inside a chamber under controlled humidity and temperature.

The samples are weighed at the thermodynamic equilibrium (which is reached when the weight remains constant over time). At the end of experiment the sludge average moisture content is determined by drying at 105°C for 24h.

The curve representing the evolution of the content of a product according to the relative humidity Hr of the air for a given temperature T is called: isotherm of desorption if it was given by a product saturated with water.

The knowledge of the isotherm of desorption makes it possible to calculate the water content at equilibrium of the product which is the limit towards which

the water content will tighten at the end of drying. The value is a parameter, which appears in particular in the models making it possible to envisage the evolution of the water content of a product during its drying [7].

2.1.3 Experimental device

The isotherms of sorption were obtained using DVS system (Dynamic System of Vapor Sorption) of the laboratory of process engineering of the ENSTIMAC. The DVS system has a microbalance with supersensitive continuous recording able to measure changes of mass of the sample lower than 1 part by 10 billion.

This type of microbalance has as principal characteristic to have a very good long-term stability and is consequently ideal for the measurement of phenomena of vapor sorption, which lasts between a few minutes and a few days. This microbalance is placed in an incubator, which makes it possible to generate a temperature of constant and precise measurement.

The required relative humidities are generated by the mixture of a dry steam flow with a saturated steam flow in proportions that are measured with a precision fluxmeter. Combined probes of moisture and temperature are located just below the nacelles of sample and reference in order to allow a checking independent of the performances of the system. The mechanism of the microbalance is very sensitive to the sorption and the desorption of moisture. DVS instrument is completely automated and controlled by computer.

2.2 Kinetics of drying

According to drying literature [4,10] the drying curve describes the evolution of evaporation flux versus the mean moisture content. It classically shows tree different phases: a short period of increasing temperature, a period of constant rate, and a period of decreasing drying rate that concludes with the stabilisation of water content at an equilibrium value at the end of drying.

2.2.1 Experimental unit

The drying experiments were carried out in a climatic chamber. This experimental device makes it possible to have a controlled aerothermic condition that can be varied during experiments.

The air flow conditions (temperature, relative humidity and velocity) were kept constant for each experiment. The mass and the temperature of sample were recorded on a computer.

The whole of the device comprises:

- The climatic box of section 180cm x100 cm and height 109cm.
- A support of surface 32cm X 26cm introduced into the climatic box and posed on an electronic balance of precision 0,01g, provided with an analogical exit.
- An adjustable ventilator of flow thanks to a variable generator. The velocity of air is measured by two thermal anemometers of type FVA645TH2/TH3 with a precision of 0.01m/s. One of them is placed at the upstream of the support and the other at the downstream.

- A thermo-hygrometrical probe of measurement of type MT8636HR of precision 2% measuring the temperature and the moisture of the air circulating in the climatic box in order to check the temperature and the hygroscopy of instruction fixed at the level of the climatic chamber.
- A thermocouple of the type K to large standard handle T 150 placed at some depth of sludge. This thermocouple makes it possible to follow the change of the temperature of sludge during the test.
- A station of acquisition of the data connected to a microcomputer equipped with software Amr-CONTROL allowing to store and treat the data.

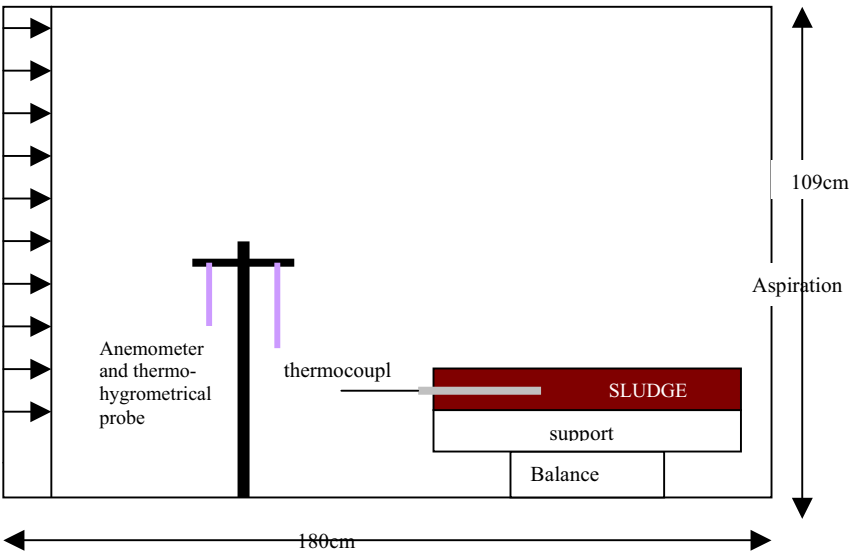


Figure 1: Climatic box.

2.2.2 Experimental protocol

The principle of the tests is simple. One fixes the air flow conditions (temperature, relative humidity and velocity), after the system be stabilized, Then one introduces into the climatic box the sludge laid out on the support in thin layer. The mass and the temperature of sample are recorded on a computer. A set of eight tests is envisaged at two temperatures (30, and 50°C), two air velocities (1.0 and 2.0m/s) and at two relative humidities (40 and 60%).

3 Experimental results

3.1 Experimental results of desorption isotherm

The desorption isotherm were established at 30°C and 50°C from water contents at equilibrium, obtained for different degrees of relative humidity.

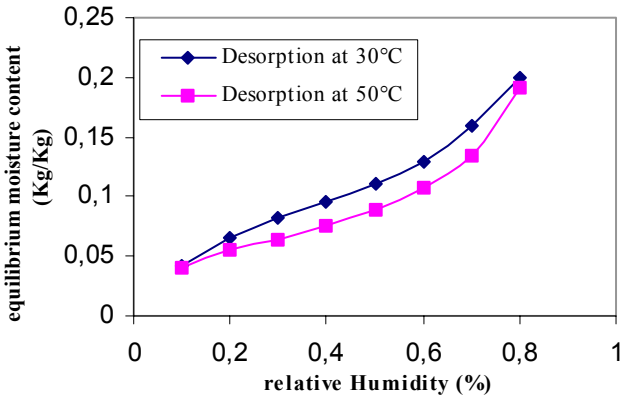


Figure 2: Isotherms of desorption at 30°C and 50°C.

The isotherms obtained were of type II, as is generally the case for urban residual sludge [1]. A large number of models have been proposed in the literature in order to describe the evolution of the equilibrium moisture content with water activity [1,5–8].

A non-linear optimization method was used to fit the parameters of every model and their suitability has been evaluated through the mean relative error (EQM: average standard deviations). According to the EQM criterion the Oswin model best fits the experimental data [3].

Oswin model

$$X_{eq} = k\left(\frac{Hr}{1-Hr}\right)^{n} \quad (1)$$

k , n are the coefficients characteristic of the product.

Table 1: Parameters of the model of Oswin and EQM relating to the adjustment.

temperature	Parameter k	Parameter n	Field of validity	EQM
30°C	0.112	0,416	0.10≤ Hr ≥0.80	3.50652E-05
50°C	0.0938	0.484	0.10≤ Hr ≥0.80	2.90608E-04

These curves indicate a relatively good agreement between the model and the experimental data.

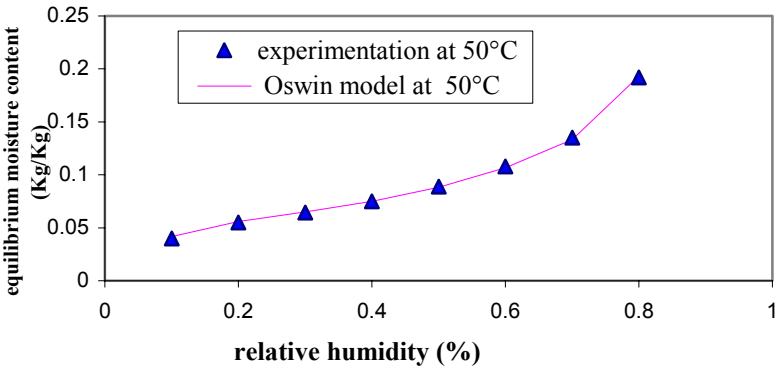


Figure 3: Model/experimentation at 50°C.

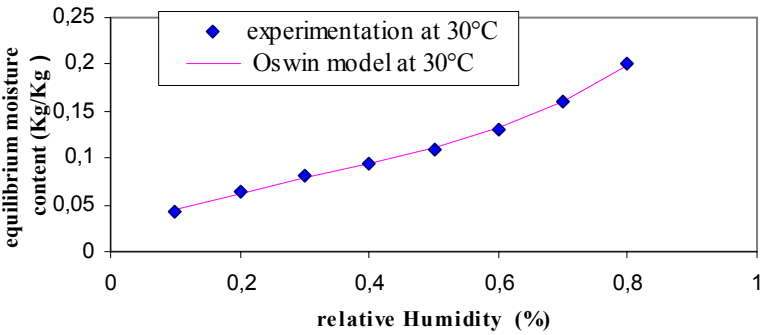


Figure 4: Model /experimentation at 30°C.

3.2 Experimental results of drying kinetics

3.2.1 Curves of drying

The curves of drying indicate, either the variations of the moisture content of sludge according to time, or that giving drying rate according to time, or even the curve proposed by Krischer and Kröll [4] drying rate according to the moisture content of sludge, or finally the reduced shape of the curve of krischer for a single representation of various conditions of drying.

The curve of drying rate can be obtained, by calculating the derivative after smoothing of the curve or directly starting from the experimental points.

3.2.2 Identification of the curve characteristic of drying

The representation of the results of various experiments for a given product, proposed by Van Meel then Krischer and Schlunder [1,2,3], makes it possible to plot the characteristic curve of drying. This curve makes possible the regrouping of the results achieved under different conditions of air (temperature, relative humidity, and velocity). The kinetics of drying are represented in the form:

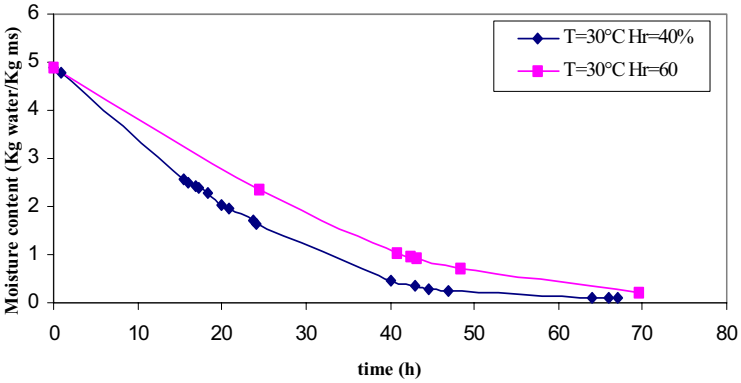


Figure 5: Moisture content for two conditions air for sludge.

$$\left(-\frac{dX}{dt}\right) = \left(-\frac{dX}{dt}\right)_1 f(X_r) \tag{2}$$

X_r is the reduced moisture content defined by:

$$X_r = \frac{X - X_{eq}}{X_{cr} - X_{eq}} \tag{3}$$

X_{eq} is the equilibrium water content measured after drying

$\left(-\frac{dX}{dt}\right)_1$ is the constant rate period $X_i \le X \le X_{cr}$

$f(X_r)$ is the normalized drying rate

Generally, the characteristic curves are represented by functions of the polynomial type or power type. In this framework we will use the polynomial function presented in the following form:

$$f(X_r) = A_1 X_r + A_2 X_r^2 + A_3 X_r^3 \tag{4}$$

The constants, A_1, A_2, A_3 are given in the experiments for fixed characteristics of air.

3.2.2.1 Determination of the first phase and the moisture content critical
The constant rate period is not easily identifiable, even for the products whose initial moisture is important. The explanation lies in the fact that the cellular walls disturb the fast migration of moisture towards the surface of the products [5]. Thus several authors [11,12] identify the moisture content critical with the initial content.

The constant rate period can be given by using a correlation, which includes the external aerodynamic conditions, and by taking in to account the deformable

character of the biological products or by using the analogy of the transfers of heat and mass through the boundary layer of a completely wet surface. This phase is comparable with the evaporation of free water. The temperature of the solid remains constant and equal to the wet bulb temperature. The constant rate (Kg of water /s) is thus equal to:

$$m_s \left(\frac{dX}{dt}\right)_1 = \frac{h\,S}{L_v}\left(T_a - T_b\right) \tag{5}$$

4 Perspective

At the end of our experimental tests, we will represent the profiles of the kinetics of drying for various values of temperature, relative humidity and velocity of air. Those profiles, will allow us:

- To identify the parameters, A_1, A_2, A_3, for each test
- To determine, the average values of A_1, A_2, A_3 and the standard deviations of these parameters for the whole of the experimental tests.

Some tests, apart from those, which made it possible to fix the curve, will allow us to validate the obtained model. These experimental tests will also allow us to show the influence of the characteristics of the air on the speed of drying.

5 Conclusion

The isotherms of desorption of sludge were obtained by using DVS system (dynamic System of vapor sorption). The obtained results were simulated by the semi-empirical model of OSWIN.

Then, the influence of drying air velocity, drying air temperature and relative humidity on the drying kinetics of sludge will be studied. The characteristic curve of drying and the expression of drying rate will be elaborated from the experimental results. This formula is necessary for programs simulating solar drying systems.

Nomenclature

A_1, A_2, A_3 Coefficients characteristic of drying.....

Hr Relative humidity of the air….....(%)

h Convection coefficient..... (W/ m^2/K)

k, n Coefficients characteristic of the product.....

l_v Latent heat of water vaporization..... (J/Kg)

m_b Mass of sludge..... (Kg)

m_s Mass Dries..... .....(kg)

S Heat-transferring surface..... (m^2)
T_a Temperature of the air drying.....(°C)
T_b Temperature of sludge.....(°C)
t Time.....(h)
U Air velocity.....(m/s)
X Moisture content dry basis.....(Kg water/kg dry solid)
$\left(\frac{dX}{dt}\right)_1$ Speed of drying with constant phase.....(Kg water/kg dry solid.h)

Subscripts

b Sludge
cr Transition moisture content: bound-free water
eq At thermodynamic equilibrium
i Initial

References

[1] Vaxelaire J, Mousques P, Bongiovanni J.M and Puiggali J.R., Desorption of domestic activated sludge Environmental Technology, vol. 21 pp 327-335 (2000).
[2] Van Meel (D.A.). – Chem. Eng. Sci., 9, p. 36 (1957).
[3] Schlunder (E.V.). – *Handbook of heat transfer.* Section 3: *Dryers,* Hemisphere Publishing Corp, (1983).
[4] Krischer (O.) et Kröll (K.). – *Technique du séchage.* cetiat Orsay, 599 p.Traduction de *Die Wissenschaftlichen Grundlagen der Trocknungstechnik*. Springer Verlag Berlin (1963).
[5] Vaxelaire J., Bongiovanni J.M and Puiggali J.R., Mechanical dewatering and thermal drying of residual sludge. Environnemental Technology, vol 20 pp 29-36 (1999).
[6] Léonard A., Etude du séchage convectif de boues de station d'épuration, suivi de la texture par microtomographie à rayons x, PhD thesis, University of Liège (2003).
[7] Nelson R.M., A model for sorption of water by cellulosic materials. Wood and Fiber Science, 15,8-22 (1983).
[8] Talla A, Jannot Y, Kaspseu C, Nganhou J., Experimental study and modelling of kinetics of drying of tropical fruits. Application to banana and to mango. Wood science, 21 499-518 (2001).
[9] Lahsasni S, Kouhila M, Mahrouz M., Experimental study of drying kinetics of cladode of opuntia ficus indica. International forum on Renewable Energies FIER 254-259 (2002).
[10] Charreau A, Cavaillé R., Séchage: Théorie et calculs. Techniques de l'ingénieur, traité Génie des procédés, J 2 480-1.

[11] Desomorieux H., Moyne C., Analysis of dryers performance for tropical foodstuffs using the characteristic drying curve concept. In: Drying 92, Elsevier Amsterdam, 834-843 (1992).
[12] Formell A., Séchage de produits biologiques par l'air chaud: calcul de séchoirs. PhD thesis, Montpellier (1979).



Experimental investigation of grid-generated turbulence using ultrasonic travel-time technique

W. Durgin & T. Andreeva
Department of Mechanical Engineering, Worcester Polytechnic Institute, USA

Abstract

This paper presents a summary of experimental work conducted by the authors in the area of acoustical wave propagation through turbulent media. The ultrasonic time-of-flight method, using dual transducers, is utilized to determine some characteristics of grid-generated turbulent flow produced in a low turbulence, low speed open circuit type wind tunnel. The experimental work utilizes the high speed Data Acquisition (DAQ) card, Labview Software connecting the experimental apparatus and computer, Low Speed Wind Channel with ultrasonic transducers placed in it and customary built grids, with heating elements inside.
Keywords: ultrasonic travel time technique, caustics.

1 Introduction

There has been an intensive research work focusing on ultrasonic flow meters and their capabilities for measuring non-ideal flows [3]. Evidence of ultrasonic technology's value to industry as effective flow diagnostic solutions can be taken from the fact that the Ultrasonic Flow Metering market size quoted in 2002 at nearly $406 Million dollars, is projected to expand to a $600 Million dollar industry by 2007. New applications for ultrasonic technology continue to emerge but its potential will depend on the innovations that take place in the future.

The classical theory of acoustic wave propagation through turbulence predicts linear increase of the first-order travel-time variance with the propagation distance. However, recent numerical and theoretical studies exhibit an almost quadratic growth of travel time variance with travel distance [4],[5],[6]. This



WIT Transactions on Engineering Sciences, Vol 52, © 2006 WIT Press
www.witpress.com, ISSN 1743-3533 (on-line)
doi:10.2495/AFM06015

effect is believed to be closely related to the occurrence of caustics.[7]-[10] If a wave propagates in a random medium, then at some distance x from the source, caustics appear. The higher the turbulence intensity, the shorter the distance at which the first caustic occurs. The probability of the appearance of the caustics in a random field was explored theoretically [8],[9],[11] and numerically. [4],[5],[10]

The fact that an acoustic wave carries some structure information of the turbulent medium after interacting with a medium makes it possible to use some statistical characteristics of the acoustic wave as a diagnostic tool to obtain some statistical information about the medium[6],[5],[12],[13],[14]. The modern theory of sound propagation in a moving random medium has been developing intensively since mid-1980s and is systematically described in Ostashev [15]. In this part of the study the goal is to demonstrate quantitatively that effect of thermal fluctuations is as much important as effect of velocity fluctuations on acoustic wave propagation. In order to do that the ultrasonic flowmeter equation is reconsidered, where the effects of turbulent velocity and sound speed fluctuations are included. The result is an integral equation in terms of correlation functions for travel time, turbulent velocity and sound speed fluctuations. Experimentally measured travel time statistic data approximated by Gaussian function and used to solve integral equation analytically. Turbulence spectral models for sound propagation in turbulent media were addressed by different authors and a summary of recent works presented in [15].

2 Experimental arrangement

Figure 1 represents a schematic diagram of the experimental setup. We consider a locally isotropic, passive temperature field coupled with a locally isotropic velocity field, which is realized by introducing a grid in a uniform flow produced in a wind tunnel with $0.3m \times 0.3m \times 1.07m$ test section. [16] Travel time moments are studied versus mean flow velocity U and travel distance L. Turbulence was produced by a bi-planar grid consisting of a square mesh of aluminum round rods with diameter 0.635 cm positioned 2.54 cm between centers. Experimental conditions were chosen similar to the experiments by previous investigators. [17]-[19] In our experiment we used two transducers working at a frequency of 100 kHz, designed for air applications, located on the upper and lower sides of the tunnel, as shown in Fig.1. Transducer- transmitter is excited by the programmable signal generator and a power amplifier by means of burst of four 100 kHz square waves with 50mV amplitude. The function generator is initiated by National Instrument Data Acquisition Card (DAQ), which produces 5V amplitude square waves with a frequency of 500 cycles/s. The ultrasound beam, send by the first transducer was received by the second one. The analog data, then, from the second transducer was transported to a CompuScope 82G DAQ with large acquisition memory and wide analog bandwidth, that transformed analog data to digital data and transferred data from CompuScope 82G card to the PC memory with the resolution of $5 \cdot 10^{-9} s$. Both DAQ cards were installed inside the PC. The National Instrument DAQ allows

one to detect the burst departure time extremely accurately and, finally, digital representation of the experimental data, provided by CompuScope 82G DAQ allowed determination of the travel time very precisely. Fig. 2 demonstrates a typical data representation obtained from CompuScope 82G DAQ, transferred to the PC and processed in Excel. The acquisition rate was $5 \cdot 10^7$ samples/s. The first signal e_1 corresponds to the burst of square waves produced by the function generated that initiate the transducer-transmitter. The second signal e_2 is the signal received by the second transducer. The measuring time for each single run was 45s (approximately 15Mb of measured data). For each measurement the travel time was averaged over more then 700 realizations.

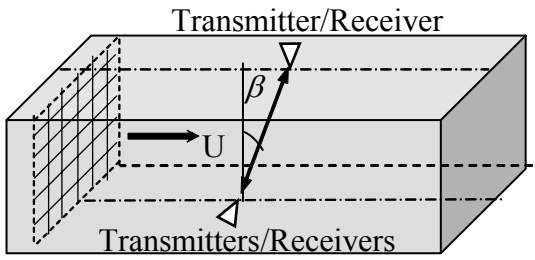


Figure 1: Wind-tunnel test section with flowmeter.

3 Experimental results and discussion

In the present work we demonstrate summary of the present work consisting of two parts: experimental demonstration of caustic effect and development of a semi-analytical model based on experimentally measured travel-time statistics for determination of statistical characteristics of grid-generated turbulence, such as correlation functions and spectral density of turbulent velocity and temperature fields.

3.1 Caustic effect

In this part two series of experiments, for heated and non-heated grids, were conducted. Experiment for a non-heated grid was devoted to a study of the travel time variance as a function of the travel path and turbulent intensity for long distances. The second set of experiments is conducted for the heated and non-heated grids at constant mean velocity for short travel distances to evaluate the effect of thermal fluctuations on travel time variances.

3.1.1 Non-heated grid experiment

Path length was changed from 0.0508m to 0.254m and the transducers were of 100 kHz working frequency. The first grid size, M_1, was $6.35 \cdot 10^{-3} m$. The measurements were collected at 0.63m downstream the grid. The mean flow

velocity U was 0m/s, 10m/s, 15m/s, 18m/s, 20m/s. The corresponding Reynolds numbers Re_{M_1} based on M_1 was 4200, 6350, 7200, 8400. We compare the travel-time variance with Chernov [20] estimates and with theoretical estimations of second-order travel time variance by Iooss *et al*. [6]

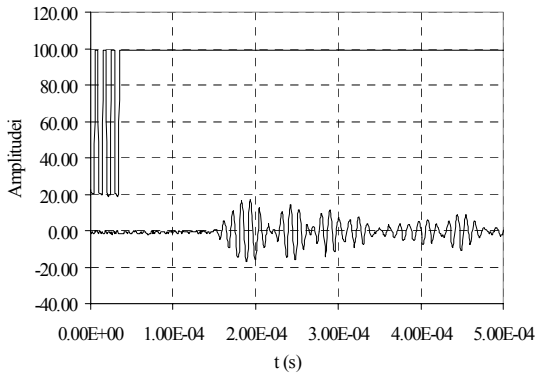


Figure 2: Transmitted (left) and received (right) waves.

Probability densities for the occurrence of caustics were calculated theoretically [4],[8]-[10],[11],[22]. For our experimental data we estimate the probability density of occurrence of caustics using theory developed by Klyatskin [11] and explored by Blanc-Benon *et al*. [9] and Iooss *et al*. [6]. The probability density function $P(\tau)$ for a plane wave propagating through 3D isotropic turbulence is defined as [8],[11]

$$P(\tau) = \frac{\alpha}{\tau^4}\exp\left(-\beta/\tau^3\right), \alpha = 1.74, \beta = 0.66 \tag{1}$$

The normalized distance τ is defined as $\tau = D^{1/3}x$,where D is the diffusion coefficient introduced by Klyatskin and x is a variable travel distance. For a Gaussian correlation function the diffusion coefficient D in a moving random medium is defined in [9] as

$$D = \frac{\sqrt{\pi}}{2L_0^3}\sigma_\varepsilon^2; \sigma_\varepsilon = \sqrt{\left\langle \varepsilon^2 \right\rangle}; \varepsilon = 2n\,, \tag{2}$$

where σ_ε is a standard deviation of an index of refraction ε and n are fluctuations in the refractive index. In Figure 3 the probability density of the occurrence of caustics is plotted along with experimental data for the travel time variance, Chernov theory for the linear propagation and results of the theoretical model developed by Iooss *et al*. as functions of normalized distance of propagation, τ. The peak of the probability density function appears at approximately $\tau = 0.85$, which corresponds to $x \approx 8.5 \cdot 10^{-2}\,\mathrm{m}$, or in non-

dimensional units $x/M_1 \cong 13.2$. It is noted in [22],[23] that strong fluctuations are connected with random focusing of acoustic waves. The level of amplitude fluctuations is expressed through the wave amplitude as $\chi = \ln(A/A_0)$ and, the variance of the log amplitude variations is $\sigma_A^2 = \left\langle \left(\chi - \langle\chi\rangle\right)^2 \right\rangle$. In Fig. 4 experimental data for the standard deviation of log amplitude variations versus actual travel distance is plotted for undisturbed medium, $10m/s$, $15m/s$, $20m/s$. Fig.4 exhibits substantial increase in standard deviation of log amplitude variations in the region, where probability density is different from zero, which has been predicted theoretically [22][23].

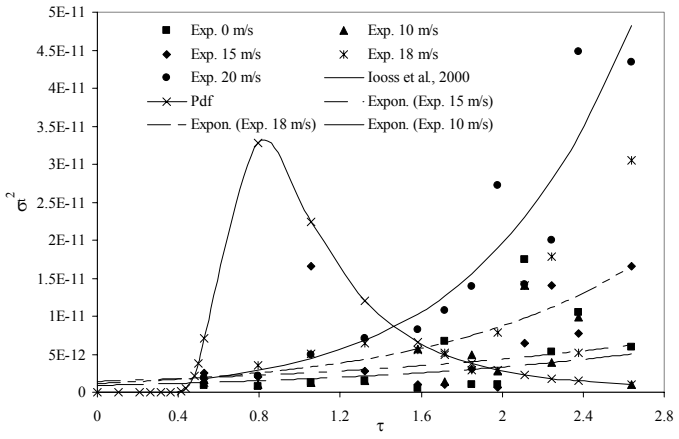


Figure 3: PDF of occurrence of caustic.

3.1.2 Heated grid experiment

Nine cases of different distances *L* for two different temperatures $T = 59^{\circ}F$ and $T = 159^{\circ}F$, were studied. The grid size was $M_3 = 2.54 \cdot 10^{-2} m$. To insure the high quality grid the heating elements were inserted in hollow aluminum rods with diameter $d = 6.35 \cdot 10^{-3} m$. The mean flow velocity was $U = 3.5$ m/s. The Reynolds number Re_M based on M and U was about $6 \cdot 10^3$ and the corresponding Péclet number $Pe_M = \mathrm{Pr}\,\mathrm{Re}_M \sim 4350$; $\mathrm{Pr} = 0.725$ for the working fluid air. The goal is to compare the dynamics of the travel-time variances for heated and non-heated grid experiments. Fig. 5 shows the travel-time variation as a function of scaled distance of propagation. It is obvious that temperature fluctuations lead to the appearance of nonlinearity in the dynamic of the travel time variance. The travel time variance at $59^{\circ}F$ is plotted for a comparison. The experimental data confirm theoretically and numerically

established theory stating that the higher the turbulent intensity, the shorter the distance at which the first caustics occurs [4].

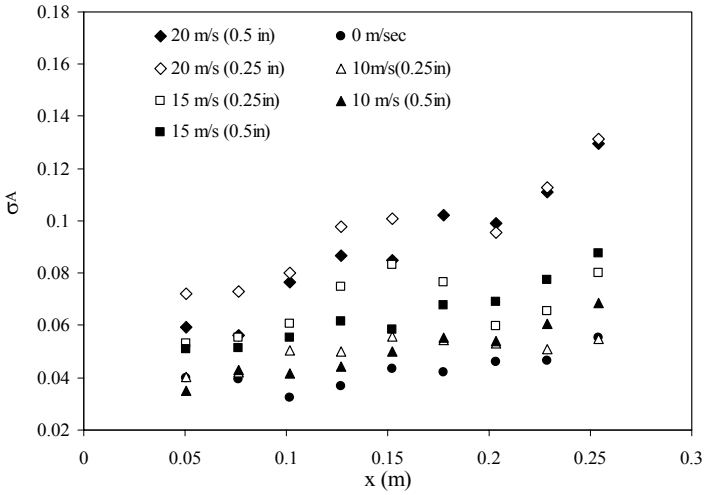


Figure 4: Standard deviation of log amplitude variations.

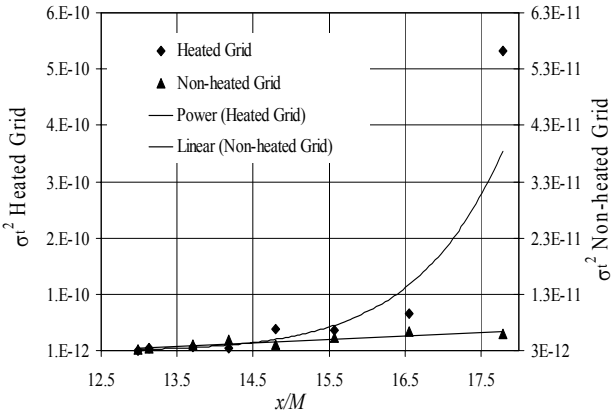


Figure 5: Experimental data for the travel time variance.

3.2 Correlation function of velocity fluctuations

The sound propagates across a grid-generated turbulence from a transmitter to a receiver separated by a distance s as shown in Fig. 1.

The angle β is changed from 0 to 40 degrees with 5-degree step. The measurements were collected at $x/M = 25$ x/M=35, where radiation effects are

negligible. The mean flow velocity U was 3.5 m/s. The Reynolds number R_M based on M and U was about 10000 and the corresponding Péclet number $Pe_M = \Pr \mathrm{Re}_M$ ~4350; $\Pr = 0.725$ for the working fluid air. . A more detailed description of the experimental particulars may be found in [24]. Basic flowmeter equation may be used to derive an expression for a travel time t of a wave traveling from the speaker to microphone.

$$t = \int_s \frac{dy}{c-u} \approx t_0 + \frac{1}{c^2}\int_s u'dy; u = U\sin\beta + u' \tag{3}$$

where t_0 is a travel time in the undisturbed media, U is a mean velocity, c is a sound speed, u' are fluctuations of the mean flow velocity. In Equation (3) we neglected the terms of order $U/c, U^2/c^2$. Introducing a new variable $t_0 = t - < t >$ and neglecting correlation between fluctuations of velocity and sound speed one gets:

$$K_{t_0}(s,s') = \frac{1}{c^4}\left[\int_s\int_{s'}\left(K_{u'}(x,x') + K_{c'}(x,x')\right)dxdx'\right] \tag{4}$$

For the case of room temperature, $T = 59^0 F$, equation (4) reduces to [24]:

$$K_{t_0}(s,s') = \frac{1}{c^4}\left[\int_s\int_{s'}\left(K_{u'}(x,x')\right)dxdx'\right] \tag{5}$$

In many practical problems, the form of the correlation function is not known. However, its general shape is often approximated by a Gaussian function.[15] We represent the correlation function in Equation (5) by

$$K_t^{59F}(s,s') = \sigma_t^2\big|_{F59}\exp\left(-(s-s')^2/l^2\right) = \sigma_t^2\big|_{F59}\exp\left(-\tau^2/l^2\right) \tag{6}$$

Here σ_t^2 is a variance of travel time fluctuations. Choice of l made on the basis of the integral length scale of the turbulence [15]. Figure 6 demonstrates correlation function of travel time obtained using experimental data as a function of separation distance x compared with Gaussian curve providing the best fit. Experimental data allows us to determine unknown coefficients, $\sigma_t^2 = 9.85e-15$ and $l^2 = 0.0036$. Integration of Equation (5) with known leads to the following form of correlation function of turbulent velocity

$$K_{u'}^{F59^\circ}(\tau) = c^4\left[2\frac{\sigma_t^2\big|_{F59^\circ}}{l^2}\exp\left(-\tau^2/l^2\right)\right] - c^4\left[4\frac{\sigma_t^2\big|_{F59^\circ}}{l^4}\tau^2\exp\left(-\tau^2/l^2\right)\right] \tag{7}$$

Figure 7 shows the correlation function of turbulent velocity for our particular experimental data. Variance of velocity fluctuations is $\sigma_{u'}^2 = 2c^4\frac{\sigma_t^2}{l^2} = 0.0801$. At

the same time we know, that $\sigma_{u'} = \left\langle u'^2 \right\rangle^{0.5}$, meaning that for our experimental conditions we have very small values of $u'^2/c^2 \sim 6.9 \cdot 10^{-7}$, which is in a very good correspondence with data [24]. The ratio of a turbulent velocity to the mean velocity is $\alpha = u'/U \cdot 100\% \sim 6\%$, which is typical for experiments performed in grid turbulence [19].

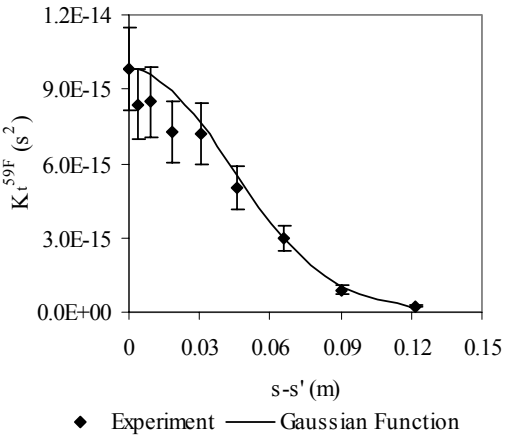


Figure 6: Correlation function of travel time.

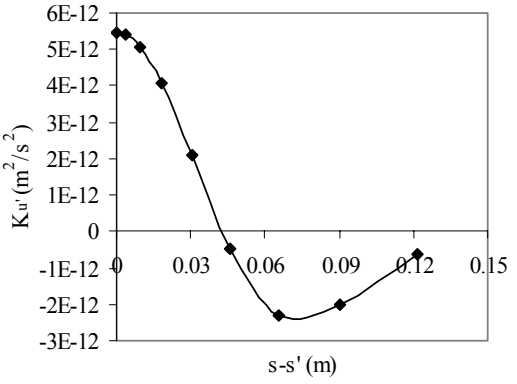


Figure 7: Experimentally obtained correlation function.

4 Conclusions

Analysis performed in laboratory conditions permit accounting for effect of temperature and velocity fluctuations resulting in occurrence of caustics, i.e., allows examining possible upgrades to travel-time meters and processing arrangements before expenditures. Semi-analytical Acoustical Model based on

travel-time measurements allows assessing the statistical properties of the flow-testing environment, while requires the knowledge of only one parameter, which is measured experimentally – travel time.

References

[1] Lynnworth, L.C., "Ultrasonic Measurements for Process Control," Academic Press, San Diego, CA, 1989.

[2] Johari, H. and Durgin, W.W., "Direct Measurements of Circulation using Ultrasound," Experiments in Fluids, Vol. 25, 1998, pp.445-454.

[3] Yeh, T.T. and Espina, P.I., "Special Ultrasonic Flowmeters for In-situ Diagnosis of Swirl and Cross Flow", Proceedings of ASME Fluids Engineering Division Summer Meeting, FEDSM2001-18037, 2001.

[4] Juvé, D., Blanc-Benon, Ph. and Comte-Bellot, G., "Transmission of Acoustic Waves through Mixing Layers and 2D Isotropic Turbulence," Turbulence and Coherent Structures, Métais and Lesieur, eds. Selected papers from Turbulence 89: Organized Structures and Turbulence in Fluid Mechanics, Grenoble, 18-21 September 1991.

[5] Karweit, M., Blanc-Benon, Ph., Juvé, D. and Comte-Bellot, G., Simulation of the Propagation of an Acoustic Wave through a Turbulent Velocity Field: a Study of Phase Variance," Journal of Acoustical Society of America, Vol. 89(1), 1991, pp. 52-62.

[6] B. Iooss, Ph. Blanc-Benon and C. Lhuillier, "Statistical moments of travel times at second order in isotropic and anisotropic random media," Waves Random Media, 10, 2000, pp. 381-394.

[7] Codona, J.L., Creamer, D.B., Flatte, S.M., Frelich, R.G. and Henyey, F.S., "Average Arrival Time of Wave Pulses Through Continuous Random Media," Physics Review Letters, Vol. 55(1), 1985, pp.9-12.

[8] Kulkarny, V.A. and White, B.S., "Focusing of Waves in Turbulent Inhomogeneous Media," Journal of Physics of Fluids, Vol. 25 (10), 1982, pp. 1779-1784.

[9] Blanc-Benon, Ph., Juvé, D., Ostashev, V.E. and Wandelt, "On the Appearance of Caustics for Plane Sound-Wave Propagation in Moving Random Media," Waves in Random Media, Vol. 5, 1995, pp. 183-199.

[10] Blanc-Benon, Ph., D. Juvé, and G. Comte-Bellot, "Occurrence of caustics for high-frequency caustic waves propagating through turbulent field," Theoret. And Comput. Fluid Dynamics 2, 1991, pp. 271-278.

[11] Klyatskin, V.I., "Caustics in Random Media," Waves in Random Media, Vol. 3, 1993, pp. 93-100.

[12] V.E. Ostashev, "Sound propagation and scattering in media with random inhomogeneities of sound speed, density and medium velocity," Waves in Random Media Vol. 4, 1998, pp. 403-428.

[13] G.A. Daigle, T.F.W. Embleton and J.E. Piercy, "Propagation of sound in the presence of gradients and turbulence near the ground," Journal of Acoustical Society of America, Vol. 79, 1986, pp.613-627.



[14] T.A. Andreeva &W.W. Durgin, "Ultrasound Technique for Prediction of Statistical Characteristics of Grid-Generated Turbulence," AIAA Journal to appear in 2002.
[15] V.E. Ostashev, "Acoustics in Moving Inhomogeneous Media," (E & FN SPON, London, UK, 1997).
[16] Andreeva, T.A, and Durgin, W.W., "Experimental Investigation of Ultrasound Propagation in Turbulent, Diffractive Media," The Journal of the Acoustical Society of America, accepted for publication, 2003 (d).
[17] K.R. Sreenivasan, S. Tavoularis, R. Henry and S. Corrsin, "Temperature fluctuations and scales in grid-generated turbulence," *J. Fluid Mech.* **100** (3), 597-621 (1980).
[18] G. Comte-Bellot and S. Corrsin, "Simple Eulerian time correlation of full- and narrow-band velocity signals in grid-generated, "isotropic" turbulence," J. Fluid Mech. 48(2), 273-337 (1971).
[19] T.T. Yeh and C.W. van Atta, "Spectral transfer of scalar and velocity fields in heated-grid turbulence," *J Fluid Mech.* **58**(2), 233-261 (1973).
[20] L. Chernov, "Wave propagation in a random medium," McGraw-Hill, New York, 1961.
[21] Blanc-Benon, Ph., Juvé, D., Ostashev, V.E. and Wandelt, R, "On the Appearance of Caustics for Plane Sound-Wave Propagation in Moving Random Media," *Waves in Random Media*, Vol. 5, 1995, pp. 183-199.
[22] Kravtsov, Yu.A., "Strong Fluctuations of the Amplitude of a Light Wave and Probability of Formation of Random Caustics," *Soviet Physics JETP*, Vol. 28(3), 1969, pp. 413-414.
[23] Tatarski, V.I., The Effect of the Turbulent Atmosphere on Waves Propagation, Israel Program for Scientific Translation, Jerusalem, 1971.
[24] Andreeva T.A. and Durgin, "Some Theoretical and Experimental Aspects in Ultrasonic Travel Time Method for Diagnostic of Grid-generated Turbulence," *World Congress on Ultrasonics* , Paris, France, September 7-10, 2003.
[25] Sepri, P., "Two-point Turbulence Measurements Downstream of a Heated Grid," *The Physics of Fluids,* Vol. 19 (12), 1976, pp. 1876-1884.



Aluminized composite solid propellant particle path in the combustion chamber of a solid rocket motor

Y. M. Xiao & R. S. Amano
Department of Mechanical Engineering, University of Wisconsin, Milwaukee, U.S.A.

Abstract

In a solid rocket motor (SRM) using aluminized composite solid propellant and a submerged nozzle, a two-phase flow needs to be investigated by both experiment and computation. The boundary conditions for the ejecting particles constrain their trajectories, hence these affect the two-phase flow calculations, and thus significantly affect the evaluation of the slag accumulation. A new method to determine the velocities of particles on the solid propellant surface was developed in the present study, which is based on the RTR (X-ray Real-time Radiography) technique and coupled with the two-phase flow numerical simulation. A method was developed to simulate the particle ejection from the propellant surface. The moving trajectories of metal particles in a firing combustion chamber were measured by using the RTR high-speed motion analyzer. Image processing software was also developed for the RTR images, so the trajectories of particles could be obtained. Numerical simulations with different propellant-surface boundary conditions were performed to calculate particle trajectories. By comparing the two trajectories, an appropriate boundary condition on the propellant surface was referred. The present method can be extended to study the impingement of particles on a wall and other related two-phase flows.
Keywords: solid rocket motor, propulsion, experiments, CFD, X-ray.

1 Introduction

Many solid rocket motors (SRMS) use aluminized propellants and submerged nozzles to improve performance. When these propellants burn, the aluminum



WIT Transactions on Engineering Sciences, Vol 52, © 2006 WIT Press
www.witpress.com, ISSN 1743-3533 (on-line)
doi:10.2495/AFM06016

powder melts to form agglomerates on the propellant surface. These agglomerates may move along the surface and then onto the case wall, or may be ejected into the gas flow in the combustion chamber where they burn almost completely to form liquid aluminum oxide (Al_2O_3) droplets. Slag is generated behind the submerged nozzle in two ways; one is that the agglomerates stream into this region along the case wall, and the other is that the droplets are trapped into this region. The entrapment is affected by the droplet diameter, bulk density, velocity and position. For boosters of the space shuttle and other larger-scale solid rocket motors the slag accumulation may reach 1000-1500 kg (Salita, 1995). Thus slag simulation is very important for SRM designers to improve the performance of the motor.

The research on slag accumulation is very active in recent years. As the cost of experiments is very high and the operation environment is very severe due to high temperature and high pressure, the research in this field is mostly focused on numerical simulation. A simulation technique requires four steps:

(1) Accurate predictions of the flow field for the gas phase (selection of a numerical method);
(2) Knowledge of the distribution of the particle size;
(3) Modeling of droplet trajectory (particle tracing);
(4) A definition of "capture rule," that determines which particles will be retained in the chamber as slag.

Boraas [1], Haloulakos [8], Hess et al [9], and Meyer [12], conducted extensive modeling of slag accumulation and obtained some useful conclusions. In 1990s, a number of two-phase compressible viscous CFD codes have been developed for modeling internal two-phase flows in a SRM, e.g., Thiokol's SHARP (Golafshani and Loh [7]), SRA's CELMINT (Sabnis et al. [17]), and Aerospace's IS (Chang [4]). In mid 1990s, Salita [16], Chauvot et al. [6], and Liaw et al. [11] focused their research on slag behavior, including combustion, evaporation, and breakup. Their work adds insight to slag accumulation process. Unfortunately, the initial velocities of particles on the solid propellant surface were chosen artificially in these researches and the conclusions were different.

There exists extensive literature on the distribution of Al_2O_3 particle size in the combustion products of aluminized composite propellants. Of all the reports, the experimental results by Braithwaite et al. [2] cover a wide range, and seem to provide a reasonable particle-size distribution. The particle-size distribution function measured by them has been widely used by many researchers.

From the above discussion it is found that use of a numerical simulation is an efficient tool to study the two-phase flow in SRM. The key is to find an experimental method to provide experimental data for some uncertain parameters in the mathematical model to validate the simulation results. As the operating environment in the combustion chamber is extremely severe (temperature may reach 3500K, pressure may be over 20×10^6 atm), it is very difficult to measure the particle velocity in the combustion chamber. The X-ray RTR is a relatively reliable technology developed in the 1980s and provides the possibility to improve this research. Xiao et al. [18] reported some experimental data and proposed a method to determine the ejection velocity of particles on the burning



surface. An improved test rocket motor is used in the present experiment and RTR images with better quality will be presented.

2 Radiography system

The details of a real-time X-ray radiography system were discussed by Char et al. [5], and thus only a brief summary is discussed in this section. A schematic diagram of the X-ray RTR system is shown in Fig. 1. The X-ray head produces a continuous stream of X-rays. The X-rays pass through an opening in the first of two lead diaphragms; attenuation occurs as the X-rays encounter the test motor and the particles in the combustion chamber. The attenuated X-rays pass through an opening in a second lead diaphragm on the other side of the test rig before reaching the image intensifier. The X-ray signal causes fluorescence of cesium iodide on the receiving screen of the image intensifier. The image intensifier transforms the X-ray image into a visible-light image with a time constant of less than 1 μs. This visible image is recorded with a high-speed video camera (up to 6000 fps), and later analysed with the image-processing system.

3 Feasibility analysis

From the above-mentioned descriptions to RTR measurement system, the following features can be deduced:

(1) The media and its thickness on the traces of X-rays affect the X-ray intensity distributions on the receiving screen of the image intensifier.
(2) If the X-ray intensifier can identify the attenuation of X-ray by the media, human's eyes may identify this signal after being augmented.
(3) The images recorded by high-speed recording system are presented by motion pictures.

The flow in the combustion chamber is a gas-solid two-phase flow. As the attenuation coefficient of the gas to X-rays is much less than that of metal particles, the attenuation of the gas to X-ray is ignored in actual applications. For a single particle its attenuation to X-ray is limited and may not be identified by the X-ray intensifier. Therefore, only those particles whose sizes are large enough to produce attenuation to the X-rays to be identified by the X-ray intensifier can be observed in the experiments. Another fact is that the X-rays have to pass through the walls with a relatively high attenuation coefficient to X-rays, and the wall thickness of the motor is much larger than the particle size. Then the intensity variation caused by large particles with a high attenuation coefficient to X-rays will be weak and it is not much clear on the image. In the present experimental system, the wall is made of Aluminium plate with thickness of 10mm, the tube voltage is 125kV. I_0, I_1, and I_2 are the X-ray intensities before penetrating the aluminium plate, in the combustion chamber, and after passing through the second aluminium plate, respectively. Table 1 shows the half-value thickness and the attenuation coefficient to X-rays of several metal materials. Figure 2 shows the layout of X-ray imaging. From the Beer's law (Char et al., 1987) the following relation can be obtained:

$$I_1 = I_0 \exp(-\beta_1 L_1) \tag{1}$$

$$I_2 = I_1 \exp(-\beta_2 L_3) \tag{2}$$

where $L_1 = L_3 = 0.01m$, $L_2 = 0.05m$, and for aluminium $\beta_1 = \beta_2 = 0.15$. As the gray range for a digit image is 256, the smallest size of a particle to be identified on the image should satisfy the following relation:

$$|\Delta I| \geq \frac{I_2}{256} \tag{3}$$

From the Beer's law we have:

$$\begin{aligned} dI &= I_0 \beta \exp(-\sum_{i=1}^{n} \beta_i L_i) dL \\ \Delta I &= -I_0 \beta \exp(-\sum_{i=1}^{n} \beta_i L_i) \Delta L \end{aligned} \tag{4}$$

and

$$\Delta L_{\min} = -\frac{\Delta I_{\min}}{I_0 \beta \exp(-\sum_{i=1}^{n} \beta_i L_i)} \tag{5}$$

From Eq. (5) and Table 1 the smallest particle sizes which can be identified in image processing for some metal materials are evaluated in Table 2.

Table 1: The smallest size to be identified by image processing with tube voltage of 150kv (μm).

Fe	Al	Cu	W	Pb
12.6	**26.1**	**11.2**	**5.50**	**8.17**

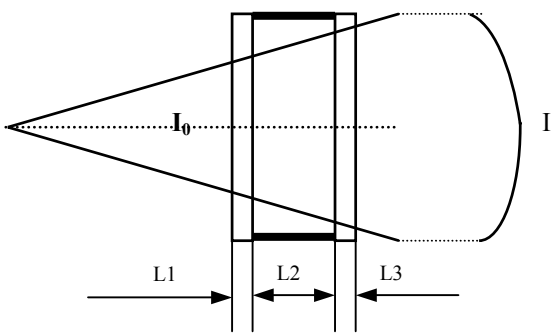


Figure 2: Layout of X-ray imaging.

The smallest sized particles listed in Table 2 were deduced from the image identification and from which we can identify most of the particles in the combustion chamber. Actually the identification of particles by the RTR technique is also constrained by the resolution of the receiving screen. As the particles with small size can flow with the gas the accumulation of slag in aft domain of the chamber is mainly formed by large size of particles. Our concern focuses on this group. The effort is still contributed to improve the propellant sample to ensure more particles on the trace of an X-ray.

4 Experimental method

From the feasibility analysis described in the preceding section it is concluded that it is possible to measure the trajectory of particle in a firing SRM combustion chamber. However, in an actual case, the operation is very difficult. Following issues should be resolved before the experiment is set up:

(1) **The ejection of metal powder**. The ejection of particles from a composite propellant burning surface needs to be imitated without scattering the particles in the entire chamber. Since if the particles are agitated the position of a moving particle will be strongly interacted with its neighbors. Therefore, the choice of an aluminized composite propellant as the propellant model is impossible. For this reason double-base propellant was chosen as the "driving force" of the metal powder. The powder ejection imitation can be accomplished by putting the metal powder in small holes or narrow slots.

(2) **The selection of metal particles**. A material with a high attenuation coefficient to X-rays should be selected as the metal particles. W powder was selected as the metal particle because of its high value of attenuation coefficient (0.78).

Figure 3 shows the layout of the test rig. The central computer sends signals to the time sequence controller to control the ignition, while the pressure signal was recorded by the computer. In order to enhance the identification of metal particles in RTR images, following techniques were employed in the experiment:

(1) Particles were injected from a narrow slot perpendicular to the flow-stream. In this way the projections of particles at the same height would be located at the same pixel on the RTR image and the attenuation to X-rays in this position would be several times higher than that for a single particle. This could greatly improve the image effect.

(2) The propellant sample and the SRM combustion chamber were made to be two-dimensional.

(3) Small focus should be used for the X-ray generator to reduce the X-ray intensity from the tube head, which would increase the ability for identifying the details.

Figure 4 shows the propellant sample model. The surfaces were insulated except the burning surface to ensure the two-dimensional. Some parameters for the test are listed as follows:



Combustion chamber: 200×60×50 (mm)
Propellant sample model: 150×12×50 (mm)
Slot: 0.5 mm
W powder: ϕ75 μm
Operation pressure: 6×10^6 Pa
Combustion temperature: 2765K

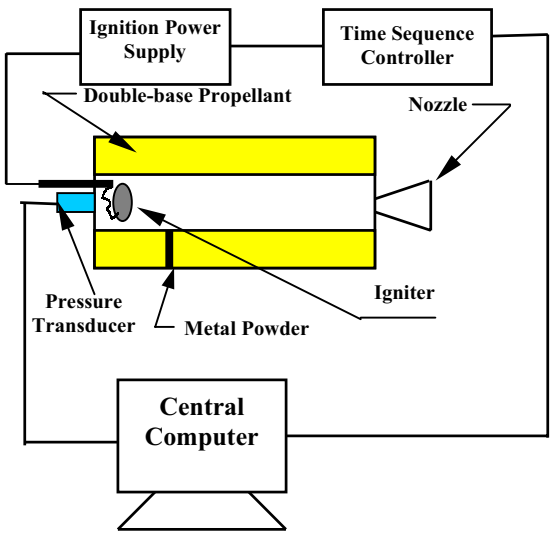


Figure 3: Layout of test rig.

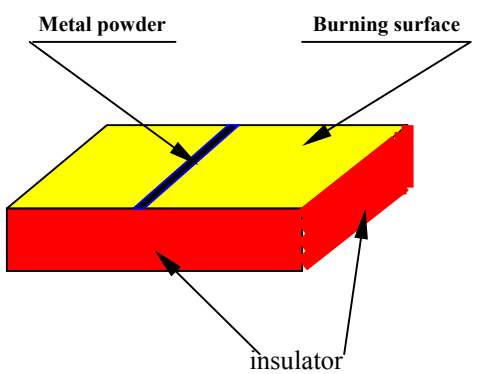


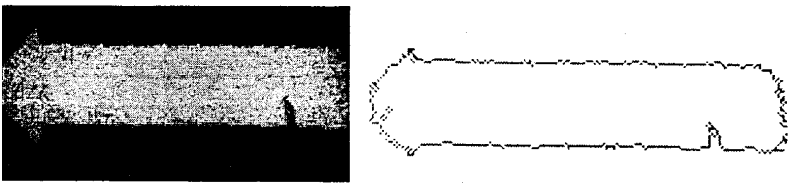
Figure 4: Layout of propellant model.

5 Results and discussion

5.1 Experimental results

From the basic principle of the generation of X-ray image it was found that the quality of the image is mainly dominated by the X-ray intensity distribution on the receiver's screen, but it is also affected by the following factors:

(1) The experimental system is off from the ideal state. In an actual case, the X-rays are not emitted from a single point, which may cause stripes or obscurity on the image. The Compton scattering induced by the walls of the motor and the propellant models will affect the intensity distribution on the screen. Environmental factors such as vibration of the test rig and fluctuation of electricity voltage will also affect the image quality.
(2) The particle is moving and the image is projected by a motion picture.
(3) The image resolution constrains from the high-speed motion analyzer. There are 239×192 pixels in one picture and this index is mainly constrained by the memory of the processor and the high-speed data transfer.



(a) Before image processing. (b) After image processing.

Figure 5: Typical initial RTR image (t=0.408s).

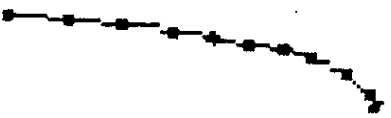


Figure 6: Particle trajectory obtained by image addition.

Figure 5 shows a typical initial RTR image. From this image it can be seen that there is a group of particles ejected to the combustion chamber from the burning surface. In any event, the quality of the image shown here is poor and it is difficult to distinguish the particles from the background. Therefore it is necessary to do some processing on the initial images to improve the quality. For this reason a image processing software was developed by the authors (Xiao et al., [18]) to deal with the RTR images, in which image addition, linear transformation of grays, neighbor-domain averaging, background subtraction, time-domain filtering, and image enhancing were all included. Applications showed that this software is valid to deal with the trajectories of particles with

large diameters (more than 75μm), and the effect is not good as it is expected. Li [10] suggested a method to improve the image quality and the resolution of the image could also be improved. This method is based on the interpolation on the local image information. A Berstein camber is constructed around the interested pixels and an interpolation can be conducted on finer grid.

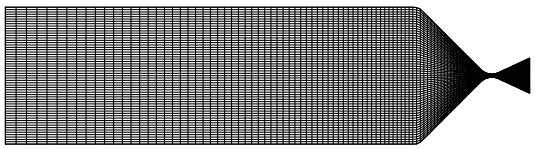


Figure 7: Grids.

5.2 Computational modelling

In order to calculate the trajectory of a particle in the combustion chamber, the gas flow field may be simulated first. For the present case, the mass fraction of particles in the combustion chamber is very low (particles was ejected from one slot), the effect of particles on the flow of gas phase is ignored. There are several methods to simulate the gas flow field in a SRM combustion chamber, such as by pressure correction methods (Patankar [14]), the AF (Approximate Factorization) method (Cai et al. [3]), etc. In the present calculation the Navier-Stokes equations are solved by AF method to calculate the flow field. As the flow is transonic flow at the throat of the nozzle, the grid distribution in axial direction is attracted to the throat. The total number is 98 × 60.

Usually there are two ways to perform the trajectory calculation: (1) Lagrangian method, in which particles are considered as a dispersed phase and each particle or particle group is followed in Lagrangian coordinate system; (2) Eulerian method, in which both gas and particles are considered as continuous phases and can be treated in an integrate method. In the present calculations the Lagrangian method is used to model the particle trajectory.

The velocity of a particle can be determined by:

$$m_p \frac{d\vec{V}_p}{dt} = \vec{F}_D + \vec{F}_w \tag{6}$$

and the position of the particle can be determined from:

$$\vec{X}_p = \vec{X}_p^0 + \int_t^{t+\Delta t} \vec{V}_p dt \tag{7}$$

the drag force $\vec{F}_D$ is calculated from:

$$\vec{F}_D = \frac{\pi}{8} \rho_g d_p^2 C_D \left| \vec{V}_g - \vec{V}_p \right| (\vec{V}_g - \vec{V}_p) \tag{8}$$

where C_D is determined by:

$$C_D = \begin{cases} \dfrac{24}{\mathrm{Re}_d}\left[1 + \dfrac{\mathrm{Re}_d^{2/3}}{6}\right] & \mathrm{Re}_d \le 1000 \\ 0.424 & \mathrm{Re}_d > 1000 \end{cases} \tag{9}$$

where the Reynolds Number Re_d is defined as:

$$Re_d = \frac{\rho_g \left| \vec{V}_g - \vec{V}_p \right| d_p}{\mu} \tag{10}$$

Upon integrating Eqs. (6) and (7) the trajectory of the particle can be obtained. However, when integrating Eq. (6) the initial conditions must be assigned: the ejection position and velocity of the particle. When there is no experimental data to provide any information to determine this velocity, one of two assumptions are usually chosen:

(a) Setting the velocity to be zero, which means the particles on the burning surface, enter the gas under the force induced by the gas drag.

(b) The particle velocity is set equal to the gas velocity, which implies that there is no delay for velocity equilibrium between the gas and the particle.

As we mentioned above, this uncertainty results in a different particle trajectory and thus in a different slag accumulation. Actually, the initial condition is one that lies between these two procedures mentioned above. The method used here is summarized as follows:

The initial velocity may be written as:

$$\vec{V}_p^{\,0} = \alpha \vec{V}_g \Big|_{surface}, \qquad 0 \le \alpha \le 1 \tag{11}$$

where $\vec{V}_g \Big|_{surface}$ is the ejection velocity of gas on the propellant burning surface and it can be obtained from:

$$\vec{V}_g = \dot{r}_p \times \frac{\rho_p}{\rho_g} \vec{n} \tag{12}$$

Then a series of values α_i ($0 \le \alpha_i \le 1$) are chosen and the corresponding $\vec{V}_p^{\,0}$ obtained. From Eqs. (11) and (12), a series of particle trajectories can be calculated. By comparing the calculated trajectory with that obtained from the RTR measurement an adequate value for this case can be deduced. Let (x_i , y_i) be the particle position of the ith node in RTR image and ($x_i, y_i^{'}$) be the particle position of the ith node on the calculated trajectory. The standard deviation between two trajectories is defined as:

$$\sigma = \sqrt{\frac{\sum_{i=1}^{N} (y_i - y_i^{'})^2}{N}} \tag{13}$$

Here the minimum value from a series of σ can be obtained and then the corresponding α is computed, which will be used to determine the ejection velocity of particles.

Burning rate of propellant is 8.3mm/s. On the burning surface, the gas ejection velocity was imposed, the front end of the combustion chamber was set to be adiabatic wall, at the exit of the nozzle, the flow was supersonic and all parameters were ex-interpolation.

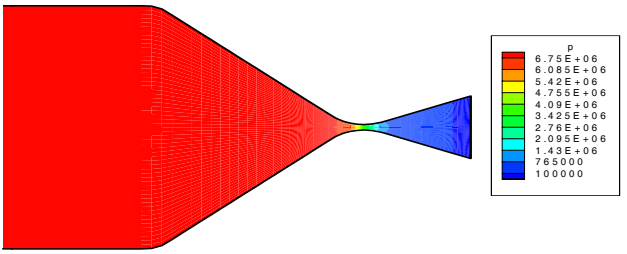


Figure 8: Pressure contour in the nozzle.

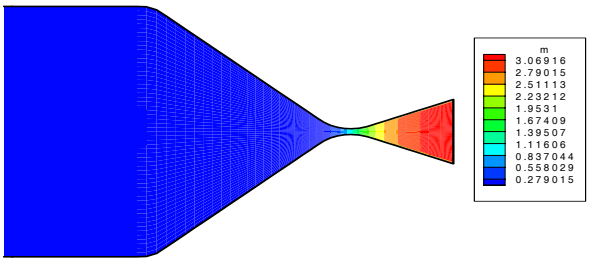


Figure 9: Mach number contour in the nozzle.

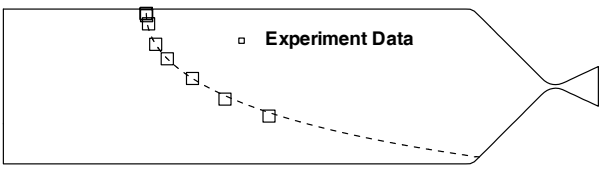


Figure 10: Comparison between calculation and experiment.

Figure 8 shows the pressure distribution in the nozzle. As the flow in the combustion is very slow, the pressure is almost kept constant. In present cases, no shock was found in the nozzle. Figure 9 shows the Mach number distribution in the nozzle. The core flow in the divergent section is approximately one-dimensional flow. In order to validate the numerical modelling, we compared the calculated trajectory with the measured one. In the present experiments, it was found that when $\alpha = 0.4$ the corresponding σ reaches minimum. Figure 10 shows the comparison between calculated trajectory and measured trajectory. It was concluded that, with the present initial conditions, the calculated trajectory agrees well with the measured one.

It was found that the particle trajectory passes through the centreline even with zero ejection velocity, which is in agreement with Zhou's conclusion [19]. Experiments with particles of small size (25μm) were done but the image processing results were poor. Using the sub-element interpolation technique to deal with the small particles is developing a new kind of image processing method and the preliminary results show that it was successful for the corresponding cases.

6 Conclusion

The moving trajectories of metal particles in a firing combustion chamber are measured by using a RTR high-speed motion analyser. Through this study the following conclusions emerge.

(1) With the 2-D test SRM combustion chamber, the propellant-sample model and particle-ejection model are successfully demonstrated.
(2) The metal particles enter into the gas with non-zero initial velocity. The velocity ratio was estimated to be approximately equal to 0.4 which was deduced from a numerical analysis.

The proposed method for determining the initial velocity of particles on the burning surface of a solid propellant is demonstrated to be successful. Appropriate boundary conditions for the numerical simulation can easily be obtained.

References

[1] Boraas, S., 1984, "Modeling Slag Deposition in the Space Shuttle Solid Rocket Motor," *Journal of Spacecraft and Rockets*. Vol. 21, No. 1, pp. 47-54.

[2] Braithwaite, P. C., Christensen, W. N., and Daugherty, V., 1988, "Quench Bomb Investigation of Aluminum Oxide Formation from Solid Rocket Propellants (Part I): Experimental Methodology," *Proceedings of the 25th JANNAF Combustion Meeting*, Vol. 1, pp. 178-184.

[3] Cai, T.M., Xiao, Y.M., and Sun, D., 1998, "Numerical Study on Internal Flow Field of SRM with Finocyl Grain and Submerged Nozzle," *The 49th International Astronautical Congress*, IAF-98-S.2.07.

[4] Chang, I.S., 1991, "An Efficient Intelligent Solution for Viscous Flows Inside Solid Rocket Motors," *AIAA Paper 91-2429*.

[5] Char, J.M., Kou, K.K., and Hsich, K.C., 1987, "Observation of Breakup Process of Liquid Jets Using Real-Time X-Ray Radiography," *AIAA Paper 87-2137*.

[6] Chauvot, J.F., Dumas, L., and Schmeisser, K., 1995, "Modeling of Alumina Slag Formation in Solid Rocket Motors," *AIAA Paper 95-2729*.

[7] Golafshani, M., and Loh, H.-T., 1989, "Computation of Two-Phase Viscous Flow in Solid Rocket Motor Using a Flux-Split Eulerian – Lagrangian Technique," *AIAA Paper 89-2785*.



[8] Haloulakos, V. E., 1991, "Slag Mass Accumulation in Spinning Solid Rocket Motors," *Journal of Propulsion and Power*, Vol. 7, No. 1, pp. 14-21.
[9] Hess, E., Chen, K., Acosta, P., Brent, D., and Fendell, F., 1992, "Effect of Aluminized-Grain Design on Slag Accumulation," *Journal of Spacecraft and Rockets*, Vol. 29, No. 5, pp. 697-703.
[10] Li, J., "A study on the motion pattern of particles in SRM," Ph.D thesis, Northwestern Polytechnic University, P.R. China, 1998.
[11] Liaw, P., Shang, H.M., and Shih, M.H., 1995, "Numerical Investigation of Slag Behavior with Cobustion/Evaporation/ Breakup/VOF Models for Solid Rocket Motors," *AIAA Paper 95-2726*.
[12] Meyer, R. X., 1992, "In-Flight Formation of Slag in Spinning Solid Propellant Rocket Motors*," Journal of Propulsion and Power*, Vol. 8, No. 1, pp. 45-50.
[13] Salita. M., Smith-Kent, R., Golafshani, M.T., Abel, R., and Pratt, D., 1990, "Prediction of Slag Accumulation in SICBM Static Flight Motors," *Thiokol TWR-10259*.
[14] Patankar, S.V., 1980, "Numerical Heat Transfer and Fluid Flow," *Hemisphere Publishing Corp*., Washington DC..
[15] Salita, M., 1995, "Predicted Slag Deposition Histories in Eight Solid Rocket Motors Using the CFD Model 'EVT'," *AIAA Paper 95-2728.*
[16] Salita, M., 1995, "Deficiencies and Requirements in Modeling of Slag Generation in Solid Rocket Motors," *Journal of Propulsion and Power*, Vol.11, No.1, pp. 10-23.
[17] Sabnis, J.S., De Jong, F.J., and Gibeling, H.J., 1992, "Calculation of Particle Trajectories in Solid Rocket Motors with Arbitrary Acceleration," *Journal of Propulsion and Power*, Vol.8, No. 5, pp. 961-967.
[18] Xiao, Y.M., R.S. Amano, Cai, T.M., and Li, J., "Numerical simulation and experimental validation on the particle trajectory in a solid propellant rocket chamber," *Proceedings of ASME 2000 International Design Engineering Technical Conferences and the international 20th Computers and Information in Engineering (CIE) Conference,* September 10-13, 2000, Baltimore, Maryland, paper No. DETC2000/CIE-14676.
[19] Zhou Xu, 1995, "A Numerical Analysis on 2-D Two-Phase Turbulent Flow in Combustor," *Journal of Propulsion and Power*, Vol. 116, No.5.



Simulation of unsteady muzzle flow of a small-caliber gun

Y. Dayan & D. Touati
Department of Computational Mechanics & Ballistics, IMI, Ammunition Group, Israel

Abstract

The present paper presents a simulation of a firing process of a 7.62mm bullet and muzzle flow out of a gun barrel. The calculation is made in two stages. First, an internal ballistics (IB) simulation via the IBHVG2 software package, is performed in order to obtain bullet travel dependent breech pressure and temperature. Following this, a simulation of unsteady muzzle flow is made, beginning at the start of bullet motion and ending one meter beyond the muzzle exit point. The second stage calculation is carried out via the CFD-FASTRAN finite volume solver package. The movement of the bullet is simulated by a chimera overset meshing technique. In general, there exists very good agreement between the computed IB and the measured muzzle velocity and pressures, and between the CFD precursors flow field, main propellant flow field calculations and the experimental shadowgraph results.
Keywords: blast, CFD-FASTRAN, chimera overset grid, first precursor, second precursor, mach disk, main propellant flow.

1 Introduction

Gun muzzle signature, blast and flash phenomena are of practical importance to the gun designer, especially their influence on firing accuracy. Overpressures and intense radiation affect the gun crew and surroundings and can be minimized by muzzle attachments that reduce the momentum of the exit flow [1, 2].

One of the challenges is to simulate the blast process numerically. The simulation results of the precursor flow field and main flow field phenomena help us to better understand the forces and present during these processes (jump phenomena). Another important aspect involves finding the forces acting on the



WIT Transactions on Engineering Sciences, Vol 52, © 2006 WIT Press
www.witpress.com, ISSN 1743-3533 (on-line)
doi:10.2495/AFM06017

bullet for asymmetric flows and their influence on the subsequent bullet's trajectory once it exits the muzzle [7–9].

Considerable progress has been made in the area of unsteady flow analyses of multiple moving bodies with the aid of CFD. One of the approaches currently used to solve the unsteady muzzle flow of a bullet (fired from a gun barrel) is to generate a grid for the bullet by a chimera/overset methodology [3], and the latter moves on the gun barrel's fixed grid via a six-degree-of-freedom model based on the theory of Etkin [4].

Figure 1 depicts the firing process of a 7.62mm bullet and muzzle flow out of a gun barrel.

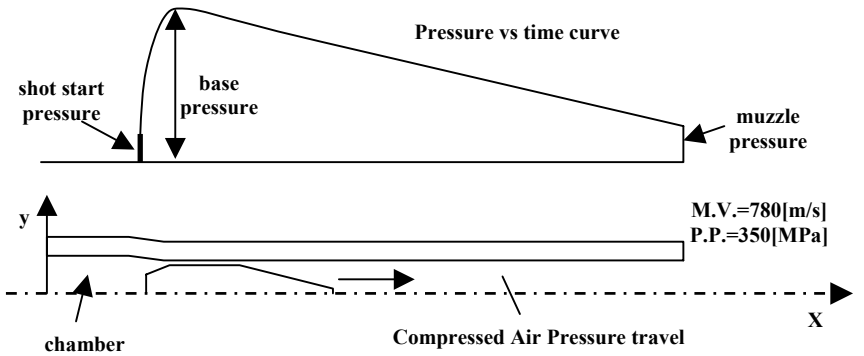


Figure 1: Pressure vs axial distance from the breech along gun tube for axisymmetric bullet.

2 Process description

One or two precursor flow fields and the main propellant gas plume are formed about the muzzle of the gun during its firing. These two or three impulsive jet flows that subsequently exit the muzzle of the gun interact with each other. The precursor flow fields are rapidly overtaken and destroyed by the main propellant flow.

The precursor flow is generated inside the gun tube due to the compression waves produced by the accelerating projectile, leaked propellant gas-particle flow. These waves rapidly coalesce into a steep precursor shock front, and then exit at the muzzle of the gun tube, expanding into the ambient atmosphere. A later stage of the precursor flow development is shown in the schematic drawing of figure 2. The air-air or gas-air interface ends laterally in a vortex due to the shear forces acting around the edge of the jet flow. The Mach disk forms and decelerates from supersonic to subsonic flow velocity. The gas-air interface in the axial direction takes the form of a distinct cap surface. The barrel shock develops undisturbed and terminates in the triple point from which the reflected shock and Mach disk originate.

After the bullet exits the gun barrel, the flow of the main propellant gases begins. The propellant gases exit the barrel at a pressure ratio of more than 500. Because the pressure ratio is much higher, the precursor blast wave is quickly overtaken.

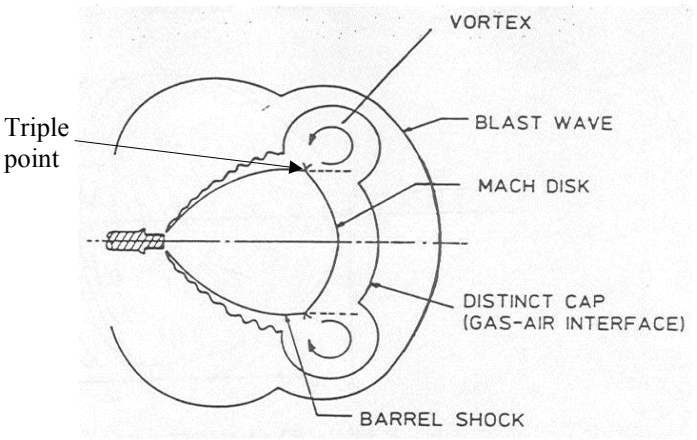


Figure 2: Later stage of precursor flow field (ref. [1]).

3 Numerical methods approach

The solution procedure involves solving the unsteady, conservative, Navier-Stokes equations. The numerical scheme employed is a finite-volume, Riemann solver with an upwind difference method for computed spatial derivatives. Fluxes are computed using Van leer's flux vector splitting scheme with second order accuracy. A fully implicit time integration scheme is employed to advance the solution in time, ensuring global time accuracy with a time step of 1.0e-007 sec and with 250 sub-iterations between each time step. The solution also includes a k-ε turbulence model with a wall function formulation.

The moving body (the bullet) problem solution involves solving the rigid body equations of motion accounting for the hot gas forces behind the bullet. The bullet is modelled by a Chimera methodology with a multi zone overlapped grid approach. It provides the flexibility of modelling geometries with multi domain grids in which different zones are allowed to overlap each other in an arbitrary manner. In the case of complex problems that involve multiple moving bodies, this methodology facilitates independent generation of grids, which could be tied together with other grids in the domain.

The major grid (gun tube) consisted of 160,000 grids points, while the minor grids (bullet) consisted of 20,000 points. The barrel length is 0.4m.

3.1 CFD-FASTRAN flow solver

The following Navier-Stokes equations are solved using the finite volume method [3]:

$$\int \frac{\partial \vec{Q}}{\partial t} dV + \int \nabla \cdot \vec{F}^{n+1} dV = 0 \tag{1}$$

where the vector $Q = (\rho, \rho u, \rho v, \rho w, E)$; the tensor $\vec{F} = (F, G, H)$ and where F and G are the inviscid and viscous flux vectors, respectively, H is the vector of source terms, V is the cell volume, and A is the surface area of the cell face.

3.2 Equation of chimera grid motion

The 6DOF motion model requires additional information to determine how the body moves, based on physical properties and forces [5]. This is achieved through the general equations of unsteady motion. The equations of motion for a rigid body with constant mass and mass moments of inertia as given by [4] are:

$$\vec{F} = m \frac{d\vec{v}}{dt} \tag{2}$$

$$\vec{M} = \frac{\partial \vec{h}}{\partial t} + \vec{\omega} \times \vec{h} \tag{3}$$

where

$\vec{F} =$ the resultant force vector of all forces
$\vec{M} =$ the moment vector about the body's centre of gravity
$m =$ the body mass
$\vec{v} =$ linear velocity vector of the centre of gravity
$\vec{h} =$ angular momentum
$\vec{\omega} =$ the angular velocity vector about the body's centre of gravity.

4 Results

The gun barrel selected for this CFD validation is a 7.62mm with a 0.4m barrel length. This configuration is characterized by two precursor flow fields and the main propellant flow field. Figures 3 through 6, present shadowgraphs (ref. [1]) and simulated density contour results starting from 370μsec before bullet ejection until 400μsec after the bullet exits the barrel.

In figure 3, (370μsec prior to bullet ejection) the outer spherical shock of the first precursor has developed (1). The outer blast wave has an identical size and shape to the CFD-FASTRAN simulation. In addition the vortex which is beginning to form, is also of similar size and shape as compared to the shadowgraph image. From the simulation, at this point in time, the bullet's position is 0.05m from the muzzle.

In figure 4 (at 40μsec prior to bullet ejection) the second precursor shock (2) appears. The simulated blast wave for the second precursor (from the CFD-FASTRAN simulation) is similar to the shadowgraph image. The Mach disk from the first precursor is clearly visible in the simulation but barely distinguishable in the shadowgraph. (it can barely be seen inside the plume turbulence). At this point in time, the bullet's position is 0.007m from the muzzle.



Figure 3: Shadowgraph (from ref. [1]) result versus simulation result of the first precursor flow field (370μsec before bullet ejection).

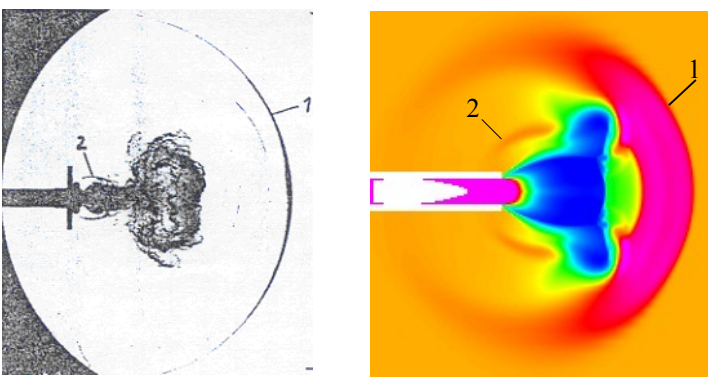


Figure 4: Shadowgraph (from ref. [1]) result versus simulation result of the first (1) and second (2) precursor flow fields (40μsec before bullet ejection).

At 60μsec after bullet ejection (see figure 5), the main propellant flow field (3) has developed. The beginning of the distortion of the first blast wave can be seen more clearly from the CFD-FASTRAN results. The blast wave of the propellant flow engulfs the base of the bullet, and a nearly vertical shock front is formed. The propellant gases ejected from the muzzle are supersonic, and they expand into the ambient region of relatively low gas pressure and low gas density.

At 400μsec after bullet ejection (figure 6), the propellant flow (3) starts to engulf the blast wave (1) of the first precursor flow and the bullet.

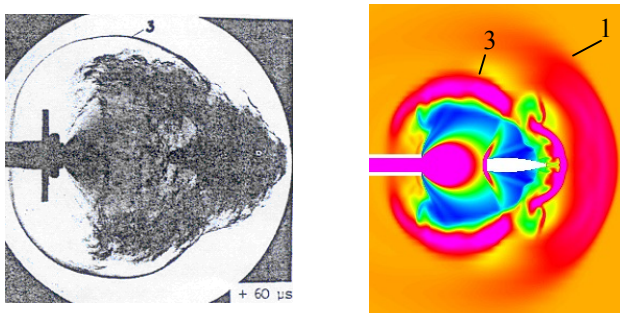


Figure 5: Shadowgraph (from ref. [1]) result versus simulation result of the first precursor flow field (1) and blast wave of main propellant flow (3) (60μsec after bullet ejection).

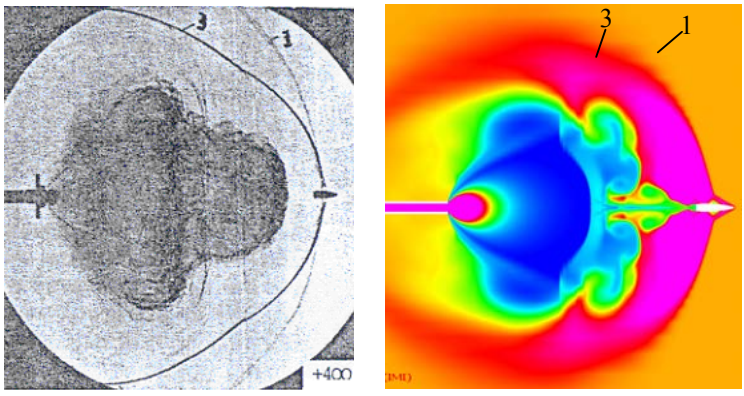


Figure 6: Shadowgraph (from ref. [1]) result versus simulation result of the first precursor flow field (1) and blast wave of main propellant flow (3) (400μsec after bullet ejection).

5 Conclusions

Several conclusions can be drawn from the CFD simulation of gun muzzle blast for a small calibre gun. These include:

- The chimera/overset grid methodology provides accurate meshing models for gun muzzle and bullet motion simulations
- The 7.62mm precursor flow fields and the main propellant flow results correspond closely to shadowgraph results

- The precursor flow fields and main propellant flow field results are very sensitive to:
  - Local ambient conditions (p_∞,ρ_∞)
  - Shape of the gun barrel and the bullet
  - Internal ballistic calculation for peak pressure (P.P), muzzle pressure (M.P.) and muzzle velocity (M.V.)

Acknowledgement

We wish to thank Mr. Aron Pila of the IMI Ammunition Group's Central Laboratory, for his assistance in editing this paper.

References

[1] N. Klingenberg and J. M. Heimerl, *Phenomenology of Gun Muzzle Flow,* In: *GUN Muzzle Blast and Flash*, AIAA, Vol. 139, pp 107-166.
[2] N. Klingenberg and J. M. Heimerl, *Blast Wave Research,* In: *GUN Muzzle Blast and Flash*, AIAA, Vol. 139, pp 167-193.
[3] CFD Research Corporation, CFD-FASTRAN User's Manual; Theory Manual, 2002.
[4] Etkin, B., *Dynamics of Flight-Stability and Control*, Second Edition, John Wiley & Sons, Inc., New-York, 1982.
[5] Z. J. Wang, V. Parthasararathy, and N. Hariharan, *A Fully Automated Chimera Methodology for Multiple Moving Body Problems*, 36th Aerospace Sciences Meeting & Exhibit, January 12-15, 1998.
[6] A. H. Klaus and T. C. Steve, *Computational Fluid Dynamics*, A Publication of engineering Education system, ISBN 0-9623731-3-3,Vol 1-3, August 2000.
[7] R. Cayzac, E. Carette, T. Alziary de Roquefort, *Intermediate Ballistics Unsteady Sabot Separation: First Computational and Validations*, 19th International Symposium of Ballistics, Switzerland, 7-11 May 2001.
[8] A. B. Crowley, and J. Szmelter, *Computational of Muzzle Flow Fields Using Unstructured Meshes*, 19th International Symposium of Ballistics, Switzerland, 7-11 May 2001.
[9] E. M. Schmidt, *Wind Tunnel Measurements of Sabot Discard Aerodynamics*, Technical Report ARBRL-TR-02246, July 1980.



This page intentionally left blank

Section 3
Hydraulics and hydrodynamics

This page intentionally left blank

Hot spots and nonhydraulic effects in surface gravity flows

T. B. Moodie[1], J. P. Pascal[2] & S. J. D. D'Alessio[3]
[1] *Applied Mathematics Institute, University of Alberta, Edmonton, Canada*
[2] *Department of Mathematics, Ryerson University, Toronto, Canada*
[3] *Department of Applied Mathematics, University of Waterloo, Waterloo, Canada*

Abstract

Surface gravity currents whose flow dynamics are modified by incoming solar radiation are of importance in the study of mechanisms related to the thermal bar in dimictic lakes as well as the spread of pollutants on the surfaces of reservoirs, lakes and oceans. We shall present results for such surface flows showing their dependence on various model parameters including the bottom slope, rate of heating and equation of state. The novel feature of this analysis is to show that the inclusion of a heat source term leads to the introduction of shear in the horizontal velocity field thereby ruling out the deployment of shallow-water theory with its depth-independent velocity field as a viable description of such flows. Calculations are presented to demonstrate that a purely hydraulic description will miss important dynamical features of the flows.
Keywords: surface gravity currents, thermal enhancement, nonhydraulic effects.

1 Introduction

A gravity current consists of the flow of one fluid within another when this flow is driven by the density difference between these fluids [1]. These currents are primarily horizontal, occurring as either top or bottom boundary currents or as intrusions at some buoyantly stable intermediate level. The density differences driving such flows may be due to salinity contrasts, as in oceanic settings [1], the presence of suspended material, as in the case of turbidity currents [2, 3], or temperature



WIT Transactions on Engineering Sciences, Vol 52, © 2006 WIT Press
www.witpress.com, ISSN 1743-3533 (on-line)
doi:10.2495/AFM06018

contrasts [4–6], as in the case to be treated here, or combinations of these mechanisms.

In the gravity current literature researchers have employed, in general, two different approaches. One direction of research has used hydraulic theory to study the time evolution of these currents from a state of rest while the other investigates the steady-state characteristics of a gravity current that has already been established without any concern for initial conditions [7]. It is, we believe, fair to say that this latter approach, which treats the current as steady, requires pressure balances that essentially rule out the inclusion of most of those physical processes that make these investigations important from the point of view of applications. Such processes would include the entrainment and sedimentation of particles that drive turbidity currents [8], the spatial and temporal influences of heating that modify the dynamics through density changes [5, 6] as well as the various flow modifications that arise from topographic forcing [9]. Adopting the former approach is not without difficulties when it comes to including these processes in the model formulation but it does offer an avenue of approach that the latter does not afford.

Our previous studies [3, 10, 11] have indicated that in the modelling of turbidity currents with sedimenting particles, horizontal gradients in particle concentrations result in a depth-dependent horizontal velocity field.

This depth dependence signifies that the deployment of shallow-water theory for these low aspect ratio flows must be brought into question. In the present analysis of thermally-enhanced surface gravity flows we will show that there is an analogous mechanism at work leading to 'hot spots' in the flow field that ultimately rules out the use of the standard shallow-water model for such flows.

In this article we develop and analyze a two layer fluid model governing the sudden release and subsequent motion of a fixed volume of light fluid whose initial density and temperature are ρ_* and T_*, respectively.These fixed volume releases have served as a paradigm for many atmospheric [12] and oceanic [1] gravity currents although it is the case that many of these flows being modelled arise not from a fixed volume release but rather from variable inflow through an opening in some barrier[13, 14]. We will provide some suggestions as to how such variable inflow problems might be approached but for now we consider our fixed volume as being released suddenly into a heavier ambient fluid of constant density $\rho_0 > \rho_*$ overlying a gently sloping bottom. The upper layer is subjected to incoming radiation and its density is assumed to decrease in time according to a general equation of state. The surface heat flux is assumed to be distributed uniformly over the local thickness of the upper layer [15]. This upper layer thickness being a function of both space and time will lead to a temperature field which is also a function of space and time with an increased heating rate for patches where upper layer thickness is diminished due to the unsteady nature of the flow. These radiation induced horizontal temperature gradients introduce distinctive $O(1)$ nonhydraulic effects into the flow field. This dependence of heating rate on the local depth of the heated fluid layer is consistent with observations in lakes and reservoir sidearms subjected to diurnal heating and cooling [15–17]. A similar mechanism is seen in bottom-hugging turbidity currents when sedimentation rate depends on the thickness of



the current [10]. In that instance sedimentation rates are greater for regions where the current is thinner leading to local decreases in the bulk density and hence the generation of horizontal gradients in the density field. It is these horizontal density gradients for both turbidity and thermally enhanced gravity currents that lead to the nonhydraulic nature of these flows.

2 Model formulation

We consider a gravity current produced by the release of a fixed volume of fluid having initial density $\rho_1 = \rho_*$ into an ambient fluid having a higher density $\rho_2 = \rho_0$(constant) overlying a mildly sloping bottom. The physical configuration is depicted in Figure 1, where $\eta(x,t)$ represents the displacement of the free surface from its undisturbed configuration, $\mathbf{u} = (u,w)$ is the fluid velocity in Cartesian coordinates with position vector $\mathbf{x} = (x,z)$, H is the mean depth of the two layer system measured from $z = 0$, $h(x,t)$ is the variable thickness of the lighter upper fluid layer and the bottom is located at $z = -sf(x)$, where $s(0 < s \ll 1)$ is a nondimensional slope parameter. In this study we will only consider a linearly varying bottom and thus set $f(x) = x$. The flow is driven by the buoyancy force arising because of the difference between the temperature dependent density $\rho_1(T)$ of the upper layer and the fixed density $\rho_2 = \rho_0$ of the ambient fluid. The relation between temperature and density for the upper layer is given in terms of an equation of state which will be assumed to have the general form

$$\rho_1(T) = \rho_0 \left[1 - \alpha(T - T_0)^n\right], \quad n = 1, 2, \tag{1}$$

wherein T_0 is the fixed temperature of the lower layer whose density is assumed fixed at ρ_0, α is the thermal expansion coefficient, and $n > 0$ is a power law index. Since the temperature of the lower layer is assumed to remain fixed we have chosen to measure the temperature $T_1 \equiv T$ of the upper layer relative to this fixed value. We shall take $T = T_* > T_0$ as the initial temperature of the release volume so that

$$\rho_1(T_*) = \rho_* = \rho_0 \left[1 - \alpha(T_* - T_0)^n\right] < \rho_0. \tag{2}$$

We have chosen to take $n = 1, 2$ in our study since these are natural choices. The case $n = 1$ corresponds to the usual description whereby the density decreases linearly with an increase in temperature. The case $n = 2$ can be used to approximate the density of fresh water near the temperature of maximum density [17], that is, $T_0 \approx 4\,^\circ$C. Here with $n = 2$ we would have $\alpha = 1.65 \times 10^{-5}\,^\circ\mathrm{C}^{-2}$.

Shown in Figure 1 is the released fixed volume of fluid which initially occupied the region $0 < z \leq H$. Assuming small temperature differences the Boussinesq approximation for the density is appropriate and will be invoked throughout our model development. We shall assume a surface heat flux I which is distributed uniformly over the local depth of the upper layer with no heating of the denser

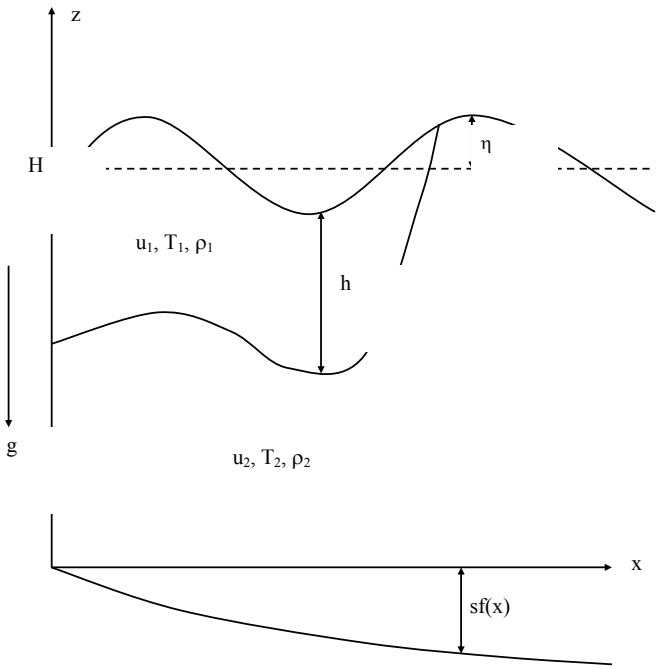


Figure 1: The flow configuration of the two layer fluid model.

ambient fluid. This leads to a heat source term in the temperature equation of the form

$$Q = \frac{I}{\rho_0 C_p h_0} \,^{\circ}\mathrm{C\ s}^{-1}. \tag{3}$$

In the above h_0 denotes a representative depth over which the heat flux I has been distributed, ρ_0 is the reference density and C_p is the specific heat at constant pressure. The magnitude of Q increases as h_0 decreases and this will give rise to horizontal gradients in temperature and hence also in the temperature dependent density which will augment the driving buoyancy forces in the flow as well as induce $O(1)$ nonhydraulic effects into the upper layer flow field. These horizontal gradients arising because of the x-dependence in the heat source term were noted by Farrow [4] in his study of the hydrodynamics of the thermal bar. Our inclusion of the variable thickness of the upper layer in the heat source term for a fully transient two layer model has, to the best of our knowledge, not been attempted in the literature to date.

In all of our development we will assume that the Reynolds numbers, Re, of the flow are sufficiently large that viscous forces are negligible and that the flow dynamics are dominated by a balance between buoyancy and inertial forces. As for the viscous effects resulting from the boundary layer formed adjacent to the bottom solid boundary, we deem these to be insignificant because the thickness

of this layer, which is $O(L/\sqrt{Re})$ with L denoting the horizontal length scale associated with the motion, remains well away from the interface of our two layer model. Hence viscous effects from the bottom are not communicated to the top layer. Further, the approximation made in ignoring the bottom boundary layer is consistent with the small aspect ratio assumption made in this work. We have taken the sole conservative body force to be that of gravity and neglected the effects of surface tension at the interface. This latter assumption requires that the Bond number $B = \rho g' L^2/\sigma \gg 1$, where g' is the reduced gravity and σ the surface tension [18]. We have further assumed that the flows are sufficiently rapid and small scale that the effect of the earth's rotation can be neglected. This requires that the Rossby number $R_0 = U/fL \gg 1$, where f is the Coriolis parameter and U and L are characteristic velocity and length scales of the flow [18]. The non-rotating case considered here is relevant to laboratory scale flows and has been employed in studies of the thermal bar [4, 15].

We now adapt the equations of mass and momentum balance to study low aspect ratio flows involving two active coupled layers consisting of an absorbing upper layer having a temperature dependent density overlying a homogeneous fluid of fixed density that is in contact with a gently sloping impermeable bottom. Our choice of non-dimensional and scaled variables are given according to the following scheme:

$$x = L\widetilde{x},\ z = h_0\widetilde{z},\ t = \frac{L}{U}\widetilde{t},\ h = h_0\widetilde{h},\ H = h_0\widetilde{H},\ (u_1, u_2) = U(\widetilde{u}_1, \widetilde{u}_2),$$
$$(w_1, w_2) = \frac{h_0 U}{L}(\widetilde{w}_1, \widetilde{w}_2),\ (p_1, p_2) = U^2\rho_0(\widetilde{p}_1, \widetilde{p}_2),\ \eta = \frac{U^2}{g}\widetilde{\eta},\ (4)$$
$$s = \delta\widetilde{s},\ \theta = T - T_0 = \theta_0\widetilde{\theta},\ U^2 = g'h_0,\ \delta = \frac{h_0}{L},$$

where we have chosen the temperature scale $\theta_0 = T_* - T_0$ to be the initial temperature difference between the two layers and the reduced gravity g' to be defined in terms of the initial density contrast, that is

$$g' = \frac{\rho_0 - \rho_*}{\rho_0} g = \alpha\theta_0^n g. \quad (5)$$

The aspect ratio $\delta = h_0/L$ is assumed small, that is, $0 < \delta \ll 1$.We have chosen the advective time scaling L/U for our model in order to be consistent with our assumption that there is no heat transfer between the fluid layers. This assumption requires that the diffusive or convective time scale given by $t_d \sim h_0^2/\kappa$, where κ is the thermal diffusivity, be much larger than the advective time scale.

In the nondimensional equations to follow, (6)–(9) provide for horizontal and vertical momentum balances in the two layers whereas (10)–(14) give the dynamic and kinematic boundary conditions at the free surface, interface and bottom boundary with tildes dropped from nondimensional quantities:

$$\frac{\partial u_1}{\partial t} + u_1\frac{\partial u_1}{\partial x} + w_1\frac{\partial u_1}{\partial z} = -\frac{\partial p_1^*}{\partial x}, \quad (6)$$



$$\delta^2\left(\frac{\partial w_1}{\partial t}+u_1\frac{\partial w_1}{\partial x}+w_1\frac{\partial w_1}{\partial z}\right)=-\frac{\partial p_1^*}{\partial z}+\theta^n, \tag{7}$$

$$\frac{\partial u_2}{\partial t}+u_2\frac{\partial u_2}{\partial x}+w_2\frac{\partial u_2}{\partial z}=-\frac{\partial p_2^*}{\partial x}, \tag{8}$$

$$\delta^2\left(\frac{\partial w_2}{\partial t}+u_2\frac{\partial w_2}{\partial x}+w_2\frac{\partial w_2}{\partial z}\right)=-\frac{\partial p_2^*}{\partial z}, \tag{9}$$

$$\alpha\theta_0^n p_1^*\left(x,H+\alpha\theta_0^n\eta,t\right)=H+\alpha\theta_0^n\eta \tag{10}$$

$$w_1\left(x,H+\alpha\theta_0^n\eta,t\right)=\alpha\theta_0^n\left(\frac{\partial\eta}{\partial t}+u_1\left(x,H+\alpha\theta_0^n\eta,t\right)\frac{\partial\eta}{\partial x}\right), \tag{11}$$

$$p_1^*\left(x,H+\alpha\theta_0^n\eta-h,t\right)=p_2^*\left(x,H+\alpha\theta_0^n\eta-h,t\right), \tag{12}$$

$$\begin{aligned}w_i\left(x,H+\alpha\theta_0^n\eta-h,t\right)&=\alpha\theta_0^n\left(\frac{\partial\eta}{\partial t}+u_i\left(x,H+\alpha\theta_0^n\eta-h,t\right)\frac{\partial\eta}{\partial x}\right)\\&\quad-\left(\frac{\partial h}{\partial t}+u_i\left(x,H+\alpha\theta_0^n\eta-h,t\right)\frac{\partial h}{\partial x}\right),\quad i=1,2,\end{aligned} \tag{13}$$

$$w_2\left(x,-sx,t\right)=-su_2\left(x,-sx,t\right). \tag{14}$$

In the above p_i^* refers to the dynamic pressure fields in the two fluids.

Under the assumption $0<\delta^2\ll 1$ we see that the horizontal velocity field in the lower layer is independent of z whereas that in the upper layer retains its z-dependence. Integrating the mass balance equation for the lower layer over the depth and applying the kinematic boundary conditions gives the mass balance to be

$$\frac{\partial}{\partial t}\left(h-\alpha\theta_0^n\eta\right)+\frac{\partial}{\partial x}\left[\left(h-\alpha\theta_0^n\eta-H-sx\right)u_2\right]=0. \tag{15}$$

Pressure continuity at the interface provides $p_2^*=\eta-\theta^n h+H(\alpha\theta_0^n)^{-1}$ leading directly to the horizontal momentum equation for the lower layer as

$$\frac{\partial u_2}{\partial t}+\frac{\partial}{\partial x}\left(\frac{1}{2}u_2^2+\eta-\theta^n h\right)=0. \tag{16}$$

Since it is straightforward to show that $\partial p_1^*/\partial x$ is a function of z it follows that $u_1=u_1\left(x,z,t\right)$. Integrating the mass balance equation for the upper layer and applying the kinematic boundary conditions gives for continuity in that layer

$$\frac{\partial h}{\partial t}+\frac{\partial}{\partial x}\left(\int_{H+\alpha\theta_0^n\eta-h}^{H+\alpha\theta_0^n\eta}u_1(x,z,t)dz\right)=0. \tag{17}$$

It now remains for us to specify the heat equation to complete the model. With the surface heat flux I assumed to be distributed uniformly over the local thickness

$h(x,t)$ of the upper layer and applying conservation principles we have that

$$\frac{\partial}{\partial t}(h\theta) + \frac{\partial}{\partial x}\left(\theta \int_{H+\alpha\theta_0^n\eta-h}^{H+\alpha\theta_0^n\eta} u_1(x,z,t)\,dz\right) = Q, \tag{18}$$

where

$$Q = \frac{I}{\rho_0 C_p h_0}{}^{\circ}Cs^{-1}, \qquad Q = \frac{U\theta_0}{L}\widetilde{Q}. \tag{19}$$

Employing (17) in (18) we can then express the heat equation as

$$\frac{\partial\theta}{\partial t} + \frac{1}{h(x,t)}\left(\int_{H+\alpha\theta_0^n\eta-h}^{H+\alpha\theta_0^n\eta} u_1(x,z,t)dz\right)\frac{\partial\theta}{\partial x} - \frac{Q}{h(x,t)} = 0. \tag{20}$$

Our model equations now consist of the lower layer mass balance and momentum equations (15) and (16), upper layer momentum and mass balance equations (6) and (17), respectively and the heat equation (20).

3 Some numerical results

All of our numerical results obtained for fixed volume releases involved first expanding $u_1(x,z,t)$ in the form of a power series about the variable position of the upper layer's lower boundary $z_0 = H + \alpha\theta_0^n\eta - h$. Substituting into the model equations and truncating the series leads to a system of eight equations in eight unknowns which can be written in vector form as

$$\frac{\partial\mathbf{U}}{\partial t} + \frac{\partial\mathbf{F}}{\partial x} = \mathbf{B}, \tag{21}$$

where $\mathbf{U}$ is a vector consisting of the flow variables, $\mathbf{F}$ is the corresponding flux vector and $\mathbf{B}$ refers to any source terms present in our system. We applied MacCormack's method [19] together with a strategy proposed by Lapidus [20] for damping spurious oscillations. Some results are displayed in Figures 2 and 3.

In Figure 2 we have plotted the evolution of the thickness of the gravity current for the hydraulic and nonhydraulic cases. The hydraulic model corresponds to the case wherein the temperature field is independent of the horizontal coordinate. This is in contrast to the model developed here wherein heating rates depend on the local thickness $h(x,t)$ of the heated layer resulting in a spatially dependent temperature field. It is clear that the gravity current speed is greater for the nonhydraulic case which will, in turn, lead to an increased rate of thinning of the current and a higher heating rate with increased buoyancy forces arising as a result of the increased density contrast between the two layers.

In Figure 3 we have plotted the total pressure field along the interface given by $z = H + \alpha\theta_0\eta - h$ for the hydraulic and nonhydraulic cases. We see that the total pressure field for the nonhydraulic case falls off more rapidly than does that associated with the hydraulic model. This is a result of the increased rate of

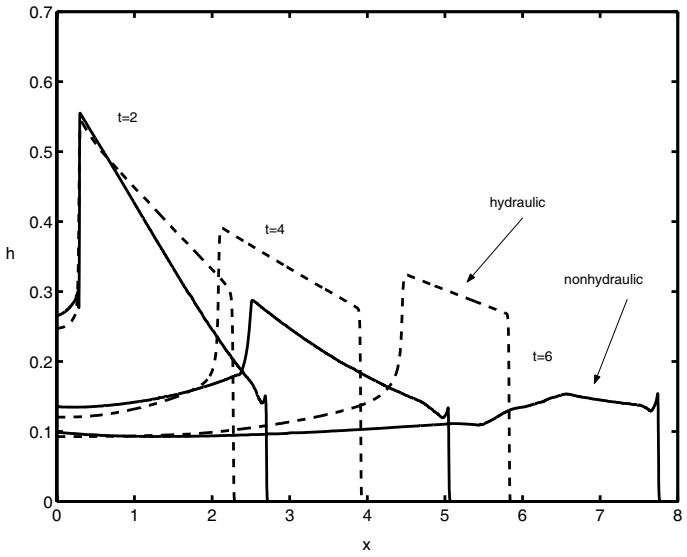


Figure 2: The evolution of the thickness of the gravity current with $n = 1, Q = 0.5, g'/g = 0.05, h_* = 0.9$.

thinning of the current in the nonhydraulic case coupled with increased heating rates. The relatively level profile for the pressure that is achieved around elapsed times $t \approx 6$ in the nonhydraulic case corresponds to the similarly level profile for the thickness of the current that is displayed in Figure 2 for the same parameter values. It is clear that there are substantial differences between the pressures for these two cases.

4 Some closing remarks

In contrast to the large amount of published theoretical and experimental material on gravity currents arising from fixed volume releases, that for variable inflow gravity currents is relatively small. This is in spite of the fact that when many gravity currents are initiated by, say, an accidental release of a fluid into an ambient environment, there is a variable discharge of fluid through an opening in a barrier. This would be the case in the situation when the rupture of a storage tank or pipeline gives rise to the release of a fluid at a variable rate over a period of time. Variable inflow gravity currents are also of great interest to those involved in the study of fluid motions in the natural environment that are not the result of contaminant releases. For example, flows of fresh water from spring run-off into lakes and fjords rarely take place with a constant flow rate, and the consequent evolution of the intrusions thus formed may be incorrectly estimated by using a constant flow model. A number of similar scenarios with flash floods, flows from volcanoes,

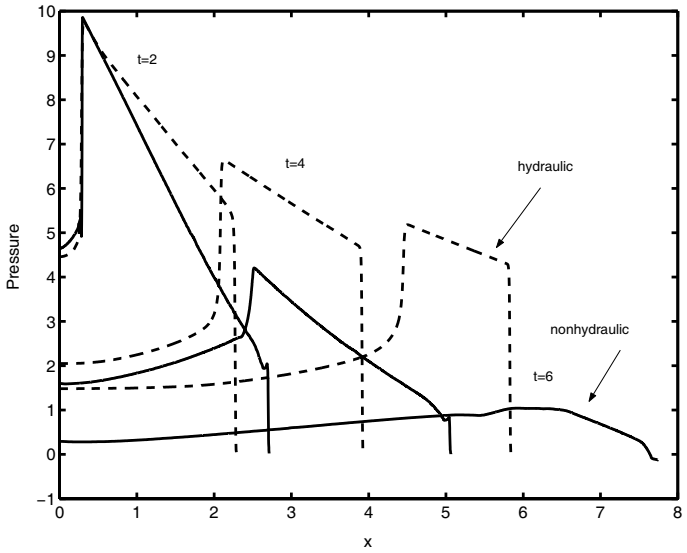


Figure 3: The evolution of the pressure at the interface between the two fluids with $n = 1, Q = 0.5, g'/g = 0.05, h_* = 0.9$.

discharges from locks in canals connecting lakes etc., all involve variable inflow buoyancy driven flows.

To develop a model for several of the above scenarios relating to variable inflow gravity currents one could consider a large volume of inviscid and incompressible fluid having a fixed temperature T_* and density ρ_* initially at rest behind a lock gate in which a small opening of height $h_0 \ll H$ is suddenly formed while a variable pressure is applied to the surface of this fluid. This mimics the conditions pertaining to the sudden rupture of an onshore storage container that then debouches its contents into a large body of water at a variable rate to create a variable inflow surface gravity current. Using energy principles and continuity it is possible to show that the average velocity through the narrow opening, $\overline{u}_1$, is governed by the forced Riccati equation

$$\frac{d\overline{u}_1}{dt} + \frac{L^2}{\overline{s}h_0}\frac{\overline{u}_1^2}{2} = \frac{L^2}{\overline{s}h_0}p(t) + \frac{L^2}{2\overline{s}h_0}, \quad \overline{u}_1(0) = 0,$$

where L is the horizontal dimension of the container and $\overline{s}$ the average length of a streamline extending from a point on the surface of the fluid in the lock to a point in the narrow orifice. Solving this initial value problem then gives a reasonable value for the variable inflow velocity.

References

[1] J.E.Simpson, *Gravity Currents: In the Environment and the Laboratory, 2nd ed.,* Cambridge University Press, Cambridge, England, 1997.

[2] R.T.Bonnecaze, H.E.Huppert, J.R.Lister, Particle-driven gravity currents, *J.Fluid Mech.,* **250**, pp.339-369, 1993.

[3] T.B.Moodie, J.P.Pascal, Non-hydraulic effects in particle-driven gravity currents in deep surroundings, *Stud.Appl.Math.,* **107**, pp.217-251, 2001.

[4] D.E.Farrow, An asymptotic model for the hydrodynamics of the thermal bar, *J.Fluid Mech.,* **289**, pp.129-140, 1995.

[5] S.J.D.D'Alessio, J.P.Pascal, T.B.Moodie, Thermally enhanced gravity driven flows, *J.Comp.Appl.Math.,* **170**, pp.1-25, 2004.

[6] T.B.Moodie, J.P.Pascal, S.J.D.D'Alessio, Non-hydraulic effects in two- layer thermally-enhanced gravity-driven flows, *Int.J.Nonlinear Mech.,* **40,** pp.11-25, 2005.

[7] T.B.Benjamin, Gravity currents and related phenomena, *J.Fluid Mech.,* **31**, pp.209-248, 1968.

[8] D.Pritchard, A.J.Hogg, On sediment transport under dam-break flow, *J.Fluid Mech.,* **473**, pp.265-274, 2002.

[9] D.Z.Zhu, G.A.Lawrence, Non-hydrostatic effects in layered shallow water flows, *J.Fluid Mech.,* **355**, pp.1-16, 1998.

[10] T.B.Moodie, J.P.Pascal, G.E.Swaters, Sediment transport and deposition from a two-layer fluid model of gravity currents on sloping bottoms, *Stud.Appl.Math.,* **100**, pp.215-244, 1998.

[11] T.B.Moodie, J.P.Pascal, J.C.Bowman, Modeling sediment deposition patterns arising from suddenly released fixed-volume turbulent suspensions, *Stud.Appl.Math.,* **105**, pp.333-359, 2000.

[12] J.B.Klemp, R.Rotunno, W.C.Skamarock, On the dynamics of gravity currents in a channel, *J.Fluid Mech.,* **269**, pp.169-198, 1994.

[13] T.Maxworthy, Gravity currents with variable inflow, *J.Fluid Mech.,* **128**, pp.247-257, 1983.

[14] J.Gratton, C.Vigo, Self-similar gravity currents with variable inflow revisited: plane currents, *J.Fluid Mech.,* **258**, pp.77-104, 1994.

[15] D.E.Farrow, J.C.Patterson, On the response of a reservoir sidearm to diurnal heating and cooling, *J.Fluid Mech.,* **246**, pp.143-161, 1993.

[16] S.Zilitinkevich, K.D.Kreiman, A.Y.Terzhevik, The thermal bar, *J.Fluid Mech.,* **236**, pp.27-42, 1992.

[17] J.Malm, S.Zilitinkevich, Temperature distribution and current system in a convectively mixed lake, *Bound. Layer Meteor.,* **71**, pp.219-234, 1994.

[18] J.Pedlosky, *Geophysical Fluid Dynamics,* 2nd Ed., Springer, New York, 1986.

[19] R.LeVeque, *Numerical Methods for Conservation Laws*, Birkhäuser, Basel, 1992.

[20] A.Lapidus, A detached shock calculation by second-order finite differences, *J.Comp.Phys.,* **2**, pp.154-177, 1967.



Finite amplitude evolution of frictionally destabilized abyssal overflows in a stratified ocean

G. E. Swaters
Applied Mathematics Institute, Department of Mathematical and Statistical Sciences and Institute for Geophysical Research, University of Alberta, Edmonton, Canada

Abstract

In the immediate vicinity of a deep sill, abyssal ocean overflows can possess current speeds greater the local long internal gravity wave speed with bottom friction and down slope gravitational acceleration playing a dominant role in the dynamics. The parameter regime for the finite amplitude transition to instability is described for marginally unstable super critical frictional abyssal overflows where there is weak coupling between the overflow and gravest-mode internal gravity waves in the overlying water column.

1 Introduction

The flow of dense water over deep sills is a source point for abyssal ocean currents. These flows, such as, for example, the Denmark Strait Overflow (hereafter DSO, e.g., [1-6]), make an important global-scale contribution to the convective overturing of the oceans. Abyssal currents of this kind are responsible, as well, for deep water replacement in marginal seas (e.g., [7]) and the along slope propagation of cold bottom intensified anomalies (e.g., [8]).

Swaters [9,10] has shown that in the near-inertial regime, super critical overflows can be destabilized by bottom friction. Within the overflow, the instabilities take the form of propagating, growing periodic bores or pulses (and are the rotational analogues of classical roll waves). In the overlying water column the instabilities take the form of amplifying internal gravity waves. For typical DSO parameter values [9], the most unstable mode has a wave length about $45\ km$,



WIT Transactions on Engineering Sciences, Vol 52, © 2006 WIT Press
www.witpress.com, ISSN 1743-3533 (on-line)
doi:10.2495/AFM06019

propagates prograde with respect to the overflow, has a period about 6 $hours$, and an $e-$folding growth time about 45 $hours$.

2 Governing equations

The density profile associated with, for example, the Denmark Strait Overflow (see Fig. 5 in [4] and the discussion in [10]) suggests that it is appropriate to consider a $2\frac{1}{2}$-layer stably stratified abyssal model with variable bottom topography (see Fig. 1). The uppermost layer, which is passive and infinitely deep, is denoted as layer one. The middle, or active upper layer is of finite thickness and is denoted as layer two. The abyssal layer, i.e., the layer immediately above the bottom topography, is denoted as layer 3. The *nondimensional* equations of motion for the upper layer are given by [10]

$$\left(\partial_t + \varepsilon\gamma^2 u_2 \partial_x\right) u_2 = -\eta_x + \frac{1}{R_e}\partial_{xx} u_2, \tag{1}$$

$$(\eta - h)_t + \gamma^2 \left\{u_2 \left[1 + \varepsilon\left(\eta - h - h_B\right)\right]\right\}_x = 0, \tag{2}$$

and, for the abyssal layer,

$$\left(\partial_t + u_3\partial_x\right) u_3 = -p_x + \frac{\partial_x\left(h\,\partial_x u_3\right)}{R_e\, h} - \frac{c_D\,|u_3|\,u_3}{h}, \tag{3}$$

$$h_t + \left(u_3 h\right)_x = 0,\ p = h + h_B + \varepsilon\gamma^2\eta, \tag{4}$$

where u_2, η, u_3, p and h are, respectively, the active upper layer horizontal velocity, the *reduced* upper layer pressure, the abyssal layer velocity, the *reduced* abyssal layer pressure and the abyssal layer thickness relative to the height of the bottom topography h_B.

The Reynolds number R_e, scaled bottom drag coefficient c_D, and the parameters ε and γ are given by, respectively,

$$R_e \equiv \frac{L\sqrt{g' h_*}}{A_H},\ c_D \equiv \frac{c_D^*}{s^*},\ \varepsilon \equiv \frac{h_*}{H}, \gamma^2 \equiv \frac{\widetilde{g} H}{g' h_*}, \tag{5}$$

where s^* a representative value for the slope of the bottom topography, h_* is a representative value for the thickness of the abyssal layer,

$$L \equiv \frac{h_*}{s^*},$$

the reduced gravities are

$$g' = \frac{g\left(\rho_3 - \rho_2\right)}{\rho_2} > 0,$$

$$\widetilde{g} = \frac{g\left(\rho_2 - \rho_1\right)}{\rho_2} > 0,$$



where

$$0 < \rho_1 < \rho_2 < \rho_3,$$

and where the horizontal eddy coefficient is A_H and the bottom drag coefficient is c_D^*.

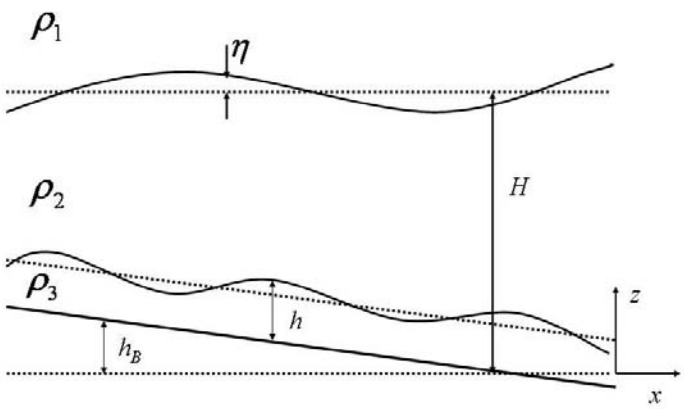


Figure 1: Model geometry used in this paper.

The parameter ε, which is the ratio of the abyssal scale thickness to the overall reference mean depth (and must be less than one), is a measure of the magnitude of the dynamical feedback of the upper layer pressure field back onto the lower layer, and is also a measure of the nonlinearity in the upper layer dynamics. The parameter γ is the ratio of the scale long internal gravity wave speeds associated with the dynamically active upper layer to the abyssal layer, respectively.

Oceanographic estimates for the dimensional parameters suggest that (see, e.g., [5,10-13])

$$\left.\begin{array}{c} \sqrt{g'h_*} \approx 46\ cm/s,\ L \approx 15\ km,\ T \approx 9\ hours, \\ c_D \approx 0.25,\ \varepsilon \approx 0.38,\ \gamma \approx 2.56,\ R_e \approx 279. \end{array}\right\} \tag{6}$$

It is assumed that $0 < \varepsilon \ll 1$, which is the expansion parameter, and that c_D, γ and R_e are formally $O(1)$.

3 Parameter regime for marginal instability

The steady abyssal flow solutions which have relevance [5] *in the near sill region*, and upon which the theory of classical roll waves has been developed, are the "slab" solutions on a linearly sloping bottom (see, e.g., [14-16]) given by

$$u_2 = \eta = 0,\ u_3 = U = \frac{1}{\sqrt{c_D}},\ h = 1,\ h_B = -x. \tag{7}$$

These uniform flows are equivalent to the "stream tube" solutions, without along-stream variation, which have been used to examine aspects of the dynamics of turbidity and abyssal currents (e.g., [17-20]).

Substitution of the perturbed solution

$$(u_2, \eta, u_3, h) \simeq \left(0, 0, \frac{1}{\sqrt{c_D}}, 1\right) + \left(\widetilde{u}_2, \widetilde{\eta}, \widetilde{u}_3, \widetilde{h}\right), \tag{8}$$

into (1) - (4), leads to the linear stability problem, after dropping the tildes and a little algebra,

$$\left(\partial_t - \frac{\partial_{xx}}{R_e}\right)(\eta - h)_t - \gamma^2 \eta_{xx} = 0, \tag{9}$$

$$\left[\left(\partial_t + \frac{\partial_x}{\sqrt{c_D}}\right)^2 - \partial_{xx} + \partial_x + (2\sqrt{c_D} - \partial_{xx})\left(\partial_t + \frac{\partial_x}{\sqrt{c_D}}\right)\right] h = 0. \tag{10}$$

Assuming a normal mode solution of the form

$$(h, \eta) = \left(\widehat{h}, \widehat{\eta}\right) \exp(ikx + \sigma t) + c.c., \tag{11}$$

where $c.c.$ means the complex conjugate of the preceding term, leads to the algebraic system, after dropping the carets,

$$\eta = \delta h, \;\; (\sigma - \sigma_+)(\sigma - \sigma_-) h = 0, \tag{12}$$

with

$$\delta \equiv \frac{\sigma\left(\sigma + k^2/R_e\right)}{\sigma\left(\sigma + k^2/R_e\right) + k^2\gamma^2}, \tag{13}$$

$$\sigma_\pm \equiv -\left(\frac{ik}{\sqrt{c_D}} + \sqrt{c_D} + \frac{k^2}{2R_e}\right) \pm \sqrt{\left(\sqrt{c_D} + \frac{k^2}{2R_e}\right)^2 - (ik + k^2)}, \tag{14}$$

where the branch cut is taken along the negative real axis. For a nontrivial solution to (12) it follows that $\sigma = \sigma_\pm$.

A mode with a given wave number k will be stable provided

$$\mathrm{Re}\,(\sigma_+) \le 0,$$

i.e.,

$$\mathrm{Re}\left(\sqrt{\left(\sqrt{c_D} + \frac{k^2}{2R_e}\right)^2 - (ik + k^2)}\right) \le \sqrt{c_D} + \frac{k^2}{2R_e}.$$

This can be considerably simplified by introducing the Euler decomposition

$$\alpha \exp(i\beta) = \left(\sqrt{c_D} + \frac{k^2}{2R_e}\right)^2 - k^2 - ik,$$



(which serves to define the real numbers α and β) allowing the above stability condition to be re-written in the form

$$\alpha\left[1+\cos\left(\beta\right)\right] \leq 2\left(\sqrt{c_D}+\frac{k^2}{2R_e}\right)^2,$$

or, equivalently, after substituting in for α and β

$$\left[\left(\sqrt{c_D}+\frac{k^2}{2R_e}\right)^2-k^2\right]^2+k^2 \leq \left[\left(\sqrt{c_D}+\frac{k^2}{2R_e}\right)^2+k^2\right]^2,$$

from which it follows that stability occurs *if and only if* (for $k \neq 0$, the flow is unconditionally stable for $k=0$)

$$\sqrt{c_D}+\frac{k^2}{2R_e} \geq \frac{1}{2}. \tag{15}$$

In the $R_e \rightarrow \infty$ limit, (15) reduces to the classical roll wave stability result

$$c_D \geq \frac{1}{4},$$

(see, e.g., [14-16]).

Note that (15) implies the existence of a high wave number cutoff if R_e is finite. If R_e is infinite, the instability problem has an ultraviolet catastrophe, which violates the *a priori* assumptions for shallow water modelling.

The marginal modes are described by

$$\sqrt{c_D}+\frac{k^2}{2R_e}=\frac{1}{2}-\varepsilon\mu$$

$$\Longrightarrow c_D=\widetilde{c}_D-2\varepsilon\mu\sqrt{\widetilde{c}_D}+\varepsilon^2\mu^2, \tag{16}$$

where

$$\widetilde{c}_D \equiv \frac{\left(1-k^2/R_e\right)^2}{4},$$

is the critical value for c_D as a function of k and R_e. The parameter $\mu \simeq O\left(1\right)$ measures the super or subcriticality. Substitution of (16) into (14) implies

$$\sigma_+=-\frac{1}{2}+\varepsilon\mu-\frac{ik}{\sqrt{c_D}}+\sqrt{\frac{\left(1-2ik\right)^2}{4}-\varepsilon\mu+\varepsilon^2\mu^2} \simeq \frac{4\varepsilon\mu k^2}{\left(1+4k^2\right)}$$

$$-ik\left\{\frac{3-k^2/R_e}{\left(1-k^2/R_e\right)}+\frac{2\varepsilon\mu\left[\left(1-k^2/R_e\right)^2+2\left(1+4k^2\right)\right]}{\left(1+4k^2\right)\left(1-k^2/R_e\right)^2}\right\}+O\left(\varepsilon^2\right), \tag{17}$$

so that the growth rate of the marginal mode will be $O\left(\varepsilon\right)$. Marginally unstable (stable) modes correspond to $\mu > (<)\ 0$, respectively. A detailed description of the nonlinear evolution of the amplitudes of the marginally unstable modes, assuming $0<\varepsilon<<1$ in (17), will be described elsewhere.



4 Conclusions

The parameter regime for the weakly nonlinear marginal destabilization of frictional supercritical abyssal overflows with weak coupling between the overflow and gravest-mode internal gravity waves in the overlying water column has been described. Necessary and sufficient stability conditions have been derived. It has been shown that in the limit of infinite Reynolds number the stability conditions reduce the known classical results. The inclusion of a finite Reynolds number removes the ultraviolet catastrophe known to exist in the stability problem when turbulent horizontal mixing is not present, violating the *a priori* assumptions for modelling with the shallow water equations.

Acknowledgement

Preparation of this extended abstract was supported in part by the Natural Sciences and Engineering Research Council of Canada.

References

[1] Worthington, L. V., An attempt to measure the volume transport of Norwegian Sea overflow water through the Denmark Strait. *Deep-Sea Res.*, 1969, **16**, 421-432.
[2] Dickson, R. R. and Brown, J., The production of North Atlantic Deep Water: Sources, rates, and pathways. *J. Geophys. Res.*, 1994, **99**, 12319-12341.
[3] Käse, R. H. and Oschlies, A., Flow through Denmark Strait. *J. Geophys. Res.*, 2000, **105**, 28527-28546.
[4] Girton, J. B. and Sanford, T. B., Synoptic sections of the Denmark Strait overflow. *Geophys. Res. Lett.*, 2001, **28**, 1619-1622.
[5] Girton, J. B. and Sanford, T. B., Descent and modification of the Denmark Strait overflow. *J. Phys. Oceanogr.*, 2003, **33**, 1351-1364.
[6] Jungclaus, J. H., Hauser, J. and Käse, R. H., Cyclogenesis in the Denmark Strait Overflow plume. *J. Phys. Oceanogr.*, 2001, **31**, 3214-3228.
[7] LeBlond, P. H., Ma, H., Doherty, F. and Pond, S., Deep and intermediate water replacement in the Strait of Georgia. *Atmos.-Ocean*, 1991, **29**, 288-312.
[8] Houghton, R. W., Schlitz, R., Beardsley, R. C., Butman, B. and Chamberlin, J. L., The middle Atlantic bight cold pool: Evolution of the temperature structure during summer 1979. *J. Phys. Oceanogr.*, 1982, **12**, 1019-1029.
[9] Swaters, G. E., Baroclinic characteristics of frictionally destabilized abyssal overflows. *J. Fluid Mech.*, 2003, **489**, 349-379.
[10] Swaters, G. E., On the frictional destabilization of abyssal overflows dynamically coupled to internal gravity waves. *Geophys. Astrophys. Fluid Dynamics*, in press, 2006.



[11] Spall, M. A. and Price, J. F., Mesoscale variability in Denmark Strait: The PV outflow hypothesis. *J. Phys. Oceanogr.*, 1998, **28**, 1598-1623.
[12] Reszka, M. K., Swaters, G. E. and Sutherland, B. R., Instability of abyssal currents in a continuously stratified ocean with bottom topography. *J. Phys. Oceanogr.*, 2002, **32**, 3528-3550.
[13] Käse, R. H., Girton, J. B. and Sanford, T. B., Structure and variability of the Denmark Strait overflow: Model and observations. *J. Geophys. Res.*, 2003, **108** (C6), 3181 10.1029/2002JC001548.
[14] Jeffreys, H., The flow of water in an inclined channel of rectangular bottom. *Phil. Mag.*, 1925, **49**, 793-807.
[15] Whitham, G. B., *Linear and Nonlinear Waves*, 1974 (Wiley: New York, Chichester, Brisbane, Toronto).
[16] Baines, P. G., *Topographic Effects in Stratified Flows*, 1995 (Cambridge University Press: Cambridge, New York, Melbourne).
[17] Smith, P. C., A streamtube model for bottom boundary currents in the ocean. *Deep-Sea Res.*, 1975, **22**, 853-873.
[18] Killworth, P. D., Mixing on the Weddell Sea continental slope. *Deep-Sea Res.*, 1977, **24**, 427-448.
[19] Price, J. F. and Baringer, O. M., Outflows and deep water production by marginal seas. *Progr. Oceanogr.*, 1994, **33**, 161-200.
[20] Emms, P. W., A streamtube model of rotating turbidity currents. *J. Mar. Res.*, 1998, **56**, 41-74.



This page intentionally left blank

Watershed models and their applicability to the simulation of the rainfall-runoff relationship

A. N. Hadadin
Department of Civil Engineering, The Hashemite University, Jordan

Abstract

With the rapid advancement in computer and information technologies, computer modeling has become a vital tool in watershed research and management practices. This paper presents a brief review of the development and application of watershed hydrologic models through the past five decades. The purpose of this study is to apply the Stanford Watershed Model (SWM) to estimate the rainfall-runoff relationship for the Wala valley (catchment area 1800km^2). The SWM has been widely accepted as a tool to synthesis a continuous hydrograph of hourly or daily streamflow. Many meteorological and hydrological data and several hydrologic parameters are required as input data. Sensitivity analysis and a trail and error adjustment technique are used for optimization of the number of parameters of the model. Comparison between estimated and measured surface runoff for the Wala valley indicates that the model is considerably efficient in predicting the total annual surface runoff from rainfall.
Keywords: watershed modeling, watershed hydrology, rainfall-runoff relationship, continuous hydrograph, streamflow, Stanford Watershed Model, surface runoff.

1 Introduction

Watershed models range widely in complexity. Some are nothing more than simple empirical equations, others perform a complex accounting of soil moisture and water in various stages of runoff. Hydrological models are divided broadly into two groups; the deterministic models seek to simulate the physical processes in the catchment involved in the transformation of rainfall to streamflow, whereas stochastic models describe the hydrological time series of



WIT Transactions on Engineering Sciences, Vol 52, © 2006 WIT Press
www.witpress.com, ISSN 1743-3533 (on-line)
doi:10.2495/AFM060020

the several measured variables such as rainfall, evaporation and streamflow involving distribution in probability.

Hydrologic synthesis technique is a powerful tool for aiding engineers and hydrologists in evaluating surface water resources. Since rainfall data is generally in abundance in comparison to runoff data, the attempt has been made to convert rainfall to runoff. Probably one of the best-known Rainfall-runoff models is the Stanford Watershed Model (SWM). It has been widely accepted as a tool to synthesis a continuous hydrograph of hourly or daily streamflow.

Many research workers throughout the world have studied extensions of the unit hydrograph principles. One of the most searching and fundamental contributions was made by Dooge [1]. Concentrating on linear mechanisms, he suggested that the response of catchment could be modeled by combining storage effects with translation effects. Inflows were obtained by the time–area method and used as distributed inputs to generalized network of linear channels and reservoirs.

A team of workers led by Eagleson [2] at the Massachusetts institute of technology (MIT) developed models using linear storages and linear channels, with several simultaneous, but different, inputs at different points in the models. The MIT models are called distributed models. The IUH for this sequence is given by the sum of the impulse responses for each reservoir and channel combination.

A different approach to determining runoff from a catchment was initiated by Laurenson in Australia [3]. He also was tackling the problem of estimating floods from ungaged catchments; the runoff-routing method he adopted gives the complete hydrograph, not just the peak flow as in the empirical formulations.

In conjunction with the Natural Environment Research Council Flood Studies, the Hydraulics Research station at Wallingford developed a simple method to derive flood hydrograph from storm rainfall [4]. The first stage of FLOUT employs the unit hydrograph method. Based on the analysis of records from many UK Catchments, the unit hydrograph is computed from recorded rainfall and runoff data for gaged catchments or from catchment characteristics for un-gaged basins.

The first major computer study to synthesize the discharge of a river was made by Linsley and Crawford [5] at Stanford University in the late 1960s. They aimed to simulate the whole of the land phase of the hydrological cycle in a catchment. The first Stanford watershed Model was soon superseded by new versions as development and experience in application brought about improvements in performance and accuracy. A great variety of data is fed into the model, which is usually programmed to produce daily river flow. Provision is made for dealing with snowmelt and, in incorporating particular of impervious area; the model can be applied to urban studies. Further elaboration compared to the O'Donnell [6] model is the subdivision of the soil moisture storage into an upper zone, from which interflow feeds into channel flow, and a lower zone, which feeds down to the groundwater storage. Evapotranspiration is allowed at the potential rate from the upper zone soil moisture storage but at a rate less than potential from the lower zone and groundwater storage. The total streamflow is



the sum of overland flow and interflow, derived by separate procedures, and baseflow from the groundwater storage. There are 34 parameters in the Stanford watershed Model IV, but most of these are obtained from physical measurements either of initial conditions or of specific catchment characteristics. Four of the parameters, infiltration and interflow indices together with the capacities of the upper and lower zone soil moisture storage, must be determined by calibration of the model with recorded data. If the snowmelt routing is omitted, the number of parameters reduces to 25.

In the UK the water Resources Board's model DISPRIN [7] (Dee Investigation simulation program for Regulating Networks) was developed for the River Dee regulation research program. The catchment is envisaged in three hydrological zones, the uplands, the hill slopes and the lower valley areas, designated bottom slopes. In each of the three zones, non- linear storage are interconnected by linear routing procedures representing over land flow and interflow (quick return flow), and these feed into a common ground water storage from which there is baseflow. There are 21 parameters for the DISPRIN model, but seven of these are starting values for the seven storages. The basic form of the model is used for small or medium sized catchment, but the drainage of a large basin can be simulated in sequence of applications.

The Institute of Hydrology mode in the UK has several different forms and can be applied over hourly or daily time periods. Although classed as a simple model, it pays particular attention to the complexities of soil moisture storage, which it represents in several layers. In addition to numerous reported studies at the Institute of Hydrology, a modified form of the model was used to investigate the effects of change in land use on East African catchment [8]. The Lambert model, developed in the former Dee and Clwyd River Authority essentially for small upland catchment, was forerunner of DISPRIN for the Dee Research program and is proving simpler to operate in practice [9]. HYSIM, developed by Manley and used in the Directorate of Operations of the Seven Trent Water Authority, is one of a suite of programs for hydrological analysis and provision of information for design and operational purposes [10]. It operates mainly on daily values of areal rainfall and potential evaporation, and produces daily values of streamflow, but the time period can be flexible. It may be used for the extension of flow data records and data validation, real time flow forecasting and flood studies, modeling of groundwater, and has also simulated successfully daily and monthly flows on ungaged catchments. The Boughton model for small or medium sized catchments was originally developed in Australia for assessing water yield from catchments in dry regions [11]. Hence its immediate concern was with quick runoff. Murray [12] modified the model to include a delayed response interflow and baseflow, and applied it to the Brenig catchment in North Wales as part of the study program carried out by the water Research Association in the late 1960s. The model operates on daily rainfall and evaporation to produce daily runoff [12].

The Stanford Watershed Model and the Boughton [11] Model have already been mentioned as originating in the USA and Australia, respectively. In addition to these pioneering studies and those of MIT, a great amount of work on



conceptual or deterministic modeling has been carried out by the large Federal Government agencies of the USA with their teams of hydrologists, mathematicians and engineers working full-time with considerable resources. The book edited by Singh [13], which is so far the most comprehensive and detailed compilation of representative, watershed hydrologic models developed in many countries around the world. Although personal bias was unavoidable as admitted by the editor, Singh [13] did a good job in selecting the twenty-six popular models and inviting the original author(s) of each model from several countries (including the USA, Canada, England, Denmark, Sweden, Australia, China and Japan) to contribute a book chapter which describes their models in details. However, notable contributions have been made in other countries in smaller government departments, in commercial organizations and by individuals or small groups in universities.

A single event model is one that is used primarily for individual storm events, although it may be of long duration and multi-peaked. Two factors usually constrain their use to single events: the continuity of soil moisture (loss rates) isn't simulated, and or the model simulates in such detail and requires time consuming computations so that it is not economical to run over long periods.

Some of the most widely used single events models are cited in DeVries [14] and McCuen [15]. Because of this strong interest in relating watershed model parameter to geographic characteristics, the Soil Conservation service's (SCS) [16] curve number technique has received much increasing interest and usage. The SCS curve number technique is the only one in which both the precipitation loss rate and the water excess to runoff transformation (unit hydrograph) can be determined from readily available geographic data. The data used are: land cover, hydrologic soil type, average slop of the watershed, and length of the main watercourse. Curve numbers have been recommended for various land cover.

2 The Stanford Watershed Model

Most of today's highly sophisticated continuous watershed is Stanford Watershed Model. Another model, developed at about the same time, is the SSARR model of the Corps of Engineering. The SSARR model does not have all of the complexity of the Stanford derived models. The Stanford watershed Model has been elaborated upon at several universities: Kentucky, Texas, Ohio, and others. Notable among these is the Kentucky version, entitled OPET, where the parameters of the model are derived automatically by an optimization routine. The National weather service also used the Stanford watershed Model as the basis for its NWSRFS model. The National Weather Service Sacramento Model has more comprehensive soil moisture accounting algorithms, but may be considered less sophisticated in its runoff transformation via linear unit graphs and the fact that it does not route streamflow in a comprehensive river system. One of the most highly developed versions, of the Stanford water Model existing today is the Hydrocomp HSP Model. The HSP system of programs incorporates the precipitation- runoff model as one piece of an array of study tools ranging



from water quality simulation to unsteady flow dam break flood routings. One of the simplest and most economical to run continuous water shed models is the STORM program. The model was originally developed by water resource Engineers, Inc. in connection with storm water runoff in the city of San Francisco. The original model was essentially a long-term hyetograph analysis with a simply rational formula type transformation to runoff [17].

3 Available data

1) Rainfall data: All the rainfall stations have been registered and named by the agencies concerned in accordance with the drainage systems. There are 12 rainfall stations in the Wala watershed. Most of these stations have been operating for period up to 20 years. The rainfall records for these station consist of few thousands of autographic charts the personnel of Water Authority of Jordan (WAJ) had reduced the mass curves on the recording charts to monthly abstracts presenting the data as hourly precipitation.
2) Evaporation data: WAJ and Meteorological Department have operated 4 evaporation stations in the area. Evaporation pans of US weather Bureau class–A of 10 in number have been installed and observed in and around the study area since 1960.
3) Other meteorological data: Other meteorological data such as air temperature (daily – maximum and minimum), sunshine hour are observed at meteorological stations operated by Meteorological Department since 1962.
4) Hydrological data: Existing water level/ discharge record, baseflow, runoff coefficient. According to the WAJ runoff ratio ranges from 4% in the desert area to 15% in the northern and western parts of the study area.

4 Model structure

The SWM is made up of a sequence of computation routine for each process in the hydrologic cycle (interception, infiltration, routing, and so on) all the moisture that was originally stored in the watershed or was input as precipitation during any time period is balanced in the continuity equation. The Stanford water model utilizes a hydrologic watershed routing technique to translate the channel inflow to the watershed outlet. The change in storage in each zone is calculated as the differences between the volume of inflow and outflow.

5 Rainfall analysis

Twelve weather stations have been established in the Wala watershed. These stations measure daily rainfall with one-station measures the streamflow at the outlet of the watershed. The existing data for precipitation is collected from these stations, the periods of rainfall data of the 12 stations varied from one station to another with some missing data. The S.W.M program required hourly rainfall depth, daily streamflow daily maximum and minimum temperature (F°) as input data in order to simulate the synthetic streamflow.



5.1 Watershed parameter

There are some parameters for Wala watershed, which were determined from a topographic map. Those parameters are:

- The watershed drainage area (AREA), which was already computed from a map of (1:50,000).
- The average ground slope of overland flow (OFSS).
- The mean length of overland flow (OFS, length of overland flow is computed by the following method:
  OFSL = 1/(2D), where D is the drainage density, D = the total length of stream with a catchment divided by the drainage area. By the aid of map the total length of stream = 480 mile. D = 480/695 = 0.69. OFSL = 0.72 mile = 3800 ft.
- The fractional stream and lake surface area (FWTR).
- The impervious fraction of the watershed surface draining directly into the stream (FIMP).
- Elevation of catchment above thermometer (ELDIF) (which is the average elevation of catchment (ft)-Elevation of thermometer station (ft)/1000).

Other parameter values such as (CHCAP) channel capacity, no criteria exists for easily obtaining CHCAP from maps, it is assumed to be equal to the maximum flood event happened in the record for Wadi Wala that is 3000 cfs. Manning's roughness parameters for flow over soil and impervious surfaces are both required as input to the program.

For the Wadi Wala the initial estimates for overland flow (OFMN) and impervious surface flow (OFMNIS) were 0.010 and 0.013, representing coefficients for light turf for over land flow and smooth concrete for impervious surface. After several trials and adjustments the values of (OFMN) and (OFMNIS) are 0.05 and 0.02 respectively.

Ratio of normal basin rainfall to normal station rainfall (RGPM) or multiplier for adjusting recorded precipitation, and (RGEXP) are assumed to be equaled 1.0 because we deal with the depth of rainfall over the total watershed not the depth of rainfall for certain rainfall station in the Wadi.

6 Trial and adjustment parameters

Several of the following parameters are determined by trial and adjustment until the comparison between simulated and recorded streamflow is satisfactory. Guidelines for establishing initial values exist for only a few of the parameters, whereas most are initially determined from suggested ranges.

For Wala watershed the parameter and initial estimates are as follows:

VINTMR: the maximum interception rate (in/hr) for a dry watershed. Crawford and Linsley suggest trial values of 0.10, 0.15 and 0.20 for grasslands, moderate forest cover and heavy forest covers respectively. The value of 0.05 was selected for wadi wala watershed, because the surface of the vegetative cover is very small.

BUZC: an index of the surface capacity to store water as interception and depression storage. This parameter normally ranges from 0.10 to 1.65 a greater

number might be indicative or the forest cover. The value of 0.10 was determined for this parameter after several trials and adjustment.

SUZC: an index of soil surface moisture storage capacity, representing the additional moisture storage capacity available during warmer months due to vegetation. Depending on the soil type, the index ranges from 0.45 to 2.0. A value of 0.45 was determined for wadi wala watershed after several trials.

LZC: a soil profile moisture storage index (in) approximately equal to the volume of water stored above the water table and below the ground surface. The LZC index depending on porosity and the specific yield of the soil, ranges from 2.0 to 20.0 and 4in plus half the mean annual rainfall can be used as an initial estimate in areas experiencing seasonal rainfall (used in coasted humid or semi humid climates. Assume an initial value for LZC equal to one quarter of the mean annual rainfall plus 4in (used in arid and semi arid regions). A final value of 4.75 in was determined after several trials.

ETLF: a soiled evaporation parameter that controls the rate of evapotranspiration losses from the lower soil zone. The parameter ranges from 0.20 to 0.90 depending on the type and extent of the vegetative cover. Also ETLF is approximately equal to the fraction of the basin covered by forest and deep-rooted vegetation. Recommendations for barren ground, grassland and heavy forest are respectively 0.20, 0.23 and 0.30.the value of 0.20 was selected for the wala watershed.

SUBWF: a parameter controlling the fraction of moisture lost or diverted from active groundwater storage through transverse flow across the drainage basin boundary. It also represents that portion of the groundwater that percolates to the deep or inactive groundwater. The SUBWF parameter can be estimated from observed changes in deep groundwater levels, or it is often assumed to be zero because these losses are small compared to the magnitudes of rainfall and runoff.

GWETF: The fraction of the total watershed over which evapotranspiration from groundwater storage is assumed to occur at the potential rate. This parameter is assumed zero unless a significant quantity of vegetation draws water directly from water table. It was selected zero because water table in the wadi wala basin is far to be reached by the plants roots.

SIAC: a factor, ranging from 0.10 to 4.0 that relates infiltration rates to evaporation rates. This parameter simply allows a more rapid infiltration rate recovery during warmer seasons. Value of 3.0 was optimal for wadi wala, after several trials.

BMIR: an index that controls the rate of infiltration, depending on the soil permeability and the volume of moisture that can be stored in the soil. This index ranges from 0.1 to 1.2. A smaller value was optimal for wadi wala after running several values.

BIVF: an index controlling the time distribution and quantities of moisture entering interflow. This index ranges from 0.55 to 4.5. A value of 0.955 was selected to Wala watershed, after several trials.

BFNLR: a daily baseflow recession adjustment factor used to produce a simulated curvilinear baseflow recession. An initial value of 1.0 for wadi wala



was selected. Later adjustments might be required in matching simulated and recorded baseflow recessions. After several trials of optimization it was found to be 0.99

UZS: the current volume (in) of soil surface moisture as interception and depression storage. Because the simulation begins on October of the first calibration year, the parameter may initially be designated as zero unless precipitation occurs during the last few days of September.
0.05 in. was optimal value for Wala stream.

LZS: the current volume (in) of soil surface moisture storage between the land surface and water table. 10% of LZC was selected to initiate the wadi wala simulation. After several trials of optimization, its best value was 0.50.

GWS: the current groundwater slope index. This index provides an indication of antecedent moisture condition. Suggested initial values fall between 0.15 and 0.25. A value of 0.15 was optimal value for Wala watershed.

7 Output from SWM

Comparison between recorded and synthesized monthly totals streamflow are shown in Figures 1 and 2 for the water year 2003-2004 and 1989-1990 respectively.

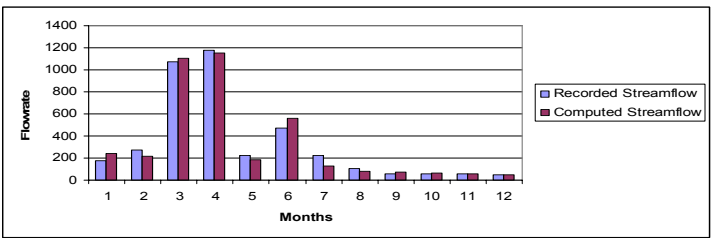


Figure 1: Comparison between monthly totals of synthesized and recorded flow rate for the water year 2003-2004.

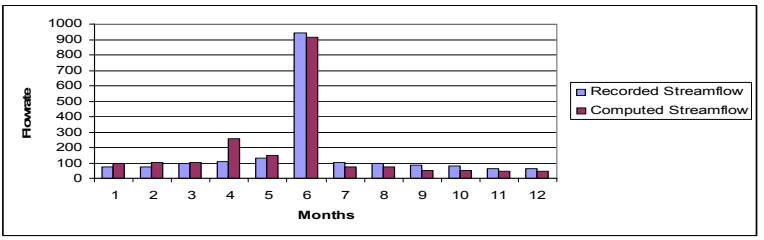


Figure 2: Comparison between monthly totals of synthesized and recorded flow rate for the water year 1989-1990.

At first the SWM is applied on the normal water year 2003-2004. The result shows a good agreement between recorded and synthesized annual streamflow volume. A summation of annual recorded streamflow is about 3950 SFD and the

synthesized stream flow 3920 SFD. The absolute difference is less than 1%. The sum of the recorded precipitation for the year is about 6.20 in., the synthesized annual evaporation is about 5.55in. A depth of 0.21 in. discharged as runoff. Dry year 1989-1990 was adopted using the same parameters the results show that the annual recorded streamflow 1930 SFD, and the synthesized streamflow is about 1960 SFD. The absolute difference is about 1.5%.

8 Conclusion

Rainfall precipitation is the primary source of water for streamflow runoff. The characteristics of the watershed govern losses within the watershed and the portion of that precipitation not lost results in surface runoff. Various techniques may be used to relate precipitation to corresponding runoff, these technique vary in complexity, as a general rule, the shortest the time period of runoff to be simulated, the more complex and sophisticated model. SWM is one of these complex models. It was applied in this research on Wala valley watershed. The choice of a model is based on the availability of records for a particular watershed. In the study the relationship between rainfall and runoff is studied by the aid of a computer program depending on the calibration and optimization of watershed parameters.

There are some differences between recorded and synthesized streamflow (of course hydrologic forecasts can not be 100% accurate). There are many sources of forecast error may be attributed. The influence of man power plays an important role, the change due to construction the dame on Wala stream causes heterogeneous of the catchment area, basic data error in the historic basic data on which the values of watershed parameters depend on, disunity of rainfall pattern, and insufficiency of the density of the rainfall station. This study drew several conclusions:

1. SWM can be applied on Wala watershed to predict the total annual streamflow and peak flood since there is a good agreement between recorded and predicted streamflow.
2. It is concluded that SWM will be accurate if it is applied on very small watershed, where you deal with one rainfall station and streamflow station, and the variety of characteristics of the watershed (geology, topography, land used, vegetation cover) is very small.
3. The model can produce results when properly calibrated. The model is difficult to calibrate because of the large number of parameters and the mass of data processing. It was difficult to know the starting values for several parameters, but this should be easier with experience.
4. The data requirements are extensive both in quantity and in the labor necessary for preprocessing.
5. The model is relatively easy to operate in terms of input instructions, file organization and manipulation.
6. The model is best studied for comprehensive river basin studies requiring analysis of both high and low flows.



7. The model can be used for all sizes of catchment, and where there are data shortages, regional values of the required inputs may be used. It has been applied to catchments throughout the world and with its great flexibility has helped to provide hydrological information for problems in civil engineering design and agricultural engineering.

References

[1] Dooge, J. C.I. (1959). A general theory of the unit hydrograph. *J.Geophys. Res.,* 64(2), pp: 241-256.
[2] Bravo, S.C.A., Harley, B.M., Perkins, F.E. and Eagleson, P.S. (1970). A linear Distributed Model of Catchment Runoff. MIT Dept. of Civil Engineering Hydrodynamics Lab., Report No. 123.
[3] Laurenson, E. M., (1964). A catchment storage model for runoff routing. *J Hydrol.* 2, pp: 141-163.
[4] Price, R.K. (1978). FLOUT a river catchment flood model. Hydraulic Research Station Report No. 168, 2nd imp. Wallingford, England.
[5] Crawford, N. H., and Linsley, R. K., (1966). Digital simulation in hydrology. Stanford Watershed Model IV. Department of Civil Engineering, Stanford.
[6] O'Donnell, T., and Dawdy, D.R., (1965). Mathematical models of catchment behavior. *Proc. ASCE. Hy4*. 91 pp: 123-127.
[7] Jamieson, D.G and Wilkinson, J.C. (1972). Application of DISPRIN to the River Dee Catchment. Water Res. 8(4), pp: 911.
[8] Blackie, J.R. (1972). The application of a conceptual model to two East Africa Catchments. Unpublished M.Sc. Dissertation. Imperial College.
[9] Lambert, A.O. (1969). A comprehensive rainfall- runoff model for upland catchment area. *J. Inst. Water Eng.,* 23(4), 231-238.
[10] Manley, R.E. (1975). A hydrological model with physically realistic parameters. Proc. *Bratislava Symposium*, IAHS Pub. No. 115.
[11] Boughton, W.C. (1966). A mathematical model for relating runoff to rainfall with daily data. *Trans. Inst. Eng. (Australia),* **7,** pp: 83.
[12] Murray, D.L. (1970). Boughton's daily rainfall- runoff model modified for the Brenig catchment. *Proc. Wellington Symposium,* IAHS Pub. No. 144-161.
[13] Singh, V.P. (ed.) (1995). *Computer Models of Watershed Hydrology*. Water Resources Publications, Highlands Ranch, Colorado, pp: 1130.
[14] DeVries, J.J. and Hromadka, T.V. (1993). Computer models for surface water. In: *Handbook of Hydrology*, D.R. Maidment (ed.), McGraw-Hill, New York, pp: 21.1-21.39.
[15] McCuen, R.H., (1998). Hydrologic Analysis and Design. 2nd, Prentice Hall Upper Saddle, River, NJ. pp: 814.
[16] The Soil Conservation Service's (SCS, 1984). Computer program for project formulation, Tech. Release No. 20 Washington, DC.
[17] Chen Y. D. (2004). Watershed Modeling: Where are we heading? Environmental Informatics Archives, Vol. 2, pp: 132-139.



Dynamic pressure evaluation near submerged breakwaters

F. T. Pinto & A. C. V. Neves
Hydraulics and Water Resources Institute, Faculty of Engineering, University of Porto, Portugal

Abstract

The increasing use of submerged breakwaters is not only due to their important role in beach protection, but also because of their low environmental impact. In their design process, an analysis of the pressure fields (near and along the structure slope) under wave flow is needed. Although a considerable amount of research has been conducted in order to improve our understanding of these structures behaviour and establish reliable formulae for design purposes, several outstanding questions remain.

This paper aims to present the evolution of dynamic pressure fields when the structure is submitted to the action of regular incident waves. These pressure fields are obtained by indirect means, through the measured horizontal wave flow velocity component as a function of the wave phase and water depth.
Keywords: submerged breakwater, wave-induced pressure fields, dynamic pressure.

1 Introduction

Submerged breakwaters are used for coastal and harbour structure protection. They are usually detached and parallel to the shoreline, with their crest heights fixed below a specified design water level to allow for the passage of some wave energy. Since they are less vulnerable to wave action and have a lower crest height, the required volume of material is less than for emerged breakwaters. A number of authors prefer submerged breakwaters for coastal protection since, in addition to defending the coastline from erosion, they (if well designed) do not disturb the landscape scenery and thus contribute to the preservation of the environment, which is one of the major design priorities at the moment. This



WIT Transactions on Engineering Sciences, Vol 52, © 2006 WIT Press
www.witpress.com, ISSN 1743-3533 (on-line)
doi:10.2495/AFM06021

type of structure also acts as an active primary defence during extreme wave climates by providing some wave energy dissipation. On the other hand, they require a more sophisticated design/project and, often, an adequate buoy/marker system to mark navigation hazards, since their crest height is near the surface (Lamberti & Mancinelli [12]).

The main purpose of submerged breakwater is to provide a "filtered" shelter for the coast on their lee-side by dissipating the highest incoming waves. Like other coastal structures, they are submitted to different kinds of wave actions which can be predicted by wave theory analysis. These actions frequently cause damage to maritime structures and can affect the overall strength and reliability of blocks structures. The role of wave-induced pressure diagrams has great importance in breakwater design, to calculate the forces acting on the structure.

In this paper a summary review of the literature will be presented, followed by an overview of the assumptions and analysis techniques used in the current study. A description of the experimental set-up and a discussion of the results will also be presented. The evolution of dynamic pressure caused by regular incident wave actions in the vicinity of submerged structure slopes, as a function of the wave phase and water depth, will also be analysed. These results were obtained indirectly, using laboratory measurements of horizontal wave velocities taken in previous research projects.

2 Wave-induced pressure fields

2.1 Introduction

Submerged breakwaters have been the subject of numerous studies and investigations. Many authors have studied the performance of submerged breakwaters in coastal protection and pointed out advantages such as their reduced visual and environmental impact and other benefits in comparison to more traditional structures. The importance of a careful design (considering the transmission coefficient, crest submergence, crest height and width, sufficient distance from the shoreline, etc.) has also been discussed.

Some numerical approaches trying to simulate a wave field near, over and after passing a submerged structure have also been carried out, as in Chen & Chen [5], Lara [13] and others.

Taveira-Pinto *et al.* ([18], [19]), Hsu *et al.* [11], Gironella & Sánchez-Arcilla [9], Browder *et al.* [2] and Groenewoud *et al.* [10] have conducted experimental studies to better understand the physical effects of submerged breakwaters on the surrounding area. Most of them are concerned with the importance of wave-structure interaction processes (e.g. wave transmission, reflection and dissipation), the crest height and width, the ratio between the freeboard and the wave length, sediment transport, turbulence, the gaps and the consequences of scour, among other factors.

Since the processes and variables involved in the design of submerged breakwaters are less understood and rather more complex than in emerged breakwaters there is still a lot of research to be done, although in recent years

there have been some studies which provide valuable information on the most important forces and processes to be considered. One of those forces is due to the wave motion, acting mostly as pressure forces (impacts) and as shear forces, on the structure slope. On impermeable and smooth breakwater slopes, percolation effects are not important, and forces depend only on the energy transformation process (Taveira-Pinto *et al.* [18]).

Determining the pressure fields caused by the wave action on a coastal structure is essential to good design, by allowing the calculation of the resultant forces. Several researchers have investigated methods of establishing these wave-induced forces, including Fuhrboter [8], Burchart [4], Allsop *et al.* [1], Martin *et al.* [15], Bullock *et al.* [3], Luís [14] and Taveira-Pinto & Neves [21]. These authors studied: (a) the wave loading on vertical, composite and perforated caisson breakwaters; (b) the effects of wave obliquity and multidirectionality on the response of the breakwaters; (c) the design methods for wave loading; (d) the scale effects and (e) compared the results from field measurements with those measured in the laboratory and predicted by theories.

An accurate estimate of wave-induced dynamic pressures is essential, therefore, as it allows calculation of the wave forces and moments acting on a structure slope.

2.2 Dynamic pressure evaluation

The wave flow interference with a submerged breakwater generates a standing or partially standing wave field (caused by the reflection of the incident wave). A part of the incident energy is transmitted and the remaining part is absorbed by the structure (Taveira Pinto [19]).

The linear theory (Demirbilek & Vincent [7] provides a good first estimate of wave parameters. Waves are considered as two-dimensional and of small amplitude, and the nonlinear terms in the boundary conditions are ignored. This is only possible when velocities are small, e.g., when waves have small amplitudes.

The pressure field, p, associated with a partially standing wave is determined from the unsteady Bernoulli equation, developed for non-rotational flows and expressed by

$$\frac{p}{\rho} + gz + \frac{1}{2}\left(u^2 + v^2\right) - \frac{\partial \phi}{\partial t} = C(t) \tag{1}$$

where p represents the pressure in a point at the depth -z, ρ the fluid mass density, g the gravitational acceleration, u and v the horizontal and vertical components of velocity, respectively, and ϕ the velocity potential.

Dean & Dalrymple [6] reduced the previous equation to

$$\frac{p}{\rho} = -gz + \frac{\partial \phi}{\partial t} \tag{2}$$

by neglecting the small velocity square terms, for a point at depth - z.

A partial standing wave is produced by the interaction of two progressive waves moving in opposite directions, with wave heights equal to half of the

standing wave height and having the same period. Thus, the velocity potential for partially standing waves is given by the subtraction of the velocity potential of two progressive waves,

$$\begin{aligned}\phi &= -\frac{H_i}{2}\frac{g}{\sigma}\frac{\cosh\left[k\,(z+d)\right]}{\cosh\,(kd)}\,\mathrm{sen}(kx-\sigma t)+\frac{H_r}{2}\frac{g}{\sigma}\frac{\cosh\left[k\,(z+d)\right]}{\cosh\,(kd)}\,\mathrm{sen}(kx+\sigma t+\varepsilon)\\ &= \frac{g}{2\sigma}\frac{\cosh\left[k\,(z+d)\right]}{\cosh\,(kd)}\left[-H_i\,\mathrm{sen}(kx-\sigma t)+H_r\,\mathrm{sen}(kx+\sigma t+\varepsilon)\right]\end{aligned} \tag{3}$$

where H_i and H_r represent the incident and the reflected wave heights respectively, k is the wave number (equal to $2\pi/L$), L is the wavelength, σ is the angular frequency (equal to $2\pi/T$), T is the wave period, d is the water depth and ε is the wave phase delay, induced by the reflection process (equal to zero in the case of theoretical total reflection).

The height of the reflected wave can be calculated by

$$H_r = C_r H_i \tag{4}$$

where C_r represents the reflection coefficient.

Rearranging equation (2), one can obtain

$$\begin{aligned}p &= -\rho g z+\rho\frac{\partial\phi}{\partial t}\\ &= \underbrace{-\rho g z}_{\substack{\text{hydrostatic}\\ \text{pressure, } p_h}}\ \underbrace{+\rho H_i\frac{g}{2}\frac{\cosh\left[k\,(z+d)\right]}{\cosh\,(kd)}\left[\cos(kx-\sigma t)+C_r\cos(kx+\sigma t+\varepsilon)\right]}_{\substack{\text{dynamic}\\ \text{pressure, } p_d}}\end{aligned} \tag{5}$$

Looking at equation (5) one can say that the resulting pressure, p, will be the contribution of two effects: the hydrostatic pressure and the dynamic pressure due to acceleration and directly related with the water elevation.

3 Indirect analysis of dynamic pressure

3.1 Introduction

The main objective of this work was to assess dynamic pressure profiles, p_d, acting on a submerged breakwater. Experimental data from the measurements undertaken in the Hydraulics Laboratory of the Faculty of Engineering of Porto and a theoretical approach were used to calculate dynamic pressure from the horizontal component of the velocity at different points along the slopes, measured during previous projects. Two structures were tested (one rough and one smooth) and horizontal velocity measurements were obtained for regular incident waves.

3.2 Dynamic pressure and the horizontal velocity component

Isolating the term corresponding to the dynamic pressure, p_d, from equation (5), gives

$$p_d = \rho H_i\frac{g}{2}\frac{\cosh\left[k\,(z+d)\right]}{\cosh\,(kd)}\left[\cos(kx-\sigma t)+C_r\cos(kx+\sigma t+\varepsilon)\right] \tag{6}$$

According to linear wave theory, the horizontal component of velocity is expressed by

$$\begin{aligned} u &= -\frac{\partial\phi}{\partial x} = \frac{g}{2\sigma}\frac{\cosh\left[k\,(z+d)\right]}{\cosh\,(kd)}\left[-kH_i\cos(kx-\sigma t)+k\,H_r\cos(kx+\sigma t+\varepsilon)\right] \\ &= -H_i\frac{g}{2\sigma}\frac{\cosh\left[k\,(z+d)\right]}{\cosh\,(kd)}(-k)\left[\cos(kx-\sigma t)-C_r\cos(kx+\sigma t+\varepsilon)\right] \\ &= H_i\frac{k}{\sigma}\frac{g}{2}\frac{\cosh\left[k\,(z+d)\right]}{\cosh\,(kd)}\left[\cos(kx-\sigma t)-C_r\cos(kx+\sigma t+\varepsilon)\right] \end{aligned} \tag{7}$$

Equation (6) can be re-typed as follows:

$$\begin{aligned} \frac{p_d}{u} &= \frac{\rho H_i\frac{g}{2}\frac{\cosh\left[k\,(z+d)\right]}{\cosh\,(kd)}\left[\cos(kx-\sigma t)+C_r\cos(kx+\sigma t+\varepsilon)\right]}{H_i\frac{k}{\sigma}\frac{g}{2}\frac{\cosh\left[k\,(z+d)\right]}{\cosh\,(kd)}\left[\cos(kx-\sigma t)-C_r\cos(kx+\sigma t+\varepsilon)\right]} \\ &= \rho\frac{\sigma}{k}\frac{\cos(kx-\sigma t)+C_r\cos(kx+\sigma t+\varepsilon)}{\cos(kx-\sigma t)-C_r\cos(kx+\sigma t+\varepsilon)} \end{aligned} \tag{8}$$

which is equal to

$$p_d = \rho u C\frac{\cos(kx-\sigma t)+C_r\cos(kx+\sigma t+\varepsilon)}{\cos(kx-\sigma t)-C_r\cos(kx+\sigma t+\varepsilon)} \tag{9}$$

where C represents the wave celerity, equal to L/T, assuming that it remains constant in the vicinity of the structure.

Hence, it can be concluded that by knowing the values of ρ, C, u, Cr and ε, one can estimate the dynamic pressure, p_d, at different *x* positions.

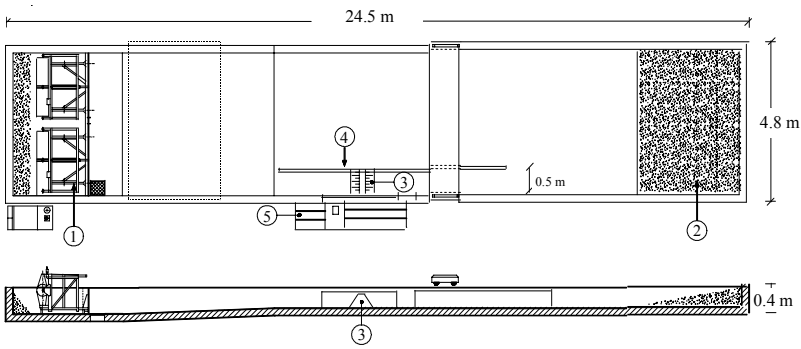


Figure 1: Layout of the FEUP Hydraulics Laboratory (1-Wavemaker; 2-Dissipating beach; 3-Model; 4-Thin dividing wall; 5-Traversing table).

4 Experimental set-up

Velocity measurements were carried out in a unidirectional wave tank at the Porto University Faculty of Engineering, schematised in Figure 1. The wave tank is 4.8 m wide, 24.5 m long, and has a maximum water depth of 0.60 and 0.40 m, near the piston-type wave generator and in the measuring section, respectively.

To avoid three-dimensional effects and wave diffraction during the tests with regular waves, a thin dividing wall was used to isolate the measuring section from the rest of the tank. A gently inclined absorbing beach was also constructed to reduce wave reflection by dissipating wave energy.

Wave probes, placed in the section where the horizontal velocity component was measured, recorded simultaneous measurements of the instantaneous water surface elevation. A detailed description of the experimental set-up can be found in Taveira-Pinto [19].

Horizontal velocity component measurements were made using a Laser Doppler Anemometry optical system (Argon-Ion Laser Spectra-Physics Stabilité 2017S operating in single-mode with 2 Watts of power and an optical system consisting of 55X modular LDA optics based on a Dantec fibre optic system and a 60 mm probe, working in a backscatter configuration). These measurements were taken in different locations, successively nearer to the breakwater and in the seaward and landward slopes, as indicated in Figure 2.

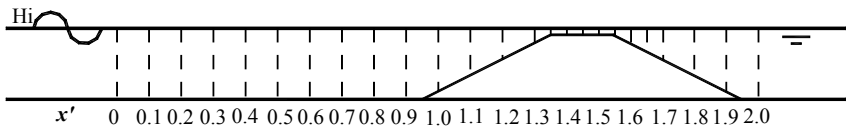


Figure 2: Location of the profiles.

Two models were tested, a rough one and a smooth one, with a crest width of 0.20 m. They had similar dimensions but different roughness qualities. The structure was 0.20 m height and had 1V:2H slopes.

5 Results and discussion

The measured regular wave conditions selected for this study were the following: water depth, d, equal to 0.22m; mean measured wave height, $\overline{H}_m$, equal to 0.037 m; mean measured wave period, $\overline{T}_m$, equal to 1.21; mean measured wave length, $\overline{L}_m$, equal to 1.56 m and mean measured wave celerity, $\overline{C}_m$, equal to 1.30 m/s.

The reflection coefficients and the wave phase delay of the smooth and the rough model were calculated, giving a reflection coefficient of 0.114 and 0.068, and a wave phase delay of 65º and 18º respectively, Taveira-Pinto [19].

The evolution of the horizontal velocity and the dynamic pressure along the wave phase were analysed for each measurement point, see Figures 3 to 6. The measured values were compared with those obtained by the linear wave theory for a reflected wave field. As mentioned before, the dynamic pressure was calculated from the mean measurements and from the theoretical (linear theory) horizontal component of the velocity. The figures represent the measurements of profile at x'=0.5 and at x'=1.0 m, for the smooth and the rough model.

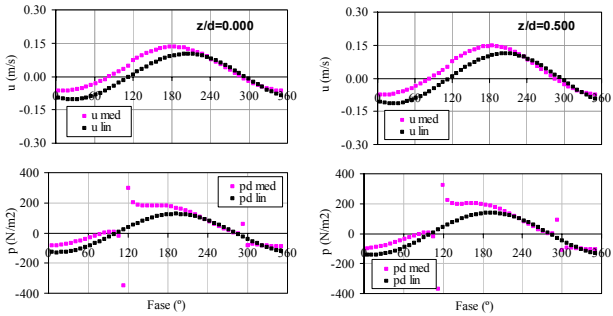


Figure 3: Evolution of horizontal velocity and dynamic pressure along the wave phase (Profile at x'=0.5 m, smooth model).

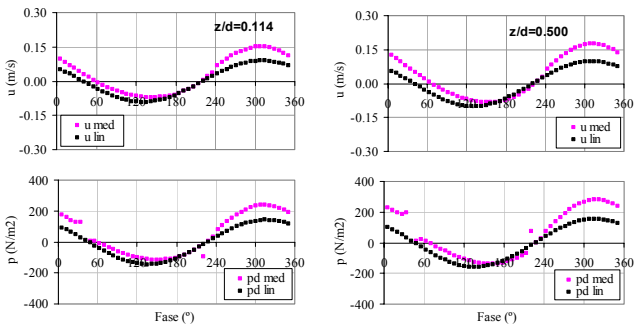


Figure 4: Evolution of horizontal velocity and dynamic pressure along the wave phase (Profile at x'=1.0 m, smooth model).

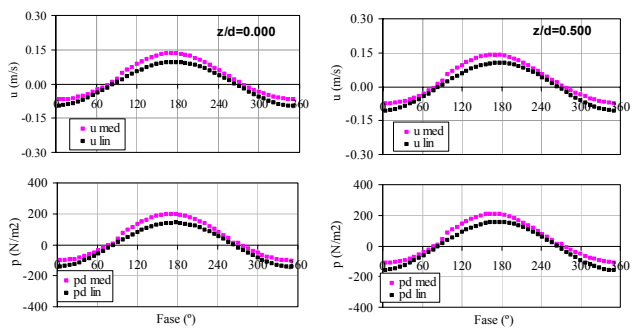


Figure 5: Evolution of horizontal velocity and dynamic pressure along the wave phase (Profile at x'=0.5 m, rough model).

During their propagation, waves deform and begin to shoal when interfering with the rising front of the model (due to the water depth reduction), giving rise to an asymmetric profile and, finally, to an unstable situation where they break (in the crest zone). When this non-linear wave decomposition process starts, the

use of the linear wave theory is no longer valid. For this reason, we have only used this approach on the seaward side of the structure and in the offshore slope until x'=1.0 m.

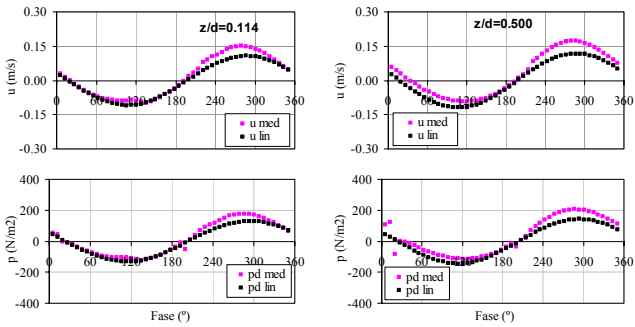


Figure 6: Evolution of horizontal velocity and dynamic pressure along the wave phase (Profile at x'=1.0 m, rough model).

The results of the dynamic pressure for the rough model seem to be in better agreement with the theory than the respective values for the smooth model. This could be explained by the small phase difference verified in the smooth model between the measured velocities and the theoretical ones, which does not occur in the rough model. The dynamic pressure (eqn. 9) depends directly on the value of $\frac{\cos(kx-\sigma t)+C_r\cos(kx+\sigma t+\varepsilon)}{\cos(kx-\sigma t)-C_r\cos(kx+\sigma t+\varepsilon)}$, which becomes very high when the theoretical horizontal velocity is near zero. If, in this instant, the measured horizontal velocity is not near zero, the dynamic pressure will be very over-predicted.

As expected, the dynamic pressures in the smooth model are higher than in the rough model, as they are not attenuated as much.

6 Summary and conclusions

This study demonstrates a methodology to determine the dynamic pressures through the horizontal wave flow velocity component. Although other tests were carried out, only one case for regular waves is presented in order to present the methodology used. Wave-induced dynamic pressure fields for the reflected field were calculated using linear wave theory using the theoretical approach presented, considering that the celerity remained constant until x'=1 m.

For all cases, high velocities and, therefore, high dynamic pressures occurred in the upper measurements, for the higher z/d values closer to the water surface. The closer the measurements were to the structure the higher were the velocities and, consequently, the dynamic pressures due to the reduction of the flow section, which led to the increasing velocities.

The calculation of the total horizontal dynamic forces by integration of the pressure field could be useful in determining the more sensitive areas of a

submerged breakwater, where special care can then be taken in its construction. These conclusions can be particularly important in further investigation on defining critical stability areas. More research, with a wider range of input conditions under regular and irregular sea states closer to prototype conditions, is also being performed.

References

[1] Allsop, N. W. H., Kortenhaus, A., Oumeraci, H., McConnel, K. J. (2000). New Design Methods for Wave Loadings on Vertical Breakwaters under Pulsating and Impact Conditions. *Proceedings of Coastal Structures '99,* Inigo Losada, Balkema, Santander, Spain, Vol. II, pp. 595-602.

[2] Browder, A. E., Dean, R. G., Chen, R. (1996). Performance of a Submerged Breakwater for Shore Protection, *Proceedings of the 25th International Conference Coastal Engineering* 1996, ASCE, Orlando, Florida,USA, Vol. II, pp. 2312-2323.

[3] Bullock G. N., Hewson P. J., Crawford A. R., Bird, P. A. D. (2000). Field and Laboratory Measurements of Wave Loads on Vertical Breakwaters. *Proceedings of Coastal Structures '99,* Inigo Losada, Balkema, Santander, Spain, Vol. II, pp. 613-621.

[4] Burcharth, H. F. (1994). The Design of Breakwaters. *Coastal, Estuarial and Harbour Engineers' Reference Book*, M. B. Abbott e W. A. Price, E & FN SPON, London, UK, pp. 381-424.

[5] Chen, B. F., Chen, P. H. (2001). Fully Nonlinear Waves Past Submerged and Floating Breakwater, *Proceedings of the XXIX IAHR Congress*, Beijing, China.

[6] Dean, R. G, Dalrymple, R. A. (1991). *Water Wave Mechanics for Engineers and Scientists*, World Scientific, Advanced Series on Ocean Engineering, Vol. II, pp. 78-90.

[7] Demirbilek, Z., Vincent L. (2002). Water Wave Mechanics. *Coastal Engineering Manual Outline*, S. Army Corps of Engineers, Washington, DC, chapter II-1, pp. 1-35.

[8] Fuhrboter, I. A. (1994). Wave Loads on Sea Dikes and Sea-Walls. *Coastal, Estuarial and Harbour Engineers' Reference Book*, M. B. Abbott e W. A. Price, E & FN SPON, London, UK, pp. 351-367.

[9] Gironella, X., Sánchez-Arcilla, A. (2000). Hydrodynamic Behaviour of Submerged Breakwaters. Some Remarks Based on Experimental Results. *Proceedings of Coastal Structures '99,* Inigo Losada, Balkema, Santander, Spain, pp. 891-896.

[10] Groenewoud, M., vand de Graaff, J., Claessen, E., van der Biezen, S. (1996). Effect of Submerged Breakwater on Profile Development. *Proceedings of the 25th International Conference Coastal Engineering 1996,* ASCE, Orlando, Florida,USA, Vol. II, pp. 2428-2441.

[11] Hsu, T. W., Ou, S. H., Hou, H. S., Shin, C. Y. (2001). Wave-induced Vortices Around a Submerged Breakwater by FLDV and PIV.



Proceedings of the International Conference Coastal Engineering 2000, ASCE, Orlando, Florida, USA, Vol. 2, pp. 2278-2291.

[12] Lamberti, A., Mancinelli, A. (1996). Italian Experience on Submerged Barriers as Beach Defence Structures. *Proceedings of the 25th International Conference Coastal Engineering 1996*, ASCE, Orlando, Florida,USA, Vol. II, pp. 2352-2365.

[13] Lara, J. (2005). A Numerical Wave Flume to Study the Functionality and Stability of Coastal Strucutres. PIANC Magazine AIPCN, International Navigation Association, nº 121 October, pp. 5-29, ISSN 0374-1002.

[14] Luís, L. (2001). Pressure in Vertical and Inclined Walls due to Wave Breaking. (in Portuguese). *MSc Thesis*, Instituto Superior Técnico, Portugal.

[15] Martin, F. L., Losada, M. A., Vidal, C., Diaz Rato, J. L. (1996). Prototype Measurements of Wave Pressures on a Wave Screen: Comparison to Physical and Analytical Models. *Proceedings of the 25th Int. Conference Coastal Engineering*, ASCE, Orlando, Florida, USA, Vol. II, pp. 1763-1775.

[16] Saitoh, T., Ishida, H. (2001). Kinematics and Transformation of New Type Wave Front Breaker Over Submerged Breakwater, *Proceedings of the 4th International Symposium Waves 200: Ocean Wave Measurement and Analysis,* ASCE, California, USA, Vol. II, pp. 1032-1041.

[17] Taveira-Pinto, F., Proença, M. F., Veloso Gomes, F. (2000). Experimental Analysis of the Behaviour of Submerged Breakwaters (in Portuguese). *Comunicação das 1as Jornadas Portuguesas de Engenharia Costeira e Portuária 1999,* AIPCN/PIANC, Porto, Portugal, pp. 71-90.

[18] Taveira-Pinto, F., Proença, M. F., Veloso-Gomes, F. (2001). Spatial Regular Wave Velocity Field Measurements Near Submerged Breakwaters. *Proceedings of the 4th International Symposium Waves 2001, San Francisco, USA,* ASCE, Vol. II, pp. 1136-1149, ISBN 0-7844-0604-9.

[19] Taveira-Pinto, F. (2002). Oscillations and Velocity Field Analysis Near Submerged Breakwaters Under the Wave Action (in Portuguese). *PhD Thesis*, Faculty of Engineering of University of Porto, Porto, Portugal.

[20] Taveira-Pinto, F., Neves, A. C. (2003). Second-Order Analysis of Dynamic Pressure Profiles, using Measured Horizontal Wave Flow Velocity Component. *Proceedings of the 6th International Conference on Coastal Engineering 2003*, Cadiz, Spain.

[21] Taveira-Pinto, F., Neves, A. C. (2003). Environmental Aspects of Using Detached for Coastal Protection Purposes. *Proceedings of the International Symposium ENVIRONMENT 2010: Situation and Perspectives for the European Union*, Porto, Portugal, paper G14, ISBN 972-98944-0-x.

[22] Tomasicchio, U. (1996). Submerged Breakwaters for the Defence of the Shoreline of Ostia - Field experiences, comparison. *Proceedings of the 25th International Conference Coastal Engineering* 1996, ASCE, Orlando, Florida,USA, Vol. II, pp. 2404-2417.



Mean flow effects in the nearly inviscid Faraday waves

E. Martín[1] & J. M. Vega[2]
[1] *E. T. S. Ingenieros Industriales, Universidad de Vigo, Spain*
[2] *E. T. S. Ingenieros Aeronáuticos, Universidad Politécnica de Madrid, Spain*

Abstract

We study the weakly nonlinear evolution of Faraday waves in a two dimensional version of a vertically vibrating annular container. In the small viscosity limit, the evolution of the surface waves is coupled to a non-oscillatory mean flow that develops in the bulk of the container. A system of equations is derived for the coupled slow evolution of the spatial phase of the surface wave and the streaming flow. These equations are numerically integrated to show that the simplest reflection symmetric steady state (the usual array of counter-rotating eddies below the surface wave) becomes unstable for realistic values of the parameters. The new states include limit cycles, steadily travelling waves (which are standing in a moving reference frame), and some more complex attractors. We also consider the effect of surface contamination, modelled by Marangoni elasticity with insoluble surfactant, in promoting drift instabilities in spatially uniform standing Faraday waves. It is seen that contamination enhances drift instabilities that lead to various steadily propagating and (both standing and propagating) oscillatory patterns. In particular, steadily propagating waves appear to be quite robust, as in the experiment by Douady *et al.* (1989).
Keywords: Faraday instability, mean flow, weakly nonlinear analysis, Marangoni elasticity.

1 Introduction

We consider the parametric excitation of waves at the free surface of a horizontal liquid layer that is being vertically vibrated. If the forcing amplitude exceeds a threshold value, the system exhibits surface waves that are named after



WIT Transactions on Engineering Sciences, Vol 52, © 2006 WIT Press
www.witpress.com, ISSN 1743-3533 (on-line)
doi:10.2495/AFM06022

Faraday [1]. These waves have attracted a great deal of attention, especially because of the rich variety of non-linear pattern forming phenomena promoted by the Faraday instability [2, 3, 4]. Unfortunately, current theoretical approaches fail to appropriately explain essential issues associated with the behavior beyond threshold, particularly in the singular limit of small viscosity. The usual nonlinear amplitude equations used to describe this weakly nonlinear regime are obtained from a strictly inviscid formulation and corrected a posteriori by adding some linear dissipation terms [2, 3]. This formulation ignores the presence of the slow non oscillatory mean flow that is driven by the boundary layers at the container walls and free surface and, in the case of a monochromatic wave only predicts standing waves (SW) after onset and fails to reproduce the drifting SWs that have been observed experimentally in annular containers [5, 6]. The object of the present paper is precisely to analyze the coupled evolution of the surface waves and the mean flow.

The remaining of the paper is organized as follows: in §2 we shall present the systems of equations for the slow time evolution of the surface waves and the mean flow, derived from a exact formulation based on the full Navier-Stokes equations. This will be done assuming either a clean free surface and a contaminated one (surface contamination is likely to be present in water, as in [5], unless care is taken in the experimental set-up). The relevant patterns obtained for large-time resulting from the primary bifurcation will be described and discussed in §3, where some conclusions will also be made.

2 Coupled amplitude-mean flow equations

We consider a horizontal 2-D liquid layer supported by a vertically vibrating plate (fig.1), and use the container's depth h and the gravitational time $\sqrt{h/g}$ for nondimensionalization. The governing equations are the following

$$u_x + v_y = 0, \tag{1}$$

$$u_t + v(u_y - v_x) = -q_x + C(u_{xx} + u_{yy}), \tag{2}$$

$$v_t - u(u_y - v_x) = -q_y + C(v_{xx} + v_{yy}), \tag{3}$$

$$u = v = 0 \qquad \text{at} \quad y = -1, \tag{4}$$

$$v = f_t + uf_x, \quad C^{1/2}(\hat{u}_n + \hat{v}_s + \kappa\hat{u}) = 0,$$

$$q - \frac{u^2 + v^2}{2} + 4\omega^2\varepsilon f\cos(2\omega t) - f + T\kappa = 2C\hat{v}_n \quad \text{at } y = f, \tag{5}$$

$$u,\ v,\ q \text{ and } f \text{ are } L\text{-periodic in } x, \tag{6}$$

where

$$s = \int_0^x \sqrt{1 + f_x^2}\, dx \quad \text{and} \quad \kappa = \frac{f_{xx}}{(1 + f_x^2)^{3/2}} \tag{7}$$

are an arch length parameter and the curvature of the free surface (defined as $y = f$), respectively, and n is a coordinate along the upward unit normal to the

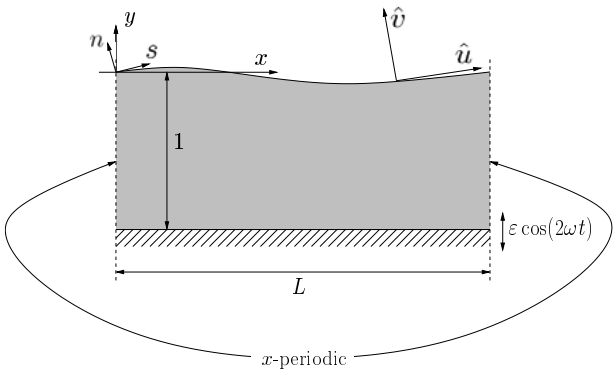


Figure 1: Sketch of the fluid domain.

free surface; $\hat{u}$ and $\hat{v}$ are the tangential and normal velocity components at the free surface $y = f$, which are related to the horizontal and vertical components u and v by

$$\hat{u} = \frac{u + f_x v}{\sqrt{1 + f_x^2}}, \quad \hat{v} = \frac{v - f_x u}{\sqrt{1 + f_x^2}}. \tag{8}$$

Equations (1)-(6) formulate the problem assuming a clean free surface, with no contamination. Nevertheless, surface contamination is likely to be present in water. The only difference between the clean and contaminated cases is seen in the boundary condition (5b), whose right hand side was zero for the clean surface and now accounts for the presence of contaminating surfactants (9), modelled in the simplest way: the resulting tangential stress includes Marangoni elasticity effects produced by a variation of surface tension with surfactant concentration

$$C^{1/2}(\hat{u}_n + \hat{v}_s + \kappa\hat{u}) = -\gamma\zeta_s. \tag{9}$$

A linear law is assumed for the variation of the surface tension T^* with the surfactant concentration ζ^*, namely $T^*(\zeta^*) = T_0^* + (dT^*/d\zeta_0^*)(\zeta^* - \zeta_0^*)$, where the derivative is calculated at the equilibrium value of the surfactant concentration ζ^*, denoted as ζ_0^*.

The nondimensional surfactant concentration $\zeta = (\zeta^* - \zeta_0^*)/\zeta_0^*$ is given by the conservation equation for an insoluble surfactant

$$\zeta_t + [(1 + \zeta)u]_s = 0 \quad \text{in } 0 < s < s_L, \qquad \zeta(s + s_L, t) = \zeta(s, t). \tag{10}$$

Here, s_L is the length of the free surface in one period and we are neglecting both cubic terms and surface diffusion of the surfactant.

Both dimensionless problems, namely (1)-(6) and (1)-(5a),(5c)-(6), (9), (10), depend on the following nondimensional parameters: the forcing frequency $2\omega = 2\omega^*\sqrt{h/g}$ and amplitude $\varepsilon = \varepsilon^*/h$, the ratio of viscous to gravitational effects

$C = \mu/(\rho\sqrt{gh^3})$ ($\rho =$ density, $\mu =$ viscosity), the Bond number $T^{-1} = \rho g h^2/T_0^*$ ($T_0^* =$ surface tension at equilibrium), the horizontal aspect ratio $L = L^*/h$ ($L^* =$horizontal length of the domain), and only for the contaminated free surface problem, the Marangoni elasticity number $\gamma = \zeta_0^*(dT^*/d\zeta_0^*)C^{1/2}/(\mu\sqrt{gh})$.

We shall consider small, nearly-resonant solutions at small viscosity and conveniently rescaled Marangoni elasticity, i.e.,

$$|u|+|v|+|q|+|f|+|\zeta| \ll 1, \quad \varepsilon \ll 1, \quad |\omega-\omega_0| \ll 1, \quad C \ll 1, \quad \gamma \sim 1, \tag{11}$$

where ω_0 is a natural frequency in the inviscid limit ($C = 0$). The assumption that $C \ll 1$ is reasonable for not too viscous fluids in not too thin layers. The assumption that $\gamma \sim 1$ is made for the Marangoni elasticity to have a significant effect both in the damping ratio of the surface waves and in the streaming flow (see [8] for more details). As explained in [7] and [9], the solution can be expanded distinguishing between an oscillating part caused by the oscillatory inviscid modes (with a $\mathcal{O}(1)$ frequency and a $\mathcal{O}(\sqrt{C})$ decay rate) and a slow non-oscillatory part generated by the viscous modes (with a $\mathcal{O}(C)$ decay rate), which produce the mean flow, denoted hereinafter by the superscript m. The solution in the bulk region, outside the boundary layers that appear at the free surface and the bottom plate, is written as follows

$$\begin{aligned}
u &= U_0(y)e^{i\omega t}[A(t)e^{ikx} - B(t)e^{-ikx}] + c.c. + u^m(x,y,t) + \cdots, \\
v &= iV_0(y)e^{i\omega t}[A(t)e^{ikx} + B(t)e^{-ikx}] + c.c. + v^m(x,y,t) + \cdots, \\
q &= Q_0(y)e^{i\omega t}[A(t)e^{ikx} + B(t)e^{-ikx}] + c.c. + q^m(x,y,t) + \cdots, \\
f &= e^{i\omega t}[A(t)e^{ikx} + B(t)e^{-ikx}] + c.c. + f^m(x,t) + \cdots, \\
\zeta &= \Xi_0 e^{i\omega t}[A(t)e^{ikx} + B(t)e^{-ikx}] + c.c. + \zeta^m(x,t) + \cdots,
\end{aligned} \tag{12}$$

where $c.c$ stands for the complex conjugate, $k = 2m\pi/L$ (with m a positive integer) is the horizontal wave number and U_0, V_0 and Q_0 are the corresponding inviscid eigenfunctions

$$U_0 = -\frac{kQ_0}{\omega_0}, \quad V_0 = \frac{Q_{0y}}{\omega_0}, \quad Q_0 = \frac{\omega_0^2 \cosh k(y+1)}{k \sinh k}, \tag{13}$$

$$\omega_0^2 = k(1+Tk^2)\tanh k. \tag{14}$$

Note that the expansion for the surfactant concentration variable (12e) is only necessary for the contaminated problem, where

$$\Xi_0 = (k\omega_0\sqrt{i\omega_0})/(\tanh k(\omega_0\sqrt{i\omega_0} - ik^2\gamma)) \tag{15}$$

cannot be obtained in the inviscid approximation. Dependence of the complex amplitudes A and B on x is ignored for simplicity, see [10] and [11] for a more complicated analysis including spatial wave modulations. The weakly nonlinear analysis requires the amplitudes A and B to be small and depend slowly on time $|A'| \ll |A| \ll 1$, $|B'| \ll |B| \ll 1$.

If we insert expansions (12a)-(12d) into the governing equations for the clean free surface case, and (12a)-(12e) into the equations for the contaminated free surface problem, take into account the boundary layers at the free surface and the bottom of the container, and apply solvability conditions, the following equations for the evolution of the complex amplitudes are obtained

$$A' = [-d_1 - id_2 + \mathrm{i}\alpha_3|A|^2 - \mathrm{i}\alpha_4|B|^2 - \mathrm{i}\frac{\alpha_6}{L}\int_{-1}^{0}\int_{0}^{L} g(y)u^m dxdy]A + \mathrm{i}\varepsilon\alpha_5\bar{B}, \tag{16}$$

$$B' = [-d_1 - id_2 + \mathrm{i}\alpha_3|B|^2 - \mathrm{i}\alpha_4|A|^2 + \mathrm{i}\frac{\alpha_6}{L}\int_{-1}^{0}\int_{0}^{L} g(y)u^m dxdy]B + \mathrm{i}\varepsilon\alpha_5\bar{A}, \tag{17}$$

which depend on the mean flow through a non local term. See [7] and [8] for a detailed derivation of the equations above and for the expressions of the coefficients and the function $g(y)$ in the non contaminated and contaminated case, respectively.

The solution of equations (16) and (17) always relaxes to a standing wave ($|A| = |B| = R_0$) of the form

$$f(x,t) = 4R_0\cos(\omega t + \phi_0)\cos[k(x-\psi)] \tag{18}$$

with constant amplitude R_0 (which depends on the amplitude of the applied forcing) and spatial phase $\psi(t)$, which remains coupled to the streaming flow through the equation

$$\psi' = \frac{\alpha_6}{kL}\int_{-1}^{0}\int_{0}^{L} g(y)u^m dxdy. \tag{19}$$

Ignoring the initial transient, taking into account the last result in expansions (12a)-(12e), and introducing these expressions in the two cases, we obtain the following equations for the mean flow outside the two boundary layers

$$\tilde{u}_x + \tilde{v}_y = 0, \tag{20}$$

$$\frac{\partial\tilde{u}}{\partial\tau} + \tilde{v}(\tilde{u}_y - \tilde{v}_x) = -\tilde{q}_x + Re^{-1}(\tilde{u}_{xx} + \tilde{u}_{yy}), \tag{21}$$

$$\frac{\partial\tilde{v}}{\partial\tau} - \tilde{u}(\tilde{u}_y - \tilde{v}_x) = -\tilde{q}_y + Re^{-1}(\tilde{v}_{xx} + \tilde{v}_{yy}), \tag{22}$$

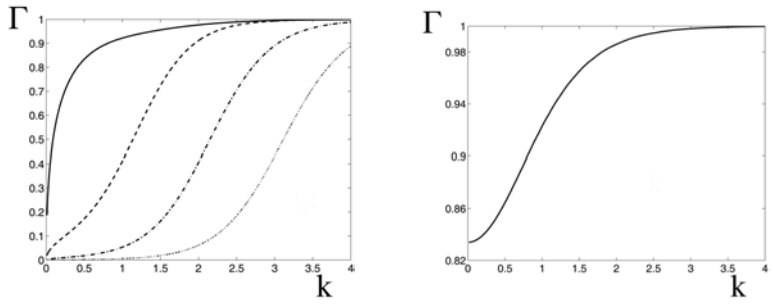
$$\tilde{u},\ \tilde{v} \text{ and } \tilde{q} \quad \text{are } x\text{-periodic, of period } L = 2m\pi/k, \tag{23}$$

$$\frac{d\psi}{d\tau} = \frac{1}{L}\int_{-1}^{0}\int_{0}^{L} G(y)\tilde{u}(x,y,\tau)dxdy, \quad G(y) = \frac{2k\cosh 2k(y+1)}{\sinh 2k} \tag{24}$$

where the bottom and free surface horizontal velocities are determined from one of the following additional conditions, either

$$\tilde{u} = -\sin[2k(x-\psi)], \qquad \tilde{v} = 0 \quad \text{at } y = -1, \tag{25}$$

$$\tilde{u}_y = 0, \quad \tilde{v} = 0, \quad \text{at } y = 0, \tag{26}$$



(a) (b)

Figure 2: The contamination parameter Γ. (a) Γ vs. k for $T = 7.42 \cdot 10^{-4}$ and: (——) $\gamma = 1$, $(- - -)$ $\gamma = 0.1$, $(- \cdot - \cdot -)$ $\gamma = 0.01$, and $(\cdot \cdot \cdot \cdot \cdot)$ $\gamma = 10^{-3}$. (b) The maximum value of Γ vs. k for $T = 7.42 \cdot 10^{-4}$ and varying γ.

or the clean free surface case, or

$$\tilde{u} = -(1-\Gamma)\sin[2k(x-\psi)], \qquad \tilde{v} = 0 \quad \text{at } y = -1, \tag{27}$$

$$\tilde{u} = -\Gamma \sin[2k(x-\psi)] + \tilde{u}_0(\tau), \quad \tilde{v} = 0, \quad \int_0^L \tilde{u}_y \, dx = 0, \quad \text{at } y = 0, \tag{28}$$

for the contaminated free surface. For convenience, we have rescaled time and mean flow variables as

$$\tau = ReCt, \quad \tilde{u} = \frac{u^m}{ReC}, \quad \tilde{v} = \frac{v^m}{ReC}, \quad \tilde{q} = \frac{q^m}{(ReC)^2}, \tag{29}$$

with the effective mean flow Reynolds number defined as follows

$$Re = \frac{2R_0^2}{C}\left(\alpha_7 + \alpha_8\right), \tag{30}$$

with

$$\alpha_7 = \frac{3\omega_0 k}{\sinh^2 k}, \quad \alpha_8 = \frac{\omega_0 k}{\tanh^2 k}\left(\frac{4\gamma k^2}{\omega_0\sqrt{i\omega_0} - i\gamma k^2} + c.c + \frac{3\gamma^2 k^4}{|\omega_0\sqrt{i\omega_0} - i\gamma k^2|^2}\right). \tag{31}$$

where γ must be substituted by 0 in (31) when considering the clean surface case. Equations for the clean case (20)-(26), hereinafter referred to as MFClean, depend on the values of the 3 parameters (Re, k, m), while the contaminated free surface problem defined by (20)-(24), (27)-(28), hereinafter MFContam, depends on an

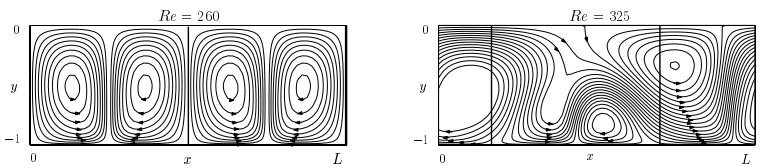
additional contamination parameter Γ that measures the relative effect of contamination in the generation of the streaming flow

$$\Gamma = \Gamma(k, T, \gamma) \equiv \frac{\alpha_8}{\alpha_7 + \alpha_8}, \tag{32}$$

and is plotted *vs.* the wavenumber k in figure 2(a) for the indicated values of γ; the selected value of the inverse of the Bond number, $T = 7.42 \cdot 10^{-4}$, corresponds to a 10 cm depth water container. It can be seen that for deep water problems, namely $k > \pi$, the contamination parameter is of the order of 1, even for quite small values of the Marangoni number γ. The maximum values of Γ are plotted in figure 2(b).

3 Results and conclusions

Problems MFClean and MFContam are both numerically solved to show that for small values of the effective mean flow Reynolds number Re, the solution relaxes to the basic standing wave (SW) with $\psi' = 0$. The mean flow associated with this basic SW consists of an array of pairs of steady counterrotating eddies. Examples are plotted in figure 3(a) for clean free surface and in fig.4(a)-4(c) for contaminated free surface. These steady solutions are $L/2$-symmetric and since they are also reflection symmetric in x, the integral (24) vanishes and the streaming flow does not affect the surface SW.



(a) (b)

Figure 3: Streamlines of the streaming flow of MFClean for $k = 2.37$, $L = 2.65$ ($m = 1$) and (a) $Re = 260$ and (b) $Re = 325$ (in moving axes $x - \psi'\tau$ with constant drift velocity). Thick vertical lines correspond to the nodes of the surface waves given by (18).

For the MFClean problem, if Re exceeds a threshold value, indicated in figure 5(a), the basic steady solution becomes unstable always through a Hopf bifurcation and a branch of time periodic solutions (PSW) appears, which produces a time periodic drift of the SW with no net drift on the free surface. These periodic solutions resemble locally the so called compression modes that have been observed in annular containers ([5], [6]) and cannot be obtained with the usual amplitude equations that ignore the coupling with the streaming flow. For some values of k and L, there are some additional bifurcations to steadily traveling waves (TWs), which move at a constant speed like the one shown in figure 3(b), and more complex oscillatory attractors, but these depend strongly on k and L (see [7]

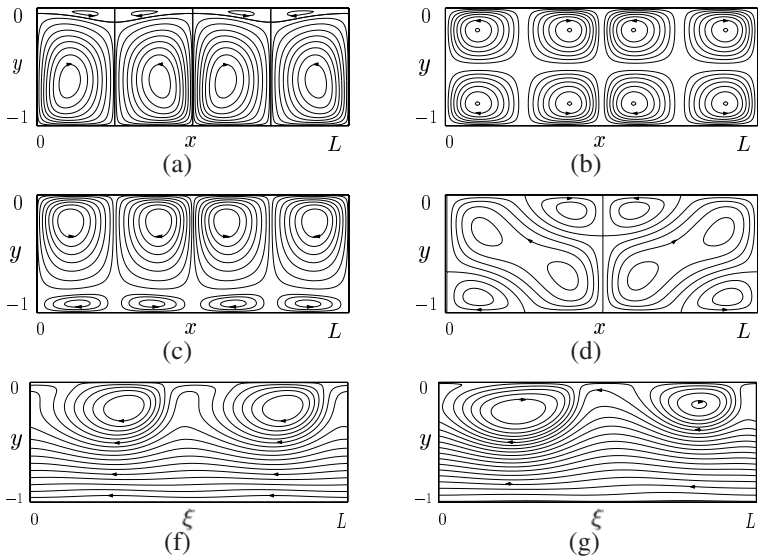


Figure 4: Streamlines of MFContam, for $k = 2.37$, $L = 2.65$ ($m = 1$), and (Re, Γ): (a) $(200, 0.1)$, (b) $(160, 0.5)$, (c) $(60, 0.9)$, (d) $(200, 0.5)$, (e) $(200, 0.9)$ in moving axes $\xi = x - \psi'\tau$ with constant drift velocity $\psi' = 0.32$ and $\tilde{u_0} = 0.49$, (f) $(600, 0.9)$ in moving axes with constant drift velocity $\psi' = 0.27$ and $\tilde{u_0} = 0.53$.

for more details). However, drift instabilities were quite robust in the experiment of Douady *et al.* [5] (Fauve, personal communication, 2003) and the MFclean problem does not seem to reproduce this feature.

In order to mimic the behavior of tap water (used in the experiment [5]) the MFContam problem is solved to obtain that the primary instability of the basic SW (SW($L/2$)) depends on the value of the contamination parameter. In figure 5(b) it can be seen that for small values of Γ the instability takes place through a Hopf bifurcation and for quite small values of Γ the contamination effect seems to stabilize the basic SWs (note that the critic Reynolds number for the clean case for the same values of k and L is marked with a large point in the horizontal axe of figure 5(b)).

This is because the only effect of contamination in this regime on the mean flow is to replace the free stress boundary condition at the free surface by a no-slip boundary condition, which reduces the strength of the mean flow. For an intermediate value of Γ a symmetry breaking bifurcation to another type of SW no longer $L/2$ symmetric (SW(L)) occurs, see figure 4(d) as an example. For larger values of the contamination parameter Γ the basic SW($L/2$) destabilizes through a parity breaking bifurcation that leads to TWs (TW($L/2$)) whose streamlines for the mean flow in a moving reference frame are similar to the one plotted in 4(e).

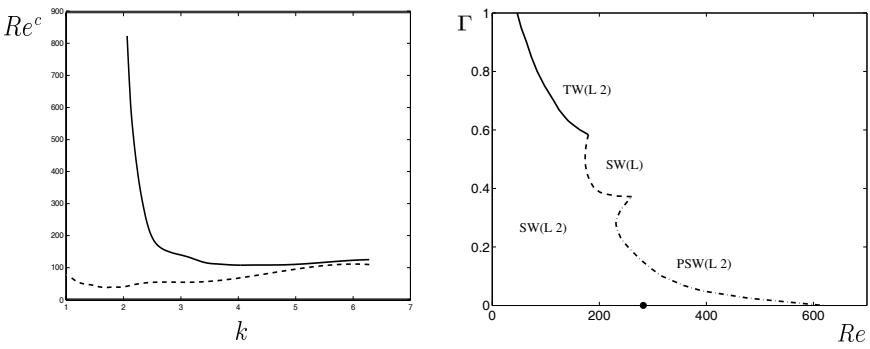


Figure 5: The primary instability of the basic SW for: (a) MFClean for different wave numbers k and (b) MFContam, for $k = 2.37$, $L = 2.65$ ($m = 1$). Figure 5(a): The bifurcation is always a Hopf bifurcation (——) ((− − −) shows the parity breaking bifurcation that takes place only if the coupling between the surface wave and the mean flow (24) it is ignored). Figure 5(b): The bifurcation is either a Hopf bifurcation ($-\cdot-\cdot-$) if $0 < \Gamma < 0.372$, a $(L/2)$-symmetry breaking bifurcation ($- - -$) if $0.372 < \Gamma < 0.584$, or a parity breaking bifurcation (——) if $0.584 < \Gamma < 1$.

Note that the mean flow is still $L/2$-symmetric. In contrast with the clean case, these TWs appear in a primary bifurcation and are quite robust (remain unchanged for larger domains and appear for all values of the wave number we have checked). Thus, contamination effects seem to play an important role in the surface waves dynamics. For larger values of the Reynolds number Re, different secondary instabilities are obtained, which include another type of TWs with no $L/2$-symmetric mean flow (figure 4(f)), pulsating traveling waves, and even chaotic attractors ([8]). For all these states that are not steady SW, the coupling with the mean flow is an essential ingredient that should not be ignored.

Acknowledgements

This work was supported by the National Aeronautics and Space Administration (Grant NNC04GA47G) and the Spanish Ministry of Education (Grant MTM2004-03808).

References

[1] Faraday, M. On the forms and states assumed by fluids in contact with vibrating elastic surfaces. *Phil. Trans. R. Soc. Lond.*, **121**, pp. 319-340, 1831.

[2] Miles, J. and Henderson D. On the forms and states assumed by fluids in contact with vibrating elastic surfaces. *Annu. Rev. Fluid Mech.*, **22**, pp. 143-165, 1990.



[3] Cross, M. and Hohenberg, P.C. Pattern formation outside of equilibrium. *Rev. Mod. Phys.*, **65**, pp. 851-1112, 1993.
[4] Kudrolli, A. and Gollub, J.P. Patterns and spatio-temporal chaos in parametrically forced surface waves: A systematic survey at large aspect ratio. *Physica D*, **97**, pp. 133-154, 1997.
[5] Douady, S. Fauve, S. and Thual, O., Oscillatory phase modulation of parametrically forced surface waves. *Europhys. Lett.*, **10**, pp. 309-315, 1989.
[6] Thual, O., Douady, S. and Fauve, S., Instabilities and Nonequilibrium Structures II. *Ed. Tirapegui, E. and Villaroel, D.*, Kluwer, pp. 227, 1989
[7] Martín, E., Martel, C. and Vega, J.M. Drift instability of standing Faraday waves. *J. Fluid Mech.*, **467**, pp. 57-79, 2002.
[8] Martín, E. & Vega, J.M. The effect of surface contamination on the drift instability of standing Faraday waves. *J. Fluid Mech.*, in press (2005).
[9] Martel C. & Knobloch, E., Damping of nearly-inviscid water waves. *Phys. Rev. E*, **56**, pp. 5544-5548, 1997.
[10] Vega, J.M., Knobloch, E. and Martel, C., Nearly inviscid Faraday waves in annular containers of moderately large aspect ratio. *Physica D*,**154**, pp. 147-171, 2001
[11] Lapuerta, V., Martel, C. and Vega, J.M., Interaction of nearly-inviscid Faraday waves and mean flows in 2-D containers of quite large aspect ratio. *Physica D*, **173**, pp. 178-203, 2002.



High frequency AC electrosprays: mechanisms and applications

L. Y. Yeo[1] & H.-C. Chang[2]
[1] *Micro/Nanophysics Research Laboratory, Department of Mechanical Engineering, Monash University, Clayton, Australia*
[2] *Department of Chemical and Biomolecular Engineering, University of Notre Dame, Notre Dame, U.S.A.*

Abstract

We have recently discovered a new electrospray phenomenon using high frequency AC electric fields beyond 10 kHz which behaves very distinctly from its DC electrospray counterpart. Experimental and theoretical findings have demonstrated that plasma charging plays a significant role in the electrohydrodynamically-driven interfacial dynamics of the electrospray. These findings show that Faradaic generation of interfacial plasma polarized layers can produce a net normal Maxwell stress that is responsible for the generation of aerosol drops. Experimental results of this plasma polarization phenomenon are presented and scaling theory is employed to elucidate the underlying plasma mechanism responsible for the phenomenon. The AC electrospray is capable of producing micron and sub-micron electroneutral drops or polymeric fibers and is a promising rapid and portable technology for drug encapsulation or biomaterials synthesis for controlled release respiratory drug delivery, wound care therapy or tissue/orthopaedic engineering.

1 Introduction

DC electric fields have mainly been used in electrohydrodynamic atomization (otherwise known as electrospraying) [1]. Several DC electrospray modes have been observed [2], the predominant mode being the cone-jet mode in which the liquids meniscus assumes the shape of a sharp cone with half angle approximately equal to the Taylor angle of 49.3°, obtained by balancing the electrostatic and capillary pressures acting on a conical surface for ideal, static equilibrium conditions [3].



WIT Transactions on Engineering Sciences, Vol 52, © 2006 WIT Press
www.witpress.com, ISSN 1743-3533 (on-line)
doi:10.2495/AFM06023

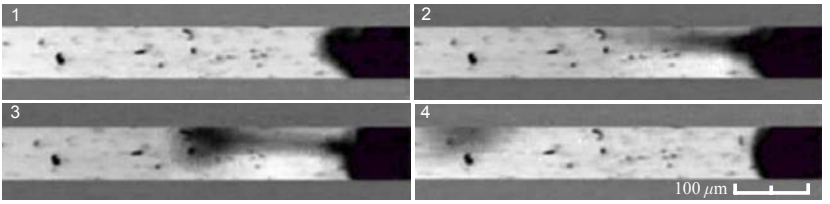


Figure 1: Image sequences at 6000 frames/s taken 300 μs apart illustrating microjet formation and subsequent drop detachment at $f = 15$ kHz and $V = 4000$ V.

Where AC fields have been utilized, these have been limited to low frequencies (< 1 kHz) such that the electrospray behavior does not significantly deviate from that of its DC counterpart [4]. Recently, the authors and their collaborators reported on a new high frequency (10–280 kHz) AC electrospray [5]. The drops generated were observed to be of larger dimensions (~ 10 μm) and were shown to carry no net charge, in contrast to that produced by DC electrosprays. In addition, none of the DC modes were observed and the drops were not ejected from the steady, well-defined Taylor cone characteristic of the stable DC modes. Instead, the drops are ejected from a round meniscus or from a peculiar microjet that protrudes intermittently from the meniscus (Fig. 1). Unlike the DC cone-jets, the microjets do not emerge from a Taylor cone and are much larger in size. In this paper, we briefly present evidence from experiments and scaling arguments to support an interfacial plasma polarization mechanism responsible for the dynamics of the AC electrospray. In addition, we also show the potential of the AC electrospray as a viable vehicle for drug encapsulation and biomaterials synthesis.

2 DC Taylor cone

In DC electrospraying, the absence of an external periodic forcing allows sufficient time for charge separation to take place in the liquid meniscus upon application of an electric field between the tip of the micro-needle from which the liquid meniscus emanates and a grounded electrode placed at a distance. Tangential ion conduction then occurs along the electric double layer formed at the interface thus resulting in co-ion accumulation and hence a singular electric field at the meniscus tip [6]. The repulsion between the co-ions at the meniscus tip then results in Coulombic fission wherein a thin liquid jet emanates from the tip once the repulsive force exceeds the surface force. The co-ion accumulation at the meniscus tip is also the reason why the drops produced as a result of various instabilities suffered by the jet carry a net charge.

For a perfectly conducting liquid, Taylor [3], by considering the static equilibrium balance between the capillary and Maxwell stresses, showed that a conical meniscus with a half angle of 49.3° is produced. Due to the assumption of the perfect conducting limit, the drop is at constant potential and hence the gas-phase

electric field is predominantly normal at the meniscus interface. It can then be shown that the normal gas phase electric field $E_{n,g}$ scales as $1/\sqrt{R}$, where R is the meniscus radius, and hence the Maxwell pressure, $p_{\mathrm{M}} \sim E_{n,g}^2$ scales as $1/R$. p_{M} therefore exactly balances the azimuthal capillary pressure $p_{\mathrm{C}} \sim \gamma/R$, where γ is the interfacial tension, for all values of R. This exact balance, and absence of a length scale selection, is responsible for the formation of a static Taylor cone.

Taylor's perfectly conducting limit was extended to allow for the effect of finite liquid conductivities by Li *et al.* [7] and Stone *et al.* [8]. Both of these studies showed that in these cases, it is the tangential electric field within the slender conical liquid meniscus that dominates. Nevertheless, it can be shown that the tangential liquid phase electric field $E_{t,l}$ also scales as $1/R$ and thus an exact balance between the Maxwell stress $p_{\mathrm{M}} \sim E_{t,l}^2$ and the capillary stress $p_{\mathrm{C}} \sim \gamma/R$ is again obtained, giving rise to a conical-like structure. The cone angle, however, depends crucially on the liquid to gas permittivity ratio $\beta \equiv \epsilon_l/\epsilon_g$, and the Taylor angle is recovered in the perfectly conducting limit as $\beta \to \infty$.

3 AC microjet

3.1 Plasma polarization mechanism

In AC electrosprays, the high frequency periodic forcing does not permit sufficient time for charge separation and hence co-ion accumulation at the meniscus tip. As a result, the generated drops are electroneutral. Moreover, the absence of tangential ion conduction also stipulates a weaker liquid phase tangential electric field, consistent with our earlier experimental findings in which the AC electrospray behavior was found to be insensitive to liquid conductitivity [5]. This passive role of the liquid phase is compounded by the formation of a thin, highly-conducting, permanent negatively charged plasma polarization layer around the liquid meniscus that gives rise to a dominant normal gas phase electric field in one AC half cycle. By imposing a flow of inert gases known to catalyze plasma ionization along the liquid meniscus, Lastochkin & Chang [9] showed that the critical voltage for drop ejection in AC electrospraying can be substantially lowered.

When ejected drops are passed through a set of parallel capacitor plates, their continuous attraction to the positive plate despite periodic reversal of the AC polarity demonstrates the existence of a permanent negatively charged plasma cloud surrounding the drop [6]. This negative charge does not originate within the drop due to the lack of time for charge separation in the liquid, as discussed above. In addition, the possibility of the drop carrying charge is ruled out since the drop ejection time, typically 10^{-3} s, is much greater than applied AC forcing period thus allowing any charge within the drop to essentially equilibrate during the ejection event. In addition, liquid conductivity again was not observed to influence the degree of drop deflection between the plates.

Given the passivity of the liquid phase, we postulate that the plasma cloud arises due to liquid vaporization from the meniscus and its subsequent ionization to produce negative ions. This is evidenced by the observation that aerosol gen-



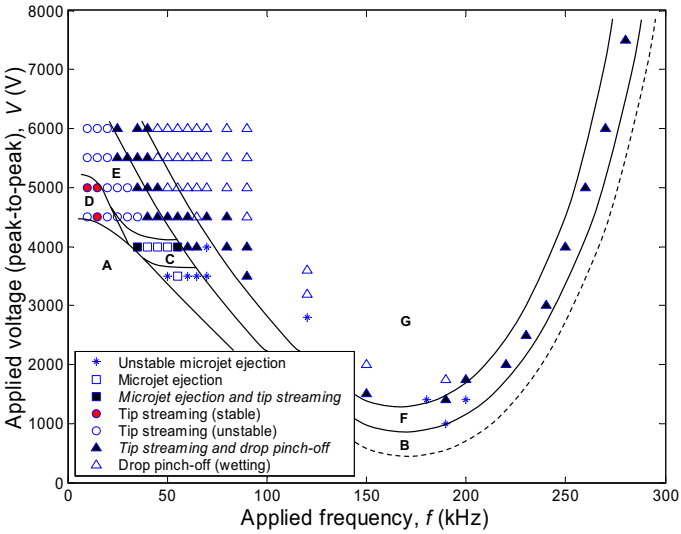


Figure 2: AC electrospray behavior indicating the optimum frequency at which the minimum in the critical voltage occurs [5]. The various spray modes are also shown: A—Capillary dominant regime (no drop ejection), B—Unstable microjet ejection, C—Microjet ejection with/without tip streaming, D—Stable tip streaming, E—Unstable tip streaming, F—Tip streaming with drop pinch-off (onset of wetting), and G—Drop pinch-off and wetting.

eration in the AC electrospray only occurs when the working liquid possesses a sufficiently high volatility (e.g. alcohols) and when the applied voltage exceeds a threshold voltage associated with the ionization potential [6]. Moreover, the V-shaped frequency dependence of the electrospray indicating a frequency optimum ($\sim$ 165 kHz) at which the critical voltage is at its minimum (Fig. 2 [5]) lends further support to the postulated plasma polarization mechanism. The gas phase ions generated around the meniscus will diffuse away unless the frequency is sufficiently high such that the ionization rate in one half AC cycle exceeds the dispersion rate. On the contrary, at extremely high frequencies, there is insufficient time for plasma ions to be generated through a Faradaic reaction mechanism. As such, an optimum frequency is anticipated at which maximum plasma polarization occurs, which thus gives rise to maximum enhancement of the local normal Maxwell field at the meniscus interface.

Other possibilities exist that can explain the existence of the permanent charge cloud [6]. Nevertheless, we will not concern ourselves with exactly how the plasma layer arises but rather the effects of its existence. In the cathodic half cycle, when the meniscus and micro-needle have the same polarity as the plasma cloud which forms a thin highly conducting layer around the meniscus, the local gas phase

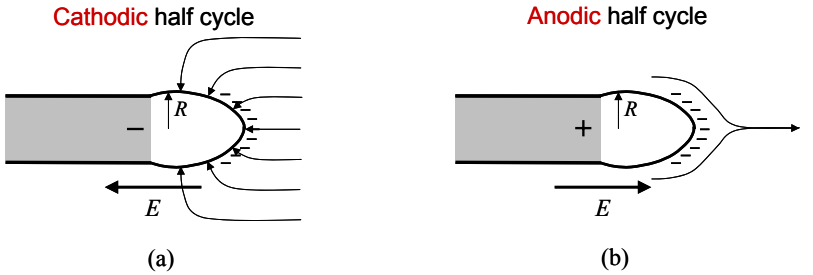


Figure 3: Postulated plasma polarization mechanism. (a) In the cathodic half cycle, the plasma cloud effectively enhances the local normal gas phase electric field. (b) In the anodic half cycle, the plasma cloud effectively screens the external field to produce a weak tangential gas phase electric field.

normal electric field at the interface is significantly enhanced, as illustrated in Fig. 3(a). This is because the meniscus and the plasma layer both resemble constant potential bodies in which the interfacial field is predominantly normal. In the anodic half cycle, however, whilst plasma is not generated, the plasma layer remains as there is insufficient time for its dispersion. The plasma layer is now oppositely charged to the meniscus and micro-needle and hence effectively screens the external field such that a weak tangential gas phase field arises, as depicted in Fig. 3(b). Consequently, it is the enhanced normal gas phase field that dominates and hence, averaged over many cycles, produces a net Maxwell stress that is responsible for the meniscus dynamics observed. Henceforth, we shall therefore restrict our analysis to this dominant normal gas phase field.

Given that both the meniscus and plasma layer resemble constant potential bodies, the solution of the Laplace equation governing the gas phase electrostatics gives rise to a specific scaling for the normal gas phase electric field $E_{n,g}$ at the interface. At this juncture, we will assume an arbitrary axisymmetric meniscus shape and not preclude the existence of a conical geometry. Thus, for a sharp conical meniscus, it can be shown from spheroidal harmonics that $E_{n,g} \sim 1/\sqrt{R}$ whereas for more slender bodies such as an elongated ellipsoid or cylinder, $E_{n,g} \sim 1/R$ [6]. Nevertheless, we note that at the meniscus tip, as $R \to 0$, the more singular $1/R$ scaling for a slender geometry dominates. It then follows that the Maxwell pressure $p_{\mathrm{M}} \sim E_{n,g}^2$ scales as $1/R^2$ and hence an exact balance with the azimuthal capillary pressure $p_{\mathrm{C}} \sim \gamma/R$ is only possible for one specific value of R. This length scale selection therefore excludes the possibility of a conical geometry and instead suggests that the meniscus is stretched to a more elongated cylinder-like geometry such as that of a microjet (regimes B and C in Fig. 2), as depicted in Fig. 1. This scaling therefore explains the appearance of a non-steady microjet instead of a steady Taylor cone in AC electrosprays.



3.2 Dynamic microjet simulation

The role of the Maxwell pressure resulting from a normal gas phase interfacial electric field that scales as $1/R$ in elongating the liquid meniscus into a cylindrical microjet structure can also be verified through a dynamic simulation in which the equations governing the coupled interactions between the hydrodynamics and electrodynamics are solved simultaneously in the longwave limit in axisymmetric polar coordinates $(r, 0, z)$. The fundamental assumption here is that the axial length scale L of the liquid meniscus and resulting jet is large compared to the radial length scale R_0, i.e. $\epsilon \equiv R_0/L \ll 1$. We adopting the following transformations,

$$(r, R) \rightarrow R_0\,(r, R_0)\,, \;\; z \rightarrow Lz, \;\; p \rightarrow \frac{\gamma}{R_0}p, \tag{1}$$
$$u \rightarrow \frac{Uu}{\epsilon}, \;\; v \rightarrow Uv, \;\; t \rightarrow \frac{R_0 t}{U}, \;\; \phi \rightarrow V\phi,$$

where u and v are the axial and radial velocities, p is the pressure and t is the time. $U \equiv \gamma/\mu$ is the characteristic velocity scale with μ being the liquid viscosity and V the applied potential.

Substituting the above transformations into the axisymmetric continuity and Navier-Stokes equations governing mass and momentum conservation in the liquid jet, together with the relevant interfacial boundary conditions (normal stress jump, tangential stress continuity and kinematic boundary conditions), and, exploiting the small value of ϵ by expanding the solutions for all variables in powers of ϵ, we then arrive at the following leading order evolution equations for the axial velocity and jet radius: [10, 6]

$$\mathrm{Re}\left(u^{(0)_t} + u^{(0)}u_z^{(0)}\right) = -\left(\frac{1}{R^{(0)}}\right)_z + Bp_{\mathrm{M}_z}^{(0)} + \frac{6R_z^{(0)}u_z^{(0)}}{R^{(0)}} + 3u_{zz}^{(0)}, \tag{2}$$

$$R_t^{(0)} + u^{(0)}R_z^{(0)} + \frac{R^{(0)}u_z^{(0)}}{2} = 0, \tag{3}$$

where $\mathrm{Re} \equiv \epsilon^2\rho U R_0/\mu$ is the Reynolds number, demoted to higher order, with ρ being the liquid density. The subscripts indicate partial derivatives in space and time. $B \equiv \varepsilon_g E_\infty^2 R_0/2\gamma$ is the Maxwell Bond number with E_∞ being the applied electric field. The leading order Maxwell pressure $p_{\mathrm{M}}^{(0)}$ is given by a composite formulation involving the Maxwell stress for a spherical cap at the meniscus tip and the Maxwell stress for a cylindrical geometry (with the same scaling as described above), connected by a weighting function [6]:

$$p_{\mathrm{M}}^{(0)} = \left[1 - \exp\left(-z/R_s\right)\right]\left(\frac{Lz}{R_0R^{(0)}}\right)^2 \tag{4}$$
$$+ \exp\left(-z/R_s\right)\left\{\cos\alpha\left[1 + 2\left(\frac{R_s\sin\alpha}{R^{(0)}}\right)^3\right]\right\}^2,$$

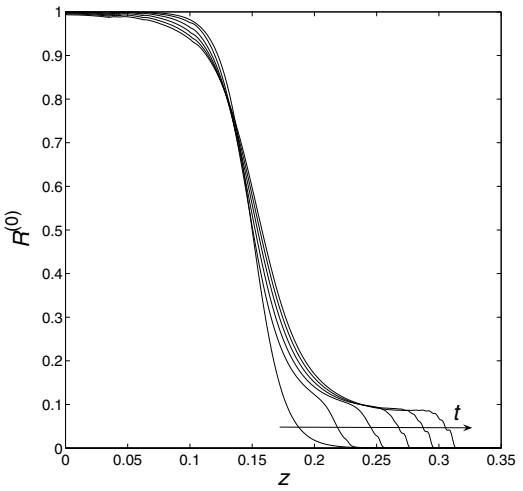


Figure 4: Typical spatio-temporal evolution profile of the meniscus interface for 5 equal time steps up to $t = 0.4$ with $B = 10$ and Re $= 100$. The initial profile is observed to elongate into a long slender microjet due to the action of the normal Maxwell stress at the interface.

with $\alpha = \tan^{-1}(R/R_s - z)$ where R_s is the radius of curvature of the spherical meniscus tip.

Equations (2) and (3) with Eq. (5) are solved numerically using the Method of Lines [11, 12] subject to the following initial conditions:

$$R^{(0)} = 0.5\left[1 - \tanh\left(\frac{z - 0.15}{0.025}\right)\right], \qquad \text{and,} \qquad u^{(0)} = 0, \tag{5}$$

and boundary conditions $R^{(0)} = 1$ and $u^{(0)} = 0$ at $z = 0$, and, $R^{(0)} \to 0$ and $u^{(0)} = 0$ as $z \to \infty$. A typical spatio-temporal evolution profile is illustrated in Fig. 4 in which the an axial pressure gradient resulting from the interfacial distribution of the normal Maxwell stress with $1/R^2$ scaling along the meniscus is observed to elongate the initially rounded meniscus and pull out a slender microjet close to that observed in Fig. 1. After a short transient, the microjet is observed to propagate forward at roughly constant velocity whilst maintaining an approximately constant radius.

4 AC electrospray applications

The main advantages of employing AC fields over DC in electrospraying are the inherent safety of employing high frequency AC, the lower critical voltages required and the electroneutrality of the ejected drops. The electroneutral drops stipulate negligible current and hence a low power requirement, which enables the

AC electrospray to be miniaturized for the design of small portable devices. Moreover, the use of high frequency AC ensures safe use, particularly in the case of consumer applications.

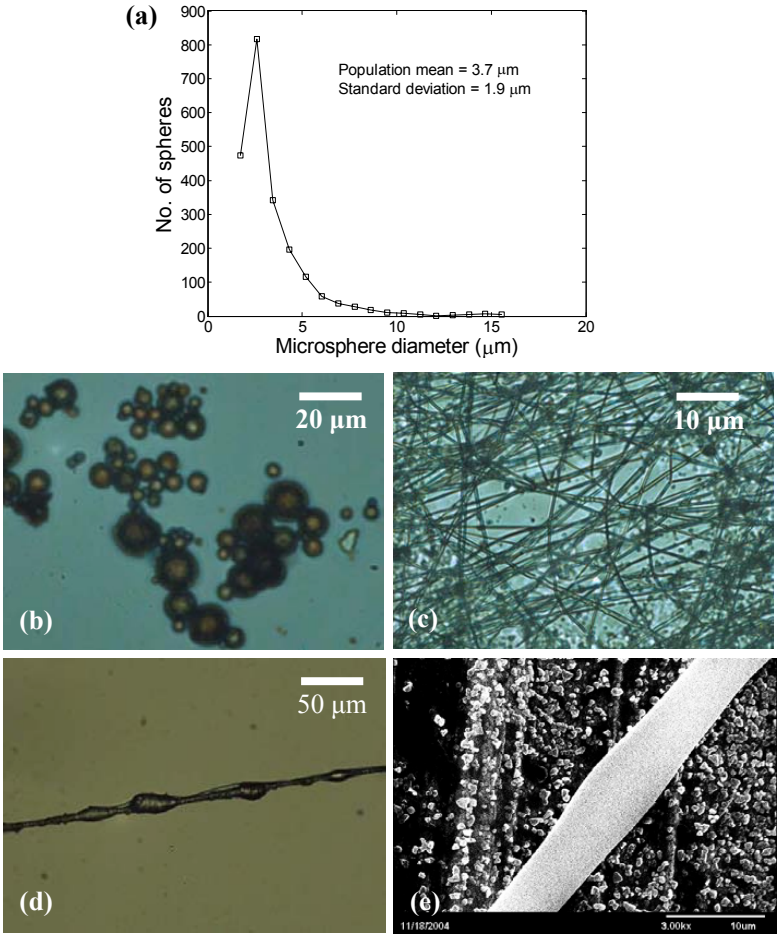


Figure 5: Synthesis of microparticles and microfibers from poly(lactic acid) using the AC electrospray. (a) Particle size distribution. (b) Water encapsulated within poly(lactic acid) microspheres. (c) Two-dimensional scaffolding network of micron sized poly(lactic acid) fibers with adjustable pore sizes. (d) 10 micron single compound poly(lactic acid) fiber. (e) Scanning electron microscope image of a micron sized fiber overlaid on a background of 100 nm poly(lactic acid) particles.

The stability of the ejected drops from Coulombic fission enables the synthesis of drug/vaccine encapsulated micron-sized spherical particles and fibers consist-

ing of biodegradable polymeric materials. Yeo *et al.* [13] discusses the relative merits of using AC fields over DC electrospraying and other conventional synthesis methods, particularly for the rapid mass production of bioscaffolds for tissue/orthopaedic engineering or for miniaturized consumer drug delivery or wound care therapy devices. In particular, the electroneutral drops prevent surface adsorption and compound ionization for in vivo applications such as drug delivery. Figure 5 shows examples of water encapsulated microparticles and microfibers made from poly(lactic acid) using the AC electrospray. Peculiarly, nanoparticles are also observed using scanning electron microscopy, as shown in Fig. 5(e), although further characterization of such is needed [13].

References

[1] Grace, J.M. & Marijnissen, J.C.M., A review of liquid atomization by electrical means. *J. Aerosol Sci.*, **25**, pp. 1005–1019, 1994.
[2] Clopeau, M. & Prunet-Foch, B. Electrohydrodynamical spraying functioning modes: a critical review. *J. Aerosol Sci.*, **25**, pp. 1021–1036, 1994.
[3] Taylor, G. I., Disintegration of water drops in an electric field. *Proc. R. Soc. Lond. A* 280 (1964) 383–397.
[4] Borra, J.P., Tombette Y. & Ehouarn, P., Influence of electric field profile and polarity on the mode of EHDA related to electric discharge regimes. *J. Aerosol Sci.*, **30**, pp. 913–925, 1999.
[5] Yeo, L.Y., Lastochkin, D., Wang, S.-C. & Chang, H.-C., A new AC electrospray mechanism by Maxwell-Wagner polarization and capillary resonance. *Phys. Rev. Lett.*, **92**, 133902, 2004.
[6] Maheshwari, S., Yeo, L.Y. & Chang, H.-C., High frequency AC electrosprays. Submitted to *Phys. Fluids*.
[7] Li, H., Halsey, T.C. & Lobkovsky, A., Singular shape of a fluid drop in an electric or magnetic field. *Europhys. Lett.*, **27**, pp. 575–580, 1994.
[8] Stone, H.A., Lister, J.R. & Brenner, M.P., Drops with conical ends in electric and magnetic fields. *Proc. Roy. Soc. Lond. A*, **455**, pp. 329–347, 1999.
[9] Lastochkin, D. & Chang, H.-C., A high frequency electrospray driven by gas volume charges. *J. Appl. Phys.*, **97**, 123309, 2005.
[10] Eggers, J., Universal Pinching of 3D axisymmetric free-surface flows. *Phys. Rev. Lett.*, **71**, pp. 3458–3460, 1993.
[11] Schiesser, W.E., *The Numerical Method of Lines*, Academic: San Diego, 1991.
[12] Yeo, L.Y., Matar, O.K., Perez de Ortiz, E.S. & Hewitt, G.F., The dynamics of Marangoni-driven local film drainage between two drops. *J. Colloid Interface Sci.*, **241**, pp. 233–247, 2001.
[13] Yeo, L.Y., Gagnon, Z. & Chang, H.-C., AC electrospray biomaterials synthesis. *Biomaterials*, **26**, pp. 6122–6128, 2005.



This page intentionally left blank

Section 4
Fluid structure interaction

This page intentionally left blank

A structured multiblock compressible flow solver SPARTA for planetary entry probes

P. Papadopoulos & P. Subrahmanyam
Department of Mechanical and Aerospace Engineering,
Center of Excellence for Space Transportation & Exploration,
San Jose State University, San Jose, CA, USA

Abstract

SPARTA is a platform independent Graphical User Interface based two-dimensional compressible flow solver on multiple block structured grids that is developed and integrated to a planetary probe database to study trajectory, aerodynamic heating and flow-field analysis. It is a time-integration solver of the Navier-Stokes equations. The flow geometry may either be planar or axisymmetric. A comprehensive database of atmospheric entry vehicles and aeroshell configurations is developed. The database comprises vehicle dimensions, trajectory data, and aero-thermal, Thermal Protection Systems data for many different ballistic entry vehicles. Material properties for Carbon and Silicon based ablators are modeled and can be accessed from the database. SPARTA provides capabilities to choose from a list of flight vehicles or enter geometry information of a vehicle in design. A fourth order Runge-Kutta integration is employed for trajectory calculations. Fay-Riddell and Sutton-Grave empirical correlations have been used for the stagnation point convective heat transfer and Tauber-Sutton for the stagnation point Radiative heat transfer calculations. An approach is presented for dynamic TPS sizing. The inputs for the flow solver come from the trajectory output. SPARTA is a trajectory based flow solver.
Keywords: aerothermodynamics, Riemann solver, relational database, trajectory, compressible flow solver, planetary probes, convective and radiative aerodynamic heating, thermal protection systems, Navier-Stokes equations.



WIT Transactions on Engineering Sciences, Vol 52, © 2006 WIT Press
www.witpress.com, ISSN 1743-3533 (on-line)
doi:10.2495/AFM06024

1 Introduction

The Unites States national vision for space exploration calls for "*The human and robotic exploration of the Solar System and beyond*". Human and Robotic exploration of the solar system is to search for evidence of life, to understand the history of the solar system and to support human exploration. But before they arrive, *planetary probes* will likely have preceded them to provide the understanding required to make further exploration possible. Advances in technology ranging from new instrumentation, sophisticated materials and improvised nanotechnology makes planetary probes a vital tool in pursuit of scientific truth and the origins.

In support of this mission, a complete computational design framework is necessary that automates the calculations for stagnation point heating, TPS sizing and CFD calculations so that better probes can be built with this analysis. An integrated planetary probe design framework that automatically computes TPS sizing and convective stagnation point heating using Fay and Riddell [1] and radiative heating based on the Tauber-Sutton correlations [2] given vehicle geometry and entry trajectory flight conditions is presented in this publication. The probe design framework includes access to existing probe designs and provides a mini-CAD like design environment for construction of new configurations based on classes consistent with existing designs. A platform independent Graphical User Interface (GUI) based, relational database and trajectory driven CFD tool called SPARTA has been developed to accurately predict aerodynamic and heating entry environments. The aero-heating environment depends on the trajectory flown, size and shape of the vehicle. Trajectory driven CFD capability is demonstrated in this article.

2 Approximate Riemann solver

2.1 Flow solver

SPARTA is a compressible multi-block flow solver in two dimensions geometries: planar or axisymmetric. It is based on the cell-centered finite-volume formulation of the Navier-Stokes equations and has a shock capturing capability through the application of a limited reconstruction scheme and an upwind-biased flux calculator. SPARTA is capable of modeling flows that include shear layers, expansions, shocks and boundary layers. The governing equations are expressed in integral form over arbitrary quadrilateral cells with the time rate of change of conserved quantities in each cell specified a summation of the fluxes: mass, momentum and energy. The integral form of the Navier-Stokes equations in Cartesian coordinates is used as the starting point of the code formulation in the flow solver. The flow domain is discretized by a structured grid and a finite-volume approach is used to discretize the conservation equations. The flow field is recorded as cell-average values at cell centers and explicit time stepping is used to update conserved quantities.



A Riemann solver is developed to calculate Inviscid fluxes across cell faces while central differences schemes are used to calculate the viscous fluxes. The governing equations for SPARTA is the set of Navier-Stokes equation which in integral form, can be expressed as

$$\frac{\partial}{\partial t}\int_V U dV = -\int_S (\overline{F}_i - \overline{F}_v)\cdot \hat{n}\ dA + \int_V Q\ dV \tag{1}$$

where V is the cell's volume, S is the bounding surface and $\hat{n}$ is the outward facing unit normal of the control surface. For two dimensional flows, V is the volume per unit depth in the z-direction and A is the area of the cell boundary per unit depth z. The array of conserved quantities per unit volume is

$$U = \begin{bmatrix} \rho \\ \rho u_x \\ \rho u_y \\ \rho E \\ \rho f_{is} \end{bmatrix} \tag{2}$$

These elements represent mass density, x-momentum per volume, y-momentum per volume, total energy per volume and mass density of species is. The flux vector is divided into inviscid and viscous components and the inviscid components, in two dimensions is:

$$\overline{F}_i = \begin{bmatrix} \rho u_x \\ \rho u_x^2 + p \\ \rho u_y u_x \\ \rho E u_x + p u_x \\ \rho f_{is} u_x \end{bmatrix} \hat{i} + \begin{bmatrix} \rho u_y \\ \rho u_x u_y \\ \rho u_y^2 + p \\ \rho E u_y + p u_y \\ \rho f_{is} u_y \end{bmatrix} \hat{j} \tag{3}$$

The viscous component is

$$\overline{F}_v = \begin{bmatrix} 0 \\ \tau_{xx} \\ \tau_{yx} \\ \tau_{xx} u_x + \tau_{yx} u_y + q_x \\ \rho f_{is} \mu_{x,is} \end{bmatrix} \hat{i} + \begin{bmatrix} 0 \\ \tau_{xy} \\ \tau_{yy} \\ \tau_{xy} u_x + \tau_{yy} u_y + q_y \\ \rho f_{is} \mu_{y,is} \end{bmatrix} \hat{j} \tag{4}$$

2.2 Gas models

A number of gas models have been developed and included in SPARTA flow solver. These include perfect gas mixtures, perfect gases and also models for air and nitrogen in chemical equilibrium. These gas models can be chosen from the drop down menu in the graphical user interface and can be assigned to the flow solver for the vehicle in design.

3 SPARTA software architecture

Figure 1 shows the software architecture of SPARTA. Once the TPS Sizing is done, it can be automatically linked to CFD tools for grid generation and analysis. A comprehensive database of ballistic reentry vehicles has been developed using the Planetary Mission Entry Vehicles manual [3]. This includes vehicle dimensions and trajectory data for all the capsules that has been flown in the past. The SPARTA GUI provides the capability to choose from a list of flight vehicle geometric information and entry trajectories. This tool is intended as a preliminary design framework for planetary entry vehicle design. The overall software architecture is shown in Figure 1. The front GUI allows the user to provide inputs for trajectory and geometry. It is connected to an extensive planetary probe database and a Matlab computational engine, which is used to generate flight trajectory data. From the trajectory data, stagnation point aerodynamic heating and TPS size requirements are computed. TPS Sizing requires the selection of materials that effectively protect the vehicle during reentry. The database has several different categories of Ablators to choose from including Carbon, Reusable Composites, Carbon-Phenolic and Silicon based ablators. With the emerging Information Technology growth, heterogeneous systems are rapidly developing and this presents a need for distributed analysis system. So, with this in mind a platform independent tool has been developed. This architecture neutral code has the capability to execute in any platform for analysis without having to recompile.

3.1 Graphical user interface

The GUI based analysis tool was developed in the Matlab platform-independent environment. Figure 2, shows the probe design options provided in the SPARTA interface. A planetary probe can be chosen from the user interface Flight vehicle drop down menu. When the flight vehicle is chosen, appropriate initial trajectory and vehicle dimensions data are populated in the input boxes from the relational database. Values in the input boxes can be changed by the user or the populated values can be used to run the trajectory simulation. The user is also able to choose a stagnation point correlation, either Fay and Riddell [1] or Sutton and Graves [4] correlations from the interface. The user can either choose a flight vehicle for trajectory analysis from the list of available probe designs in the planetary probe database as explained above or construct a new configuration. This is achieved by calling the Geometry Engine from within the GUI. After the

vehicle is constructed, the trajectory is computed by calling the computational engine from within the GUI.

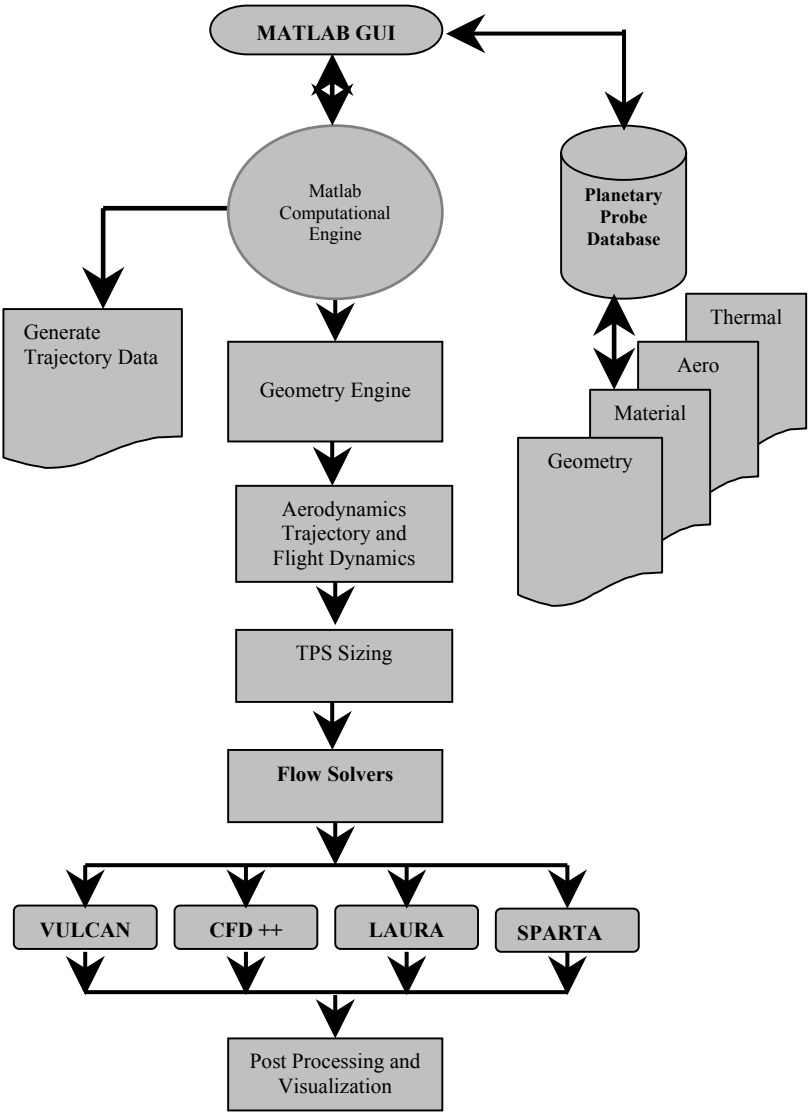


Figure 1: SPARTA software architecture.

3.2 Atmospheric model

SPARTA design environment also links the trajectory code to appropriate planetary empirical atmospheric models depending on the planetary probe that is

chosen. The 1976 US Standard Atmosphere for Earth called GAME – General Atmospheric Model for Earth is modeled as a subroutine that calculates pressure, density, temperature, Reynolds number and speed of sound as a function of altitude. Global Reference Atmospheric Models (GRAM) [5] of Mars, Venus, Titan, and Neptune has been used to compute the atmospheric pressure, density and temperature profiles.



Figure 2: SPARTA graphical user interface.

4 Trajectory driven CFD

4.1 Probe model

The probe model developed for this trajectory is a point-mass model with two translations and one rotation (3-DOF) around a spherical planet. It integrates the equations of motions of a vehicle on a ballistic entry trajectory so that no lift is generated and the body acts only on gravity. The vehicle model is build from a number of parameters defining the geometry of the probe including body diameter, cone half-angle, nose and shoulder radius. The aerodynamic properties of the probe are subsequently derived from the geometry of the vehicle.

4.2 Trajectory calculations

The Apollo capsules were chosen for demonstration of the trajectory analysis capability. A sample trajectory data is shown in Table 1 and in figures 3(a) to 3(d).

4.3 Test cases and CFD results

The aeroshell analyzed is the Pathfinder configuration with a spherically blunted, 70° cone with a nose radius R_N of 0.020 m, and the edge radius of the shoulder

R_S of 0.0020 m. The freestream conditions are $P_\infty = (7.1208)(10^{-5})$ kg/m^3, $T_\infty = 217$ K, $V_\infty = 6571.7$ m/s.

Table 1: Sample output of trajectory calculated by SPARTA.

Trajectory Analysis for Flight Vehicle: Apollo 4					
Altitude (ft)	Velocity (ft/sec)	Flight Path Angle (deg) γ	Mach Number	Stag Point Pressure (lbf/ft^2)	Stag Point Heat Transfer rate $\dot{q}_{conv}$ (W/cm^2)
250000.00	**22500.00**	**12.00**	**23.83**	**30.70**	**191.30**
249000.00	**22501.37**	**12.00**	**23.80**	**32.16**	**195.82**
248000.00	**22502.75**	**12.01**	**23.77**	**33.69**	**200.44**

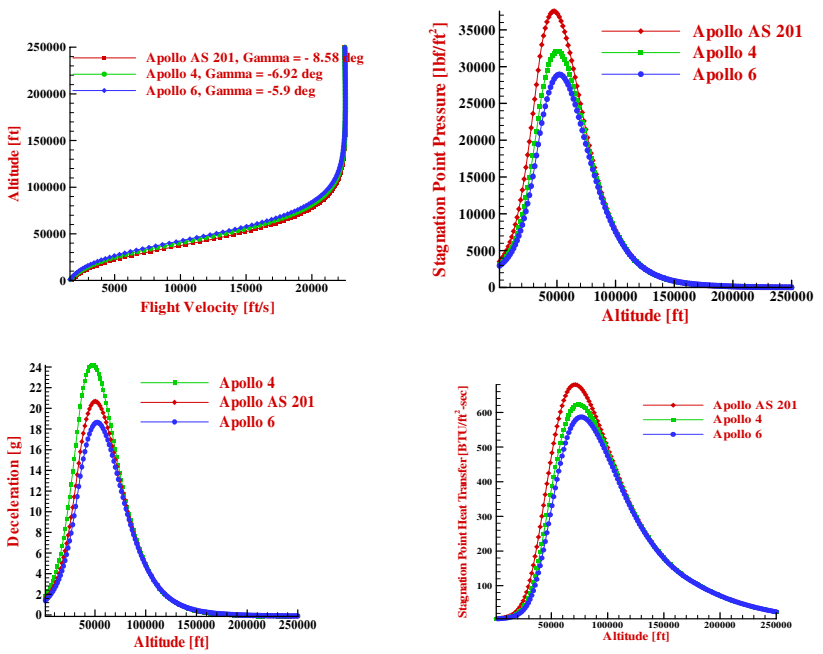


Figure 3: Trajectory data: flight velocity, Stagnation point heating, stagnation point pressure, deceleration vs. altitude.

4.4 Planetary probe relational database and flight vehicle architecture

The geometry of the flight vehicle is either constructed from the GUI for user specifications or generated from the SPARTA database for existing probes. The user specified inputs include vehicle dimensions such as the planetary probe's nose radius, forebody conical angle, corner radius, afterbody frustrum conical angle, and any additional base geometry specifications. Other design variables

such as the probe mass, reference area and ballistic coefficient are also required to define the vehicle architecture. The user must also indicate the vehicle's angle-of-attack and freestream flight conditions along the reentry trajectory. A comprehensive database of existing planetary probe designs is provided in the SPARTA framework. Trajectory and geometry data are stored for each probe in the database. In addition to the capsule shapes, base areas, nose radii, payload masses and the ballistic coefficients of the probes are stored in the database. Pathfinder, Viking and Apollo class vehicle configurations can be generated from the database. The user can modify the existing vehicle designs by changing geometric features available in the GUI.

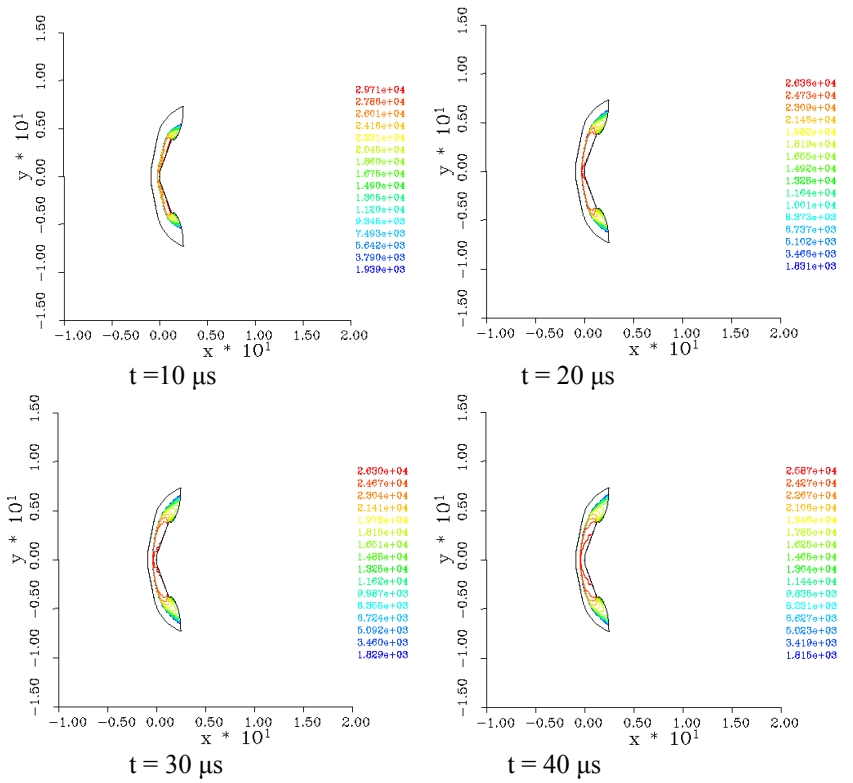


Figure 4: Transient flow over MARS Aeroshell at times t=10 μs, 20 μs, 30 μs and 40 μs.

5 Conclusions

A trajectory based two-dimensional compressible flow solver CFD tool SPARTA is developed to solve multiple block structured grids. It is integrated to a comprehensive planetary probe database to study aerodynamic heating and flow-field analysis. It is a time-integration solver of the Navier-Stokes equations.

The code calculates all flight conditions along the trajectories including aerodynamic and Aerothermodynamic stagnation point quantities. The code has been extensively benchmarked successfully against the industry standard trajectory codes. SPARTA is a platform-independent standalone Matlab based flight vehicle-database driven graphical user interface application to do the preliminary investigation of reentry vehicles. Appropriate atmospheric profiles have been developed and integrated with the code. For Venus, Mars and Neptune, the GRAM models have been used. Empirical correlations for estimating the stagnation point convective and radiative heat transfer have been modeled using Fay-Riddell and Tauber-Sutton correlations.

References

[1] J. Fay and F. Riddell, "Theory of Stagnation Point Heat Transfer in Dissociated Air" *Journal of Aeronautical Sciences* 25 (2), Feb 1958.

[2] Tauber, M. E., Sutton, K., "Stagnation Point Radiative Heating Relations for Earth and Mars Entries", *Journal of Spacecraft and Rockets*, Vol 28, No 1, 1991, pp.40-42.

[3] C. Davies, "Planetary Mission Entry Vehicles," Quick Reference Guide, Ver. 2.1, NASA-ARC, 2002.

[4] K. Sutton, R.A Graves, "A General Stagnation Point Convective Heating Equation for Arbitrary Gas Mixture", NASA TR-376, 1971.

[5] Justus, C.G., and Johnson, D.L, Mars Global Reference Atmospheric Model 2001 Version (MARS- GRAM 2001) Users Guide, NASA/TM-2001-210961, April 2001.



This page intentionally left blank

Eulerian simulations of oscillating airfoils in power extraction regime

G. Dumas & T. Kinsey
Laval University, Quebec, Canada

Abstract

A wing that is both heaving and pitching simultaneously may extract energy from an oncoming flow, thus acting as a turbine. The theoretical performance of such a concept is investigated here through unsteady, two-dimensional laminar flow simulations using the finite volume, commercial CFD code FLUENT$^{\mathrm{TM}}$. Computations are performed in the heaving reference frame of the airfoil, thus leaving only the pitching motion of the airfoil to be dealt with through a rigid-body mesh rotation and a circular, non-conformal sliding interface. This approach offers the benefit of second order time accurate simulations. For a NACA 0015 airfoil at a Reynolds number of $Re = 1\,100$, a heaving amplitude of one chord ($H_0 = c$), and a pitching axis at the third chord ($x_p = c/3$), we present a mapping of power extraction efficiency in the frequency and pitching amplitude domain: $0 < fc/U_\infty < 0.25$ and $0 < \theta_0 < 90°$. Remarkably, efficiency as high as 34% is observed as well as a large parametric region above $\theta_0 > 55°$ of better than 20% results. Impact of varying some of the fixed parameters is also addressed.
Keywords: oscillating wing, pitching and heaving airfoil, unsteady aerodynamics, power extraction, turbine, wind energy, flow simulation, finite volume method, accelerated reference frame.

1 Introduction

Following the work of McKinney and DeLaurier [1], it has been proposed in recent years to use systems of oscillating wings, heaving and pitching with large amplitudes, to develop alternative turbine designs for applications in air (wind turbine) and in water (tidal energy system). Our ongoing investigation [2] aims to establish the actual potential of the concept.

In this paper, we restrict ourselves to the canonical case of low-Reynolds number, 2-D incompressible laminar flows for which modern CFD tools can yield reli-



WIT Transactions on Engineering Sciences, Vol 52, © 2006 WIT Press
www.witpress.com, ISSN 1743-3533 (on-line)
doi:10.2495/AFM06025

able predictions at an affordable cost. This latter consideration is particularly critical here considering the great number of physical parameters involved, and thus the great number of cases that need to be computed. In addition, one should keep in mind that for a given set of parameters, the power extraction efficiency can only be evaluated once the simulation has reached its time-periodic response after several cycles of oscillation, requiring typically well above 10 000 timesteps.

2 Problem description

We consider a symmetric airfoil undergoing a combined motion of pitching $\theta(t)$ and heaving $h(t)$ such as shown in figure 1. Restricting to a pitching axis located on the chord line at position x_p from the leading edge, one express the airfoil motion as:

$$\theta(t) = \theta_0 \, \sin(\gamma \, t) \quad \longrightarrow \quad \Omega(t) \, = \, \theta_0 \, \gamma \, \cos(\gamma \, t) \tag{1}$$

$$h(t) = H_0 \, \sin(\gamma \, t + \phi) \quad \longrightarrow \quad V_y(t) = H_0 \, \gamma \, \cos(\gamma \, t + \phi) \tag{2}$$

where H_0 and θ_0 are respectively the heaving and pitching amplitudes, V_y is the heaving velocity, Ω the pitching velocity, γ the angular frequency ($= 2\pi \, f$), and ϕ is the phase shift between the two motions which is kept fixed in this study ($\phi = 90°$).

The effective angle of attack α and effective upstream velocity experienced by the airfoil during its cyclic motion are obviously functions of time. Their maximum values in the cycle are expected to have major impact on the peak forces generated, and on the probability of dynamic stall occurrence. In particular, one has $\alpha(t) = \theta(t) + \arctan(\, V_y(t)/U_\infty \,)$, for which we approximate the maximum value (exact approximation in most cases) by its quarter-period value: $\alpha_{max} \approx \alpha_{T/4} = \theta_0 - \arctan(\gamma H_0/U_\infty)$.

One must realize that an oscillating symmetric airfoil can operate in two different regimes, namely propulsion and power extraction, depending on the value of the "feathering parameter", i.e.,

$$\chi \, = \, \frac{\theta_0}{\arctan(H_0 \gamma / U_\infty)} \, . \tag{3}$$

Based on a simple quasi-steady argument [2], which leads to necessary but not precisely sufficient conditions (in a mean sense over the cycle), one can show that $\chi < 1 \; \Rightarrow$ propulsion; $\chi > 1 \; \Rightarrow$ power extraction. An example of the latter case is shown in the schematic representation of figure 2 which presents a time sequence viewed in a reference frame moving with the farfield flow, so that the effective angle of attack $\alpha(t)$ is made visible from the apparent trajectory of the airfoil. In that figure, $\mathbf{R}$ is first constructed from typical lift and drag forces (right-hand side), and then decomposed into X and Y components (left-hand side). One easily infers on figure 2 that the resultant aerodynamic force $\mathbf{R}$ would have a vertical component Y that is in the same direction as the vertical displacement of the airfoil. The flow would thus make a positive work on the airfoil, and therefore,



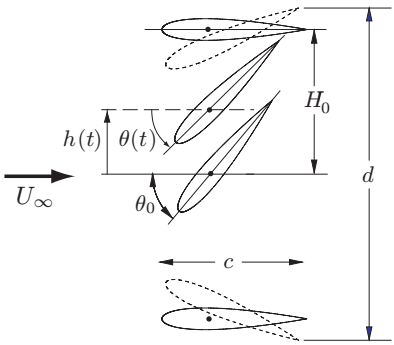


Figure 1: Imposed motion.

power would be extracted as long as no negative work is involved with respect to the horizontal component X. This is precisely the case of interest here since our airfoil is not moving horizontally, but only pitching and heaving into a uniform flow from left to right of speed U_∞.

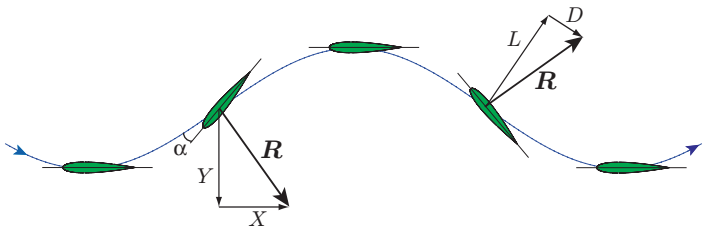


Figure 2: Power extraction regime ($\chi > 1$) of an oscillating airfoil.

3 Numerics

High resolution, two-dimensional unsteady computations have been performed in this study at Reynolds numbers from 500 to 2400 with the finite volume code FLUENT 6.1 [4] which allows for the use of moving meshes. Initially solving the Navier-Stokes equations in a fixed, inertial frame of reference, a proper meshing strategy taking advantage of the dynamic mesh and remeshing capabilities of the code was developed [2]. Both heaving and pitching motion of the airfoil were then taken into account through mesh motion. However, this approach in FLUENT required the use of first order time integration which therefore imposed the use of very small timestep sizes in order to control the inherent numerical diffusion.

To circumvent this constraint, a new meshing strategy has been developed in this work. In the present approach, the problem is set in a heaving reference frame (vertical translation) attached to the airfoil. This implies the use of time varying boundary conditions on exterior boundaries and the addition of the reference frame

acceleration as a new source term in the Navier-Stokes equation. The pitching portion of the airfoil motion on the other hand is left as such, i.e., the airfoil is actually pitching in the heaving reference frame, and this body motion is taken into account by the use of a moving mesh involving a circular, non-conformal sliding interface. As can be seen on figure 3, this interface is located at five chords around the airfoil, and the grid inside is pitching in rigid body with the airfoil. The grid outside the interface is not moving. This strategy offers the significant advantage of allowing for the use of second order time integration scheme rather than only first order.

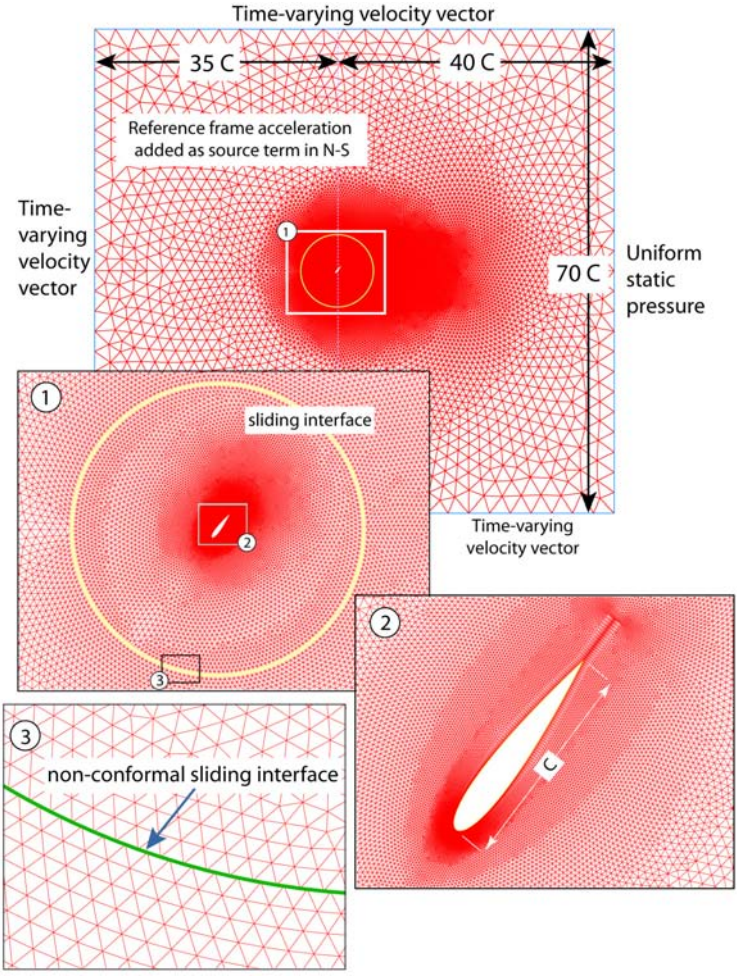


Figure 3: Grid details with two zoom levels showing its circular, non-conformal sliding interface (typical grid size: 72 000 cells).

In order to reach the long-term, periodic flow response after the impulsive start in each of our simulations, a few cycles are first computed with a relaxed timestep size. The precise number of cycles computed at that stage depends on the period of oscillation $T = 1/f$. This transitory period should provide at least 20 convective time units, i.e., time enough for the early wake to get sufficiently far away from the body. From that point on, we compute more cycles using a finer time resolution given by

$$\Delta t \;=\; \min\left\{ \frac{T}{2000} \;;\; \frac{c\,/\|V\|}{100} \right\}$$

where $\|V\|$ is a velocity norm representing the maximum instantaneous convective flux velocity in the domain which takes into account U_∞, the heaving boundary condition and the pitching mesh velocity. Normalized flow diagnostics are thereafter monitored so as to assert the periodicity of the final cycles. A criterion of less than 0.5% variation in mean statistics between final cycles is typically used. Flow quantities and aerodynamic forces of the last cycle are then used to compute mean values as well as efficiency. Typical run time for a whole simulation is about 100 hours on a single P4/3.2GHz processor.

A great deal of attention and rigor has been paid in this numerical investigation to assure good prediction accuracy throughout the targeted parametric space. Several auto-validation tests were carried out until force predictions independency was satisfactorily achieved with respect to all modelling aspects: mesh refinement and isotropy near the body, grid relaxation away from the airfoil, timestep size, domain size, periodicity criterion, sliding interface position, as well as implementation of user-defined functions (UDF) for unsteady boundary conditions and unsteady momentum source terms. In addition, numerous comparisons with several other studies were realized, in particular with the works of Blackburn and Henderson [5], Ohmi *et al.* [6], Jones *et al.* [3], and Pedro *et al.* [7]. Very good agreement was in general achieved, or, if need be, discrepancies successfully explained. This will be reported separately elsewhere (but in full details in: T. Kinsey, 2006, M.Sc. thesis, Laval University).

4 Results

The instantaneous power extracted from the flow (per unit depth) when $\chi > 1$ comes from the sum of a heaving contribution $P_y(t) = Y(t)\,V_y(t)$ and a pitching contribution $P_\theta(t) = M(t)\,\Omega(t)$, where M is the resulting torque about the pitching center x_p. The mean power extracted over one cycle can thus be computed in non-dimensional form ($C_P \equiv \frac{P}{\frac{1}{2}\,\rho\,U_\infty^3\,c}$) as:

$$\overline{C}_P = \overline{C}_{P_y} + \overline{C}_{P_\theta} = \int_0^1 \left\{ C_Y(t)\,\frac{V_y(t)}{U_\infty} \;+\; C_M(t)\,\frac{\Omega(t)\,c}{U_\infty} \right\} d(t/T)\,. \quad (4)$$

We further define the power extraction efficiency η as the ratio of the mean total power extracted $\bar{P}$ to the total power available P_a in the oncoming flow passing

through the swept area (the "flow window"):

$$\eta \equiv \frac{\bar{P}}{P_a} = \frac{\bar{P}_y + \bar{P}_\theta}{\frac{1}{2}\rho U_\infty^3 d} = \overline{C}_P \frac{c}{d} \tag{5}$$

where d is the overall, vertical extent of the airfoil motion (see figure 1).

4.1 Efficiency — basic case

A partial mapping of the predicted efficiencies (over 42 simulations) in the parametric space $(f^*,\ \theta_0)$ is provided in figure 4 for our basic case: NACA 0015 airfoil, $Re = U_\infty c/\nu = 1\,100$, $H_0/c = 1$ and $x_p/c = 1/3$. Note that the dimensionless frequency is defined here as $f^* \equiv fc/U_\infty$.

First, we find that the highest efficiency achieved, $\eta_{\max} \approx 34\%$, is obtained for high pitching amplitudes, $\theta_0 \approx 70 - 80°$, and at non-dimensional frequencies in the range $f^* \approx 0.12 - 0.18$. As a reference, let us recall here the theoretical limit of Betz (from actuator disk theory) at 59% which should apply to the present

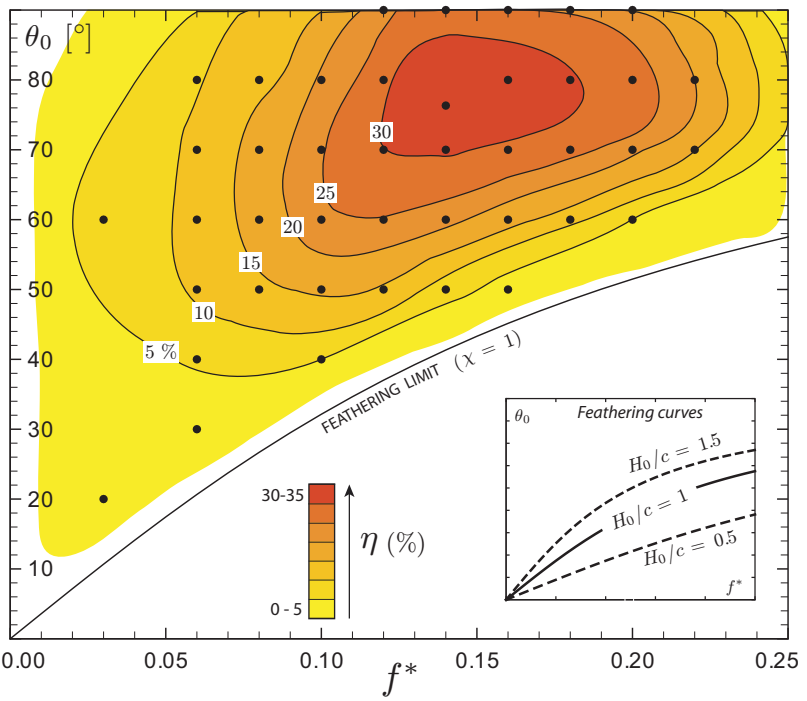


Figure 4: Preliminary mapping of efficiency η in the parametric space $(f^*,\ \theta_0)$ for a NACA 0015 at $Re = 1\,100$, $H_0/c = 1$ and $x_p/c = 1/3$. Simulated cases are shown with black circles. Note that the iso-efficiency contours have been sketched approximately.

oscillating wing problem since a cycle-averaged, stationary flow concept may be defined. In any case, efficiencies higher than 30% for a single oscillating airfoil appear quite encouraging from a practical point of view for the present turbine concept.

We further note that the best efficiency cases in figure 4 correspond to operating conditions of roughly $V_{y_{max}}/U_\infty = 2\pi f^* H_0/c \approx 1$ (maximum heaving velocity comparable to free stream velocity). At the same time, these cases are found to involve effective angles of attack (see Section 2) reaching as high as 35° during their cycles. With such large values of angle of attack, it is no surprise to observe some dynamic stall vortex shedding taking place during the motion. Indeed, leading edge vortex shedding (LEVS) is seen to occur during the cycles of most of the efficient cases (see figure 5). In fact, one finds that well-timed LEVS, occurring each half period just prior to $t \approx 0$ and $t \approx T/2$, is a very important mechanism to maximize the power extraction efficiency as can be illustrated with the help of figure 5.

The case shown in figure 5a corresponds to a typically smooth aerodynamic flow with a moderate efficiency of $\eta = 11\%$ while the case of figure 5b, which is at a slightly lower frequency but higher pitching amplitude, exhibits dynamic stall vortex shedding and reaches a mean efficiency of nearly 34%. The straight horizontal line corresponding to the theoretically available power C_{P_a} has been added to the figures as a reference level.

The main feature revealed by figure 5 is that case (a), without LEVS, shows a poor synchronization between V_y and C_Y (i.e., exhibiting opposite signs at times) causing the total power curve to go negative in some parts. On the other hand, case (b) exhibiting dynamic stall, shows good timing in the sign switch of V_y and C_Y, resulting in positive values of total extracted power over almost all of the cycle. It is clearly the shed vortices and their suction effect on the airfoil that are responsible for maintaining a negative Y force much closer to the mid-cycle time at $t/T = 0.5$. In this particular case, one notes further that the shedding at each half-cycle has also a favourable impact on the pitching contribution P_θ which can play a positive role momentarily in the cycle, despite its small overall mean contribution.

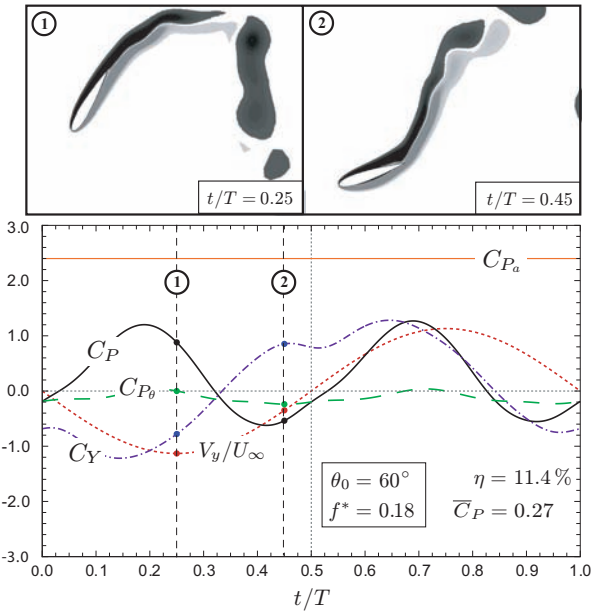
Indeed, one finds in this study that for most cases of interest, the heaving contribution P_y significantly dominates the pitching contribution P_θ. One may thus write $P(t) \approx Y(t)\, V_y(t)$. Consequently, one concludes that there are three major aspects affecting the level of power extracted:

- synchronization between the vertical force $Y(t)$ and the heaving velocity $V_y(t)$ $\longrightarrow$ both have to be of the same sign most of the cycle to avoid negative power occurrences;
- the magnitude of the heaving velocity $V_y(t)$ $\longrightarrow$ being proportional to H_0 and f, see Eq.(2), higher frequencies and/or higher heaving amplitude appear favourable;
- the magnitude of the vertical force $Y(t)$ $\longrightarrow$ complex dependency on both maximum effective angle of attack and maximum effective velocity.

It is clear that increasing the effective velocity by increasing V_y (through H_0/c and/or f^*) leads to increased effective dynamic pressure, and thus increased aero-



(a)



(b)

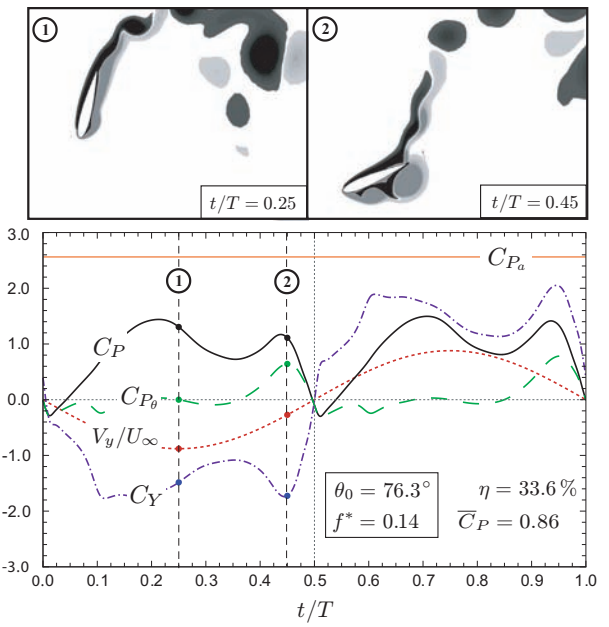


Figure 5: Contours of vorticity at two instants in the cycle (top), and time evolution (bottom) of total power coefficient C_P — as well as V_y/U_∞, C_Y, and C_{P_θ} — for two power extraction cases of figure 4. (a) A moderate efficiency case: No leading edge vortex shedding (LEVS); poor synchronization of Y vs V_y. (b) A typical high efficiency case: Occurrence of LEVS; optimal synchronization.

dynamic forces. However, the vertical force component Y may at the same time start decreasing due to decreasing effective angle of attack and reduced vertical projection. Indeed, increasing either the frequency f or the heaving amplitude H_0 (everything else being the same) inevitably moves us towards the feathering limit, which ultimately has a detrimental effect past a certain level. As suggested in figure 4, there has to be an optimum in those parameters.

4.2 Parametric study — preliminary

An extensive parametric investigation is currently underway in order to qualify, and quantify as much as possible, the effects of all the parameters involved in the characterization of an oscillating wing in power extraction. Several of the numerous parameters that had been set fixed are now varied: heaving amplitude H_0, pitching axis location x_p, airfoil geometry, phase angle ϕ, heaving and pitching functions, and Reynolds number. Preliminary results briefly discussed below concern the effects of airfoil thickness, heaving amplitude and Re number.

What we find with respect to airfoil thickness (NACA 0002 up to NACA 0020) is that global efficiency is little sensitive to the details of the geometry. The aerodynamics at play here is very much inertial, and governed by the forced, large amplitude oscillation. Although dynamic stall, thus boundary layer separation, is seen to play an important role in some cases, the precise location of flow separation along the airfoil is apparently not so critical. Indeed, for airfoil thickness varying from 2% to 20% chord, we obtain for the case of figure 5(a), $11.0 \leq \eta \leq 11.6\%$, while for the case of figure 5(b), efficiency varies slightly more in the range $32.0 \leq \eta \leq 33.6\%$. Again, from a practical point of view, these observations are rather favourable and encouraging.

Table 1: Effect of a larger heaving amplitude.

Case	$H_0/c = 1.0$		$H_0/c = 1.5$	
(f^*, θ_0)	$\overline{C}_P$	η (%)	$\overline{C}_P$	η (%)
(0.18, 60.0°)	0.27	11.4	−0.69	–
(0.14, 76.3°)	0.86	33.6	0.98	28.5

The impact of varying the heaving amplitude is much more complex and significant since it affects directly the oscillating velocities (at a given frequency), thus inertia, and the size of the flow window swept by the airfoil. Referring again to the two basic cases considered in figure 5, we find that although efficiency tends to decrease with an increase in amplitude (table 1), it may not be so for the power coefficient. This point would have to be kept in mind when applying the concept in practice. Table 1 also provides an example of a $\chi > 1$ case, thus above its feathering limit (but only slightly), that does not, in the mean, extract power from the flow



($\overline{C}_P < 0$). As mentioned previously, actual operating conditions have to remain away from the feathering limit.

Finally, the effect of viscosity has been addressed by simulating again our two basic cases of figure 5 for a lower (500) and a larger ($2\,400$) Re number. We find that efficiency tends to increase slightly with Re, from 9.8 to 11.9% for case (a), and from 32.7 to 36% for case (b). It is expected that at even higher Re numbers, turbulence might have a more significant impact on the power extraction efficiency. To address this, we plan to conduct URANS simulations in the near future.

5 Conclusion

The power extraction potential of an oscillating airfoil has been investigated in this study. For low-Re number and 2-D flow conditions, it has been shown that efficiencies as high as 34% can be obtained for reduced frequency $f^* \approx 0.15$ and under high pitching amplitude $\theta_0 \approx 75°$. For the parameters considered, efficiencies above 20% require a minimum pitching amplitude of about $55°$. Dynamic stall vortices have also been observed to play a key role in achieving optimal efficiency. It has also been confirmed that the physics of such oscillating airfoils is dominated by the imposed motion of large amplitude, and very little sensitive (in terms of efficiency) to the airfoil thickness and the level of viscous diffusion.

Acknowledgements

Financial support from NSERC Canada is gratefully acknowledged.

References

[1] McKinney W. & DeLaurier J., *The Wingmill: An Oscillating-Wing Windmill*, J. of Energy, Vol. **5**, No.2, pp. 109-115, 1981.

[2] Dumas G. & Kinsey T., *Unsteady Forces on Flapping Airfoils*, Paper CASI-257, 11th Aerod. Symp., Canadian Aeronautics and Space Institute, April 26-27, 2005, Toronto, Canada.

[3] Jones, K.D., Lindsey, K. and Platzer, M.F., *An Investigation of the Fluid-Structure Interaction in an Oscillating-Wing Micro-Hydropower Generator*, Fluid Structure Interaction II, Chakrabarti, Brebbia, Almorza and Gonzalez-Palma Eds., WIT Press, pp. 73-82, 2003.

[4] Fluent 6.1 User's Guide, Fluent Inc. 2003, http://www.fluent.com

[5] Blackburn H. M. & Henderson R. D., *A study of two-dimensional flow past an oscillating cylinder*, J. of Fluid Mech. **385**, pp. 255-286, 1999.

[6] Ohmi K., Coutanceau M., Daube O. and Loc T. P., *Further experiments on oscillating airfoils*, J. of Fluid Mech. **225**, pp. 607-630, 1991.

[7] Pedro G., Suleman A. and Djilali N., *A numerical study of the propulsive efficiency of a flapping hydrofoil*, Int. J. Numer. Meth. Fluids, Vol. **42**, 493-526, 2003.



Laboratory tests on flow field around bottom vane

M. M. Hossain[1], Md. Zahidul Islam[1], Md. Shahidullah[1],
A. de Weerd[2], P. van Wielink[2] & E. Mosselman[3]
[1]*Bangladesh University of Engineering and Technology (BUET), Bangladesh*
[2]*Avans Hogeschool, The Netherlands*
[3]*WL/Delft Hydraulics & Delft University of Technology, The Netherlands*

Abstract

Bottom vanes are vortex generating devices that are mounted on the river bed at an angle to the prevailing flow direction. They can be used effectively for sediment management and training of alluvial rivers. We tested the three-dimensional flow field generated by bottom vanes in a 45.6 m long and 2.45 m wide straight flume at the open-air physical modelling facility of BUET in Dhaka, Bangladesh, for all combinations of 4 vane heights, 5 vane angles and 2 bed topographies. Both topographies were moulded in concrete. The two bed topographies consisted of a flat bed and a bed with scour holes recorded in preceding mobile-bed experiments. Vanes at an angle of 30° to the flow were found to generate the strongest vortices. The scour holes did not weaken the vortices appreciably. We conclude therefore that local scour does not jeopardize the effectiveness of bottom vanes.
Keywords: helical flow, vortex, bottom vanes, laboratory experiments.

1 Introduction

Bottom vanes are vortex generating devices that are mounted on the river bed at an angle to the prevailing flow direction. The pressure difference between the pressure and suction sides of the vanes produces vortices that alter the transverse slope of the alluvial river bed in a zone downstream of the vanes. Thus bottom



WIT Transactions on Engineering Sciences, Vol 52, © 2006 WIT Press
www.witpress.com, ISSN 1743-3533 (on-line)
doi:10.2495/AFM06026

vanes can be used to modify river cross-sections (Potapov & Pyshkin [1], Remillieux [2], Odgaard & Kennedy [3] Odgaard & Spoljaric [4]). This might offer opportunities for low-cost interventions in the numerous rivers of Bangladesh that are responsible for enormous erosion and siltation problems throughout the country every year. An optimal design of bottom vanes for a particular situation requires good insight in the three-dimensional flow generated by the vanes. The three-dimensional flow field around a bottom vane was therefore tested in laboratory experiments for different vane heights as well as different vane angles to the flow. A specific issue was the effect of local scour holes that develop around bottom vanes, because there were some doubts whether those holes would disturb or even eliminate the vane-generated vortex. In the preceding year, the formation of scour holes had been investigated by experiments using a mobile sand bed (Hossain *et al.* [5]). However, the turbidity resulting from sediment transport hampered measurements of the associated flow field. The present fixed-bed experiments were therefore carried out for both a flat bed and one of the topographies found in the preceding mobile-bed experiments.



Figure 1: Overview of physical model facility at BUET.

2 Experimental set-up

2.1 Test facility

The experiments were carried out in a 45.6 m long and 2.45 m wide straight flume at the open-air physical modelling facility of BUET in Dhaka, Bangladesh (Figure 1). The flume has a re-circulating water supply system with pre-pump

storage pool, post-pump upstream reservoir, tailgates, sediment trap and stilling basin. The water discharge could be measured at two sharp-crested Rehbock weirs, one between the upstream reservoir and the flume and one in the re-circulation channel. Having established during trial experimentations that no water was lost in the system, only the Rehbock weir in the re-circulation channel was used to measure the discharge on a routine basis at half-hour intervals. Three point gauges along the flume were used to measure water levels and, hence, streamwise water level gradients at one-hour intervals. Flow velocities were measured using a programmable electromagnetic current velocity meter (P-EMS), mounted on a movable measurement carriage. The sensor of this instrument determines flow velocity components in two dimensions only, but three-dimensional flow velocity vectors could be obtained by rotating the sensor over 90° during part of the measurements. P-EMS positions and readings were calibrated daily, as the instrument was removed every evening and re-installed every morning to prevent theft.

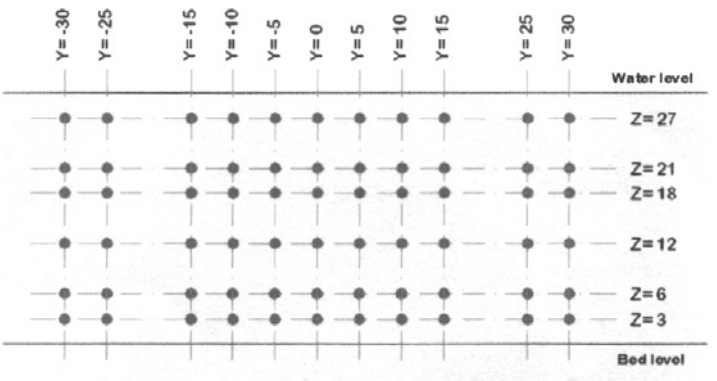


Figure 2: Cross-sectional measurement grid for flow velocity measurements.

2.2 Co-ordinate system and basic flow and vane parameters

Streamwise co-ordinates are denoted by x, cross-stream co-ordinates by y (positive to the right) and vertical co-ordinates by z (positive upward). The vane was installed at the centre of the flume (y = 0) at streamwise co-ordinate x = 15.00 m. Flow velocities were measured in 10 cross-sections at x = 14.00 m, 14.40 m, 14.80 m, 15.00 m, 15.20 m, 15.40 m, 15.60 m, 16.00 m, 16.50 m and 16.90 m. Figure 2 shows the fixed (y,z) locations where for each cross-section the components of the flow velocity vectors were measured. A flow depth of 0.30 m was maintained in combination with a discharge of 200 l/s. The flume being 2.45 m wide, these settings implied an average streamwise flow velocity of

0.27 m/s. The vane was made of durable Perspex, 0.40 m long and 8 mm thick. Vane heights and vane angles with respect to the flow were varied during the experiments.

2.3 Construction of scour holes in fixed bed

Mobile-bed experiments had been carried out during the preceding year to study the effects of bottom vanes on a sand bed topography (Hossain *et al.* [5]). The resulting topographies had been recorded for 20 test runs with different vane heights and vane angles. The topography resulting from a height of 0.18 m and an angle of 20° was moulded in a concrete bed for a detailed study of the corresponding three-dimensional flow field. This topography consisted of two scour holes, one around the vane (A) and one 2 m downstream (B), as shown in Figure 3. A special mould system was developed for an accurate reproduction of the original topography. An hourglass-shaped area of the fixed concrete bed was kept open for the positioning of the vane in different configurations (Figure 4). For each experimental run, the central part of scour hole A was remoulded in this gap using concrete of a low cement-sand ratio that could be broken away easily to prepare the next experimental run.

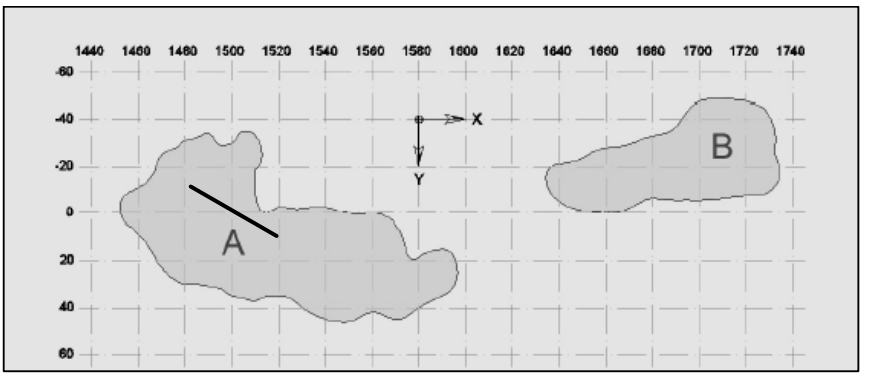


Figure 3: Scour hole planform.

2.4 Test runs

Test were carried out for 4 vane heights and 5 vane angles on both the flat bed and the scour bed, leading to a total of $4 \times 5 \times 2 = 40$ test runs. Table 1 gives an overview of the different experimental settings.

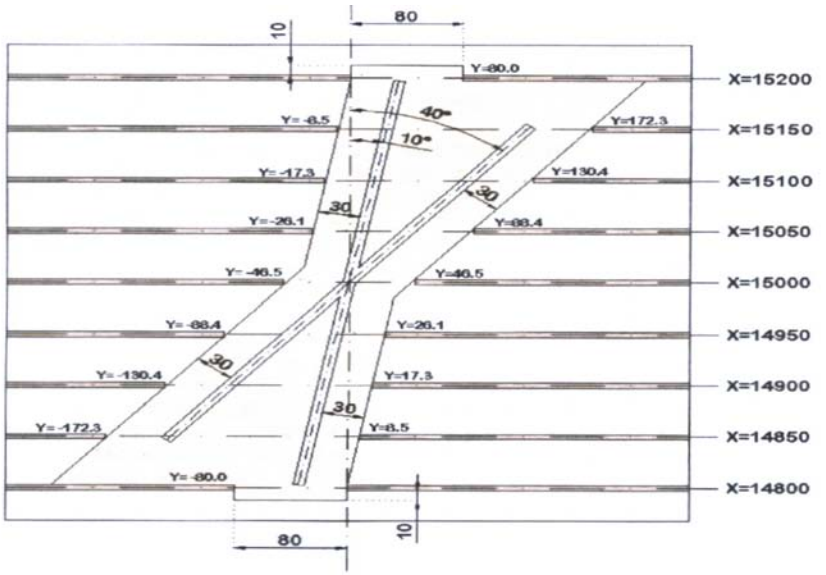


Figure 4: Hourglass-shaped vane gap.

Table 1: Overview of experimental settings.

Vane height (m)	Vane angle (deg)	Bed topography
0.06	10	flat
0.09	15	scour holes
0.12	20	
0.18	30	
	40	

3 Results and discussion

The 40 experiments were carried out during a period of 14 months and produced a dataset of 33 000 flow velocity vectors for the flat-bed experiments and 36 000 flow velocity vectors for the scour-bed experiments, all measured and entered into a computer manually. Figures 5 to 8 present some of the results for different vane heights, H, and vane angles, α, on the flat bed and the scour bed. They show that a 30° vane angle yielded the strongest vortex for the 0.18 m high vane. The vortices generally attenuated by a factor 0.3 to 0.6 over a streamwise distance of 5.7 times the water depth. The presence of scour holes affected the flow, but did not weaken the vortices appreciably.

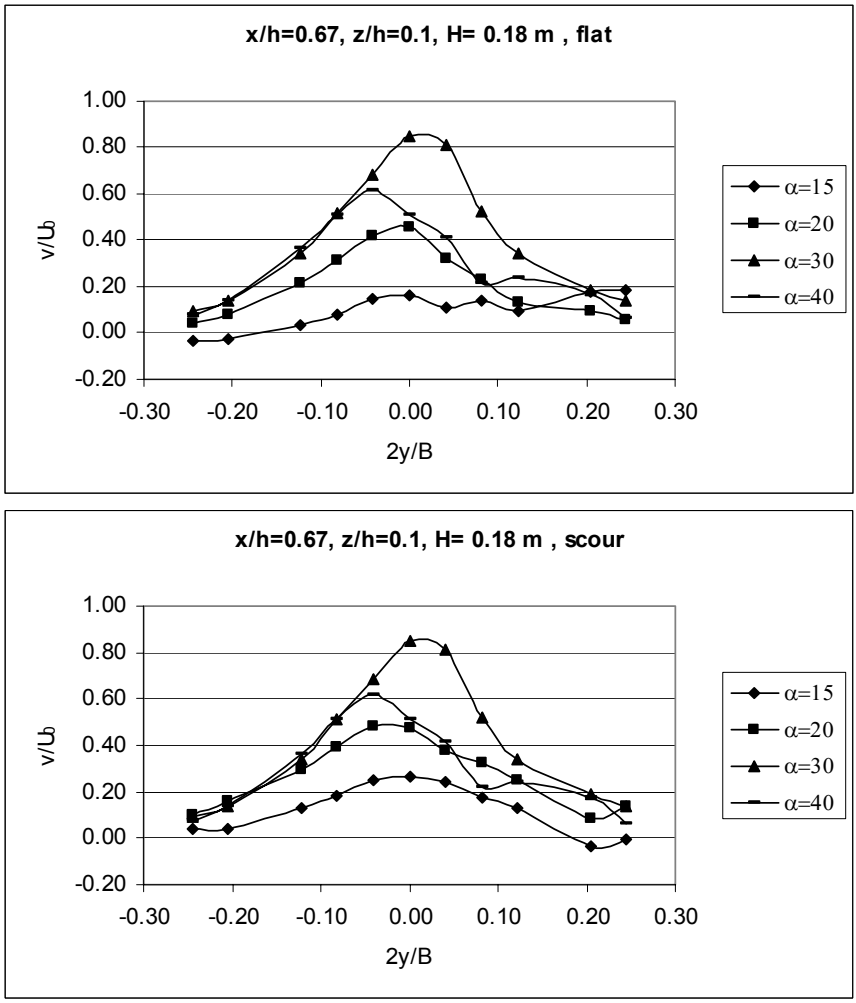


Figure 5: Cross-stream distribution of near-bed cross-stream flow velocity near trailing end of 0.18 m high vane: flat bed (above) and scour bed (below).

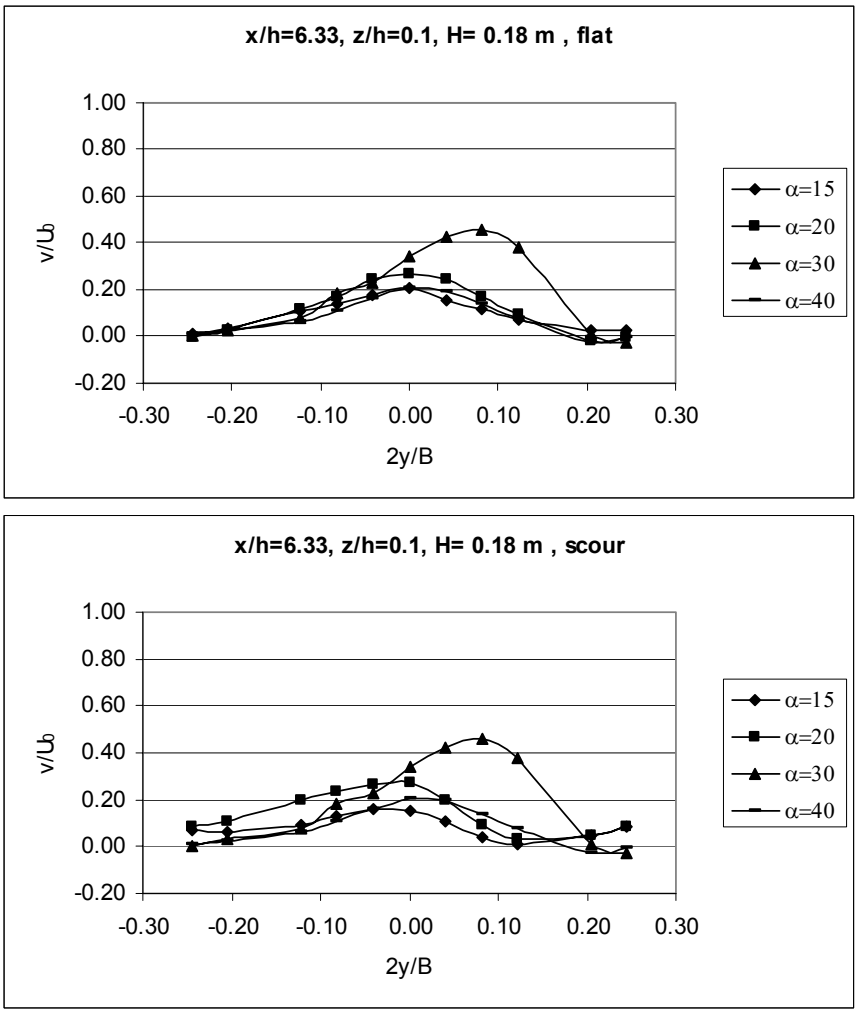


Figure 6: Cross-stream distribution of near-bed cross-stream flow velocity at 6 m downstream of 0.18 m high vane: flat bed (above) and scour bed (below).

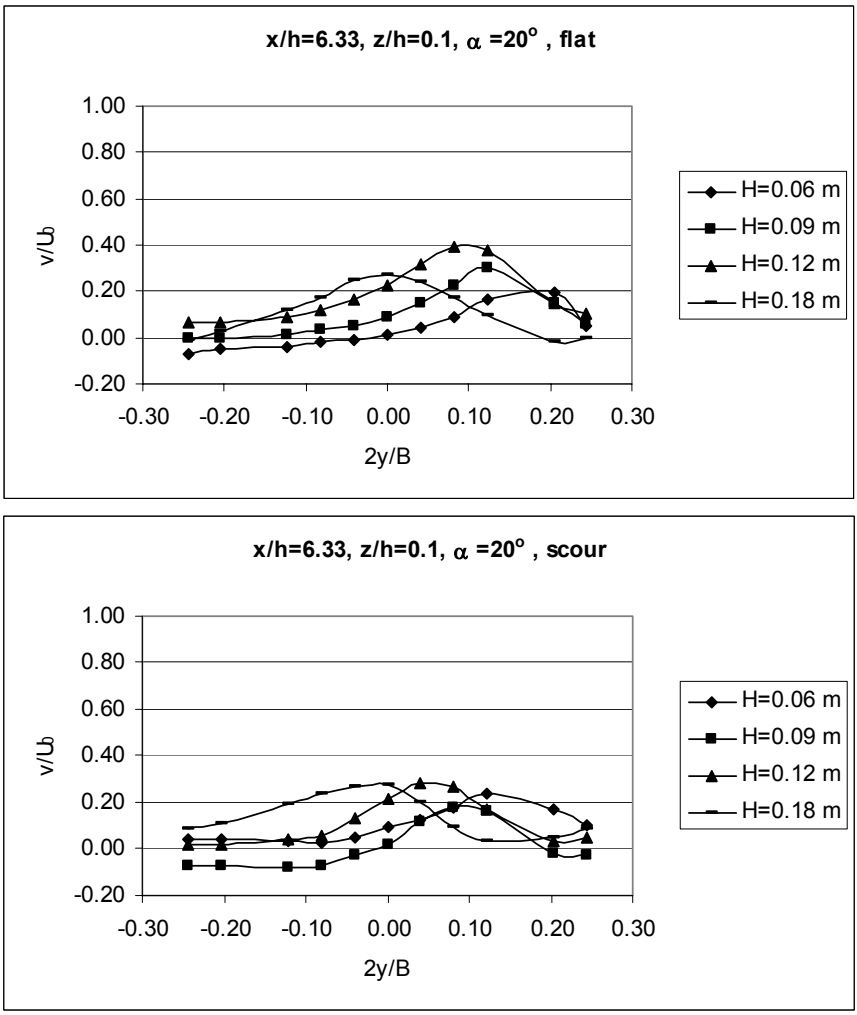


Figure 7: Cross-stream distribution of near-bed cross-stream flow velocity at 6 m downstream of vane under 20° to the flow: flat bed (above) and scour bed (below).

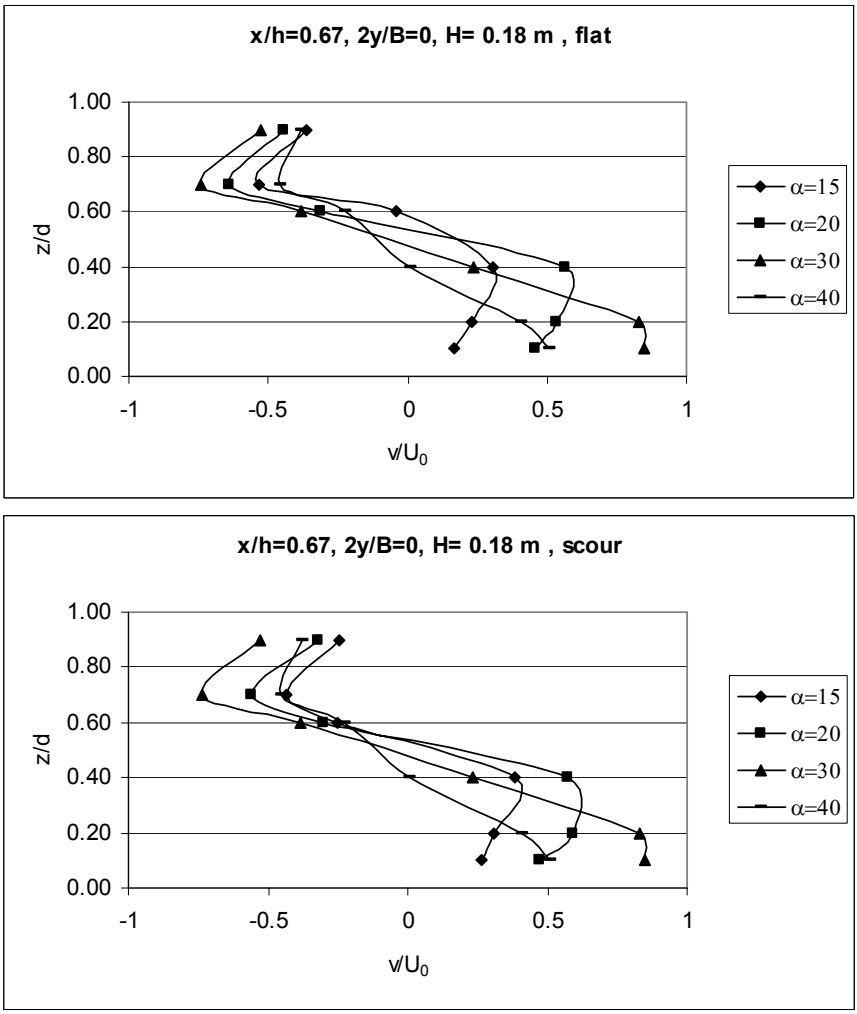


Figure 8: Vertical distribution of cross-stream flow velocity at centre-line near trailing end of 0.18 m high vane: flat bed (above) and scour bed (below).

4 Conclusions

The laboratory tests have produced a rich database that reveals the three-dimensional turbulence-averaged flow structure around bottom vanes of different heights and angles, above a flat bed as well as above a bed with two depressions in the shape of natural scour holes.

The scour holes have been found to affect the flow without appreciably weakening the vane-induced vortices. Hence scour holes are concluded not to jeopardize the effectiveness of bottom vanes for river training purposes.

References

[1] Potapov, M.V. & Pyshkin, B.A., *Metod poperechnoy tsirkulyatsii i ego primenenie v gidrotekhnike*, Izd. Ak. Nayk. SSSR: Moscow and Leningrad, in Russian, 1947.

[2] Remillieux, M., Development of bottom panels in river training. *Journal of Waterways, Harbors and Coastal Engineering Division*, **98(2)**, pp.151-162, 1972.

[3] Odgaard, A.J. & Kennedy, J.F., River-bend bank protection by submerged vanes. *Journal of Hydraulic Engineering*, **109(8)**, pp.1161-1173, 1983.

[4] Odgaard, A.J. & Spoljaric, A., Sediment control by submerged vanes. *Journal of Hydraulic Engineering*, **112(12)**, pp.1164-1181, 1986.

[5] Hossain, M.M., Islam, M.R., Saha, S., Ferdousi, S., Van Zwol, B., Zijlstra, R. & Mosselman, E., Laboratory tests on scour around bottom vanes. *Proc. of the 2nd Int. Conf. on Scour and Erosion*, eds. Y.-M. Chiew, S.-Y. Lim & N.-S. Cheng, Stallion Press: Singapore, vol.2, pp.245-251, 2004.



Section 5
Convection, heat and mass transfer

This page intentionally left blank

Velocity vorticity-based large eddy simulation with the boundary element method

J. Ravnik, L. Škerget & M. Hriberšek
University of Maribor, Faculty of Mechanical Engineering, Maribor, Slovenia

Abstract

A large eddy simulation using velocity-vorticity formulation of the incompressible Navier-Stokes equations in combination with the turbulent heat transfer equation is proposed for the solution of the turbulent natural convection drive flow in a 1:4 enclosure. The system of equations is closed by an enstrophy based subgrid scale model. The Prandtl turbulent number is used to estimate turbulent diffusion in the heat transfer equation. The boundary element method is used to solve the kinematics equation and estimate the boundary vorticity values. The vorticity transport equation is solved by the finite element method. The numerical example investigated in the paper is the onset of a turbulent flow regime occurring at high Rayleigh number values ($Ra = 10^7 - 10^{10}$). The formation of vortices in the boundary layer is observed, along with buoyancy driven diffusive convective transport. Quantitative comparison with the laminar flow model and the work of other authors is also presented in terms of Nusselt number value oscillations.

1 Introduction

Over the last few decades two-dimensional buoyancy driven flows have been investigated thoroughly by several authors. Natural convection in a rectangular enclosure is present in many industrial applications, such as the cooling of electronic circuitry, nuclear reactor insulation and ventilation of rooms.

A benchmark solution for two-dimensional flow of Boussinesq fluid in a square differentially heated enclosure was presented by De Vahl Davies [1]. They used the stream function-vorticity formulation. 2D DNS was preformed by Xin and Le Quéré [2] for an enclosure with aspect ratio 4 up to Rayleigh number based on the enclosure height 10^{10} using expansions in series of Chebyshev polynomials.



WIT Transactions on Engineering Sciences, Vol 52, © 2006 WIT Press
www.witpress.com, ISSN 1743-3533 (on-line)
doi:10.2495/AFM06027

Salat et al. [3] compared the results of modelling turbulent natural convection at high Rayleigh number between an experiment, 2D LES, 2D DNS and 3D LES computations. They reported that only minor differences are observed between the 2D and 3D results and concluded that a 2D calculation could be used as a first approximation for general flow structure in cavities at Rayleigh number about 10^{10}.

In the present work we have studied the onset of natural convection in a $1:4$ differentially heated enclosure within the incompressible Boussinesq approximation. Transition from two-dimensional steady laminar flow at enclosure width based Rayleigh number $Ra = 10^6$ via oscillatory motion at $Ra = 10^7, Ra = 10^8$ to chaotic (turbulent) fluid flow at $10^9, 10^{10}$ is simulated. The planar Large Eddy Simulation (LES) is used for velocity-vorticity formulation of the incompressible Navier-Stokes equations. The velocity vorticity formulation of the Navier-Stokes equations in combination with the boundary element method is a promising concept for numerical solution of fluid flow problems. Solution of the kinematics equation is obtained by the boundary element method (BEM) and provides boundary vorticity values and hence a well posed vorticity transfer equation. We propose the usage of BEM because of its unique advantage for solving the boundary. Unfortunately, solution of a Poisson type equation with BEM requires huge integral matrices, which poses computer storage problems and limits the maximum number of nodes. We have used a wavelet transform technique proposed by Ravnik et al. [4] to compress the matrices of integrals and thus decrease the storage requirements. The LES based vorticity transport equation is solved by the finite element method (FEM).

2 $\vec{v}$ $\vec{\omega}$ LES

Incompressible viscous fluid flow within the Boussinesq approximation is governed by the following system of equations. Mass conservation can be stated by

$$\vec{\nabla} \cdot \vec{v} = 0, \tag{1}$$

while conservation of momentum is

$$\frac{\partial \vec{v}}{\partial t} + (\vec{v} \cdot \vec{\nabla})\vec{v} = -\frac{Ra}{PrRe^2} T\vec{g} - \frac{1}{Eu}\vec{\nabla}p + \frac{1}{Re}\nabla^2\vec{v}, \tag{2}$$

and the energy equation is

$$\frac{\partial T}{\partial t} + (\vec{v} \cdot \vec{\nabla})T = \frac{1}{RePr}\nabla^2 T. \tag{3}$$

The system is fully defined by specifying the Euler, Reynolds, Prandtl and Rayleigh numbers. Vorticity is defined by $\vec{\omega} = \vec{\nabla} \times \vec{v}$ and is also divergence free. When



introducing the velocity vorticity formulation (Škerget et al. [5]) one combines the velocity and vorticity into the kinematics equation

$$\nabla^2 \vec{v} + \vec{\nabla} \times \vec{\omega} = 0, \tag{4}$$

which connects the velocity and vorticity fields at all points in space and time.

We define the filtering operation of an arbitrary function $u(\vec{x}, t)$ with the following convolution integral

$$\bar{u}(\vec{x}, t) = \int_{\Omega} G(\vec{r}, \vec{x}) u(\vec{x} - \vec{r}, t) d\vec{r}, \tag{5}$$

where $G(\vec{r}, \vec{x})$ stands for the filter kernel, integration encompasses the whole domain Ω. By choosing a homogenous filter kernel filtering commutes differentiation with respect to coordinate, thus the filtered kinematics equation is

$$\overline{\nabla^2 \vec{v} + \vec{\nabla} \times \vec{\omega}} = \nabla^2 \overline{\vec{v}} + \vec{\nabla} \times \overline{\vec{\omega}} = 0. \tag{6}$$

In order to derive the velocity vorticity based LES we will rewrite the transport equation for momentum (2) into a transport equation for vorticity and filter it. The advection term (second on the left hand side of (2)) may be rewritten as

$$(\vec{v} \cdot \vec{\nabla}) \vec{v} = \frac{1}{2} \vec{\nabla} v^2 - \vec{v} \times \vec{\omega}. \tag{7}$$

We use (7) in equation (2) and rewrite the last term on the right hand side of (2) with the aid of the kinematics equation, arriving at

$$\frac{\partial \vec{v}}{\partial t} + \frac{1}{2} \vec{\nabla} v^2 - \vec{v} \times \vec{\omega} = -\frac{Ra}{PrRe^2} T\vec{g} - \frac{1}{Eu} \vec{\nabla} p - \frac{1}{Re} \nabla \times \vec{\omega}. \tag{8}$$

When a curl of the whole equation (8) is taken, both gradient terms vanish. Thus pressure is eliminated from the equation. Bearing in mind the vorticity definition, we have

$$\frac{\partial \vec{\omega}}{\partial t} - \vec{\nabla} \times (\vec{v} \times \vec{\omega}) = -\frac{Ra}{PrRe^2} \vec{\nabla} \times T\vec{g} - \frac{1}{Re} \vec{\nabla} \times \nabla \times \vec{\omega}. \tag{9}$$

When equation (9) is filtered, commutation properties of the homogenous filter are used to write

$$\frac{\partial \overline{\vec{\omega}}}{\partial t} - \vec{\nabla} \times \overline{(\vec{v} \times \vec{\omega})} = -\frac{Ra}{PrRe^2} \vec{\nabla} \times \overline{T}\vec{g} - \frac{1}{Re} \vec{\nabla} \times \nabla \times \overline{\vec{\omega}}. \tag{10}$$

The difference between the unfiltered (9) and the filtered (10) vorticity transport equation is in the nonlinear advection term. Filter of the vector product of velocity and vorticity fields is not equal to a vector product of filtered fields. Equation (10) will be rewritten in a form that is equivalent to the form of (9) with an additional term, which will account for the contribution of the filtered field. The additional,

subgrid term will be modelled in such manner, that it will have a dissipative effect. Therefore we introduce the residual vorticity vector as the difference between the filter of the vector product of velocity and vorticity fields and a vector product of filtered fields $\vec{\tau}^{\omega} = \overline{\vec{v} \times \vec{\omega}} - \overline{\vec{v}} \times \overline{\vec{\omega}}$. With this, equation (10) may be rewritten

$$\frac{\partial \overline{\vec{\omega}}}{\partial t} - \vec{\nabla} \times (\overline{\vec{v}} \times \overline{\vec{\omega}}) = -\frac{Ra}{PrRe^2} \vec{\nabla} \times \overline{T}\vec{g} - \frac{1}{Re} \vec{\nabla} \times \nabla \times \overline{\vec{\omega}} + \vec{\nabla} \times \vec{\tau}^{\omega}. \quad (11)$$

According to the turbulent vorticity transfer theory of Taylor [6], the subgrid term $\vec{\nabla} \times \vec{\tau}^{\omega}$ describes the dissipation of vorticity due to subgrid scales. To derive the final form of the filtered vorticity transfer equation we make use of $\vec{\nabla} \times \vec{\nabla} \times \overline{\vec{\omega}} = -\nabla^2 \overline{\vec{\omega}}$ and $\vec{\nabla} \times (\overline{\vec{v}} \times \overline{\vec{\omega}}) = (\overline{\vec{\omega}} \cdot \vec{\nabla})\overline{\vec{v}} - (\overline{\vec{v}} \cdot \vec{\nabla})\overline{\vec{\omega}}$:

$$\frac{\partial \overline{\vec{\omega}}}{\partial t} + (\overline{\vec{v}} \cdot \vec{\nabla})\overline{\vec{\omega}} = (\overline{\vec{\omega}} \cdot \vec{\nabla})\overline{\vec{v}} - \frac{Ra}{PrRe^2} \vec{\nabla} \times \overline{T}\vec{g} + \frac{1}{Re} \nabla^2 \overline{\vec{\omega}} + \vec{\nabla} \times \vec{\tau}^{\omega}. \quad (12)$$

The Stokes derivative of vorticity on the right hand side of equation (12) is equal to the twisting and stretching term, buoyancy, viscous diffusion and the subgrid term. The equation is nonlinear due to the product of velocity and vorticity, which are kinematically depended quantities. In two dimensions, only the component of vorticity that is perpendicular to the plan of flow is nonzero, thus vorticity may be regarded as a scalar quantity. The vortex twisting and stretching term vanishes is cases of planar flow. The buoyancy term, which includes the temperature, binds the vorticity transport equation to the energy equation.

Before filtering of the energy equation (3) we rewrite the advection term with $\vec{\nabla} \cdot (T\vec{v}) = (\vec{v} \cdot \vec{\nabla})T$:

$$\frac{\partial \overline{T}}{\partial t} + \vec{\nabla} \cdot (\overline{T\vec{v}}) = \frac{1}{RePr} \nabla^2 \overline{T}. \quad (13)$$

The nonlinear term is rewritten by introducing the residual temperature vector $\vec{\tau}^{h} = \overline{T\vec{v}} - \overline{T}\,\overline{\vec{v}}$. The final form of the filtered energy equation is

$$\frac{\partial \overline{T}}{\partial t} + \vec{\nabla} \cdot (\overline{T}\,\overline{\vec{v}}) = \frac{1}{RePr} \nabla^2 \overline{T} - \vec{\nabla} \cdot \vec{\tau}^{h}. \quad (14)$$

With an analogy to molecular viscosity, which drains the energy of the flow, we will describe the residual vectors by introducing subgrid scale viscosity and diffusivity

$$\vec{\tau}^{\omega} = -\nu_{sgs} \vec{\nabla} \times \overline{\vec{\omega}}, \qquad \vec{\tau}^{h} = \alpha_{sgs} \vec{\nabla} \overline{T}. \quad (15)$$

The subgrid scale viscosity was modelled by the Mansour et al. [7] model, which is based on the local enstrophy of the large scales

$$\nu_{sgs} = (C\Delta)^2 \sqrt{\vec{\omega} \cdot \vec{\omega}}. \quad (16)$$

The filter width is $\Delta = (\Delta_x \Delta_y \Delta_z)^{\frac{1}{3}}$ in 3D and $\Delta = (\Delta_x \Delta_y)^{\frac{1}{2}}$ in 2D. In the vicinity of walls, the model constant C will be damped with Piomelli and/or Van

Driest damping function. Based on experimental findings on isotropic turbulence, the subgrid scale viscosity is comparable to subgrid scale diffusivity, their relationship being close to linear. The turbulent Prandtl number is used to connect the two: $\alpha_{sgs} = \frac{\nu_{sgs}}{Pr_t}$.

3 Numerical method

Sufficiently dense meshes must be used in order for the LES simulation to be successful. BEM requires fully populated matrices of integrals. Their size grows rapidly with the number of grid points. In order to be able to obtain the solution we have made the following simplifications: (i) let the flow be planar, vorticity is a scalar, (ii) we shall use wavelet compressed BEM for the solution of the boundary with the kinematics equation only and (iii) use FEM for the transport equations. In the following we shall briefly describe the wavelet compressed BEM and give the computational algorithm at the end of this section. Detailed derivation and explanation of the numerical method may be found in Ravnik et al. [8].

Using BEM for the calculation of boundary vorticity values, one arrives at the following system of linear equations

$$[D^{\Gamma}]\{\overline{\omega}^{\Gamma}\} = ([C] + [H])\{\overline{v}_t\} + [H^t]\{\overline{v}_n\} - [D^{\Omega\setminus\Gamma}]\{\overline{\omega}^{\Omega\setminus\Gamma}\}, \qquad (17)$$

where matrices of integrals $[D^{\Gamma}]$, $[C]$, $[H]$ and $[H^t]$ are square, full, non-symmetric and have number of boundary nodes rows and columns. Although full, the these matrices do not require a lot of storage, since they are for boundary only. On the other hand, the matrix $[D^{\Omega\setminus\Gamma}]$ is rectangular and also full and non-symmetric. It has number of boundary nodes rows and number of internal nodes columns. In the discretized system of equations it must be multiplied with a vector of internal vorticity values $\{\overline{\omega}^{\Omega\setminus\Gamma}\}$ to form the right hand side of the system of equations.

The matrix vector product $[D^{\Omega\setminus\Gamma}]\{\overline{\omega}^{\Omega\setminus\Gamma}\}$ will be calculated with the aid of wavelet compression. The matrix will be compressed written in compressed row storage format and thus require less storage.

Let W be the discrete wavelet transform matrix for vectors of arbitrary length introduced in Ravnik et al. [4]. Since the product of the wavelet matrix with its transpose is the identity matrix, we may write

$$[D^{\Omega\setminus\Gamma}]\{\overline{\omega}^{\Omega\setminus\Gamma}\} = W^T(\underbrace{W[D^{\Omega\setminus\Gamma}]W^T}_{[D_W^{\Omega\setminus\Gamma}]} W\{\overline{\omega}^{\Omega\setminus\Gamma}\}). \qquad (18)$$

The wavelet compressed matrix of integrals $[D_W^{\Omega\setminus\Gamma}] = W[D^{\Omega\setminus\Gamma}]W^T$ is calculated only once, prior to the start of the iterative process. In absolute sense small matrix elements are thresholded and compressed row storage format is used for remaining nonzero elements.

A parallel code has been written to perform the wavelet compression, since the full matrix does not fit into single computer memory. Clusters of single processor



nodes have been used. Communication was preformed via MPI. During compression, multiplication with random test vectors is done to establish the relative error ϵ of the matrix vector product.

Without further details, the computational algorithm may be summarised as follows: Solve kinematics equation for boundary vorticity values using internal vorticities from previous nonlinear iteration step using wavelet compressed BEM. Solve the kinematics equation again for domain velocities by FEM, using new boundary vorticities obtained from BEM in the previous step to form right hand side vector. Solve the energy equation to obtain the new temperature field by FEM. Solve vorticity transport equation for domain vorticities by FEM, using the new velocity field and use boundary vorticities from kinematics as boundary conditions. Use under-relaxation for computing new domain vorticity values and loop until convergence is achieved.

4 Validation

Using wavelet compression in the numerical algorithm introduces an error. In order to estimate the largest compression ratio, that does not effect the accuracy of a high Re computation, we have preformed a standard lid driven cavity benchmark test at $Re = 10^4$. Results were compared with Ghia et al. [9] benchmark. Table 1 gives different compression rations tested, while Figure 1 presents the results. We have found, that the solution obtained is virtually identical for $\epsilon = 10^{-6}$ and $\epsilon = 10^{-5}$ and differs only slightly for lower relative error values. Therefore, we decided that the limit $\epsilon = 10^{-5}$, will be used for compression. The test also showed, that increasing mesh density enables higher compression for the same accuracy.

Table 1: Wavelet compression of domain integrals matrix on a square mesh with 182×180 nine node Lagrange elements. Total number of nodes in the mesh is 131765. Number of all elements in the matrix is 188699016.

share of thresholded elements	relative error of multiplication ϵ
0.7652	$1.4 \cdot 10^{-6}$
0.9217	$1.0 \cdot 10^{-5}$
0.9761	$1.0 \cdot 10^{-4}$
0.9870	$1.2 \cdot 10^{-3}$

5 Differentially heated enclosure

We consider an enclosure with width to height ratio of $1 : 4$. The left vertical wall is heated, the right vertical wall is cooled, both are kept at constant temperatures.



The Rayleigh number is defined by the temperature difference and the enclosure width. The top and bottom horizontal walls are adiabatic. The no-slip velocity boundary condition is employed on all solid walls.

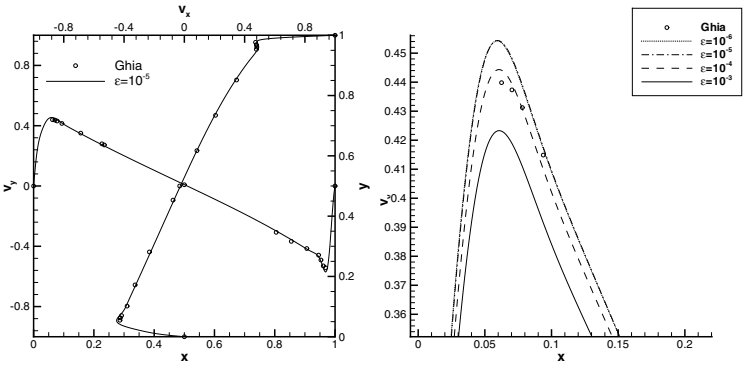


Figure 1: Comparison of velocity profiles in a lid driven cavity at $Re = 10^4$ for different compression ratios with the benchmark solution of Ghia et al. [9].

The enclosure is filed with air ($Pr = 0.71$), the subgrid scale constant was $C = 0.1$, the turbulent Prandtl number was set to $Pr_t = 0.6$. Two meshes were used in simulations: up to Rayleigh number $Ra \leq 10^9$ a mesh with 128×200 nine node Lagrange elements with approximately 10^5 nodes and at Rayleigh number 10^{10} a 170×300 mesh with $2 \cdot 10^5$ nodes.

Steady state temperature field for $Ra = 10^6$ and averaged temperature fields at $Ra = 10^7$ without subgrid scale model and LES with Piomelli damping for $Ra = 10^8$, $Ra = 10^9$ and $Ra = 10^{10}$ are shown in Figure 2. While at $Ra = 10^6$ steady state is reached, at $Ra = 10^7$ the boundary layer becomes unstable and vortices are formed along the top of the hot wall and along the bottom part of the cold wall. Eddies are transported by convection up the hot wall and down the cold wall thus mixing the top and bottom parts of the enclosure. In the central part the temperature field is stratified and the flow virtually steady. The whole flow field is oscillatory and symmetric. At $Ra = 10^8$ the eddies are formed more frequently. The formation takes place in the top half of the hot wall and in the bottom half of the cold wall. The stratified central core becomes smaller, but still exists. The flow field is no longer symmetric (although the initial $Ra = 10^6$ flow field was) length scales of the structures in the flow are becoming smaller. There is no difference between calculations with and without the subgrid scale model. At $Ra = 10^9$ eddies are formed along the whole length of both vertical walls, most of them being formed at mid height. The central core is now thoroughly mixed and one can no longer speak of temperature stratification. The flow field includes eddies of various scales and is non-repeating, irregular and chaotic. At $Ra = 10^{10}$ the whole flow field is turbulent. The difference between calculation with and without

subgrid scale model is evident at this Rayleigh number. Comparing heat transfer with benchmark proved that the LES simulation give the correct results.

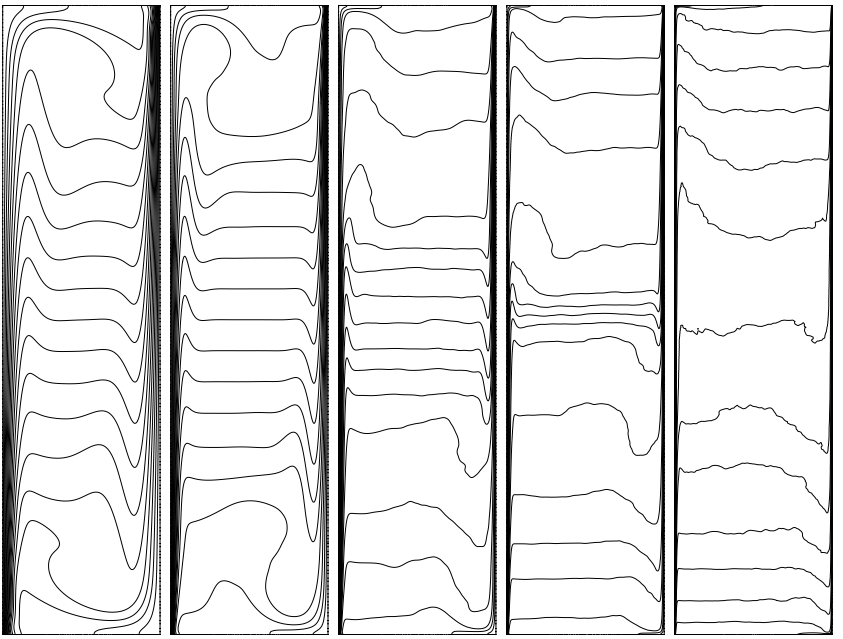


Figure 2: Temperature fields (1(0.05)0): left to right: steady state at $Ra = 10^6$, time averaged field at $Ra = 10^7$ without a subgrid scale model, time averaged LES field with damped subgrid scale model for $Ra = 10^8$, $Ra = 10^9$ and $Ra = 10^{10}$.

The heat transfer through the walls is represented by the average Nusselt number value, defined for our geometry by $Nu = \frac{1}{H}\int_0^H \frac{\partial T}{\partial x} dy$. The Nusselt number versus time graphs are shown on Figure 3. The average values are compared with benchmark results of Xin and Le Quéré [2] in Table 2. Very good agreement is obtained.

6 Conclusions

The velocity vorticity formulation of LES in combination with the wavelet transform based boundary element method presented in this paper shows good potential for solving turbulent fluid flow problems with the large eddy simulation approach. Solution of boundary vorticity values with wavelet based BEM provides boundary conditions for the transport equations, which we are solving by FEM. Using the wavelet transform with the boundary element method enabled us to use meshes

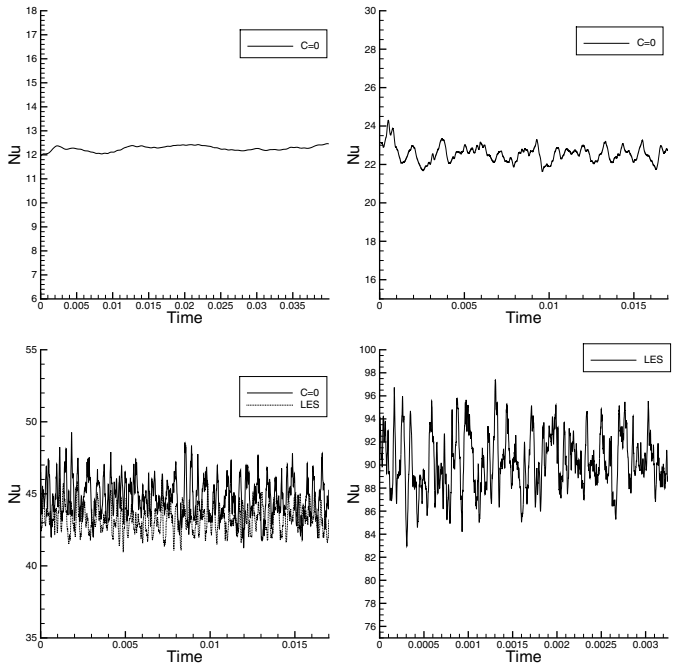


Figure 3: Time traces of Nusselt number for: $Ra = 10^7$ (upper left), $Ra = 10^8$ (upper right), $Ra = 10^9$ (lower left) in $Ra = 10^{10}$ (lower right).

Table 2: Average Nusselt number Nu and correlation comparison with benchmark DNS results of Xin et al. [2]. Piomelli damped (LES_p) as well as Van Driest damped (LES_{vd}) results are presented. (*) For Nu at $Ra = 10^8$ and $Ra = 10^9$ Xin's values were predicted using their $Nu/Ra^{1/4}$ relationship. (+) Nu prediction using our $Nu/Ra^{1/4}$ relationship.

	Nu				$Nu/Ra^{1/4}$	
Ra	$C = 0$	LES_p	LES_{vd}	Xin [2]	present	Xin [2]
10^7	12.27			12.3	0.2181	0.2185
$3.125 \cdot 10^7$		16.91^+		16.62		
10^8	22.5	22.5		22.56^*	0.2256	
$1.56 \cdot 10^8$		25.57^+		25.25		0.2256
10^9	44.77	43.25	43.67	43.63^*	0.2432	
10^{10}			90.25			

with $2 \cdot 10^5$ nodes. Higher mesh densities will be possible in the near future, as well as the extension of the code to 3D, by the use of domain decomposition and parallel computing.

Acknowledgements

The first author gratefully acknowledges the support of the parallel computer centres HLRS and CINECA in the framework of the EC-funded HPC-Europa project under contract number 506079.

References

[1] Davies, G.D.V., Natural convection of air in a square cavity: a bench mark numerical solution. *Int J Numer Meth Fl*, **3**, pp. 249–264, 1983.
[2] Xin, S. & Le Quéré, P., Direct numerical simulations of two-dimensional chaotic natural convection in a differentially heated cavity of aspect ratio 4. *J Fluid Mech*, **304**, pp. 87 – 118, 1995.
[3] Salat, J., Xin, S., Joubert, P., Sergent, A., Penot, F. & Le Quéré, P., Experimental and numerical investigation of turbulent natural convection in a large air-filled cavity. *Int J Heat Fluid Fl*, **25**, pp. 824–832, 2004.
[4] Ravnik, J., Škerget, L. & Hriberšek, M., The wavelet transform for BEM computational fluid dynamics. *Eng Anal Bound Elem*, **28**, pp. 1303–1314, 2004.
[5] Škerget, L., Alujeviè, A., Brebbia, C.A. & Kuhn, G., *Topics in Boundary Element Research*, Springer-Verlag: Berlin, volume 5, chapter Natural and Forced Convection Simulation Using the Velocity-Vorticity Approach, 1989.
[6] Taylor, G.I., The transport of vorticity and heat through fluids in turbulent motion. *Proc R Soc London Ser A*, **135**, pp. 685–705, 1932.
[7] Mansour, N.N., Ferziger, J.H. & Reynolds, W.C., Large-eddy simulation of a turbulent mixing layer. Report TF-11, Thermosciences Div., Dept. of Mech. Eng., Standford University., 1978.
[8] Ravnik, J., Škerget, L. & Hriberšek, M., 2D $\vec{v} - \vec{\omega}$ LES for the solution of natural convection in a differentially heated enclosure by wavelet transform based BEM and FEM. *Eng Anal Bound Elem*, submitted.
[9] Ghia, U., Ghia, K. & Shin, C., High-Re solutions for incompressible flow using the Navier-Stokes equations and a multigrid method. *J Comput Phys*, **48**, pp. 387–411, 1982.



Flow and heat transfer characteristics of tornado-like vortex flow

Y. Suzuki & T. Inoue
Department of Mechanical Sciences and Engineering,
Tokyo Institute of Technology

Abstract

A tornado-like vortex flow has been investigated for both effective local ventilation from the floor of a room and local heat transfer control without the circumferential thermal diffusion. A relatively stable axisymmetrical tornado-like vortex is generated in a water tank by a vertically uniform swirl. The overall flow structure of the tornado-like vortex has been categorized into three regions: the outer free vortex region, the inflow layer (the Ekman boundary layer), and the vortex tube. The present tornado-like vortex flow was investigated experimentally and also agrees qualitatively with this flow structure. In the free vortex region, the tangential velocity distribution shows a Rankine-like vortex and has good agreement with an approximate formula characterized by the radius and the maximum tangential velocity of the forced vortex. A numerical analysis using an axisymmetrical laminar flow model is carried out. To eliminate the effect of swirl supplying methods, a virtual cylindrical surface of the radius (R_{out}) is considered, where an axisymmetrical flow is established. All experimental and computational data of the flow characteristics of the tangential velocity profile in the free vortex region are well-arranged by the Reynolds number based on the flow rate and the swirl Reynolds number based on R_{out}. The flow structure in the Ekman boundary layer is characterized by the tangential velocity profile in the free vortex region and the height where the radial velocity is half its maximum value. The heat transfer characteristics of the heated plate with uniform heat flux located on the bottom are investigated both experimentally and computationally. The forced convective heat transfer of the tornado-like swirling flow is handled in the same way as the laminar forced convective heat transfer on a flat plate, by using the maximum radial velocity component in the Ekman boundary layer.
Keywords: tornado-like vortex, swirl flow, flow structure, heat transfer control.



WIT Transactions on Engineering Sciences, Vol 52, © 2006 WIT Press
www.witpress.com, ISSN 1743-3533 (on-line)
doi:10.2495/AFM06028

1 Introduction

The tornado is an intensive forced columnar vortex with a strong updraft above a lower boundary. For a better understanding of the dynamics of naturally occurring intense vortices such as tornadoes, there are a number of approaches from both meteorological and mechanical points of view [1]. A tornado-like swirling flow has been more prospective for effective local ventilating from the room floor where polluted air and dust arise, and for local heat transfer control on the base without the circumferential thermal diffusion. We have investigated the local ventilation and heat transfer characteristics of the tornado-like swirling flow by using the top rotating vortex generator [2]. However, the velocity field and heat transfer characteristics of the tornado-like vortex have not been clarified enough for handling of such a system.

The objective of the present work is as follows: to clarify the flow structure of the tornado-like swirling flow generated by a vertically uniform swirl flow from the peripheral surface and a suction from the center top, and to investigate the heat transfer on the heated bottom plate.

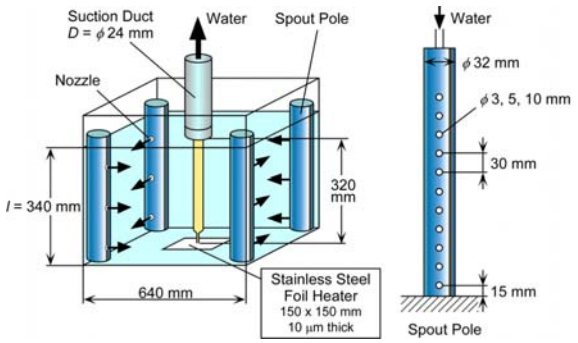


Figure 1: Experimental setup.

2 Experimental apparatus and procedures

The experimental apparatus is shown in Fig. 1. A tornado-like vortex flow is generated in a square water tank made of acrylic resin, which size is 640 mm square. The water level is fixed in height l = 340 mm. A relatively-stable axi-symmetrical tornado-like vortex is generated by a vertically-uniform swirl from four cornered poles with water nozzles and the suction from the duct (inner diameter, D = 24 mm) installed at a height of 320 mm from the base in the center of the tank. The suction and supply flow rate (Q) is varied between 1.0 to 5.0 l/min. The swirl intensity is varied by the diameter of the water nozzle (d = 3, 5, 10 mm). The supply water is controlled at a constant temperature without the influence of the bulk temperature change. The velocity components of the tornado-like vortex flow are measured by PTV. To obtain the detail of velocity field of the vortex boundary layer near the base, the radial and tangential velocity components are measured by 2D-LDV put under the base plate.

The same experimental apparatus is used to obtain the local heat transfer coefficient through knowledge of the fixed surface heat flux, the bulk temperature, and the local wall temperature. For measuring the local wall temperature, 57 T-type thermocouples are installed on the backside of the stainless steel foil heater (150 mm square, 10 μm thick) radially from the center of the tank. The fixed surface heat flux is varied between 1.7×10^2 and 2.7×10^3 W/m^2.

3 Results and discussion

3.1 Flow structure of tornado-like swirling flow

3.1.1 Overall flow structure

The present tornado-like vortex flow is visualized as shown in Fig. 2. The dye put on the base is concentrated at the center of the vortex, lifted up and evacuated from the suction duct. The vortex breakdown is shown near the base. An overall flow structure of the tornado-like vortex has been categorized into three regions [1]: a center vortex tube with a spiral upward flow, the outer free vortex region with a tangential velocity profile of a Rankine-like vortex, and an inflow layer near the base called as the Ekman boundary layer. The present tornado-like swirling flow also agrees qualitatively with this flow structure as shown in Fig.3.

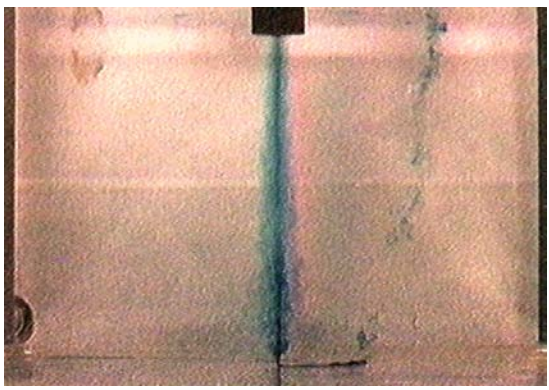


Figure 2: Visualization of tornado-like vortex flow: Q = 5.0 *l*/min, d = 3 mm.

3.1.2 Tangential velocity distribution in free vortex region

In the free vortex region, which comprises a large part of a tornado-like swirling flow, the tangential velocity distribution shows a Rankine-like vortex. The tangential velocity distributions are almost same at any height except near the suction duct and in the Ekman boundary layer. The larger flow rate and swirl intensity provide the higher maximum velocity ($v_{\theta\,\max}$) and the smaller radius of the forced vortex (R_F).

In the present experimental apparatus, it is very difficult to estimate the tangential velocity component in the outer flow region, $v_{\theta\,\text{out}}$, from the initial velocity of the water nozzles as the given boundary condition. To eliminate the

effect of swirl supplying methods, a virtual peripheral cylindrical surface of the radius R_{out} is considered, where an axisymmetrical flow is established. In this case, R_{out} = 200 mm. An approximate expression of the tangential velocity distribution in the free vortex region is considered as Eq. (1), which superimposes the effect of the outer given swirling flow on a Rankine-like vortex flow.

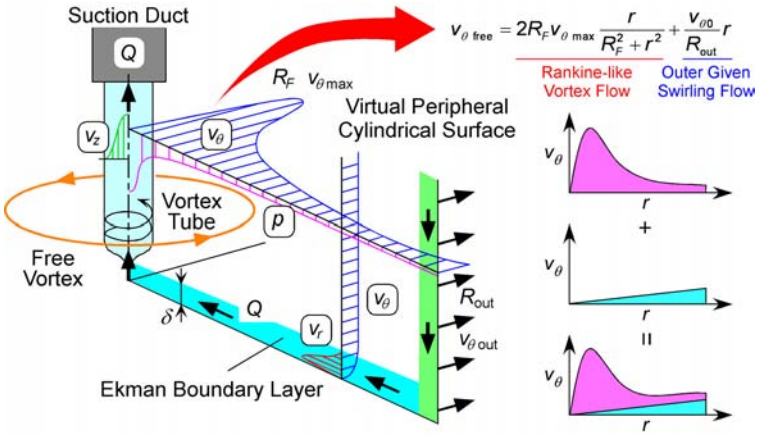


Figure 3: Structure of tornado-like vortex flow.

$$v_{\theta\,\mathrm{free}} = 2R_F v_{\theta\,\max} \frac{r}{R_F^2 + r^2} + \frac{v_{\theta 0}}{R_{\mathrm{out}}} r \tag{1}$$

The tangential velocity distribution has good agreement with Eq. (1), which is characterized by the radius and the maximum tangential velocity of the forced vortex (R_F and $v_{\theta\,\max}$). The tangential velocity at virtual cylindrical surface ($v_{\theta\,\mathrm{out}}$) is obtained by setting $r = R_{\mathrm{out}}$ in Eq. (1).

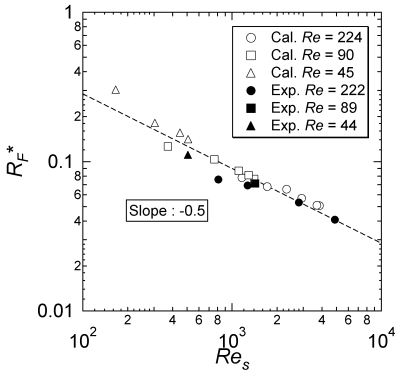
3.1.3 Numerical simulation

A numerical analysis using an axisymmetrical laminar flow model is carried out to investigate the structure of the tornado-like vortex flow. The calculation domain is $14D \times 12D$ in the z and r directions on the basis of the suction duct diameter D. The calculation grids are set by 320 × 280 with non-uniform grid spacing near the center and the wall regions. The inflow boundary conditions at $r = 12D$ are uniform velocities of the radial and tangential components (v_r and v_θ) respectively. The radius of the virtual cylindrical surface corresponds to $R_{\mathrm{out}} = 8.33D$. As the dominant parameters for the flow field, the Reynolds number Re based on the flow rate and the swirl Reynolds number Re_s based on the circulation at the virtual surface are defined as $Re = (Q/l)/\nu$, $Re_s = (R_{\mathrm{out}}\, v_{\theta\,\mathrm{out}})/\nu$.

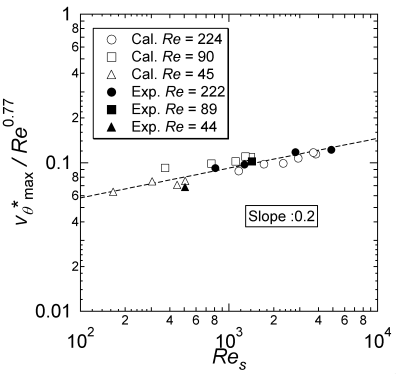
The dimensionless form of Eq. (1) is given by using the radius and the velocity of the virtual cylindrical surface (R_{out} and $v_{\theta\,\mathrm{out}}$) as follows.

$$v_{\theta\,\mathrm{free}}^{*} = 2R_F^{*} v_{\theta\,\max}^{*} \frac{r^{*}}{R_F^{*2} + r^{*2}} + C^{*} r^{*} \tag{2}$$

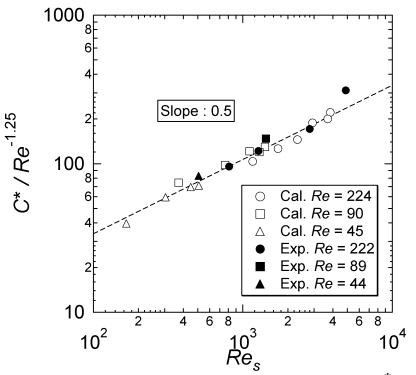
The computational results for the tangential velocity profiles in the free vortex region have good agreement with Eq. (2) as well as experimental results. Both experimental and computational flow characteristics of the tangential velocity profile in the free vortex region of this swirling flow are well-arranged by *Re* and Re_s as shown in Fig. 4. These flow characteristics are estimated as follows:



(a) Radius of forced vortex, R_F^*



(b) Maximum tangential velocity, $v_{\theta}^{*}{}_{\max}$



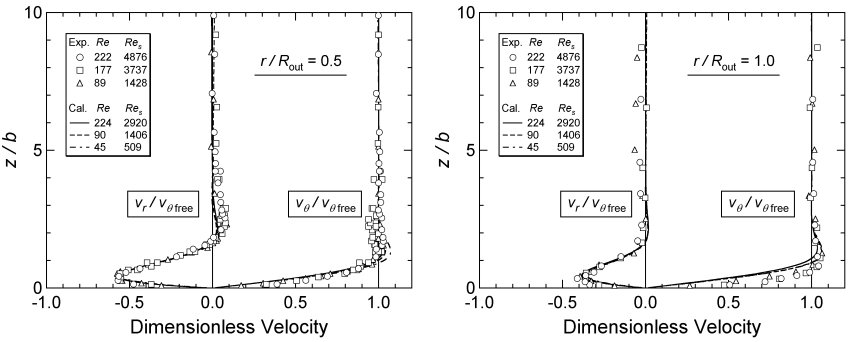
(c) Tangential velocity ratio, C^*

Figure 4: Flow characteristics in free vortex region.

$$\left.\begin{aligned} R_F^* &\equiv \frac{R_F}{R_{\text{out}}} \approx 2.84\ Re_s^{-0.5} \\ v_{\theta\max}^* &\equiv \frac{v_{\theta\ \max}}{v_{\theta\ \text{out}}} \approx 0.0231\ Re^{0.77} Re_s^{0.2} \\ C^* &\equiv \frac{v_{\theta 0}}{v_{\theta\ \text{out}}} \approx 3.38\ Re^{-1.25} Re_s^{0.5} \end{aligned}\right\}, \tag{3}$$

where the constant numbers are considered as dependent values on geometric parameters such as an aspect ratio which is constant in the present work. The radius of the forced vortex R^*_F is not dependent on *Re*, that is the total flow rate, but in proportion to $Re_s^{-0.5}$. This result is consistent with Khoo et al. [3].

Meanwhile, the maximum tangential velocity $v^*_{\theta\,\max}$ is rather influenced by *Re*. Here $v_{\theta 0}$ means the tangential velocity of the totally forced vortex that is generated by the outer swirling flow without the base plate. Thus, 1-C^* is considered as the ratio of the angular momentum transported from the outer flow region to the vortex center through the Ekman boundary layer. The larger flow rate and the lower swirl intensity provide the higher transport ratio.



(a) $r^* = r / R_{\text{out}} = 0.5$ (b) $r^* = 1.0$

Figure 5: Dimensionless velocity profile in Ekman boundary layer.

3.1.4 Flow structure in Ekman boundary layer

The velocity distributions of the Ekman boundary layer is investigated both experimentally and computationally. Figure 5 shows the radial and tangential velocity profiles by using 2D-LDV and calculating. The normalization by the tangential velocity of the free vortex region ($v_{\theta\,\text{free}}$) and the height (*b*) where $|v_r| = v_{r\,\max}/2$ brings the consistent velocity profiles at each radius. Furthermore, the radial profiles of the maximum radial velocity component and the characteristic height *b* are shown in Fig. 6 and estimated as follows:

$$\left.\begin{aligned} \frac{v_{r\,\max}}{v_{\theta\,\text{free}}} &\approx -0.46\, r^* + 0.83 \\ b^* \equiv \frac{b}{R_{\text{out}}} &\approx \left(2.28 - 0.60\exp\left(-6.21\, r^{*2}\right)\right) Re^{0.23} Re_s^{-0.65} \end{aligned}\right\}, \tag{4}$$

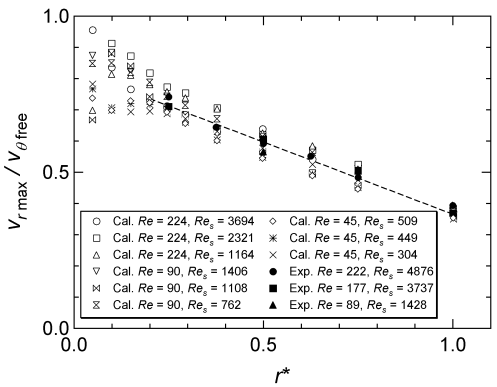
except near the vortex center where the upward flow has large influence. The maximum radial velocity is increasing linearly as the radius is decreasing. The radial profile of the Ekman boundary layer thickness is estimated as 1.7*b*. This estimation has good agreement with results of the boundary layer visualization. The Ekman boundary layer thickness is decreasing as the radius is decreasing.

3.2 Effect of tornado-like vortex on heat transfer from heated bottom plate

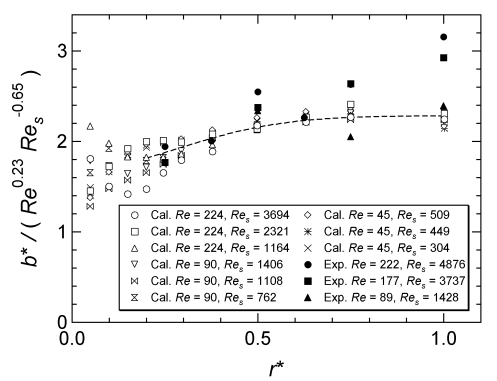
3.2.1 Local heat transfer coefficient

Additionally, the heat transfer characteristics of the heated plate with uniform heat flux located on the bottom surface of the tornado-like vortex are investigated experimentally. Since the value of the fixed surface heat flux has no

difference in the heat transfer characteristics, the results of the maximum heat flux ($q = 2.7\times10^3$ W/m^2) in this work are discussed. This means that the forced convection of the tornado-like vortex flow is more dominant than the natural convection. As the swirl intensity is higher, the higher temperature region concentrates near the heater center, and the overall temperature on the heater surface goes down. The temperature distribution has rotational symmetries through 90 degrees. On the diagonal line of the heater, the relatively higher temperature region is confirmed. Thus, the profile of the local heat transfer coefficient ($h = q/(T_w - T_b)$) on the transversal lines crossing the center and the diagonal lines of the heater surface are examined as shown in Fig. 7. The effect of the heat concentration to the center brings the decreasing of the heat transfer coefficient near the vortex center, but the overall improvement is occurred with increasing of the swirl intensity. The flow quite near the base goes approximately straight toward the center. The heat transfer characteristics on the square heater have the path dependency, and are concerned with between the heater shape and the radial velocity component in the Ekman boundary layer.

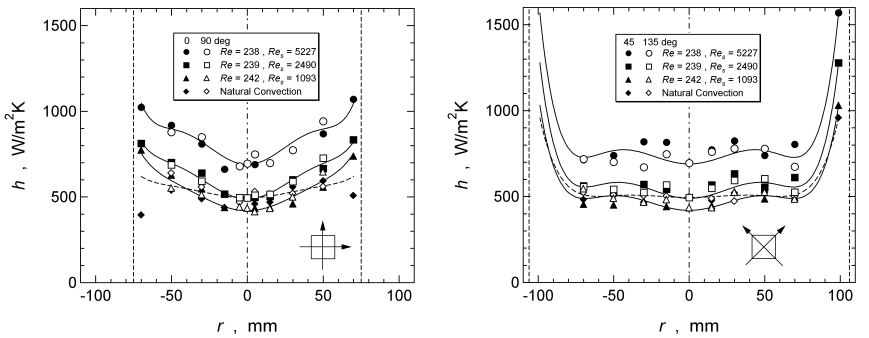


(a) Dimensionless maximum radial velocity profile, $v_{r\,max} / v_{\theta\,free}$



(b) Dimensionless characteristics scale profile, b^*

Figure 6: Flow characteristics in Ekman boundary layer.



(a) Profile on transversal lines (b) Profile on diagonal lines

Figure 7: Heat transfer coefficients on heated bottom plate.

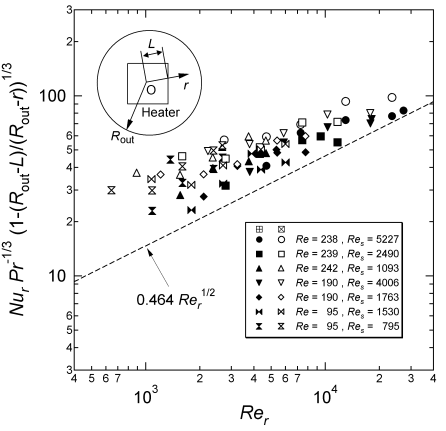


Figure 8: Correlation between Nu_r and Re_r on heated bottom plate.

3.2.2 Local Nusselt number and local Reynolds number

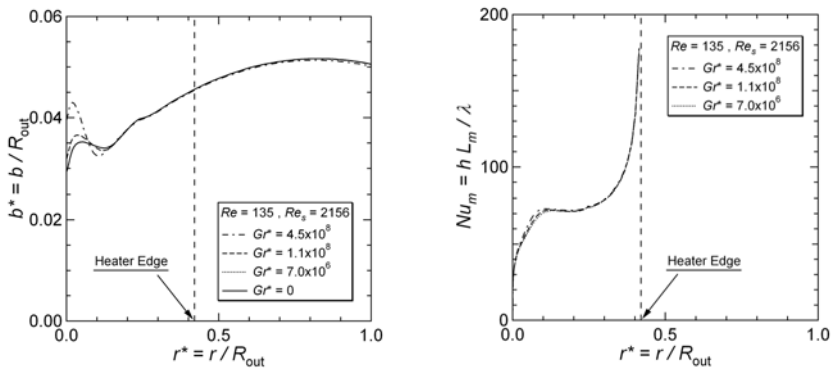
The forced convective heat transfer characteristics on the line from the virtual peripheral cylindrical surface to the heater center through the unheated section and the uniform heat flux section are investigated. The local Nusselt number and the local Reynolds number are defined as follows: $Nu_r = h(R_{out} - r)/\lambda$ and $Re_r = v_{r\,max}(R_{out} - r)/\nu$, where $v_{r\,max}$ is the maximum radial velocity component in the Ekman boundary layer, to which the above Eqs. (2) and (3) in the flow characteristics of the tornado-like vortex flow are applied. Figure 8 shows the correlation between Nu_r and Re_r referred to an unheated starting length problem of a laminar forced convective heat transfer on a flat plane, where L means the slant distance from the center to the edge of the heater. In Fig. 8, the data on both the axes and the diagonal are distributed on an almost same straight line. The local Nusselt number is rather large than a laminar forced convective heat transfer on a flat plane with a uniform heat flux through an unheated starting length shown as Eq. (5) [4], but it demonstrates a qualitatively almost same

tendency without reference to the flow rate (Re) and the swirl intensity (Re_s) of the tornado-like vortex flow.

$$Nu_r = 0.464 Pr^{1/3} Re_r^{1/2} \left(1 - \frac{R_{out} - L}{R_{out} - r}\right)^{-1/3} \tag{5}$$

3.2.3 Effect of free convection from heated bottom plate

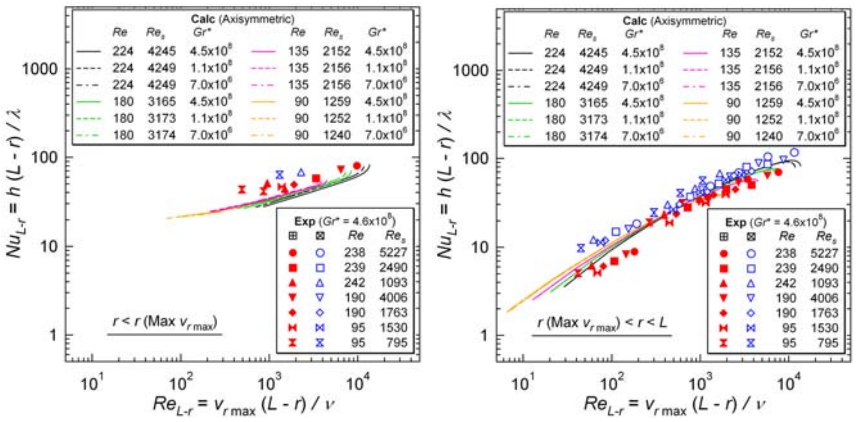
The forced convective heat transfer is dominant above the surface of the heated bottom plate. The effect of free convection from the heated bottom plate is investigated computationally. A numerical analysis using a same axisymmetrical laminar flow model above the circular heater with the uniform heat flux is carried out. The radius of the circular heater (L_m) is set as same surface area as the experiments. The modified Grashof number is defined as $Gr^* = g\beta q L_m^4 / \nu^2 \lambda$. In case of $Gr^* \leq 7.0\times10^6$, flow characteristics are almost never affected by the free convection. In case of $Gr^* > 7.0\times10^6$, as the heat flux is increasing, the flow concentrates in the vortex center in the Ekman boundary layer. The Ekman boundary layer thickness near the center is thinner as shown in Fig. 9(a). Furthermore, the mean Nusselt number ($Nu_m = h\ L_m\ /\ \lambda$) near the center is increasing as shown in Fig. 9(b). However, in almost all area except the center of vortex, the free convection has no influence upon the flow and heat transfer characteristics.



(a) Ekman boundary layer thickness (b) Mean Nusselt Number

Figure 9: Effect of free convection on heated bottom plate.

The correlations between the local Nusselt number ($Nu_{L\text{-}r} = h(L - r)/\lambda$) and the local Reynolds number ($Re_{L\text{-}r} = v_{r\ max}(L - r)/\nu$) based on the distance from the heater edge ($L - r$), are shown in Fig. 10. In the case that the forced convective heat transfer is dominant (Fig. 10(b)), both experimental and computational results have good agreement with $Nu_{L\text{-}r} \propto Re_{L\text{-}r}^{0.5}$ without the influence of Gr^*. On the other hand, the upward flow depend on the free convection brings the lower heat transfer near the center of vortex (Fig. 10(a)).



(a) $r < r(\text{Max } v_{r\,\max})$ (b) $r(\text{Max } v_{r\,\max}) < r < L$

Figure 10: Correlation between $Nu_{L\text{-}r}$ and $Re_{L\text{-}r}$ on heated bottom plate.

4 Conclusions

(1) In the free vortex region of the tornado-like swirling flow, the forced vortex radius, the maximum tangential velocity, and the tangential velocity ratio is in proportion to $Re_s^{-0.5}$, $Re^{0.77}Re_s^{0.2}$, and $Re^{-1.25}Re_s^{0.5}$ respectively.

(2) The flow structure in the Ekman boundary layer is characterized by the tangential velocity profile described as above in the free vortex region, and the characteristic scale b defined as the height where the radial velocity is half its maximum value. The Ekman boundary layer thickness is estimated as $1.7b$.

(3) On the base of the tornado-like swirling flow, the forced convective heat transfer is dominant except the center of vortex, and handled as same as the laminar forced convective heat transfer on a flat plate, by using the maximum radial velocity component in the Ekman boundary layer.

References

[1] Snow, J.T., A Review of Recent Advances in Tornado Vortex Dynamics. *Reviews of Geophysics and Space Physics*, **20(4)**, pp. 953-964, 1982.

[2] Hijikata, K., Suzuki, Y., Aizawa, Y. & Kozawa, Y., Local Ventilation by Tornadolike Vortex. *Transactions of the Japan Society of Mechanical Engineers* (in Japanese), **61(587) B**, pp. 401-407, 1995.

[3] Khoo, B.C., Yeo, K.S. & Yao, S.E., Effusing Core at the Center of a Potential Vortex. *Experimental Thermal and Fluid Science*, **7**, pp. 307-318, 1993.

[4] The Japan Society of Mechanical Engineers, *JSME Mechanical Engineers' Handbook, A6: Thermal Engineering* (in Japanese), Maruzen: Tokyo, 1985.

Modeling fluid transport in PEM fuel cells using the lattice-Boltzmann approach

L.-P. Wang & B. Afsharpoya
Department of Mechanical Engineering, University of Delaware, Newark, U.S.A.

Abstract

Three viscous flow problems relevant to fuel cell modeling are considered with the lattice Boltzmann approach. The first problem is a 3D viscous flow through a section of serpentine channel and the second is a 2D channel filled or partially filled with a porous medium. In the first case, attention is given to the implementation details such as inlet-outlet boundary conditions, nonuniform grid, and forcing. In the second case, the effects of multiple time scales and interface between the porous medium and clear channel are considered. In the third problem, these techniques are combined to simulate flow in a serpentine channel with GDL. Results are compared with other studies based on Navier-Stokes CFD and experimental observations.
Keywords: lattice Boltzmann approach, simulation, fuel cells, serpentine channel, porous medium, pressure loss.

1 Introduction

Fuel cells are electrochemical reactors generating electricity directly from oxidation reactions of fuels. Due to their high efficiency (typically twice of the energy conversion efficiency of internal combustion engines), near-zero emissions, low noise, and portability, fuel cells are being considered as a potentially viable energy-conversion device for mobile, stationary, and portable power. The low operation temperature of the proton-exchange membrane fuel cell (PEMFC) makes it a preferred fuel-cell type for automotive applications. A PEMFC unit consists of two thin, porous electrodes (an anode and a cathode) separated by a membrane-electrode assembly. Reactants (e.g., hydrogen and air) are brought into the cell through flow distribution channels (Fig. 1(a)). Computational models of increas-



WIT Transactions on Engineering Sciences, Vol 52, © 2006 WIT Press
www.witpress.com, ISSN 1743-3533 (on-line)
doi:10.2495/AFM06029

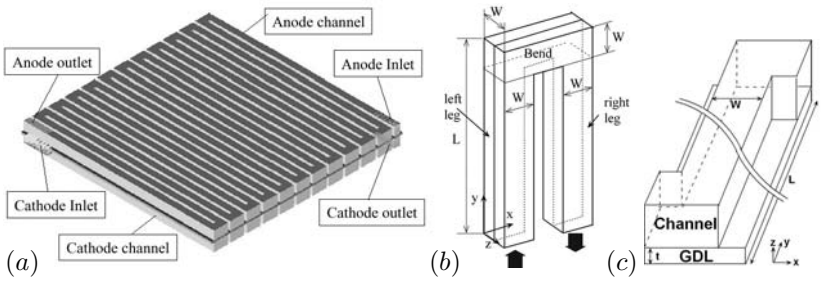


Figure 1: (a) Sketch of serpentine flow channels in PEM fuel cell; (b) A section of the channel being modeled in section 2; (c) A section of the channel with GDL being modeled in section 4.

ing complexity are currently being developed to better understand issues related to the performance of PEMFC, such as pressure loss and temperature distribution in the flow channels, species transport through porous gas diffusion layers (GDL), and water management on the cathode side. Wang [1] provides a review of recent modeling efforts using traditional computational fluid dynamics (CFD) based on macroscopic conservation equations.

In this paper we explore the use of lattice Boltzmann (LB) approach as a modeling tool for predicting fluid flows relevant to PEMFC. The LB approach is based on a kinetic formulation and could have certain advantages over the traditional CFD [2]. While LB models capable of addressing thermal flows, flows through porous media, multiphase flows, electro-osmotic flows, and contact line, *etc.*, have been proposed in recent years, two general aspects remain to be studied before they can be applied to fuel cell modeling. The first aspect concerns the accuracy and reliability of these models for practical applications. Since these models have typically only been tested for idealized problems, their applications to PEMFC flow problems need to be critically examined and different possible LB models be compared. The second aspect concerns a variety of implementation issues when dealing with practical applications, such as nonuniform grid, forcing implementation, boundary conditions, and porous-medium interface.

2 Flow through a serpentine channel without GDL

As a first example, we investigate the pressure distribution and flow pattern in a section of serpentine channel over a range of Reynolds numbers encountered in PEMFC. The channel has a square cross section of width W and a side length L (Fig. 1(b)). As a first step, we consider isothermal laminar flow and neglect the flow into the GDL so that the back wall is treated as a no-slip wall. This similar flow was studied recently by Matharudrayya *et al.* [3] using a traditional finite-volume CFD code and by Martin *et al.* [4] using particle imaging velocimetry (PIV).

The LB equation for the distribution function (DF) f_i of the particle with velocity $\mathbf{e}_i$

$$f_i(\mathbf{x}+\mathbf{e}_i\delta_t, t+\delta_t) - f_i(\mathbf{x},t) = -\frac{1}{\tau}\left[f_i(\mathbf{x},t) - f_i^{(eq)}(\mathbf{x},t)\right] + \psi_i(\mathbf{x},t) \quad (1)$$

is solved with a prescribed forcing field ψ_i designed to model the pressure difference between the inlet and the outlet, so that a periodic boundary condition can still be applied to f_i between the inlet and outlet. This minimizes the density fluctuations associated with f_i which could otherwise be significant considering the large L/W ratio here and the augmented pressure loss through the bend. The D3Q19 model is used with the following equilibrium distribution function

$$f_i^{(eq)}(\mathbf{x},t) = \omega_i\rho\left[1 + \frac{\mathbf{e}_i\cdot\mathbf{u}}{c_s^2} + \frac{\mathbf{uu}:(\mathbf{e}_i\mathbf{e}_i - c_s^2\mathbf{I})}{2c_s^4}\right], \quad (2)$$

where ω_i is the weight and the sound speed c_s is $1/\sqrt{3}$.

Two different methods of specifying the forcing term were tested. The first method specifies ψ_i and macroscopic variables as

$$\psi_i(\mathbf{x},t) = \omega_i\mathbf{e}_i\cdot\mathbf{F}/c_s^2,\ \rho = \sum_i f_i,\ \rho\mathbf{u} = \sum_i f_i\mathbf{e}_i,\ p = \rho c_s^2 + p_0(\mathbf{x}) \quad (3)$$

where ρ, $\mathbf{u}$, and p are the fluid density, velocity, and pressure, respectively. The macroscopic force field is defined as $\mathbf{F} = (0, A(1-y/L_1), 0)$ for the left leg of the channel and $\mathbf{F} = (0, -A(1-y/L_1), 0)$ for the right leg, with $L_1 = L - W$. In the bend region, $\mathbf{F} = 0$. This force field amounts to an auxiliary pressure field of $p_0(\mathbf{x}) = A(L_1-y)^2/(2L_1)$ in the left leg and $p_0(\mathbf{x}) = -A(L_1-y)^2/(2L_1)$ in the right leg and a total pressure difference of AL_1 between the inlet and outlet (the driving force for the flow). The coefficient A was set to $8\rho\nu v_0/W^2$, where the kinematic viscosity is related to the relaxation time as $\nu \equiv (\tau - 0.5)c_s^2\delta_t$ and v_0 is a velocity scale (of similar magnitude as the mean flow speed u_0). Guo *et al.* [5] showed that the forcing term in the above formulation introduces some lattice effects to the Navier-Stokes equation. They were able to remove the lattice effects by modifying the definitions of ψ_i and $\mathbf{u}$ [5]. For the current problem, we found, however, that the two methods gave almost identical results.

A nonuniform mesh along the $y-$direction (Fig. 1(b)) is necessary for computational efficiency. We have developed a Lagrangian interpolation method to compute DF at a grid point from the DFs on a shifted grid defined by the streaming step. The method generalizes the interpolation-supplemented LB method of He *et al.* [6] and is easier to implement than the Taylor series expansion and least squares-based LB method of Shu *et al.* [7]. The walls are located in the middle of lattice links so a second-order accuracy is achieved with a simple bounce-back algorithm.

Fig. 2 shows a typical pressure distribution along the centerline of the channel. If the channel is made very long ($L >> W$), the pressure should change linearly with distance away from the bend region at both the inlet and outlet, with a same



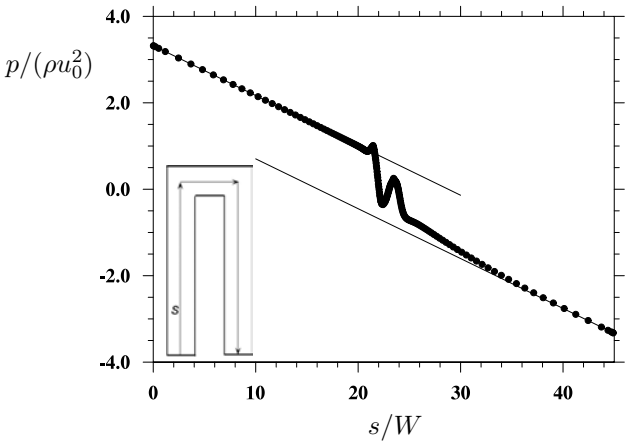


Figure 2: The pressure as a function of the distance s along the centerline of the channel when $Re = 127$.

slope. This slope away from the bend can be used to define a friction factor for a straight channel (i.e., $f = W\Delta p/(L\rho u_0^2/2)$) and the results are shown in Fig. 3(a) as a function of flow Reynolds number Re. This friction factor can be well modeled by the friction factor in a circular pipe (i.e., $f = 64/Re$) with diameter defined as $D = 2W/\sqrt{\pi}$, namely, diameter corresponding to same cross-sectional area. The deviation at large Re could be due to the influence of the bend since the value of L used ($L = 22W$) is not long enough.

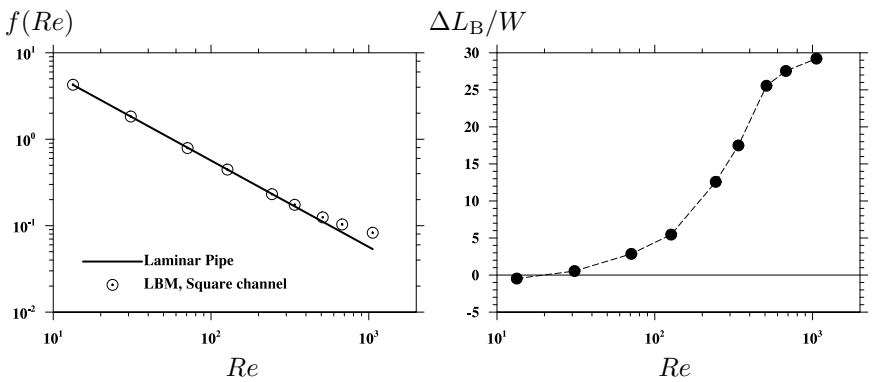


Figure 3: (a) The friction factor for the straight portion of the channel away from the bend. (b) The augmented loss due to the bend measured as the equivalent length of a straight channel.

A finite jump in pressure due to the bend exists, as indicated by the vertical distance between the two thin parallel lines in Fig. 2. This is referred to as the

bend pressure loss. The ratio of this jump to the slope away from the bend region defines a normalized, equivalent length for the bend pressure loss, $\Delta L_{\mathrm{B}}/W$. This equivalent length is shown in Fig. 3(b) as a function of Re. Of importance is that this length increases quickly with Re to values comparable to the actual single-path length in a typical PEMFC, implying that the bend pressure loss must be considered in fuel cell flow modeling. The slight negative value at the lowest Re is due to the fact that the flow can make 180-degree turn along the inner bend at such low Re.

Finally, we found that the flow in the bend region becomes unstable and small-scale vortices form at $Re \approx 1000$. To our knowledge, no accurate simulations for this Re range for a serpentine channel were made previously. Further analysis of this Re dependence will be reported in detail in a separate paper.

3 Flow through a channel filled or partially filled with porous medium

This section is motivated by the need to consider the interface between porous medium and flow channel in PEMFC modeling. We first consider flow in a 2D channel filled with porous medium of given porosity ϵ and permeability K. The macroscopic variables averaged over a representative elementary volume (REV) [8, 9] are considered and they are governed by the following momentum equation incorporating a Brinkman-extended Darcy law

$$\begin{aligned} \frac{\partial \mathbf{u}}{\partial t} + (\mathbf{u}\cdot\nabla)\left(\frac{\mathbf{u}}{\epsilon}\right) &= -\frac{1}{\rho}\nabla(\epsilon p) + \nu_e \nabla^2 \mathbf{u} + \mathbf{F} \\ \text{with } \mathbf{F} &= -\frac{\epsilon\nu}{K}\mathbf{u} - \frac{\epsilon F_\epsilon}{\sqrt{K}}|\mathbf{u}|\mathbf{u} + \epsilon\mathbf{G}, \end{aligned} \tag{4}$$

where the REV-averaged velocity $\mathbf{u}$ is assumed to be divergence-free, ν is fluid viscosity, ν_e is an effective viscosity, G represents the driving force for the flow. The geometric factor F_ϵ depends on the porosity and the microscopic configuration of porous medium (for details, see [8, 9]). This approach recovers the usual Navier-Stokes equation if $\epsilon \to 1$.

An LB model for the above macroscopic partial differential equation has been rigorously derived by Guo and Zhao [9]. The LB equation is identical to Eq. (1), but with f_i^{eq} and ψ_i modified as

$$f_i^{(eq)} = \omega_i \rho \left[1 + \frac{\mathbf{e}_i\cdot\mathbf{u}}{c_s^2} + \frac{\mathbf{uu}:(\mathbf{e}_i\mathbf{e}_i - c_s^2\mathbf{I})}{2\epsilon c_s^4}\right], \tag{5}$$

$$\psi_i = \omega_i\left(1 - \frac{1}{2\tau}\right)\left[\frac{\mathbf{e}_i\cdot\mathbf{F}}{c_s^2} + \frac{\mathbf{uF}:(\mathbf{e}_i\mathbf{e}_i - c_s^2\mathbf{I})}{\epsilon c_s^4}\right]. \tag{6}$$

We first apply the above model to a 2D channel of width H filled with porous medium. The flow is initially at rest and is driven by a constant pressure gradient G along the flow direction. In this case, the unidirectional transient flow subjected

to the boundary conditions $u(y=0,t)=u(y=H,t)=0$ can be solved analytically, giving

$$u(y,t)=\frac{GK}{\nu}\left\{1-\frac{\cosh[r(y-0.5H)]}{\cosh[0.5rH]}\right\}-\sum_{k=1,3,5,\ldots}^{\infty}\frac{4GK}{\nu}\frac{(\pi k)^2}{(\pi k)^2+(rH)^2}\times\sin\frac{\pi k y}{H}\exp\left\{-\left[(\pi k)^2+(rH)^2\right]\frac{\nu_e t}{H^2}\right\},\qquad(7)$$

where $r\equiv\sqrt{\nu\epsilon/(\nu_e K)}$. The analytical solution implies that there are two time scales in this problem, a diffusion time scale due to the channel walls $T_1\equiv H^2/(\pi^2\nu_e)$ and a diffusion time scale within the porous medium $T_2\equiv K/(\epsilon\nu)$. The ratio of the two time scales T_2/T_1 is equal to $\pi^2 Da/\epsilon$, which can be very small if the permeability is small. Here the Darcy number is defined as K/H^2. We find that in the implementation of the above LB scheme, it is necessary to use a very small Darcy velocity or a large H to ensure that both T_1 and T_2 are such larger than one. Otherwise, an apparent slip may be present near the walls, regardless whether the midway bounce-back or the nonequilibrium extrapolation method [10] was used on the walls. This slip disappears and the analytical solution can be precisely recovered when $T_1>>1$ and $T_2>>1$. A permissible lower bound for the time scales is found to be about 50 lattice time units.

We then simulated flow in a channel partially filled with porous medium so there is an interface inside the channel. The velocity varies continuously across the interface only when a very small Dracy velocity was used, for the reason indicated above. Two different treatments near the interface were tested. The first method places the interface in between the lattice nodes so that only the streaming step lead to exchanges of DF between two sides of the interface. The second method treats the interface as a boundary using the nonequilibrium extrapolation method, with the density and velocity taken as the average value from the two neighboring lattice points on the two sides of the interface. The results from the two treatments are almost identical. The results are also compared with the experimental data of Gupte and Advani [11]. The discrepancy in the clear channel region near the interface may be caused by the fact that the interface is not sharply defined in the experiment. Further investigation is underway to understand the origin of this discrepancy.

4 Flow through a serpentine channel with GDL

In this section, we combine the LB models discussed above to simulate fluid flow through a serpentine channel with GDL. A similar flow problem was recently studied by Pharoah [12] using a commercial, Navier-Stokes package (i.e., Fluent). Experimental measurements of fluid flow with the similar setting were performed by Feser [13].

For computational efficiency, a minimum periodic domain (see Fig 1(c)) with $0\le x\le 2W, 0\le y\le L, 0\le z\le (t+W)$ was considered, following the

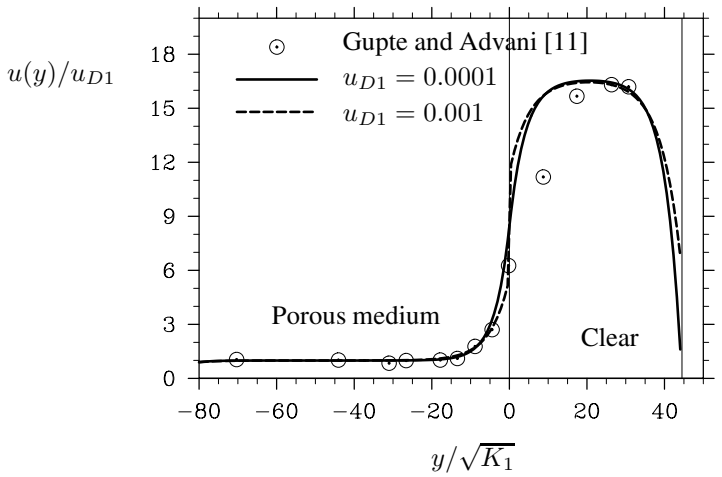


Figure 4: Velocity profile in a channel partially filled with porous medium. Parameters are: $\epsilon = 0.07$, $Re = 0.107$, $K_c/K_1 = 16.634$, and $Da = 5.611e-5$. Only a part of the channel is shown. The interface is located at $y = 0$.

analytical work of Feser [13]. Here L is the total length of the fuel cell, W is the width of the square flow channel, and t is the height of the GDL. The domain covers half of a complete serpentine loop. The inlet section at $x = 0$ consists of the cross section of the channel and the full section of GDL layer at the middle of a bend. The outlet is a cut through the middle of the immediate, opposite bend. The periodic boundary condition is

$$\mathbf{u}(0, y, z) = \mathbf{u}(2W, L - y, z), \quad \text{for } 0 \leq y \leq L \text{ and } 0 \leq z \leq (t + W). \tag{8}$$

In our simulations, we assumed that $L/W = 38$, $t/W = 1/3$, and W is 36 lattice units. A constant forcing per unit fluid mass of magnitude $F_0 = 8u_0\nu(L+W)/W^3$ is applied in the x direction to drive the flow in the LB equation. The forcing is added back when defining the macroscopic pressure field, namely, $p \equiv c_s^2 \sum f_i + \rho F_0(2W - x)$.

The results are compared with those of Pharoah [12] in Table 1. Note that Pharoah [12] used $L/W = 40$ and $t/W = 0.25$. The symbols in the table are: Re is the Reynolds number based on the total volumetric flow rate Q and W, Re_C is the Reynolds number based on the average velocity at the inlet channel and W, Re_{GDL} is the Reynolds number based on the average velocity at the GDL inlet and t, Q_C is the volumetric flow rate through the inlet channel only, and the pressure drop was normalized by $\rho(Q/W^2)^2$ or equivalently by $Re^2\rho(\nu/W)^2$. The air density and viscosity in Pharoah [12] are assumed to be 1 kg/m^3 and 0.17 cm^2/s, respectively. Several observations can be made: (1) the percentage of fluid flux through the channel decreases quickly with the Darcy number ($Da = K/W^2$)

Table 1: Flow partition and pressure drop in a serpentine channel with GDL.

	Re	Re_C	Re_{GDL}	Da	Q_C/Q	$\lvert\Delta\tilde{p}\rvert$
Run1	257.0	224.6	0.85	10^{-5}	87.4%	9.46
Run2	572.1	475.5	2.53	10^{-5}	83.2%	5.74
Run3	509.8	227.4	7.43	10^{-4}	44.6%	2.40
Run4	1624	268.1	35.7	10^{-3}	16.5%	0.24
Pharoah (2005)	200.0			10^{-5}	$\sim$90%	~ 10.9
Pharoah (2005)	400.0			10^{-5}	$\sim$87%	~ 6.81
Pharoah (2005)	400.0			10^{-4}	$\sim$50%	~ 3.03
Pharoah (2005)	400.0			10^{-3}	$\sim$22%	~ 0.54

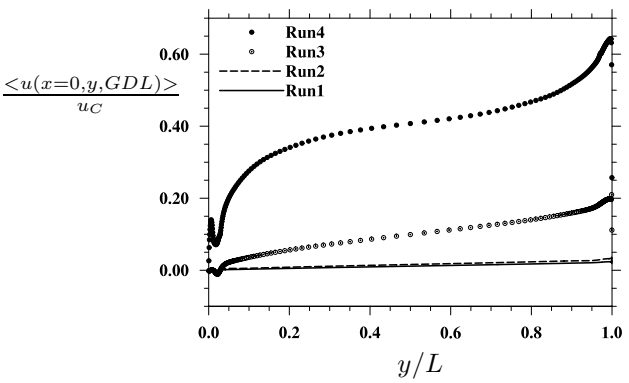


Figure 5: The z-averaged, x-component velocity through the middle of the GDL layer (i.e., x=0).

when $10^{-5} \leq Da \leq 10^{-3}$; (2) the percentage of fluid flux through the channel decreases slightly with flow Reynolds number, (3) both the pressure drop and the percentage of flow in channel agree reasonably well with the results of Pharoah [12], and finally (4) since our flow Reynolds number is higher, the percentage of flow in channel is lower than the values of Pharoah [12]. It is possible to match exactly the flow Reynolds numbers by adjusting the magnitude of u_0 appeared in the forcing F_0.

The vertically averaged, x-component velocity through the DGL at $x = 0$ is shown in Fig. 5 for the same four runs shown in table 1. In general, the velocity increases with y since the pressure difference on the two neighbouring channels above the GDL increases. At large Da, the flows through the channel and GDL are strongly coupled so that the convection velocity in GDL is strongly affected by the channel bends.

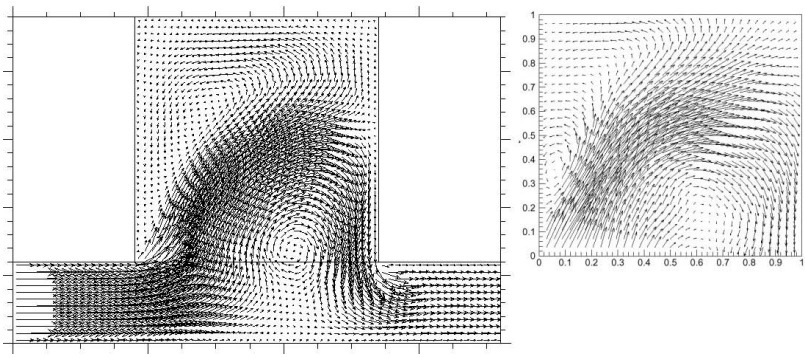


Figure 6: A snapshot of the quasi-steady velocity field in the $x - z$ plance, at a y location of one W before the exit bend. The left panel is from run4 and the right panel from PIV study of Feser [13].

Finally, the velocity field through an $x-z$ plane near the exit bend ($y = L-2W$) is compared with the PIV results of Feser [13]. The velocity is normalized by the average velocity u_C through the channel inlet. A strong convection flow through GDL generates secondary flows in the channel. This secondary flow differs from the self-generated secondary flow due to channel bends.

5 Conclusions

Three flow problems relevant to PEMFC are simulated with the LB approach. A 3D viscous flow through a section of serpentine channel without GDL was simulated and shown to depend sensitively on the flow Reynolds number. The pressure distribution along both the straight portion and bend region of the channel can be quantitatively modeled. We also demonstrate that flow through a porous medium with an interface can be treated with the LB approach, provided that the existence of multiple macroscopic time scales is taken into consideration. Finally, 3D flows through a serpentine channel with GDL were considered and it is shown that results on pressure drop and flow convection through GDL agree well with other Navier-Stokes CFD and PIV results.

Acknowledgements

This study is supported by the U.S. Department of Energy. The authors thank Professors Advani and Prasad of the University of Delaware for helpful discussions.

References

[1] Wang, C.Y., Fundamental models for fuel cell engineering. *Chem. Rev.* **104**, pp.4727-4766, 2004.

[2] Chen, S. and Doolen, G.D., Lattice Boltzmann method for fluid flows, *Annu. Rev. Fluid Mech.* **30**, 329-364, 1998.
[3] Maharudrayya, S., Jayanti S., & Deshpande, A.D., pressure losses in laminar flow through serpentine channels in fuel cell stacks. *J. Power Sources* **138**, pp.1-13, 2004.
[4] Martin, J., Oshaki, P., & Djilali, N., Flow structures in a u-shaped fuel cell flow channel: quantitative visualization using particle imaging velocimetry. *J. Fuel Cell Sci. Technol.*, in press.
[5] Guo, Z.L., Zheng, C.G., and Shi, B.C., Discrete lattice effects on the forcing term in the lattice Boltzmann method. *Phys. Rev. E.* **65**, 046308, 2002.
[6] He, X., Luo, L.-S., & Dembo, M., Some progress in lattice Boltzmann method. Part I. Nonuniform mesh grids. *J. Comp. Phys.* **129**, pp.357-363, 1996.
[7] Shu, C., Niu, X.D., & Chew, Y.T., Taylor series expansion and least squares-based lattice Boltzmann method: Three-dimensional formulation and its applications. *Int. J. Modern Physics C* **14**, pp.925-944, 2003.
[8] P. Nithiarasu, K.N. Seetharamu, and T. Sundararajan, Natural convective heat transfer in a fluid saturated variable porosity medium. *Int. J. Heat Mass Transfer* **40**, pp.3955-3967, 1997.
[9] Guo, Z.L. & Zhao, T.S., Lattice Boltzmann model for incompressible flows through porous media. *Phys. Rev. E.* **66**, 036304, 2002.
[10] Guo, Z.L., Zheng, C.G., and Shi, B.C., Non-equilibrium extrapolation method for velocity and pressure boundary conditions in the lattice Boltzmann method. *Chinese Phys.* **11**, pp.366-374, 2002.
[11] Gupte, S. & Advani, S.G., Non-Darcy flow near the permeable boundary of a porous medium: An experimental investigation using LDA. *Exp. in Fluids* **22**, pp.408-422, 1997.
[12] Pharoah, J.G., On the permeability of gas diffusion media used in PEM fuel cells. *J. Power Sources*, **144**, pp.77-82, 2005.
[13] Feser, J. Convective Flow Through Polymer Electrolyte Fuel Cells. M.S. thesis, University of Delaware, Newark, Delaware, USA, 2005.



Painlevé analysis and exact solutions for the coupled Burgers system

P. Barrera[1] & T. Brugarino[2]
[1] *Dipartimento di Meccanica, Università di Palermo, Facoltà d'Ingegneria, Palermo, Italia*
[2] *Dipartimento di Metodi e Modelli Matematici, Università di Palermo, Facoltà d'Ingegneria, Palermo, Italia*

Abstract

We perform the Painlevé test to a system of two coupled Burgers-type equations which fails to satisfy the Painlevé test. In order to obtain a class of solutions, we use a slightly modified version of the test. These solutions are expressed in terms of the Airy functions. We also give the travelling wave solutions, expressed in terms of the trigonometric and hyperbolic functions.

1 Introduction

The nonlinear diffusion-convection equations

$$\begin{cases} u_t(x,t) = u_{xx}(x,t) + \mu u(x,t)u_x(x,t) + \lambda_{11}v(x,t)u_x(x,t) \\ \qquad\qquad + \lambda_{12}u(x,t)v_x(x,t) \\ v_t(x,t) = v_{xx}(x,t) + \nu v(x,t)v_x(x,t) + \lambda_{21}v(x,t)u_x(x,t) \\ \qquad\qquad + \lambda_{22}u(x,t)v_x(x,t) \end{cases} \tag{1}$$

have a lot of applications in physics, chemistry and biology [1-3], particularly in the study of porous media [4], in polydispersive sedimentation [5], in dynamic of growing interfaces [6] and in the study of integrable coupled Burgers-type equations [7], [8].

The paper is organized as follows: in sect. **2** we show that system (1), for arbitrary coefficients, is not integrable in Painlevé sense; in sect. **3** a slightly modified version of the truncated Painlevé test is used to obtain analytic solutions for particular values of the coefficients; in sect. **4** we determine some exact solutions of



WIT Transactions on Engineering Sciences, Vol 52, © 2006 WIT Press
www.witpress.com, ISSN 1743-3533 (on-line)
doi:10.2495/AFM06030

the system with the aid of the Airy, the trigonometric and the hyperbolic functions. The last section is devoted to brief conclusions.

2 Painlevé analysis

It is possible to study the complete integrability of a system of partial or ordinary differential equations by using the so-called Painlevé test [9], [10]. The Painlevé test for the integrability of a system of partial differential equations

$$\mathbf{u}_t = \mathbf{K}(x, t, \mathbf{u}) \tag{2}$$

presented by Weiss-Tabor-Carnevale [9] involves seeking solutions of eq. (2) as expansion of the form of a Laurent series:

$$\mathbf{u}(x,t) = \phi(x,t)^{\mathbf{a}} \sum_{j=0}^{\infty} \mathbf{u}_j \phi(x,t)^j$$

where each vector $\mathbf{u}_j$ is a function of x and t, and the $\phi(t,x) = 0$ defines an arbitrary noncharacteristic movable singular manifold. The Painlevé method consists of the following main steps:

(i) determination of the leading behaviour;
(ii) identification of the powers at which arbitrary functions can enter in to the Laurent series, called resonances;
(iii) verifying that at resonance values a sufficient number of arbitrary functions exists without the introduction of the movable critical points.

First, we show that the system (1) fails to satisfy the Painlevé test. We assume that the solutions of the system (1) take the form:

$$u(x,t) = \phi(x,t)^a \sum_{j=0}^{\infty} u(x,t)_j \phi(x,t)^j \tag{3}$$

$$v(x,t) = \phi(x,t)^b \sum_{j=0}^{\infty} v(x,t)_j \phi(x,t)^j \tag{4}$$

where a and b are negative integers. By leading order analysis, we find that $a = b = -1$. Inserting in system (1) the expansions (3) and (4), we obtain

$$\begin{cases} \mu {u_0}^2 \phi_x + \lambda_{11} u_0 v_0 \phi_x + \lambda_{12} u_0 v_0 \phi_x - 2 u_0 \phi_x^2 = 0 \\ \lambda_{21} u_0 v_0 \phi_x + \lambda_{22} u_0 v_0 \phi_x + \nu {v_0}^2 \phi_x - 2 v_0 \phi_x^2 = 0 \end{cases} \tag{5}$$

Solving eqns. (5), we have

$$\begin{cases} u_0 = \frac{2(\lambda_{11}+\lambda_{12}-\nu)\phi_x}{\lambda_{11}(\lambda_{21}+\lambda_{22})+\lambda_{12}(\lambda_{21}+\lambda_{22})-\mu\nu} \\ \\ v_0 = \frac{2(\lambda_{21}+\lambda_{22}-\mu)\phi_x}{\lambda_{11}(\lambda_{21}+\lambda_{22})+\lambda_{12}(\lambda_{21}+\lambda_{22})-\mu\nu} \end{cases} \tag{6}$$



We take the meaningful values of u_0 and v_0. Substituting the Laurent series (3) in eqns. (1), collecting the coefficients of ϕ_x^{r-3} and utilizing eqns. (6), we finally obtain the resonance values:

$$r_1 = -1, \quad r_2 = 2$$

$$r_{3,4} = 3\lambda_{11}\lambda_{21} + 5\lambda_{12}\lambda_{21} + \lambda_{11}\lambda_{22} + 3\lambda_{12}\lambda_{22} - 2\lambda_{12}\mu - 2\lambda_{21}\nu - \mu\nu$$
$$\pm\sqrt{(\lambda_{11}(3\lambda_{21}+\lambda_{22}) + \lambda_{12}(5\lambda_{21}+3\lambda_{22}-2\mu) - (2\lambda_{21}+\mu)\nu)^2 -}$$
$$\overline{8(\lambda_{21}+\lambda_{22}-\mu)(\lambda_{11}+\lambda_{12}-\nu)((\lambda_{11}+\lambda_{12})(\lambda_{21}+\lambda_{22}) - \mu\nu)}\times$$
$$(2(\lambda_{11}+\lambda_{12})(\lambda_{21}+\lambda_{22}) - 2\mu\nu)^{-1}$$

Because the values of $r_{3,4}$ are not integer, for any value of λ_{hk}, the system (1) does not possess the Painlevé property.

3 Truncated Painlevé analysis

Now we use the truncated version of the Painlevé test to look for solutions of a system of differential equations [9] and [11].

The invariant formalism of truncated Painlevé [10], [12] implies looking for a solutions of eqns. (1) as:

$$\begin{cases} u = U_1\omega + U_0 \\ v = V_1\omega + V_0 \end{cases} \tag{7}$$

where the $\omega = \Psi_x/\Psi$.

The variable ω satisfies the Riccati equations

$$\omega_x = -\omega^2 - \frac{S}{2}$$

$$\omega_t = C\omega^2 - \omega C_x + \frac{CS + C_{xx}}{2}$$

and the variable Ψ satisfies the linear equations

$$\Psi_{xx} = -\frac{1}{2}S\Psi \tag{8}$$

$$\Psi_t = \frac{1}{2}C_x\Psi - C\Psi_x$$

The coefficients are related by the cross-derivative condition

$$S_t + 2SC_x + CS_x + C_{xxx} = 0$$

where S, the Schwarzian derivative of ϕ, and C are defined by:

$$S = \frac{\phi_{xxx}}{\phi_x} - \frac{3}{2}\left(\frac{\phi_{xx}}{\phi_x}\right)^3 \qquad C = -\frac{\phi_t}{\phi_x}$$

Substituting eqns. (7) in eqns. (1), then for eqns. (7) to be a solution, we must have:

For $j = 1$:

$$U_1 = \frac{2(\lambda_{11} + \lambda_{12} - \nu)}{(\lambda_{11} + \lambda_{12})(\lambda_{21} + \lambda_{22}) - \mu\nu}$$

$$V_1 = \frac{2(\lambda_{21} + \lambda_{22} - \mu)}{(\lambda_{11} + \lambda_{12})(\lambda_{21} + \lambda_{22}) - \mu\nu}$$

for $j = 2$:

$$U_0 = -\frac{(\lambda_{11} + \lambda_{12} - \nu)C}{(\lambda_{11} + \lambda_{12})(\lambda_{21} + \lambda_{22}) - \mu\nu}$$

$$V_0 = -\frac{(\lambda_{21} + \lambda_{22} - \mu)C}{(\lambda_{11} + \lambda_{12})(\lambda_{21} + \lambda_{22}) - \mu\nu}$$

therefore

$$u = \frac{\lambda_{11} + \lambda_{12} - \nu}{(\lambda_{11} + \lambda_{12})(\lambda_{21} + \lambda_{22}) - \mu\nu}(2\omega - C)$$

$$v = \frac{\lambda_{21} + \lambda_{22} - \nu}{(\lambda_{11} + \lambda_{12})(\lambda_{21} + \lambda_{22}) - \mu\nu}(2\omega - C)$$

and, for $j = 3$:

$$C_t + CC_x - S_x - 2C_{xx} = 0 \tag{9}$$

and, of course, the cross-derivative condition

$$S_t + 2SC_x + CS_x + C_{xxx} = 0 \tag{10}$$

4 Exact solutions

Now we able to obtain solutions of system (1), by solving eqns. (9), (10) and (8). A possible set of solutions of eqns. (9) and (10) is:

$$C = at + c$$

$$S = ax - \frac{a^2t^2}{2} - act + d \tag{11}$$

while eqn. (8):

$$\Psi_{xx} + \left(ax - \frac{a^2t^2}{2} - act + d\right)\frac{\Psi}{2} = 0 \tag{12}$$

is now an ordinary differential equation of Airy type [13], the variable t acting as a parameter. We consider three cases.



4.1 $a \neq 0$

The Airy equation has the following general solution

$$\Psi = k_1 \mathrm{Ai}\left(\sqrt[3]{(2/a)^2}\left(\frac{a^2t^2+2act-2d}{4}-\frac{ax}{2}\right)\right)+$$
$$k_2 \mathrm{Bi}\left(\sqrt[3]{(2/a)^2}\left(\frac{a^2t^2+2act-2d}{4}-\frac{ax}{2}\right)\right)$$

therefore, the solutions of system (1) are:

$$u=\frac{\lambda_{11}+\lambda_{12}-\nu}{(\lambda_{11}+\lambda_{12})(\lambda_{21}+\lambda_{22})-\mu\nu}\left(at+c+\right.$$
$$\left.\sqrt[3]{4a}\frac{\mathrm{Ai}'\left(\sqrt[3]{4a}\left(\frac{at^2}{4}+\frac{ct}{2}-\frac{d}{2a}-\frac{x}{2}\right)\right)+k\mathrm{Bi}'\left(\sqrt[3]{4a}\left(\frac{at^2}{4}+\frac{ct}{2}-\frac{d}{2a}-\frac{x}{2}\right)\right)}{\mathrm{Ai}\left(\sqrt[3]{4a}\left(\frac{at^2}{2}+\frac{ct}{2}-\frac{d}{2a}-\frac{x}{2}\right)\right)+k\mathrm{Bi}\left(\sqrt[3]{4a}\left(\frac{at^2}{2}+\frac{ct}{2}-\frac{d}{2a}-\frac{x}{2}\right)\right)}\right)$$

$$v=\frac{\lambda_{22}+\lambda_{21}-\mu}{(\lambda_{11}+\lambda_{12})(\lambda_{21}+\lambda_{22})-\mu\nu}\left(at+c+\right.$$
$$\left.\sqrt[3]{4a}\frac{\mathrm{Ai}'\left(\sqrt[3]{4a}\left(\frac{at^2}{4}+\frac{ct}{2}-\frac{d}{2a}-\frac{x}{2}\right)\right)+k\mathrm{Bi}'\left(\sqrt[3]{4a}\left(\frac{at^2}{4}+\frac{ct}{2}-\frac{d}{2a}-\frac{x}{2}\right)\right)}{\mathrm{Ai}\left(\sqrt[3]{4a}\left(\frac{at^2}{2}+\frac{ct}{2}-\frac{d}{2a}-\frac{x}{2}\right)\right)+k\mathrm{Bi}\left(\sqrt[3]{4a}\left(\frac{at^2}{2}+\frac{ct}{2}-\frac{d}{2a}-\frac{x}{2}\right)\right)}\right)$$

where Ai and Bi are the Airy functions, the prime denotes the derivative with respect to the argument, and k is an arbitrary constant.

4.2 $a = 0, d = \quad \delta\ (\delta > 0)$

The eqn. (12) has the general solution expressed in terms of the hyperbolic functions, so that the solutions of system (1) are:

$$u=\frac{\lambda_{11}+\lambda_{12}-\nu}{(\lambda_{11}+\lambda_{12})(\lambda_{21}+\lambda_{22})-\mu\nu}\times$$

$$\frac{c+\sqrt{2\delta}+k(c-\sqrt{2\delta})(\cosh\sqrt{2\delta}(x-ct)+\sinh\sqrt{2\delta}(x-ct))}{1+k(\cosh\sqrt{2\delta}(x-ct)+\sinh\sqrt{2\delta}(x-ct))}$$

$$v=\frac{\lambda_{22}+\lambda_{21}-\mu}{(\lambda_{11}+\lambda_{12})(\lambda_{21}+\lambda_{22})-\mu\nu}\times$$

$$\frac{c+\sqrt{2\delta}+k(c-\sqrt{2\delta})(\cosh\sqrt{2\delta}(x-ct)+\sinh\sqrt{2\delta}(x-ct))}{1+k(\cosh\sqrt{2\delta}(x-ct)+\sinh\sqrt{2\delta}(x-ct))}$$

4.3 $a = 0, d = \delta$ $(\delta > 0)$

In this case, analogously, eqn. (12) has the general solution expressed in terms of the trigonometric functions, and the solutions of system (1) are:

$$u = \frac{\lambda_{11} + \lambda_{12} - \nu}{(\lambda_{11} + \lambda_{12})(\lambda_{21} + \lambda_{22}) - \mu\nu} \times$$

$$\frac{c - \sqrt{2\delta}k + (ck + \sqrt{2\delta}) \tan\left((x - ct)\sqrt{\delta/2}\right)}{1 + k \tan\left((x - ct)\sqrt{\delta/2}\right)}$$

$$v = \frac{\lambda_{22} + \lambda_{21} - \mu}{1 - (\lambda_{11} + \lambda_{12})(\lambda_{21} + \lambda_{22}) - \mu\nu} \times$$

$$\frac{c - \sqrt{2\delta}k + (ck + \sqrt{2\delta}) \tan\left((x - ct)\sqrt{\delta/2}\right)}{1 + k \tan\left((x - ct)\sqrt{\delta/2}\right)}$$

5 Conclusions

In this note we obtain for the system (1), in addition to the usual travelling wave solutions corresponding to the constant values of the invariant S and C, another type of interesting analytic solutions, related to Airy functions, where S and C are not constant.

References

[1] B. H. Gilding, R. K. Kersner, The characterization of reaction-convection-diffusion processes by travelling waves, J. Diff. Eqns. **124** (1996) 27.
[2] M. P. Edwards, P. Broadbridge, Exact transient solutions to nonlinear diffusion-convection equations in higher dimensions, J. Phys. A **27** (1994) 5455.
[3] P. Barrera, T. Brugarino, Traveling waves of two coupled nonlinear diffusion convection equations, 14^{th} Symposium Transport and Air Pollution **II** (2005) 9, Graz.
[4] A. Klute, Soil Sci. 73 (1952) 105.
[5] S. E. Esipov, Coupled Burgers equations: A model of polydispersive sedimentation, Phys. Rev. 52 (1995) 3711.
[6] M. Kardar, G. Parisi, Y. C. Zhang, Dynamic scaling of growing interfaces, Phys. Rev. Lett. 56 (1986) 889.
[7] M. V. Fursov, On integrable coupled Burgers-type equations, Physics Lett. A **272** (2000) 57.
[8] L. Zeng-Ju, C. Li-Li, L. Sen-Yue, Painlevé property, symmetries and symmetry reductions of the coupled Burgers system, Chinese Phys. **14** (2005) 1486.



[9] J. Weiss, M. Tabor, G. Carnevale, The Painlevé Property for Partial Differential Equations, J. Math. Phys. **24** (1983) 522.
[10] R. Conte, Universal Invariance Properties of Painlevé Analysis and Bäcklund Transformation in Nonlinear Partial Differential Equations, Physics Lett. A **134** (1988) 100.
[11] P. Barrera, T. Brugarino, L. Pignato, Analytic solutions of two coupled reaction-diffusion equations, Air Pollution **XI** (2003) 135, Catania.
[12] T. Brugarino, Exact Solutions of two Coupled Burgers Equations, Proceedings **SIMAI** (2002), Cagliari.
[13] M. Abramowitz, I. A. Stegun, *Handbook of Mathematical functions*, (1972), Dover.



This page intentionally left blank

Section 6
Boundary layer flow

This page intentionally left blank

New scaling parameter for turbulent boundary layer with large roughness

C. S. Subramanian & M. Lebrun
Department of Mechanical and Aerospace Engineering,
Florida Institute of Technology, Melbourne, Florida

Abstract

Nikuradse uses the equivalent sand-grain roughness to characterize the effect of roughness. While this approach works when the roughness is contained in the inner layer, it does not apply in recent studies with a larger roughness. Various techniques have been applied in the past to scale the mean velocity and the Reynolds stress profiles for a zero pressure gradient boundary layer, the classical scaling using the friction velocity u* to normalize the velocity profiles. However none of these techniques holds universally.

This study attempts to improve the understanding that we have of the way roughness affects the inner layer behaviour and aims to find an alternative scaling parameter for cases where roughness is large compared to the inner layer. Measured mean and turbulent velocity profiles on a large regular roughness show a non-zero wall normal pressure is caused which contributes to the velocity deficit in the near wall rough boundary layer velocity profile. The normal turbulent stresses are also increased. Hence a pressure gradient velocity rather than the friction velocity is defined to capture the pressure effects induced by roughness. The power law seems to give a better representation of the velocity profiles than the log law in this case.
Keywords: large roughness, boundary layer, friction velocity, turbulent velocity, pressure gradient velocity, log law, power law.

1 Introduction

Some of the most recent studies of the effects of surface roughness on boundary layer structure were performed by Perry et al. [2], Bandyopadhyay and Watson [3], Barenblatt [4], Acharya et al. [5] and Keirsbulk et al. [6]. Roughness may be



WIT Transactions on Engineering Sciences, Vol 52, © 2006 WIT Press
www.witpress.com, ISSN 1743-3533 (on-line)
doi:10.2495/AFM06031

classified in various ways depending on the geometry of the roughness elements. It may be deterministic (regular) or stochastic (random). Most of the research has been done on "regular" roughness patterns such as sand grain roughness.

Nikuradse [1] and Schlichting [7] were the first ones to introduce the concept of equivalent sand grain roughness size, ks, to characterize and quantify roughness effects on the boundary layers. But in many cases, a single parameter is not enough to characterize the hydrodynamics of a surface. The logarithmic velocity profile relationship is stated as:

$$\frac{u}{u^*} = \frac{1}{\kappa}\ln\left(\frac{y.u^*}{\nu}\right) + C \tag{1}$$

where, u^* is the friction velocity, κ is the Karman constant, C is the additive constant.

The classical framework established by Nikuradse [1] predicts that the effect of roughness on the mean-velocity distribution is confined to a thin wall layer. Many researchers have verified through experiments the existence of the log-law region of the boundary layer for flows with a range of pressure gradients (Klebanoff and Diehl [8]; Clauser [9]; and many others). However values of C and κ are still debated.

Durbin and Belcher [12] defined a viscous pressure-gradient velocity which is derived in Subramanian's research [13] where he shows that if you define the characteristic velocity as u_p given by

$$u_p^3 = \frac{\nu}{\rho}.\frac{dP_s}{dx} \tag{2}$$

where P_s is the surface mean pressure, independent of y but function of x, an equation can be derived with only one characteristic velocity u_p and one characteristic length scale ν/u_p, and its boundary conditions are homogeneous (both u and the shear stress are zero at y=0) which would yield a solution similar to the law-of-the-wall as (1).

u_p seems to be a better scale in situations where the friction velocity, u^*, is ill defined or tends to zero and the local pressure gradient is the influencing parameter.

The purpose of this research was to gain some fundamental and practical knowledge of these flows and to find an alternative scaling parameter for flows where the roughness is very strong and where the "log law" does not apply anymore.

2 Experimental set up and method

All the experiments were conducted in the boundary layer wind tunnel located at the FloridaTech laboratories.

The wind tunnel test section is 1.7 m in length, 0.54 m in width and 0.54 m in height. Three test plates (0.34 m x 0.27 m) were designed to go on the boundary layer plate as an insert. The first one follows the smooth pattern of the plate, the



second one has the two-dimensional roughness, and the third one has the three-dimensional rough elements. Figure 1 shows where the roughness is located on the boundary layer plate. The type of roughness used is k type, where the ratio of the gap width over the height of the roughness elements is greater than 1. The gap width is 7 mm, the height is 6 mm. Each roughness element width is 3 mm. The plate containing the 3D roughness has pressure taps in both x (longitudinal) and the z (transverse) directions to measure the pressure at all the experimental points. A trip wire was attached at 1 cm from the leading edge in order to obtain a fully turbulent flow over the plate.

The boundary layer test section is fitted with a boundary layer flat plate. The leading edge of the test plate was shaped to mimic the forward position of an airfoil. In order to measure the boundary layer pressure gradient, 3 surface static pressure taps were placed on the plate; more were placed on the inserts. Table 1 gives the location of the pressure taps, including on the insert.

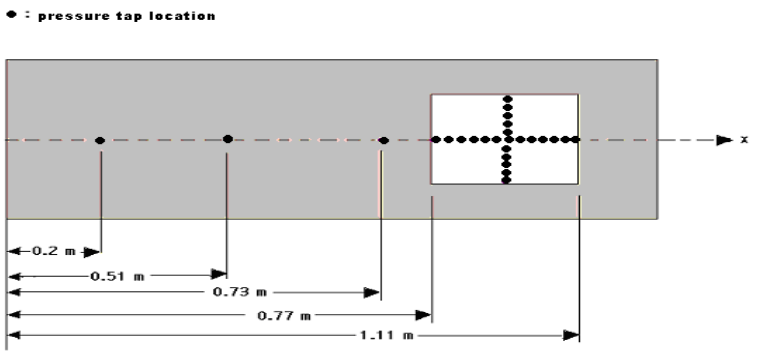


Figure 1: Location of pressure taps on the boundary layer plate.

Table 1: Location of the pressure taps on the 3 inserts in cm.

Smooth	20	51	73	81.5	86	90.5	95	99.5	104	
2D	77.5	79	80.5	83	85.5	87	89.5	91	92.5	95
Rough	96.5	98	100.5	102	103.5	106	107.5	109	110.5	
3D	77.5	79	80.5	82	84	85.5	87	89	90.5	92
Rough	94	95.5	97	99	100.5	102	104	105.5	107	
	-14	-12.5	-10.5	-9	-7.5	-5.5	-4	-2	0	
	1.5	3	5	6.5	8	10	11.5	13	14.5	

Three probes were used to measure the boundary layer profile. The first probe was a boundary layer pitot tube which measured total pressure, in conjunction with the surface static pressure taps located on the plate. The second probe was a hotwire probe Model TSI 1218-10 serial B460 with a 5-micron diameter single fibre-film probe used in conjunction with a Dantec 56C17 constant temperature anemometer. It is made of platinum film and has a nominal resistance of 5.30 ohms. The third probe is an x-wire (Model 55R53) mounted on a Dantec long probe support (Model 55H25) and used in conjunction with the

Dantec 56C17 constant temperature anemometer. This probe has a nominal resistance of 4.99 ohms and 4.74 ohms. Each probe was attached to a vertical traverse to take data at different height locations. The initial location from the surface was determined approximately by eyeballing which introduces offset errors. The first position of the pitot probe was taken to be 0.63 times the diameter thickness of the probe to account for the wall proximity error on the velocity. The probes were traversed from 0 to 20 mm in 1 mm intervals then from 20 to 50 mm in 2 mm intervals. The traverse's stepper motor resolution is 0.127 mm. The probe traversing and the data acquisition were automated. The data acquisition system used for this experiment consisted of National Instruments (NI) PCI 6024E 100ks/s multi-function card, Lab View 6.0 software, and a personal computer. Data acquisition from the pressure transducer was done at 1,000 samples/second with a total of 10,000 samples, which were used for velocity statistics. Data acquisition from the anemometer was set at 10,000 samples/second with a total of 20,000 samples, which were used for velocity statistics.

3 Results and discussion

Pitot tube, pitot static tube, Preston tube, single wire anemometry, cross-wire anemometry and visualization techniques were performed to obtain measurements. The data uncertainty for the probes are 6% for the pitot static tube, 14% for the Preston probe, 2% for the hotwire and 3% for the x-wire. At all time of the experiment ambient conditions were noted. The average temperature among all the experiments was 24.0°C with an average relative humidity of 71% and an average atmospheric pressure of 1015.0 hPa. The following air properties are derived from the above listed ambient conditions. The average air density was 1.189 kg/m^3, the average absolute viscosity was 1.839-05 Nm^2/s and the average kinematic viscosity was 1.547E-05 m^2/s. The boundary layer thickness, δ_{99}, and the skin friction coefficient, C_f, estimated by the Clauser method give values that are consistent with the empirical correlation results found in many textbooks for a nominal smooth-wall turbulent boundary.

For estimating the u_p values, the longitudinal surface pressure gradients are measured with respect to the immediate upstream tap. The surface pressure distribution was checked along the plate at 15 different points to determine the differences caused by the roughness. Figure 2 shows the plot of the surface pressure distribution along the centerline on the 2D and on the 3D roughness. The dynamic pressure is plotted and the reference pressure used is P_∞. The accuracy of the pressure measurements is ± 5 Pa. The magnitude of the surface pressure is small but it is clearly non-zero and increases with respect to the free stream on the local roughness. Figure 2 shows that the pressure increases rapidly at the very first point on the roughness then decreases on the rough surface. The pressure stabilizes around the smooth plate value far downstream. The estimated pressure velocities, although relatively small, are considered a better indicator of the local pressure change. Therefore the surface pressures should be measured at

close intervals and with a sensitive transducer to get a good estimation of the pressure velocity for surfaces where variations due to roughness are large.

Extensive flow measurements were taken first on the smooth plate then on the 2D rough plate to compare the two. Measurements were performed with the pitot tube, the hotwire and the x-wire measuring u and v components at 10 stream wise locations on the rough plate. The u velocity deficit in the inner layer increases with the downstream distance, which suggests that the inner layer flow adjusts to the smooth wall condition only further downstream. The profiles are in agreement with previous finding that the overlap region is the most affected by the roughness. The longitudinal component of turbulent direct stress increases as much as twice the value of the smooth wall near the wall by the roughness. The stress level increases as we go downstream, showing that it extends in to the outer region. This might be due to enhanced diffusion. All profiles asymptote to the same value in the outer layer. The same observations can be made for the normal component of the turbulent direct stress. The normal component of the turbulent direct stress is mostly responsible for inducing the normal pressure gradients along the wall. There is more increase of this stress due to roughness than of the longitudinal component of direct stress. The shear stress profiles in Figure 3 show that the stress level is higher near the wall due to roughness. The constant shear stress region that is usually present in the smooth wall profiles is practically non-existent. Therefore the wall similarity law may not be used in this case. The peak stress occurs closer to the wall than for a smooth wall, therefore abrupt velocity gradients are expected at the wall when the roughness is strong.

The results obtained on the 3D roughness are very similar. It seems that the flow is even less turbulent than with the 2D roughness. Measurements were taken with the pitot tube and the hotwire at 8 stream wise locations, along the centre line, alternatively on and within the roughness, at 10 and 15 m/s free stream speeds. Velocity profiles can be seen on Figure 4 and we can conclude that along the roughness, the u velocity near the wall is dramatically reduced compared to smooth wall. For 3D roughness, as well as for 2D rough elements, the coefficient of friction cannot be found using the Clauser chart for the log law does not exist anymore.

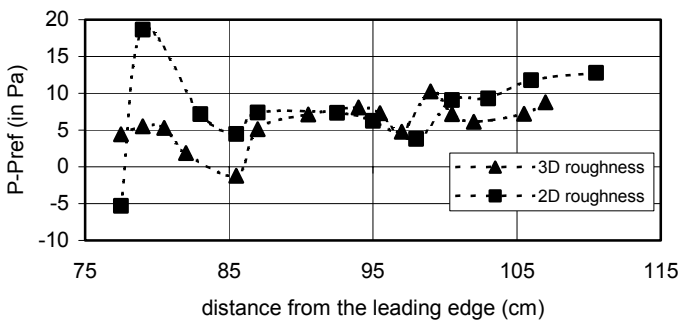


Figure 2: Variation of surface pressure with roughness at 10 m/s.

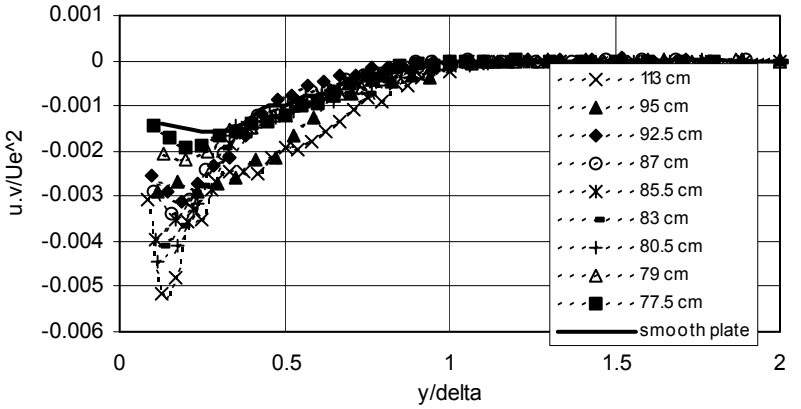


Figure 3: Turbulent shear stress profiles along the centreline.

For the 3D roughness, the velocity profiles in the z (transverse) direction are shown in Figure 5. On the rough plate, the flow does not follow the $1/7^{th}$ power law. There is no pattern as we go further left or further right from the centreline. The mean profile is laminar like unlike what we saw on the 2D insert. It seems that the 3D roughness, since it has less blockage than the 2D roughness (the roughness elements are now cubes that allow more air to flow between them) turns the mean velocity profile into a laminar profile but we cannot consider the flow as laminar because it still has a high turbulent intensity.

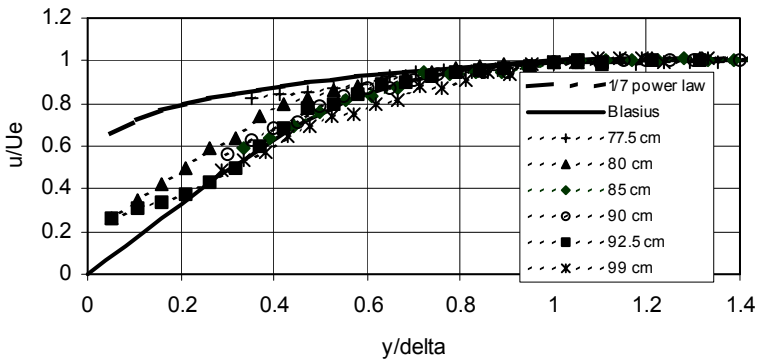


Figure 4: u-velocity profile development on 3D roughness with hotwire.

We are looking for a better scaling parameter for cases where the roughness is large. The parameter u_p defined earlier seems to be a better scaling parameter than the usual skin friction velocity u*. u_p is calculated using Eq. (2). The pressure transducer gives us series of surface pressure measurement, from that

the static pressure is found at each experimental point and dP_s/dx can be calculated. From there we can deduce u_p at each experimental point.

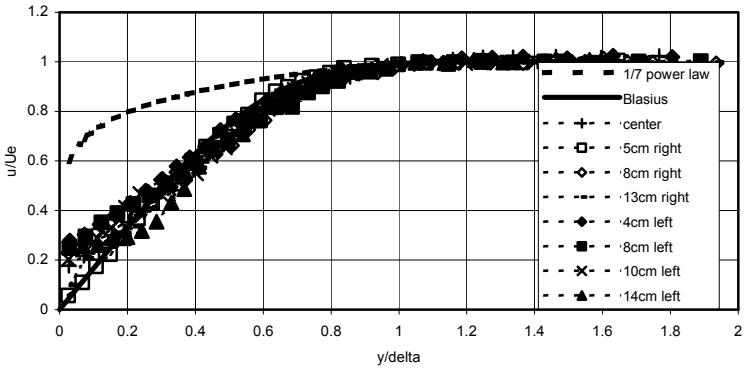


Figure 5: Transversal velocity across the 3D plate at x=92 cm and 15 m/s.

Figure 6 shows the distribution of u_p on the 2D rough plate at 10 m/s. There does not seem to be a pattern but on the other hand, we cannot conclude anything for the points contained within the limits of uncertainty. The uncertainty on the pressure is ± 5 Pa with gives us an uncertainty on u_p of ± 0.13 m/s. Figure 7 shows a semi log plot of the longitudinal mean velocity profiles plotted using the new scaling parameter u_p both on the smooth and on the rough surface. A linear log-law region is noticeable but a more accurate estimate of the u_p might be needed. Stratford's zero-wall shear stress velocity profile gives a log-law distribution with a similar scaling with a slope of 5 and an intercept of 8. In our case, the wall shear stress is not zero and therefore we do not have a first order equation: a second order velocity correction term is required.

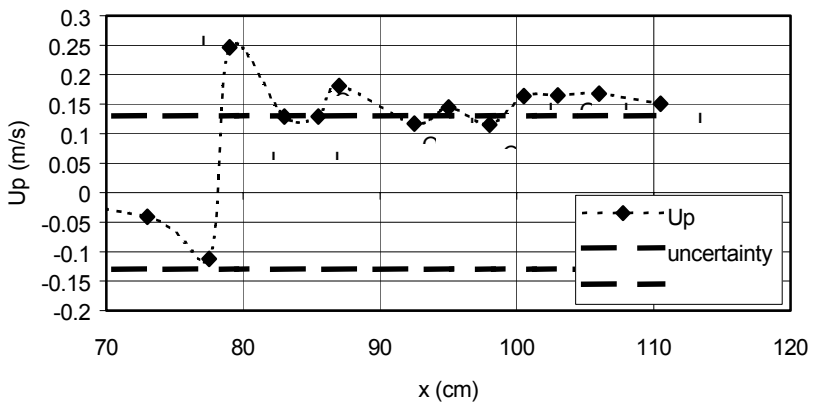


Figure 6: u_p distribution on the 2D rough plate at 10 m/s.

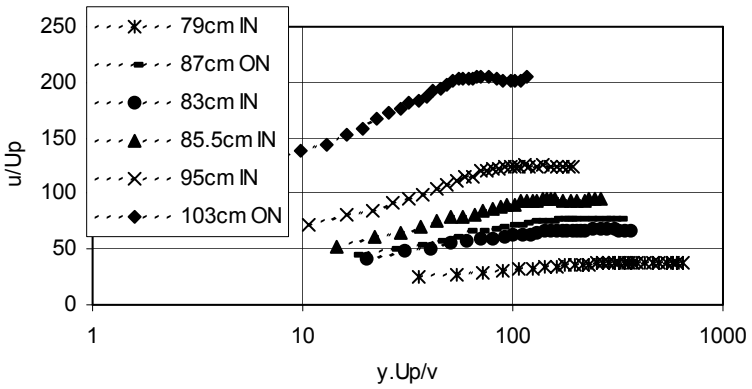


Figure 7: Longitudinal mean velocity profiles based on u_p scaling, z=0.

If we plot the shear stress profile using the u_p and ν/u_p normalization, the negative peak magnitude of shear stress increases and moves away from the surface with the increase of streamline distance. Downstream of the roughness, some constant shear stress region is seen. We can see that the u, v and w fluctuations are greater close to the wall (i.e. the inner layer) compared to the smooth wall data. Away from the wall, the fluctuations seem to decrease as the distance from the leading edge increases therefore the outer layer of the turbulent boundary layer are affected by the roughness.

The span wise size of the roughness elements plays an important role in determining whether the outer layer is going to be altered by the roughness or not. The local roughness can be expressed in different ways, as suggested by Subramanian et al. [13] to define the roughness using Ra, the average roughness height over a square mm area, Rt, the difference between the largest positive deviation and the largest negative deviation from the mean line in a 1 mm square area and Rq the root mean square roughness.

We find: Rt = 6 mm and Rq = 4.24 mm for the 2D and the 3D roughness. Ra is 6 mm on the 2D roughness and 3 mm on the 3D plate. The ratio Ra/Rt appears to be a good indicator of the roughness, for the 2D roughness, Ra/Rt is 1 meaning that the local peaks and valleys are of the same size. For the 3D roughness, Ra/Rt is 0.5 showing that the roughness occupies only half the area that it did in the 2D case. Recent research has been done on scaling the power law velocity profile, which is a good alternative to the log law in cases like ours with large roughness. Afzal [14] proposes the relation and Barenblatt et al. [15] the correlations of power law constants:

$$\frac{u}{U^*}=C\left(\frac{y.U^*}{\nu}\right)^{\alpha} \tag{3}$$

$$\alpha=\frac{3}{2.\ln R_e} \quad \text{and} \quad C=\frac{1}{\sqrt{3}}\ln R_e+\frac{5}{2} \tag{4}$$

If we apply Eq. (3) using Barenblatt's coefficients (Eq. (4)) and using u_p instead of u*, we get a perfect correlation on the 2D roughness as can be seen on

Figure 8. Same thing for the 3D roughness. We obtain 2 nearly identical linear fits. This results proves that u_p is a more adequate velocity scaling parameter than u* which cannot be found easily on the rough surfaces.

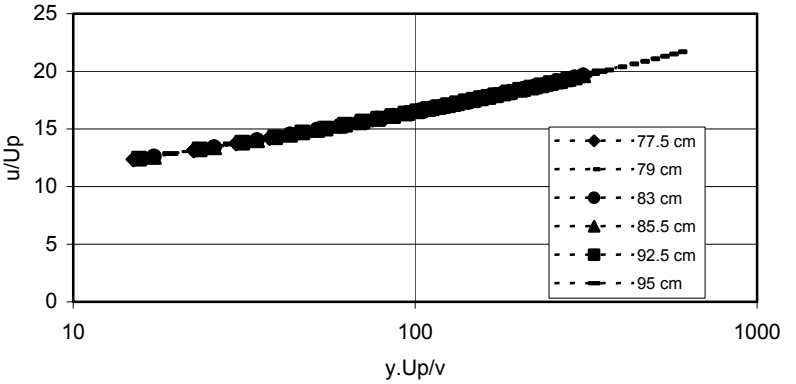


Figure 8: Longitudinal mean velocity profiles based on the scaling law and the scaling parameter u_p on the 2D roughness.

4 Conclusions

Surface roughness is a defining feature of many of the high Reynolds-numbers flows found in engineering. The higher the Reynolds number, the more significant will the effects of roughness be. Unfortunately, the impact of surface roughness is not entirely understood. The turbulent boundary layer over a rough surface contains a roughness sublayer within which the flow is directly influenced by the local roughness elements and is therefore not spatially homogeneous. The height of this sublayer presumably depends upon the height of the roughness elements as well as their shape and density distribution in the lateral directions.

The rough-wall boundary layers can be categorized according to whether or not the surface roughness affects the outer layer. In this region, the inner log-law may be altered or destroyed, the existence of the log-law cannot be assumed anymore. All the scaling laws used so far are based only on its effect on the viscous drag even though several recent studies suggest that the turbulence structural changes caused by roughness are very profound in the inner layer.

The specific conclusions of this research are that the large regular roughness decreases the mean longitudinal velocity in the near wall layers and affects the overlap log-law layer. The mean velocity profiles follow the $1/7^{th}$ power law on the smooth plate insert, the $1/4^{th}$ power law on the 2D rough insert and the Blasius-like profile on the 3D rough insert. Large roughness increases all the turbulence quantities in the inner layer; the shear stresses are increased by a factor of 2 times the smooth wall value. There seems to be an effect of roughness not only on the inner layer but also on the outer layer structure of the boundary layer. The roughness causes a normal pressure gradient, invalidating the thin boundary layer assumption. The near wall pressure is higher than the free stream

pressure. Inner layer recovery of the mean flow is slow downstream of the roughness. This research shows that the log law is not valid in cases were the roughness is large and it is necessary to find a scaling parameter that will work in those cases. A new scaling parameters was found and applied to our experimental data but, we still need to do more research to find a scaling parameter that can be applied to any boundary layer analysis.

The validity of the experiment and sources of error were confirmed. Among these is the inability to measure velocities near the surface, at less than 0.25 mm and without introducing flow obstructions.

References

[1] Nikuradse, J.: *Laws of flow in rough pipes*, NACA TM 1292, National Advisory Committee on Aeronautics, 1933.

[2] Perry, A.E., Lim, K. L. and Henbest, S. M.: An experimental study of the turbulence structure in smooth and rough wall boundary layers, *J. Fluid Mech.* **177**, pp. 437-466, 1987.

[3] Bandyopadhyay, Promode R. and Watson, Ralph D.: Structure of rough-wall turbulent boundary layers, *Phys.Fluids* **31**, pp.1877-1883, 1988.

[4] Barenblatt G.I.: *Turbulent Boundary Layers at a very large Reynolds number*, Lawrence Berkeley National Laboratory, California, 2003.

[5] Acharya M., Bornstein J. and Escudier M.P.: Turbulent Boundary Layers on Rough Surfaces, *Exp. Fluids*, **4**, pp. 33-47, 1986.

[6] Keirsbulck L., Labraga L., Mazouz A. and Tournier C.: Surface Roughness Effects on Turbulent Boundary Layer Structures, *ASME J. Fluids Eng*. **124**, pp. 127-135, 2003.

[7] Schlichting, H.: *Experimental investigation of the problem of surface roughness*, NACA TM 832, National Advisory Committee on Aeronautics, 1936.

[8] Kebanoff, P.S. and Diehl, Z.W., Natl. Advisory Comm. Aeronaut. Tech. Notes. No. 2475, 1951

[9] Clauser, F. H., "The turbulent boundary layer," Adv. Appl. Mech. 4, pp. 1--51, 1956

[10] White, Frank M.: *Viscous Fluid Flow*, Second edition, McGraw-Hill, N.Y., 1991.

[11] Townsend A.A.: *The structure of turbulent shear flow*, Second edition, Cambridge University Press, Cambridge, 1976.

[12] Durbin P.A and Belcher S.E.: Scaling of adverse-pressure-gradient turbulent boundary layers, *J. Fluid Mech.*, **238**, pp. 699-722, 1992.

[13] Subramanian, Chelakara S., King, Paul I., Reeder, Mark F., Ou, Shichuan, Rivir, Richard B.: Effects of Strong Irregular Roughness on the Turbulent Boundary Layer, *Flow, Turbulence & Comb*, **74(2-4)**, pp.349-368, 2004.

[14] Afzal, Noor: Scaling of Power Law Velocity Profile in Wall-Bounded Turbulent Shear Flows, *43rd Aerospace Science Meeting*, Reno, NV, 2005.

[15] Barenblatt, G.I., Chorin, A.J., Prostokishin, V.M.: A model of a turbulent boundary layer with a nonzero pressure gradient, *Proc. US NAS*, **99(9)**, pp. 5772-5776, April 2002.



Stratified flow over topography: wave generation and boundary layer separation

B. R. Sutherland & D. A. Aguilar
Department Mathematical and Statistical Sciences, University of Alberta, Edmonton, Canada

Abstract

We have performed laboratory experiments to study wave generation over and in the lee of model topography. We have chosen to use periodic, finite-amplitude hills which are representative of the Earth's major mountain ranges as well as the repetitious topographic features of the ocean floor. The topographic shapes are selected to encompass varying degrees of roughness, from smoothly-varying sinusoidal hills to sharper triangular and rectangular hills.

Contrary to linear theory predictions, the (vertical displacement) amplitude of the internal waves directly over the hills is generally much smaller than the hill height. This is because fluid is trapped in the valleys between the hills effectively reducing the amplitude of the hills. Thus the experiments serve to emphasize the importance of boundary layer separation upon internal waves generated by flow over rough topography.

1 Introduction

Internal waves propagate through fluids whose density, effectively, decreases continuously with height. Like surface waves, fluid parcels associated with internal waves move up and down due to buoyancy. However, the motion is not confined to an interface and so it is possible for internal waves to move vertically as well as horizontally through the fluid.

The strongest source of internal waves in the atmosphere results when stratified air flows over mountain ranges. For hills that are periodic and sufficiently small amplitude, linear theory predicts that waves are generated in the overlying air with the same period as the time for flow from one hill crest to the next. The waves propagate vertically away from the hills provided this period is longer than the



WIT Transactions on Engineering Sciences, Vol 52, © 2006 WIT Press
www.witpress.com, ISSN 1743-3533 (on-line)
doi:10.2495/AFM06032

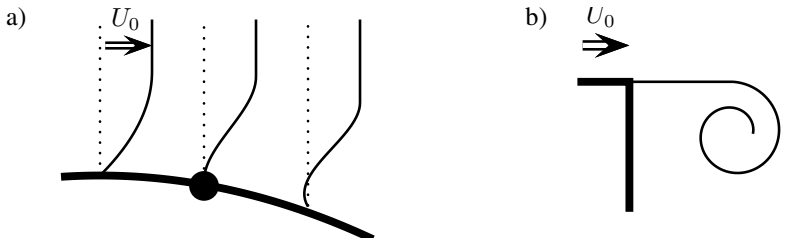


Figure 1: a) Flow profiles surrounding a separation point (solid circle) in the lee of a hill crest. b) Boundary layer separation from a sharp corner.

buoyancy period, which is the natural period of vertical oscillations of the stratified fluid. The buoyancy period is shorter of the stratification is stronger.

Linear theory also predicts that the vertical-displacement amplitude of the waves is half the hill-to-valley distance. Again this assumes the hills are such small amplitude that the air can flow over the surface with negligible change to its speed. If the hills are sufficiently large amplitude, however, we expect the air to move significantly more slowly in the valleys than over the hills.

This occurs due to two reasons. In uniform-density fluid, it is well known that an adverse pressure gradient can develop in an expanding flow leading to deceleration and ultimately reversal of the flow at the boundary, as depicted in fig. 1a. The point where the shear at the boundary is zero, and hence where there is no surface stress, is called a separation point. When such boundary-layer separation occurs the downstream flow typically is unstable. Streamlines wrap into vortices (fig. 1b) and eventually break down turbulently,

In a stratified fluid, boundary layer separation can also occur because the fluid in a valley is significantly more dense than the fluid at the surrounding hill tops. The kinetic energy of the flow relative to the available potential energy of the fluid in the valley in part dictates the location of the separation point.

But the situation is more complicated than this. When unstratified or sufficiently weakly stratified air flows over a set a hills, a perturbation pressure field is established with relatively low pressure overlying hill crests and high pressure at the base of the valleys, fig. 2a. Thus an adverse pressure gradient is established in the lee of the crest and this can lead to boundary layer separation.

However, if the fluid is more strongly stratified so that the forcing period is long compared to the buoyancy period, then internal waves are generated and the pressure variation on the surface changes. Now the centre of low pressure lies at the midpoint between the hill and valley on the lee of the crest (fig. 2b). Meanwhile, the high now lies at the midpoint on the facing side of the hill. This means that the adverse pressure gradient is strongest at the valley floor and so the separation point will shift downslope from its position in the absence of waves. That is, internal waves retard or at least forestall the formation of separated boundary layers.

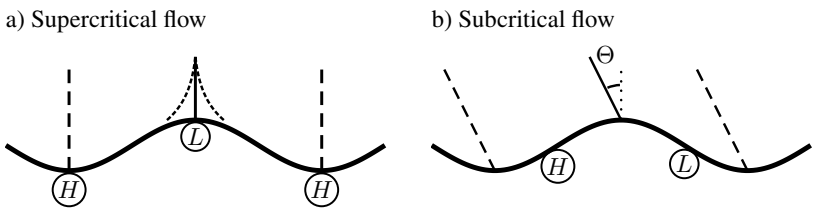


Figure 2: a) Vertical phase lines and surface pressure associated with evanescent disturbances for which Fr $>$ 1. Such disturbances have exponentially decreasing amplitude with height as illustrated by the short dashed lines above the hill crest. b) Tilted phase lines associated with vertically propagating internal waves for which Fr $<$ 1.

Although the literature on boundary layer separation in uniform density fluids is vast, remarkably few studies have examined the influence of stratification. Baines and Hoinka [1] examined boundary layer separation and resulting boundary-trapped lee waves behind an isolated hill and Baines [2] examined separation due to flow over an isolated valley. Both studies ignored the influence of internal waves upon separation and, conversely, ignored the impact of boundary layer separation upon internal wave generation. In experiments studying stratified flow over a step [3], vertically propagating waves and boundary-trapped lee waves were found to couple resonantly. The period of both was an approximately constant fraction of the buoyancy period.

By way of numerical simulations, Welch *et al.* [4] were the first to study internal waves generated above large amplitude sinusoidal hills. They showed that the wave amplitude increases with the hill height until the hills were so tall that separation occurs. At still larger hill heights they showed that wave amplitudes remained fixed and the depth of the fluid trapped in the valleys increased. These results were corroborated in laboratory experiments [5] examining flow over moderate and large-amplitude sinusoidal hills.

Although these studies have focused upon flow over smooth topography, recent ocean observations [6] suggest that substantial mixing and associated internal wave activity occurs as a result of tidal flow over abyssal canyons associated with the Mid-Atlantic Ridge.

This raises the issue of the influence of topographic shape upon boundary layer separation and internal wave generation, and is the point of the work presented here.

2 Experimental set-up

Details of the experimental setup are given by Aguilar *et al.* [5]. All experiments were performed in a 197 cm long and 17.5 cm wide glass tank. The tank was filled with uniformly salt-stratified fluid to a depth of 27 cm. The resulting density gra-

dient is proportional to the squared buoyancy frequency, which in the Boussinesq approximation is given by

$$N^2 = -\frac{g}{\rho_0}\frac{d\bar{\rho}}{dz}. \tag{1}$$

Here g is the acceleration of gravity and ρ_0 is a characteristic density. The buoyancy period is $2\pi/N$.

One of four model hills was then suspended on the surface of this stratified fluid. Each topographic shape consisted of four hills with crest-to-crest distance $\lambda = 13.7\,\text{cm}$. Three of the hills had half crest-to-trough amplitude $h_0 = 1.30\,\text{cm}$ having either sinusoidal, triangular or rectangular shape. The fourth hill was sinusoidal but had amplitude $h_0 = 0.65\,\text{cm}$ ($h_0/\lambda \sim 0.047$). The qualitative discussion here will focus on the three large-amplitude hills, although amplitude measurements will also include data from the moderate-amplitude hill experiments.

From an initial state of rest, the hills were towed at constant horizontal speed, U, until they reached the end of the tank. Whether or not internal waves are generated by periodic topography is determined by the value of the Froude number

$$\text{Fr} \equiv \frac{Uk}{N}, \tag{2}$$

in which $k = 2\pi/\lambda$ is the wavenumber based on the crest-to-crest distance, λ, of the hills.

Nonlinear effects associated with the half crest-to-valley hill height, h_0, can be represented nondimensionally in a variety of ways. A measure of the influence of stratification upon boundary layer separation is given by a quantity sometimes called an inverse vertical Froude number. For convenience as well as conceptual accuracy [2], here we call it the 'Long number', after Robert Long [7]. Explicitly, we define the Long number by

$$\text{Lo} \equiv \frac{Nh_0}{U}. \tag{3}$$

We expect stratification to play an important role if $\text{Lo} \gg 1$. In the limit $\text{Lo} \ll 1$, linear theory should be valid. But, with N and h_0 fixed, this limit corresponds to increasing flow speed. So boundary layer separation may still occur due to adverse pressure gradients in the lee of a hill crest.

A stratification-independent non-dimensional parameter that represents the importance of boundary-layer separation is $h_0/\lambda = \text{Lo}\,\text{Fr}/2\pi$, the aspect ratio of the hills. For the three large-amplitude model hills, $h_0/\lambda \sim 0.094$. Because topographic shape is relevant to this study, we define a third parameter S_{max}, which is the maximum slope of the hills. For large amplitude sinusoidal hills, $S_{\text{max}} = \text{Lo}\,\text{Fr} \simeq 0.60$, for triangular hills, $S_{\text{max}} \simeq 0.38$, and for rectangular hills $S_{\text{max}} \to \infty$.

Internal waves and boundary layer separation were observed in experiments using synthetic schlieren [8], by which a digital camera records how an image of horizontal black and white lines becomes distorted when the stratified fluid between them is disturbed. In this sense the fluid acts like a time-varying lens.



If fluid separates from a boundary, the associated density gradients are large and greatly distort the image both at the separation point and along the separated streamline. Where the flow is turbulent but still stratified, the image is distorted to such a degree that it blurs and the black and white lines can no longer be distinguished.

The distortion associated with propagating internal waves is not so large and the disturbance field in the tank can be treated as quasi two-dimensional. Knowing how light travels through such a disturbance, the degree of image distortion can straightforwardly be related back to the amplitude of the waves.

For convenience, the results are presented here in terms of the time rate of change of the buoyancy frequency, ${N^2}_t$,

$$ {N^2}_t = \frac{\partial}{\partial t}\left(-\frac{g}{\rho_0}\frac{\partial \rho}{\partial z}\right). \tag{4} $$

in which $\rho = -\bar{\rho}'\xi$ is the perturbation density field. For periodic waves, the ${N^2}_t$ field is proportional to ξ. Using power spectra to measure peak frequencies and horizontal wavenumbers of the observed waves, the vertical-displacement amplitude, A_ξ, is thereby determined [5].

Although the experiments are conducted so that waves move downward from topography towed along the surface, for conceptual convenience, all the images shown here will be flipped upside-down so that it will appear as if disturbances and waves occur above the hills. Within the Boussinesq approximation, there is no dynamical distinction between upward and downward propagating disturbances.

3 Experimental results

3.1 Qualitative results

First we examine boundary layer separation in experiments with three different topographic shapes towed at relatively slow speeds so that in all three cases Fr $\simeq$ 0.4 and Lo $\simeq 1.5$. The distortion pattern associated with streamlines separating in the lee of hill crests is shown in fig. 3. These time series illustrate increased density gradients in the tank where the image of black and white lines behind the tank is magnified.

Separation behind the sinusoidal and triangular hills occurs midway between the hill crests and troughs and the detached streamline reconnects with the following hill near its crest. Apparently the presence of the cusp at the triangular hill crests does not influence boundary layer separation. However, separation occurs right at the lee-side corner of the rectangular-shaped hills and a substantially larger proportion of fluid is trapped between hills. Thus we expect the effective hill height to be relatively smaller for flow over rectangular hills.

In fig. 4 we examine the effect of increasing U (and, hence, increasing Fr and decreasing Lo) upon boundary layer separation. As Fr increases, the separation point occurs further below the hill crest. In part, this is because faster flow has



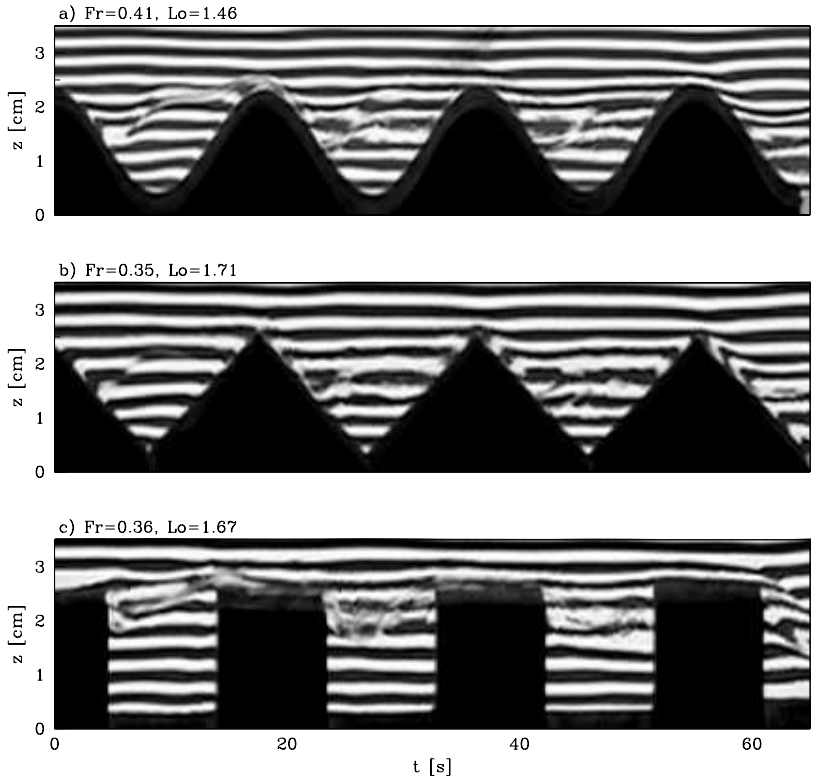


Figure 3: Time series showing distorted image due to flow over a) sinusoidal, b) triangular and c) rectangular topography. In all three cases the flow is subcritical with Fr $\simeq 0.4$.

more kinetic energy with which to sweep dense fluid out of the valleys. But is also because the pressure in the lee of the hills decreases as the flow speed increases and so fluid is sucked into the valleys.

Stratification plays less of a role than adverse pressure gradients in establishing a separation point as Fr increases. Although Lo correspondingly decreases to values much smaller than unity, the experiments show that the flow becomes increasingly turbulent as evident from the blurring of the image in figs. 4e and f.

The results are shown for rectangular topography experiments, but the conclusions are qualitatively similar for all three topographic shapes. This serves as a reminder that Lo alone does not establish whether the flow regime is linear or not.

Next we examine the effect of boundary layer separation upon wave excitation. Fig. 5 shows the near hill flow structure up to 5 cm above the hill valleys and shows the wave field between 5 and 20 cm. In the three subcritical cases (figs. 5a,b,c), waves are generated above the hills with phase lines tilting upstream at the slope

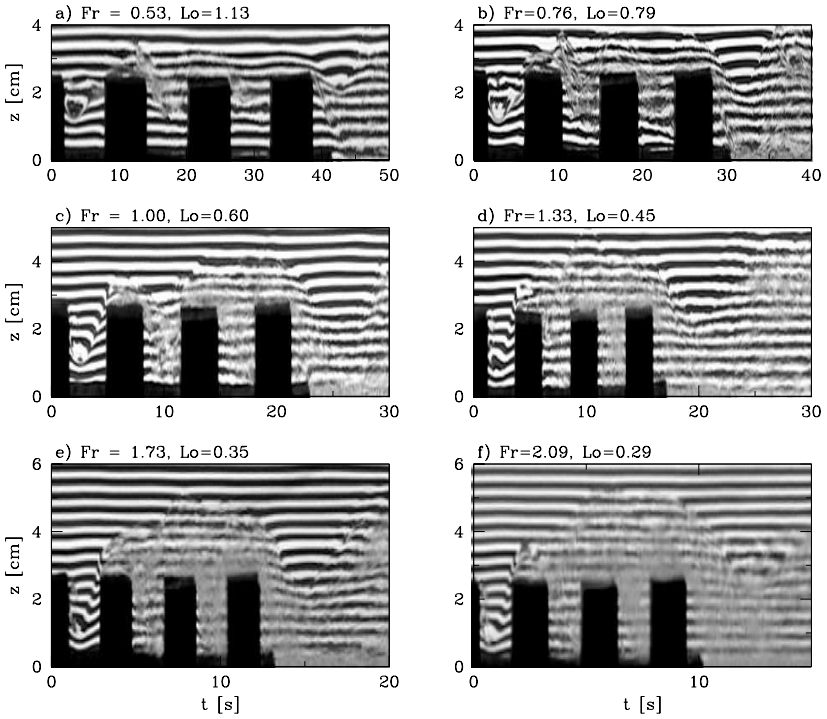


Figure 4: As in fig. 4 but for flow over rectangular topography with successively larger flow rates as indicated by the Froude number.

predicted by linear theory. As expected from our boundary layer separation observations, the wave amplitudes are largest above the sinusoidal and triangular-shaped hills.

In the three supercritical cases (figs. 5d,e,f) shown the waves directly over the hills are evanescent. However, vertically propagating waves are excited in the lee of the four hills in part as a consequence of the low pressure behind the trailing hill. Because there is no fluid trapping behind this hill the streamlines descend much closer to the surface. The flow then rebounds dynamically in response to buoyancy forces, as is evident from measurements showing that the rebound frequency is a nearly constant fraction of N [5].

3.2 Quantitative results

From measurements of the amplitude of the ${N^2}_t$ field and the corresponding wave frequencies and horizontal wavelengths, we compute the vertical displacement amplitude of the waves. These are plotted in fig. 6.

Fig. 6a shows the measured amplitude of the waves observed directly over the

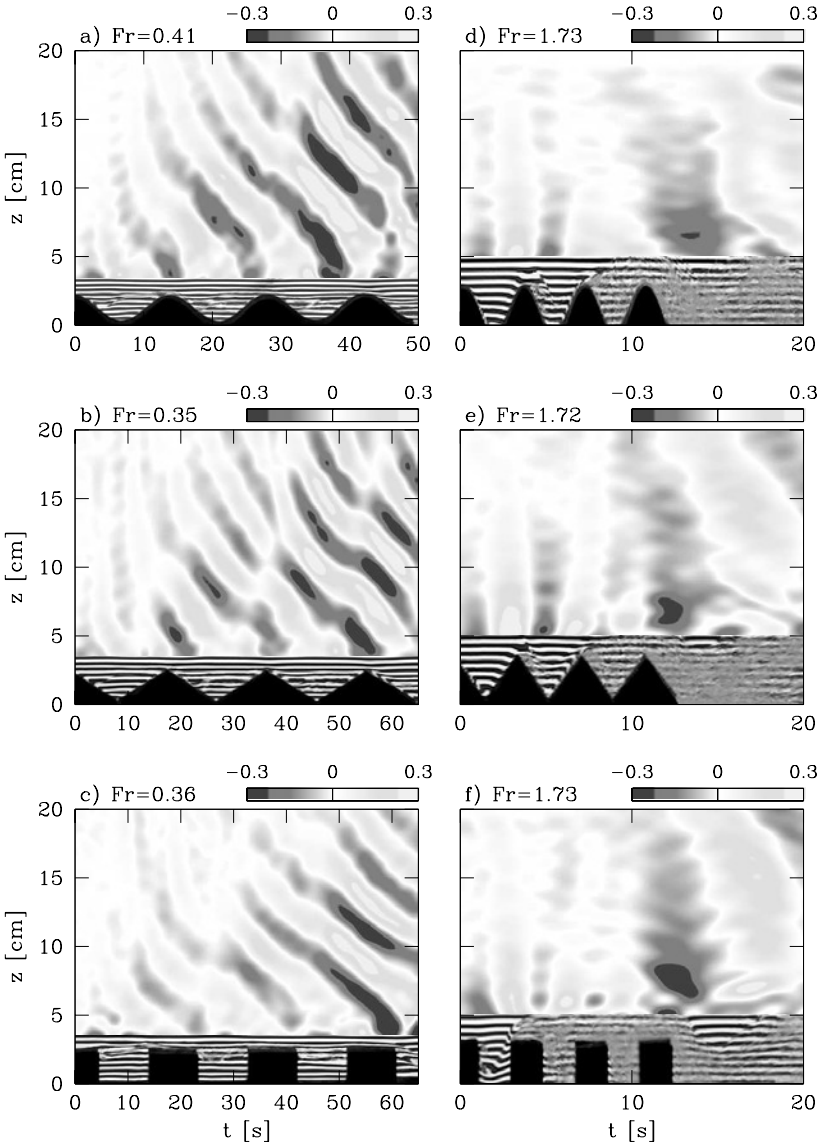


Figure 5: Raw image of near-hill flow and processed images showing $N^2{}_t$ fields associated with internal waves generated by subcritical flow over a) sinusoidal, b) triangular and c) rectangular topography and by supercritical flow over d) sinusoidal, e) triangular and f) rectangular topography. Colour contours correspond to values of the $N^2{}_t$ field measured in units of s^{-3}.

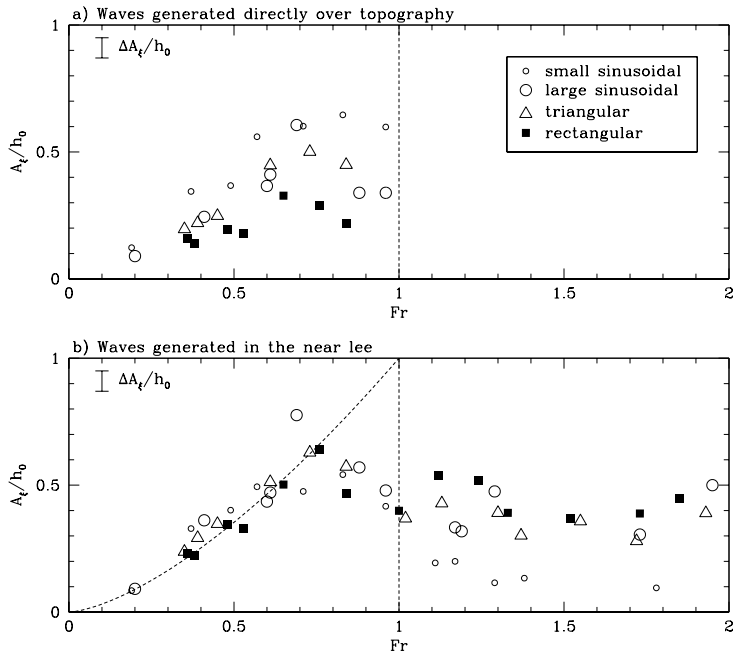


Figure 6: Propagating internal wave amplitudes measured a) over and b) in the lee of 4 sets of hills with shapes indicated in the legend. The dashed line in b) corresponds to the curve $A_\xi/h_0 = \mathrm{Fr}^{3/2}$.

hills which, consistent with linear theory, were non-evanescent only for subcritical flow with Fr < 1. Whereas linear theory predicts the amplitude should equal the topographic height, the experiments show that the waves are consistently smaller. The discrepancy is greater for smaller Fr because Lo correspondingly increases, meaning that stratification more strongly influences blocking. Consistent with this hypothesis, we see that the relative amplitudes of waves above small-amplitude sinusoidal hills is larger than those above large-amplitude hills. Presumably for even smaller amplitude hills, and corresponding smaller Lo, the relative amplitude should approach unity.

In the lee of subcritical topography at fixed Fr (fig. 6b), the relative amplitude of the lee waves is approximately the same for all experiments independent of shape and hill amplitude. Crudely, we find $A_\xi \simeq (\mathrm{Fr})^{3/2} h_0$ for Fr < 0.8. In supercritical experiments with Fr > 1, the relative amplitude of waves in the lee of small sinusoidal hills is smaller than that of waves in the lee of large-amplitude hills. For a range of supercritical Froude numbers, the amplitude behind the large hills is approximately $0.38h_0$.

4 Conclusion

The laboratory experiments reported upon here show is little qualitative or quantitative distinction between the results of the triangular and sinusoidal hill experiments. At fixed Fr and Lo, boundary layers separate at similar locations and internal waves have comparable amplitudes. This gives some hope that the roughness associated with mountain ranges may not play so significant a role in influencing wave excitation.

On the other hand, we find that internal waves have substantially smaller amplitude when generated directly over rectangular topography. This occurs because enhanced boundary layer separation traps fluid in the valleys between the hills and so reduces the effective hill height. This result is important when taken in connection with internal wave generation above the rough, canyon-shaped topography associated with the Mid-Atlantic Ridge.

Acknowledgements

The discussion regarding the influence of internal waves upon boundary layer separation came out of discussions with Richard Rotunno. We are grateful to Caspar Williams for his assistance in preparing some of the figures. This research was supported by the Canadian Foundation for Climate and Atmospheric Science (CFCAS).

References

[1] Baines, P.G. & Hoinka, K.P., Stratified flow over two-dimensional topography in fluid of infinite depth: a laboratory simulation. *J Atmos Sci*, **42**, pp. 1614–1630, 1985.
[2] Baines, P.G., *Topographic Effects in Stratified Flows*. Cambridge University Press: Cambridge, England, p. 482, 1995.
[3] Sutherland, B.R., Large-amplitude internal wave generation in the lee of step-shaped topography. *Geophys Res Lett*, **29(16)**, p. art. no 1769, 2002.
[4] Welch, W.T., Smolarkiewicz, P., Rotunno, R. & Boville, B.A., The deepening of a mixed layer in a stratified fluid. *J Atmos Sci*, **58(12)**, pp. 1477–1492, 2001.
[5] Aguilar, D., Sutherland, B.R. & Muraki, D.J., Generation of internal waves over sinusoidal topography. *Deep-Sea Res II*, p. in press, 2006.
[6] Ledwell, J.R., Montgomery, E., Polzin, K., St.Laurent, L.C., Schmitt, R. & Toole, J., Evidence for enhanced mixing over rough topography in the abyssal ocean. *Nature*, **403**, pp. 179–182, 2000.
[7] Long, R.R., Some aspects of the flow of stratified fluids. III Continuous density gradients. *Tellus*, **7**, pp. 341–357, 1955.
[8] Sutherland, B.R., Dalziel, S.B., Hughes, G.O. & Linden, P.F., Visualisation and measurement of internal waves by "synthetic schlieren". Part 1: Vertically oscillating cylinder. *J Fluid Mech*, **390**, pp. 93–126, 1999.



Group analysis and some exact solutions for the thermal boundary layer

P. Barrera[1] & T. Brugarino[2]
[1] *Dipartimento di Meccanica, Università di Palermo, Facoltà d'Ingegneria, Palermo, Italia*
[2] *Dipartimento di Metodi e Modelli Matematici, Università di Palermo, Facoltà d'Ingegneria, Palermo, Italia*

Abstract

We perform the group analysis of the thermal boundary layer in laminar flow. We obtain the classification of the solutions in terms of the asymptotic velocity. Some solutions of the boundary layer equations, for some distributions of outer flow velocity, are obtained also.

1 Introduction

It is very important to have the similarity solutions for the partial differential equations for the flow field near a body in a fluid flow. Generally the solutions of these equations are obtained by means of dimensional analysis which is a particular case of the group analysis. This is based on the theory of S. Lie developed more than one hundred years ago in order to have solutions of ordinary and partial, linear and non linear differential equations [1–6].

Considering systems of partial differential equations containing an arbitrary number of dependent and independent variables, the group analysis provides similarity solutions reducing the original system to a system with a reduced number of independent variables [7–9].

Now we turn our attention to the group analysis of the equations of the thermal boundary layer for some particular cases.

2 Group analysis

We show in brief the theory of one-parameter Lie groups of transformations for a partial differential equation in which the number of independent variables is equal



WIT Transactions on Engineering Sciences, Vol 52, © 2006 WIT Press
www.witpress.com, ISSN 1743-3533 (on-line)
doi:10.2495/AFM06033

to two. We can generalize the results to systems of partial differential equations containing an arbitrary number of dependent and independent variables.

Consider the partial differential equation (dependent variable c, independent variables x and t) of second order

$$F(c, x, t, c_x, c_t, c_{xx}, c_{xt}, c_{tt}) = 0 \tag{1}$$

In what follows c_x denotes $\frac{\partial c}{\partial x}$, c_t denotes $\frac{\partial c}{\partial t}$, ...

Consider an one-parameter (ϵ) group of transformations:

$$\left\{ \begin{array}{lcl} c^* & = & c^*(x, t, c; \epsilon) \\ x^* & = & x^*(x, t, c; \epsilon) \\ t^* & = & t^*(x, t, c; \epsilon) \end{array} \right. \tag{2}$$

When $\epsilon = 0$ the (2) correspond to identical transformation

$$\left\{ \begin{array}{lcl} c^* & = & c \\ t^* & = & t \\ x^* & = & x \end{array} \right.$$

Expanding the (2) about the identity $\epsilon = 0$ we obtain

$$\left\{ \begin{array}{lclcll} c^* & = & c & + & \epsilon\gamma(x, t, c) & + & O(\epsilon^2) \\ x^* & = & x & + & \epsilon\xi(x, t, c) & + & O(\epsilon^2) \\ t^* & = & t & + & \epsilon\tau(x, t, c) & + & O(\epsilon^2) \end{array} \right.$$

where γ, ξ and τ are the *infinitesimal generators* of the transformations (2).

The $c^*_{x^*}$, $c^*_{t^*}$, ... are the transformed derivatives determined from (2)

$$\left\{ \begin{array}{lcl} c^*_{x^*} & = & c^*_{x^*}(x, t, c, c_x, c_t; \epsilon) \\ c^*_{t^*} & = & c^*_{t^*}(x, t, c, c_x, c_t; \epsilon) \\ c^*_{x^*x^*} & = & c^*_{x^*x^*}(x, t, c, c_x, c_t, c_{xx}, c_{xt}, c_{tt}; \epsilon) \\ c^*_{x^*t^*} & = & c^*_{x^*x^*}(x, t, c, c_x, c_t, c_{xx}, c_{xt}, c_{tt}; \epsilon) \\ c^*_{t^*t^*} & = & c^*_{x^*x^*}(x, t, c, c_x, c_t, c_{xx}, c_{xt}, c_{tt}; \epsilon) \end{array} \right. \tag{3}$$

In similar way for the (3) we have

$$\left\{ \begin{array}{lclcll} c^*_{x^*} & = & c_x & + & \epsilon[c_x] & + & O(\epsilon^2) \\ c^*_{t^*} & = & c_t & + & \epsilon[c_t] & + & O(\epsilon^2) \\ c^*_{x^*x^*} & = & c_{xx} & + & \epsilon[c_{xx}] & + & O(\epsilon^2) \\ c^*_{x^*t^*} & = & c_{xt} & + & \epsilon[c_{xt}] & + & O(\epsilon^2) \\ c^*_{t^*t^*} & = & c_{tt} & + & \epsilon[c_{tt}] & + & O(\epsilon^2) \end{array} \right. \tag{4}$$

where $[c_x]$, $[c_t]$, $[c_{xx}]$ are the *infinitesimal generators* of the transformed derivatives determined from the (2).



Because the (2) determine the (4), the transformed derivatives $[c_x]$, $[c_t]$, $[c_{xx}]$, $[c_{xt}]$ and $[c_{tt}]$ can be expressed in terms of γ, ξ, τ.

We have for example

$$[c_x] = \frac{D\gamma}{Dx} - \frac{\partial c}{\partial x}\frac{D\xi}{Dx} - \frac{\partial c}{\partial t}\frac{D\tau}{Dx}$$

where $\frac{D}{Dx}$ is the total derivative. In a similar way we proceed for $[c_t]$.

Higher order transformed derivatives can be derived from recurrence formulas. The differential equation (1) is invariant under the group of transformations (2) if

$$\begin{aligned} &F(c, x, t, c_x, c_t, c_{xx}, c_{xt}, c_{tt}) = \\ &F(c + \epsilon\gamma + \cdots, x + \epsilon\xi + \cdots, t + \epsilon\tau + \cdots, c_x + \epsilon[c_x] + \cdots, c_t + \epsilon[c_t] + \cdots, \\ &\qquad c_{xx} + \epsilon[c_{xx}] + \cdots, c_{xt} + \epsilon[c_{xt}] + \cdots, c_{tt} + \epsilon[c_{tt}] + \cdots) \end{aligned} \tag{5}$$

Expanding the right member of the (5), we have

$$\begin{aligned} &F(c, x, t, c_x, c_t, c_{xx}, c_{xt}, c_{tt}) = F(c, x, t, c_x, c_t, c_{xx}, c_{xt}, c_{tt}) + \\ &\epsilon(F_c\gamma + F_x\xi + F_t\tau + F_{c_x}[c_x] + F_{c_t}[c_t] + F_{c_{xx}}[c_{xx}] + F_{c_{xt}}[c_{xt}] + F_{c_{tt}}[c_{tt}]) + \cdots \end{aligned}$$

and so the *invariance condition* of the equation is

$$F_c\gamma + F_x\xi + F_t\tau + F_{c_x}[c_x] + F_{c_t}[c_t] + F_{c_{xx}}[c_{xx}] + F_{c_{xt}}[c_{xt}] + F_{c_{tt}}[c_{tt}] = 0$$

If the solution is invariant under the group of transformations, the solution must map into itself, i.e.

$$c^* = c(x^*, t^*) = c(x + \epsilon\xi, t + \epsilon\tau) \tag{6}$$

In terms of the transformation functions, eq. (6) can be written as.

$$c(x + \epsilon\xi, t + \epsilon\tau) = c(z, t) + \epsilon\gamma(z, t, c) + O(\epsilon^2) \tag{7}$$

Expanding the left-hand side of eq. (7) and equating the coefficients of ϵ, we get

$$\gamma = c_x\xi + c_t\tau \tag{8}$$

The eq. (8) is the *invariant surface condition*. We can call the eq. (7) also as *invariance condition of the solution*. The general solution of eq. (7) is obtained by solving the characteristic equation

$$\frac{\mathrm{d}x}{\xi} = \frac{\mathrm{d}t}{\tau} = \frac{\mathrm{d}c}{\gamma} \tag{9}$$

In principle, the general solution of eq. (8) can be found. It involves two constants, one becomes the independent variable $\xi(c, x, t)$, called the *similarity variable* and the other is the dependent variable $f(\xi)$. We obtain the *similarity solution*

$$c = \mathcal{F}(t, x, \xi, f(\xi)) \tag{10}$$

with the dependence of $\mathcal{F}$ on x, t and the arbitrary function $f(\xi)$ known explicitly. Substitution of (10) into (1) results an ordinary differential equation for the function $f(\xi)$.

The application of the group analysis, also for modest systems of differential equations, involves long and tedious computations. Symbolic packages are very useful for such computations.

3 Thermal boundary layer equations

If the properties c_p, μ and k can be assumed independent of temperature and the pressure gradient in the x-direction is different from zero, the thermal boundary layer equations for two-dimensional incompressible steady fluid flow are (see Schlichting [10], Schlichting and Gersten [11] and Rosenhead [12]):

$$\begin{cases} \frac{\partial\Psi}{\partial y}\frac{\partial^2\Psi}{\partial x\partial y} - \frac{\partial\Psi}{\partial x}\frac{\partial^2\Psi}{\partial y^2} &= \nu\frac{\partial^3\Psi}{\partial y^3} + U(x)\frac{\mathrm{d}U(x)}{\mathrm{d}x} \\ \\ \frac{\partial\Psi}{\partial y}\frac{\partial T}{\partial x} - \frac{\partial\Psi}{\partial x}\frac{\partial T}{\partial y} &= \frac{k}{\rho c_p}\frac{\partial^2 T}{\partial y^2} + \frac{\nu}{c_p}\left(\frac{\partial^2\Psi}{\partial y^2}\right)^2 - \frac{1}{c_p}\frac{\partial\Psi}{\partial y}U(x)\frac{\mathrm{d}U(x)}{\mathrm{d}x} \end{cases} \tag{11}$$

where:

- $\Psi(x,y) \Rightarrow$ Stream function ($u = \frac{\partial\Psi}{\partial y}, v = -\frac{\partial\Psi}{\partial x}$);
- $U(x) \Rightarrow$ Outer flow velocity;
- $T(x,t) \Rightarrow$ Fluid temperature;
- $\nu \Rightarrow$ Kinematic viscosity;
- $k \Rightarrow$ Thermal conductivity;
- $c_p \Rightarrow$ Specific heat at constant pressure;
- $\rho \Rightarrow$ Density.

The boundary conditions for eqs. (11) are:

$$\begin{cases} u = v = 0 & \text{at} \quad y = 0 \\ u = U(x) & \text{as} \quad y \to \infty \\ T = T_w & \text{at} \quad y = 0 \\ T = T_\infty & \text{as} \quad y \to \infty \end{cases}$$

where :

- $T_w \Rightarrow$ Wall temperature
- $T_\infty \Rightarrow$ Free stream temperature

Consider the following one-parameter Lie group of transformations in order to leave invariant the eqs. (11):

$$\begin{cases} x' = x + \epsilon\xi^1(x,y,\Psi,T) + \cdots \\ y' = y + \epsilon\xi^2(x,y,\Psi,T) + \cdots \\ \Psi' = \Psi + \epsilon\eta(x,y,\Psi,T) + \cdots \\ T' = T + \epsilon\tau(x,y,\Psi,T) + \cdots \end{cases} \tag{12}$$

The invariance conditions for eqs. (11) give us the following equations for the infinitesimal generators of the transformations (12) and for the free-stream flow

velocity $U(x)$:

$$\begin{cases} \xi_y^1 = \xi_\Psi^1 = \xi_T^1 = \xi_\Psi^2 = \xi_T^2 = \eta_x = \eta_y = \eta_T = \tau_y = \eta_\Psi = 0 \\ \xi_{yy}^2 = \xi_{xy}^2 = \eta_{\Psi\Psi} = \tau_{TT} = 0 \\ \xi_y^2 + \eta_\Psi - \xi_x^1 = 0 \\ 2(\xi_y^2 - \eta_\Psi) + \tau_T = 0 \\ -UU_{xx}\xi^1 - 3UU_x\xi_y^2 + UU_x\eta_\Psi - U_x^2\xi^2 = 0 \\ -UU_{xx}\xi^1 - UU_x\xi_y^2 - UU_x\eta_\Psi + \tau_t UU_x - \xi^1 U_x^2 + \frac{\tau_x}{\nu} = 0 \end{cases} \tag{13}$$

The system (13) admits the following solution:

$$\begin{cases} \xi^1 = (A + C)x + D \\ \xi^2 = Ay + M(x) \\ \eta_{=} C\Psi + B \\ \tau = 2(C - A)T + R \end{cases}$$

where A, B, C, D, R are arbitrary constants and $M(x)$ is an arbitrary but regular function of x. For the free stream flow velocity we obtain the following differential equation [13]:

$$(3A - C)\frac{\mathrm{d}U^2}{\mathrm{d}x} + ((A + C)x + D)\frac{\mathrm{d}^2U^2}{\mathrm{d}x^2} = 0 \tag{14}$$

We performed the calculations of the generators of transformations group on a PC using the REDUCE and MATHEMATICA packages.

Each of the constants A, B, C, D, R and the function $U(x)$ can be taken in turn to generate a similarity form for the solution.

4 Similarity solutions

Let us look at particular similarity solutions.

4.1 $C \neq A = 1, D = B = R = M = 0, A + C \neq 0$

The characteristic equations are:

$$\frac{\mathrm{d}x}{(1 + C)x} = \frac{\mathrm{d}y}{y} = \frac{\mathrm{d}\Psi}{C\Psi} = \frac{\mathrm{d}T}{2(C - 1)T} \tag{15}$$

It is possible to have the following invariants

$$\begin{cases} I_1 = yx^{-\frac{1}{1+C}} \\ I_2 = \Psi x^{-\frac{C}{1+C}} \\ I_3 = Tx^{2\frac{1-C}{1+C}} \end{cases} \tag{16}$$

The invariant $I_1 = yx^{-\frac{1}{1+C}}$ is the similarity variable ξ and the similarity solutions are:

$$\begin{cases} \Psi = x^{\frac{C}{1+C}} f(yx^{-\frac{1}{1+C}}) \\ T = x^{-2\frac{1-C}{1+C}} \theta(yx^{-\frac{1}{1+C}}) \end{cases} \tag{17}$$

The functions $f(\xi)$ and $\theta(\xi)$ satisfy the following equations obtained from eqs. (11)

$$\begin{cases} \frac{1-C}{1+C} f'^2 + \frac{C}{1+C} f f'' + \nu f''' + \alpha = 0 \\ 2\frac{C-1}{1+C} f'\theta - \frac{C}{1+C} f\theta' - \frac{k}{\rho c_p}\theta'' - \frac{\nu}{c_p} f''^2 + \frac{\alpha}{c_p} f' = 0 \end{cases} \tag{18}$$

where α is a constant.

The free stream flow velocity, considering eq. (14), is solution of the equation:

$$UU_x = \alpha x^{\frac{C-3}{C+1}}$$

We have

$$U^2 = U_l^2 \left(\frac{x}{l}\right)^{2n} + U_0^2 \tag{19}$$

if:

$$C = \frac{1+n}{1-n} \qquad \text{and} \qquad U_l^2 = n\alpha l^{2n} \qquad (n \neq 1)$$

The eq. (19) correspond to the flow past a wedge, in the neighborhood of the leading edge [11].

In particular, if $C = 0$ $(n = -1)$ we obtain:

$$U^2 = U_l^2 \left(\frac{l}{x}\right)^2 + U_0^2$$

(flow in converging or diverging channel [11]).

4.1.1 Flow past a wedge, in the neighborhood of the leading edge

If $U_0 = 0$, we have:

$$U = U_l \left(\frac{x}{l}\right)^n$$

In this case the component u of the velocity is:

$$u = x^n f(yx^{\frac{n-1}{2}})$$

and the boundary conditions become

$$\begin{cases} f(0) & = & f'(0) = 0 \\ f'(\infty) & = & \frac{U_l}{l^n} \\ \theta(0) & = & \theta_0 \\ \theta(\infty) & = & 0 \end{cases}$$

If we assume $C = \frac{1}{2}$, then $n = -\frac{1}{3}$ [11]. The first of eqs. (18) become:

$$\frac{1}{3}f'^2 + \frac{1}{3}ff'' + \nu f''' - 3U_l^2 l^{\frac{2}{3}} = 0 \tag{20}$$

The eq. (20) is analytically integrable. Integrating the equation twice and using the boundary conditions, we obtain:

$$K\xi + \frac{1}{6}f^2 + \nu f' - \frac{3}{2}U_l^2\xi^2 l^{\frac{2}{3}} = 0 \tag{21}$$

The eq. (21) is a Riccati equation [14] and its solution is:

$$f(\xi) = \left\{ 3\sqrt{2lU_l^3\nu}\left(K^2 - 18lU_l^3\nu\right) C_1 \mathrm{H}_{\frac{A^2}{36lU_l^3\nu}-\frac{3}{2}}\left(\frac{3l^{\frac{2}{3}}U_l^2\xi - K}{3\sqrt{2lU_l^3\nu}}\right) + \left(K - 3l^{\frac{2}{3}}U_l^2\xi\right) \times \right.$$

$$\left[18lU_l^3\nu \left(C_1 \mathrm{H}_{\frac{K^2}{36lU_l^3\nu}-\frac{1}{2}}\left(\frac{3l^{\frac{2}{3}}U_l^2\xi - K}{3\sqrt{2lU_l^3\nu}}\right) + {}_1\mathrm{F}_1\left(\frac{\left(K - 3l^{\frac{2}{3}}U_l{}^2\xi\right)^2}{18lU_l{}^3\nu}; \frac{1}{4} - \frac{K^2}{72lU_l{}^3\nu}, \frac{1}{2}\right)\right) + \right.$$

$$\left.\left.\left(K^2 - 18lU_l{}^3\nu\right) {}_1\mathrm{F}_1\left(\frac{\left(K - 3l^{\frac{2}{3}}U_l{}^2\xi\right)^2}{18lU_l{}^3\nu}; \frac{5}{4} - \frac{K^2}{72lU_l{}^3\nu}, \frac{3}{2}\right)\right]\right\} \times$$

$$\left\{ 18l^{\frac{4}{3}}U_l^4\nu \left[C_1 \mathrm{H}_{\frac{K^2}{36lU_l^3\nu}-\frac{1}{2}}\left(\frac{3l^{\frac{2}{3}}U_l^2\xi - K}{3\sqrt{2lU_l^3\nu}}\right) + {}_1\mathrm{F}_1\left(\frac{\left(K - 3l^{\frac{2}{3}}U_l{}^2\xi\right)^2}{18lU_l{}^3\nu}; \frac{1}{4} - \frac{K^2}{72lU_l{}^3\nu}, \frac{1}{2}\right)\right]\right\}^{-1}$$

where ${}_1\mathrm{F}_1(-;-,-)$ is the Kummer confluent hypergeometric function and $\mathrm{H}_-(-)$ the Hermite function; the constant K and C_1 are determined by boundary conditions.

4.1.2 Flow converging or diverging channel

If $C = 0$ and $U_0 = 0$, then we have $n = -1$:

$$U = U_l\frac{l}{x}$$

The component u of the velocity is:

$$u = x^{-1}f'(yx^{-1})$$

the boundary conditions become

$$\begin{cases} f(0) &= f'(0) = 0 \\ f'(\infty) &= U_l l \\ \theta(0) &= \theta_0 \\ \theta(\infty) &= 0 \end{cases}$$

The first of eqs. (18) becomes:

$$f'^2 + \nu f''' - U_l^2 l^2 = 0 \tag{22}$$

The eq. (22) is analytically integrable.

The transformation: $h(\xi) = f'(\xi)$ reduces eq. (22) to the equation:

$$h^2 + \nu h'' - U_l^2 l^2 = 0 \tag{23}$$

The eq. (23) is a Painlevé type equation (see [15]); its solution is expressed in term of Weierstrass elliptic function $\wp$. The equation eq. (23) is equivalent to

$$(h')^2 = \frac{2}{\nu}(lU_l)^2 h - \frac{2}{3\nu}h^3 - H$$

The substitution $h(\xi) = -6\nu z(\xi)$ leads to the equation:

$$(z')^2 = 4z^3 - \frac{(lU_l)^2}{3\nu^2}z - H$$

The solution of this equation is:

$$z(\xi) = \wp\left(\xi - C_1; \frac{(lU_l)^2}{3\nu^2}, H\right)$$

where $\wp(-; g_2, g_3)$ is the Weierestrass elliptic function.

The solution of eq. (22) is therefore:

$$f(\xi) = 6\nu\zeta\left(\xi - C_1; \frac{(lU_l)^2}{3\nu^2}, H\right) + K$$

where $\zeta(-; g_2, g_3)$ ($\zeta' = -\wp$) is the Weierestrass ζ-function (see [16]), the constant H, C_1 and K are determined by boundary conditions. It is worthy of remark that for $\Delta = g_2^3 - 27g_3^2 = 0$ and for particular values of g_2 and g_3, the Weierestrass $\wp$-function degenerates to the hyperbolic function [16]; in this case we have the Pohlhausen solution [10].

4.2 $A = D = B = R = 0, M \neq 0, C \neq 0$

From the characteristic equations we have:

$$\begin{cases} \Psi = xf(y - h(x)) \\ T = x^2\theta(y - h(x)) \end{cases} \tag{24}$$

where $h(x)$ is an arbitrary function. The similarity equations are:

$$\begin{cases} f'^2 - ff'' - \nu f''' - \alpha = 0 \\ 2f'\theta - f\theta' - \frac{k}{\rho c_p}\theta'' - \frac{\nu}{c_p}f''^2 + \frac{\alpha}{c_p}f' = 0 \end{cases} \tag{25}$$

where α is a constant. If we put

$$\alpha = \frac{U_l^2}{l^2}$$



the free stream flow velocity is:

$$U^2 = \frac{U_l^2}{l^2}x^2 + U_0^2$$

If

$$U_0 = 0$$

we have

$$U = U_l\frac{x}{l}$$

This is the flow with forward or rear stagnation point [12]. In this case the component u of the velocity is ($h(x) = 0$):

$$u = xf'(y)$$

and the boundary conditions become

$$\begin{cases} f(0) & = & f'(0) = 0 \\ f'(\infty) & = & \frac{U_l}{l} \\ \theta(0) & = & \theta_0 \\ \theta(\infty) & = & 0 \end{cases}$$

4.3 $A + C = B = R = M = 0, D = 1$

In this case:

$$\begin{cases} \Psi = \mathrm{e}^{Cx} f(y\mathrm{e}^{Cx}) \\ T = \mathrm{e}^{4Cx}\theta(y\mathrm{e}^{Cx}) \end{cases} \tag{26}$$

The similarity solutions are

$$\begin{cases} 2Cf'^2 - Cff'' - \nu f''' - \alpha = 0 \\ 4Cf'\theta - Cf\theta' - \frac{k}{\rho c_p}\theta'' - \frac{\nu}{c_p}f''^2 + \frac{\alpha}{c_p}f' = 0 \end{cases} \tag{27}$$

where α is a constant. The free stream flow velocity is:

$$U^2 = U_l^2 + \frac{\alpha}{2C}\left(\mathrm{e}^{4Cx} - \mathrm{e}^{4Cl}\right)$$

If we assume:

$$U_l = \frac{\alpha}{2C}\mathrm{e}^{4Cl}$$

then

$$U = \sqrt{\frac{\alpha}{2C}}\mathrm{e}^{2Cx}$$

In this case [10] the component u of the velocity is:

$$u = \mathrm{e}^{2Cx} f'(y\mathrm{e}^{Cx})$$

and the boundary conditions become

$$\begin{cases} f(0) & = & f'(0) = 0 \\ f'(\infty) & = & \sqrt{\frac{\alpha}{2C}} \\ \theta(0) & = & \theta_0 \\ \theta(\infty) & = & 0 \end{cases}$$

4.4 $D = B = R = M = 0, A = C = 1, U =$ constant

The stream function and the temperature are:

$$\begin{cases} \Psi = x^{\frac{1}{2}} f(yx^{-\frac{1}{2}}) \\ T = \theta(yx^{-\frac{1}{2}}) \end{cases} \tag{28}$$

The functions f and θ satisfy the following equations:

$$\begin{cases} \frac{1}{2} f f'' + \nu f''' = 0 \\ \frac{1}{2} f\theta' + \frac{k}{\rho c_p}\theta'' + \frac{\nu}{c_p} f''^2 = 0 \end{cases} \tag{29}$$

This solution corresponds to semi-infinity flat plat (Blasius solution).

5 Conclusions

Therefore we can be sure that the group analysis, compared to dimensional analysis or *ad hoc* position, enable to have with methodical work similarity solutions: all the solutions derived in standard text [10], [11] and [12] are therefore group invariant solutions.

References

[1] S. Lie, *Theorie der Transformation Gruppen*, Chelsea, 1974.
[2] G. W. Bluman and J. D. Cole, *Similarity Methods for Differential Equations*, Springer-Verlag, 1974.
[3] W. F. Ames, *Nonlinear Partial Differential Equations*, Academic Press, 1965-1972.
[4] L. V. Ovsiannikov, *Group analysis of differential equations*, Academic Press, 1982.
[5] G. W. Bluman and S. Kumei, *Symmetries and Differential Equations*, Springer-Verlag, 1989.
[6] P. O. Olver, *Applications of Lie Groups to Differential Equations*, Springer, 1993.
[7] P. Barrera and T. Brugarino, *Similarity Solutions of the Generalized Kadomtsev Petviashvili-Burgers Equations*, Il Nuovo Cimento B, **92**, 2, (1986), 142–156.



[8] P. Barrera and T. Brugarino, *Group analysis and similarity solutions of the compressible boundary layer equations*, Meccanica, **24** (1989), 211–215.
[9] P. Barrera, T. Brugarino and L. Pignato, *Solutions for a Diffusion Process in non Homogeneous Media*, Il Nuovo Cimento B, **116**, 8, (2001), 951–958.
[10] H. Schlichting, *Boundary Layer Theory*, Mc Graw-Hill, 1968.
[11] H. Schlichting and K. Gersten *Boundary Layer Theory*, Springer-Verlag, 2000.
[12] L. Rosenhead, *Laminar Boundary Layery* Oxford University Press, 1963.
[13] P. Barrera, T. Brugarino, *Analisi gruppale delle equazioni dello strato limite*, IX Congresso AIDAA, 1987.
[14] A. D. Polyanin and V. F. Zaitsev *Handbook of Exact Solutions for Ordinary Differential Equations*, CRC Press, 1995.
[15] H. T. Davis, *Introduction to Nonlinear Differential and Integral Equations*, Dover Publications, 1962.
[16] M. Abramowitz and I. Stegun, *Handbook of Mathematical Functions*, Dover Publications, 1972.



This page intentionally left blank

Section 7
Multiphase flow

This page intentionally left blank

Cavity length and re-entrant jet in 2-D sheet cavitation

I. Castellani
Department of Mechanical and Structural Engineering, University of Trento, Italy.

Abstract

Some features of hydrodynamic cavitation have been investigated in this experimental study to understand the role of the re-entrant jet in the formation of sheet (or cloud) 2-D cavitation. Velocity profiles, frequency contents of the cavity, pressure coefficients and pressure pulses spectrum have been measured in isothermal conditions. Physical quantities of interest were found to be greatly affected by the rate of pressure increase. Flow separation, surge instability, hysteresis, rebounds, splashes, choking and re-entrant jets have been observed. A correlation has been found between the cavitation number and the cavity length. The frequency content was detected by a new method that produces a spectrum at high Strouhal numbers. A large band without a peak was observed for the highest frequencies, e.g. greater than 1000 Hz. The role of the re-entrant jet in breaking the cavity was not found to be as much important as it is currently believed. The present results, obtained through thousands of experiments, may be of interest to predict cavity formation.
Keywords: cavitation, re-entrant jet, frequency content, laser measurements, pressure pulses, wall effects, choke, hysteresis, rebound, splash.

1 Introduction

The present work originates from previous literature results about sheet-cloud 2-D cavitation, e.g. Astolfi *et al.* [8], Franc and Lauterborn [9], Lindau [12] and Sato and Shimojo [14], who discussed features such as periodicity, re-entrant jet, pressure gradient, rebound, wall effect and morfology.

The experimental apparatus is described at length in Castellani [15, 16]. It comprises a high speed water tunnel, a centrifugal pump (120 l/min and 25 m maximum head) and a vacuum pump. The temperature was always kept constant at



WIT Transactions on Engineering Sciences, Vol 52, © 2006 WIT Press
www.witpress.com, ISSN 1743-3533 (on-line)
doi:10.2495/AFM06034

20°C and the pressure could rise up to 7 bar. The test chamber is a perspex Venturi channel, where a perspex hydrofoil is allocated on the floor, at the minimum area section (*throat*) of the chamber. The x-axis is horizontal and oriented streamwise; the y-axis is vertical, upward; the z-axis follows the left-handed cartesian rule. The channel width (in z direction) is 80 mm, while the throat height is 9.8 mm. The undisturbed flow reference station, labelled "0", has been chosen for computing velocity, static pressure, cavitation index and pressure coefficient. The chord length of the hydrofoil is $c = 44.42$ mm at a fixed angle of attack $\alpha = 5°$. The hydrofoil has a spanwise groove, located at the throat section, which helps in fixing exactly the starting point of the cavity. The volumetric flow rate Q, the static pressure p_0 and the temperature T could be independently controlled.

The relevant nondimensional parameters are:

(i) the cavitation index σ_0, where σ_{0i} stands for the inception index;
(ii) the pressure coefficient C_p;
(iii) the Strouhal number St, based on the double of the cavity length $2L$.

All of the experiments were performed under steady state conditions. The cavitation stages were always obtained by decreasing the pressure at given velocities. The velocity fields was measured by the LDA technique. The wall effect was taken into account performing spanwise measurements: a distance from the wall $z = 5$ mm was found to be sufficient to overcome the boundary layer influence.

At a given V_0, the static pressure p_0 was reduced until the cavitation inception (σ_{0i}) was reached, then it was further reduced step by step, recording the cavitation index for each condition, until $L/c \simeq 0.66$. The pressure was then increased until the cavitation disappeared. This cycle was repeated five times at any tested velocity to detect a possible hysteresis.

The frequency measurements of cavity were performed in three ways:

(i) by a high speed video camera of the *scattered* (indirect) or direct laser light;
(ii) by a mean speed acquisition of the whole cavity;
(iii) by a piezoresistive pressure transducer (180 kHz response and 140 bar), allocated into the hydrofoil.

The acquisition interval is about 5.5 μs and may detect the *rebound* and the *splash* phenomena.

The speed of the camera was 2900 fps, with a pixel matrix of 64×64, i.e. a visual field of 2×2 mm, resulting in a *local* measurement. On each series a FFT was performed and three frequency peaks were found: very low (1-2 Hz), mean (about 40 Hz) and high (from 100 to 1300 Hz). Among the physical quantities involved, it was calculated that the maximum relative error occurred for the cavitation index (about 2.6%). The repeatability of the present experiments was verified by three different methods.

2 Experimental results

Interested readers are referred to Castellani [15, 16] for the comprehensive presentation of results.

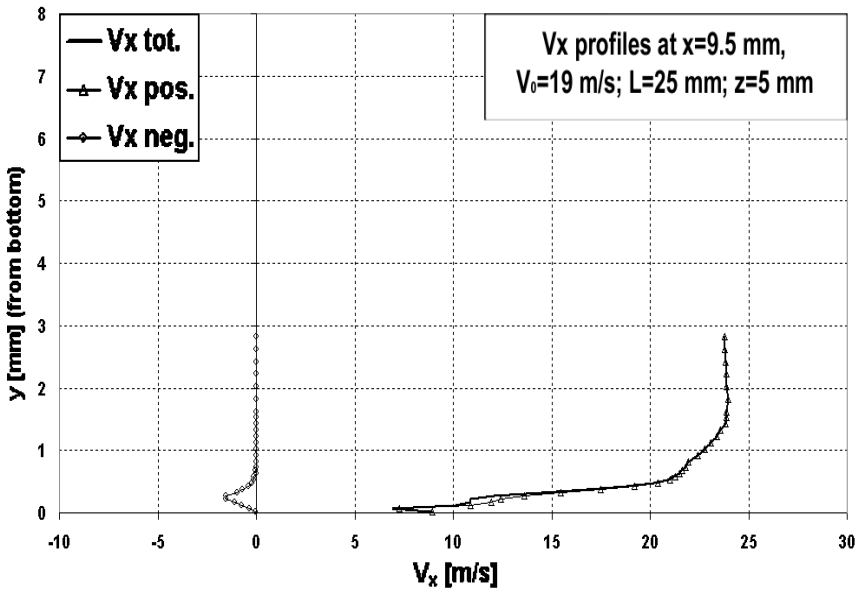


Figure 1: Negative V_x for $L/c = 0.56$ and $V_0 = 19$ m/s.

The boundary layer detached at $x/c \simeq 0.6$ in any tested condition. It has also been numerically predicted. The experiments with cavitation were carried out at $L/c = 0.34$ and 0.56, $V_0 = 19$, 21 and 29 m/s. Due to wall effects, it was not possible to produce a greater cavity length. The flow was chocked at $L/c \simeq 0.79$. The transitional cavitation was observed for $L/c \geq 0.5$; beyond this limit, surge cavitation appeared. The downstream turbulent transition is indicated by streaks on the cavity surface. The thickness of the cavity was deduced by differences between local and mean velocities and by the very high RMS of V_x.

At $x/c \simeq 0.5$, flow detachment is seen at the end of the cavity, where vapor is created and, for $L/c > 0.5$, clouds. This is clear from fig. 1. Remarkably enough, this phenomenon occurs only at this location and *does not* depend on the cavity length L/c. For $x/c = 0.5$ flow detachment is observed.

The profile shape seems to depend more on V_0 than on σ_0, suggesting that σ_0 alone may not wholly describe the phenomenon. The potential flow hypothesis has been verified by comparing the local measured velocity at the top border of the cavity with the theoretical one (Bernoulli's theorem).

A *negative* V_x have been measured for $L/c = 0.56$, starting from $x/c = 0.21$: a clear evidence of the re-entrant jet (fig. 1). The negative V_x profile is maximum at ~ 0.3 mm from the hydrofoil. This does not happen in other downstream stations, possibly indicating the upward rising of the jet.

The experiments to relate σ to L were carried out at constant velocity V_0. The tested range was $\sigma_0 \in [0.72; 0.88]$. It was not possible to decrease σ_0 below 0.72

(corresponding roughly to $L/c = 0.68$) because of choking. The surge instability produces great cavity variations for small variations in σ_0 and was always detected for $L/c > 0.67$. The wall effect caused this instability to be active for L/c *less* than the literature value 0.75 (Watanabe [11]).

Incipient (i) and desinent (d) cavitation were investigated at $V_0 = 17$, 19, 21, 24, 26 and 28 m/s. The difference between σ_{0i} and σ_{0d} was strongly affected by the time elapsed to vary the parameters (p_0, V_0, ...): the slower the variation, the greater the difference. Generally speaking, the diagrams $\sigma_0 - L/c$ show an almost linear decrease of σ_0 and also a possible hysteretic behaviour. However experimental errors do not allow a doubtless interpretation for that matter.

The wall effect played an important role: in fact the variations of L, p_0 and V_0 were not simultaneous. The decrease of V_0 follows an increase of p_0, which in turn causes a decrease of L, in a self-induced cycle.

The pressure coefficient C_p was measured along the hydrofoil at $V_0 \in [15; 28]$ m/s and $L/c \in [0; 0.8]$. In *ideal* conditions, the minimum pressure during cavitation would be p_v: whence $\sigma_i = -C_{p,min}$. As a matter of fact, $p_{min} \leq p_v$ typically, resulting in $\sigma_i \leq -C_{p,min}$. This parameter is useful to predict the starting location of the cavity and represents a limit for σ_i. It becomes important to know the difference between σ_i and $C_{p,min}$ because it shows the difference between theoretical and experimental conditions.

The diagrams C_{P0} vs. x/c show an initial flat region, roughly corresponding to the cavity attached to the wall; then C_{p0} increases. It appears that the pressure coefficient is useful to describe the *fixed part* of the cavity. The flat region is actually shorter than the visually observed (by stroboscopic light, 2200 RPM) cavity length and this indicates that the re-entrant jet travels upstream under the cavity so that the pressure gauges are exposed directly to pure jet water and not to the vapor-water mixture of the cavity. An important result is that *the extension of the flat region does not depend on the mean flow velocity*.

The greatest difference between cavitating and non-cavitating flow has been observed for $L/c > 0.5$.

The difference $\sigma_0 - (-C_p)$ was plotted vs. x/c. In the flat region, this value is about 0.1 and it indicates that it is always $p_{min} > p_v$. An useful graphical compact representation is showed in fig. 2 which shows an upper limit for C_p depending on cavity length and x-location.

Three distinct frequencies were detected by means of a *new* non-intrusive method based on the recording of the laser scattered light at cavity closure: a laser beam was focused on the cavity surface and the scattered (indirect) light was recorded from a direction normal to the beam. Another setting made the beam to incide directly on the camera. The tested velocities were in the range $[15; 29.1]$ m/s, while $L/c = 0.3, 0.4$ and 0.5. This phenomenon does not pertain to the bubble collapse, but to the *local* interface vibration (indirect beam configuration) and to the vapour clouds motion (direct beam configuration).

There was not a well defined peak at the highest frequencies, but rather a *frequency band*, sometime as large as 400 Hz.

The time scale for the mean flow to travel the distance L can be defined as



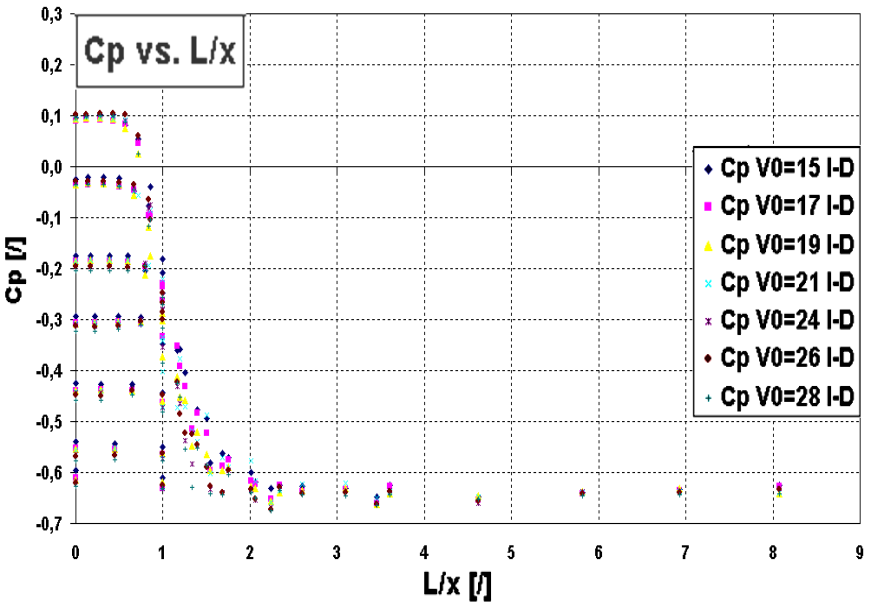


Figure 2: C_p vs. L/x for different velocities.

$\tau := L/V$, whereas $1/f$ is the time scale for the cavity to travel the distance L twice (down- and upstream). The proposed Strouhal number is herein defined with $2L$ as the length scale:

$$St := \frac{2fL}{V} = \frac{f}{1/2\tau} \tag{1}$$

The literature value for the vortex shedding behind a cylinder ranges around $St \approx 0.3$.

The very low frequency peaks (2-3 Hz) are not typical of the cavity, and depend on the tunnel geometric configuration. Following Franc *et al.* [9], it can be defined a *system instability*. The same is true for the 40 Hz frequency, while the 100 Hz or greater frequencies seem quite specific.

The frequency content does not appear to depend upon L/c, but only on V_0. fig. 3 shows this dependence for St related to the peak and to the starting (*min*) and ending (*max*) frequency of each peak. St is always decreasing with σ_0. The highest frequency band may possibly indicate a chaotic interaction of different phenomena, where the spectrum is partly the sum and partly the convolution. Peaks were even observed at 200-300 Hz and at 1200-1300 Hz. According to Kjeldsen [10], this is supposed to be the range governed by the re-entrant jet ($\sigma_0/2\alpha > 4$). St attains values up to 4, an information not reported in the literature.

The instantaneous cavity length and thickness have also been measured. It is a *global* measure. The minimum recorded length is clearly increasing with V_0, fig. 4,

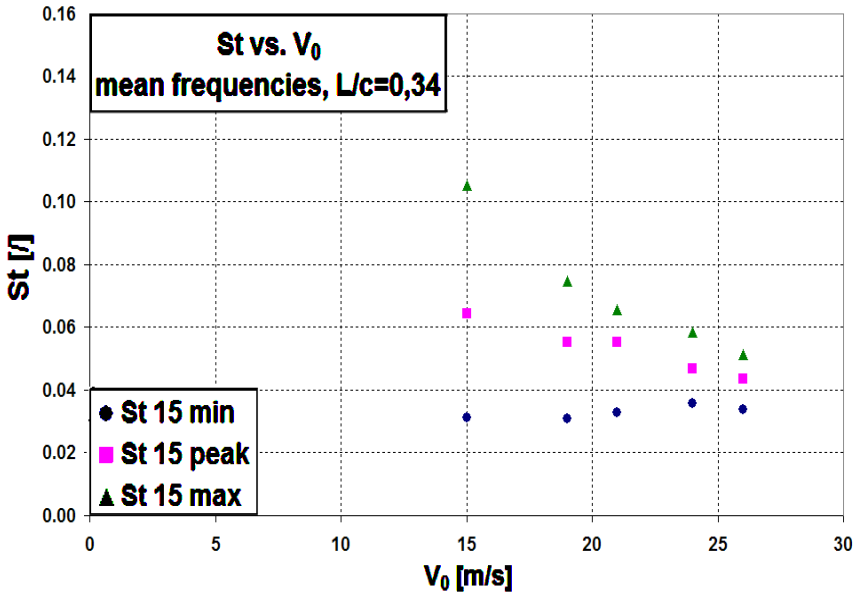


Figure 3: Strouhal number trend with velocity.

indicating that the length of the fixed part of the cavity is proportional to the length of the cavity. This fact may prevent *the re-entrant jet to reach the upstream end of the cavity for long cavities*. This is probably due to the low pressure gradient because of the wall effect. There are differences between this speculation and the results of Franc *et al.* [4, 5] and Kawanami *et al.* [6].

This result is confirmed also by the percentage of zero instantaneous thicknesses recorded for different velocities and lengths: for low velocities the cavity disappears, while this is not true at higher velocities.

St referred to L_c is increasing with V_0 and L/c. If we consider the fixed part of the cavity, given by the minimum of L_c, we obtain an increasing trend with V_0 for all of the cavity lengths. This leads to an important consideration. If, according to Kawanami [6], L_c is the cavity length, L_{cut} is the *fixed* cavity length and, following Franc [5], $\beta := V_j/V_0 = 0.84$, where V_j is the velocity of the re-entrant jet, it may be deduced that:

$$\frac{fL_c}{V} = \frac{fL_{cut}}{V} + \beta\frac{T_j}{T_c} \rightarrow \frac{T_j}{T_c} = \frac{L_c - L_{cut}}{\beta V}$$

If $V = V_c$, where $V_c := \sqrt{1+\sigma_0}$ (Bernoulli), then:

$$\frac{T_j}{T_c} = \frac{L_c - L_{cut}}{0.84V_0\sqrt{1+\sigma_0}} \tag{2}$$

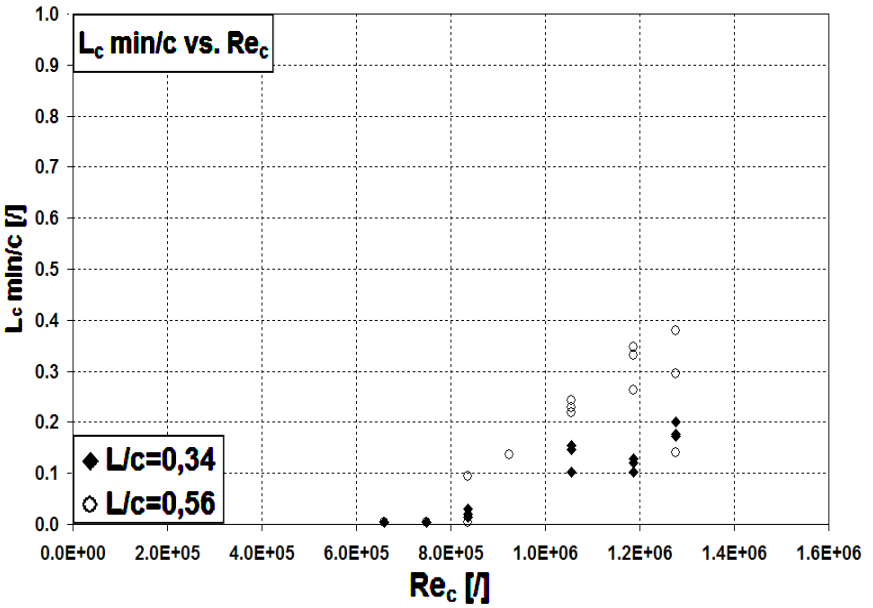


Figure 4: Minimum recorded cavity length for different Re.

Since the ratio T_j/T_c decreases when V_0 increases, the time needed for the re-entrant jet to travel upstream, compared with the time of cavity oscillation (f^{-1}), decreases. This is reasonable because that ratio is acting as a Strouhal number of the *mobile* part of the cavity, scaled to β. The travel time of the re-entrant jet increases less than the corresponding increase of the cavity break time, so that the jet breaks shorter parts of the cavity. That means also that *the cavity rebuilding velocity increases less than the velocity of the re-entrant jet*.

As a result, the role of the re-entrant jet in breaking the cavity is not as much important as it is commonly thought. No correlation between frequency peaks and flow velocity have been detected.

As for the instantaneous pressure peaks, the experiments were performed at $V_0 \in [18.5; 29]$ m/s and $L/c = 0.56$ and the measurements were taken at $x/c \equiv L/c$. Not only a decrease of σ_0 but also an increment of V_0 can produce surge instability, because of wall effects.

Analyzing directly the shape of the time series, fig. 5, it can be noticed (for low velocity, i.e. 18-24 m/s) some "valley", 10-20 ms wide, with high peaks inside. Outside the valley there were generally no peaks. These valleys represent the transit of the cavity border, or vapour clouds, while the peaks represent the pressure pulses given by bubbles implosions. Actually, the peak has a basis ~ 1 ms wide in time and shows typically four damped oscillations. Moreover each sub-peak of this oscillation has often two spires, at an interval of some 0.05 ms. These results are in agreement with the literature: the damped oscillation is related to the *rebound*,

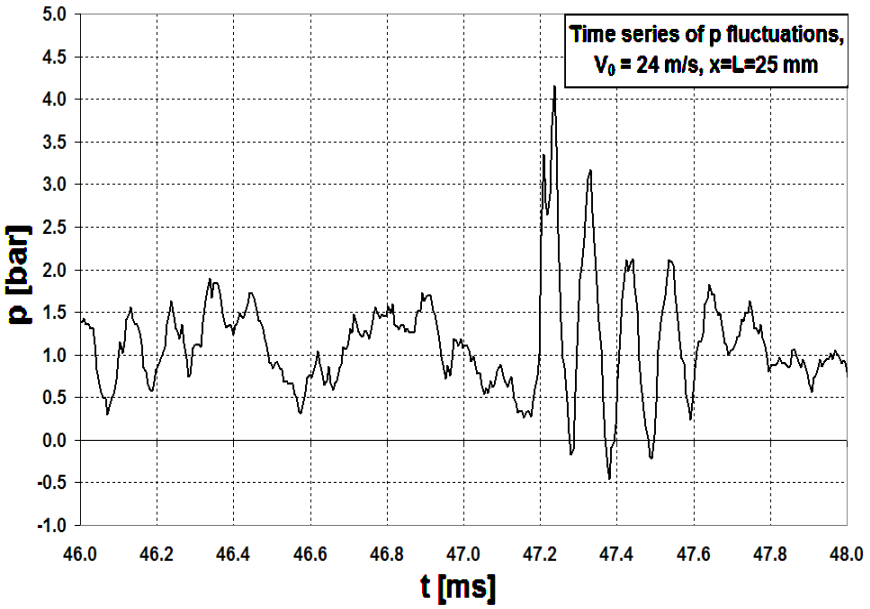


Figure 5: Visualization of *rebound* and *splash* phenomena.

and the double spire can be interpreted as the *splash* phenomenon, observed in Tong *et al.* [7].

The following parameters have been calculated:

$$I1 := \frac{1}{t}\sum_{i=1}^{N} n_i a_i \tag{3}$$

which is an index of the cavitation intensity, and

$$A1 := \frac{\sum_{i=1}^{N} n_i a_i}{\sum_{i=1}^{N} n_i} \tag{4}$$

which is an index of the average width of the peak, where n_i is the peaks number in the *i*-class and a_i is the *i*-class width. These parameters are both clearly increasing with V_0 and this indicates that, for the same σ_0, the cavity is stronger and more dangerous for higher velocities.

3 Conclusions

Sheet cavitation was observed, with a surge behaviour for high L/c, transitional behaviour for $L/c = 0.56$ and choke for $L/c = 0.79$. A great influence of the downstream pressure gradient was observed and $x/c \simeq 0.5$ was seen to be a threshold between two cavitation types (sheet-cloud) and a point of flow separation. The

velocity profile was found to depend more upon V_0 than upon σ_0, so that the cavitation number cannot be exhaustive. The slowness of the parameter variation was found to dramatically affect the incipient cavitation. The wall effect was found to have a great importance. The cavitation number increases slowly with V_0 and only for $V_0 > 25$ m/s. A limit point was found again for $L/c = 0.55$. The observed negative velocities indicates the presence of the re-entrant jet. The extension of the constant C_{p0} region (attached and fixed cavity) was found not to be influenced by the velocity. The cavity actual pressure p_c was always greater than p_v.

The frequency content of cavitation was spread on three regions: very low (2-3 Hz), low (about 40 Hz), possibly related to a system instability, and high (up to 1300 Hz), which produces Strouhal numbers greater than those detected in the literature. A *new* method of cavity vibration measurement is proposed that is based on recording the *scattered laser light* at the cavity interface. The velocity of cavity rebuilding is not wholly controlled by the re-entrant jet, as eqn. (2) shows, suggesting that the role of the re-entrant jet in breaking the cavity should be partly reconsidered.

Three different methods of frequency detection have been compared and found in agreement. The Strouhal number for the highest frequencies of pressure pulses agrees with literature data (see Chandrashekhar and Syamala Rao [1]).

References

[1] Chandrashekhar, D.V., Syamala Rao, B.C., Effect of pressure on the length of cavity and cavitation damage behind circular cylinders in a venturi, *Journal of Fluid Engineering*, June 1973.

[2] Fry, S.A., The damage capacity of cavitating flow from pulse height analysis, *Journal of Fluid Engineering*, Vol. 102, December 1989.

[3] Ramamurthy, A.S., Balachandar, R., A note on choking cavitation flow past bluff bodies, *Journal of Fluid Engineering*, Vol. 114, September 1992.

[4] Franc, J.P., Michel, J.M., Le, Q., Partial cavities: pressure pulse distribution around cavity closure, *Journal of Fluid Engineering*, Vol. 115, June 1993.

[5] Franc, J.P., Michel, J.M., Le Q., Partial cavities: global behavior and mean pressure distribution, *Journal of Fluid Engineering*, Vol. 115, June 1993.

[6] Kawanami, Y., Kato, H., Yamaguchi, H., Three-dimensional characteristics of the cavities formed on a two-dimensional hydrofoil, *Third International Symposium on Cavitation*, Grenoble, 1998.

[7] Tong, R.P., Schiffers, W.P., Shaw, S.J., Blake, J.R., Emmony, D.C., The role of "splashing" in the collapse of a laser-generated cavity near a rigid boundary, *Journal of Fluid Mechanics*, Vol. 380, 1999.

[8] Astolfi, J.A., Dorange, P., Billard, J.Y., Cid, T.I., An experimental investigation of cavitation inception and development on a two dimensional Eppler hydrofoil, *Journal of Fluid Engineering*, Vol. 122, March 2000.

[9] Franc, J.P., Partial cavity instabilities and re-entrant jet, *Fourth International Symposium on Cavitation*, Pasadena, USA, 2001.

[10] Kjeldsen, M., Arndt, R.E.A., Joint time frequency analysis techniques: a



study of transitional dynamics in sheet-cloud cavitation, *Fourth International Symposium on Cavitation*, Pasadena, USA, 2001.
[11] Watanabe, S., Tsusjimoto, Y., Furukawa, A., Theoretical analysis of transitional and partial cavity instabilities, *Journal of Fluid Engineering*, Vol. 123, September 2001.
[12] Lindau, O., Lauterborn, W., Cinematographic observation of the collapse and rebound of a laser-produced cavitation bubble near a wall, *Journal of Fluid Mechanics*, Vol. 479, 2002.
[13] Saito, Y., Sato, K., Cavitation bubble collapse and impact in the wake of a circular cylinder, *Fifth International Symposium on Cavitation*, Osaka, Japan, 2003.
[14] Sato, K., Shimojo, S., Detailed observations on a starting mechanism for shedding of cavitation cloud, *Fifth International Symposium on Cavitation*, Osaka, Japan, 2003.
[15] Castellani, I., *Hydrodynamic 2D cavitation - experimental database*, Mechanical and Structural Engineering Department, University of Trento, Laboratory report, Trento, 2005.
[16] Castellani, I., *Studio di un profilo cavitante in un ugello venturi* [Study of a cavitating hydrofoil in a Venturi channel], Ph.D thesis, Udine, 2005.



Numerical results for coagulation equation with bounded kernels, particle source and removal

C. D. Calin, M. Shirvani & H. J. van Roessel
Department of Mathematical and Statistical Sciences, University of Alberta, Edmonton, Alberta, Canada

Abstract

Numerical approaches for the coagulation equation with source and removal terms, and kernels that are bounded independently of the particle size, are investigated. A few classes of exact solutions are provided.
Keywords: coagulation, polymers, exact solution, source, removal, numerical solution.

1 Introduction

There is considerable literature on the mathematical theory of coagulation, deterministic and stochastic, discrete and continuous, beginning with the pioneering work of Smoluchowski in 1917 on modelling binary coalescence of particles. For a very comprehensive survey of work up to 1970, including applications, different derivations of the equation from physical assumptions, and discrete versions of the equation, see Drake [1]. The pioneering works of Melzak [2] (on cloud formation) include some of the earliest applications of the theory, and more applications can be found in Drake [1], Lee [3], Krivitsky [4].

The presence of external particle sources, and the removal of particles from the system, however, has not received a great deal of mathematical attention, the work of Simons [5] being a notable recent exception. In Shirvani and Van Roessel [6], the discrete version with constant kernel and source terms is investigated. Laurençot [7] and Norris [8] are two comprehensive recent studies of coagulation/fragmentation for unbounded kernels (but without source and removal effects).

An example of application to the coagulation equation is in the manufacturing of aluminium alloys. Here, molten metal is kept in a holding furnace for several hours while particles of titanium diboride are added for further solidification and casting.



WIT Transactions on Engineering Sciences, Vol 52, © 2006 WIT Press
www.witpress.com, ISSN 1743-3533 (on-line)
doi:10.2495/AFM06035

During this process these foreign particles can agglomerate and be lost from the melt by attachment to the furnace walls, thus jeopardizing the desired properties of the alloy, and increasing manufacturing costs (see, e.g. Wattis et al [9]). Although there have been significant studies regarding the size distribution in molten aluminum, still not much is known about the kinetics of the coagulation in this system. This is an example of an industrial process where one may wish to increase or modify the number of particles of a particular size. The only way to achieve this would be by the introduction or removal of particles of some prescribed size to enable the coagulation process to arrive at some desired limiting state.

The equation being investigated in this paper is

$$\frac{\partial u}{\partial t}(x,t) = \frac{1}{2}\int_0^x K(x-y,y,t)u(x-y,t)u(y,t)\,dy - u(x,t)\int_0^\infty K(x,y,t)u(y,t)\,dy + g(x,t) - r(x,t)u(x,t) \quad (1)$$

subject to the initial condition

$$u(x,0) = u_0(x) \geq 0. \quad (2)$$

For a detailed description of the terms in eqn. (1) see for example Drake [1] and Melzak [2]. In this paper, the coagulation kernel K is assumed to be bounded (for the precise mathematical form of these assumptions see Calin et al [10]). Bounded kernels are of fundamental importance both practically as well as theoretically (for investigating unbounded kernels, using the method of truncation). They were first investigated by Melzak [2] in the case where no source term is present.

The source g is the rate of addition of new particles to the system, and r determines the rate of removal of particles from the system. For physical reasons, the source and removal terms are assumed to be non-negative. None of the functions K, g, r is assumed to be continuous.

In this article we provide information about the numerical approaches to the solution of (1, 2), and comment on how the solutions depend on factors such as the kernel K or the source term g (see Section 2). The two most reliable methods (collocation and adaptive power series) are described in some detail. In Section 3 we comment on explicit solutions for particular choices of K and g (closed-form solutions cannot be expected to exist in the general case).

2 Numerical results

In applications (industrial or otherwise), even the kernel K may not be known analytically, and the question of finding a reliable numerical solution to (1, 2) becomes important. There are two distinct problems here.

One is the question of computing the values of $u(x,t)$ for a bounded, predetermined range of values $0 \leq x \leq X$ and $0 \leq t \leq T$. This is the correct setting in many industrial problems, where the physical limits X on particle size and T on



reaction time arise naturally. In such cases we may, if desired, find constants a, b, c such that the change of variables

$$x = ax^*, \qquad t = bt^*, \qquad u = cu^*,$$

transforms (1, 2) into an analogous equation with the same K, but with $0 \leq x^*, t^* \leq 1$ (or any other finite upper limits; the modification is in u_0, g, r being multiplied by various constants). In other words, in this type of problem it is legitimate to confine x and t to a pre-determined range of values.

The other problem (which we shall not discuss here) typically involves a change of variables $t^* = \psi(t)$, the function ψ being chosen in such a way that the entire interval $0 \leq t < \infty$ corresponds to $0 \leq t^* < 1$; a popular choice is $t^* = \left[\int_0^\infty (u_0(x) - u(x,t))dx\right] / \left[\int_0^\infty u_0(x)\,dx\right]$. This is most suitable for studying the long-time properties of $u(x,t)$, since $t \to \infty$ corresponds to $t^* \to 1^-$. The method, however, appears to be less reliable numerically for bounded ranges of the values of t. In recent years, several numerical studies have been devoted to (1), (see, e.g. Filbet and Laurençot [12], Krivitsky [4], Lee [3]).

Our numerical results are presented for $0 \leq x \leq 5$ and $0 \leq t \leq 1$ following the comments at the beginning of this section. Quite a few numerical schemes were looked at, and the two methods giving the most accurate results (when tested in the cases where exact solutions are known) were found to be the weighted residual method (collocation method) and the method of power series at successive points (the adaptive PS). A description of the methods follows.

One of the more reliable methods of obtaining numerical solutions to (1) turns out to be the use of power series. If K is independent of time, and we have

$$u(x,t) = \sum_{i=0}^{\infty} \gamma_i(x) t^i, \quad g(x,t) = \sum_{i=0}^{\infty} \delta_i(x) t^i$$

for some interval of values of x and t, then substitution into (1) (again with $r = 0$) evidently leads to $\gamma_0(x) = u_0(x)$, and for $n \geq 0$,

$$(n+1)\gamma_{n+1}(x) = \delta_n(x) + \frac{1}{2} \sum_{i+j=n} \int_0^x K(y, x-y)\gamma_i(y)\gamma_j(x-y)dy - \sum_{i+j=n} \gamma_i(x) \int_0^\infty K(x,y)\gamma_j(y)dy \tag{3}$$

The question of the convergence of the series $\sum_{i=0}^{\infty} \gamma_i(x) t^i$ is a very interesting one, not least because there is more than one sense in which the series can converge. The question of convergence and an example of its use will be discussed in Calin et al [10]. For additional comments on the method of power series expansions in terms of the small parameter $t^* = \psi(t)$, see Martynov and Bakanov [11]. They comment that, for certain kernels, using 10 terms in the series gave reasonable

results only for $t^*x \leq 2$. This is only practical for the initial stages of the evolving spectrum. Drake [1] suggests the use of power series combined with asymptotic methods for obtaining global numerical solutions.

In using a partial sum $u(x,t) \sim \sum_{i=0}^{m} \gamma_i(x)t^i$ for relatively large times t, a modification is found to be useful. Let $\delta > 0$ be small, and suppose we want to find the value of $u(x,t)$ at $t = n\delta$ for some large n. Beginning with $\gamma_0 = u_0$, compute $\gamma_1, \ldots, \gamma_m$ from (3), and then obtain $u(x,\delta) \sim u^{(1)}(x) = \sum_{i=0}^{m} \gamma_i(x)\delta^i$. However, to compute $u(x,2\delta)$, it is better to start with a new $\gamma_0^{(2)} = u^{(1)}$, re-compute the corresponding $\gamma_1^{(2)}, \ldots, \gamma_m^{(2)}$ from (3), and then use $u(x,2\delta) \sim u^{(2)}(x) = \sum_{i=0}^{m} \gamma_i^{(2)}(x)\delta^i$ (this is tantamount to computing the Taylor series at $t = \delta$, which is in turn equivalent to shifting the origin of time to $t = \delta$, and then solving the initial-value problem). Proceeding in this way, the numerical results were found to be much more precise than when a single series $\sum_{i=0}^{m} \gamma_i(x)t^i$ was used for increasingly larger values of t.

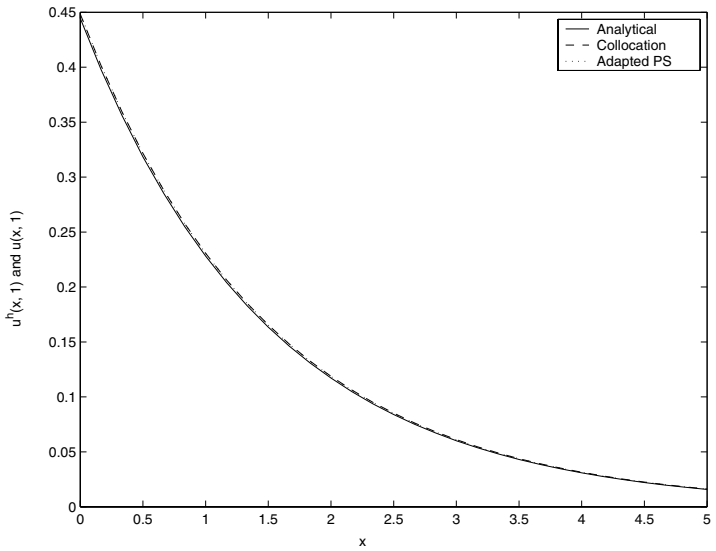


Figure 1: Plot of the numerical solution $u^h(x,1)$ using the collocation and the adaptive power series methods and analytical solution $u(x,1)$.

The version of the collocation method used here is the one suggested in Sandu [13]. Taking the collocation points to be the same as the nodal points, the integral terms of the coagulation equation were evaluated by using Gaussian numerical quadrature. Having performed the pointwise evaluation of the terms of the coagulation equation at the nodal points, the original partial integro-differential equation is transformed into a set of ordinary differential equations, where the dependent variables are at the same points. This system was then solved by the semi-implicit Euler for the time-discretization. Our experiments showed excellent

accuracy even with piecewise-linear elements and with a small number of size bins.

Even though the collocation method requires integration only at the nodal points and seems to have good accuracy even with linear elements, computationally speaking it is an expensive method. For instance, using 31 bins yields a maximum error of 1.67×10^{-3} with the collocation method, and a maximum error of 5×10^{-3} for the adaptive power series method (with terms up to and including t^2) in the example presented below (the errors were found to be of a similar order of magnitude in other examples).

Our conclusion from repeated testing is that, for examining the *qualitative* behaviour of the solutions, the adaptive power series (even with as few as three terms) is quite accurate, while for more precise numerical solutions, the collocation method is preferable.

Letting u^h denote the numerical solution, Figure 1 shows the graph of $u^h(x, 1)$ for the case $K = 1$, $g = 0$, and $u_0(x) = e^{-x}$. The exact solution $u(x, t) = (1 + t/2)^{-2} e^{-2x/(2+t)}$ is obtained in Example 3.1 (with $\eta(t) = 0$ in the notation of that example).

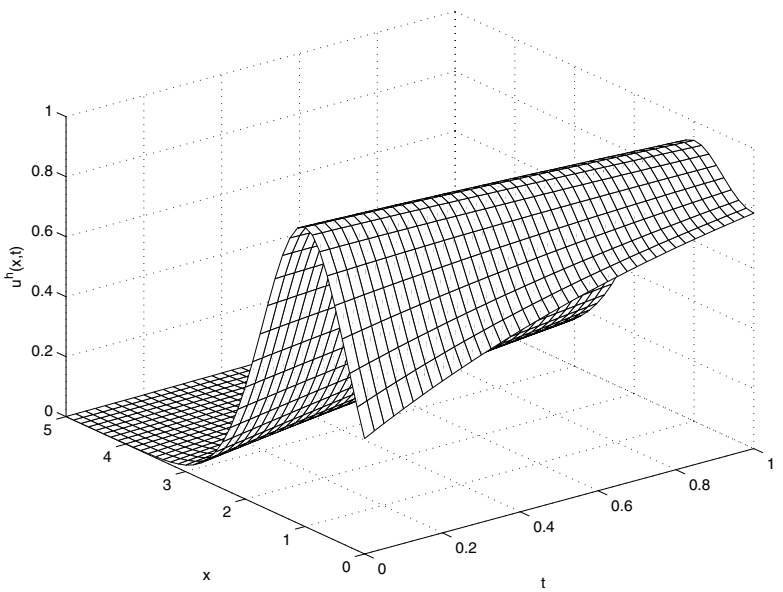


Figure 2: $K(x, y) = 1/(1 + x + y)$, $\quad g(x, t) = e^{-x}$, $\quad u(x, 0) = e^{-(x-1)^2}$.

The above picture shows the propagation of an initial global maximum through time. The adaptive power series method was used in this and subsequent graphs. Longer time periods can be investigated by a suitable change of variables as indicated earlier in this section, but result in no qualitative change in behaviour. No analytical solution is known in general for this kernel.

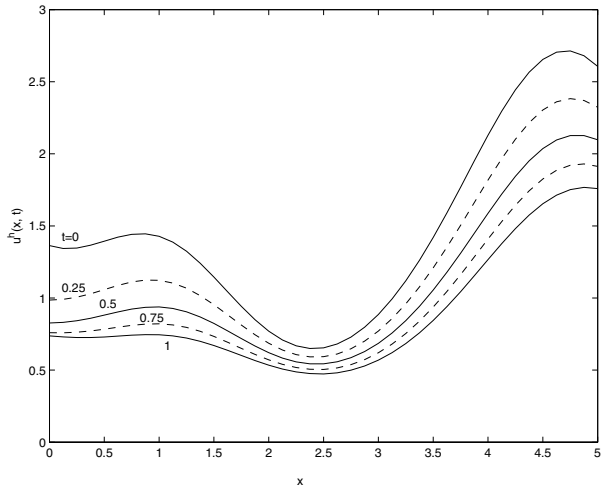


Figure 3: The graph of the numerical solution $u^h(x,t)$ at times $t = 0, 0.25, 0.5, 0.75, 1$ assuming the initial condition $u(x,0) = e^{-\sin x} + e^{-(x-1)^2}$ has two maxima and $K(x,y) = 1/(1+x+y)$, $g(x,t) = e^{-x}$.

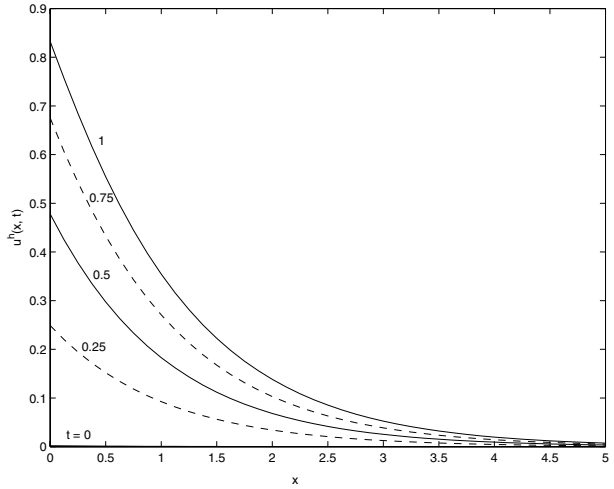


Figure 4: $K(x,y) = 1/(1+x+y)$, $g(x,t) = e^{-x}$, $u(x,0) = 0$.

The graph in Figure 4 shows the influence of the source term on the solution. The solution increases from its initial value of $u_0(x) = 0$. The series of graphs in Figure 4 also indicates the fact that the kernel K exerts a relatively small and

transient influence on the form of the solutions, with the initial conditions u_0 and the source term g being the more dominant factors.

Our next example (Figure 5) is that of another intractable kernel, $K(x,y) = e^{-(x^2+y^2-1)^2} = e^{-(r^2-1)^2}$ (in polar coordinates). Observe that the maxima of K initially appear in the solution before being smoothed out by the coagulation process.

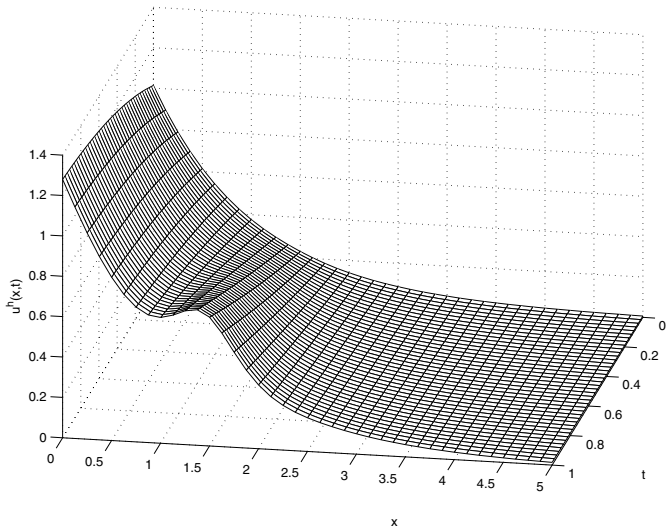


Figure 5: $K(x,y) = e^{-(x^2+y^2-1)^2}$, $\quad g(x,t) = e^{-x}$, $\quad u(x,0) = e^{-x}$.

3 A few examples of exact solutions for (1)

In this section we look at exact solutions to (1). For more examples of exact, formal and asymptotic solutions see Calin et al [10]. It is worth mentioning that no closed-form solution of (1) is known when $K = 0$ outside a bounded interval (except in trivial cases).

Example 3.1 *Our first example is an explicit solution to (1). Assume that* $K \equiv 1$. *Let* $\eta(t)$ *be a non-decreasing, non-negative function for all* $t \geq 0$, *such that* $\eta(0) = 0$. *Set* $\alpha(t) = 2/[2 + \int_0^t e^{\eta(s)}\, ds]$. *If the source term is* $g(x,t) = \eta'(t)\alpha^2(t)e^{\eta(t)-x\alpha(t)}$ *and the initial condition is* $u_0(x) = e^{-x}$, *then it can be verified by a direct substitution that* $u(x,t) = \alpha^2(t)e^{\eta(t)-x\alpha(t)}$ *is the solution of (1).* $\square$

Example 3.2 *The next example shows that, in general, separable, non-negative solutions cannot be expected to exist for all* x. *To see this, suppose* $u(x,t) = u_0(x)\beta(t)$ *for* $(x,t) \in [0,N] \times [0,\infty)$ *for some* $N > 0$, *where* $\beta(0) = 1$. *Substi-*

tuting into (1) with $r = 0$ and re-arranging, we find that

$$\frac{g}{\beta u} = \frac{\beta'}{\beta^2} + \int_0^N K(x,y)u_0(y)dy - \frac{1}{2}\int_0^x \frac{K(y,x-y)u_0(y)u_0(x-y)}{u_0(x)}dy.$$

Now let

$$p(N) = \inf_{x\in[0,N]}\Big[\int_0^N K(x,y)u_0(y)dy - \frac{1}{2}\int_0^x \frac{K(y,x-y)u_0(y)u_0(x-y)}{u_0(x)}dy\Big].$$

Then of course

$$\frac{g}{\beta u} \geq \frac{\beta'}{\beta^2} + p(N).$$

If $p(N) \geq 0$, then the most general function β for which the right-hand side of the above equation remains non-negative is

$$\beta(t) = \frac{1}{1 + p(N)t - \eta(t)}$$

where η is any non-decreasing function of t such that $\eta(0) = 0$ and $\eta(t) < 1 + p(N)t$ for all t. The simplest choice is $\eta(t) = 0$ for all t. In order for a separable non-negative solution to exist for all $x \geq 0$, we require that $\lim_{N\to\infty} p(N) \geq 0$. We do not know of any examples (even with $K = 1$) where the above condition holds (the limit is $-\infty$ in the examples we have looked at). □

References

[1] Drake, R.L., A general mathematical survey of the coagulation equation, In: G. Hidy and J. R. Brock, editors, *Topics in Current Aerosol Research 3 (Part 2)*, Pergamon Press, 1972.

[2] Melzak, Z.A., A scalar transport equation, *Trans. Amer. Math. Soc.*, **85**, pp. 547-560, 1957.

[3] Lee, M.H., A survey of numerical solutions to the coagulation equation, *J. Phys. A*, **34**, pp. 10219-10241, 2001.

[4] Krivitsky, D.S., Numerical solution of the Smoluchowski kinetic equation and asymptotics of the distribution function, *J. Phys. A*, **28**, pp. 2025-2039, 1995.

[5] Simons, S., On the solution of the coagulation equation with a time-dependent source-application to pulsed injection, *J. Phys. A:Math. Gen.*, **31**, pp. 3759-3768, 1998.

[6] Shirvani, M. & van Roessel, H.J., Existence and uniqueness of solutions of Smoluchowski's coagulation equation with source terms, *Quarterly of Applied Mathematics.*, **LX (1)**, pp. 183-194, 2002.

[7] Laurençot, P., On a class of continuous coagulation-fragmentation equations, *J. Diff. Eqns.*, **167**, pp. 245-274, 2000.



[8] Norris, J.R., Smoluchowski's coagulation equation: uniqueness, nonuniqueness and a hydrodynamic limit for the stochastic coalescent, *The Annals of Applied Probability*, **9(1)**, pp. 78-109, 1999.
[9] Wattis, J.A.D, McCartney, D.G. & Gudmundsson, T., Coagulation equations with mass loss, *Journal of Engineering Mathematics*, **49**, pp. 113-131, 2004.
[10] Calin, C.D., Shirvani, M. & van Roessel, H.J., The coagulation equation with bounded kernels, and particle source and removal, to appear, *AMI, Technical Reports*, University of Alberta, 2006.
[11] Martynov, G.A. & Bakanov, S.P., Solution of the kinetic equation for coagulation, In: B. Derjaguin, editor, *Surface Forces*, 1961.
[12] Filbet, F. & Laurençot, P., Numerical simulation of the Smoluchowski coagulation equation, *SIAM J. Sci. Comput.*, **25**, pp. 2004-2028, 2004.
[13] Sandu, A., A framework for the numerical treatment of aerosol dynamics, *Applied Numerical Mathematics*, **45**, pp. 475-497, 2003.



This page intentionally left blank

Volume of fluid model applied to curved open channel flows

T. Patel & L. Gill
Department of Civil, Structural and Environmental Engineering, Trinity College, University of Dublin, Ireland.

Abstract

An attempt has been made to simulate secondary flows in curved open channels using three-dimensional CFD analysis. Besides the classical center-region cell, a counter rotating outer bank cell is often observed which could play an important role in the mechanism of sediment transport. The CFD analysis is carried out on the 120° curved open channel bend using the commercial software package *Fluent*. The volume of fluid (VOF) model is used to simulate the air-water interaction at the free surface and the turbulence closure was obtained using the Reynolds stress model (RSM). It is observed that the RSM model was able to predict both circulation cells successfully. The results show that the core of maximum velocities is found close to the separation between both circulation cells and below the free surface which agrees well with the experimental data.
Keywords: open channel, secondary flows, computational fluid dynamics, volume of fluid, free surface, turbulence modeling.

1 Introduction

Secondary flows are a significant feature of flow in open-channel bends. They are formed due to a local imbalance between the pressure gradient and centrifugal force at any given section. They tend to redistribute the mean velocity, alter the boundary shear stress and erode the outer bank. Most of the research on flows in bends over the past decade has concentrated on the central portion of the flow, whereas the flow characteristic at the outer bank (where a small counter-rotating circulation cell is present) has often been neglected. Earlier studies indicate that the center-region circulation cell has been captured successfully using a two-equation turbulence model. Patel and Gill [1],



WIT Transactions on Engineering Sciences, Vol 52, © 2006 WIT Press
www.witpress.com, ISSN 1743-3533 (on-line)
doi:10.2495/AFM06036

Rameshwaran and Naden [2, 3] and Ye and McCorquodale [4] were able to simulate the same using the κ-ε turbulence model. Booij [5] also concluded that κ-ε turbulence model was unable to predict the outer bank cell but was able to reproduce the center-region cell. Blanckaert and Graf [6] stressed the importance of high-resolution experimentation to fully understand the mechanism underlying the generation of the outer bank cell and also mentioned that the lack of proper experimental data has hampered the verification of investigations to date by means of numerical investigation. Blanckaert and de Vriend [7] also found that the decreasing velocities towards the water surface ($\partial v/\partial z<0$) and turbulent anisotropy are an important generation mechanism for the outer-bank cell. Unlike the two-equation model, the RSM model is capable of simulating cross-stream turbulent anisotropy in compound straight channels [8].

It has been also cited that the discretization schemes (for the non-linear terms in the momentum equations) can also be responsible for accurate results [9]. They indicated that the single order unwinding scheme might result in numerical diffusion especially if the flow is skewed relative to the numerical mesh. Nicholas [10] attempted to study the flow behaviour in straight open channels using *Fluent* [11] and also mentioned the importance of the grid resolution near the bottom wall to capture the detailed flow characteristics.

This paper reports the simulation of both circulation cells in a 120° curved open channel using the RSM turbulence model. The air-water interaction is modeled using the VOF method as developed by Hirt and Nicholls [12]. It should also be noted here that VOF model has not been applied previously to the study of curved open channel flows.

2 Problem formulation

CFD analysis was carried out on the 120º curved open channel experiment conducted by Blanckaert and Graf [6]. Figure 1 shows the geometrical layout and the cross-sectional details at the test section. The hydraulic parameters for the fluid flow are also shown in Table 1. The test case was selected to imitate the real flow conditions which include variable bed topography, as found in nature. The test location is at 60º into the bend and the measurements are taken at the outer half of the section.

2.1 Computational method

The computations were performed on an adaptive grid using *Fluent*, a general purpose CFD software. The governing flow equations for mass and momentum conservations are as follows:

$$\frac{\partial \rho}{\partial t} + \frac{\partial}{\partial x_i}(\rho u_i) = 0 \tag{1}$$

$$\frac{\partial(\rho u_i)}{\partial t} + \frac{\partial}{\partial x_j}(\rho u_i u_j) = -\frac{\partial p}{\partial x_i} + \frac{\partial}{\partial x_j}\left[\mu\left(\frac{\partial u_i}{\partial x_j} + \frac{\partial u_j}{\partial x_i} - \frac{2}{3}\delta_{ij}\frac{\partial u_k}{\partial x_k}\right)\right] + \frac{\partial}{\partial x_j}\left(-\rho\overline{u_i' u_j'}\right)_i \tag{2}$$

Table 1: Experimental characteristics.

Radius of Curvature (m)	Depth of flow (m)	Channel width (m)	Mean Velocity U(m/s)	Discharge Q(l/s)	Reynolds Number
2	0.114	0.4	0.38	17	67260

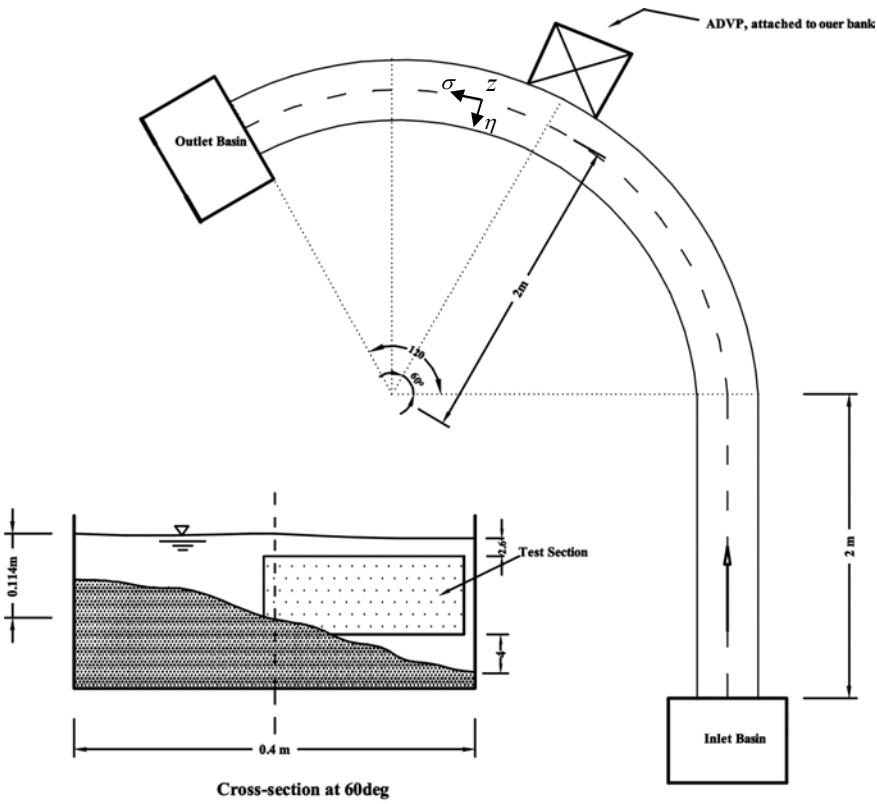


Figure 1: Geometric layout of channel.

where, δ_{ij} is the Kronecker delta, and $-\rho\overline{u_i' u_j'}$ is the Reynolds stress. The Reynolds stress equation is given by:

$$\underbrace{\frac{\partial}{\partial t}\left(\rho\overline{u_i' u_j'}\right)}_{Local\,Time\,Derivative} + \underbrace{\frac{\partial}{\partial x_k}\left(\rho u_k \overline{u_i' u_j'}\right)}_{C_{ij}\equiv Convection} = \underbrace{-\frac{\partial}{\partial x_k}\left[\rho\overline{u_i' u_j' u_k'} + \overline{p\left(\delta_{kj}u_i' + \delta_{ik}u_j'\right)}\right]}_{D_{T,ij}\equiv Turbulent\,Diffusion}$$

$$+ \underbrace{\frac{\partial}{\partial x_k}\left[\mu\frac{\partial}{\partial x_k}\left(\overline{u_i' u_j'}\right)\right]}_{D_{L,ij}\equiv Molecular\,Diffusion} - \underbrace{\rho\left(\overline{u_i' u_k'}\frac{\partial u_j}{\partial x_k} + \overline{u_j' u_k'}\frac{\partial u_i}{\partial x_k}\right)}_{P_{ij}\equiv Stress\,\Pr oduction} + \underbrace{\overline{p\left(\frac{\partial u_i'}{\partial x_j} + \frac{\partial u_j'}{\partial x_i}\right)}}_{\phi_{ij}\equiv \Pr essure\,Strain} - \underbrace{2\mu\overline{\frac{\partial u_i'}{\partial x_k}\frac{\partial u_j'}{\partial x_k}}}_{\varepsilon_{ij}\equiv Dissipation} \tag{3}$$

It should be noted here that the unsteady solver is used only to get the steady flow results, and not intended to obtain time-accurate solutions. Time derivative terms are discretized using the first order accurate backward implicit scheme. Convection terms are discretized using the third order Monotone upstream-centered schemes for conservation laws (MUSCL) scheme, while diffusion terms are discretized using the second order accurate central differencing scheme. The pressure-velocity coupling is achieved using the SIMPLE algorithm [13].

As mentioned earlier, the VOF method has been employed to simulate the air-water interaction at the free surface. The VOF method which was developed by Hirt and Nichols [12] is a type of interface-capturing method which relies on the fact that two or more fluids/phases are not interpenetrating and for each additional phase, a new variable that is the volume fraction of the phase in the computational cell is introduced. The mass conservation equation for the qth phase is given by:

$$\frac{\partial \alpha_q}{\partial t} + \vec{v}.\nabla\alpha_q = 0 \tag{4}$$

It should be noted here that the volume fraction equation is not solved for the primary phase, but is based on the constraint that in each cell, the volume fraction of all phases must sum to unity,

$$\left(\sum_{q=1}^{n}\alpha_q = 1\right).$$

A single momentum equation is solved throughout the domain, and the resulting velocity field is shared among the phases. The momentum equation depends on the volume fractions of all the phases through the fluid properties, which are determined by the presence of the component phases in each control volume, e.g.,

$$\rho = \alpha_q\rho_q + (1-\alpha_q)\rho_p \tag{5a}$$

$$\mu = \alpha_q\mu_q + (1-\alpha_q)\mu_p \tag{5b}$$

where subscripts *p* (air) and *q* (water) denote the primary and secondary phases respectively for open channel flows. In addition, the complexity of implementing

boundary conditions on the surface has been avoided since the water surface is the interface between the air and the water. For an unsteady fluid flow, the cells currently filled with air provide the space for the water when the water level rises. Thus, this method allows free movement of the water at the interface.

2.2 Grid generation and boundary conditions

Numerical grids were constructed with the *Gambit* preprocessor available in the CFD package *Fluent*. The flow domain was divided into number of non-overlapping unstructured (T-grid) meshes. The total number of meshes increased to 1,144,662 after grid adaptation. The boundary conditions for the flow domain are as follows:

I. *Inlet.* A new boundary condition 'Open Channel' (available in *Fluent* [11]) is defined at the inlet. Two separate inlets are defined for air and water with the same group ID. Mass flow rates are defined for both the phase depending upon the velocity and the inlet area. The depth of the flow is known in advance from the experimental results which help in defining the free surface level before starting the simulations. The flow domain is initialized with the volume fraction of secondary phase (i.e. water) equal to 1 up to the free surface level. This procedure also helps in the convergence of the problem.

II. *Outlet.* Pressure Outlet boundary condition is applied at the outlet. The pressure is kept at atmospheric pressure (i.e. gauge pressure =0). Here also two separate outlets are kept with the same group id.

III. *Top Surface.* As discussed earlier the boundary condition at the interface is avoided by using the VOF model. The top surface above which is air is initially kept at symmetry (a boundary condition) in which all the normal gradients ($\partial/\partial z$=0) and the normal components are zero. Once the solution stabilizes the top surface boundary condition is changed to ambient pressure conditions to represent the real flow conditions more accurately.

IV. *Wall.* The bottom and side surfaces are defined as *Wall* boundary condition. In this, study, the standard wall function has been employed, which may be expressed as follows:

$$\frac{u_p u^*}{\tau_w/\rho} = \frac{1}{\kappa}\ln\left(E\frac{\rho u^* y_p}{\mu}\right) - \Delta B \tag{6a}$$

$$u^* = C_\mu^{1/4}\kappa^{1/2} \tag{6b}$$

$$\Delta B = \frac{1}{\kappa}\ln f_r \tag{6c}$$

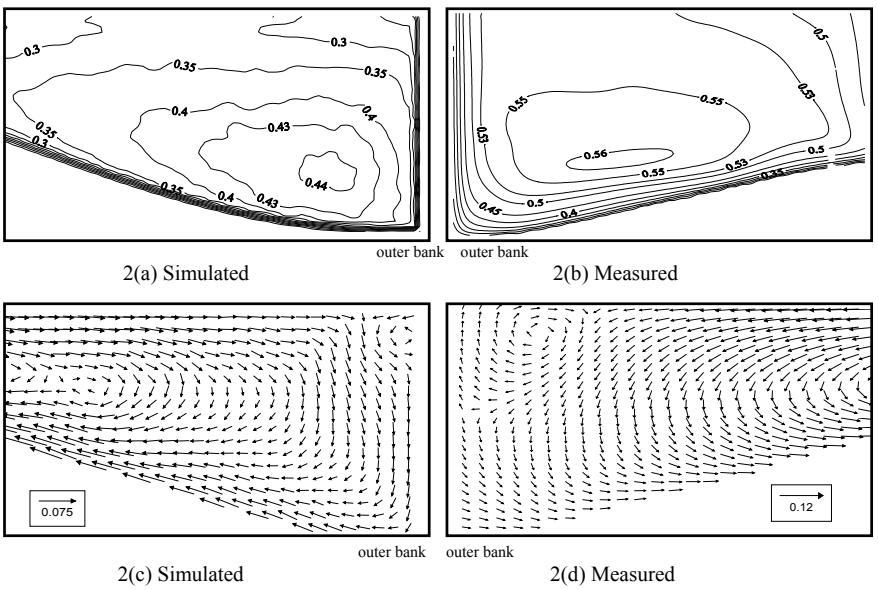
where, f_r is the measure of the roughness of the bed/wall. It should also be noted here that fine grid resolution near the wall has been avoided by using the wall function which also helps in reducing the computational time.

3 Results and discussion

3.1 Mean velocity field

The comparisons between the experimental and the predicted flow fields are shown in Figure 2(a-d). As described earlier the test section is located at 60º downstream into the bend and focused at the outer half of that section. The figure shows that both the circulation cells are captured successfully using the RSM model. Before the RSM model is activated, the κ-ε model was applied to prepare the flow field. This also confirmed the inability of κ-ε model to simulate outer bank cell. The velocity fields are plotted by taking their components at 60º as *Fluent* uses a Cartesian reference system. The validation results are shown for the outer half section at 60º since this is where the original measurements were taken.

It can be seen that the distribution of velocity contours is not symmetric and is shifted outwards towards the outer bank of the bend owing to the presence of secondary flows. The value approaches zero near the side walls from the maximum velocity (near the outer bank) due to boundary layer formation. The average velocity of flow is 0.38m/s. The model predicts a maximum value of around 0.44m/s whereas the experimental plot shows the same value as 0.56m/s. The location of the maximum velocity contour is also of interest and is found well below the free surface. The horizontal position of the maximum velocity contour is found at the intersection of both the circulation cells which agrees well with the experimental data.



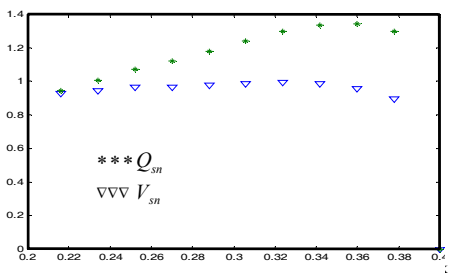
2(a) Simulated 2(b) Measured

2(c) Simulated 2(d) Measured

Figure 2: Simulated and measured (a, b) velocity contours and (c, d) vectors at 60º section.

Blanckaert and de Vriend [7] indicated that the resulting decreasing velocities towards the water surface are an important generation mechanism for the outer-bank cell. The predicted vector plot (Figure 2c) shows that both the circulation cells are well simulated. In the measured vector plot, the velocity vectors at the bottom are pointing horizontally which must be due to a lack of proper experimentation near the bed, so care should be taken with their interpretation with the measured values. The simulation underestimates the strength of both the circulation cells. It can also be observed that the predicted length of the outer bank cell is less than that of the measured one. This also leads to the conclusion that the underestimation of the strength of the centre region cell leads to the underestimation of the outward increase of the longitudinal velocity contours. Blanckaert and Graf [6] also concluded that the outer bank cell has a protective effect on the outer bank because the outer bank cell keeps the core of the maximum velocity away from the bank.

Figure 3 presents the normalized distribution of the downstream velocity, V_{sn}, and the unit discharge, $Q_{sn,}$ in the outer half-section. It can be seen that the flow is concentrated over the deeper part of the section and the majority of the discharge flows through the investigated half-section. The depth-averaged values of the downstream velocity remain almost constant throughout the outer half-section and reduce to zero near the side wall. The value for normalized velocity and discharge is calculated by:



$$V_{sn} = \frac{1}{h}\int_{z_b}^{z_t} v_s dz$$

$$Q_{sn} = V_{sn} Bh / Q$$

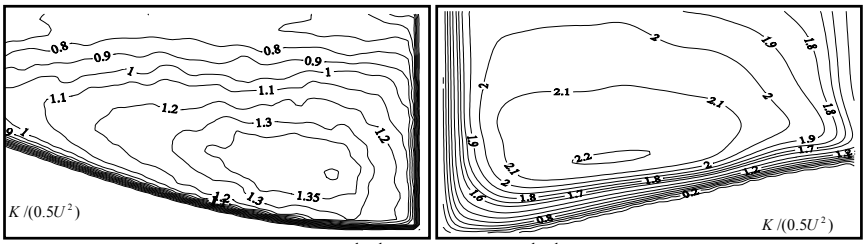
where 'B' is width, 'h' is local depth of flow, subscript 't' and 'b' denotes free surface and bottom of the channel

Figure 3: Normalized depth-averaged velocity (V_{sn}), and normalized unit discharge (Q_{sn}).

3.2 Mean-flow kinetic energy

Figure 4 shows the normalized distribution of mean kinetic energy. The kinetic energy per unit mass is defined as:

$$K = \frac{1}{2}\left(V_\sigma^2 + V_\eta^2 + V_z^2\right)$$



(a) Simulated (b) Measured

Figure 4: (a) Simulated and (b) measured mean-flow kinetic energy.

The figure depicts that the simulated results match well with the measured ones. The variation of kinetic energy contours is more or less similar to the longitudinal velocity contours where the respective maximum value is near the outer bank owing to the presence of secondary flows. The computational model predicts the maximum value of around 1.35 whereas the measured plot shows the same value is 2.2. This difference in the magnitude between the two can be ascribed to the under prediction of velocity contours. The comparison between the longitudinal velocity contours and kinetic energy contours shows that the longitudinal component of the velocity dominates the kinetic energy and contains about 98% of the flow. The K.E. contour values are relatively higher because K.E. varies according to the square of the velocity.

As it can be observed, some discrepancy exists between the experimental and simulated results and more research is required to improve the understanding of the mechanism underlying the formation of outer-bank cell and the under prediction of the velocity magnitudes.

4 Conclusions

Secondary flows are significant phenomena of curved open channels which strongly influence the flow behaviour within the natural rivers and estuaries. Besides the classical center-region cell, a counter rotating cell is also observed near the outer bank. The standard κ-ε model has been shown to be unable to simulate this outer-bank cell which confirms the results of previous studies. However, it has been concluded that the RSM model is able to simulate both the circulation cells successfully. The main flow features of the flow field are captured reasonably well although it has not been possible to remove all discrepancies between the model and experimental results. More simulations are being undertaken presently to further improve the predictions with the help of CFD.

Acknowledgements

The first author would like to thank RPS-MCOS, Ireland for providing funds to carry out research.

References

[1] Patel, T. & Gill, L., Flow characteristics of curved open channel using computational fluid dynamics, ISSEC Annual Symposium, pp. 28, 2005.
[2] Rameshwaran, P. & Naden, P.S., Modeling turbulent flow in two-stage meandering channels, Proc. ICE, Water Management 157, pp. 159-173, 2004.
[3] Rameshwaran, P. & Naden, P.S., Three-dimensional modeling of free surface variation in a meandering channel, J. of Hydraulic Research, 42(6), pp. 603-615, 2004.
[4] Ye, J. & McCorquodale, J.A., Simulation of curved open channel Flows by 3D hydrodynamic model, J. of Hydraulic Engineering, ASCE, 124(7), pp. 687-698, 1998.
[5] Booij, R., Measurements and large eddy simulations of the flows in some curved flumes, J. of Turbulence, 4, pp. 1-17, 2003.
[6] Blanckaert, K., & Graf, W.H., Mean flow and turbulence in open-channel bend, J. of Hydraulic Engineering, ASCE, 127(10), pp. 835-847, 2001.
[7] Blanckaert, K., & de Vriend, H.J, Secondary flow in sharp open channel bends, J. of Fluid Mechanics, 498, pp. 353-380, 2004.
[8] Cokljat, D., & Younis, A., Second-order closure study of open-channel flows, J. of Hydraulic Engineering, ASCE, 121(2), pp. 94-107, 1995.
[9] Leschziner, M.A., & Rodi, W., Calculation of annular and twin parallel jets using various discretization schemes and turbulence-model variations, J. of Fluid Engineering, ASME Transactions, 103(6), pp. 352-360, 1981.
[10] Nicholas, A.P., Computational fluid dynamics modeling of boundary roughness in gravel-bed rivers: an investigation of the effects of random variability in bed elevation, Earth Surfaces Processes and Landforms, 26, pp. 346-362, 2001.
[11] Fluent Software Manual, version 6.2.16, 2005.
[12] Hirt, C.W., & Nichols, B.D., Volume of Fluid (VOF) method for the dynamics of free boundaries, J. of Computational Physics, 39, pp. 201-225, 1981.
[13] Patankar, S.V., Numerical heat transfer and fluid flow, Hemisphere Publishing, 1980.



This page intentionally left blank

Drag reduction in two-phase annular flow of air and water in an inclined pipeline

A. Al-Sarkhi[1], E. Abu-Nada[1] & M. Batayneh[2]
[1]*Department of Mechanical Engineering, Hashemite University, Zarqa, Jordan*
[2]*Department of Civil Engineering, Hashemite University, Zarqa, Jordan*

Abstract

Measurements of drag reduction for air and water flowing in an inclined 0.0127 m diameter pipe were conducted. The fluids had an annular configuration. The injection of drag reducing polymers (DRP) solution produced drag reductions as high as 71% with a concentration of 100 ppm in the pipeline. A maximum drag reduction that is accompanied (in most cases) by a change to a stratified or annular stratified pattern. The drag reduction is sensitive to the gas and liquid superficial velocities and the pipe inclination. Maximum drag reduction was achieved in the case of pipe inclination of 1.28^{o} at the lowest superficial gas velocity and the highest superficial liquid velocity.
Keywords: inclined pipeline, annular gas-liquid flow, drag reducing polymers, injection method.

1 Introduction

The injection of small amounts of high molecular weight long-chain polymers into a single-phase liquid flow can cause large decreases in the frictional resistance at the wall; this interesting finding was first published by (Toms, [1]).

Two-phase gas liquid flow in pipes is regularly encountered and is of great commercial importance in the natural gas and petroleum industries. This paper presents results of experiments in which drag-reducing polymers were added to the flow of water and air in an inclined pipe, with a diameter of 0.0127 m. The gas velocity was large enough that an annular flow existed. This pattern commonly occurs in natural gas/ condensate pipelines. It is characterized by a situation in which a part of the liquid flows along the wall as a liquid layer and part as drops entrained in the gas in the core of the pipe.



WIT Transactions on Engineering Sciences, Vol 52, © 2006 WIT Press
www.witpress.com, ISSN 1743-3533 (on-line)
doi:10.2495/AFM06037

At low gas and liquid rates the liquid flows along the wall in a stratified manner. At high enough superficial gas velocity, U_{SG}, drop mixing and deposition is such that the film on the side walls becomes thick enough for groups of large amplitude irregular waves to form intermittently. These disturbances are sites for atomization and the fluid in them has characteristics similar to turbulence. They greatly enhance the ability of liquid to climb up the wall in opposition to the gravitational force and called disturbance waves (Lin and Hanratty, [2]).

A similar previous study of the effect of drag-reducing polymers on annular gas-liquid flow was carried out by Sylvester and Brill [3] for air-water in a horizontal pipe with a diameter of 1.27 cm and a length of 6.1 m. A polymer solution with 100 ppm of polyethlene oxide, contained in a holding tank, was pumped to a tee where it was mixed with the gas. The data are plotted as pressure gradient versus liquid flow rate for superficial gas velocities 86 m/s and 111 m/s. The percent change in the pressure gradient from what was observed in the absence of polymer varied from zero to about 37. No explanation for these changes was given.

Sylvester et al. [4] studied the effect of liquid flow rate and gas flow rate on drag reduction in horizontal natural gas-hexane pipe flow in three different diameter (1, 2 and 3 inch). Drag reduction of 34% was obtained. It was found that drag reduction increased with decreasing gas rate.

Al-Sarkhi and Hanratty [5] found that the injection of a concentrated drag reducing polymers into an air-water in a 9.53 cm pipe changed an annular pattern to a stratified by destroying the disturbance waves in the liquid film. Drag reduction of 48% was realized. In a following study in a 2.54 cm pipe, Al-Sarkhi and Hanratty [6] observed similar results and obtained drag reduction as high as 63%.

Soleimani et al. [7] studied experimentally the effect of drag reducing polymers on pseudo-slugs-interfacial drag and transition to slug flow. They revealed that the transition to slug flow is delayed by drag reducing polymers and the pressure drop can increase or decrease when polymers are added.

Al-Sarkhi and Soleimani [8] conducted a series of experiments to investigate the effect of drag reducing polymer on two-phase flow pattern in a horizontal 2.54cm pipe. The characteristics of two phase flow with and without drag reducing polymers were described. It is noted that the interfacial shear stress decreases sharply by adding polymers and flow pattern map is changed.

Studies of the effect of the drag-reducing polymer on frictional losses have been made by Rosechart et al. [9] and by Otten and Fayed [10] for bubbly and plug flows. Kang et al. [11] studied the influence of an additive (which is not identified) on three-phase flow (oil, water and carbon dioxide). They found a drag-reduction of 35 percent at the two highest superficial gas velocities that were studied, U_{SG} =13, 14 m/s. A review of work on this area by Manfield et al. [12] concludes that understanding of the influence of drag-reducing polymers on multiphase flows is not satisfactory.

The present study used technology developed by Al-Sarkhi and Hanratty [5] for injecting the polymers directly in the liquid film in the pipeline. It differs

from all of the studies listed above in that a concentrated polymer solution was injected at the wall without using a pump. The concentration in the pipeline was controlled by varying the flowrate of the injected polymer concentrated solution. Gas and liquid superficial velocities of 19-38 m/s and 0.04-0.1 m/s were used.

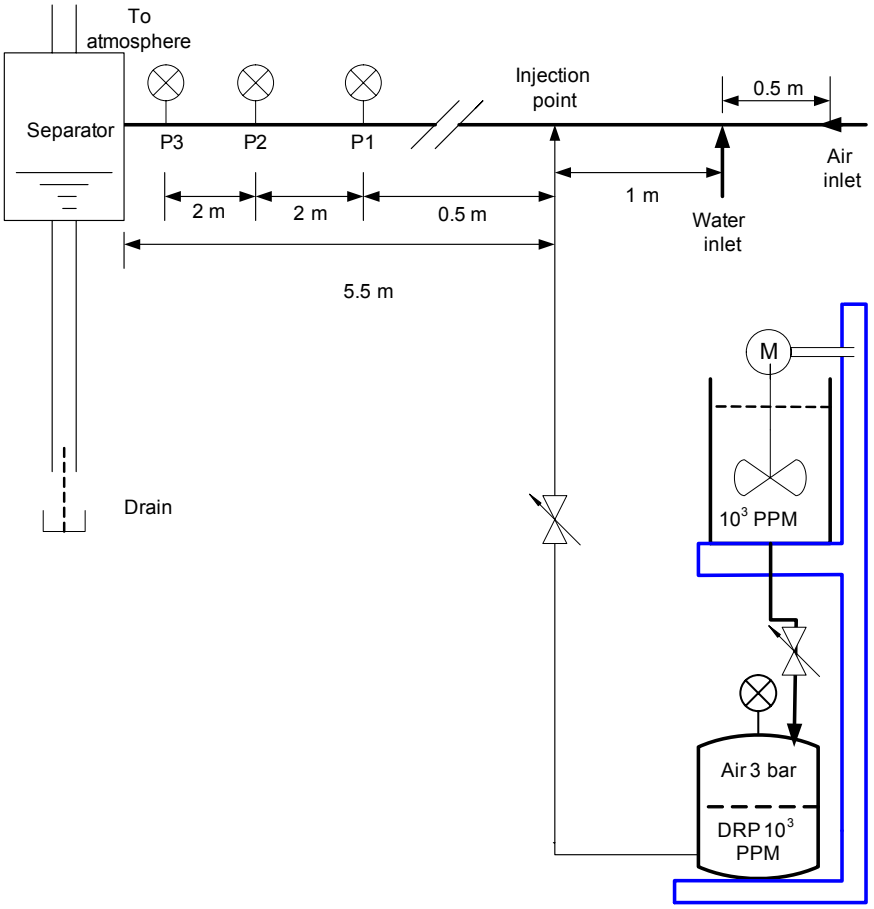


Figure 1: Experimental setup.

2 Experimental setup

The 0.0127 m pipeline used in this study has a length of 7 m. The pipe sections were constructed from Plexiglas to allow visual observations. The air and water were combined in a tee-section at the entry. The water flowed along the run of the tee. The air discharged to the atmosphere so the pressure was slightly above the atmospheric. A detailed description of the loop is shown in fig. 1.

The master polymer solution was prepared the day before an experiment was performed. MAGNAFLOC 110L is a high molecular weight anionic

polyacrylamide flocculant as a liquid dispersion grade (produced by Ciba) was mixed gently with water in a 150-liter tank with a concentration of 1000 ppm (weight basis). The master solution was transferred by gravity to a smaller tank, which was pressurized with air at 3 bar (see fig. 1). The flow rate out of the tank was measured by a rotameter. These methods for transferring the concentrated polymer solution were used in order to avoid the degradation that would have occurred if a pump were used.

The polymer solution was injected into the flow loop by introducing of the master solution into the liquid through a hole with a diameter of 2 mm that was located at the bottom of the pipe, 1.0 m downstream of the tee where the air and water were mixed. This method involved injection at a location where the annular pattern was developed, i. e., 1.0 m from the mixing tee. In this way the polymer was rapidly mixed with liquid flowing along the wall. A polymer concentration of 100 ppm was used. A U-tube manometer was used to measure the pressure drop over a 2 m length of pipeline. The first pressure tap was located 0.5 m from the downstream injection point.

3 Results

3.1 Visual observations

Visual observations of the air-water flow revealed a turbulent liquid film with intermittent disturbance waves around the whole pipe circumference. These were longer and more intense at the bottom, as would be expected, since the average height of the film is distributed asymmetrically (Williams at al., [13]).

Detail explanation of the effect of the addition of polymer to the flow on the flow pattern is listed in Table 1. The air and water without DRP has an annular configuration with liquid film wetting the whole pipe circumference and the presence of a large-scale disturbance wave. The forth, fifth and sixth column represent the flow of air and water with 100 ppm of polymer added to the liquid for horizontal, and 1.28^{o} and 2.4^{o} of pipe inclination. The flow pattern at lowest gas and liquid superficial velocities (U_{SG} =19, 24 m/s and U_{SL}=0.04, 0.05 and 0.07 m/s) shows a stratified flow with a relatively smooth surface and a negligible amount of entrained drops in the gas phase. These results can be interpreted by noting that the polymers damped the disturbance waves. This, in turns, reduces the rate of atomization and the ability of liquid to spread upward along the wall. A secondary effect is a damping of the waves on the stratified flow that finally results.

At the lowest superficial gas velocities (19 and 24 m/s) and highest superficial liquid U_{SL} (U_{SL} =0.1). Considering the horizontal case; the flow pattern with 100 ppm of polymer injected to the liquid film, the new flow pattern characterized by a thin liquid film at the top of the pipe and a thick film at the lower half of the pipe with no disturbance waves shown in the pipe. This flow configuration is called Annular–Stratified as in Al-Sarkhi and Hanratty [9]. The case for the angle 1.28^{o} the final configuration with DRP was stratified but for the angle 2.4^{o}, the final pattern was pseudo slug.

Table 1: Flow patterns with and without 100 ppm polymers (Ann means annular and Strt means Stratified).

U_{SG} m/s	U_{SL} m/s	Without DRP all angles	With DRP (θ=0°)	With DRP (θ=1.28°)	With DRP (θ=2.4°)
38	0.10	Ann	Ann w/o D.W	Ann w/o D.W	Ann w/o D.W
38	0.08	Ann	Ann w/o D.W	Ann w/o D.W	Ann w/o D.W
38	0.07	Ann	Ann-Strat	Ann w/o D.W	Ann w/o D.W
38	0.05	Ann	Ann-Strat	Ann w/o D.W	Ann w/o D.W
38	0.04	Ann	Ann-Strat	Ann w/o D.W	Ann w/o D.W
33	0.10	Ann	Ann-Strat	Ann-Strat	Ann w/o D.W
33	0.08	Ann	Ann-Strat	Ann-Strat	Ann w/o D.W
33	0.07	Ann	Ann-Strat	Ann-Strat	Ann w/o D.W
33	0.05	Ann	Ann-Strat	Ann-Strat	Ann w/o D.W
33	0.04	Ann	Ann-Strat	Stratified	Ann w/o D.W
28	0.10	Ann	Ann-Strat	Stratified	Ann w/o D.W
28	0.08	Ann	Ann-Strat	Stratified	Ann-Strat
28	0.07	Ann	Stratified	Stratified	Ann-Strat
28	0.05	Ann	Stratified	Stratified	Stratified
28	0.04	Ann	Stratified	Stratified	Stratified
24	0.10	Ann	Ann-Strat	Stratified	Annular - pseudo slug
24	0.08	Ann	Ann-Strat	Stratified	Ann-Strat
24	0.07	Ann	Stratified	Stratified	Stratified
24	0.05	Ann	Stratified	Stratified	Stratified
24	0.04	Ann	Stratified	Stratified	Stratified
19	0.10	Ann	Ann-Strat	Stratified	Ann -pseudo slug
19	0.08	Ann	Ann-Strat	Stratified	Stratified
19	0.07	Ann	Stratified	Stratified	Stratified
19	0.05	Ann	Stratified	Stratified	Stratified
19	0.04	Ann	Stratified	Stratified	Stratified

At the highest U_{SL} and U_{SG} the annular air and water flow contains many of the high amplitude disturbance waves. The pressure gradient is very high. Adding small amount of polymers to the flow causes the pressure gradient to start to drop down and the disturbance waves to start to disappear. With adding enough polymers (reaching 100 ppm) maximum drag reduction is achieved and beyond that amount there was no more drag reduction with adding more polymers, this situation is described as an annular with out disturbance waves (Annular w/o D.W). At lower gas velocity (33 m/s) and same U_{SL} = 0.1 m/s the same sequences happened but the final pattern was stratified-annular instead of an annular for the horizontal and 1.28^o angles and annular with out disturbance waves (Annular w/o D.W) for the 2.4^o angle.

3.2 Drag reduction

The effectiveness of the polymer is expressed in terms of the drag-reduction (DR) defined as in eqn. (1), where $\Delta P_{withDRP}$ is the pressure drop when drag-reducing polymer was present and $\Delta P_{withoutDRP}$ is the pressure drop in the absence of drag-reducing polymer.

$$\mathrm{DR} = \frac{\Delta P_{withoutDRP} - \Delta P_{withDRP}}{\Delta P_{withoutDRP}} \tag{1}$$

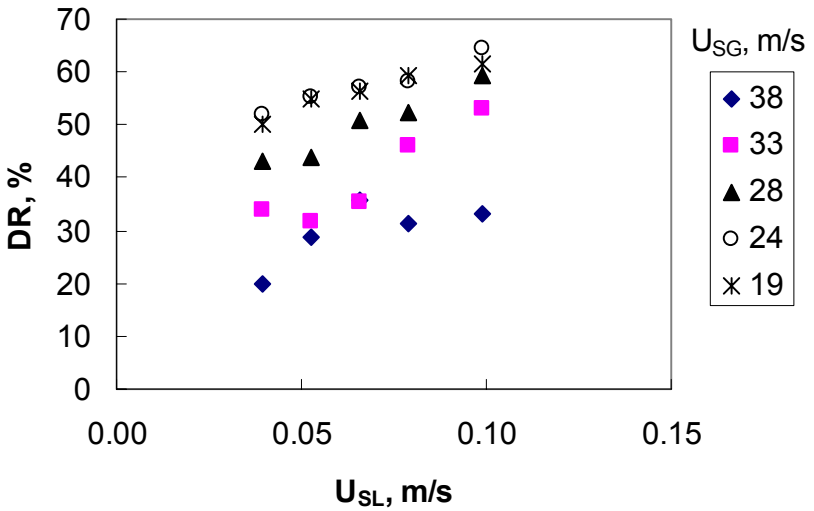


Figure 2: Drag reduction variation with superficial liquid velocity, θ=0°.

Figures 2 to 7 show plots for maximum DR versus U_{SL} and U_{SG} respectively. Figures show that DR is very sensitive to U_{SG} and U_{SL}. The DR and pressure drop increases with increasing U_{SL}. Drag reduction increases with increasing U_{SG} at lower U_{SG} values and then decreases with increasing U_{SG} at higher U_{SG} values. Effect of pipe inclination can be appeared on two things; the first is the changes on the flow pattern with addition of the DRP and the second on the DR. In general, all angles have the same trend of DR with U_{SL} and U_{SG}. The case of 1.28° inclination has the highest DR and the case of 2.4° has the lowest DR. The maximum DR among all experiments occurs at 1.28° inclination and lowest U_{SL} and highest U_{SG}. The effect of pipe inclination also appears on the changes of the flow pattern with adding DRP. At the lowest two U_{SG} (19 and 24 m/s) and the highest U_{SL} (0.1 m/s) the final pattern for air and water with 100 ppm of DRP at inclination of 2.4° was pseudo slug while at 1.28° was stratified and at zero inclination was an annular-stratified. Noting that the maximum DR occurs for the case of 1.24° inclination in which the flow pattern changes from the annular to stratified.

This behaviour agrees with all previous studies, which indicated that the maximum DR accompanied always with change in the flow pattern from annular to stratified.

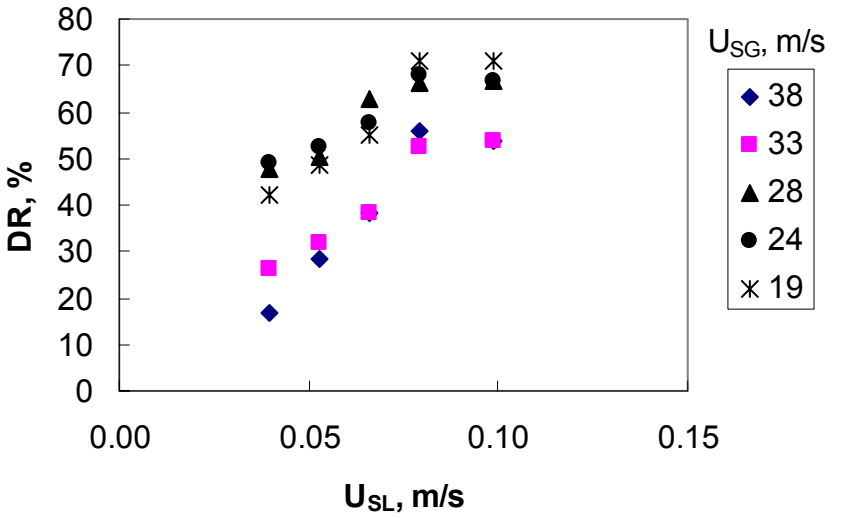


Figure 3: Drag reduction variation with superficial liquid velocity, $\theta = 1.28^{o}$.

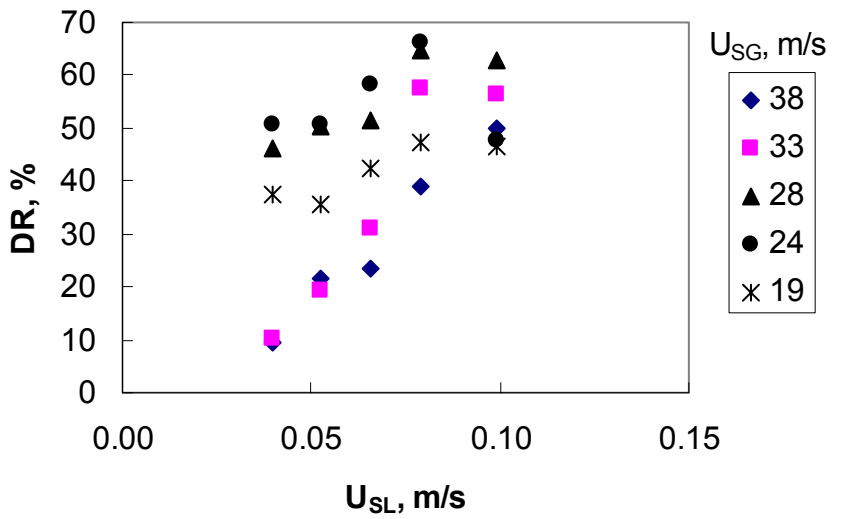


Figure 4: Drag reduction variation with superficial liquid velocity, $\theta = 2.4^{o}$.

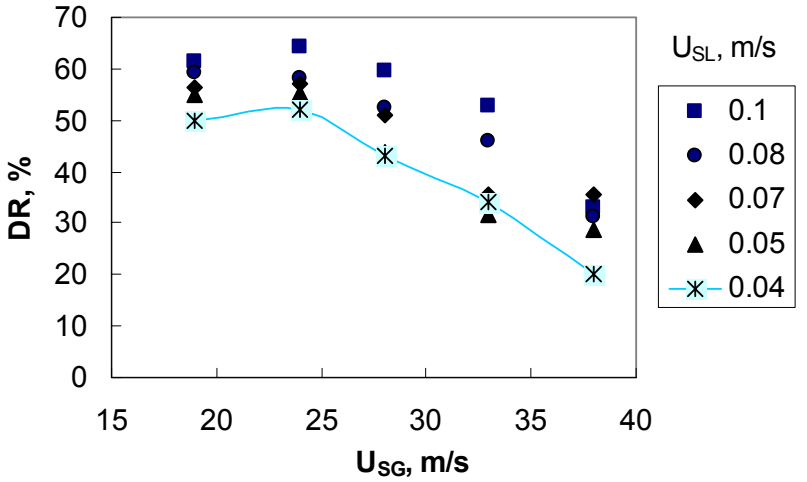


Figure 5: Drag reduction variation with superficial gas velocity, $\theta = 0^{o}$.

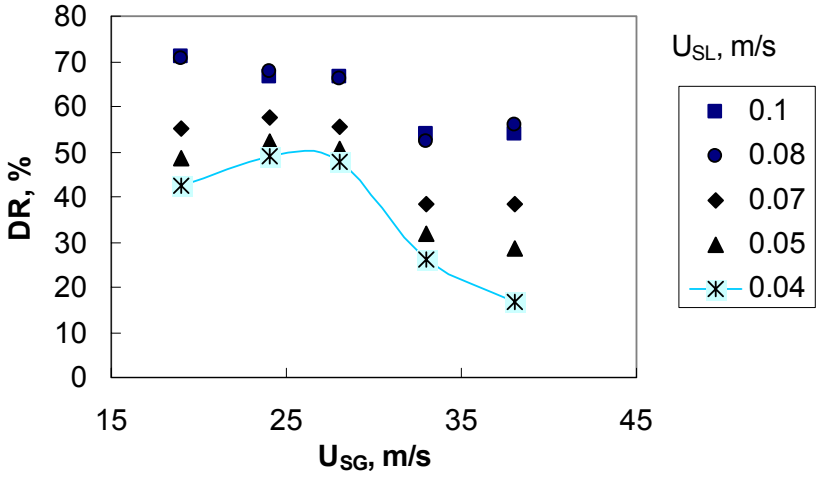


Figure 6: Drag reduction variation with superficial gas velocity, $\theta = 1.28^{o}$.

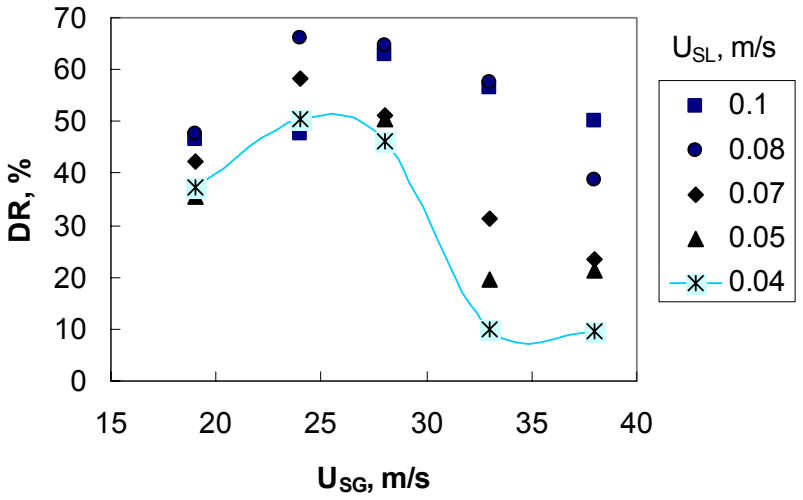


Figure 7: Drag reduction variation with superficial gas velocity, $\theta = 2.4^{o}$.

4 Discussion and conclusions

The injection of polymer solution into an air-water flow that has an annular configuration in an inclined 1.28° pipe can produce drag-reductions of about 71%. The polymer destroys the turbulent disturbance waves, which are the cause of drop formation and which help the water film to spread upward around the pipe circumference.

Visual observation of the pattern changes due to injection of polymers to an annular flow revealed that an annular flow pattern changes to stratified pattern at low superficial liquid and gas velocities. An annular flow pattern changes to an annular-stratified at higher gas and liquid velocities and finally, at highest superficial liquid and gas velocities an annular flow remains an annular but without disturbance waves.

At lowest gas velocities, highest liquid velocity, and highest pipe inclination (2.4°) an annular flow changes to pseudo slug in the presence of DRP which is expectable due to the tendency of accumulation of the liquid at the inlet of pipe with increasing the pipe inclination. The pressure gradient of annular patterns of air and water in the absence of polymers are higher than that of air and water at same liquid and gas rates in the presence of polymers. The maximum drag reduction was achieved in the case of pipe inclination of 1.28° at the lowest superficial gas velocity and the highest superficial liquid velocity. The minimum drag reduction was achieved in the case of pipe inclination of 2.4° and at highest superficial gas velocity and lowest superficial liquid velocity.

Acknowledgement

This work was supported by the Deanship of Research at Hashemite University under grant 29/15/425.

References

[1] Toms, B. A., Some observations on the flow of linear polymer solutions through straight tubes at large Reynolds numbers. *Proceeding. 1st Int. Congress on Rheology*. North Holland publication company, Amsterdam, 2, pp. 135-141, 1948.

[2] Lin, P. G. & Hanratty, T. J., Effect of pipe diameter on flow patterns for air water flow in horizontal pipes, *Int. J. Multiphase Flow* 13, pp. 549-563, 1987.

[3] Sylvester, N. D. & Brill, J.P., Drag-reduction in two-phase annular mist flow of air and water. *AIChE J.* 22 (3), pp. 615-617, 1976.

[4] Sylvester, N.D., Dowling, R. H. and Brill, J.P., Drag Reductions in Concurrent Horizontal Natural Gas-Hexane Pipe Flow, Polymer Engineering and Science, 20, No. 7, pp. 485, 1980.

[5] Al-Sarkhi, A. and Hanratty, T. J., Effect of drag reducing polymer on annular gas-liquid flow in a horizontal pipe. *Int. J. Multiphase flow* 27, pp. 1151-1162, 2001a.

[6] Al-Sarkhi, A. and Hanratty, T. J., Effect of pipe diameter on the performance of drag reducing polymers in annular gas-liquid flows. Trans IChemE 79, Part A pp. 402-408, 2001b.

[7] Soleimani, A., Al-Sarkhi, A. and Hanratty T. J., Effect of drag reducing polymers on Pseudo-slugs-interfacial drag and transition to slug flow. Int. J. Multiphase flow 28, pp. 1911-1927, 2002.

[8] Al-Sarkhi, A. and Soleimani, A., Effect of drag reducing polymer on two-phase gas-liquid flow in a horizontal pipe. Trans IChemE 82 (A12) pp. 1583-1588, 2004.

[9] Rosehart, R. G., Scott, D. & Rhodes, E., Gas-liquid slug flow with drag-reducing polymer solutions, *A.I.Ch.E.J.* 18(4), pp. 744-750, 1972.

[10] Otten, L. & Fayed, A. S., Pressure drop and drag-reduction in two-phase non-Newtonian slug flow, *Can. J. Chem. Eng*. 54, pp. 111-114, 1976.

[11] Kang C., Vancko, R. M., Green, A., Kerr, H. & Jepson, W. Effect of drag-reducing agents in multiphase flow pipelines. *Journal of Energy Resources Technology* 120, pp. 15-19, 1997.

[12] Manfield, C. J., Lawrence C. & Hewitt, G., Drag-reduction with additive in multiphase flow: A Literature Survey. *Multiphase Science and Technology* 11, pp. 197-221, 1999.

[13] Williams, L. R., Dykhno, L. A. and Hanratty, T. J., Droplet flux distributions and entrainment in horizontal gas-liquid flows. *Int. J. Multiphase Flow* 22, No. 1, pp. 1-18, 1996.



Fluid flow simulation in a double L-bend pipe with small nozzle outlets

A. Rigit[1], J. Labadin[2], A. Chai[1] & J. Ho[1]
[1]*Faculty of Engineering, University Malaysia Sarawak, Sarawak, Malaysia*
[2]*Faculty of Computational Science and Information Technology, University Malaysia Sarawak, Sarawak, Malaysia*

Abstract

The results of fluid flow simulation in a double L-bend pipe with small nozzle outlets are presented in this paper. The pipe geometry represents a sparger for a mixing process in a tank. The flow simulation was performed with a commercially available computational fluid dynamics package, Star-CD. The effects of the L-bend and small nozzle outlets on the velocity and pressure distributions in the pipe are discussed. The discussion will lead to an improved design of the sparger with the objective of obtaining a uniform fluid discharge from the nozzle outlets.
Keywords: flow simulation, computational fluid dynamics, velocity and pressure distributions.

1 Introduction

The primary process in manufacturing computer hard discs is the process of coating nickel sulphamate solution onto the discs. The nickel solution is normally fed into a mixing tank via a double L-bend pipe, which represents a sparger with small nozzle outlets. However, the coating process may be affected by non-uniform distribution of the nickel solution inside the mixing tank, resulting in an uneven nickel coating thickness at the discs surface. It is therefore desirable to have a uniform fluid discharge from the pipe nozzle outlets in order to obtain a uniform distribution of the nickel solution inside the mixing tank. The variables that may be changed in order to get the optimum results would be the pipe geometry, design or even the control of pressure of the fluid flow as



WIT Transactions on Engineering Sciences, Vol 52, © 2006 WIT Press
www.witpress.com, ISSN 1743-3533 (on-line)
doi:10.2495/AFM06038

previously discussed by Morrison [1] and Aroussi et al. [2, 3] on CFD and experimental studies for a gas phase flow in a double elbows pipe problem.

The objectives of this paper are to present the fluid flow visualization in the pipe and to decide which variables that should be changed in order to obtain a uniform fluid discharge from the nozzle outlets.

2 Computational modelling

2.1 The configuration examined

The computational fluid dynamics (CFD) explores the effects of a double 90° L-bend and a series of equally spaced small nozzles along one side of the pipe horizontal arm on the fluid flow. The configuration used in the study is shown in Fig. 1. The pipe geometry is a double L-bend configuration with both elbows perpendicular to each other. The length of the smooth pipe is modelled to be equivalent to 20 times the diameter of the pipe. This double L-bend configuration also replicates many pipe structures present in a range of pipe networks.

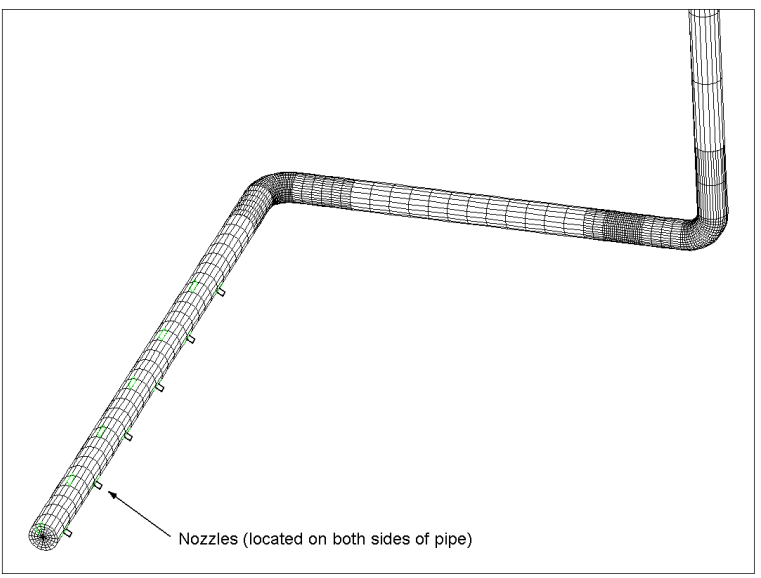


Figure 1: The configuration of the double L-bend pipe with series of nozzles located after the 2nd bend.

2.2 The CFD model

The flow predictions were carried out using a commercially available CFD package, Star-CD 3.15. The solid geometries were modelled using SolidWorks,

which are then imported into ProStar of Star-CD. The grid generation and meshing were created using manual-generation of vertices and splines.

Star-CD provides various differencing scheme in the package in order to produce fluid simulation that best describes the problem nature. The central-differencing (CD) scheme was chosen over the other schemes such as upwind-differencing (UD) and self-filtered central differencing (SFCD) since the CD scheme:

a) is of higher order scheme (second-order accuracy),
b) interpolates linearly on the nearest neighbouring values, and
c) produces less numerical diffusion;

SFCD blends UD and CD together and thus making it a second-order accurate. However, this scheme was not chosen due to the fact that it has the possibility of generating additional non-linearity. An example of the CD scheme being applied to flow simulation is described by Mendonça et al. [6].

The mass and momentum conservation equations solved by Star-CD for general incompressible and compressible fluid flows and a moving coordinate frame (essentially, the Navier-Stokes equations) are, in Cartesian tensor notation [7]:

$$\frac{1}{\sqrt{g}}\frac{\partial}{\partial t}(\sqrt{g}\,\rho)+\frac{\partial}{\partial x_j}(\rho\,\tilde{u}_j) = s_m$$

$$\frac{1}{\sqrt{g}}\frac{\partial}{\partial t}(\sqrt{g}\,\rho\,u_i)+\frac{\partial}{\partial x_j}(\rho\,\tilde{u}_j\,u_i-\tau_{ij}) = -\frac{\partial p}{\partial x_i}+s_i \qquad \text{(1a\&b)}$$

where

t	—	time
x_i	—	Cartesian coordinate (i = 1, 2, 3)
u_i	—	absolute fluid velocity component in direction x_i
$\tilde{u}_j$	—	$u_j - u_{cj}$, relative velocity between fluid and local (moving) coordinate frame that moves with velocity u_{cj}
p	—	piezometric pressure = $p_s - \rho_0 g_m x_m$ where p_s is static pressure, ρ_0 is reference density, the g_m are gravitational field components and the x_m are coordinates from a datum, where ρ_0 is defined
ρ	—	density
τ_{ij}	—	stress tensor components
s_m	—	mass source
s_i	—	momentum source components
$\sqrt{g}$	—	determinant of metric tensor

In the case of laminar flows, Star-CD caters for both Newtonian and non-Newtonian fluids that obey the following constitutive relation

$$\tau_{ij} = 2\mu s_{ij} - \frac{2}{3}\mu \frac{\partial u_k}{\partial x_k}\delta_{ij} \tag{2}$$

where μ is the molecular dynamic fluid viscosity and, δ_{ij}, which is the Kronecker delta, is unity when $i = j$ and zero otherwise and finally, s_{ij} , the rate of strain tensor, is given by

$$s_{ij} = \frac{1}{2}\left(\frac{\partial u_i}{\partial x_j} + \frac{\partial u_j}{\partial x_i}\right) \tag{3}$$

The governing equations are then discretize using the central-differencing scheme with a blending factor of 1. Relaxation factors were set at 0.8 and 0.5 for the momentum in the vertical direction and pressure solver parameters respectively. The sparger model has 35420 fluid-cells with 320 partial boundaries.

2.3 The CFD simulations

The periodic cross-sectional contour-plots of the velocity-magnitude within the 2nd L-bend of the sparger is shown in Fig. 2. It is observed at the middle-part of the pipe, the plots tend to exhibit horizontal-forms of contour-plots. This signifies the fluid-flow interaction around the boundary-regions of the nozzles.

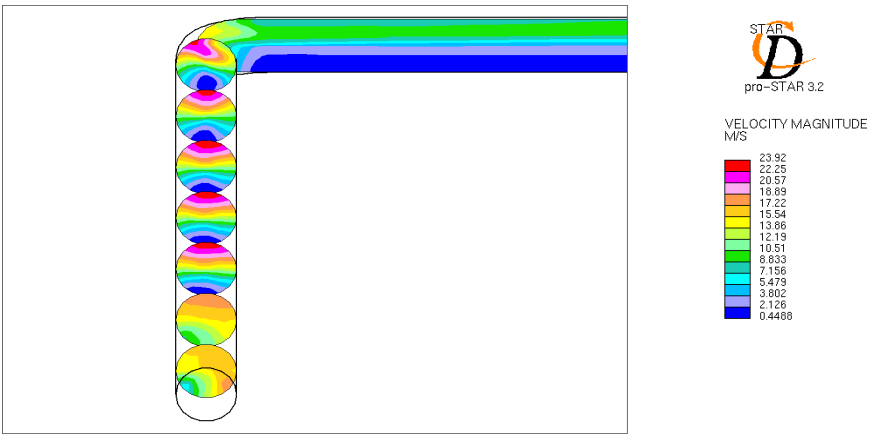


Figure 2: Periodic cross-sectional velocity-magnitude in contour-plot.

Figure 3 shows the particle-tracking plot with ribbon-widths of 0.1 model units and a twist-magnification of 1. The ribbons are also plotted with mesh-plotting. This plot allows a much closer observation on the fluid-flow within the sparger at the 2nd L-Bend. It is observed that the fluid flow is experiencing a vortex flow.

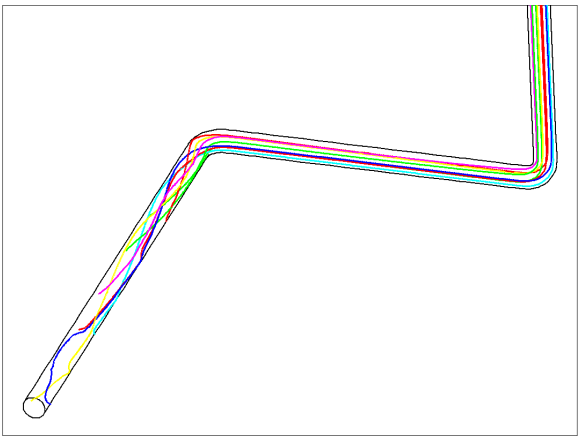


Figure 3: Particle-tracking in ribbon-form at 2nd L-Bend of sparger in isometric view.

Figures 4 and 5 depicted the velocity and total pressure magnitude respectively for the whole pipe configuration. The fluid flow at the 1st L-bend showing adverse pressure gradient indicating the occurrence of wake. However, downstream of the pipe before the 2nd L-bend, the flow settles and the distribution shows that the flow tends to be uniform. On the other hand, this flow is not observed after the 2nd L-bend.

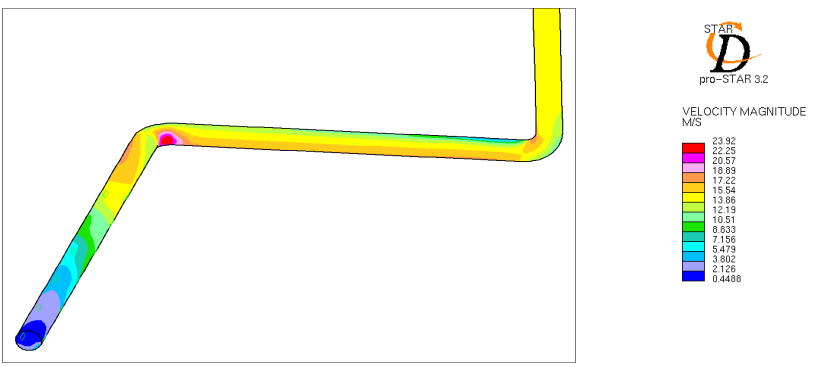


Figure 4: The velocity distribution in the pipe.

This is clearly shown in Figure 6, where 20 contour-plots of the velocity magnitude at this section of the pipe are presented, that the flow is circulating.

3 Discussion

The results from the CFD simulations show that there exists a secondary flow in both bends, which is due to the dynamic pressure differences created on each

bend. This phenomena is described in detail in many standard fluid mechanics textbooks, such as Munson et al. [4] and Çengel and Cimbala [5]. To reduce swirls and disturbances as observed in such flows, Munson et al. [4] suggest to use carefully designed guide vanes that help to direct the flow so that it stays uniform.

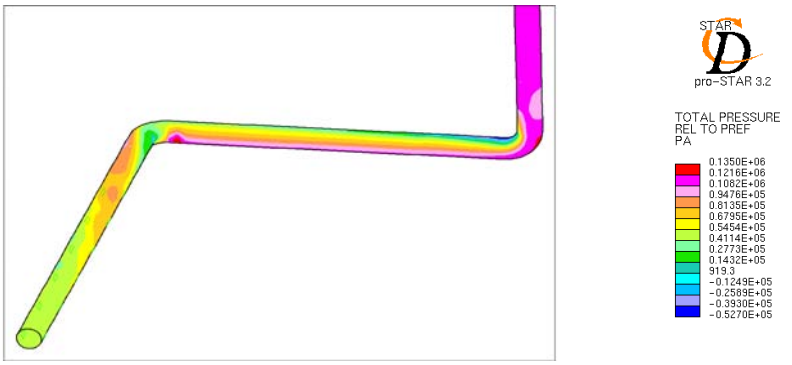


Figure 5: The total pressure distribution for the pipe.

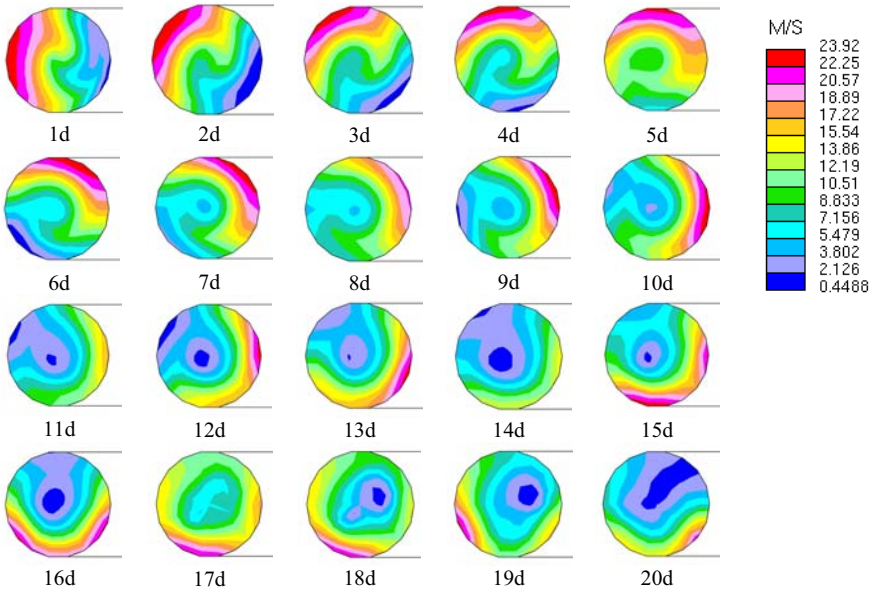


Figure 6: 20 contour-plots of the velocity magnitude at cross-sectional view.

Nevertheless, further upstream of the pipe bend without any guiding vanes, the velocity profiles should settle into a more uniform distribution (see Figure 4 and 5). The length of the pipe plays significant role in ensuring this statement as what has been concluded in Aroussi et al. [2] that the secondary flow patterns

depends on the pipe geometry. However, this fully developed uniform flow pattern is not observed when the series of nozzles are included on the outlet arm. The flow becomes erratic whereby the streamlines follows a wave-like pattern (see Figure 3). This suggests that the fluid injected through the nozzles will not be of the same volume. In order to address this non-uniformity of fluid discharge from the nozzles, the location of the nozzle along the pipe and the size of the nozzle diameter could be varied as a function of the pipe length.

4 Conclusions

In order to obtain a uniform fluid discharge from the nozzles, the fluid flow past the second bend must be controlled so that the secondary flows will not occur. This suggests that the pipe configuration and design needs to be improved, perhaps by including guided vanes on the L-bends and adjusting the position of the nozzles and their diameter along the pipe.

Acknowledgements

Our gratitude to University Malaysia Sarawak for financial support (Fundamental research grant Code 02(55)/465/2004(202)), the Malaysian Ministry of Science, Technology and Innovation for student sponsorship (Almon Chai), and Komag USA (Malaysia) Ltd. for research collaboration.

References

[1] Morrison, G.L., Flow field development downstream of two in plane elbows. *Proc. of the ASME Fluids Engineering Division Summer Meeting*, Vancouver, British Columbia, Canada, Paper No: FEDSM97-3021, 1997.

[2] Aroussi, A., Roberts, J., and Rogers, P., Investigation of secondary flows in double pipe elbows: CFD study. *Proc. of the 11th Int. Symp. on Flow Visualizations*, Notre Dame, Indiana, USA, Paper No: 39, 2004.

[3] Aroussi, A., Roberts, J., Rogers, P., and Box, G., Investigation of secondary flows in double pipe elbows: an experimental study. *Proc. of the 11th Int. Symp. on Flow Visualizations*, Notre Dame, Indiana, USA, Paper No: 40, 2004.

[4] Munson, B. R., Young, D. F. and Okiishi, T. H., *Fundamentals of Fluid Mechanics (4th Ed.)*, John Wiley & Sons: USA, pp. 486, 2002.

[5] Çengel, Y. A. and Cimbala, J. M., Flow in pipes (Chapter 8). *Topics in Fluid Mechanics: Fundamentals and Applications*, McGraw-Hill: New York, pp. 335-354, 2005.

[6] Mendonça, F., Allen, R., Charentenay, J.D., and Lewis, M., Towards understanding LES and DES for Industrial Aeroacoustic Predictions. *Proc. Int. Workshop on 'LES for Acoustics'*, Göttingen, Germany, 2002.

[7] Star-CD Methodology, Star-CD Ver. 3.15A, Computational Dynamics Ltd., UK, 2002.



This page intentionally left blank

Stability analysis of dredging the flow sediment regiment upstream a dam

G. Akbari
Civil Engineering Department, University of Sistan & Baluchestan, Iran

Abstract

The overall aim of this study was to investigate stability of flow-sediment regime upstream from a dam, to develop and calibrate a one-dimensional flow-sediment transport numerical model to deal with the many river-reservoir sedimentation problems including river reservoir dredging upstream from a dam. The basic physical principles of the conservation of mass and momentum are used to describe the fluid flow. The conservation of mass and semi-empirical equations governing sediment particle movement are adopted to establish the interaction between the sediment movement and fluid flow. The resulting mathematical formulation is highly non-linear and complex. It is impractical, if not impossible, to solve them analytically. Therefore the three governing equations of water continuity, sediment continuity, and momentum were solved numerically. The three governing equations were solved in an approximate linear form as well as in the more complete non-linear form. Also, by ignoring certain terms, the sediment continuity equation was uncoupled from the other two. Algorithms were developed for linear or non-linear and coupled or uncoupled solutions.
Keywords: dredging upstream, linear, non-linear, coupled, uncoupled, water-sediment phases.

1 Introduction

In recent years, many major projects have caused serious difficulties as proper account has not been taken of their relationship with the surrounding environment. It has been estimated that nearly 14000 mega tonnes of sediment is carried annually by rivers worldwide and is deposited in man made reservoirs. This reduces the capacity of reservoirs which leads to an equivalent loss of 6 billion dollars per annum [5]. Dredging river reservoir upstream a dam is a



WIT Transactions on Engineering Sciences, Vol 52, © 2006 WIT Press
www.witpress.com, ISSN 1743-3533 (on-line)
doi:10.2495/AFM06039

necessary measure for stabilizing river flow condition upstream a dam. This can slow down the energy when the release of sediment free water from the dam results in considerable downstream erosion of banks and riverbeds. The release of clear water from the Imperial dam after its closure in 1938 caused the scour of large amounts of sand and silt from the riverbed downstream, creating large difficulties. The same is the case at Hoover, Parker, Garison and many dams worldwide. Due to the erosion downstream of the Senner Dam located south of Khartoum in the Sudan, the costs of repairs are assessed to be around 16 million dollars which will be more than the original cost of the dam [6]. The sediment-free water below the dam flows faster and tends to re-acquire a normal sediment load. The resulting erosion may be dangerous for the foundations of hydraulic structures existing downstream of the dam and dam itself. For example the resulting erosion downstream of Aswan High Dam threatens to undermine the foundations of 3 dams and 550 bridges between the Aswan High Dam and the sea [2]. However, case studies of past projects show that the effects of changes in flow regimes can help in comprehensive planning of the dam and reservoir projects and environmental losses can be controlled. The construction of the Trans Florida Barrage Canal was abandoned in the USA because from the calculations it was felt that adverse environmental effects due to the changes in the river regime outweighed the proposed benefits.

2 Simulation of sediment-laden flow upstream a dam

Numerical models can be used to predict the water-surface profile during floods, the effect of river engineering works at one location on the rest of the system, and long-term maintenance requirements. Sediment transport phenomena are very complex and time variant even when the flows are steady. For example flow upstream and downstream of newly constructed obstruction or flow in a newly dredged channel until regime conditions is achieved. To simulate time-dependent transient flow in open channels, the unsteady flow of sediment-laden water can be formulated in terms of three one-dimensional partial differential equations. These equations can be represented as:
Modified St. Venant Eqn. for sediment mass flow:

$$\partial Qs/\partial x + p_{or}\partial Ad/\partial t + \partial ACs/\partial t = q_{ls} \tag{1}$$

Modified St. Venant Eqn. for water mass flow:

$$\partial Q/\partial x + \partial A/\partial t + \partial Ad/\partial t = q_l \tag{2}$$

Modified Hydro dynamic St. Venant Eqn. for sediment-laden mass flow:

$$\rho\partial Q/\partial t + \beta\,\partial/\partial x[\rho\, Q^2/A + \rho g\, A/T\, dA/\partial x - \rho g A\,(S - S_f) - \rho\, q_l\, Q/A +$$

$$\rho\, Q/A\ \partial Ad/\partial = 0 \tag{3}$$

The different parameters used in above equations are: $\boldsymbol{Q}$ is the discharge; $\boldsymbol{A}$ is the area of cross-section; $\boldsymbol{A_d}$ is the volume of sediment deposited/eroded per unit

length of channel; x is the distance along the channel; t is the time; q_l is the lateral flow per unit length of channel; β is the momentum correction factor; g is the acceleration due to gravity; T is the channel top width; S is the bed slope and S_f the friction slope; Q_S is the sediment discharge, C_S is the sediment concentration = Q_S/Q, p_{or} represents the volume of sediment in unit volume of bed layer and q_{lS} is the lateral sediment flow. The friction slope S_f and sediment load Q_S need to be defined by what may be called the supplementary equations (see [6]). Prior knowledge of some of the parameters embedded in these supplementary equations is required in order to route flow and sediment down a river reach.

3 Flow-sediment dredging upstream

A steady flow problem involving dredging upstream was attempted to investigate the relative performances of the four different numerical solutions. The same data used here are as follows.

3.1 Channel characteristics

A wide rectangular channel was selected. The reach length was taken as 20 km with special increment of Δx = 500m and the bed slope, S =0 .0005. The initial flow was assumed to be $5m^3/s$ per unit width at the upstream end. The normal initial depths were assumed as 3m and then the depth at the upstream end was made 5m due to the dredging of 2m.

3.1.1 Upstream boundary condition

A steady flow of 5 m^3/s per unit width was imposed (U/S boundary condition), and a second boundary condition was defined by using a constant bed level condition at node-1.

3.1.2 Downstream boundary condition

The downstream boundary condition was defined by the Manning's equation.

3.1.3 Frictional slope

It is possible to use any roughness equation such as Chezzy, Colebrook-White, or Manning formula to estimate riverbed roughness. For this case study, the frictional slope was calculated by a general form of Manning equation as follows.

$$S_f = [\alpha Q / A R^{\beta}]^2 \tag{4}$$

where, S_f is bed resistance, α and β are empirical parameters need to be adjusted, Q, A, R are flow discharge, cross sectional area, and hydraulic radius respectively.

3.1.4 Sediment characteristics

A uniform sediment bed material was selected. The value of volume of sediment per unit volume of bed layer, p_{or}, was 0.8, and effective grain size (d_{35}) was taken as 0.8 mm. Sediment discharge, Q_S, was calculated using the simple equation as follows.

$$Q_S = \alpha\,(Q/A)^{\beta}\,Q/y\,d_m^{\gamma} \tag{5}$$

where, α, β *and* γ are the sediment parameters to be optimized. Such simplified forms of the equations are acceptable when the parameters are specifically fitted to a particular situation by optimization methods [6]. The bed level at the upstream end was dredged by 2 m.

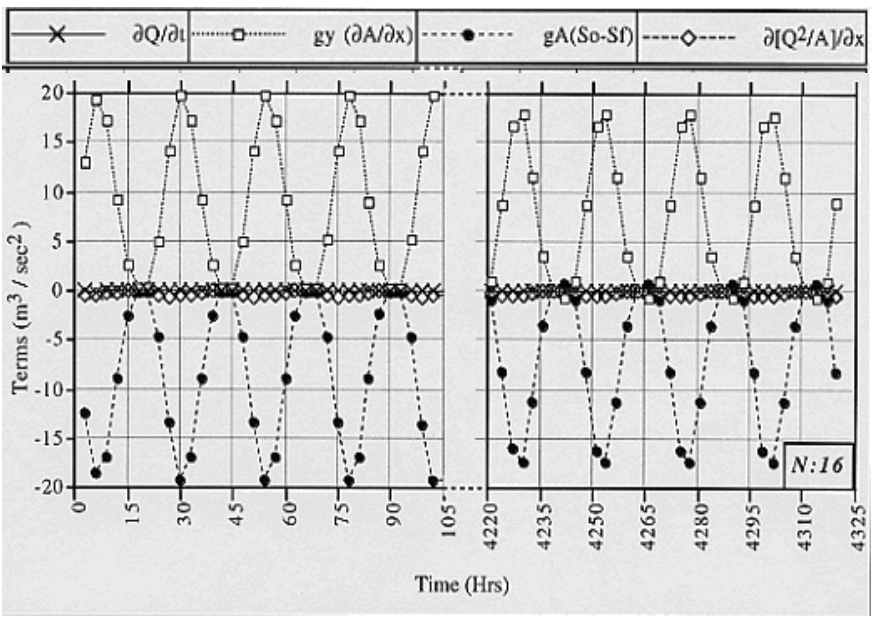


Figure 1: Magnitude of non-linear terms in the flow-sediment equation.

4 Results and discussion

Comparison of results for different models is shown in figures 2 to 5. As can be seen, all of the models developed by author produced stable flow-sediment configuration. In particular the implicit non-linear and linear solutions are not significantly different for stable flow-sediment regime upstream a dam. This means that the linearization of the non-linear terms in the governing equations (1-5) did not affect the result, because the second and higher order partial differential terms of each variable between two successive nodes were so small for each time step. This confirms that when flow-sediment regime was stable, no

large spatial or/and temporal changes occurred in the variables Q, A, A_d etc., the errors due to ignoring the derivatives of non-linear terms [$\partial(Q^2/A)/\partial x$ and gA/T ($\partial A/\partial x$)] in the momentum equation was insignificant. The linear models (LCM and LUM) can therefore be used here as satisfactorily as the non-linear (NCM and NUM) models. De-coupling the hydraulic and sediment variables in the uncoupled models, may lead to an ill-posed problem for which a general boundary condition cannot be satisfied. However, an upstream boundary provided constant discharge to the system, with the sufficient initial conditions, may result in a well-posed problem. That is also the reason why coupled and uncoupled models bring stable results. Further analysing the results shown in the figures, it shows that for dredging upstream, coupling and uncoupling the system of equations only had very little effect on the solution at the upstream end. This is due to the boundary condition at the upstream, which is mainly affected by the dredging at the upstream. Also as discussed earlier, the sediment continuity and momentum equations are implicitly coupled through the bed and frictional slope terms in the momentum equation.

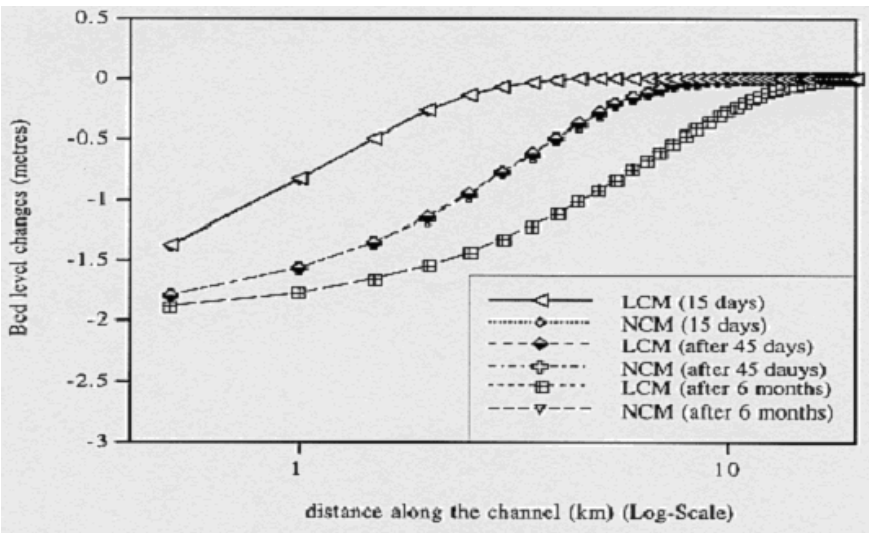


Figure 2: Comparison of coupled linear/non-linear models stable regime upstream.

For a stable flow regime the result of uncoupled models has shown satisfactory results, but the general problem with the uncoupled models is that they are unable to satisfy an arbitrary boundary condition. This is because the uncoupled solution of the equations (2) and (3) gives Q and A values at all nodes, from which A_d values are determined using equation (1). Different numerical solutions were implicated can differ from each other in one way or another, for instance non-linear/linear implicit coupled and uncoupled models are quite different solution techniques.

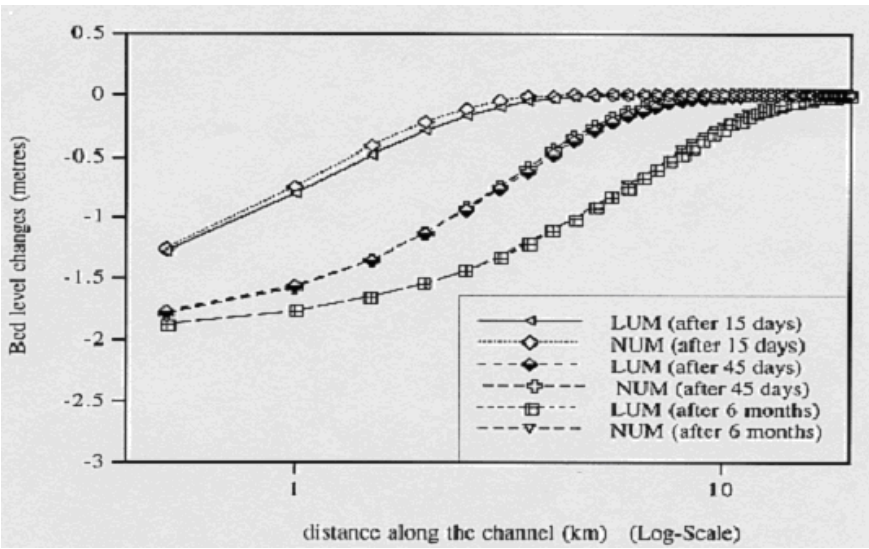


Figure 3: Comparison of uncoupled models stable regime upstream a dam.

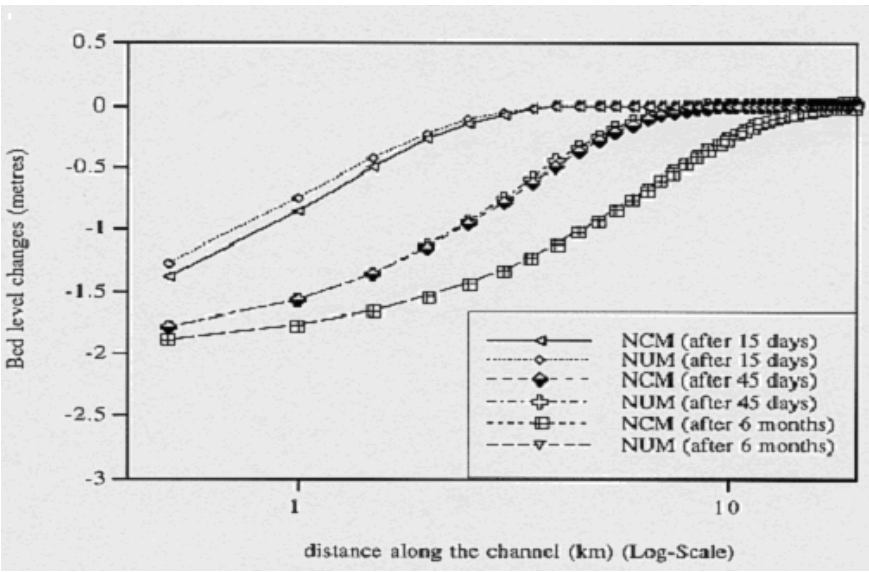


Figure 4: Comparison of coupled uncoupled non-linear models stable regime upstream.

However, when applying these models to a particular case (e.g. the stable flow regime upstream) they have almost the same results. This is mainly because of the implicit coupling in the uncoupled models through bed and frictional

slopes in the momentum equation [bed and frictional slopes are treated in a similar way to other variables and discredited by weighted approximations in an implicit scheme. A conclusion may reach here that for some cases (e.g. the case study at the hand) neither the non-linear nor linear implicit solution to the governing equations can be better than the others. Because, each of these model could produce almost the same result, when the same values of the parameters Δx and Δt were used.

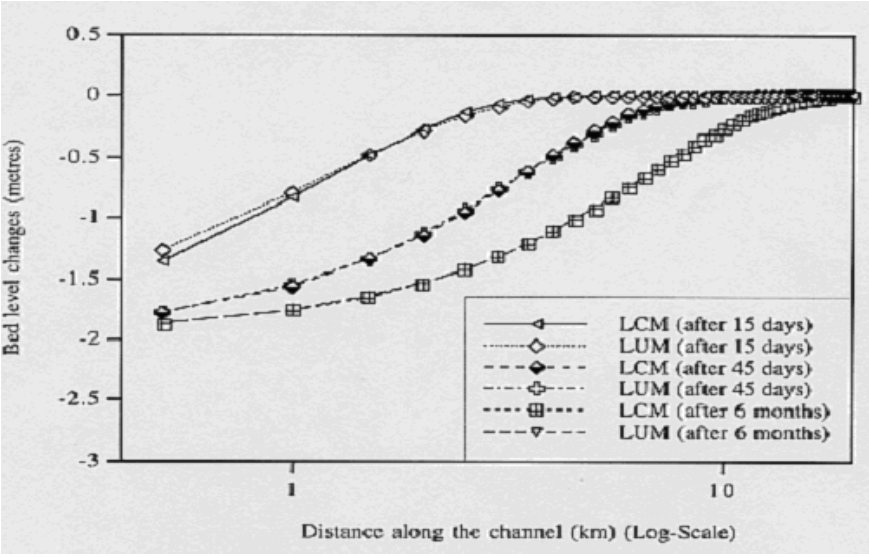


Figure 5: Comparison of coupled uncoupled linear models stable regime upstream.

References

[1] Ackers, P., and White, W.R., "Sediment Transport-New Approach and Analysis," Journal of the Hydraulics Division, ASCE, Vol. 99, No. HY11, November, 1973, 2041-2060.

[2] Akbari, G.H., Wormleaton, P.R., Ghumman, A.R., "A Numerical Model for Estimation of Sedimentation in Reservoirs," Proceedings of International Conference on Aspects of Conflicts in Reservoir Development and Management, pp. 731-41, City university, London, 3-5 Sept. 1996.

[3] Akbari, G.H., Wormleaton, P.R., Ghumman, A.R., "A Simple Bed Armoring Algorithm for Graded Sediment Routing in Rivers", Water for a Changing Global Community, 27th IAHR Congress, 10-15 August 1997 San Francisco, USA.

[4] Akbari, G.H., "Sensitivity analysis of flow-sediment transport parameters", 6th Seminar of Iranian students in Europe, UMIST, Manchester, UK, 1999.
[5] Akbari, G.H., "Fully coupled non-linear mathematical model for flow-sediment routing through rivers", PhD Thesis, Q.M. University of London, 2003.
[6] Chin, C.O., Melville, B.W., Raudkivi, A.J. "Armoring Development" J. Hyd. Engg. ASCE, Vol. 120, No. 8, pp. 899-918, 1994.
[7] Correia, L.P. "Numerical Modeling of Unsteady Channel Flow Over a Mobile Boundary", These No 993 (1992), Ecole Polytechnique Federal De Lausanne.
[8] Fisher, K.R. "Manual of Sediment Transport in Rivers" HR, Wallingford Report SR 359, May 1995.
[9] Ghumman A. R, Wormleaton P.R, Akbari G.H, "Estimation of Changes in Flow Regimes After Construction of a Dam", Proceedings of International Conference on Aspects of Conflicts in Reservoir Development and Management, pp. 749-55, 3-5 Sept, London, 1996.
[10] Ghumman A. R, Wormleaton P.R, Hashmi H.N, Akbari G.H, "Parameter identification for Sediment Routing in Rivers" IAHR, Journal of Hyd. Research, Vol. 34-1996.
[11] Little, W.C., Mayer, R.G., "The Role of Sediment Gradation on Channel Armoring", Pub. No. ERC-0672, School of Civil Engg, Georgia Instit. Of Technology, Atlanta, Georgia, 1972.
[12] NAG, "NAG Fortran Library Manual", QMW, Univ. of London, 1985.
[13] Nakato, T. "Tests of Selected Sediment Transport Formulae", J. Hyd. Engg, ASCE, Vol. 116, No. 3, pp. 362-379, 1990.
[14] Wormleaton, P.R., Ghumman, A., R., and Akbari G., H., "A Comparison of the Performance of Coupled/Uncoupled Non-linear Models for Sediment Routing in Rivers", Proceedings of the Regional Conf. on Water Resources Management (WRM 95), Isfahan, Iran, 1995.
[15] Wormleaton, P.R., Ghumman, A., R., and Akbari G., H., "Degradation Numerical Models for the Missouri River", Proceedings of International Conference on Aspects of Conflicts in Reservoir Development and Management, pp. 759-67, 3-5 Sept, London, 1996.



Section 8
Non-Newtonian fluids

This page intentionally left blank

Viscous spreading of non-Newtonian gravity currents in radial geometry

V. Di Federico[1], S. Cintoli[1] & G. Bizzarri[2]
[1]*D.I.S.T.A.R.T. - Idraulica, Università di Bologna*
[2]*Dipartimento di Architettura, Università di Ferrara*

Abstract

A gravity current originated by a power-law viscous fluid propagating in axisymmetric geometry on a horizontal rigid plane below a fluid of lesser density is examined. The intruding fluid is considered to have a pure power-law constitutive equation. The set of equations governing the flow is presented, under the assumption of buoyancy-viscous balance and negligible inertial forces. The conditions under which the above assumptions are valid are examined and a self-similar solution in terms of a nonlinear ordinary differential equation is derived for the release of a fixed volume of fluid. The space-time development of the gravity current is discussed for different flow behavior indexes.
Keywords: non-Newtonian fluid, density current, gravity current, viscous flow, self-similar solution.

1 Introduction

Gravity currents, also termed density or buoyancy currents, are usually defined as flow of one fluid into another, driven by a density difference. These currents are mainly horizontal and are a common feature in many natural and artificial phenomena. Spreading of a gravity current along a rigid horizontal surface is governed by an interplay between buoyancy, inertial, and viscous forces. In the process, a gravity current passes through several distinct flow regimes which are characterized by the relative balance of forces. Immediately after its release, a gravity current usually experiences an adjustment phase that is strongly influenced by the release conditions. Subsequently, the balance between the buoyancy and inertial forces governs flow (this phase being thus termed the inertial regime) and holds until the current becomes so thin that viscous effects


WIT Transactions on Engineering Sciences, Vol 52, © 2006 WIT Press
www.witpress.com, ISSN 1743-3533 (on-line)
doi:10.2495/AFM06040

become comparable with the inertia of the current, if this ever happens. In this later stage (the viscous regime), flow is governed by the buoyancy and viscous forces. Typical currents which eventually evolve into the viscous regime include mudflows, lava flows, and those originating by discharge of effluents into rivers or lakes.

A large body of literature exists on gravity currents in different geophysical [1], environmental and industrial applications: for a review see Simpson [2, 3]. Horizontal gravity currents were studied by Hoult [4], Huppert and Simpson [5] and Didden and Maxworthy [6] among others. Huppert [7] derived, under a lubrication approximation, a spreading relationship (rate of advance of the front) for plane and axisymmetric gravity currents in the buoyancy-inertia and buoyancy-viscous regimes. His theoretical findings are in a good agreement with the experimental work by Huppert and Simpson [5], Didden and Maxworthy [6] and Maxworthy [8] for the release of a constant volume or constant inflow rate. Rottman and Simpson [9] extended these experimental results to the slumping phase of an inertial gravity current. There also exists a number of stability analyses of analytical solutions for inertial gravity currents [10, 11, 12] and for viscous gravity currents [13]. Thomas et al. [14] and Marino and Thomas [15] included a porous substrate in their analysis of the inertial gravity currents. Ross et al. [16] incorporated in their analysis the effect of a sloping lower boundary.

Despite significant progress in understanding gravity currents of Newtonian fluids, there is a relatively poor number of studies of this phenomenon for non-Newtonian fluids. However, many fluids of geophysical or industrial interest exhibit a non-Newtonian rheology, with or without a yield stress. The simplest non-Newtonian rheological model is the Ostwald power-law model [17], which may be successful in describing the behavior of colloids, suspensions, fresh magma, and polymeric liquids. The power-law rheological model can also be seen as the asymptotic behavior of the Herschel-Bulkley model (in the limit as the yield stress tends to zero), which is widely adopted to describe flow of fine sediment-water mixtures [18, 19, 20]. Adopting a pure power-law model may facilitate the derivation of exact similarity solutions, such as that of Wilson and Burgess [21] for two-dimensional steady-state flow down a sloping plane. In the present paper, we derive the similarity solution for radial flow of a constant volume of a non-Newtonian power-law fluid with arbitrary flow behavior index. We do so in a way that generalizes earlier results of Huppert [7] obtained for a Newtonian fluid. Analogous results for the release of a fixed volume of fluid in plane geometry were obtained in [22] and later generalized for time dependent influx volume in [23].

2 Flow modeling

Consider a horizontal, radial gravity current of an incompressible non-Newtonian fluid of density ρ at the bottom of an ambient fluid of depth H and density ρ-$\Delta\rho$. (For the coordinate system see Fig. 1). In the shallow water approximation, the pressure distribution is hydrostatic, so that pressure satisfies (see [7]).

$$p = p_0 + (\rho - \Delta\rho)g(H - h) + \rho g(h - z) \tag{1}$$

where h is the non-Newtonian fluid depth and p_0 is the constant pressure at $z = H$. Neglecting inertial forces, while accounting for buoyancy, gravitational, and viscous forces, results in the following momentum balance in cylindrical coordinates

$$\frac{\partial p}{\partial r} + \frac{\partial \tau_{zr}}{\partial z} = 0 \tag{2}$$

where r, z are the radial and axial and coordinates, respectively; p is pressure and τ_{zr} is shear stress. The validity of the simplified buoyancy-viscous balance (2) is explored in the Appendix, where the ratio between inertial and viscous forces is shown to be a decreasing function of time; thus, inertial forces are negligible for $t >> t_1$, where t_1 is a threshold time value that renders equal inertial and viscous forces; its expression is derived explicitly in the Appendix.

An intruding fluid is considered to obey a pure power-law constitutive equation (see [17]).

$$\tau_{zr} = -m\left|\frac{\partial u}{\partial z}\right|^{n-1}\frac{\partial u}{\partial z} \tag{3}$$

where u is radial velocity, m consistency index, n flow behavior index (a positive real number). When $n < 1$, the model describes pseudoplastic (shear-thinning) behavior, whereas $n > 1$ represents dilatant (shear-thickening) behavior. When n equals unity, (3) reduces to the constitutive equation for a Newtonian fluid and m becomes Newtonian viscosity μ.

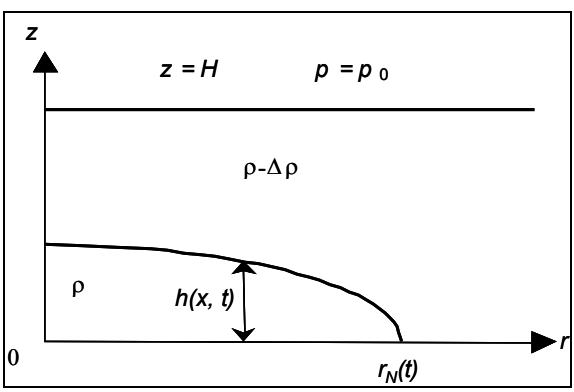


Figure 1: Sketch of flow domain.

Substituting (1) and (3) in (2) gives

$$\rho g' \frac{\partial h}{\partial r} - mn\left|\frac{\partial u}{\partial z}\right|^{n-1}\frac{\partial^2 u}{\partial z^2} = 0 \tag{4}$$

where $g' = g\,\Delta\rho/\rho$ is reduced gravity. Eq. (4) is subject to the boundary conditions

$$u(z=0)=0;\quad \frac{\partial u}{\partial z}(z=h)=0 \tag{5}$$

The second condition in (5) implies that shear stress at the interface between the two fluids is much smaller than within the current. Validity of this assumption in the regime of a buoyancy-viscous balance can be demonstrated by following the argument of Huppert ([7], see his Appendix B). Integration of (4) with (5) yields the following expression for the velocity *u*

$$u = -\frac{n}{(n+1)\dfrac{\rho g'}{m}\dfrac{\partial h}{\partial r}}\left\{\left[\frac{\rho g'}{m}\frac{\partial h}{\partial r}(z-h)\right]^{\frac{n+1}{n}} - \left[-\frac{\rho g'}{m}h\frac{\partial h}{\partial r}\right]^{\frac{n+1}{n}}\right\} \tag{6}$$

For one-dimensional transient flow, the mass conservation takes the form

$$\frac{\partial h}{\partial t} + \frac{1}{r}\frac{\partial}{\partial r}\int_0^h rh(r,t)dz = 0 \tag{7}$$

Substituting (6) into (7) yields

$$\frac{\partial h}{\partial t} + \frac{n}{2n+1}\frac{1}{r}\frac{\partial}{\partial r}\left[rh^{\frac{2n+1}{n}}\left(-\frac{\rho g'}{m}\frac{\partial h}{\partial x}\right)^{\frac{1}{n}}\right] = 0 \tag{8}$$

Equation (8) defines the problem together with the global continuity equation requesting a fixed volume *Q* to be released

$$Q = 2\pi\int_0^{r_N(t)} rh(r,t)dr \tag{9}$$

where *rN(t)* is the radial coordinate of the head of the current.

3 Solution to the problem and discussion

Choosing $\bar{h} = Q^{1/3}$ as a typical length-scale, dimensionless (primed) variables are defined as [22, 23]:

$$r = r'\bar{h};\quad r_N = r'_N\bar{h};\quad h = h'\bar{h};\quad t = t'\Big/\left(\frac{\rho g'\bar{h}}{m}\right)^{\frac{1}{n}} \tag{10}$$

This recasts (8)-(9) in the dimensionless form (primes are dropped for convenience)

$$\frac{\partial h}{\partial t}+\frac{n}{2n+1}\frac{1}{r}\frac{\partial}{\partial r}\left[rh^{\frac{2n+1}{n}}\left(-\frac{\partial h}{\partial r}\right)^{\frac{1}{n}}\right]=0 \tag{11}$$

$$2\pi\int_0^{r_N(t)} rh(r,t)dr=1 \tag{12}$$

By introducing the similarity variable

$$\xi=\left(\frac{2n+1}{n}\right)^{\frac{n}{3n+5}} rt^{-\frac{n}{3n+5}} \tag{13}$$

and denoting the value of ξ for $r = rN(t)$ by ξN, the similarity solution of (11)-(12) takes the form

$$h(r,t)=\xi_{\mathrm{N}}^{(n+1)/(n+2)}\left(\frac{2n+1}{n}\right)^{\frac{2n}{3n+5}} t^{-\frac{2n}{3n+5}}\Psi(\xi/\xi_{\mathrm{N}}) \tag{14}$$

Substituting (13)-(14) in (11)-(12) yields respectively

$$\frac{d}{dz}\left[z\Psi^{\frac{2n+1}{n}}\left(-\frac{d\Psi}{dz}\right)^{\frac{1}{n}}\right]-\frac{n}{3n+5}z^2\frac{d\Psi}{dz}-\frac{2n}{3n+5}z\Psi=0 \tag{15}$$

and

$$\xi_{\mathrm{N}}=\left(2\pi\int_0^1 z\Psi dz\right)^{-\frac{n+2}{3n+5}} \tag{16}$$

where

$$z=\frac{\xi}{\xi_{\mathrm{N}}} \tag{17}$$

The solution to (15) is

$$\Psi(z)=\left(\frac{n}{3n+5}\right)^{n/(n+2)}\left(\frac{n+2}{n+1}\right)^{1/(n+2)}\left(1-z^{n+1}\right)^{\frac{1}{n+2}} \tag{18}$$

Substituting (18) into (16) gives

$$\xi_{\mathrm{N}}=\left\{2\pi\frac{1}{3n+5}\left(\frac{n}{3n+5}\right)^{n/(n+2)}\left(\frac{n+2}{n+1}\right)^{1/(n+2)}\frac{\Gamma\left[2/(n+1)\right]\Gamma\left[1/(n+2)\right]}{\Gamma\left[(3n+5)/((n+1)(n+2))\right]}\right\}^{-(n+2)/(3n+5)} \tag{19}$$

Finally, the (dimensionless) length of the gravity current is

$$R=r_{\mathrm{N}}(t)=\xi_{\mathrm{N}}\left(\frac{n}{2n+1}\right)^{\frac{n}{3n+5}}t^{\frac{n}{3n+5}} \tag{20}$$

For $n = 1$, governing equations and results reduce to those valid for a Newtonian fluid (see [1], [7]).

4 Discussion and results

Fig. 2 shows the shape of the function $\Psi(z)$ for n = 0.50, 0.75, 1.00, 1.25, 1.50. The corresponding dynamics of the dimensionless current length is presented in Fig. 3. For $t < 1$, the head of the current advances farther as n decreases; the reverse is true for larger times.

Figs. 4, 5, and 6 illustrate how the gravity current develops in space and time, respectively for n = 0.50 (pseudoplastic fluid), n = 1.00 (Newtonian fluid), n = 1.50 (dilatant fluid). In all cases, the rate of advance decreases (currents slow down) as time increases, as implied by (20). The prescribed fluid volume released slumps down more rapidly for dilatant gravity currents than for pseudoplastic ones: as a result, profiles of the former are more elongated than profiles of the latter.

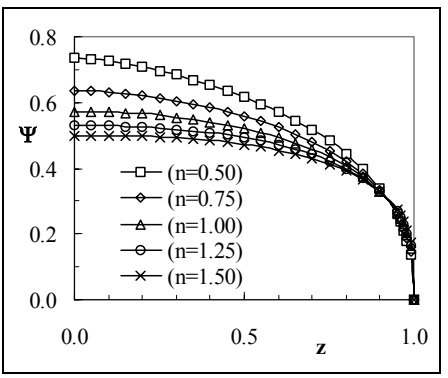


Figure 2: Shape of the current $\Psi(z)$ for various n.

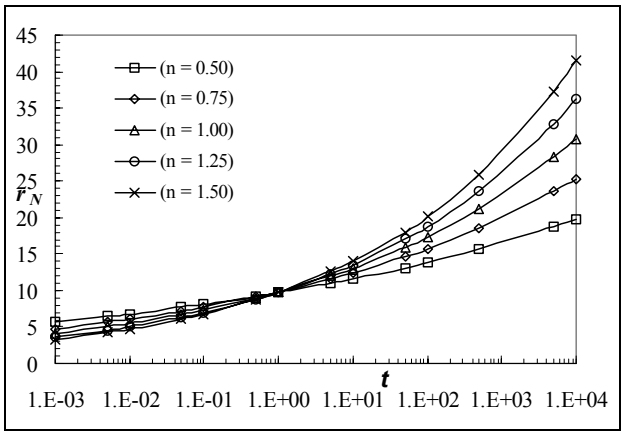


Figure 3: Dimensionless current length as a function of time for various n.

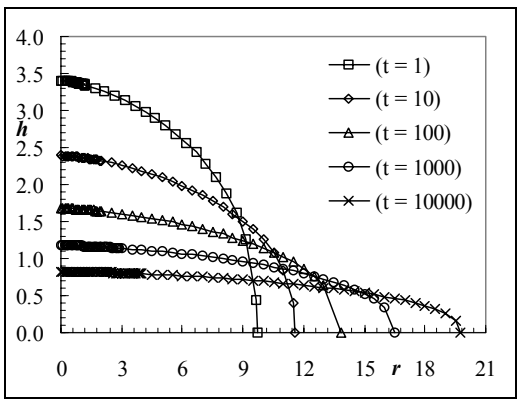


Figure 4: Profile of the current at different times for n = 0.50.

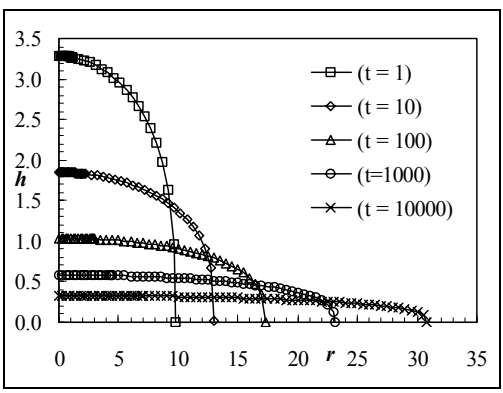


Figure 5: Profile of the current at different times for n = 1.00.

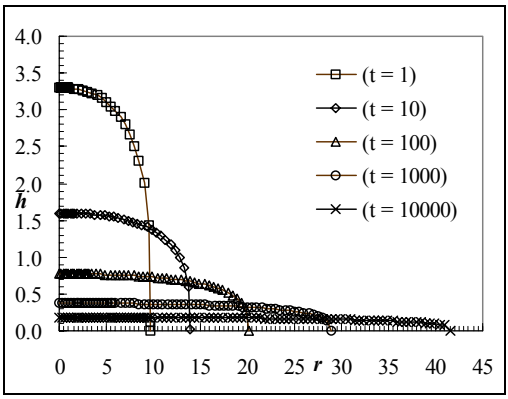


Figure 6: Profile of the current at different times for $n = 1.50$.

5 Summary and conclusions

Our work leads to the following major conclusions: when studying horizontal gravity currents, at large times inertial forces are negligible as compared to buoyancy and viscous forces. Under the above assumption, we derive a set of equations which describe gravity currents of an incompressible power-law non-Newtonian fluid at the bottom of an ambient fluid of lower density propagating on a horizontal plane. The intruding fluid is considered to have a pure power-law constitutive equation. A self-similar solution is then derived for the release of a fixed volume of fluid, allowing one to study the development of the gravity current as a function of time and flow behavior index.

Appendix range of validity of viscous regime

The purpose of this Appendix is to determine the transition time t_1 when inertial and viscous forces are comparable. The order of magnitude of the fluid volume is $\approx h_0 R^2$, where $h_0 = Q/R^2$ is a representative thickness of the current and R its radius. Buoyancy, F_g, inertial, F_i, and viscous, F_v, forces are given by

$$F_g \approx \rho g' h_0^2 R = \rho g' Q^2 R^{-3} \tag{A1}$$

$$F_i \approx \rho U^2 h_0 R = \rho Q R t^{-2} \tag{A2}$$

$$F_v = m(U/h_0)^n R^2 = m Q^{-n} R^{2+3n} t^{-n} \tag{A3}$$

where $U = R/t$ is a representative velocity of the current. For a current propagating in the inertial-buoyancy regime, equating (A1) and (A2) yields

$$R = \left(g'Q\right)^{\frac{1}{4}} t^{\frac{1}{2}} \tag{A4}$$

as obtained by Huppert ([7], see Eq. (A5b)). Equating (A2) and (A3) under a viscous-buoyancy regime, and deriving R from the dimensional form of (20), yields

$$\frac{F_i}{F_v} = \left(\frac{\rho^4 Q^{n+3}}{m^4 g'^{3n+1}}\right)^{\frac{1}{3n+5}} t^{-2\frac{n+5}{3n+5}} \tag{A5}$$

Thus the (dimensional) transition time at which inertial and viscous forces are comparable is

$$t_1 = \left(\frac{\rho^4 Q^{n+3}}{m^4 g'^{3n+1}}\right)^{\frac{1}{2(n+5)}} \tag{A6}$$

Finally, it is worth noting that for $n = 1$ all expressions in this Appendix reduce to the corresponding ones derived for a Newtonian fluid by Huppert ([7], see Appendix A).

References

[1] Huppert, H.E., The intrusion of fluid mechanics into geology, J. Fluid Mech., 173, pp. 557-594, 1986.

[2] Simpson, J.E., Gravity currents in the laboratory, atmosphere, and ocean, Ann. Rev. Fl. Mech., 14, pp. 213-234, 1982.

[3] Simpson, J.E., Gravity currents: in the environment and the laboratory, 2nd edition, Cambridge University Press, Cambridge, 1997.

[4] Hoult, D.P., Oil spreading on the sea, Ann. Rev. Fl. Mech., 4, pp. 341-368, 1972.

[5] Huppert, H.E. and Simpson, J.E., The slumping of gravity currents, J. Fluid Mech., 99, pp. 785-799, 1980.

[6] Didden, N. and Maxworthy, T., The viscous spreading of plane and axysymmetric gravity currents, J. Fluid Mech., 121, pp. 27-42, 1982.

[7] Huppert, H.E., The propagation of two-dimensional and axisymmetric viscous gravity currents over a rigid horizontal surface, J. Fluid Mech., 121, pp. 43-58, 1982.

[8] Maxworthy, T., Gravity currents with variable inflow, J. Fluid Mech., 128, pp. 247-257, 1983.

[9] Rottman, J.W. and Simpson, J.E., Gravity currents produced by instantaneous release of a heavy fluid in a rectangular channel, J. Fluid Mech., 135, pp. 95-110, 1983.

[10] Grundy, R.E. and Rottman, J.W., The approach to self-similarity of the solution for the shallow water equations representing gravity currents releases, J. Fluid Mech., 156, pp. 39-53, 1985.



[11] Grundy, R.E. and Rottman, J.W., Self-similar solutions of the shallow water equations representing gravity currents with variable inflow, J. Fluid Mech., 169, pp. 337-351, 1986.
[12] Gratton, J. and Vigo, C., Self-similar gravity currents with variable inflow revisited: plane currents, J. Fluid Mech., 258, pp. 77-104, 1994.
[13] Snyder, D. and Tait, S., A flow-front instability in viscous gravity currents, J. Fluid Mech., 369, pp. 1-21, 1998.
[14] Thomas, L.P., Marino, B.M. and Linden, P.F., Gravity currents over porous substrates, J. Fluid Mech., 366, pp. 239-258, 1998.
[15] Marino, B.M. and Thomas, L.P., Spreading of a gravity current over a permeable surface, J. of Hydr. Eng. ASCE, 128-5, pp. 527-533, 2002.
[16] Ross, A.N., Linden, P.F. and Dalziel, S.B., A study of three-dimensional gravity currents down a uniform slope, J. Fluid Mech., 453, pp. 239-261, 2002.
[17] Bird, R.B., Stewart, W.E. and Lightfoot, E.N., Transport Phenomena, Wiley, New York, 1960.
[18] Battaglia, M. and Borgia, A., Laminar flow of fine sediment water mixtures, J. Geophys. Res., 105-B3, pp. 5939-5945, 2000.
[19] Coussot, P., Proust, S. and Ancey, C., Rhelogical interpretation of deposits of yield stress fluids, J. Non-Newtonian Fluid Mech., 66, pp. 55-70, 1996.
[20] Di Federico, V., Permanent waves in slow free-surface flow of a Herschel-Bulkley fluid, Meccanica, 33-2, pp. 127-137, 1998.
[21] Wilson, S.D.R. and Burgess, S.L., The steady, spreading flow of a rivulet of mud, J. Non-Newtonian Fluid Mech., 79, pp. 77-85, 1998.
[22] Di Federico, V. and Guadagnini, A., Propagation of a plane non-Newtonian gravity current, Proc. of the 28th IAHR Congress, Graz, Austria 1999, Abstract Volume (Papers on CD-ROM), p. 284, 1999.
[23] Di Federico, V., Cintoli, S. and Malavasi, S., Viscous spreading of non-Newtonian gravity currents on a plane, Meccanica, in press, 2006.



Axisymmetric motion of a second order viscous fluid in a circular straight tube under pressure gradients varying exponentially with time

F. Carapau[1] & A. Sequeira[2]
[1] *Department of Mathematics and CIMA/UE, University of Évora, Portugal*
[2] *Department of Mathematics and CEMAT/IST, IST, Portugal*

Abstract

The aim of this paper is to analyze the axisymmetric unsteady flow of a non-Newtonian incompressible second order fluid in a straight rigid and impermeable tube with circular cross-section of constant radius. To study this problem, we use the one dimensional (1D) nine-directors Cosserat theory approach which reduces the exact three-dimensional equations to a system depending only on time and on a single spatial variable. From this system we obtain the relationship between mean pressure gradient and volume flow rate over a finite section of the tube. Assuming that the pressure gradient rises and falls exponentially with time, the 3D exact solution for unsteady volume flow rate is compared with the corresponding 1D solution obtained by the Cosserat theory using nine directors.
Keywords: Cosserat theory, nine directors, unsteady rectilinear flow, axisymmetric motion, pressure gradient, second order fluid.

1 Introduction

A possible simplification to a three-dimensional model for an incompressible viscous fluid inside a domain is to consider the evolution of average flow quantities using simpler one-dimensional models. Usually, in the case of flow in a tube, the classical 1D models are obtained by imposing additional assumptions and integrating both the equations of conservation of linear momentum and mass over the cross section of the tube. Here, we introduce a 1D model for non-Newtonian Rivlin-Ericksen fluids of second order in an axisymmetric tube, based on the nine-



WIT Transactions on Engineering Sciences, Vol 52, © 2006 WIT Press
www.witpress.com, ISSN 1743-3533 (on-line)
doi:10.2495/AFM06041

director approach developed by Caulk and Naghdi [4]. This theory includes an additional structure of directors (deformable vectors) assigned to each point on a space curve (Cosserat curve), where a three-dimensional system of equations is replaced by a one-dimensional system depending on time and on a single spatial variable. The use of directors in continuum mechanics goes back to Duhen [7] who regards a body as a collection of points together with associated directions. Theories based on such a model of an oriented medium were further developed by Cosserat and Cosserat [6] and have also been used by several authors in studies of rods, plates and shells (see *e.g*. Ericksen and Truesdell [8], Truesdell and Toupin [17], Green and Naghdi [10, 11] and Naghdi [13]). An analogous hierarchial theory for unsteady and steady flows has been developed by Caulk and Naghdi [4] in straight pipes of circular cross-section and by Green and Naghdi [12] in channels. The same theory was applied to unsteady viscous fluid flow in curved pipes of circular and elliptic cross-section by Green *et al*. [9]. Recently, the nine-director theory has been applied to blood flow in the arterial system by Robertson and Sequeira [16] and also by Carapau and Sequeira [2, 3], considering Newtonian and shear-thinning flows, respectively. The relevance of using a theory of directed curves is not in regarding it as an approximation to 3D equations, but rather in their use as independent theories to predict some of the main properties of the three-dimensional problems. Advantages of the director theory include: (i) the theory incorporates all components of the linear momentum; (ii) it is a hierarchical theory, making it possible to increase the accuracy of the model; (iii) there is no need for closure approximations; (iv) invariance under superposed rigid body motions is satisfied at each order and (v) the wall shear stress enters directly in the formulation as a dependent variable.

This paper deals with the study of the initial boundary value problem for an incompressible homogeneous second order fluid model in a straight circular rigid and impermeable tube with constant radius, where the fluid velocity field, given by the director theory, can be approximated by the following finite series:

$$\boldsymbol{v}^* = \boldsymbol{v} + \sum_{N=1}^{k} x_{\alpha_1} \dots x_{\alpha_N} \boldsymbol{W}_{\alpha_1 \dots \alpha_N}, \tag{1}$$

with

$$\boldsymbol{v} = v_i(z,t)\boldsymbol{e}_i, \quad \boldsymbol{W}_{\alpha_1 \dots \alpha_N} = W^i_{\alpha_1 \dots \alpha_N}(z,t)\boldsymbol{e}_i, \tag{2}$$

(latin indices subscript take the values $1, 2, 3$; greek indices subscript $1, 2$, and the usual summation convention is employed over a repeated index). Here, $\boldsymbol{v}$ represents the velocity along the axis of symmetry z at time t, $x_{\alpha_1} \dots x_{\alpha_N}$ are the polynomial weighting functions with order k (this number identifies the order of hierarchical theory and is related to the number of directors), the vectors $\boldsymbol{W}_{\alpha_1 \dots \alpha_N}$ are the director velocities which are symmetric with respect to their indices and $\boldsymbol{e}_i$ are the associated unit basis vectors. When we use the director theory, the 3D system of equations governing the fluid motion is replaced by a system which depends only on a single spatial and time variables, as previously mentioned. From this new



system, we obtain the unsteady relationship between mean pressure gradient and volume flow rate, and the correspondent equation for the wall shear stress.

The aim of this paper is to develop a nine-director theory ($k = 3$ in equation (1)) for the unsteady flow of a second order fluid in a straight tube with constant radius, to compare the corresponding volume flow rate with the 3D exact solution given by Soundalgekar [15], when the pressure gradient rises and falls exponentially with time.

2 Equations of motion

We consider a homogeneous fluid moving within a circular straight and impermeable tube, the domain Ω (see fig.1) contained in $\mathbb{R}^3$. Its boundary $\partial\Omega$ is composed by, the proximal cross-section Γ_1, the distal cross-section Γ_2 and the lateral wall of the tube, denoted by Γ_w.

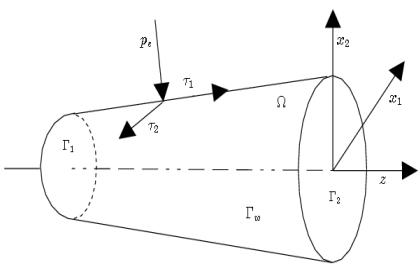


Figure 1: Fluid domain Ω with the components of the surface traction vector τ_1, τ_2 and p_e.

Let x_i $(i = 1, 2, 3)$ be the rectangular Cartesian coordinates and for convenience set $x_3 = z$. Consider the axisymmetric motion of an incompressible fluid without body forces, inside a straight circular tube, about the z axis and let $\phi(z, t)$ denote the radius of that surface at z and time t. Using the notation adopted in Naghdi *et al*. [4, 9], the three-dimensional equations governing the fluid motion are given by

$$\begin{cases} \rho\Big(\dfrac{\partial \boldsymbol{v}^*}{\partial t} + v^*_{,i}\boldsymbol{v}^*_i\Big) = t_{i,i}, \\ \qquad\qquad\qquad\qquad\qquad\qquad in\ \ \Omega \times (0,T), \\ v^*_{i,i} = 0, \\ \\ t_i = -p^*\boldsymbol{e}_i + \sigma_{ij}\boldsymbol{e}_j,\ \boldsymbol{t} = \vartheta^*_i t_i, \end{cases} \tag{3}$$

with the initial condition

$$\boldsymbol{v}^*(x, 0) = \boldsymbol{v}_0(x) \ \text{ in } \ \Omega, \tag{4}$$

and the boundary condition

$$\boldsymbol{v}^*(x,t) = 0 \ \text{ on } \ \Gamma_w \times (0,T), \tag{5}$$

where $\boldsymbol{v}^* = v_i^* \boldsymbol{e}_i$ is the velocity field and ρ is the constant fluid density. Equation $(3)_1$ represents the balance of linear momentum and $(3)_2$ is the incompressibility condition. In equation $(3)_3$, p^* is the pressure, σ_{ij} are the components of the extra stress tensor, $\boldsymbol{t}$ denotes the stress vector on the surface whose outward unit normal is $\vartheta^* = \vartheta_i^* \boldsymbol{e}_i$, and t_i are the components of $\boldsymbol{t}$.

For a general incompressible Rivlin-Ericksen fluid of second order, the components of the extra stress tensor, in the constitutive equation $(3)_3$, are given by (see *e.g.* Coleman and Noll [5])

$$\sigma_{ij} = \mu A_{ij} + \alpha_1 S_{ij} + \alpha_2 A_{ik} A_{kj}, \quad i,j,k = 1,2,3 \tag{6}$$

where μ is the constant viscosity, α_1, α_2 are material constants (*normal stress moduli*) and A_{ij}, S_{ij} are the first two Rivlin-Ericksen tensors, defined by (see Rivlin and Ericksen [14])

$$A_{ij} = \frac{\partial v_i^*}{\partial x_j} + \frac{\partial v_j^*}{\partial x_i}, \tag{7}$$

and

$$S_{ij} = \frac{\partial A_{ij}}{\partial t} + v_k^* \frac{\partial A_{ij}}{\partial x_k} + A_{ik} \frac{\partial v_k^*}{\partial x_j} + \frac{\partial v_k^*}{\partial x_i} A_{kj}. \tag{8}$$

Note that, if $\alpha_1 = \alpha_2 = 0$ in equation (6) we obtain the classical Newtonian incompressible model.

We assume that the lateral surface Γ_w of the axisymmetric tube is defined by

$$\phi^2 = x_\alpha x_\alpha, \tag{9}$$

and the components of the outward unit normal to this surface are

$$\vartheta_\alpha^* = \frac{x_\alpha}{\phi\left(1+\phi_z^2\right)^{1/2}}, \quad \vartheta_3^* = -\frac{\phi_z}{\left(1+\phi_z^2\right)^{1/2}}, \tag{10}$$

where the subscript variable denotes partial differentiation. Since equation (9) defines a material surface, the velocity field must satisfy the kinematic condition

$$\phi\phi_t + \phi\phi_z v_3^* - x_\alpha v_\alpha^* = 0 \tag{11}$$

on the boundary (9).

Averaged quantities such as flow rate and average pressure are needed to study 1D models, in particular the unsteady relationship between mean pressure gradient and volume flow rate over a finite section of the tube. Consider $S(z,t)$ as a generic axial section of the tube at time t defined by the spatial variable z and bounded by

the circle defined in (9) and let $A(z,t)$ be the area of this section $S(z,t)$. Then, the volume flow rate Q is defined by

$$Q(z,t) = \int_{S(z,t)} v_3^*(x_1, x_2, z, t)da, \tag{12}$$

and the average pressure $\bar{p}$, by

$$\bar{p}(z,t) = \frac{1}{A(z,t)} \int_{S(z,t)} p^*(x_1, x_2, z, t)da. \tag{13}$$

In the sequel, this general framework will be applied to the specific case of the Cosserat nine-director theory in a rigid tube, i.e. $\phi = \phi(z)$. Using condition (1) it follows from Caulk and Naghdi [4] that the approximation for the three-dimensional velocity field $\boldsymbol{v}^*$ is given by

$$\begin{aligned}\boldsymbol{v}^* = &\Big[x_1\big(1 - \frac{x_1^2 + x_2^2}{\phi^2}\big)\frac{2\phi_z Q}{\pi\phi^3}\Big]\boldsymbol{e}_1 + \Big[x_2\big(1 - \frac{x_1^2 + x_2^2}{\phi^2}\big)\frac{2\phi_z Q}{\pi\phi^3}\Big]\boldsymbol{e}_2 \\ &+ \Big[\frac{2Q}{\pi\phi^2}\big(1 - \frac{x_1^2 + x_2^2}{\phi^2}\big)\Big]\boldsymbol{e}_3\end{aligned} \tag{14}$$

where the volume flow rate $Q(t)$ is

$$Q(t) = \frac{\pi}{2}\phi^2(z)v_3(z,t). \tag{15}$$

We remark that the initial condition (4) is satisfied when $Q(0) = ct$. Also, from Caulk and Naghdi [4] the stress vector on the lateral surface Γ_w is given by

$$\begin{aligned}\boldsymbol{t}_w = &\Big[\frac{1}{\phi(1+\phi_z^2)^{1/2}}\Big(\tau_1 x_1\phi_z - p_e x_1 - \tau_2 x_2(1+\phi_z^2)^{1/2}\Big)\Big]\boldsymbol{e}_1 \\ &+ \Big[\frac{1}{\phi(1+\phi_z^2)^{1/2}}\Big(\tau_1 x_2\phi_z - p_e x_2 + \tau_2 x_1(1+\phi_z^2)^{1/2}\Big)\Big]\boldsymbol{e}_2 \\ &+ \Big[\frac{1}{(1+\phi_z^2)^{1/2}}\Big(\tau_1 + p_e\phi_z\Big)\Big]\boldsymbol{e}_3.\end{aligned} \tag{16}$$

Instead of satisfying the momentum equation $(3)_1$ pointwise in the fluid, we impose the following integral conditions

$$\int_{S(z,t)} \Big[t_{i,i} - \rho\Big(\frac{\partial \boldsymbol{v}^*}{\partial t} + \boldsymbol{v}^*_{,i}v_i^*\Big)\Big]da = 0, \tag{17}$$

$$\int_{S(z,t)} \Big[t_{i,i} - \rho\Big(\frac{\partial \boldsymbol{v}^*}{\partial t} + \boldsymbol{v}^*_{,i}v_i^*\Big)\Big]x_{\alpha_1}\ldots x_{\alpha_N}da = 0, \tag{18}$$

where $N = 1, 2, 3$.

Using the divergence theorem and integration by parts, equations $(17)-(18)$ for nine directors, can be reduced to the four vector equations:

$$\frac{\partial \boldsymbol{n}}{\partial z}+\boldsymbol{f}=\boldsymbol{a},\ \frac{\partial \boldsymbol{m}^{\alpha_1\ldots\alpha_N}}{\partial z}+\boldsymbol{l}^{\alpha_1\ldots\alpha_N}=\boldsymbol{k}^{\alpha_1\ldots\alpha_N}+\boldsymbol{b}^{\alpha_1\ldots\alpha_N}, \tag{19}$$

where $\boldsymbol{n},\ \boldsymbol{k}^{\alpha_1\ldots\alpha_N},\ \boldsymbol{m}^{\alpha_1\ldots\alpha_N}$ are resultant forces defined by

$$\boldsymbol{n}=\int_S \boldsymbol{t}_3 da,\ \ \boldsymbol{k}^{\alpha}=\int_S \boldsymbol{t}_\alpha da,\ \boldsymbol{k}^{\alpha\beta}=\int_S \Big(\boldsymbol{t}_\alpha x_\beta+\boldsymbol{t}_\beta x_\alpha\Big)da, \tag{20}$$

$$\boldsymbol{k}^{\alpha\beta\gamma}=\int_S \Big(\boldsymbol{t}_\alpha x_\beta x_\gamma+\boldsymbol{t}_\beta x_\alpha x_\gamma+\boldsymbol{t}_\gamma x_\alpha x_\beta\Big)da, \tag{21}$$

$$\boldsymbol{m}^{\alpha_1\ldots\alpha_N}=\int_S \boldsymbol{t}_3 x_{\alpha_1}\ldots x_{\alpha_N} da. \tag{22}$$

The quantities $\boldsymbol{a}$ and $\boldsymbol{b}^{\alpha_1\ldots\alpha_N}$ are inertia terms written as follows

$$\boldsymbol{a}=\int_S \rho\Big(\frac{\partial \boldsymbol{v}^*}{\partial t}+\boldsymbol{v}^*_{,i}v^*_i\Big)da, \tag{23}$$

$$\boldsymbol{b}^{\alpha_1\ldots\alpha_N}=\int_S \rho\Big(\frac{\partial \boldsymbol{v}^*}{\partial t}+\boldsymbol{v}^*_{,i}v^*_i\Big)x_{\alpha_1}\ldots x_{\alpha_N} da, \tag{24}$$

and $\boldsymbol{f},\ \boldsymbol{l}^{\alpha_1\ldots\alpha_N}$, which arise due to surface traction on the lateral boundary, are given by

$$\boldsymbol{f}=\int_{\partial S}\Big(1+\phi_z^2\Big)^{1/2}\boldsymbol{t}_w ds,\ \ \boldsymbol{l}^{\alpha_1\ldots\alpha_N}=\int_{\partial S}\Big(1+\phi_z^2\Big)^{1/2}\boldsymbol{t}_w x_{\alpha_1}\ldots x_{\alpha_N} ds. \tag{25}$$

The equation relating the mean pressure gradient with the volume flow rate will be obtained using these quantities.

3 Results and discussion

We consider the case of a straight circular rigid and impermeable walled tube with constant radius, i.e. $\phi=ct$. Replacing the results $(20)-(25)$ obtained for the nine-director model into equations (19), we get the unsteady relationship

$$\bar{p}_z(z,t)=-\frac{8\mu}{\pi\phi^4}Q(t)-\frac{4\rho}{3\pi\phi^2}\Big(1+6\frac{\alpha_1}{\rho\phi^2}\Big)\dot{Q}(t), \tag{26}$$

were the notation $\dot{Q}$ is used for time differentiation. Flow separation occurs when the axial component τ_1 of the stress vector on the lateral surface (*cf.* (16)) is in

the direction of the flow, i.e. $\tau_1 > 0$. The expression for the wall shear stress τ_1 is given by

$$\tau_1 = \frac{4\mu}{\pi\phi^3}Q(t) + \frac{\rho}{6\pi\phi}\Big(1 + 24\frac{\alpha_1}{\rho\phi^2}\Big)\dot{Q}(t). \tag{27}$$

Integrating equation (26), over a finite section of the tube, between z_1 and position z_2 ($z_1 < z_2$), we get the mean pressure gradient

$$G(t) = \frac{\bar{p}(z_1,t) - \bar{p}(z_2,t)}{z_2 - z_1} = \frac{8\mu}{\pi\phi^4}Q(t) + \frac{4\rho}{3\pi\phi^2}\Big(1 + 6\frac{\alpha_1}{\rho\phi^2}\Big)\dot{Q}(t). \tag{28}$$

Now, let us consider the following dimensionless variables

$$\hat{z} = \frac{z}{\phi},\ \ \hat{t} = \omega_0\, t,\ \ \hat{Q} = \frac{2\rho}{\pi\phi\mu}\, Q,\ \ \hat{\bar{p}} = \frac{\phi^2\rho}{\mu^2}\,\bar{p}, \tag{29}$$

where ϕ is the characteristic radius of the tube and ω_0 is the characteristic frequency for unsteady flow. Substituting the new variables (29) into equation (26), we obtain

$$\hat{\bar{p}}_{\hat{z}} = -4\hat{Q}(\hat{t}) - \frac{2}{3}\Big(1 + 6\mathcal{W}_e\Big)\mathcal{W}_0^2\dot{\hat{Q}}(\hat{t}), \tag{30}$$

where $\mathcal{W}_0 = \phi_0\sqrt{\rho\omega_0/\mu}$ is the *Womersley number* and $\mathcal{W}_e = \alpha_1/(\rho\phi^2)$ is a viscoelastic parameter, also called the *Weissenberg number*. The dimensionless number $\mathcal{W}_0$ is the most commonly used parameter to reflect the unsteady pulsatility of the flow. Integrating (30) over a finite section of the tube between $\hat{z}_1$ and $\hat{z}_2$, we get the relationship between mean pressure gradient and volume flow rate given by

$$\hat{\bar{G}}(\hat{t}) = 4\hat{Q}(\hat{t}) + \frac{2}{3}\Big(1 + 6\mathcal{W}_e\Big)\mathcal{W}_0^2\dot{\hat{Q}}(\hat{t}). \tag{31}$$

Moreover, the dimensionless form of equation (27) is

$$\hat{\tau}_1 = 2\hat{Q}(\hat{t}) + \frac{1}{12}\Big(1 + 24\mathcal{W}_e\Big)\mathcal{W}_0^2\dot{\hat{Q}}(\hat{t}) \quad \text{with} \quad \hat{\tau}_1 = \frac{\phi^2\rho}{\mu^2}\,\tau_1.$$

Next we compare the exact solution for a rectilinear motion (given by Soundalgekar [15]) with the solution obtained by the nine-director theory in a straight circular rigid tube with constant radius ϕ, when the pressure gradient rises and falls exponentially with time.

3.1 Pressure gradient rising exponentially with time

Let us assume the following pressure gradient

$$-\frac{1}{\rho}p_z^* = k\ exp(\theta^2 t), \tag{32}$$

where k and θ are constants, with θ^2 being the characteristic frequency. Then the velocity field solution obtained by Soundalgekar [15], with $\mid \beta\phi \mid \ll 1$ and

$\mid \beta\sqrt{x_1^2+x_2^2} \mid \ll 1$, is given by

$$v_3^* = \Big[\frac{k\beta^2}{4\theta^2}\Big(\phi^2 - \big(x_1^2+x_2^2\big)\Big)exp(\theta^2 t)\Big]\boldsymbol{e}_3, \tag{33}$$

where $\beta^2 = \rho\theta^2/\big(\mu+\alpha_1\theta^2\big)$. From (33) the volume flow rate reduces to

$$Q(t) = \frac{k\phi^4\pi\rho}{8\big(\mu+\alpha_1\theta^2\big)}exp(\theta^2 t). \tag{34}$$

Using the nondimensional variables

$$\hat{t} = \theta^2 t, \;\; \hat{Q} = \frac{8\mu}{k\phi^4\pi\rho}Q, \tag{35}$$

into equation (34), we obtain the nondimensional volume flow rate

$$\hat{Q}(\hat{t}) = \frac{1}{1+\mathcal{W}_e\mathcal{W}_0^2}\; exp\big(\hat{t}\big). \tag{36}$$

In view of the pressure gradient (32) and equation (31) given by the nine-director theory, we get the following nondimensional volume flow rate

$$\hat{Q}(\hat{t}) = \frac{1}{12+2\mathcal{W}_0^2+12\mathcal{W}_0^2\mathcal{W}_e}\Big[3\; exp(\hat{t}) + exp\big(\frac{-6\hat{t}}{\mathcal{W}_0^2+6\mathcal{W}_0^2\mathcal{W}_e}\big)\Big(\frac{9+2\mathcal{W}_0^2+9\mathcal{W}_0^2\mathcal{W}_e}{1+\mathcal{W}_e\mathcal{W}_0^2}\Big)\Big]. \tag{37}$$

Next, we compare the relationship between the volume flow rates (36) and (37), for a fixed Womersley number and different values of the Weissenberg number. Results in fig.2 show that for $\mathcal{W}_0 = 0.5$, the solutions (36) and (37) have the same qualitative behavior for increasing Weissenberg numbers, but show a large deviation in time. Numerical simulations for different Womersley numbers have shown similar results.

3.2 Pressure gradient falling exponentially with time

We consider the pressure gradient given by

$$-\frac{1}{\rho}p_z^* = k\; exp(-\theta^2 t). \tag{38}$$

The velocity field solution obtained by Soundalgekar [15], with $\mid \zeta\phi \mid \ll 1$ and $\mid \zeta\sqrt{x_1^2+x_2^2} \mid \ll 1$, is given by

$$v_3^* = \Big[\frac{k\zeta^2}{4\theta^2}\Big(\phi^2 - \big(x_1^2+x_2^2\big)\Big)exp(-\theta^2 t)\Big]\boldsymbol{e}_3, \tag{39}$$



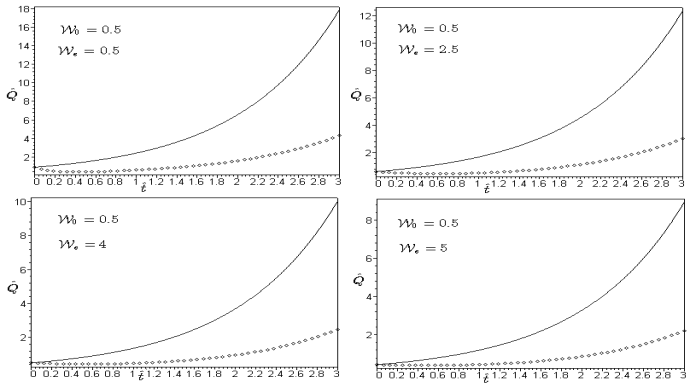


Figure 2: Volume flow rate when the pressure gradient is rising exponentially with time for different values of Weissenberg number, with fixed Womersley number ($\mathcal{W}_0 = 0.5$): nine-directors solution (37) (dotted line) and exact 3D solution (36) (dark line).

where $\zeta^2 = \rho\theta^2/\big(\mu - \alpha_1\theta^2\big)$ and the corresponding volume flow rate is

$$Q(t) = \frac{k\phi^4\pi\rho}{8\big(\mu - \alpha_1\theta^2\big)} exp(-\theta^2 t). \tag{40}$$

Using the dimensionless variables (35) into the preceding equation, we obtain

$$\hat{Q}(\hat{t}) = \frac{1}{1 - \mathcal{W}_e\mathcal{W}_0^2}\, exp\big(-\hat{t}\big). \tag{41}$$

Taking into account the pressure gradient (38) and the nine-directors equation (31), we obtain the following nondimensional volume flow rate

$$\hat{Q}(\hat{t}) = \frac{1}{-12 + 2\mathcal{W}_0^2 + 12\mathcal{W}_0^2\mathcal{W}_e}\Big[-3\, exp(-\hat{t}) + exp\Big(\frac{-6\hat{t}}{\mathcal{W}_0^2 + 6\mathcal{W}_0^2\mathcal{W}_e}\Big)\Big(\frac{9 - 2\mathcal{W}_0^2 - 9\mathcal{W}_0^2\mathcal{W}_e}{\mathcal{W}_e\mathcal{W}_0^2 - 1}\Big)\Big]. \tag{42}$$

In fig.3 we illustrate the behavior of the nine-directors solution versus the exact 3D solution, for a fixed Womersley number and different values of the Weissenberg number. The solutions show a small deviation for short times and approach asymptotically when time increases. Several numerical tests have also been performed for other Womersley numbers showing similar results.

4 Conclusion

The Cosserat nine-director theory applied to the axisymmetric unsteady flow behavior of a second order fluid in a straight tube, with uniform circular cross-section, has been evaluated by comparing its solution with the 3D exact solution

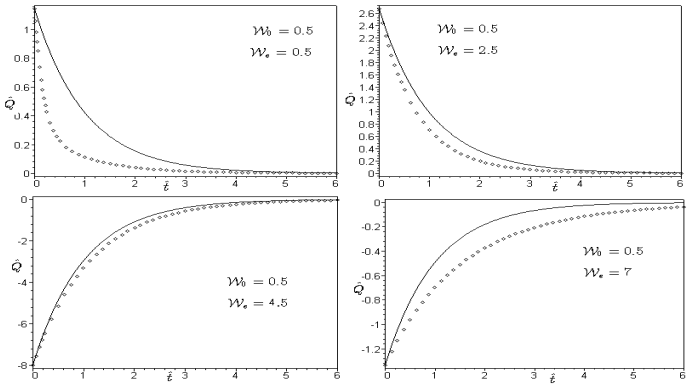


Figure 3: Volume flow rate with pressure gradient is falling exponentially with time for different values of Weissenberg number, with fixed Womersley number ($\mathcal{W}_0 = 0.5$): nine-directors solution (42) (dotted line) and exact 3D solution (41) (dark line).

for unsteady flows, given by Soundalgekar [15]. For fixed Womersley number, when the pressure gradient rises exponentially with time, both solutions have the same qualitative behavior, but show a large deviation for increasing time. However, when the pressure gradient is falling exponentially with time, the solutions show a small deviation for short times and approach asymptotically in time. One of the important extensions of this work is the application of the Cosserat 1D theory to non-Newtonian second order fluids in a straight tube with non-constant radius. A more detailed discussion of this issue can be found in [1].

Acknowledgements

The authors are grateful to Professor A. M. Robertson (Univ. Pittsburgh, USA) for helpful discussions. This work has been partially supported by projects POCTI/MAT/41898/2001, HPRN-CT-2002-00270 of the European Union and by the research centers CEMAT-IST and CIMA-UE, through FCT´s funding program.

References

[1] Carapau, F., *Development of 1D Fluid Models Using the Cosserat Theory. Numerical Simulations and Applications to Haemodynamics*, PhD Thesis, IST, Lisbon, Portugal, 2005.

[2] Carapau, F., & Sequeira, A., Axisymmetric flow of a generalized Newtonian fluid in a straight pipe using a director theory approach, *Proceedings of the 8th WSEAS International Conference on Applied Mathematics*, pp. 303-308, 2005.

[3] Carapau, F., & Sequeira, A., 1D Models for blood flow in small vessels using the Cosserat theory, *WSEAS Transactions on Mathematics*, Issue 1, Vol.5, pp. 54-62, 2006.
[4] Caulk, D.A., & Naghdi, P.M., Axisymmetric motion of a viscous fluid inside a slender surface of revolution, *Journal of Applied Mechanics*, Vol.54, pp. 190-196, 1987.
[5] Coleman, B.D., & Noll, W., An approximation theorem for functionals with applications in continuum mechanics, *Arch. Rational Mech. Anal.*, Vol.6, pp. 355-370, 1960.
[6] Cosserat, E. & Cosserat, F., Sur la théorie des corps minces, *Compt. Rend.*, Vol.146, pp. 169-172, 1908.
[7] Duhem, P., Le potentiel thermodynamique et la pression hydrostatique, *Ann. 'Ecole Norm*, Vol.10, pp. 187-230, 1893.
[8] Ericksen, J.L. & Truesdell, C., Exact theory of stress and strain in rods and shells, *Arch. Rational Mech. Anal.*, Vol.1, pp. 295-323, 1958.
[9] Green, A.E. & Naghdi, P.M., A direct theory of viscous fluid flow in pipes: II Flow of incompressible viscous fluid in curved pipes, *Phil. Trans. R. Soc. Lond. A*, Vol.342, pp. 543-572, 1993.
[10] Green, A.E., Laws, N. & Naghdi, P.M., Rods, plates and shells, *Proc. Camb. Phil. Soc.*, Vol.64, pp. 895-913, 1968.
[11] Green, A.E., Naghdi, P.M. & Wenner, M.L., On the theory of rods II. Developments by direct approach, *Proc. R. Soc. Lond. A*, Vol.337, pp. 485-507, 1974.
[12] Green, A.E. & Naghdi, P.M., A direct theory of viscous fluid flow in channels, *Arch. Ration. Mech. Analysis*, Vol.86, pp. 39-63, 1984.
[13] Naghdi, P.M., *The Theory of Shells and Plates,* Flügg´s Handbuch der Physik, Vol. VIa/2, Berlin, Heidelberg, New York: Springer-Verlag, pp. 425-640, 1972.
[14] Rivlin, R.S., & Ericksen, J.L., Stress-deformation relations for isotropic materials, *J. Rational Mech. Anal.*, Vol.4, pp. 323-425, 1955.
[15] Soundalgekar, V.M., The flow of a second order viscous fluid in a circular tube under pressure gradients varying exponentially with time, *Indian J. Phys*, Vol.46, pp. 250-254, 1972.
[16] Robertson, A.M. & Sequeira, A., A director theory approach for modeling blood flow in the arterial system: An alternative to classical 1D models, *Mathematical Models & Methods in Applied Sciences*, Vol.15, nr.6, pp. 871-906, 2005.
[17] Truesdell, C. & Toupin, R., *The Classical Field Theories of Mechanics*, Handbuch der Physik, Vol. III, pp. 226-793, 1960.



This page intentionally left blank

The flow of power law fluids between parallel plates with shear heating

M. S. Tshehla, T. G. Myers & J. P. F. Charpin
Department of Mathematics and Applied Mathematics, University of Cape Town, South Africa

Abstract

A mathematical model for the flow and heat transfer between two parallel plates is studied, using the power law model. The flow due to a pressure gradient and flow due to a moving upper plate are investigated. In the derivation the Navier-Stokes and energy equations is reduced in line with the lubrication theory to provide scalar differential equations. The velocity and temperature profiles are determined analytically and the results show that the power law index $n = 1$ compares favourably with Newtonian profiles. The temperature field is increasing when n increases. The Brinkman number Br, also shows a significance increase of the temperature field when Br increases.
Keywords: lubrication theory, non-Newtonian flow, power law viscosity, shear heating.

1 Introduction

In a typical operating situation lubricants can be subjected to extreme conditions, such as high temperature, high pressure and shear rate. External heating and high shear rates can lead to high temperature being generated within a fluid. Viscosity is the most sensitive fluid property that represents a material's internal resistance to deform, see [8, 9]. In this paper the main focus will be on the effect of viscosity variation due to the power law model see, [3, 5, 6] for example. However for possible prediction of the results, the viscosity is considered to be constant in section 2.1 and is allowed to vary in section 2.2. Similar laws are discussed, see Andersson and Valnes [1] and Zheng and Zhang [10] in their study of boundary layer flow along lubricated surface and for squeeze flow in Lian *et al* [4]. Conclusion is included in section 3. Fluids in which, viscosity is the only property to



WIT Transactions on Engineering Sciences, Vol 52, © 2006 WIT Press
www.witpress.com, ISSN 1743-3533 (on-line)
doi:10.2495/AFM06042

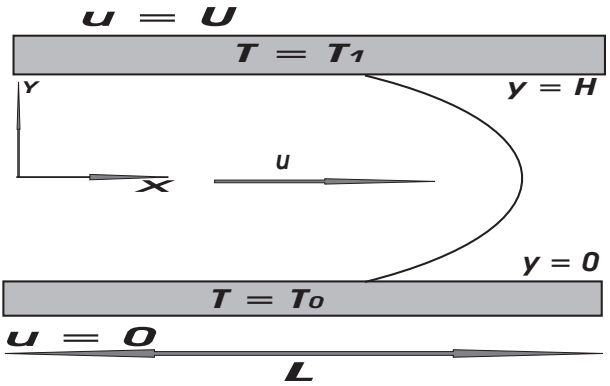


Figure 1: Schematic representation of the problem.

vary are termed generalised non-Newtonian fluids, see Schetz and Fuhs [7] and Shames [8]. Considering a basic flow configuration, where the fluid flows between parallel plates, will isolate the effect of viscosity variation. The temperature at the top and bottom plates is fixed. The lubrication theory will be exploited to reduce the governing equations to a more tractable form.

2 Governing equations

Two parallel plates geometrically define the problem in fig. 1. The independent variables x denote the horizontal distance along the channel, y the vertical distance, H the distance apart and L denotes typical length. The pressure and shear driven cases are combined. For the pressure driven case both plates are fixed. For the shear driven case the upper plate is moving at the speed U relative to the lower plate. The upper and lower plates are maintained at T_1 and T_0 respectively. With the hypothesis established above, the appropriate equations for modelling of this problem, the continuity, Navier-Stokes and energy equations are now stated. Initially the dynamic viscosity, density, thermal conductivity and the coefficient of thermal expansion denoted by μ, ρ, κ and β respectively are assumed to be constants. The Navier-Stokes equations are combined with the energy equations to solve for the velocity u, the pressure p and the temperature T of the fluid. See [2, 7, 9].

For incompressible fluids the governing equations may be written,
Continuity:

$$\rho \ (\bigtriangledown \ \cdot \ \mathbf{u}) \ , = 0 \tag{1}$$

Navier-Stokes equation:

$$\rho \left(\frac{\partial \mathbf{u}}{\partial t} + (\mathbf{u} \cdot \bigtriangledown) \, \mathbf{u} \right) = - \bigtriangledown p + \rho \mathbf{g} + \bigtriangledown^2 (\mu \, \mathbf{u}) \, , \tag{2}$$

Energy equation:

$$\rho\, c_p \left(\frac{\partial T}{\partial t} + (\mathbf{u} \cdot \bigtriangledown)\, T\right) = \beta\, T \left[\frac{\partial p}{\partial t} + (\mathbf{u} \cdot \bigtriangledown)\, p\right] + \bigtriangledown \cdot (\kappa \bigtriangledown T) + \Phi\,. \quad (3)$$

where,

$$\Phi = \mu \left[2\left(\frac{\partial u}{\partial x}\right)^2 + 2\left(\frac{\partial v}{\partial y}\right)^2 + \left(\frac{\partial u}{\partial y} + \frac{\partial v}{\partial x}\right)^2\right].$$

The components of the velocity vector $\mathbf{u}$ are denoted (u, v) in the (x, y) direction, t denotes time. The notation is discussed in the nomenclature table 1. Since the fluid is considered to flow in a thin layer, the governing equations can be simplified using this geometrical property. To determine the leading order terms, the governing equations will be non-dimensionalised. An asymptotic simplification known as lubrication theory may be used to simplify the governing equations. This method is valid when the film is thin and the flow regime is laminar. See [7, 8, 9]. The variables are scaled in the following manner,

$$x = Lx', \qquad y = Hy', \qquad u = Uu',$$
$$v = \frac{HU}{L}v', \qquad t = \frac{L}{U}t', \qquad \mu = \mu_0\mu',$$
$$T = T_0 + \Delta T_0 T', \qquad p = Pp' = \frac{\mu_0 UL}{H^2}p'.$$

where all quantities with prime denote non-dimensional parameters. Since the film is thin the aspect ration $\epsilon = H/L \ll 1$. Using the scaled parameters eqns. (1)-(3) may now be reduced to their final form:

$$\frac{\partial u}{\partial x} + \frac{\partial v}{\partial y} = 0\,, \quad (4)$$

$$-\frac{\partial p}{\partial x} + \frac{\partial}{\partial y}\left(\mu\, \frac{\partial u}{\partial y}\right) = 0\,, \quad (5)$$

$$\frac{\partial p}{\partial y} = 0\,, \quad (6)$$

$$\frac{\partial^2 T}{\partial y^2} + \mu\, Br \left(\frac{\partial u}{\partial y}\right)^2 = 0\,. \quad (7)$$

where $Br = (\mu_0 U^2/\kappa_0 \Delta T_0)$, $Pe = (\rho_0 c_p UL/\kappa_0)$ and $Re = (\rho_0 UL/\mu_0)$ represents the Brinkman, the Peclet and Reynolds numbers respectively. Despite the fact that the Peclet number is large, the reduced Peclet number $\epsilon^2 Pe$ and the reduced Reynolds number $\epsilon^2 Re$ are small and may be neglected in the governing equations. The Brinkman number may be close to a unity and may be retained.

Derivation of the velocity and temperature profiles may be completed after the boundary conditions associated with eqns. (4)-(7) are stated. A no slip boundary

condition is applied at the bottom of the channel. The velocity at the top of the plate moves at a constant velocity U hence the boundary conditions are listed as,

$$y = 0\,,\;\; u = 0\,, \tag{8}$$

$$y = 1\,,\;\; u = U = 1\,. \tag{9}$$

The temperature at the top and bottom of the plate are given as follows,

$$y = 0\,,\;\; T = 0\,, \tag{10}$$

$$y = 1\,,\;\; T = 1. \tag{11}$$

The final equations will be solved using the boundary conditions above.

2.1 Newtonian model with constant viscosity

In this case for prediction of the correct results, we start with a simple case when the viscosity is constant. In the latter stage the viscosity will be allowed to vary. Now if the viscosity is considered to be constant, the velocity is determined by integrating eqn. (5) with respect to y. Using the boundary conditions (8) and (9) respectively to obtain,

$$u = \frac{1}{2}\left[\frac{\partial p}{\partial x}\left(y^2 - y\right)\right] + Uy\,. \tag{12}$$

The first term on the right hand side is the standard parabola for the pressure driven flow. The last term is the classical straight line for the shear driven flow. The flux is determined by integrating eqn. (12) from $y = 0$ to $y = 1$. If the flux is constant the final integration leads to a linear pressure profile along the channel

$$p = -3Q(x - x_0) + \frac{3U}{2}(x - x_0) + p_0, \tag{13}$$

where p_0 is the pressure and x_0 is the position at the inlet. The governing equation for the temperature profiles requires the velocity gradient, this gradient may be determined by differentiating eqn. (12) with respect to y and combined with eqn. (7) to obtain,

$$\frac{\partial^2 T}{\partial y} = -\frac{Br}{4}\left[\left(\frac{\partial p}{\partial x}\right)^2 \left(4y^2 - 4y + 1\right) + 2U\,\frac{\partial p}{\partial x}\left(2y - 1\right) + U^2\right]\,. \tag{14}$$

Integrating eqn. (14) twice with respect to y, applying the boundary conditions (10) and (11) yields,

$$T = -\frac{Br}{4}\,\left[\frac{1}{12}\left(\frac{\partial p}{\partial x}\right)^2\left[\left(4y^4 - 8y^3 + 6y^2 - 2y\right) + \frac{U}{3}\frac{\partial p}{\partial y}\left(2y^3 - 3y^2 + y\right)\right]\right.$$

$$+\frac{U^2}{2}\left(y^2-y\right)\Bigg]+y\,. \tag{15}$$

The first term in the square brackets shows that the temperature is quartic in y and it occurs due to the pressure gradient. The second term appears due to the combination of the pressure and the shear. The last term is the straight-line distribution. When the viscosity is not constant this simple analysis cannot be followed through. In the next section, a specific case will be studied where the flow regime obeys the power law model.

2.2 The power law model for variable viscosity in conduits

In the previous section the study was conducted for constant viscosity, in this section the power law model with varying viscosity will be investigated. The velocity and the temperature profiles will be derived using the power law model:

$$\mu = m\left|\frac{\partial u}{\partial y}\right|^{n-1}. \tag{16}$$

where m is a constant and n is the power law index, $(\partial u/\partial y)$, is the shear rate. Setting $n=1$ and $m=\mu$, the Newtonian case will be retrieved. With $n\neq 1$, Eqn. (16) represent shear-thinning fluids, for $n<1$, represent pseudo-plastic fluids and $n>1$ a dilatant fluids. The absolute value sign may lead to a regularized power law model; consider the following two assumptions,

- Case (a), $\Longrightarrow$, $(\partial u/\partial y)\geq 0$:
- Case (b), $\Longrightarrow$, $(\partial u/\partial y)\leq 0$:

Integrating eqn. (5) with respect to y yields

$$\mu\,\frac{\partial u}{\partial y} = \left(G_x y + C_1\right)\,, \tag{17}$$

where $G_x=(\partial p/\partial y)$, Combining eqns. (16) and (17) gives,

$$\left|\frac{\partial u}{\partial y}\right|^{n-1}\frac{\partial u}{\partial y} = \frac{\left(G_x\,y+C_1\right)}{m}\,. \tag{18}$$

Using case (a) above, the positive velocity gradient is given by,

$$\frac{\partial u}{\partial y} = \left[\frac{\left(G_x\,y+C_1\right)}{m}\right]^{\frac{1}{n}}\,. \tag{19}$$

Integrating eqn. (19) with respect to y, and applying the boundary conditions (8) and (9) gives the velocity profile as,

$$u = \frac{n\,m}{(n+1)G_x}\left[\left(\frac{G_x}{m}y+\frac{C_1}{m}\right)^{\frac{n+1}{n}}-\left(\frac{C_1}{m}\right)^{\frac{n+1}{n}}\right]\,, \tag{20}$$

where C_1 will be computed from,

$$U = \frac{n\,m}{(n+1)G_x}\left[\left(\frac{G_x}{m}+\frac{C_1}{m}\right)^{\frac{n+1}{n}} - \left(\frac{C_1}{m}\right)^{\frac{n+1}{n}}\right]. \tag{21}$$

To determine the temperature profile, eqns. (7) and (19) are combined to give,

$$\frac{\partial^2 T}{\partial y^2} = -m\,Br\,\left[\left(\frac{G_x\,y}{m}+\frac{C_1}{m}\right)^{\frac{n+1}{n}}\right]. \tag{22}$$

Integrating eqn. (22) twice with respect to y, and applying the boundary conditions (10) and (11) to eliminate the constants of integration gives the temperature profile as,

$$\begin{aligned} T = &-A_1\left[\left(\frac{G_x y}{m}+\frac{C_1}{m}\right)^{\frac{3n+1}{n}}\right] \\ &+ A_1\left[\left(\left(\frac{G_x}{m}+\frac{C_1}{m}\right)^{\frac{3n+1}{n}} - \left(\frac{C_1}{m}\right)^{\frac{3n+1}{n}}\right)y - \left(\left(\frac{C_1}{m}\right)^{\frac{3n+1}{n}}\right)\right] + y, \end{aligned} \tag{23}$$

where $A_1 = \frac{\left(n^2\ m^3\ Br\right)}{((2n+1)\ (3n+1)\ G_x^2)}$.

For the case (b) above, the same procedure may be followed to obtain the velocity and temperature profiles. The results for case (a), will be plotted and discussed quantitatively.

2.3 Results and discussions

Three curves representing the velocity profiles for eqn. (12) are shown in fig.2. Curve (a) represents the parabolic profile for the pressure driven flow. The maximum velocity of the flow appears at the centre of plate. Curve (b) represents a linear profile for the shear driven flow, as expected from eqn. (12) the velocity increases linearly from 0 at the lower boundary to 1 at the upper boundary. Curve (c) is the combination of both the shear and pressure driven flow. We observe a parabolic profile with its maximum velocity near the moving upper plate.

Three temperature profiles corresponding to eqn. (15) are shown in fig. 3. Curve (a) represents the shear driven case. This is a parabolic profile with its maximum temperature near the moving plate. Curve (b) represents the pressure driven case, and curve (c) represents the combination of both the pressure and shear driven cases, the parabolic type profiles with its maximum temperature towards the moving plate are shown. These results are standard for lubrication theory and may be retrieved in [8, 9].

Fig. 4, represent three velocity profiles for eqn. (21). Each curve corresponds to three different values of the power law index $n = 0.8$, $n = 1$ and $n = 1.5$

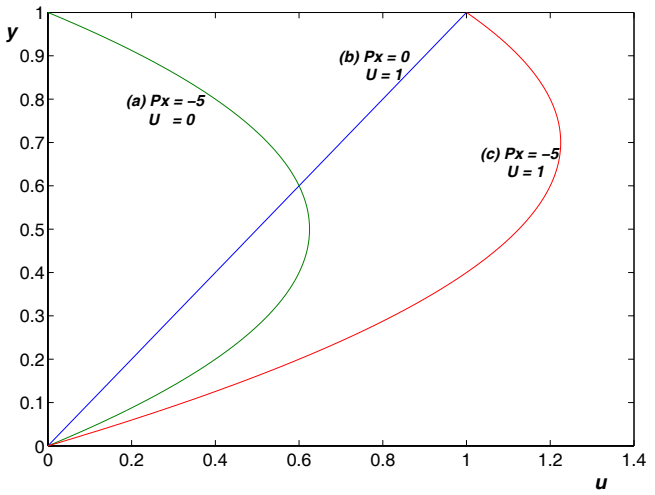


Figure 2: The velocity profile for eqn (12).

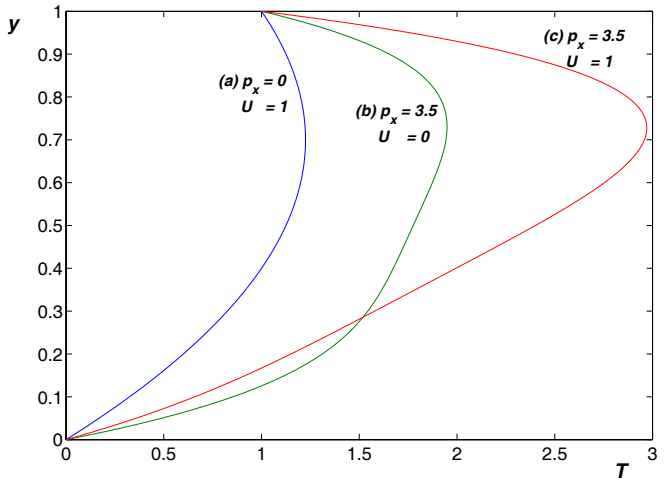


Figure 3: The temperature profile for eqn. (15).

respectively. All these curves are parabolic in shape and begin at the origin due to the boundary conditions. These curves show an increasing velocity profile with their maximum velocities towards the upper plate. Curve (b) with $n = 1$ compares closely with the Newtonian case. The velocity profiles increase with an increasing power law index n.

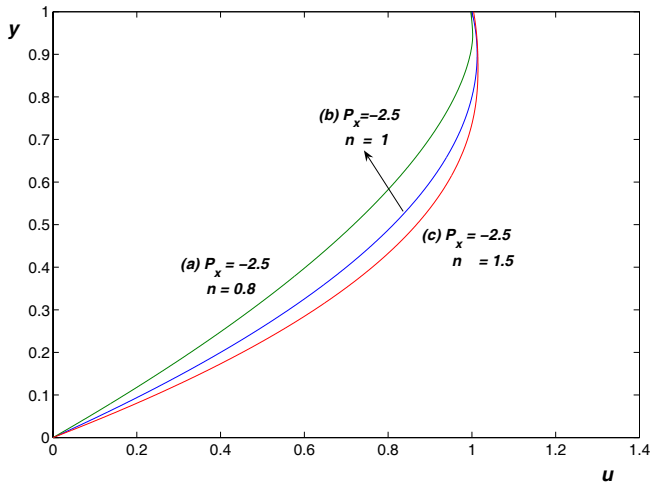


Figure 4: The velocity profile for eqn. (21).

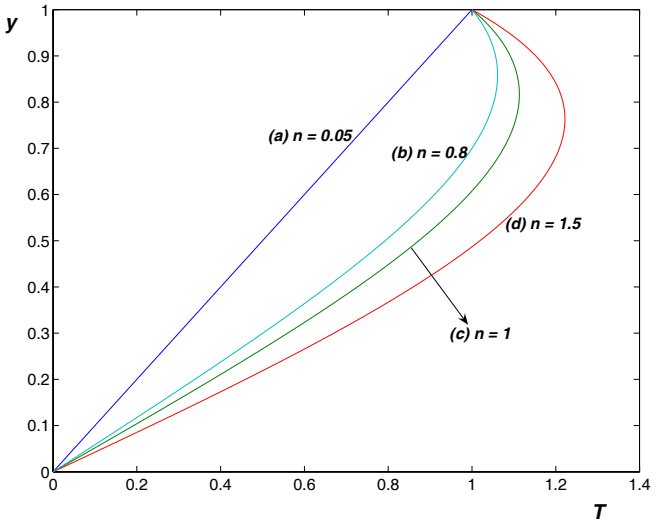


Figure 5: The temperature profile for eqn. (23).

On fig. 5, four curves representing the temperature profile for eqn. (23) are shown. Different values for n namely $n = 0.05$, $n = 0.8$, $n = 1$ and $n = 1.5$ are shown respectively on the corresponding curves. A linear profile is observed in curve (a) with its maximum temperature $T = 1$ at $y = 1$. Three parabolic type

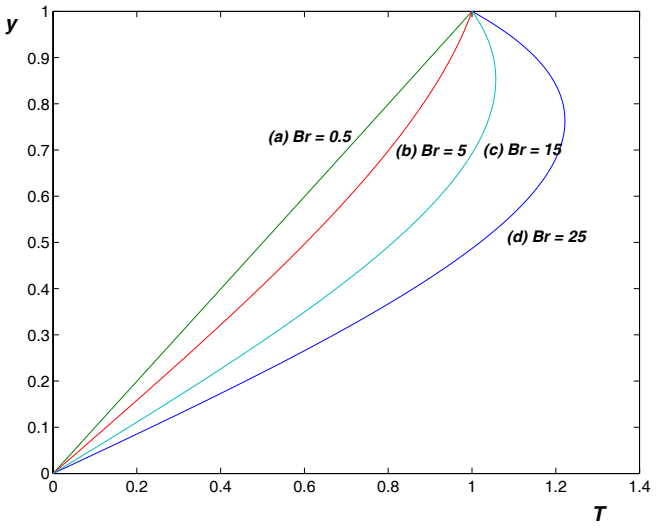


Figure 6: The temperature profile for eqn. (23) with varying Br.

temperature profiles are observed in curves (b), (c) and (d) respectively. When n increases the viscosity increases, and the temperature increases. The more viscous is the fluid the higher the temperature.

The effect of Brinkman number is investigated. Large values of Br means that the viscosity of the fluid is high. Fig. 6, shows four curves representing the temperature profile as shown in fig. 5, (b). Each curve corresponds to different values of Br, namely $Br = 0.5$, $Br = 5$, $Br = 15$ and $Br = 25$ respectively. A linear profile is observed in curve (a) which is increasing across the layer to the top plate $T = 1$ at $y = 1$. Curve (b) also increases nonlinearly across the layer to the upper plate. Curves (c) and (d) shows parabolic profiles with their maximum temperatures $T = 1.03$, at $y = 0.86$ and $T = 1.22$, at $y = 0.78$ respectively. When Br increases, a significant increase in the temperature field is observed. This shows that the temperature rise due to heat dissipation is significant when Br increases from $Br = 0.5$ to $Br = 25$.

3 Conclusion

In this paper the problem of applying a thin layer of a power-law fluid between parallel plates has been examined using the lubrication theory. The hydrodynamics of equivalently Newtonian model with constant viscosity was studied. The integral solutions for the velocity and temperature are presented and their flow patterns were compared. It is clear that the Newtonian results compares closely with power law model results particularly when the power law index $n = 1$, see figs. 2 and 4.

The results shown in figs. 3 and 5, a significance increase in the power law index n results in a significance increase in the both the velocity and temperature profiles. Fig. 6 clearly shows an increase in Br also influences the temperature. In future we hope to improve the model by allowing the temperatures at the plate to vary in the direction of the flow.

Acknowledgements

The authors acknowledge the support of this work by the National Research Foundation of South Africa, under grant number 2053289. Mr Tshehla acknowledges the department of Defence for the continuous support. Dr Charpin acknowledges the support of the Claude Leon Foundation.

Nomenclature

The following dependent variables are taken into consideration.

Name	Symbol	Typical value	Unit
$Br = \eta_0 U^2/(k\Delta T_m)$	Brinkman number	0.01-0.5	
c_p	Heat capacity	2000	J·kg^{-1}·K^{-1}
H	Channel height	10^{-6}	m
k	Thermal conductivity	0.17	W·m^{-1}·K^{-1}
L	Channel length	0.005	m
P	Pressure scale	10^9	Pa
p	Pressure		Pa
$Pe = \rho c_p LU/k$	Peclet number	10^5	
$Re = \rho UL/\eta_0$	Reynolds number	40-2000	
t	Time		s
T	Temperature		K
ΔT	Temperature drop	100	K
U	Velocity scale	5	m/s
(u, v)	Cartesian velocity		m/s
(x, y)	Cartesian coordinates		m
ϵ	Aspect ratio of the flow	10^{-4}	
η	Dynamic viscosity		kg·m^{-1}·s^{-1}
η_0	Typical dynamic viscosity	0.01-0.5	kg·m^{-1}·s^{-1}
ρ	Fluid density	1000	kg·m^{-3}



References

[1] Andersson, H. I. & Valnes, O. A., Slip-flow boundary conditions for non-Newtonian lubrication layers. *Fluid Dynamic Research*, **24**, pp. 211-217, 1999.
[2] Constatinescu, V. N., *Laminar Viscous flow*, Springer-Verlag: New York, pp. 127-134, 1995.
[3] Gupta, R. C., On developing laminar no-Newtonian flow in pipes and channels. *Nonlinear Analysis*, **2**, pp. 171-193, 2001.
[4] Lian, G. Xu, Y. Huang, W., & Adams, M. J., On the squeeze flow of a power law between rigid spheres. *Journal of non-Newtonian fluid Mechanics*, **100**, pp. 151-164, 2001.
[5] Rao, B. K., Heat transfer to falling power law. *Heat and Fluid flow*, **20**, pp. 429-436, 1999.
[6] Ross, A. B. Wilson, S. K. & Duffy, B. R., Blade coating of power-law fluid. *Physics of Fluids*, **11(5)**, pp. 958-970, 1999.
[7] Schetz, J. A. & Fuhs, A. E., *Fundamentals of fluid mechanics*, John Wiley and Sons: USA, pp. 243, 1999.
[8] Shames, I. H., *Mechanics of fluids*, McGraw-Hill: USA, pp. 14, 1992.
[9] White, F. M., *Viscous fluid flow*, McGraw-Hill: USA, pp. 235-238. 1991.
[10] Zheng, L. C. & Zhang X. X., Skin friction and heat transfer in power-law fluid laminar boundary layer along a moving surface. *International Journal of Heat Mass transfer*, **45**, pp. 2667-2672, 2002.



This page intentionally left blank

Section 9
Wave studies

This page intentionally left blank

Second-order wave loads on offshore structures using the Weber's transform method

M. Rahman[1] & S. H. Mousavizadegan[2]
[1] *Department of Engineering Mathematics, Dalhousie University, Canada*
[2] *Department of Mechanical Engineering, Dalhousie University, Canada*

Abstract

The second-order wave loads are computed for the diffraction of monochromatic waves by a surface-piercing vertical cylinder in the finite and infinite fluid depths. The Weber transform method which is essentially a Hankel transform method with a more general kernel, is applied to compute the second-order force due to the second-order velocity potential. Suitable closed contours in the complex plane are used to derive the analytical solution of the improper integrals involved in this study. This makes the present solution distinct from the other available solution of the second-order forces.

1 Introduction

The fluid viscosity and the irrotational flow are important in determining the wave induced loads on offshore structures. The wave loading estimations for small volume structures are based on the well-known "Morison Equation" which involves both viscous drag and inertia forces. If the characteristic dimension of the structure is comparable to the wavelength, the diffraction theory should be applied to find the wave induced loads upon the structure.

There are some fundamental second-order phenomena that can not be predicted in the linearized wave theory. The second-order phenomena in monochromatic waves are the steady mean drift forces and the oscillating forces with a frequency twice the first order frequency. The force oscillating with the difference of frequencies that cause slow-drift motion of moored structures and the loads with sum frequencies that cause springing on TLPs are the second-order phenomena in multi-chromatic waves.



WIT Transactions on Engineering Sciences, Vol 52, © 2006 WIT Press
www.witpress.com, ISSN 1743-3533 (on-line)
doi:10.2495/AFM06043

Hunt and Baddour [2] derived a second-order solution for the diffraction of a nonlinear progressive wave in fluid of infinite depth, incident on a vertical, surface-piercing, circular cylinder. They applied a modified form of Weber's integral theorem to obtain the second-order diffracted velocity potential and the associated wave force. Newman [5] analyzed the second-order wave force on a vertical cylinder by the application of the Weber transformation to derive the second-order potential. Solutions for the second-order forces associated with the first and the second-order velocity potentials are evaluated directly from pressure integration over the cylinder surface for the case of infinite fluid depth. He extended the solution to the case of finite fluid depth.

Rahman [6] extended the Lighthill's [3] second-order theory to the cases of intermediate and shallow fluid depth waves. Buldakov et al. [1] studied the diffraction problem of a unidirectional incident wave group by a bottom-seated cylinder. The amplitude of the incoming wave was assumed to be small in comparison with other linear scales of the problem to develop the corresponding second-order perturbation theory. They used the Fourier transform to treat time variation and separated spatial variables in solving the non-homogeneous second-order problem. The Weber transform is adopted to find the solution of the second-order velocity potential and the associated wave force. The computations are carried out in fluid of finite and infinite depths.

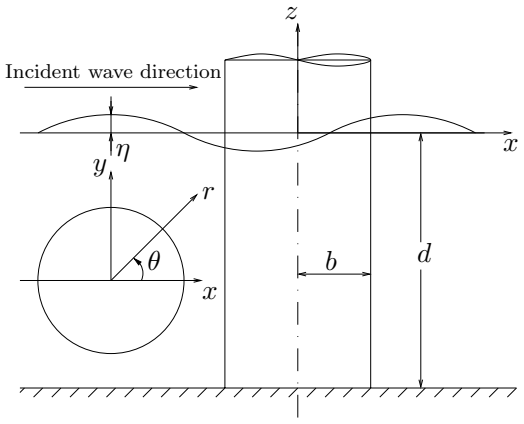


Figure 1: Schematic diagram of the circular surface piercing cylinder of radius b.

2 Governing mathematical equations

A rigid vertical cylinder of radius b is acted upon by a train of regular progressive surface waves of amplitude A (Fig.1). It is assumed that the fluid is incompressible, inviscid and the motion is irrotational. The fluid flow field can be defined by a scalar function called velocity potential and denoted by $\Phi(r, \theta, z, t)$. If the analysis

is approximated up to the second-order, it can be written that $\Phi = \Phi_\ell + \Phi_q$, where Φ_ℓ and Φ_q are the linear and the quadratic diffraction velocity potentials. The motion of the fluid is subjected to the Laplace equation in fluid domains, a free-surface kinematic boundary condition and a free-surface dynamic boundary condition. The fluid flow field is also subjected to a bottom condition that indicates no flux of mass through the bottom of the fluid, a radiation condition at a large distance from the body and a body surface boundary condition.

The total horizontal force acting upon the surface of the cylinder is obtained by the integration of the pressure along the surface of the cylinder. The fluid pressure is determined using Bernoulli's equation. The second-order force is partly due to the contribution of the first-order potential and partly due to the effect of the second-order potential. Using Weber's transform the contribution of the second-order potential is derived and computed by direct integration of the attributed pressure along the surface of the cylinder.

3 The second-order velocity potential

This section is devoted to obtain the explicit expression of the second-order potential with the help of Weber's transform for the infinite and finite depth ocean. The mathematical developments are given below for each case.

3.1 Infinite fluid depth

The second-order velocity potential may be written in the form of $\Phi_q = \phi_q e^{-i\,2\omega t}$. The time independent quadratic potential ϕ_q can be expressed by the Fourier series in the form of

$$\phi_q(r,\theta,z) = \sum_{n=0}^{\infty} \phi_q^{(n)}(r,z)\cos n\theta, \tag{1}$$

where the Fourier coefficients $\phi_q^{(n)}(r,z) = \frac{\alpha_n}{2\pi}\int_0^{2\pi} \phi_q(r,\theta,z)\cos n\theta\; d\theta$ in which $\alpha_0 = 1$ and $\alpha_n = 2$ for $n \geq 1$.

The modified Weber transform that is an extension of the Hankel's transform with a more general kernel is applied to find the solution of the second-order velocity potential. If the term $\hat{\phi}(k)$ is denoted as the transformation of $\phi(r)$, the transform pairs are

$$\hat{\phi}^{(n)}(k) = \int_b^{\infty} \phi^{(n)}(r) W_n(kb,kr) r dr$$

$$\phi^{(n)}(r) = \int_0^{\infty} \hat{\phi}^{(n)}(k) \frac{W_n(kb,kr)}{{J'_n}^2(kb) + {Y'_n}^2(kb)} k dk, \tag{2}$$

where $W_n(kb,kr) = J_n(kr)Y'_n(kb) - Y_n(kr)J'_n(kb)$ is the kernel for the integral transformation.

Substituting (1) in the Laplace equation in cylindrical coordinates and taking the Weber transform of it, an ordinary differential equation is obtained,

$$\hat{\phi}^{(n)}_{zz}(k,z) - k^2\hat{\phi}^{(n)}(k,z) = 0 \tag{3}$$

The solution $\hat{\phi}^{(n)}(k,z) = \hat{\phi}^{(n)}(k)e^{kz}$ satisfies (3). Using the transformation (2), a solution for the θ-independent quadratic velocity potential is constructed in the form

$$\phi^{(n)}_q(r,z) = \int_0^\infty \hat{\phi}^{(n)}_q(k)e^{kz}W_n(kb,kr)\frac{k\,dk}{J_n'^2(kb) + Y_n'^2(kb)}. \tag{4}$$

This solution satisfies the body surface boundary and bottom boundary conditions. The multiplication of the solution (4) by $\cos n\theta$ also satisfies the Laplace equation. The solution (4) satisfies the free surface boundary condition provided that

$$\hat{\phi}^{(n)}(k) = \frac{2\,\omega\nu A^2\alpha_n}{k - 4\nu}\hat{S}^{(n)}(k), \tag{5}$$

where $\hat{S}^{(n)}(k)$ is the transformation of $S^{(n)}(\nu r)$. The function $S^{(n)}(\nu r)$ is defined by

$$S^{(n)}(\nu r) = i^{\,n+1}\sum_{m=0}^{\infty}(-1)^m B_{mn}(\nu r) + \frac{i^{\,n+1}}{2}\sum_{p=1}^{n-1}C_{pn}(\nu r) \tag{6}$$

where

$$B_{mn}(\nu r) = A_m(\nu r)A_{m+n}(\nu r) + A'_m(\nu r)A'_{m+n}(\nu r) + \frac{m(m+n)}{\nu^2 r^2}A_m(\nu r)A_{m+n}(\nu r)$$

$$C_{pn}(\nu r) = A_p(\nu r)A_{n-p}(\nu r) + A'_p(\nu r)A'_{n-p}(\nu r) - \frac{p(n-p)}{\nu^2 r^2}A_p(\nu r)A_{n-p}(\nu r).$$

The time-independent quadratic velocity potential may be expressed in the form

$$\phi_q(r,\theta,z) = 2\,\omega\nu A^2\sum_{n=0}^{\infty}\alpha_n\cos n\theta\int_0^\infty \frac{\hat{S}^{(n)}(k)}{k-4\nu}e^{kz}W_n(kb,kr)\times \frac{k\,dk}{J_n'^2(kb) + Y_n'^2(kb)} \tag{7}$$

that satisfies the governing equations and all the boundary conditions.

3.2 Finite fluid depth

The second-order time-independent velocity potential may be expressed for the case of finite fluid depth as

$$\phi_q(r,\theta,z) = \frac{2gK^2A^2}{\omega}\sum_{n=0}^{\infty}\alpha_n\cos n\theta\int_0^{\infty}\hat{T}^{(n)}(k)\frac{\cosh k(z+d)}{k\sinh kd - 4\nu\cosh kd}\frac{W_n(kb,kr)}{{J'_n}^2(kb)+{Y'_n}^2(kb)}\,k\,dk, \tag{8}$$

where $\hat{T}^{(n)}(k)$ is the Weber transform of $T^{(n)}(Kr)$ and

$$T^{(n)}(Kr) = S^{(n)}(Kr) + \frac{3}{2}i^{\,n+1}sech^2Kd\;E^{(n)}(Kr). \tag{9}$$

The function $S^{(n)}(Kr)$ is expressed in (6) and $E^{(n)}(Kr)$ is the extra term due to the limitation of the fluid depth,

$$E^{(n)}(Kr) = \sum_{m=0}^{\infty}(-1)^m\Big[\lambda_m H_m^{(1)}(Kr)A_{m+n}(Kr) + \lambda_{m+n}H_{m+n}^{(1)}(Kr)\times J_m(Kr)\Big] + \sum_{p=1}^{n-1}\Big[\lambda_p H_p^{(1)}(Kr)A_{n-p}(Kr) + \lambda_{n-p}H_{n-p}^{(1)}(Kr)J_p(Kr)\Big].$$

The complete derivation of the velocity potentials in infinite and finite fluid depth can be found in Mousavizadegan [4].

4 The quadratic force

This section contains the evaluation of second-order forces for the infinite and finite depth ocean. The analytical solutions are described below.

4.1 Infinite fluid depth

The quadratic force may be expressed in the form

$$F_q = \Re\left\{f_q e^{-i\,2\omega t}\right\}, \tag{10}$$

where $\Re$ stands for the real part. The contribution of the solution $\phi_q(r,\theta,z)$ to the time-independent quadratic force stems only from the term $n=1$ in (7). The non-dimensional time independent quadratic force $\hat{f}_q = \frac{f_q}{\rho g A^2 b}$ can be obtained by

integrating the transient second-order pressure along the surface of the cylinder. Carrying out the integration, it can be written that

$$\hat{f}_q = -\frac{4i\nu}{b}\int_b^\infty G(\nu r)S^{(1)}(\nu r)r\ dr, \tag{11}$$

where

$$G(\nu r) = 4\nu\int_0^\infty \frac{W_1(kb,kr)}{J_1'^2(kb)+Y_1'^2(kb)}\frac{dk}{k(k-4\nu)}. \tag{12}$$

The integral in (12) is evaluated by the contour integration in the complex k-plane. The suitable contour for this problem is the semi-circular contour of infinite radius on the right side of the imaginary axis which contains the first and fourth quadrants. There exists one singularity $k = 4\nu$ which lies on the path of integration along the real axis.

Finally, the quadratic force can be obtained from,

$$\hat{f}_q = \frac{id_0(\nu b)}{\nu b}\Big\{\int_0^\infty \frac{K_0(4\nu by)}{y^2(1+y^2)K_1'(4\nu by)}dy - \frac{\pi}{2}\Big[\frac{H_0^{(2)}(4\nu b)}{H_1'^{(2)}(4\nu b)} + \frac{H_0^{(1)}(4\nu b)}{H_1'^{(1)}(4\nu b)}\Big]\Big\}$$
$$+\frac{4i}{b}\int_b^\infty\Big\{\int_0^\infty \frac{K_1(4\nu ry)}{y(1+y^2)K_1'(4\nu by)}dy - \frac{\pi}{2}\Big[\frac{H_1^{(2)}(4\nu r)}{H_1'^{(2)}(4\nu b)} + \frac{H_1^{(1)}(4\nu r)}{H_1'^{(1)}(4\nu b)}\Big]\Big\}Z(\nu r)dr, \tag{13}$$

where

$$d_0(\nu b) = \frac{2i}{\pi}\sum_{m=0}^\infty (-1)^m\epsilon_m\lambda_m, \quad Z(\nu r) = \sum_{m=1}^\infty d_m(\nu b)H_m^{(1)}(\nu r)A_m(\nu r),$$
$$d_m(\nu b) = (-1)^{m+1}m(\lambda_{m+1}-\lambda_{m-1}) \quad m\geq 1, \qquad \lambda_m = \frac{J_m'(\nu b)}{H_m'^{(1)}(\nu b)}.$$

This result is similar to the one obtained by Newman [5]. The difference is in the solution of the contour integral for $G(\nu r)$. Here, the solution is a combination of the first and second kind of Hankel's functions. In contrast, Newman's result is expressed only by the second kind of the Hankel function.

4.2 Finite fluid depth

Because of orthogonal properties of the cosine functions, only the term proportional to $\cos\theta$ in (8) contributes to the second-order force due to the second-order potential. The second-order force coefficient can be obtained for the case of finite fluid depth by

$$\hat{f}_q = -\frac{4iK}{b}\int_b^\infty G(Kr)T^{(1)}(Kr)\ r\ dr, \tag{14}$$

where

$$G(Kr) = \frac{2K}{i}\int_0^\infty \Big\{\frac{H_1^{(2)}(kr)}{H_1^{(2)'}(kb)} - \frac{H_1^{(1)}(kr)}{H_1^{(1)'}(kb)}\Big\}\frac{k^{-1}\sinh kd\, dk}{k\sinh kd - 4\nu\cosh kd}$$
$$= \frac{2K}{i}(I_2 - I_1) \tag{15}$$

The integral I_1 can be computed by using the contour integration along a semicircular contour above the real axis. The integral I_2 is computed using a semicircular contour below the real axis. The integrand contains a singular point along the real axis and infinite number of singular points along the imaginary axis.

The final solution for the quadratic force coefficient is found for the case of finite fluid depth as

$$\hat{f}_q = \frac{4id_0(Kb)}{b}\Big\{\sum_{n=1}^{\infty}\frac{g_n K_0(\kappa_n b)}{\kappa_n K_1'(\kappa_n b)} - \frac{g_0}{\kappa_0}\Big[\frac{H_0^{(1)}(\kappa_0 b)}{H_1'^{(1)}(\kappa_0 b)} + \frac{H_0^{(2)}(\kappa_0 b)}{H_1'^{(2)}(\kappa_0 b)}\Big]\Big\}$$
$$+ \frac{4i}{b}\int_b^\infty \Big\{\sum_{n=1}^{\infty} g_n\frac{K_1(\kappa_n r)}{K'1(\kappa_n b)} - g_0\int_b^\infty \Big[\frac{H_1^{(1)}(\kappa_0 r)}{H_1'^{(1)}(\kappa_0 b)} + \frac{H_1^{(2)}(\kappa_0 r)}{H_1'^{(2)}(\kappa_0 b)}\Big]\Big\}Z(Kr)dr$$
$$+ \frac{6iK}{b}sech^2 Kd\int_b^\infty \Big\{\sum_{n=1}^{\infty} g_n\frac{K_1(\kappa_n r)}{K'1(\kappa_n b)}$$
$$- g_0\int_b^\infty \Big[\frac{H_1^{(1)}(\kappa_0 r)}{H_1'^{(1)}(\kappa_0 b)} + \frac{H_1^{(2)}(\kappa_0 r)}{H_1'^{(2)}(\kappa_0 b)}\Big]E^{(1)}(Kr)rdr\Big\}, \tag{16}$$

where coefficients g_0 and g_n are defined by

$$g_0 = 2\pi K\left\{\frac{4\nu/\kappa_0}{\kappa_0^2 d + 4\nu - 16\nu^2 d}\right\}, \qquad g_n = 4\pi K\left\{\frac{4\nu/\kappa_n}{\kappa_n^2 d - 4\nu + 16\nu^2 d}\right\}. \tag{17}$$

The terms denoted by κ_0 and κ_n , $n = 1, 2, 3\ldots$ are the roots of the transcendental equations $\kappa_0\tanh\kappa_0 d = 4\nu$ and $\kappa_n\tan\kappa_n d = -4\nu$, respectively. The first and the second part of (16) are the same as the force equation (13) for the infinite fluid depth case. The last part is an extra term due to the limitation of the fluid depth.

5 Results and discussion

The solutions contain considerable interactions of the Bessel and the modified Bessel functions of various kinds and orders. These functions are evaluated with double-precision routines. All computations are carried out using a PC with an Intel(R) Pentium(R) 4 CPU $1.80Ghz$ and total memory of $384MB$.

The second-order force coefficient $\hat{f}_q$ is obtained through the solution of (13) for the case of infinite fluid depth. The force equation (13) consists of four parts. The calculation of the second part is straightforward. There are three infinite integrals. The integrand of the first consists of a combination of the modified Bessel function of second kind. The second integral is a double infinite integral. The integrand of this integral consists of a combination of the modified Bessel function of the

second kind of order one and an infinite series. This series consists of the Bessel and Hankel functions of the first kind of different orders. The integrand of the third infinite integral consists of a combination of the Hankel function of the first and the second kinds. It also consists of the infinite series as explained already. These integrals are calculated by the Simpson three-eights rule.

The computation of the first integral is straightforward. The solution for each $\nu b = const.$ is carried out in two steps. First the infinite interval is divided into small segments of $2^k - 2^{k-1}$, $k = 0, 1, 2, \cdots$ and $k - 1 \geq 0$. The result on each subinterval is obtained for a convergence error in order of 10^{-6}. The solutions for the segments are added together to reach an error less than 10^{-8}. The second integral is a double infinite integral. The computation are carried out for each step ($\nu b = const.$), while r is varied from b to infinity. The result for the infinite series is obtained with an error less than 10^{-8}. The result of the infinite internal integral is obtained in the same way as mentioned in the last paragraph. The third integral is also found by the Simpson method of three-eights rule with an error less than 10^{-6}. However, the integrand of this integral has a very oscillatory nature. The computations are very time-consuming for large values of νr.

The solutions for the real and imaginary parts of the second-order force coefficients $\hat{f}_q$ are displayed in Fig. 2. They are compared with the published results of Newman [5]. The imaginary part of both solutions has the same sign and almost the same value. The real part of solutions has a different sign due to the different direction of the incoming waves. The values of the real part for small values of the νb are also different. The differences are due to the different contours that are used in the integration process. It seems that our computations are more reliable due to the fact that the function $G(\nu r)$ in (10) is a real function. Newman's solution [5] for (10) is a complex function, while ours is a real one.

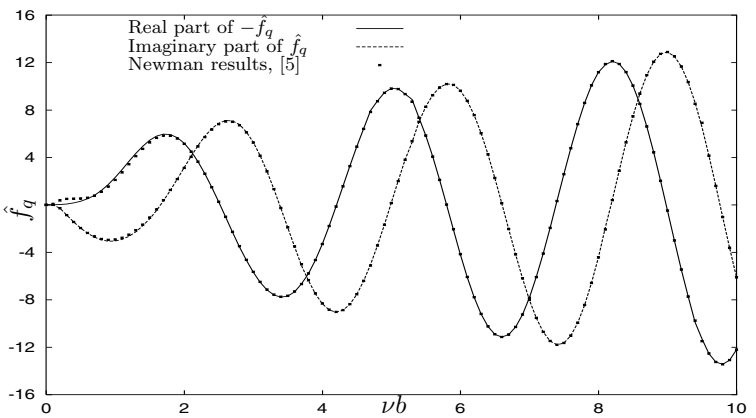


Figure 2: Real and imaginary parts of the non-dimensional quadratic force in infinite fluid depth.

The quadratic force coefficient in finite depth is obtained through the solution of (16) for different depth-radius ratios. The first and second parts in (16) are the same as (10) in the case of infinite fluid depth. However, the infinite integrals from zero to infinity are replaced by an infinite series that has very good convergence properties and makes the computations faster. The third part is an extra term due to the limitation of the fluid depth.

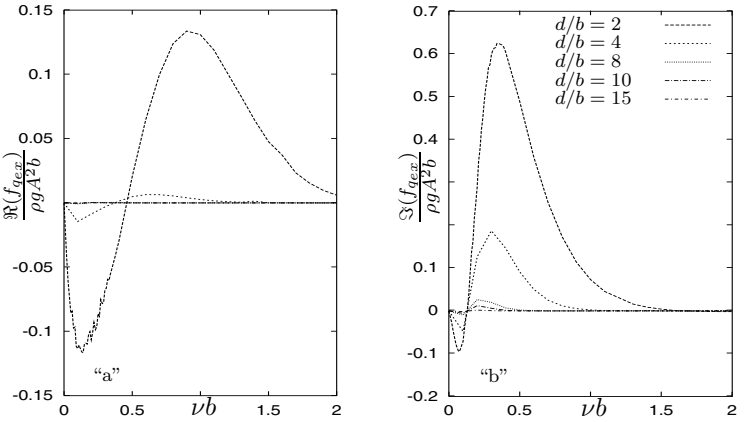


Figure 3: Real and imaginary parts of the extra term due to the limitation of the fluid depth.

The extra part is denoted by $\hat{f}_{q_{ex}}$. This part consists of two infinite integrals. The computation of the first integral is quite fast due to the proper behavior of the modified Bessel function. The second integral is very oscillatory and converges slowly. This part of the computation is the most time-consuming part. The real and imaginary parts of $\hat{f}_{q_{ex}}$ are depicted in Fig. 3. The contribution of this part is relatively small to the quadratic force. The quadratic force coefficient $\hat{f}_q$ is shown in Fig. 4. The infinite integral was solved using the Simpson three-eights rule with an error less than 5×10^{-6}. The infinite series converged with an error of order 10^{-8} or less. The effect of the limitation of depth is obvious and diminishes with an increase in the depth to radius ratio. This part of the wave force is affected by the limitation of fluid depth in a wide range of frequency spectrum.

6 Conclusions

Using the Weber transform, the second-order diffraction potential is evaluated in both cases of infinite and finite fluid depths. The quadratic force coefficients, due to the effect of the second-order velocity potential, are obtained using the direct integration of the related transient pressure around the cylinder surface. The resulting force coefficient is an integral along a horizontal distance from the vicinity of the

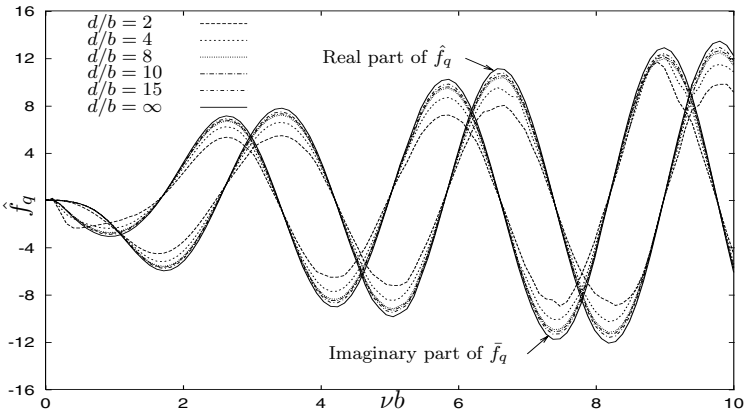


Figure 4: Real and imaginary parts of the quadratic force in various depth to radius ratios.

cylinder to infinity. The integrand of this integral contains an improper integral from zero to infinity of a real function. The expected solution is also a real function for the internal integral. The contour integration rule is adopted to obtain the solution of the internal integrals. The solutions are real functions for both infinite and finite fluid depth.

Acknowledgement

The Natural Sciences and Engineering Research Council (NSERC) of Canada is gratefully acknowledged.

References

[1] E. V. Buldakov, R. Eatock-Taylor, and P. H. Taylor, Local and far-field surface elevation around a vertical cylinder in unidirectional steep wave groups, *Ocean Engineering*, Vol. 31 , pp. 833–864, 2004.

[2] J. N. Hunt and R. E. Baddour, The diffraction of nonlinear progressive waves by a vertical cylinder, *Quarterly Journal of Mechanics and Applied Mathematics*, Vol. 34, pp. 69–88, 1981.

[3] M. J. Lighthill, Waves and hydrodynamic loading, *Proc. 2nd int. conf. on behavior of offshore structures*, Vol. 1, pp. 1–40, 1979.

[4] S. H. Mousavizadegan, Analytical and numerical approaches to determine the second-order forces in wave-body interactions, *Ph.D. thesis*, Dalhousie University, Sept. 2005.

[5] J. N. Newman, The second-order wave force on a vertical cylinder, *J. Fluid Mech.*, Vol. 320, pp. 417–443, 1996.

[6] M. Rahman, Nonlinear hydrodynamic loading on offshore structures, *Theoret. Comput. Fluid Dynamics*, Vol. 10, pp. 323–347, 1998.



Rear shock formation in gravity currents

S. J. D. D'Alessio[1], J. P. Pascal[2] & T. B. Moodie[3]
[1] *Department of Applied Mathematics, University of Waterloo, Canada*
[2] *Department of Mathematics, Ryerson University, Canada*
[3] *Department of Mathematical and Statistical Sciences, University of Alberta, Canada*

Abstract

Considered in this study is the gravity driven flow of a two-fluid system arising from the motion of a heavy fluid in a rectangular channel having a flat bottom. The mathematical model is based on shallow-water theory in connection with a two-layer Boussinesq fluid. By means of a scaling argument, it can be shown that for small density differences the gravity current can be successfully modelled by a two-by-two hyperbolic system in conservation form together with a pair of algebraic relations. This reduced system is referred to as the weak stratification model. A weakly nonlinear analysis is performed on this weak stratification model to elicit information concerning the formation of a rear shock which may form on the back side of the head of the gravity current. Predictions made by the analytical technique are then verified by numerical simulations.
Keywords: shallow-water theory, Boussinesq approximation, two-layer model, hyperbolic system, multiple scales analysis.

1 Introduction

A gravity current refers to the flow of one fluid within another which is driven by the density difference between these two fluids. Gravity currents play an important role in many known natural phenomena as well as human-related activities ranging from turbidity currents to the accidental release of industrial pollutants.

Although it is obviously the case that the initial flow following the release of a gravity current of finite volume is a complex three-dimensional unsteady flow, soon after release the current will have spread sufficiently that its length is very much greater than its thickness. The thickness $h(x,t)$ will at this stage be slowly



WIT Transactions on Engineering Sciences, Vol 52, © 2006 WIT Press
www.witpress.com, ISSN 1743-3533 (on-line)
doi:10.2495/AFM06044

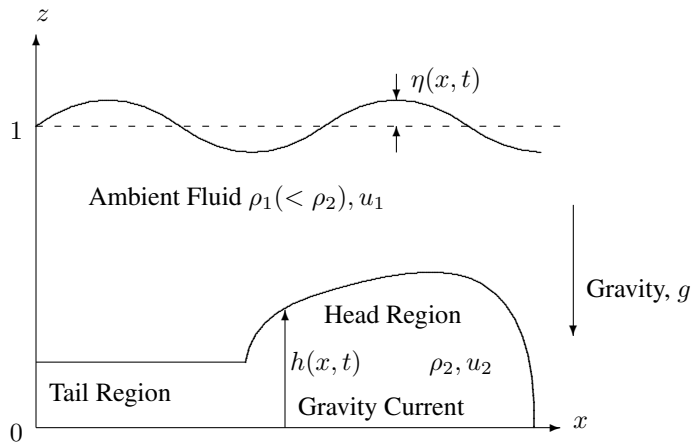


Figure 1: The flow configuration of the two-fluid system and the general structure of a bottom gravity current.

varying over the horizontal position x and in time t. This approach to gravity currents has been exploited successfully by numerous researchers in the past and we refer the reader to the book by Simpson [1] for an extensive bibliography and comparisons between theory based on this low aspect ratio approach and experiments. The general structure of a bottom gravity current is shown in Figure 1.

A distinguished feature of these flows, which is the focus of this study, is the formation of a rear shock behind the head of the gravity current. Experiments executed by Rottman and Simpson [2] examined instantaneous releases for $0 < h_i \leq 1$, where h_i is the initial depth ratio between the released heavy fluid and the total depth of the two-fluid system in the rectangular channel. Their observations revealed that for h_i equal to or slightly less than unity the disturbance generated at the proximal end wall has the appearance of an internal hydraulic drop. On the other hand, for smaller values of h_i ($\lesssim 0.7$) this disturbance is a long wave of depression. Currently there are no theoretical model-based calculations that can accurately predict this bifurcation in behaviour which occurs in the experimental results as h_i is varied. These experiments did however serve to emphasize the importance of including the effects of the ambient fluid on the bottom boundary current when the current initially occupies a large fraction of the total depth.

D'Alessio *et al* [3] employed a two-layer shallow-water model to study bottom gravity currents released from rest. Using MacCormack's method [4] to integrate numerically the hyperbolic system they were able to achieve good qualitative agreement with the experimental results of Rottman and Simpson [2]. Also, employing multiple scales arguments they were able to show analytically the dependence of internal bore formation (i.e. rear shock) on initial fractional depth of the release volume. Their analysis, however, did not confirm the value of $h_i \simeq 0.7$ referred to earlier but rather gave the lower value of $h_i = 0.5$ as the minimum

fraction for bore initiation. This is perhaps not surprising when one contrasts the relative simplicity of a shallow water (hydraulic) model for what is a complex flow involving possible nonhydrostatic effects in various regions of the flow due to streamline curvature, unresolved small scale dissipation and other effects.

The goal of the present work is to extend the analysis in [3] to include bottom gravity currents released with an arbitrary constant initial velocity in a rectangular channel.

2 Formulation

The flow configuration and general structure of the gravity current is depicted in Figure 1. Here, $\eta(x,t)$ represents the dimensionless displacement of the free surface from its undisturbed height, (u_1, u_2) are the dimensionless fluid velocities in Cartesian coordinates (x, z). In dimensionless form the mean depth of the two layer system measured from $z = 0$ is taken to be unity, and $h(x,t)$ is the dimensionless fractional thickness of the bottom layer (or gravity current). The flat bottom of the rectangular channel is located at $z = 0$. The flow is driven by the buoyancy force arising because of the difference between the density ρ_2 of the bottom layer and the density ρ_1 of the ambient fluid.

In dimensionless variables the governing shallow-water equations take the form:

$$\frac{\partial u_1}{\partial t} + u_1 \frac{\partial u_1}{\partial x} + \frac{\partial \eta}{\partial x} = 0 \ , \tag{1}$$

$$\frac{\partial}{\partial t}(h - \frac{g'}{g}\eta) + \frac{\partial}{\partial x}[(1 + \frac{g'}{g}\eta - h)u_1] = 0 \ . \tag{2}$$

$$\frac{\partial u_2}{\partial t} + u_2 \frac{\partial u_2}{\partial x} + \left(1 - \frac{g'}{g}\right) \frac{\partial \eta}{\partial x} + \frac{\partial h}{\partial x} = 0 \ , \tag{3}$$

$$\frac{\partial h}{\partial t} + \frac{\partial}{\partial x}(h u_2) = 0 \ . \tag{4}$$

In the above $g' = g(\rho_2 - \rho_1)/\rho_2$ is the reduced gravity and the parameter g'/g is a measure of the stratification of this two-fluid system. As explained in [3], it is also a measure of the importance of the free surface on the flow since letting $g'/g \to 0$ filters out surface wave phenomena. The system of equations (1)-(4) is posed as an initial value problem subject to the initial conditions

$$u_1(x,0) = 0 \ , \ u_2(x,0) = u_{20} \ , \ \eta(x,0) = 0 \ , \ h(x,0) = G(x) \ , \tag{5}$$

the impermeability conditions

$$u_1(0,t) = 0 \ , \ u_2(0,t) = 0 \ , \tag{6}$$

the slope conditions

$$\frac{\partial \eta}{\partial x}(0,t) = \frac{\partial h}{\partial x}(0,t) = 0 \ , \tag{7}$$

and lastly the far-field conditions

$$u_1(x,t) \to 0\ ,\ u_2(x,t) \to 0\ ,\ \eta(x,t) \to 0\ ,\ h(x,t) \to 0 \text{ as } x \to \infty\ . \tag{8}$$

In the above $G(x)$ specifies the initial configuration of the two-fluid system. We are particularly interested in initial rectangular configurations of the form

$$G(x) = \begin{cases} h_0 & \text{if } 0 \le x \le x_0 \\ 0 & \text{if } x > x_0 \end{cases}\ , \tag{9}$$

where h_0 is the nondimensional initial thickness of the gravity current and u_{20} is its corresponding initial velocity. The parameter h_0 is thus the ratio of the initial depth of the heavy fluid to that of the two-fluid system.

An important simplified model is the **weakly stratified** model wherein we neglect terms of $O(g'/g)$ on the assumption that the initial density difference is small. It has been shown in [3] that in this limit the governing equations can be reduced to the two-by-two system

$$\frac{\partial u_2}{\partial t} + \left(u_2 + \frac{\partial \eta}{\partial u_2}\right)\frac{\partial u_2}{\partial x} + \left(1 + \frac{\partial \eta}{\partial h}\right)\frac{\partial h}{\partial x} = 0\ , \tag{10}$$

$$\frac{\partial h}{\partial t} + \frac{\partial}{\partial x}(hu_2) = 0\ , \tag{11}$$

together with the two algebraic relations given by

$$\eta = \eta(u_2, h) = -\frac{u_2^2 h}{1-h} - \frac{1}{2}h^2\ , \tag{12}$$

$$u_1 = -\frac{hu_2}{1-h}\ . \tag{13}$$

Alternatively, the above can be expressed more compactly as

$$\frac{\partial u_2}{\partial t} + \frac{(1-3h)}{(1-h)}u_2\frac{\partial u_2}{\partial x} + \left(1 - h - \frac{u_2^2}{(1-h)^2}\right)\frac{\partial h}{\partial x} = 0\ , \tag{14}$$

$$\frac{\partial h}{\partial t} + \frac{\partial}{\partial x}(hu_2) = 0\ . \tag{15}$$

Another more simplified model worth mentioning is the **weakly stratified deep ambient layer** model given by

$$\frac{\partial u_2}{\partial t} + u_2\frac{\partial u_2}{\partial x} + \frac{\partial h}{\partial x} = 0\ , \tag{16}$$

$$\frac{\partial h}{\partial t} + \frac{\partial}{\partial x}(hu_2) = 0\ . \tag{17}$$

This model applies when $h \ll 1$.

In the next section we carry out a multiple scales analysis on the weakly stratified model equations to elicit information regarding rear shock formation.

3 Weakly nonlinear analysis

In this section we will analytically investigate the formation of the rear shock behind the head of the gravity current. Since shock formation is a nonlinear phenomenon, we employ a weakly nonlinear analysis, similar to that in [3], on the weakly stratified model equations given by (14) and (15). We first expand the flow variables about the basic state given by $(u, h) = (u_0, h_0)$, taking $u \equiv u_2$, which corresponds to the initial configuration. The weakly stratified model equations can then be reduced to the following quadratically nonlinear system:

$$\frac{\partial \hat{u}}{\partial t} + \left(\frac{u_0(1-3h_0)}{(1-h_0)} + \frac{(1-3h_0)}{(1-h_0)}\hat{u} - \frac{2u_0}{(1-h_0)^2}\hat{h} \right) \frac{\partial \hat{u}}{\partial x}$$
$$+ \left(\frac{(1-h_0)^3 - u_0^2}{(1-h_0)^2} - \frac{2u_0}{(1-h_0)^2}\hat{u} - \frac{[(1-h_0)^3 + 2u_0^2]}{(1-h_0)^3}\hat{h} \right) \frac{\partial \hat{h}}{\partial x} = 0 \ , \quad (18)$$

$$\frac{\partial \hat{h}}{\partial t} + (h_0 + \hat{h})\frac{\partial \hat{u}}{\partial x} + (u_0 + \hat{u})\frac{\partial \hat{h}}{\partial x} = 0 \ , \quad (19)$$

where the hat denotes the deviation from the basic state (u_0, h_0).

Linearizing the above equations and assuming a wave-like solution

$$u(x,t) = u(\xi) \ , \ h(x,t) = h(\xi) \text{ where } \xi = x - ct$$

(dropping the hats) we find that the linearized speeds

$$c_\pm = \left(\frac{1-2h_0}{1-h_0} \right) u_0 \pm \sqrt{\frac{h_0}{1-h_0}} \sqrt{(1-h_0)^2 - u_0^2} \ , \quad (20)$$

guarantee a nontrivial solution. For $0 \le u_0 \le 1$ it is clear that the speeds are real in the triangular region $h_0 \le 1 - u_0$.

Equations (18) and (19) can be combined to yield a single equation given by (again dropping the hats)

$$h_{tt} + a_1 h_{xt} + a_2 h_{xx} = -(uh)_{xt} + a_3(uu_x)_x - a_4(hh_x)_x - a_5(uh)_{xx} \ , \quad (21)$$

with subscripts denoting partial differentiation and

$$a_1 = \frac{2u_0(1-2h_0)}{(1-h_0)} \ , \ a_2 = \frac{u_0^2(1-3h_0+3h_0^2) - h_0(1-h_0)^3}{(1-h_0)^2} \ ,$$

$$a_3 = \frac{h_0(1-3h_0)}{(1-h_0)} \ , \ a_4 = \frac{h_0[(1-h_0)^3 + 2u_0^2]}{(1-h_0)^3} \ , \ a_5 = \frac{u_0(1-2h_0+3h_0^2)}{(1-h_0)^2} \ .$$

We next introduce

$$\xi = x - c_- t \ , \ \eta = x + c_- t \ , \ T = \varepsilon t \ , \ h = \varepsilon \tilde{h} \ , \ u = \varepsilon \tilde{u} \ . \quad (22)$$

In addition, we expand the variables in the following series

$$\tilde{h} = h^{(0)} + \varepsilon h^{(1)} + O(\varepsilon^2) \text{ and } \tilde{u} = u^{(0)} + \varepsilon u^{(1)} + O(\varepsilon^2) \, . \tag{23}$$

The leading order equations then become

$$\alpha h^{(0)}_{\eta\eta} - \beta h^{(0)}_{\eta\xi} = 0 \, , \tag{24}$$

$$c_-(u^{(0)}_\eta - u^{(0)}_\xi) + \frac{u_0(1-3h_0)}{(1-h_0)}(u^{(0)}_\eta + u^{(0)}_\xi) = \\ -\frac{[(1-h_0)^3 - u_0^2]}{(1-h_0)^2}(h^{(0)}_\eta + h^{(0)}_\xi) \, , \tag{25}$$

with $\alpha = c_-^2 + a_1 c_- + a_2$ and $\beta = 2(c_-^2 - a_2)$. The solutions have the form

$$h^{(0)} = \phi(\xi, T) + \psi(\eta + \frac{\alpha}{\beta}\xi, T) \, , \tag{26}$$

$$u^{(0)} = \frac{\Gamma}{\gamma}\phi(\xi, T) - \frac{(1+\frac{\alpha}{\beta})\Gamma}{\omega}\psi(\eta + \frac{\alpha}{\beta}\xi, T) \, , \tag{27}$$

where ϕ and ψ are arbitrary functions and

$$\Gamma = \frac{[(1-h_0)^3 - u_0^2]}{(1-h_0)^2} \, , \; \gamma = c_- - \frac{u_0(1-3h_0)}{(1-h_0)} \, ,$$

$$\omega = \left(1 - \frac{\alpha}{\beta}\right) c_- + \left(1 + \frac{\alpha}{\beta}\right) \frac{(1-3h_0)u_0}{(1-h_0)} \, .$$

As we will shortly see, of importance to our analysis is the function ϕ.

Carrying the analysis to the next order enables us to find the correction $h^{(1)}$. After some algebra the following equation for $h^{(1)}$ emerges

$$\alpha h^{(1)}_{\eta\eta} - \beta h^{(1)}_{\eta\xi} = A(\xi, T) + B(\xi, \eta, T) \, , \tag{28}$$

where

$$A(\xi, T) = (2c_- - a_1)\phi_{T\xi} + \frac{s}{2}(\phi^2)_{\xi\xi} \, , \tag{29}$$

with $s = 2\Gamma(c_- - a_5)/\gamma + \Gamma^2 a_3/\gamma^2 - a_4$. To ensure that $h^{(1)}$ remains bounded as $\xi, \eta \to \pm\infty$ we impose $A = 0$ as a solvability condition. We note that the function B does not enter into the analysis.

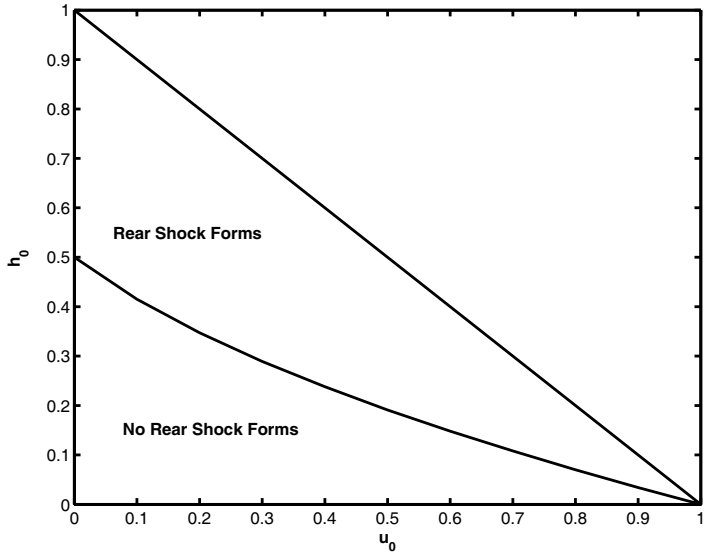


Figure 2: Analytical predictions showing initial configurations which should result in a rear shock.

Integrating $A = 0$ with respect to ξ gives

$$\phi_T + b\phi\phi_\xi = 0 \ , \ b = \frac{s}{2c_- - a_1} \ , \tag{30}$$

where it was assumed that ϕ has compact support. If we let $\phi(\xi, 0) = f(\xi)$ represent the initial condition, then the solution to the above can be expressed implicitly in parametric form in terms of the parameter τ as

$$\phi(\xi, T) = f(\tau) \text{ along } \xi = bTf(\tau) + \tau \ . \tag{31}$$

Shock formation occurs when $|\phi_\xi| \to \infty$ where

$$\phi_\xi = \frac{f'(\tau)}{1 + bTf'(\tau)} \ , \tag{32}$$

which becomes infinite when $T = -1/bf'(\tau)$. Along the back side of a smooth curve $f(\tau)$, where $f'(\tau) > 0$, a shock will form if $b < 0$. In terms of the initial configuration specified by u_0 and h_0, with u_0 replacing u_{20} in equation (5), this condition can be expressed as

$$2F_1F_2F_3 + F_1^2F_4 - F_2^2F_5 < 0 \ , \tag{33}$$

where

$$F_1 = \frac{(1-h_0)^3 - u_0^2}{(1-h_0)^2} \ , \ F_2 = \frac{u_0h_0}{1-h_0} + \sqrt{\frac{h_0}{1-h_0}}\sqrt{(1-h_0)^2 - u_0^2} \ ,$$

$$F_3 = -\frac{u_0 h_0(1+h_0)}{(1-h_0)^2} + \sqrt{\frac{h_0}{1-h_0}}\sqrt{(1-h_0)^2 - u_0^2}\,,\ F_4 = \frac{h_0(1-3h_0)}{(1-h_0)}\,,$$

$$F_5 = \frac{h_0[(1-h_0)^3 + 2u_0^2]}{(1-h_0)^3}\,.$$

A plot of the region satisfying the above inequality is shown in Figure 2. As a check, if we set $u_0 = 0$ then the above condition collapses to simply $h_0 > 1/2$ which is in full agreement with our previous result reported in [3].

We conclude this section by mentioning that if the above analysis is repeated on the weakly stratified deep ambient layer model equations (16)-(17), the prediction is that a rear shock should always form. This result, however, is not consistent with our numerical simulations. Thus, the further simplifications inherent in these equations render them inadequate in capturing the essential physics of the flow.

4 Numerical results and discussion

We next discuss the technique used to numerically integrate the weakly stratified equations. The goal here is to validate the analytical predictions derived in the previous section.

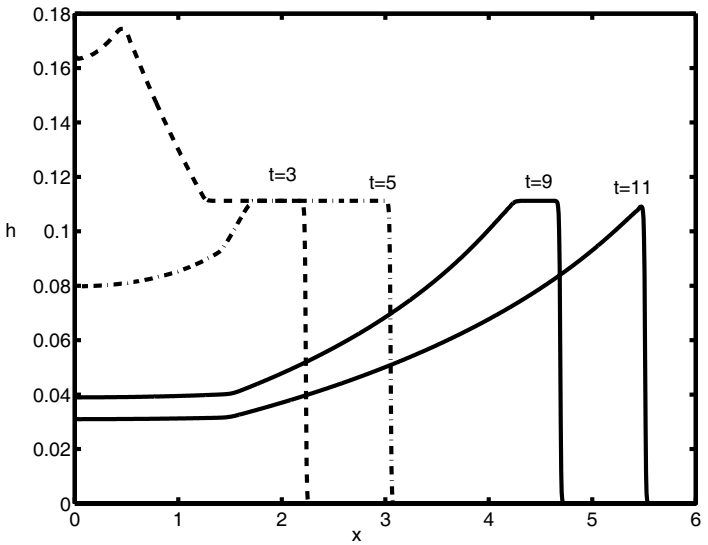


Figure 3: The evolution of the gravity current with $x_0 = 1, h_0 = 0.3$ and $u_0 = 0$.

In order to obtain numerical solutions to the weakly stratified equations we employed the SLIC method which is a conservative high-order TVD scheme [5]. Based on the MUSCL-Hancock approach, second-order accuracy is obtained by

considering a piecewise linear reconstruction of the cell-averaged approximations over computational cells of the spatial domain. A slope limiter is applied in order to obtain non-oscillatory results.

The cell-averaged approximate solution is updated at the subsequent time level by a finite-volume scheme. The numerical flux employed is the FORCE flux, which is given by the arithmetic mean between the Lax-Friedrichs flux and the two-step Lax-Wendroff flux. The resulting scheme is thus centred and as such does not require the information provided by the decomposition of the Jacobian of the flux vector into characteristic fields which is essential for upwind based methods.

Shock formation can be determined from the numerical solution by examining the solution for $h(x,t)$ as a function of x for a fixed value of t. This distribution reveals the structure of the gravity current at a particular time. In Figure 3 we present the evolution of the gravity current resulting from the release from rest of a fixed volume of fluid with $h_0 = 0.3$. As expected, due to the low value of h_0 the disturbance generated at the proximal end wall evolves into a long wave of depression on the back side of the head of the gravity current.

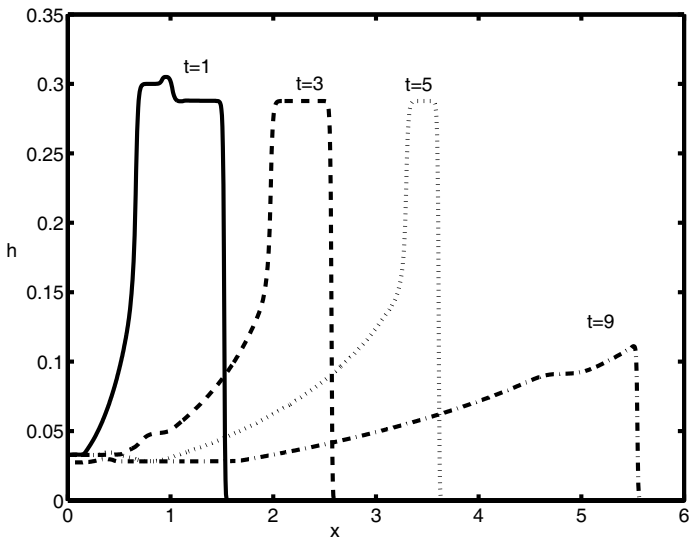


Figure 4: The evolution of the gravity current with $x_0 = 1, h_0 = 0.3$ and $u_0 = 0.5$.

The evolution presented in Figure 4 indicates that with the same initial depth ratio of $h_0 = 0.3$, an initial velocity of $u_0 = 0.5$ is sufficiently large to generate a gravity current exhibiting the formation of a rear shock. To illustrate the dependence of the generation of a rear shock on the initial velocity of the heavy fluid, in Figure 5 we display the structure of the gravity current corresponding to different values of u_0 at a fixed time. It can clearly be seen that as u_0 increases the back

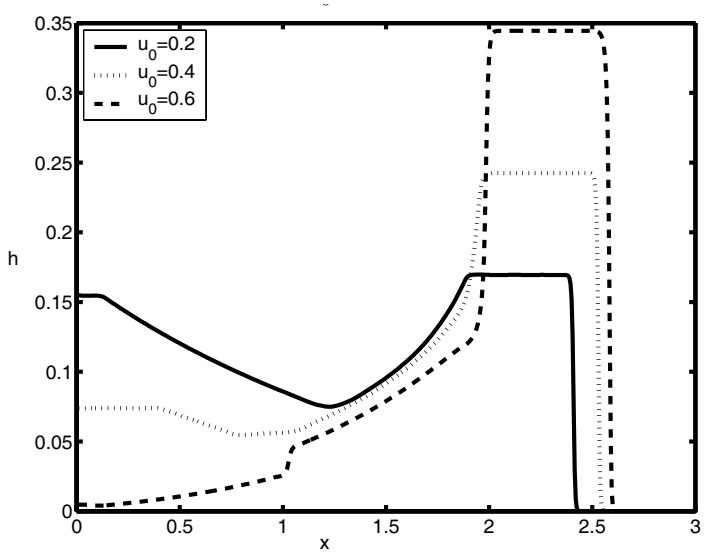


Figure 5: The structure of the gravity current with $x_0 = 1$ and $h_0 = 0.3$ at $t = 3$.

side of the head of the gravity current steepens. Our numerical experiments indicate that the critical initial velocity for the formation of the rear shock is in good agreement with the analytical prediction for various values of h_0.

5 Concluding remarks

Discussed in this paper are bottom gravity currents flowing on a flat bottom of a rectangular channel. In particular, the interest here was on the formation of a rear shock formed behind the head of the gravity current. Under conditions of weak stratification a simplified model has been constructed and is amenable to analytical treatment. A weakly nonlinear analysis was successful in predicting when a rear shock should form. These predictions were confirmed by extensive numerical experiments.

Acknowledgements

Financial support for this research was provided by the Natural Sciences and Engineering Research Council of Canada.

References

[1] Simpson, J.E., *Gravity Currents: In the Environment and the Laboratory*, 2nd Ed., Cambridge University Press, Cambridge, UK, 1997.



[2] Rottman, J.W., & Simpson, J.E., Gravity currents produced by instantaneous releases of a heavy fluid in a rectangular channel, *J. Fluid Mech.* **135**, pp. 95-110, 1983.
[3] D'Alessio, S.J.D., Moodie, T.B., Pascal, J.P., & Swaters, G.E., Gravity currents produced by sudden release of a fixed volume of heavy fluid, *Stud. Appl. Math.* **96**, pp. 359-385, 1996.
[4] Le Veque, R., *Numerical Methods for Conservation Laws*, Birkhäuser, Basel, Switzerland, 1992.
[5] Toro, E.F., *Riemann Solvers and Numerical Methods for Fluid Dynamics*, Springer, Berlin, Germany, 1999.



This page intentionally left blank

Nonlinear dynamics of Rossby waves in a western boundary current

L. J. Campbell
School of Mathematics and Statistics, Carleton University, Ottawa, Canada

Abstract

This paper examines the nonlinear dynamics of a Rossby wave propagating longitudinally in a north-south shear flow. The flow configuration is an idealized model for a western boundary current in an ocean basin. It is assumed that there is a critical layer in the flow, where the shear flow speed is the same as the wave phase speed. The nonlinear critical-layer evolution of the wave depends on the direction of propagation of the wave. Numerical simulations show that an eastward-propagating wave incident on the critical layer from the west is absorbed by the mean flow at early times. This is the same situation that is known to occur for small-amplitude waves, according to the linear theory. At later times, however, nonlinear waves may be reflected from the critical layer. In contrast, a westward-propagating wave incident on the critical layer from the east passes through largely unaffected. An approximate analytic solution of the linearized equations is also presented to give further insight into the evolution of the critical layer.
Keywords: critical layer, Rossby waves, nonlinear wave interactions, western boundary current, shear flow, numerical simulations.

1 Introduction

An idealized model for the dynamics of Rossby waves in a western boundary current in an ocean basin consists of a latitudinally-periodic Rossby wave propagating horizontally in the zonal direction in a north-south shear flow [6, 7, 8]. This paper examines the nonlinear interactions between the waves and the current in the vicinity of a critical layer. A critical layer is a region surrounding a longitude at which the shear flow velocity is equal to the phase speed of the wave. When the governing linearized inviscid equations are solved numerically or analytically it is seen that



WIT Transactions on Engineering Sciences, Vol 52, © 2006 WIT Press
www.witpress.com, ISSN 1743-3533 (on-line)
doi:10.2495/AFM06045

the behaviour of a small-amplitude wave incident on the critical layer depends on the direction of propagation of the wave. An eastward-propagating wave incident on the critical layer from the west is absorbed, *i.e.* its momentum is transferred to the mean flow, but a westward-propagating wave forced to the east of the critical layer passes through without attenuation [3, 7].

However, the fate of large-amplitude waves which are governed by nonlinear theory remains unclear. The question is whether a nonlinear wave incident on a critical layer in a north-south flow would be absorbed or transmitted as in the linear theory. Another possibility is that the wave would be reflected at the critical layer. This is the situation that occurs in the related problem in which a Rossby wave, periodic in the zonal direction, propagates southwards towards a critical latitude in a zonal shear flow. In that configuration, it is well-known that, according to the linear theory, waves incident on the critical layer are completely absorbed [5, 10]. Large-amplitude (nonlinear) waves are absorbed at the critical layer at early times; however, the nonlinear effects eventually become important and the critical layer then becomes a reflector of the incident waves [1, 9, 11].

In the present study, the governing nonlinear equations for a longitudinally-propagating Rossby wave in a north-south shear flow are solved numerically in order to determine whether the wave is absorbed, reflected or transmitted. Both eastward- and westward-propagating waves are considered. It is found that an eastward-propagating wave incident on the critical layer from the west is absorbed by the mean flow at early times, but at later times there is wave reflection. On the other hand, a westward-propagating wave incident on the critical layer from the east passes through unaffected; this is the same situation that occurs in the linear theory. An approximate analytic solution of the linearized equations is also presented.

2 Formulation

The governing equation in this study is the barotropic vorticity equation. It is written in terms of non-dimensional variables as

$$\nabla^2\Psi_t + \Psi_x\nabla^2\Psi_y - \Psi_y\nabla^2\Psi_x + \beta\Psi_x - Re^{-1}\nabla^4\Psi + B(x) = 0, \qquad (1)$$

where $\Psi(x, y, t)$ is the total streamfunction and the subscripts denote partial differentiation with respect to time t and the two space variables x (longitude) and y (latitude). The parameter Re is the Reynolds number and β is the non-dimensional gradient of planetary vorticity. The term $B(x)$ represents a body force such as that due to topography and is included in order that the basic flow quantities, which are functions of x, can satisfy the governing equation. The Laplacian operator in (1) is non-dimensional with the y-derivative in the operator being multiplied by a factor $\delta = L_x^2/L_y^2$, where L_x and L_y are typical length scales in the zonal and meridional directions respectively. The parameter δ is the square of the aspect ratio.

The streamfunction is written as

$$\Psi(x, y, t) = \bar{\psi}(x) + \varepsilon\psi(x, y, t). \qquad (2)$$

where $\bar{\psi}$ is the streamfunction of the meridional basic flow and ψ is the disturbance streamfunction. The basic flow is taken to be the initial y-independent flow. It is assumed that both $\bar{\psi}$ and ψ are $O(1)$, so that the parameter ε gives a measure of the magnitude of the perturbation relative to that of the basic flow. The basic velocity is related to the basic streamfunction by

$$\bar{v}(x) = \bar{\psi}'(x),$$

where the prime denotes differentiation with respect to x. In the rest of this paper, the body force term in (1) is set to $B(x) = -\beta\bar{v}(x)$, in order that the basic streamfunction $\bar{\psi}(x)$ satisfies (1).

The assumption (2) leads to the nonlinear equation

$$\left(\frac{\partial}{\partial t} + \bar{v}\frac{\partial}{\partial y}\right)\nabla^2\psi + \beta\psi_x - \bar{v}''\psi_y + \varepsilon(\psi_x\nabla^2\psi_y - \psi_y\nabla^2\psi_x) = 0. \quad (3)$$

If it is assumed that $\varepsilon \ll 1$, one is justified in neglecting the nonlinear terms in this equation. This gives

$$\left(\frac{\partial}{\partial t} + \bar{v}\frac{\partial}{\partial y}\right)\nabla^2\psi + \beta\psi_x - \bar{v}''\psi_y = 0. \quad (4)$$

By writing the disturbance streamfunction in the neutral mode form

$$\psi(x, y, t) = \mathrm{Re}\{\phi(x)e^{il(y-ct)}\}, \quad (5)$$

where l is the meridional wavenumber and c is the phase speed, the following amplitude equation is derived:

$$(\bar{v} - c)(\phi_{xx} - \delta l^2\phi) - \frac{i\beta}{l}\phi_x - \bar{v}''\phi = 0. \quad (6)$$

This equation is singular at any point $x = x_c$ where $\bar{v}(x) = c$. This is the critical line and the region surrounding it is the critical layer. Using the method of Frobenius and expanding about the point x_c, it can be shown that two linearly independent power series solutions of this equation are

$$\phi_a(x - x_c) = 1 + \frac{il\bar{v}_c''}{\beta}(x - x_c) + \ldots \quad (7)$$

and

$$\phi_b(x - x_c) = (x - x_c)^{1+i\gamma} + \frac{\bar{v}_c''}{2\bar{v}_c'}\frac{(2 - i\gamma(1 + i\gamma))}{2 + i\gamma}(x - x_c)^{2+i\gamma} + \ldots, \quad (8)$$

where $\gamma = \beta/\delta l\bar{v}_c'$ and the subscript c denotes evaluation of $\bar{v}$ and its derivatives at x_c. The solution ϕ_b is singular at the point $x = x_c$. East and west of the singular



point, ϕ_b can be written as

$$\phi_b^+(x - x_c) = (x - x_c)e^{i\gamma \log|x-x_c|} + \ldots, \tag{9}$$

and

$$\phi_b^-(x - x_c) = (x - x_c)e^{-|\gamma|\theta}e^{i\gamma \log|x-x_c|} + \ldots, \tag{10}$$

respectively, if, when $x < x_c$, the logarithm is defined to be

$$\log(x - x_c) = \log|x - x_c| + i\theta \ \mathrm{sgn}(\bar{v}_c^{'}), \tag{11}$$

with $\theta = -\pi$. Thus, the amplitude of the ϕ_b solution decreases by a factor of $e^{-|\gamma|\pi}$ as the wave crosses the critical line from west to east.

Using group velocity arguments, it can be shown [7] that the nonsingular solution ϕ_a corresponds to an westward-propagating wave. It has a long zonal wavelength and is non-divergent. The discontinuous solution ϕ_b corresponds to an eastward-propagating wave with short zonal wavelength and its momentum flux divergence is in general nonzero. Thus, the behaviour of the solution depends on whether the perturbation is forced to the west or east of the critical layer.

In the rest of this paper, the amplitude of the disturbance is assumed to be time-dependent. In section 3, linear time-dependent solutions are presented and we shall see that these solutions satisfy properties analogous to those of the corresponding steady solutions (7) and (8). The results of some nonlinear numerical simulations are presented in section 4.

3 Analytic solution of the linear time-dependent equation

Writing the disturbance streamfunction as

$$\psi(x, y, t) = \mathrm{Re}\{\phi(x, t)e^{ily}\} \tag{12}$$

in the linear equation (4) gives the amplitude equation

$$\left(\frac{\partial}{\partial t} + il\bar{v}\right)(\phi_{xx} - \delta l^2\phi) + \beta\phi_x - il\bar{v}^{''}\phi = 0. \tag{13}$$

The domain of definition of the solution is assumed to be semi-infinite in both time and space, *i.e.* $t \geq 0$ and either $-\infty < x \leq x_1$ or $x_1 \leq x < \infty$. At the forced boundary $x = x_1$, the perturbation streamfunction is set to

$$\psi(x_1, y, t) = \mathrm{Re}\{e^{il(y-ct)}\}, \tag{14}$$

which means that

$$\phi(x_1, t) = e^{-ilct}. \tag{15}$$

On defining the Laplace transform of $\phi(x, t)$ by

$$\tilde{\phi}(x, s) = \int_0^\infty \phi(x, t)e^{-st}dt \tag{16}$$

and taking the transform of each term in (13), one obtains

$$(s + il\bar{v})\,(\tilde{\phi}_{xx} - \delta l^2\tilde{\phi}) + \beta\tilde{\phi}_x - il\bar{v}''\tilde{\phi} = 0, \tag{17}$$

with the boundary condition

$$\tilde{\phi}(x_1, s) = \frac{1}{(s + ilc)}. \tag{18}$$

The solution of (17) is a linear combination of the power series $\phi_a(x - x_s)$ and $\phi_b(x - x_s)$, where x_s is the point where $\bar{v}(x) = -is/l$, and ϕ_a and ϕ_b are defined in (7) and (8) respectively. For the special case where the aspect ratio δ is zero and the basic velocity is $\bar{v}(x) = x$, the functions ϕ_a and ϕ_b are simply equal to the leading order terms in each of their respective series, *i.e.* $\phi_a = 1$ and $\phi_b = (x - x_s)^{1+i\gamma}$.

On applying the boundary condition and inverting the Laplace transform, ϕ is found to be

$$\phi(x,t) = \frac{1}{2\pi i}\int_{\alpha-i\infty}^{\alpha+i\infty} \frac{e^{st}}{(s + ilc)}\,\frac{a(s)\phi_a(x - x_s) + b(s)\phi_b(x - x_s)}{a(s)\phi_a(x_1 - x_s) + b(s)\phi_b(x_1 - x_s)}\,ds, \tag{19}$$

where the real constant α is chosen so that the contour of integration will lie to the right of all the singularities of the integrand. The functions $a(s)$ and $b(s)$ depend on the boundary conditions and determine the direction of propagation of the waves. For the case where $b(s) = 0$, the only singularity of the integrand is the pole at $s = -ilc$, so the integral is evaluated by a simple residue calculation and the solution is found to be

$$\phi(x,t) = \lim_{s\to -ilc}\left[e^{st}\,\frac{\phi_a(x - x_s)}{\phi_a(x_1 - x_s)}\right] = e^{-ilct}\,\frac{\phi_a(x - x_c)}{\phi_a(x_1 - x_c)}. \tag{20}$$

Thus, the solution in this case is simply the steady westward-propagating solution (7) multiplied by a periodic function of t. The amplitude of the wave is unaffected by an encounter with a critical layer, there is no $-\pi$ phase change, and the solution does not contribute to the nonlinear dynamics of the critical layer.

If $b(s) \neq 0$, then the integral is equal to the sum of the contributions from three singularities: the pole at $s = -ilc$, and the branch points at $s = -ilx$ and $s = -ilx_1$. If both $a(s)$ and $b(s)$ are non-zero, then the solution is the sum of a westward-propagating disturbance of the form (20) and a singular solution with eastward group velocity which is discontinuous at the critical layer. The former does not contribute to the nonlinear dynamics of the critical layer; it is the latter solution that is of interest. Let us therefore consider the case $a(s) = 0$, $b(s) \neq 0$. In that case, the contribution to the solution from the residue at the pole $s = -ilc$ is $e^{-ilct}\phi_b(x - x_c)\,\{\phi_b(x_1 - x_c)\}^{-1}$. This is added to the contributions from the branch points to give an approximate solution of (13). In this paper, we only present the solution in the outer region, *i.e.* away from the critical layer.

In the outer region where $|x - x_c|t \gg 1$, and for $t \gg 1$, ψ is found to leading order to be

$$\psi(x,y,t) \sim \frac{e^{ily}}{2}\left\{e^{-ilct}\phi_\infty(x) + e^{-ilxt}h_1(x)t^{-2-i\gamma} + h_2(x)t^{i\gamma} + O(t^{-1})\right\} + \text{c.c.}, \quad (21)$$

where

$$\phi_\infty(x) = \frac{\phi_b(x - x_c)}{\phi_b(x_1 - x_c)}, \quad (22)$$

$$h_1(x) \sim (x - x_c)^{-1}(x_1 - x)^{-1-i\gamma} \quad (23)$$

and

$$h_2(x) \sim (x_1 - x_c)^{-1}(x_1 - x)^{1+i\gamma}. \quad (24)$$

The outer solution breaks down as $x \to x_c$. In the critical layer where $|x - x_c|t \sim O(1)$, $t \gg 1$ and $|x - x_c| \ll 1$, an inner solution is derived and matched to the outer solution. The outer and inner solutions of the linear equation can be used as a starting point for deriving an approximate solution of the nonlinear equation (3) following the procedure used by [2]. The detailed derivation of the linear and nonlinear analytic solutions will be given in a subsequent paper.

4 Numerical solution of the nonlinear equation

The nonlinear equation (3) is solved numerically in a rectangular domain in the xy-plane. The numerical methods used are based on those of [4]. The numerical solution of the linear equation (4) was described in [3] for a case where the forcing took the form of a wave packet localized in the y-direction and comprising a continuous spectrum of meridional wavenumbers. In the present study, the forcing comprises a single meridional wavenumber. At the forced boundary $x = x_1$, the streamfunction is set to $\psi = \cos l(y - ct)$. As in [3], the basic velocity is set $\bar{v}(x) = \tanh x$. At the other boundary $x = x_2$, two types of boundary conditions are employed. In cases where the disturbance is transmitted through the critical layer, a radiation condition, which is described in [3], is used. In cases where there is a negligible amount of transmission, it suffices to set ψ to zero at the outflow boundary. Periodic boundary conditions are assumed at the southern and northern boundaries of the computational domain, which are at $y = -2\pi$ and $y = 2\pi$, respectively.

The parameters β, δ, l and c are chosen to satisfy the requirements that the disturbance be propagating without decay away from the forced boundary and that any part of the disturbance transmitted beyond the critical layer decays. If v_1 denotes the local value of $\bar{v}(x)$ near the forced boundary $x = x_1$ and v_2 denotes

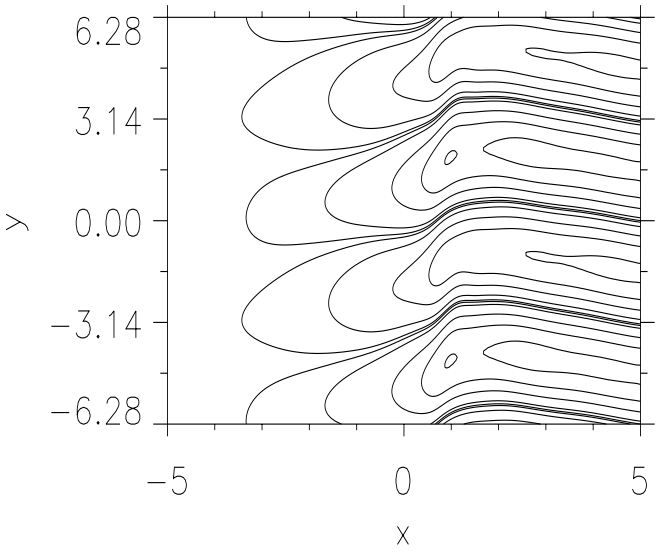


Figure 1: Nonlinear simulation of a westward-propagating Rossby wave forced to the east of its critical layer: Perturbation streamfunction ψ at $t = 200$.

the local value at the opposite boundary $x = x_2$, then these conditions lead to the inequality

$$\delta^{1/2} l^2 |v_1 - c| \leq \beta < 2\delta^{1/2} l^2 |v_2 - c|. \tag{25}$$

For the hyperbolic tangent profile used here, this means that when the forcing is imposed at the western boundary so that $v_1 = -1$ and $v_2 = 1$, then c must be negative, and when the forcing is imposed at the western boundary so that $v_1 = 1$ and $v_2 = -1$, then c must be positive. We therefore set $c = \tanh(-1)$ in the simulations with a eastward-propagating wave and $c = \tanh(1)$ in the simulations with a westward-propagating wave. We also set $\beta = 1$, $\delta = 1$ and $l = 1$.

According to the linear solution (20), a westward-propagating wave forced to the east of the critical layer passes through. Figure 1 shows the result of a nonlinear simulation for this configuration. The amplitude parameter ε has been set to 0.02. Contours of the perturbation streamfunction are shown at time $t = 200$. The critical line is located at $x = 1$. As in the linear case, the wave passes through the critical layer. With this choice of input parameters, the amplitude of the transmitted wave decays from the critical layer to the outflow boundary. Thus, although the radiation condition is linear, it continues to work up until about $t = 350$. Around this time, the wave amplitude becomes large near the outflow boundary and numerical instabilities develop. To continue the simulations beyond this time a nonlinear radiation condition would be needed.

Figure 2 shows the results of a nonlinear simulation in which the wave is forced at the western boundary of the domain. The critical line is located at $x = -1$. At

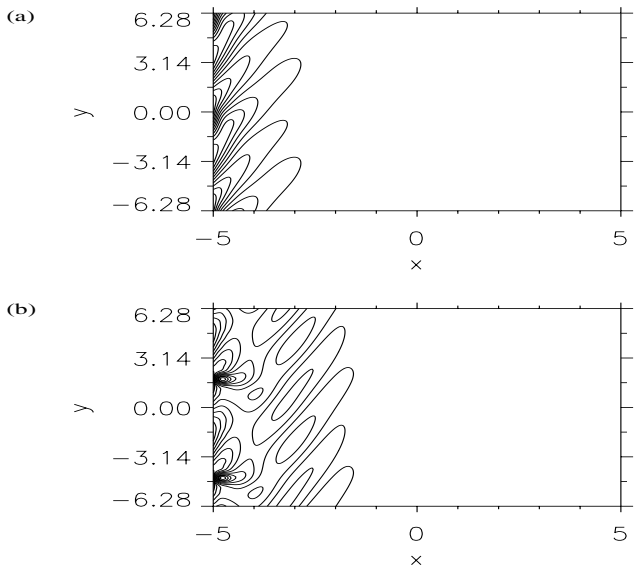


Figure 2: Nonlinear simulation of an eastward-propagating Rossby wave forced to the west of its critical layer: Perturbation streamfunction ψ at (a) $t = 20$, (b) $t = 200$.

early time (Figure 2(a)) the wave is completely absorbed at the critical layer, as predicted by the linear solution. Continuing the simulation to $t = 200$ (Figure 2(b)), we see evidence of a reflected wave near the forced boundary.

We can verify that wave reflection is indeed taking place in Figure 2(b) by evaluating the discontinuity across the critical layer of the meridional average of the zonal momentum flux. This is defined as $F(x,t) = (\overline{\psi_x \psi_y})$, where the overbar denotes an average taken over a meridional wavelength $2\pi/l$. The difference $[F]$ in this quantity between two points on either side of the critical layer is analogous to the "Reynolds stress jump" in the more familiar case of southward-propagating waves in a zonal shear flow. The evolution of $[F]$ with time is shown in Figure 3. Negative values correspond to time regimes in which the waves are being absorbed, while zero and positive values indicate critical layer reflection. The graph shows that the critical layer alternates between these states.

5 Conclusions

This paper discussed the critical-layer dynamics of a Rossby wave propagating longitudinally in a north-south shear flow. An approximate solution of the governing linearized equation was presented. Numerical solutions of the governing nonlinear equation were described. These solutions show that an eastward-propagating wave incident on the critical layer from the west is absorbed by the mean flow at

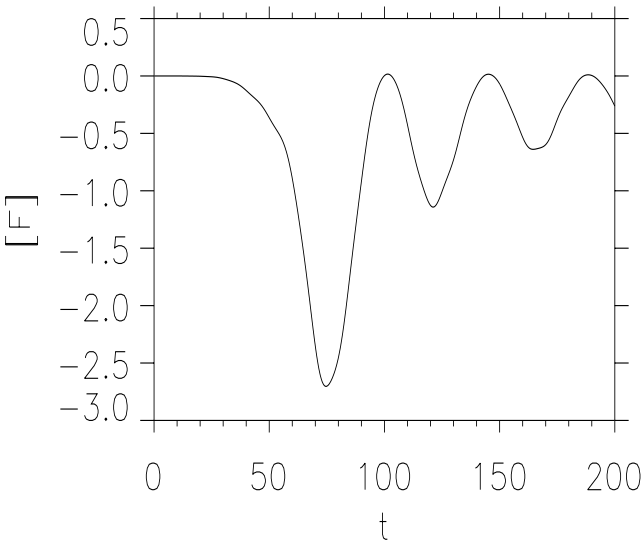


Figure 3: Nonlinear simulation of an eastward-propagating Rossby wave forced to the west of its critical layer: Momentum flux discontinuity $[F]$ plotted as a function of t.

early times, but at later time the wave may be reflected from the critical layer. On the other hand, a westward-propagating wave incident on the critical layer from the east passes through the critical layer.

References

[1] Béland, M., Numerical study of the nonlinear Rossby wave critical level development in a barotropic zonal flow, *J. Atmos. Sci.*, **33** pp. 2066–2078, 1976.

[2] Campbell, L.J., Wave–mean-flow interactions in a forced Rossby wave packet critical layer, *Stud. Appl. Math*, **112**, pp. 39–85, 2004.

[3] Campbell, L.J. & Maslowe, S.A., Forced Rossby wave packets in barotropic shear flows with critical layers, *Dyn. Atmos. Oceans*, **28**, pp. 9–37, 1998.

[4] Campbell, L.J. & Maslowe, S.A., A numerical simulation of the nonlinear critical layer evolution of a forced Rossby wave packet in a zonal shear flow, *Math. Comp. in Simulation* **55**, pp. 365–375, 2001.

[5] Dickinson, R.E., Development of a Rossby wave critical level, *J. Atmos. Sci.*, **27**, pp. 627–633, 1970.

[6] Fantini, M. & Tung, K.K., On radiating waves generated from barotropic instability of a western boundary current, *J. Phys. Oceanography*, **17**, pp. 1304–1308, 1979.



[7] Geisler, J.E. & Dickinson, R.E., Critical level absorption of barotropic Rossby waves in a north-south flow, *J. Geophys. Res.*, **80**, pp. 3805–3811, 1975.
[8] Ierley, G.R., Young, W.R., Viscous instabilities in the western boundary layer, *J. Phys. Oceanography*, **21**, pp. 1323–1332, 1991.
[9] Stewartson, K., The evolution of the critical layer of a Rossby wave, *Geophys. Astrophys. Fluid Dyn.*, **9**, pp. 185–200, 1978.
[10] Warn, T. & Warn, H., On the development of a Rossby wave critical level, *J. Atmos. Sci.*, **33**, pp. 2021–2024, 1976.
[11] Warn, T. & Warn, H., The evolution of a nonlinear critical level, *Stud. Appl. Math.*, **59**, pp. 37–71, 1978.



Section 10
Industrial applications

This page intentionally left blank

Assessment of aerodynamic noise in an industrial ventilation system

A. M. Martins & A. C. Mendes
Universidade da Beira Interior,
Laboratory of Fluid Mechanics and Turbomachinery, Covilhã, Portugal

Abstract

This paper deals with the assessment of aerodynamic noise level generated by an industrial ventilation system. The system incorporates an axial flow fan operating with airfoil rotor blades. Measurements were performed using a modular digital sonometer of high precision, equipped with a microphone and a frequency analyser. The procedure that was followed enabled us to account for both the global level and the equivalent frequency level of noise, in the intermediate range of audible frequencies, using a filter of 1/3 of the octave.
Keywords: aerodynamic noise, axial flow fans, industrial ventilation systems.

1 Introduction

Sound is a form of energy associated with the vibration of material particles in a medium. The displacements of the oscillating particles are transferred throughout the matter as acoustic energy, which travels under the form of a sound wave. Acoustics is the science that studies the generation and transmission of such sound waves. It concerns not only the phenomenon that occurs in air, which is audible to humans, but also other phenomena governed by the same basic laws. Sound may as well be transmitted through solids, liquids and gases. In all cases we are mainly concerned with the study of a wave motion which is, however, very distinct from the motion of the individual particles in the medium. Sound is effectively a mechanical wave motion whose propagation depends on the physical properties of matter. To be transmitted, sound relies on the elasticity and inertia of the material in question [1].

Noise, on the other hand, is a sonorous stimulus that is unpleasant to our hearing and without significant information to its receptor. It can become nevertheless an issue of primary importance in what refers to human health and



WIT Transactions on Engineering Sciences, Vol 52, © 2006 WIT Press
www.witpress.com, ISSN 1743-3533 (on-line)
doi:10.2495/AFM06046

environmental quality. Noise will be caused by a number of factors, for instance by friction between mechanical components, like in bearings and gears, by the vibration induced by floating masses in internal combustion engines, or even by cavitation induced vibrations in hydraulic pumps and turbines. Eventually, the noise arising in industrial equipment will be caused by the same factors that contribute to its loss of efficiency. Therefore, it can be expected that a gain in the performance of any machine will result in a lower level of noise in the installation [2].

In the specific case of fans and compressors, aerodynamic instabilities play a decisive role in the global noise level of the system. Aerodynamic noise, as is usually called, is mainly caused by separation of boundary layer flow at the upper surface of the rotor blades [3]. The noise level can be significant, especially in axial-flow compressors operating close to stall conditions. Another important cause of aerodynamic noise in axial machines is vortex shedding from the blades trailing edge. The noise frequency depends, in this case, essentially upon the blade profile and velocity. As this velocity varies along the blade, the noise generated by the interaction between the rotor and working fluid covers a wide range of frequencies. In the case of rotors presenting a great number of blades, another relevant source of noise appears to be the interaction between the wake of one blade with the adjacent one. These interactions become more important as the rotational speed of the machine increases.

An inadequate tip clearance between the rotor of an axial-flow machine and its casing may also be at the origin of noise production and loss of efficiency. This is essentially associated with undesired secondary flow effects [4]. Moreover, turbulent flow is also an important cause of noise, in particular for airflow velocities higher than 5m/s.

Finally, the stability of the entire ventilation system is crucial in what concerns noise level. Vibrations induced by the rotor upon its casing and adjacent ducts may become intense, especially near structural resonance.

In order to measure the noise that is generated by ventilation systems it is often used a sonometer of high precision. In a first step the equivalent continuous sound level of the installation is usually assessed. However, this parameter in itself is not a sufficient indication of what is felt by the human hearing. In reality we are more sensitive to sound frequencies between 500 Hz and 4 KHz. On the other hand, sound frequencies lower than 20 Hz or higher than 20 KHz become unperceptive. Consequently, it is also necessary to perform measurements of the equivalent sound level in frequency. For that purpose sound meters usually include a frequency analysis module, with a filter of an octave or $^1/_3$ of the octave band, for the frequencies belonging to the audible frequency bandwidth. Measurements requiring a good precision must inclusively be conducted in an anechoic test facility [5].

The present work deals with the assessment of aerodynamic noise level generated by an industrial fan equipped with airfoil rotor blades. Measurements were performed using a modular digital sonometer of high precision. The procedure followed enables us to present herein the equivalent continuous sound



level and the equivalent frequency level of noise generated by the fan, in the intermediate range of audible frequencies, using a filter of 1/3 of the octave.

2 Experimental apparatus

An industrial fan currently under investigation at the Turbomachinery Laboratory of UBI [6] has been tested in the axial-flow test bench (Fig. 1). The experimental apparatus consists of a tubular duct that is fully instrumented in view of making the performance analysis of axial-flow fans. Below we describe this experimental facility.

2.1 Test bench

The main body of the test facility is a four-element steel duct having a circular cross-section. These four elements are assembled together with the casing of the fan to be tested. The location of the machine is directly related to obtaining uniform flow conditions at the inlet of the rotor. A valve placed at the outlet section of the duct, downstream of the fan, controls the flow rate. The velocity of the flow is measured by a telescopic Prandtl tube, positioned upstream of the rotor. The data acquired by the probe covers the width of the bench cross-section. The axial mean velocity of the flow is assessed by another Prandtl probe, which in turn is placed downstream of the machine. The head rise of the working fluid across the rotor is measured at eight static pressure inlets, four of these before and four after the fan rotor. Static and total pressure heads are red in mm of alcohol, by means of a U-tube panel having a variable inclination. The rotational speed of the rotor is measured with the help of a tachometer. A digital thermometer and a barometer monitor the atmospheric temperature and pressure.

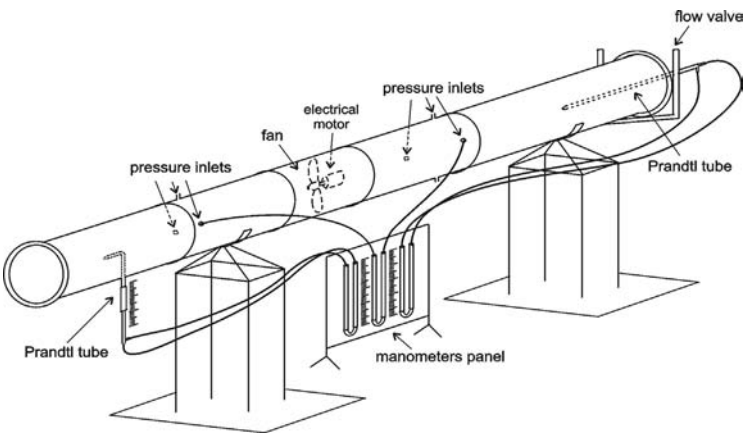


Figure 1: Axial-flow fans test bench.

2.2 Axial-flow fan

The machine to be tested is an axial-flow fan whose rotor is driven by an electrical motor. The machine is mounted in its circular casing and later on assembled to the test bench (see Fig. 2).

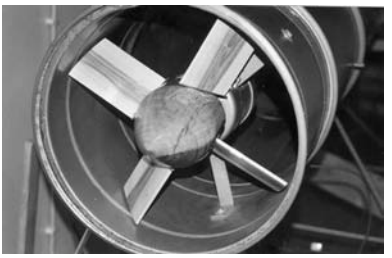


Figure 2: Axial-flow fan under investigation.

In order to obtain a flexible installation, the hub is able to accommodate different rotor blades with a pre-defined geometry. Two sets of blades have been produced, all manufactured in wood. The axial-flow fan that makes the object of the present study was equipped with four blades especially adapted to working at low Reynolds Number. In nominal conditions for this machine Re is of the order of 5×10^4. Tab. 1 summarises the characteristics of the fan rotor. The angle of attack of the blade wing sections may be conveniently controlled, in order to get the best flow entry at the leading edge. On the other hand, the hub was designed in such a way that it offsets the electrical motor and, hence, reduces the overall resistance associated with the central core of the machine.

Table 1: Geometrical characteristics of the fan rotor.

Rotor diameter (D)	295 [mm]
Hub diameter (d_c)	101,6 [mm]
Number of blades (n)	4
Blade length (l)	98 [mm]
Blade chord (c)	70 [mm]
Pitch at mean radius (t)	193 [mm]
Pitch-chord ratio at mean radius $\left(t/c\right)$	2,76
Maximal blade thickness	9,35% of the chord
X-coordinate of maximal thickness point	26,3% of the chord
Maximal y-coordinate of the camber line	3% of the chord
x-coordinate of inflexion point at the upper surface	39,8% of the chord
Camber angle at leading edge (θ_1)	13 [º]
Camber angle at the trailing edge (θ_2)	8 [º]
Camber line angle (θ)	21 [º]

In order to conduct the performance analysis of the fan, the machine was firstly inserted in the test bench and driven at a rotor speed of N=1466 *rpm*. The stagger angle of the blades was selected at $\lambda = 48^{\circ}$. Total head across the rotor was then measured for different working conditions, as the flow rate is varied by means of the valve at the end of the experimental facility. Fig. 3 shows the evolution of the internal efficiency η of the fan, i.e. the ratio between the hydraulic power and the power available at the shaft of the electric motor. The fan efficiency is here represented as a function of flow rate coefficient $\phi = Q/ND^3$.

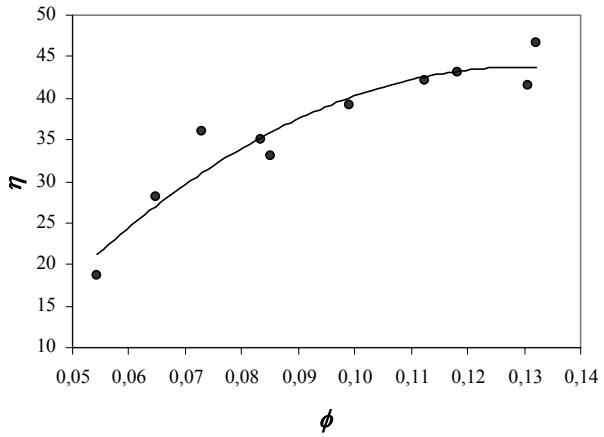


Figure 3: Internal efficiency versus flow-rate coefficient.

The analysis of the curve shows that nominal conditions correspond to the highest values of flow rate, of the order of Q=510*l/s*, for which the fan efficiency is about $\eta = 42\%$. It is expected that noise level will be less significant under these working conditions.

3 Noise assessment

In this section we present and discuss the noise measurements that were carried out while the fan was being tested in the ventilation bench. The noise in the ventilation system was measured by means of a modular digital sonometer of high precision, model 2231, produced by Brüel and Kjær [7]. This device is equipped with a microphone (model 4155) and a module for frequency analysis (model BZ 7103). We may print the results of the measurements directly on paper by using the printer of the equipment (model 2318/ZI 0054).

The sonometer was placed at the rear end of the test facility, facing the back of the rotor, as is shown in Fig. 4. Two series of measurements were conducted. Firstly the global level of noise was assessed, while running the fan for different

flow-rate conditions. After this the level of noise in frequency was assessed at maximal flow-rate conditions, i.e. by keeping the valve at the end of the bench 100% open. All the measurements were recorded for a rotating speed corresponding to nominal working conditions $(N = 1466rpm)$ and blades stagger angle $\lambda = 48°$.

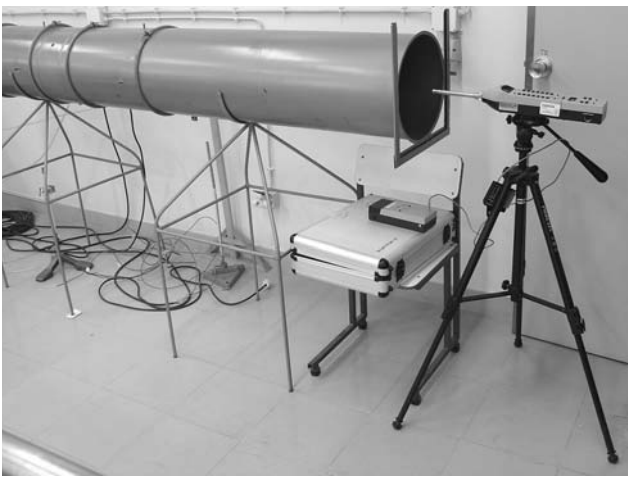


Figure 4: Equipment for noise assessment.

Table 2: Sonometer set-up parameters.

Module #:	5 (BZ 7103)
Mic.Corr:	+ 0.0 dB
S.I.Corr:	"FRONTAL"
Time W. :	"FAST"
Freq.W. :	"A"
B.W. :	1/3 Oct.
Time/Cha:	Variable
Pr.No.Sp:	1
RG. (dB):	10.0 - 83.0

3.1 Sonometer set-up

The Table (Tab. 2) shows the set-up parameters that were selected for the sonometer before starting the measurements. *S.I.Corr*. is associated with the choice of the microphone and its orientation, with respect to the source of noise. This parameter was selected as *frontal* in accordance with CEI Standards, as the microphone is directed towards the fan rotor. Parameter *Time W* corresponds to time weighting; it was prescribed as *fast*, because we are confronted with oscillating noise, which is typical for industrial equipment. *Freq W* is the frequency weighting parameter, here defined as *A*, according to CEI 651

Standard. *B.W.* parameter determines the frequency step at which noise levels are recorded; in the present case we have assumed $1/3$ of the octave, for the central frequencies of the audible range (20 Hz to 20 kHz). *Time/Cha* parameter, defined internally by the sonometer as *variable*, is the time interval for data acquisition in each of the considered frequencies. Finally *RG* (in dB) defines the range of values for $L_{eq,f}$, i.e. the minimal and maximal values of the sound power level.

3.2 Equivalent continuous sound level

The equivalent continuous sound level (L_{eq}) is the temporal mean of sound pressure level (*SPL*), taken during the time interval *T*:

$$L_{eq,T} = 10\log_{10}\frac{1}{T}\int_0^T \left(\frac{p(t)}{p_r}\right)^2 dt \tag{1}$$

Here p_r is the sound pressure of reference $(20\mu Pa)$, $p(t)$ is the sound pressure measured as a function of time, and T is the period of measurement. Fig. 5 presents the values of L_{eq} that have been recorded placing the microphone at the end of the ventilation duct. They are represented as a function of ϕ. These values were obtained for the fan nominal working speed, by varying the flow-rate valve between 50% and 100% of the duct opening, and taking $T = 30s$.

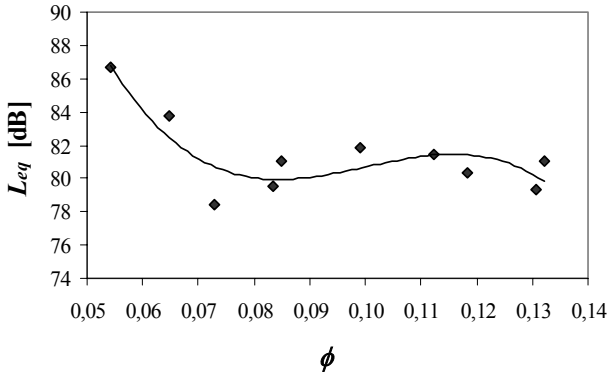


Figure 5: Equivalent continuous sound level as a function of flow-rate coefficient.

As we can observe, the range of the fan nominal working conditions coincides with the minimum values of L_{eq}. On the other hand, for reduced values of flow-rate the noise level increases exponentially. This corresponds in fact to a recognizable zone of instability for this type of machine.

3.3 Equivalent sound level at frequency f

Another important parameter in this context is the equivalent sound level at frequency f $\left(L_{eq,f}\right)$. This parameter represents the mean value of the sound pressure level at each of the sampling rate frequencies, which are the central frequencies of the standard $1/3$ octave band. Such a parameter is important for the identification of frequency bands for which the sound pressure level is higher than the equivalent continuous sound level.

In this series of tests the sonometer was placed once again at the outlet of the test bench, facing the rear of the fan. $L_{eq,f}$ was then recorded for the central frequencies of $1/3$-octave of the audible spectrum, between $20Hz$ and $20kHz$. Tab. 3 shows the values that were printed by the frequency analyser of the sonometer.

Table 3: Equivalent sound level at frequency f, for $\lambda = 48º$ and N=1466 *rpm.*

Frequency [Hz]	$L_{eq,f}$ **[dB]**	**Frequência [Hz]**	$L_{eq,f}$ **[dB]**
20	50,0±0,1	800	75,8±0,1
25	51,8±0,1	1000	75,3±0,1
31,5	54,4±0,1	1250	74,8±0,1
40	56,3±0,1	1600	74,1±0,1
50	58,7±0,1	2000	72,4±0,1
63	60,2±0,1	2500	70,7±0,1
80	63,7±0,1	3150	69,3±0,1
100	66,9±0,1	4000	67,2±0,1
125	69,3±0,1	5000	64,4±0,1
160	71,6±0,1	6300	62,0±0,1
200	72,7±0,1	8000	58,2±0,1
250	74,8±0,1	10000	55,2±0,1
315	74,9±0,1	12500	51,7±0,1
400	75,4±0,1	16000	47,8±0,1
500	75,0±0,1	20000	45,6±0,1
630	75,8±0,1		

As it can be observed for this range of frequencies the level of noise in the installation varies between $45{,}6dB$ and $75{,}8dB$. Moreover, the maximal values appear to occur in the frequency range f=200*Hz*–2*kHz*. We may notice that the sound level presents a smooth evolution in the entire range of the audible frequencies.

4 Conclusions

Most of the aerodynamic noise that is generated by industrial axial-flow fans is propagated to the environment via the inlet and outlet ends of the ventilation system. In reality, less than 5% of this noise is propagated directly through the walls of the ventilation duct. On the other hand, noise transmission along the ventilation ducts is quite efficient, unless appropriate noise dissipaters are used. The design of such devices, however, must take into consideration that no significant head losses are to be introduced in the system.

One way to meet this purpose is to use noise absorbent materials to isolate the duct and overall system housing. It is an expensive technique that gains importance nowadays, especially in large factories, where the level of noise is sometimes so high that any small reduction is important, in terms of human comfort. This solution is equally applicable in auditoriums and public theatres, where noise should be unperceptive and a constant ventilation of the space is nevertheless indispensable. In the case of axial machines this technique is particularly useful to mitigate noise at frequencies above 500 Hz [8].

By comparing our results with other results published for industrial axial-flow fans [9], we may conclude that they are of the same order of magnitude of those obtained for fans with similar characteristics, at least in what concerns the equivalent continuous sound level. The frequency analysis of sound is, however, of fundamental importance when we wish to reduce noise levels that were not detected in measurements of equivalent continuous sound level. For the central frequencies of $1/3$-octave of the audible spectrum, the level of noise in our installation varied between $45{,}6dB$ and $75{,}8dB$, with its maximal values in the frequency range f=$200Hz$–$2kHz$. We have also noticed that the sound level presents a smooth evolution in the entire range of the audible frequencies.

Another important source of noise could be the structural vibration that is induced by the fan on the ventilation system, particularly if near resonance. The ducts should be well fixed and the use of appropriate supporting elements, capable of damping these induced vibrations, should be considered.

Acknowledgements

The present work was carried out at the Laboratory of Fluid Mechanics and Turbomachinery of Universidade da Beira Interior, in Portugal. The authors are indebted to the Aerospace Sciences Department of UBI, for the use of their equipment of noise measurement.

References

[1] Pierce, A.D., Acoustics - An Introduction to Its Physical Principles and Applications, McGraw-Hill Book Co., New York, 1981.

[2] Envia, E., Fan Noise Reduction – An Overview, AIAA–2001-0661, Glenn Research Center, Cleveland, 2001.



[3] Hay, N., Mather, J. & Metcalfe, R., Fan Blade Selection for Low Noise, Proc. Seminar of Fluid Machinery Committee, pp. 51-57, Beccles, 1987.
[4] Neuhaus, L. & Neise, W., Active Flow Control to Reduce the Tip Clearence Noise and Improve the Aerodynamic Performance of Axial Turbomachines, Proc. Fan Noise Int. Symposium, 8 pp., Senlis, 2003.
[5] Jansson, D., Mathew, J., Hubner, P., Sheplak, M. & Cattafesta, L., Design and Validation of an Aeroacoustic Anechoic Test Facility, Proc. 8th AIAA/CEAS Aeroacoustics Conference, pp. 1-10, Breckenridge, 2002.
[6] Mendes, A.C., Martins, A.M., Marques, B.T. & Pascoa, J.C., Design and Performance Analysis of a Rotor for an Industrial Axial Flow Fan (in Portuguese), Proc. VI Congresso Ibero-Americano de Engenharia Mecânica, Vol. II, pp. 1531-1536, ed. A. M. Dias, Coimbra, 2003.
[7] Brüel & Kjær, Modular Precision Sound Level Meter plus Integrating SLM Application Module, Instruction Manual (2231 + BZ 71103), Nærum, Denmark, 1987.
[8] Osborne, W., The Selection and Use of Fans, Engineering Design Guides 33, pp. 1-17, Oxford, 1980.
[9] Soler & Palau, Industrial Catalog, Spain, 2001.



Airflow modeling analysis of the Athens airport train station

M. Gr. Vrachopoulos[1], F.K. Dimokritou[2], A.E. Filios[3] & A. Fatsis[1]
[1]*Technological University of Chalkis, Department of Mechanical Engineering, Greece*
[2]*Harvard University, Environmental Science and Engineering, USA*
[3]*ASPAITE University, Department of Mechanical Engineering, Greece*

Abstract

The present work aims to investigate the maximum CO distribution in the Athens-Greece airport train station platform for long-term exposure. A model based on the numerical solution of the three-dimensional flow field of the Athens-Greece airport train station was developed for this reason The work was performed using the CFD package called *FLOVENT*® V3.2.

The initial study of the CO level at the train station was performed without mechanical ventilation at the train station platform. Three different cases were examined by varying the wind magnitude and direction. Subsequently, four extra scenarios were examined with and without mechanical ventilation. The results obtained from the scenario with mechanical ventilation were compared to the ones from the scenario without mechanical ventilation. In all the above cases, the CO emissions from the vehicles in the two nearby highways were also taken into account. It is concluded that the maximum CO level in the case with mechanical ventilation is higher than in the case without. This is due to recirculation zones that create locally high levels of CO in the platform area. On the other hand, the average level of CO is lower at the platform with the ventilation on.
Keywords: emissions level, mechanical ventilation, numerical prediction.

1 Introduction

A study undertaken to investigate the CO levels in the Athens-Greece Airport train station platform is presented in the present article. Several external wind conditions will be studied and these will be compared to cases with mechanical


WIT Transactions on Engineering Sciences, Vol 52, © 2006 WIT Press
www.witpress.com, ISSN 1743-3533 (on-line)
doi:10.2495/AFM06047

ventilation at the train station platform. The work was performed using the Computational Fluid Dynamics tool called FLO*VENT*® V3.2.

The primary objective of the study is to determine the CO levels on the train station platform under different external wind conditions. The CO level should not exceed 25 ppm for long term exposure (i.e. 8 hrs), per World Health Organization Recommendations, [1].

2 Model description and results

Airflow and heat transfer within a fluid are governed by the principles of conservation of mass, momentum and thermal energy. These conservation laws may be expressed in terms of partial differential equations, the solution of which forms the basis of computational fluid dynamics (CFD).

The finite volume based approach was used, requiring the region modelled to be sub-divided into a number of small volumes or grid cells. During the program solution, the developed CFD model integrates the relevant differential conservation equations [2] over each computational grid cell, assembling a set of algebraic equations which relate the value of the variable in a cell to the value in adjacent cells. Since the equations display strong coupling (variables are dependant upon surrounding values and other variables) the solution is carried out iteratively.

2.1 Baseline cases

2.1.1 Model assumptions

The following assumptions were done in the present study:

- The wind speed is 15 m/s from the North direction. A velocity profile was applied at the North face of the solution domain, which varied from 1 m/s at ground to 15 m/s at 10 m. This is based upon local meteorological data. Additional Iterations were performed with different wind speeds and directions. See Table 1.
- Ambient temperature is 32 C.
- Total CO release rate is 1.9E-3 kg/s.
- 400 cars are releasing CO at a rate 2.61g/mile.
- The CO source was uniformly distributed along the roadways.
- Small items, which do not affect the general airflow patterns, were not included in the model.
- Thermal loading from lights, people, trains, etc, were considered insignificant and were not included.
- The CFD solution domain size is 350m x 350m x 50m with 801,248 grid cells. The maximum aspect ration is 15.6.
- The model was solved on a system with dual 2.4 GHz CPUs and 2.0 G RAM. The model solved in approximately 550 iterations and in 5.1 hours.

2.1.2 Model geometry

The model geometry and boundary conditions are shown in the following figure.

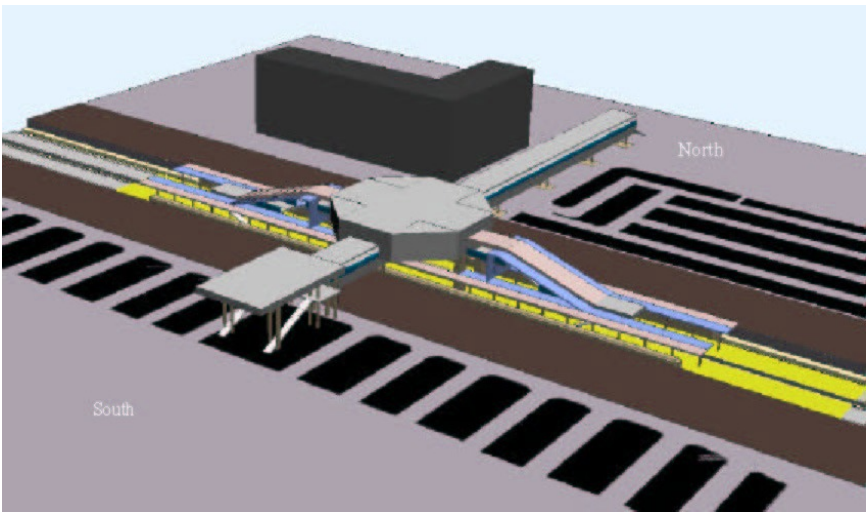


Figure 1: Isometric view of the Athens-Greece train station (viewing in the North West direction).

2.1.3 Baseline results

The CO levels along the train platform are well below the limit of 25 ppm. The maximum level in the platform area is 0.5 ppm. The following figures show the airflow patterns around the train station and CO level plots with an external wind speed of 15 m/s from the North.

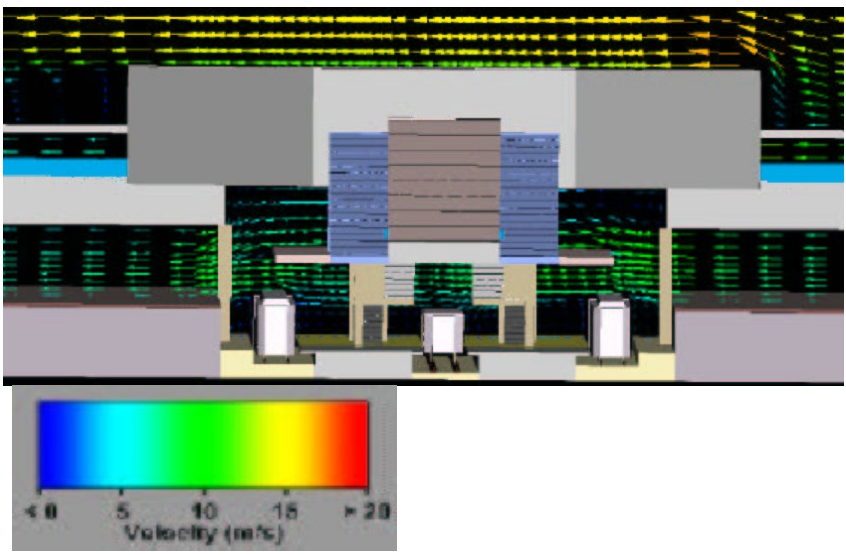


Figure 2: Airflow velocity plot through the center of the building (viewing in the West direction).

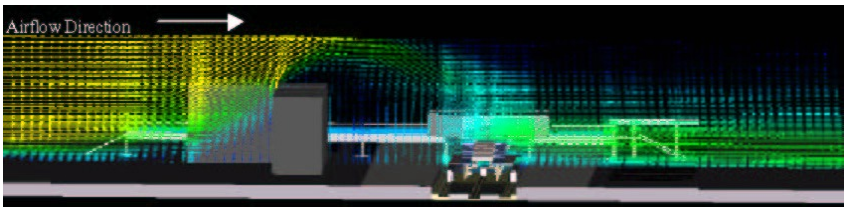


Figure 3: Airflow velocity plot across the Hotel (viewing in the East direction).

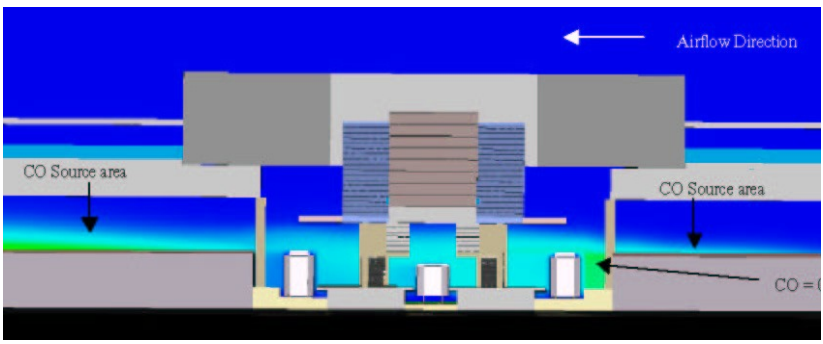


Figure 4: CO plot through the center of the building showing the platform area. The maximum platform CO level is 0.2 ppm.

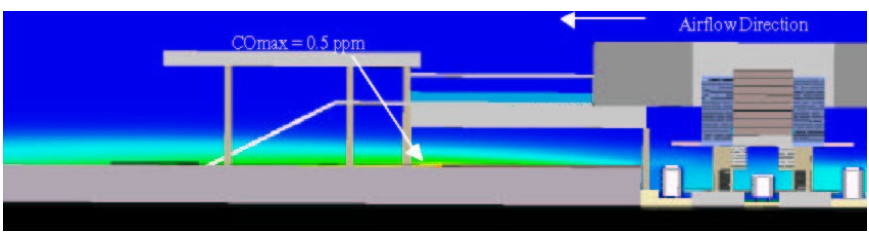


Figure 5: CO plot through the center of the building. The maximum CO level is 0.5 ppm along the ground below the Southern walkway.

2.1.4 Baseline case with different external conditions

Three additional Iterations were studied and compared to the Baseline results to determine the affect on the CO levels at the train station platform. The results are summarized in the following Table.

In all cases analyzed, the maximum CO levels are outside of the train platform area and are well below the limit of 25 ppm. The location of the maximum CO varies depending upon the wind direction. The CO levels along

the train platform are, also, well below the limit (more than 5 times lower than the limit of 25 ppm).

Table 1: Summary of CO levels with different wind conditions.

Case	**Summary of Results**		*COmax (ppm)*
		COmax (ppm)	***above the platform***
Baseline	15 m/s North direction	0.5	0.2
Iteration 1	15 m/s West direction	1.1	0.15
Iteration 2	1 m/s West direction	16.5	2.2
Iteration 3	1 m/s North direction	7.9	2.8

The following CO plots show the results of the Baseline and Iteration 1–3. The plots are 2 m above the train station platform.

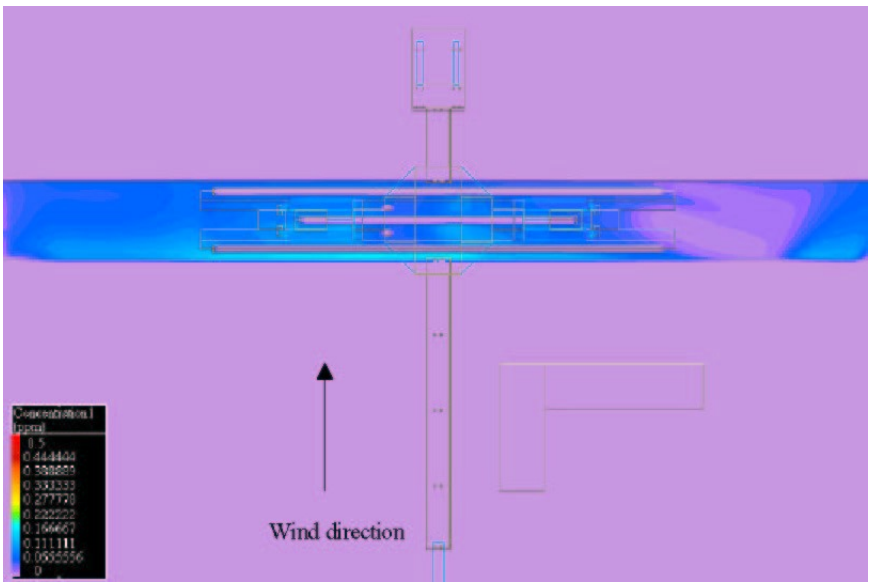


Figure 6: CO plot at 2 m height from the platform. North wind direction at 15 m/s. The maximum CO level on this plane is 0.2 ppm.

2.2 Mechanical venting case

2.2.1 Model assumptions

- The wind speed is 1 m/s from the North direction. A velocity profile was applied at the North face of the solution domain, which varied from 0.1 m/s at ground to 1 m/s at 10 m.
- Ambient temperature is 32 ^{o}C.
- Total CO release rate is 1.9E-3 kg/s.

- 400 cars are releasing CO at a rate 2.61 g/mile.
- The CO source was uniformly distributed along the roadways.
- Small items, which do not affect the general airflow patterns, were not included in the model.
- Thermal loading from lights, people, trains, etc, were considered insignificant and were not included.
- The CFD solution domain size is 350 m x 350 m x 50 m with 920,856 grid cells. The maximum aspect ration is 15.6.

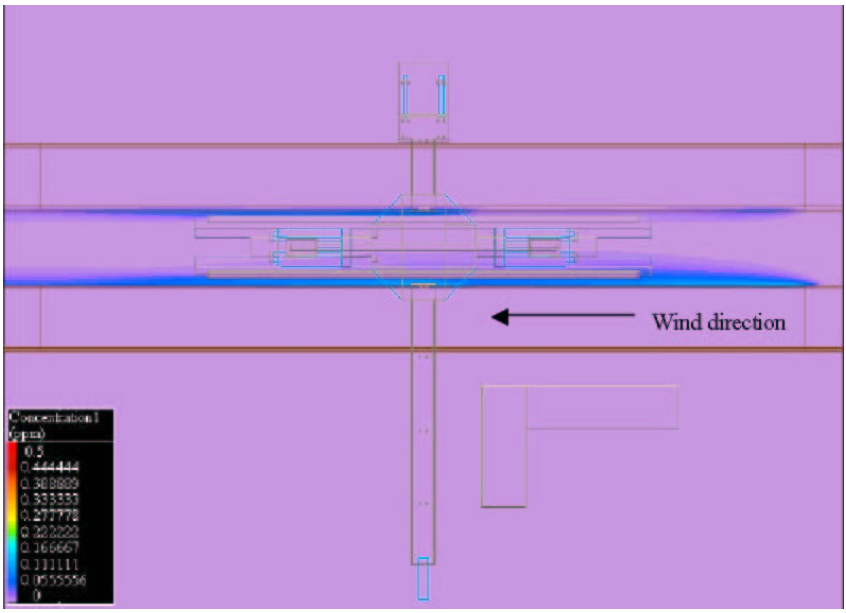


Figure 7: Iteration 1 - CO plot at 2 m height from the platform. West wind direction at 15 m/s. The maximum CO level on this plane is 0.15 ppm.

The model was solved on a system with dual 2.4 GHz CPUs and 2.0 G RAM. The model solved in approximately 750 iterations and in 8.2 hours.

2.2.2 Model geometry

The model geometry and Autocad drawings for the Mechanical Venting Case are shown in the figure 10.

Figures 11 and 12 compare the CO distribution along the train station platform with the same wind conditions with the venting on and off. The CO plot with venting on shows less dispersion of CO along the platform. There are regions where the CO levels are approximately 1.5 ppm without the venting and these are below 1 ppm when the venting is on. The following table shows the maximum CO levels for all cases analyzed.

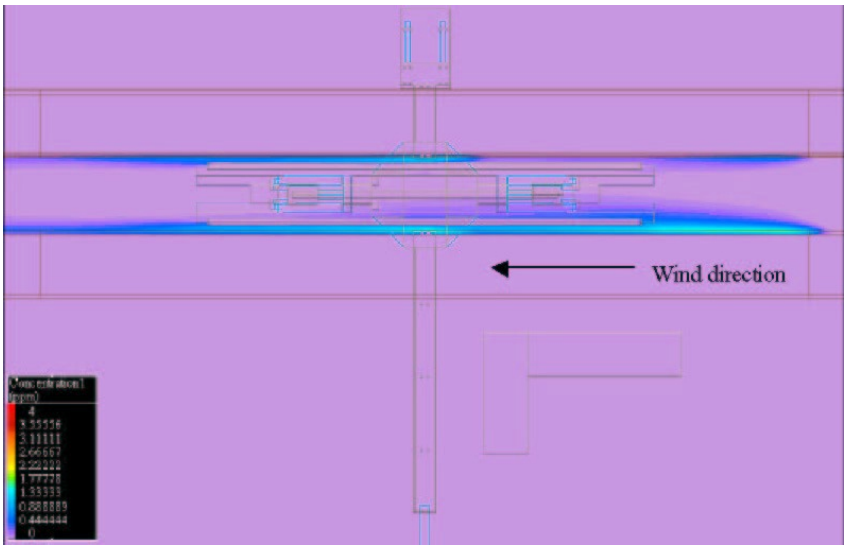


Figure 8: Iteration 2 - CO plot at 2 m height from the platform. West wind direction at 1 m/s. The maximum CO level on this plane is 2.2 ppm.

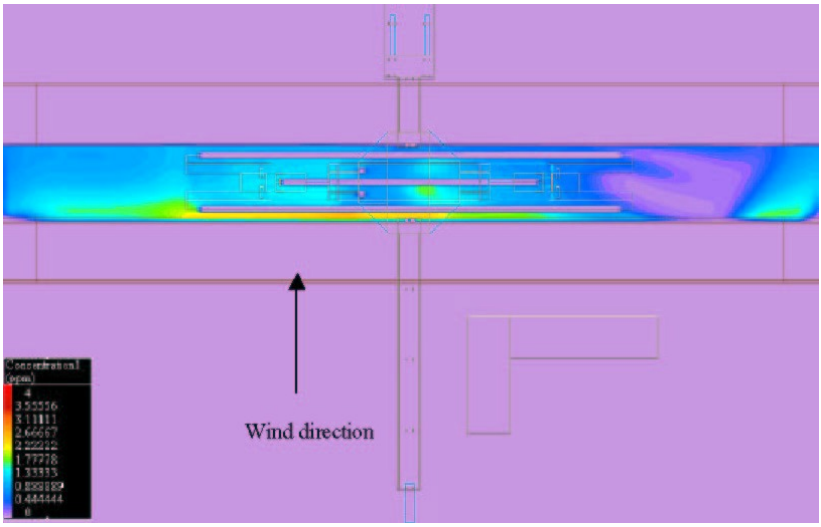


Figure 9: Iteration 3 - CO plot at 2 m height from the platform. North wind direction at 1 m/s. The maximum CO level on this plane is 2.8 ppm.

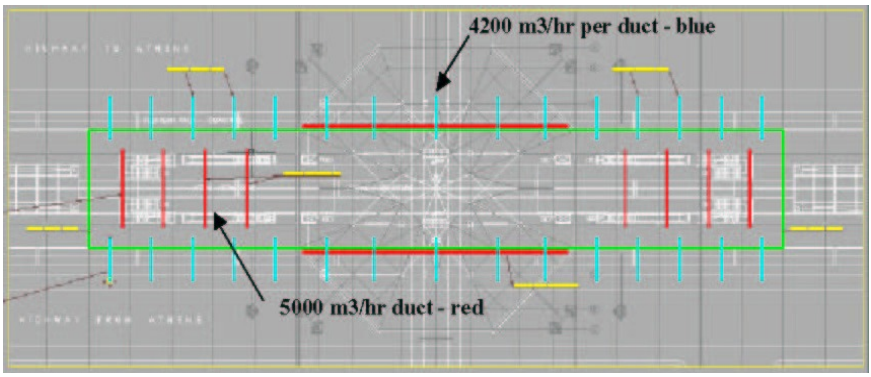


Figure 10: Plan view of the mechanical venting location and flow rates.

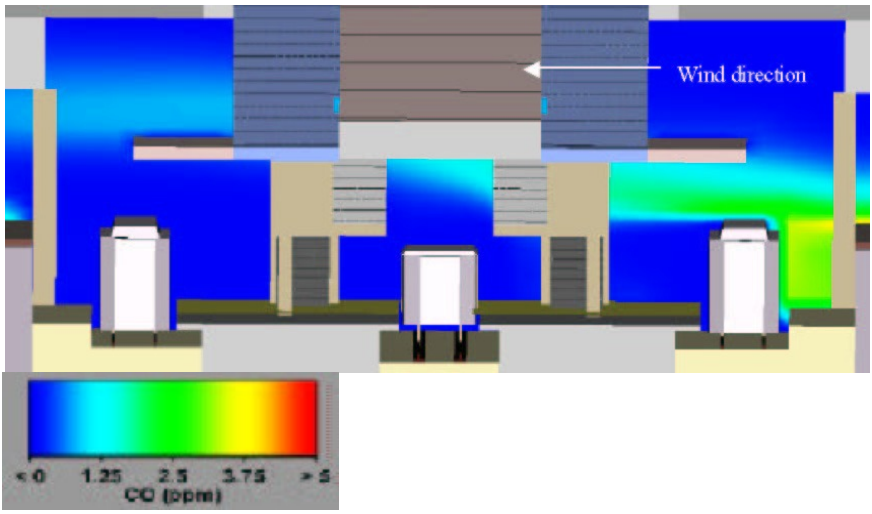


Figure 11: CO plot across the centreline on the platform with a 1 m/s North wind and mechanical venting.

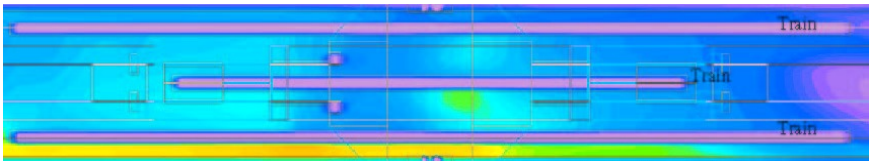


Figure 12: Plan view CO plot of Iteration 3 – 1 m/s North wind; no venting.

The maximum CO levels for scenario 4 are higher than a similar case (Scenario 3) without venting. This is due to recirculation zones in Scenario 4, which created increased levels of CO in the platform area. Overall, the average CO levels are less at the platform with the ventilation on.

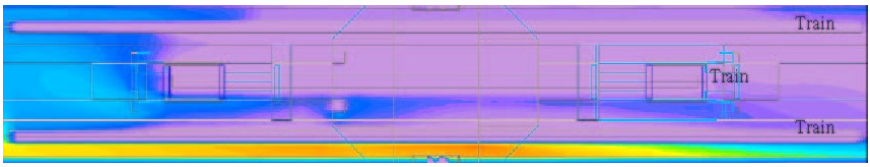


Figure 13: Plan view CO plot of Iteration 4 – 1 m/s North wind; with venting.

Table 2: Summary of CO levels with different wind conditions – all cases.

Case	**Summary of Results**	***COmax ppm)***	***COmax (ppm) above platform***
Baseline	15 m/s North direction off	0.5	0.2
Scenario 1	15 m/s West direction off	1.1	0.15
Scenario 2	1 m/s West direction off	16.5	2.2
Scenario 3	1 m/s North direction off	7.9	2.8
Scenario 4	1 m/s North direction on	9.7	3.4

3 Conclusions

Airflow modelling of the Athens-Greece Train Station was performed to determine the CO levels along the train platform. The CO levels from the baseline model and four simulation scenarios are well below the 25 ppm limit, that is the upper limit for long-term exposure (i.e. 8 hrs) as per World Health Organization Recommendations. These simulations included different wind speeds and direction, as well as, one Scenario with mechanical ventilation. The average CO levels at the platform with the ventilation on have decreased when compared to a similar case without ventilation under the same external wind conditions.

Acknowledgement

This publication was accomplished in the framework of Archimedes II-Support of Research Programs ΕΠΕΑΕΚ ΙΙ.

References

[1] Krarti and Ayari, “Overview of Existing Regulations for Ventilation Requirements of Enclosed Vehicular Parking Facilities”, ASHRAE paper 4274 (RP-945), 1999, **105**, page 6.
[2] Patankar, S V, "Numerical Heat Transfer and Fluid Flow", Hemisphere Publishing Corporation.
[3] Weather forecast data from the Athens airport whether forecast station.
[4] Weather forecast data from the central Athens whether forecast station.

This page intentionally left blank

An industrial method for performance map evaluation for a wide range of centrifugal pumps

A. Fatsis[1], M. Gr. Vrachopoulos[1], S. Mavrommatis[1],
A. Panoutsopoulou[2], N. Vlachakis[1] & V. Vlachakis[3]
[1]*Technological University of Chalkis,*
Department of Mechanical Engineering, Greece
[2]*Hellenic Defence Systems S.A., Greece*
[3]*Virginia Polytechnic Institute and State University,*
Department of Mechanical Engineering, USA

Abstract

Centrifugal pumps are designed and manufactured in order to be fitted to installations and work over a wide range of operating conditions. In such cases the prediction of performance constitutes an important challenge for the pump designer. The challenge becomes particularly difficult when it is necessary to predict the performance of different types of centrifugal pumps varying from low to high volume flow rates. Even if one possesses the rig to measure the performance of a pump, it is useful and time saving to predict numerically the overall pump characteristics. The present method is a simple and easy to apply numerical tool for pump performance curve estimation. It requires a minimum of pump geometrical data and it can be advantageous to pump designers providing them with an initial performance curve estimation during the design process, before they advance to the detailed design of the pump and its experimental verification on the test rig. From the cases examined, it is concluded that the proposed method provides a satisfactory approximation of industrial centrifugal pumps' performance curves, constituting a potential tool for pump manufacturers.
Keywords: performance curve, characteristic line, centrifugal pump, numerical prediction.


WIT Transactions on Engineering Sciences, Vol 52, © 2006 WIT Press
www.witpress.com, ISSN 1743-3533 (on-line)
doi:10.2495/AFM06048

1 Introduction

Prediction of centrifugal pump performance constitutes an important challenge when a pump has to be manufactured in order to be fitted in a given installation and to work over a wide range of operating conditions, Samani [1]. The challenge becomes particularly difficult when is needed to predict the performance of different types of centrifugal pumps varying from low to high volume flow rates Pfeiderer [2]. Characteristic curves are not always available to evaluate the adequacy of the pump's performance for a particular situation, Engeda [3]. Even if one possesses the rig to measure the performance of a pump, it is useful and time saving to predict numerically the overall pump characteristics.

Significant numerical work was done over the past years to estimate the flow and the performance characteristics of centrifugal pumps [1–10]. An interesting method was presented by Engeda [3] for the Head prediction. It has been demonstrated by Engeda [3] that predictions based on the Euler's method and airfoil theory, sometimes produce unrealistic results. Sophisticated three-dimensional methods including the interaction between impeller and volute, Lakshminarayana [11] are time consuming, require detailed three-dimensional geometrical data of the impeller and volute and they are not suited as an engineering tool for performance prediction, but for the detailed flow analysis inside the pump.

The present study presents a fast method requiring only a few pump geometrical data to estimate performance characteristics of centrifugal pumps. Not only the Head, but also the overall efficiency and the required power of the motor to drive the pump are estimated. Numerical predictions are compared to experimental data that was either obtained in the test rig or found in the literature, for centrifugal pumps delivering low, medium and high volume flows. The results show that the proposed method can be used as a tool to provide a quick assessment of performance curves to the pump designer.

2 Numerical method

The maximum head produced by a centrifugal pump corresponds to throttling conditions, where the volume flow is zero, Bohl [14]. The maximum theoretical head is proportional to the square of the impeller rotational speed and of the impeller tip diameter, i.e. available head can be approximated as:

$$H_{theor} \approx \left(n \cdot D_2\right)^2 \tag{1}$$

Taking into account that according to Japikse [5] the main sources of losses inside a centrifugal pump are mechanical losses, impeller losses, disk friction losses and leakage losses in the gap between impeller and casing, the maximum available head can be written as:

$$H_{\max} = K_1 \cdot \left[\left(n \cdot D_2\right)^2\right] \tag{2}$$

where n is the impeller rotational speed in rev/*s and* D_2 is the impeller tip diameter in *m*. The coefficient K_1 involved in this formula is a loss coefficient at throttling. It is defined as $K_1 = 0.6$ that it can be able to capture all types of losses referred previously at throttling conditions (i.e. when $Q = 0$). The constant K_1 has the units so that the Head is expressed in S.I. units. Similar choice of the loss coefficient at throttling conditions was done in the past by Stepanoff [15].

To simulate the pump behaviour for all other operation points up to the maximum flow that the pump can deliver, the non-dimensional flow rate, namely ξ is introduced. The coefficient ξ is semi-empirical and is defined by the volume flow at any operating point as well as easily attainable pump data, such as D2x,, b_2, d_P, n:

$$\xi(Q) = K_2 \cdot \frac{Q}{d_p \cdot b_2 \cdot n \cdot D_{2x}} \tag{3}$$

It should vary from 0 at throttling conditions (where $Q = 0$) to a value close to 1 indicating at that point the maximum estimated flow delivered by the pump. The non-dimensional coefficient K_2 is defined as $K_2 = 0.3$ to approximate the maximum predicted flow rate as close as possible to the one obtained in the test rig.

Due to the fact that a lot of pump manufacturers use the pump discharge diameter d_P and the impeller tip diameter D_{2x} to group pump categories, these two geometrical data were deliberately used in equation (3).

Characteristic curves based on experimental data by Vlachakis [16], Inoue and Cumpsty [17], show a slight curvature in the area of throttling where the volume flow is zero and an almost linear behaviour elsewhere. This behaviour was thought to be captured in the best way by using a cosine function to an exponent. The exponent 0.2 guarantees an almost linear behaviour of the H-Q curve, for the values of ξ of interest, $\xi \in [0,1]$, that is close to the real (measured) performance of centrifugal pumps:

$$H = K_1 \cdot \left[\left(n \cdot D_{2X} \right)^2 \right] \cdot \left[\cos\left(\frac{\pi}{2} \cdot \xi \right) \right]^{0,2} \tag{4}$$

Additionally, it can be easily verified that the slope $dH/d\xi$ is always negative, for the values of $\xi \in [0,1]$ which means that the proposed approximation warrantees monotonic behaviour of the performance curve.

3 Validation of the method

The numerical model described in the section 2 was in a first stage validated against experimental data found in the literature. As test cases, the same pump data used by Amminger and Bernbaum [8] and by Yedidiah [18] were chosen to be compared to the numerical results obtained by the present work.

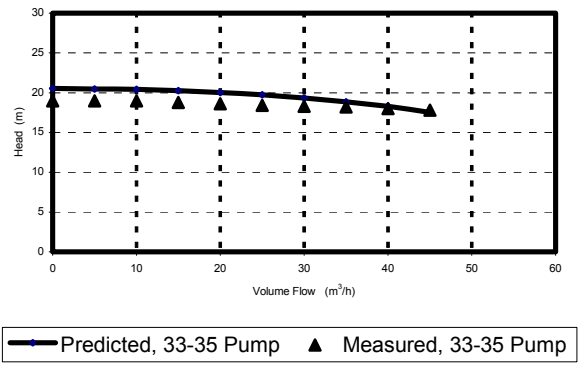


Figure 1: Predicted versus experimental performance curves for the centrifugal pump named 33-35 in Amminger and Bernbaum [8].

Figure 1 shows the comparison between predictions and experimental data from the so-called 33-35 pump for which experimental data presented by Amminger and Bernbaum [8]. It can be seen from this figure that Head predictions show very good agreement to experimental data. In the same article there are experimental data of the so-called 26-14 pump. Figure 2 shows the comparison between numerical and experimental data. The agreement is good for the maximum head as well as the head distribution up to maximum capacities.

Figure 3 presents the comparisons between predictions and experimental data for two different tip impeller diameters, for D_{2x}=136 *mm* and for D_{2x}=16m *mm*. Comparing numerical and experimental data, one observes a good agreement for all the range of flow capacities.

4 Comparison of predictions to measurements obtained in the test rig

After it had been validated, the present numerical model was applied to more than 30 different pumps tested in the test rig of the University of Chalkis. Since it is not possible to present all these results here, only some typical cases were selected that reveal the applicability limits as well as the constraints of the present method. The experimental set-up will not be commented in the present work because the purpose here is the presentation of the prediction method and

not of the measurement chain. The results obtained are grouped in three sections; pumps that deliver low, medium and high volume flows.

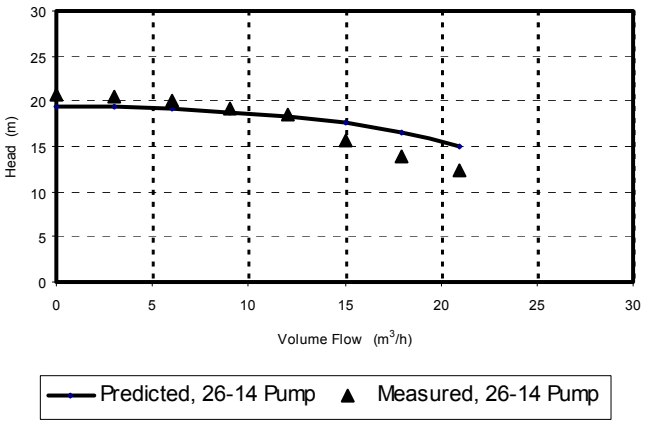


Figure 2: Predicted versus experimental performance curves for the centrifugal pump named 26-14 in Amminger and Bernbaum [8].

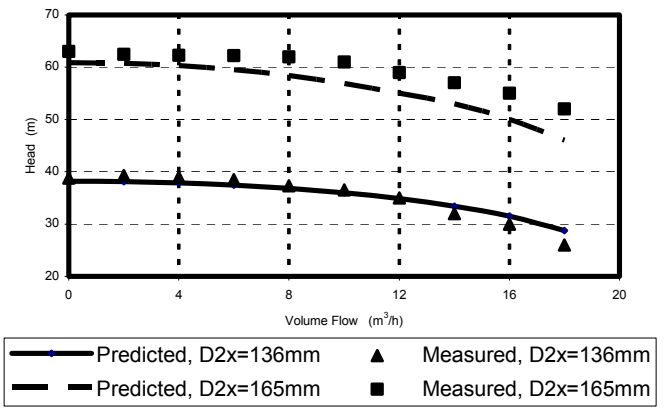


Figure 3: Predicted versus experimental performance curves for the centrifugal pump of figure 2 of Yedidiah [18].

4.1 Low volume flow pumps

A centrifugal pump category with nominal impeller tip diameter D_2= 200 *mm* having discharge diameter d_p= 32 *mm,* running at 1450 rpm. Two sets of centrifugal impellers were used: One having D_{2x}= 215 *mm* and another having

D_{2x}= 185 *mm*. Numerical predictions show an over- prediction of the Head of the pump for both diameters used, when compared to experimental data, figure 4.

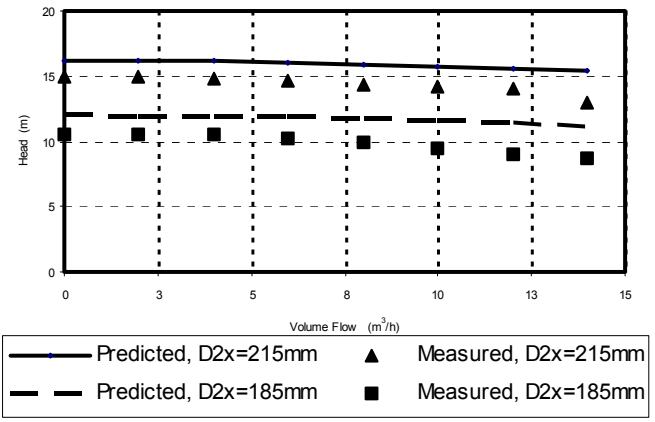


Figure 4: Predicted versus experimental performance curves for centrifugal pumps with nominal D_2=200 *mm*, d_p=32 *mm* running at 1450 *rpm*.

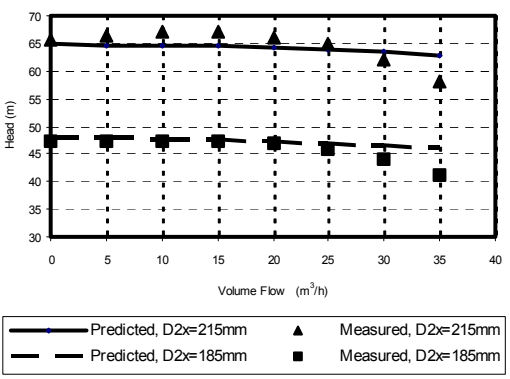


Figure 5: Predicted versus experimental performance curves for centrifugal pumps with nominal D_2=200 *mm*, d_p=40 *mm* running at 2900 *rpm.*

4.2 Medium volume flow pump

Comparisons between predictions and experimental data for another medium flow pump category are shown in figure 5. This centrifugal pump has nominal impeller tip diameter D_2=200 *mm*, discharge diameter d_p=40 *mm* running at 2900 *rpm.* Two sets of centrifugal impellers were tested: One having D_{2x}=215 *mm* and another having D_{2x}=185 *mm*. The Head prediction is in good agreement to experimental data.

4.3 High volume flow pump

Figure 6 shows the predicted versus the experimental head for a centrifugal pump with nominal impeller tip diameter D_2= 400 *mm*, discharge diameter d_p=250 *mm,* running at 1480 *rpm*. Two cases were examined: one with D_{2x}=400 *mm* and another one with D_{2x}= 350 *mm*. The comparison between the predicted and measured Head is again very good for all the range of volume flows.

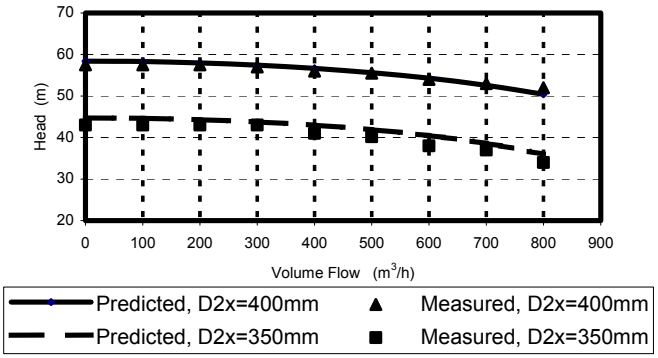


Figure 6: Predicted versus experimental performance curves for centrifugal pumps with nominal D_2=400 *mm*, d_p=250 *mm* running at 1480 *rpm*.

5 Conclusions

A simple and fast method was presented attempting to predict performance curves of industrial centrifugal pumps. For all centrifugal pumps examined, delivering low, medium and high volume flows, the same semi-empirical coefficients and equations were deliberately used in the model. To validate the model, centrifugal pumps for which experimental data were found in the literature, were tested with satisfactory results. Comparisons between numerical and experimental data obtained in the test rig show that the proposed model can satisfactorily predict performance characteristics of centrifugal pumps, for the cases examined. In the most of the cases it seems that the present numerical model over-predicts the Head distribution for low volume flow pumps, while it gives better predictions for medium and high volume flow pumps. This feature of the model seems to underestimate the losses at throttling for low capacity centrifugal pumps, whereas for medium and maximum capacity pumps it provides a better estimation of the maximum head. For the cases examined the assessment of the Head at throttling conditions where Q=0 proved satisfactory using equation (2) whereas the shape and the rate of decrease of the Head as the volume flow is increasing is adequately predicted using equation (4).

The present method is a simple and easy to apply numerical tool for pump performance curves' estimation. It requires a minimum of pump geometrical data

and it can be advantageous to pump designers providing them with an initial performance curve estimation during the design process, before they advance to the detailed design of the pump and its experimental verification on the test rig. Furthermore, in cases where pump's characteristics are not available, the present method works as a quick assessment tool to give an educated guess to the question whether a particular pump is suitable to fulfil the installation's requirements.

Acknowledgement

This publication was accomplished in the framework of Archimedes I-Support of Research Programs ΕΠΕΑΕΚ ΙΙ.

References

[1] Samani, Z., 1991, "Performance estimation of close-coupled centrifugal pumps". American Society of Agricultural Engineers, **7**, pp.563-565.
[2] Pfeiderer, C., 1938, "Vorausbestimmung der Kennlinien schnellläufiger Kreiselpumpen." VDI, Düsseldorf.
[3] Engeda, A., 1987, Untersuchungen an Kreiselpumpen mit offenen und geschlossenen Laufrädern im Pumpen- und Turbinenbetrieb. Ph.D. thesis *TU Hannover.*
[4] Gülich, J.F., 1988, "Bemerkungen zur Kennlinienstabilität von Kreiselpumpe". *Pumpentagung Karlruhe*, B3.
[5] Japikse, D., Marscher, W.D., Furst, R.B., 1997. *Centrifugal Pump Design and Performance,* Concepts ETI Inc., Vermond.
[6] Karassik, I.J., Krutzsch, W.C., Fraser, W.H. and Messina J.P., 1976, *Pump Handbook*, McGraw-Hill Book Co, New York.
[7] Gülich, J.F., 1999, *Kreiselpume,* Springer-Verlag, Berlin.
[8] Amminger, W.L., Bernbaum, H.M. 1974. "Centrifugal pump performance prediction using computer aid", Computers and Fluids, **2**, pp.163-172.
[9] Yedidiah S., 2003, "An overview of methods for calculating the head of a rotordynamic impeller and their practical significance*",* Proceedings of the Institution of Mechanical Engineers, Part A: Journal Process Mechanical Engineering, **217(3)**, pp.221-232.
[10] Fatsis, A., 1993, "Three-dimensional unsteady flow calculations in radial components", von Karman Institute Lecture Series 1993-01 'Spacecraft Propulsion'.
[11] Lakshminarayana, B., 1991, "An assessment of computational fluid dynamic techniques in the analysis of turbomachinery", ASME Journal of Fluids Engineering, **113**, pp.315-352.
[12] Gülich, J.F. 1994. "Berechung von Kreiselpumpen mit Navier-Stokes-Verfahren – aus der Sicht des Anwendes". Forsch Ingenieurwes **60**, pp.307-316.



[13] Zhou W., Zhao, Z., Lee, T.S., Winoto S.H. 2003. "Investigation of Flow Through Centrifugal Pump Impellers using Computational Fluid Dynamics", International Journal of Rotating Machinery, **9(1)**, pp.49-61.
[14] Bohl, W., 1988, *Stroemungsmachinen I, II,* V*ogel-Verlag, Berlin*.
[15] Stepanoff, A. J. 1957. *Centrifugal and axial flow pumps: Theory, design and applications,* John Wiley and Sons, New York.
[16] Vlachakis N. 1974. "Vergleich zweier Geschwindigkeitansätze für die radiale Spaltrichtung in Bezug auf das Drehmoment der rotierenden Scheibe". Bericht Uni Karlsruhe.
[17] Inoue M, Cumpsty, N.A. 1988. "Experimental study of centrifugal discharge flow in vaneless and vaned diffusers". ASME Journal of Engineering Gas Turbines and Power, **106**, pp.455-467.
[18] Yedidiah S. 2001. "Practical applications of a recently developed method for calculating the head of a rotordynamic impeller". Proceedings of the Institution of Mechanical Engineers, Part E: Journal of Power and Energy, **215**, pp.119-131.



This page intentionally left blank

Large eddy simulation of compressible transitional cascade flows

K. Matsuura[1] & C. Kato[2]
[1]*Department of Intelligent Machinery and Systems, Kyushu University, Japan*
[2]*Institute of Industrial Science, The University of Tokyo, Japan*

Abstract

The large eddy simulation (LES) of compressible transitional flows in a low-pressure turbine cascade is performed by using 6th-order compact difference and 10th-order filtering method. The numerical results without free-stream turbulence and those with about 5% of free-stream turbulence are compared. In these simulations, separated-flows in the turbine cascade accompanied by laminar-turbulent transition are realized, and the present results closely agree with past experimental measurements in terms of the static pressure distribution around the blade. In the case where no free-stream turbulence is taken into account, unsteady pressure field essentially differs from that with strong free-stream turbulence. In the no free-stream turbulence case, pressure waves that propagate from blade's wake region have noticeable effects on the separated-boundary layer near the trailing-edge, and on the neighboring blade. Also, based on Snapshot Proper Orthogonal Decomposition (POD) analysis, dominant behaviors of the transitional boundary layers are investigated.
Keywords: large eddy simulation, low pressure turbine, compressible flow, transition.

1 Introduction

In low-pressure turbines or small-sized turbines, Reynolds number based on the chord length and the throat exit velocity becomes as small as in the order of 10^4-10^5 due to decrease in density, resulting in increase in kinematic viscosity or the small length scale. The boundary layer on the blade in such a turbine thus



WIT Transactions on Engineering Sciences, Vol 52, © 2006 WIT Press
www.witpress.com, ISSN 1743-3533 (on-line)
doi:10.2495/AFM06049

becomes transitional and unsteadiness of the cascade flows becomes evident. At the same time, the boundary layers are affected by the strong free-stream turbulence with about 5-20% intensity that originates in the combustion chamber or wakes of the upstream blade rows [1].

Conventionally, Reynolds-averaged Navier-Stokes Simulation (RANS) has been widely used for the prediction of transitional flows. In this method, transition is treated empirically, e.g. by correlating the transition point or transition length with the momentum thickness of the boundary layer, or by assuming production rate of turbulent spots based on Emmons' spot theory [2]. However, the transition location or the spot production rate is usually estimated from limited and scattered experimental data. Therefore, the accuracy of the prediction deteriorates when it is applied to those operating conditions that are beyond the assumptions of the empirical transition treatments, and/or to three-dimensional complex shapes.

Recently, numerical methods that solve Navier-Stokes equation as directly as possible have been developed and applied to the prediction of transitional flows. These methods are capable of directly treating temporal evolution of flow disturbances and frequency contents of free-stream disturbances that are vital in the transitional processes. Among these methods, large eddy simulation (LES) can predict turbulent flows with a reasonable accuracy at a smaller computational cost than is needed for direct numerical simulation (DNS) and therefore its applications are expected to spread in a wide range of engineering flows.

DNS and LES of transitional flows in a low-pressure turbine were made by several researchers [3-6], and physical aspects of the flows have been revealed gradually. In the studies mentioned above [3-6], unsteady behaviors of a separation bubble near the trailing-edge of a low-pressure turbine have been investigated in detail in relation with no free-stream turbulence case. Also investigated in these studies are the changes in transition mode of a cascade for different types of free-stream turbulence.

However, it is not thoroughly understood what would result from the unsteady behaviors near the trailing-edge in the cascade passages, or how unsteady separation and/or boundary layer transition in a low-pressure turbine changes according to the change in free-stream turbulence. Investigation into these issues is important not only for predicting transitional boundary layers accurately but also for understanding the mechanism of noise generation from aeroacoustical point of view.

In this paper, after a validation of the numerical method for bypass transition on a flat plate, large eddy simulations of a low-pressure turbine cascade flow subjected to free-stream turbulence are performed. Based on the computed results investigations are presented on the effects of the free-stream turbulence on the boundary layer transition, and behavior of the pressure waves that originate near the trailing-edge with its effects on the separation/transition of the boundary layer [6]. Also presented in this paper are the dominant unsteady behaviors in the transitional boundary layers that are extracted by Snapshot Proper Orthogonal Decomposition (POD) Analysis [7].



2 Governing equations and numerical methods

The governing equations are the unsteady three-dimensional compressible Favre-filtered Navier-Stokes equations. The equations are solved by finite-difference method. In the current study, no explicit subgrid scale (SGS) model is used. Instead, energy in the grid scale (GS) transferred to SGS eddies is dissipated by a 10^{th}-order spatial filter mentioned below with removing numerical instabilities at the same time. The validity and effectiveness of the numerical method for the current problems are confirmed in the next chapter.

Spatial derivatives which appear in metrics, convective and viscous terms are evaluated by the 6^{th}-order tridiagonal compact scheme [8]. Time-accurate solutions to the governing equations were obtained by the implicit approximately-factored finite-difference algorithm of Beam & Warming based on the three-point-backward formulation. In the method, computational efficiency is enhanced by the Pulliam & Chaussee's diagonalization. Three Newton-like subiterations per time-step are employed to reduce errors induced by linealization, factorization and diagonalization. The final accuracy of the time integration is 2^{nd}-order.

In addition to the spatial discretization and the time integration, 10^{th}-order implicit filter shown below [9] is used to suppress numerical instabilities due to the central differencing in compact scheme.

$$\alpha_f \hat{\phi}_{i-1} + \hat{\phi}_i + \alpha_f \hat{\phi}_{i+1} = \sum_{n=0}^{5} \frac{a_n}{2} (\phi_{i+n} + \phi_{i-n}). \tag{1}$$

Here, ϕ denotes a conservative quantity, $\hat{\phi}$ a filtered quantity at each grid point. Regarding coefficients a_n (n=0,…,5), the values in [9] are used in the present study. The parameter α_f is set to be 0.46.

Not only the accuracy of the filter but also the value of α_f have considerable influence on both the accuracy and the stability of a calculation. In the present study, the above value is used in order to keep the stability of the calculation while maintaining the high-accuracy of the calculation results.

3 Validation of numerical methods

3.1 Computational details

Computed flow is a spatially growing boundary layer on a flat plate. Free-stream Mach number is 0.3 and free-stream turbulence intensity is 6%. Streamwise Reynolds number Re_x of the computational domain extends from 6.625×10^3 to 4.26×10^5. Grid points used are 1134, 70 and 76, and the grid resolutions are Δx^+=14-38, Δy^+=1-76 and Δz^+=15 for the streamwise, wall-normal and spanwise directions, respectively. In particular, Δx^+ is gradually decreased from 38 to 14 for $Re_x=1.04\times10^5$- 2.08×10^5 and gradually increased from 14 to 30 for $Re_x=2.08\times10^5$- 4.26×10^5. The wall units are based on the friction velocity just after transition is complete.

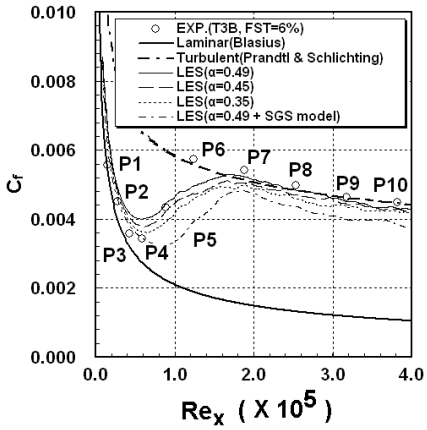


Figure 1: Variation of skin friction coefficient C_f with respect to Re_x.

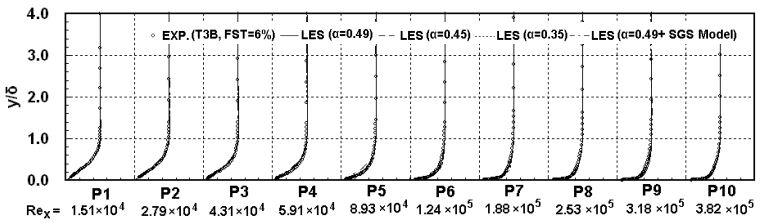


Figure 2: Profiles of streamwise velocity at each streamwise position.

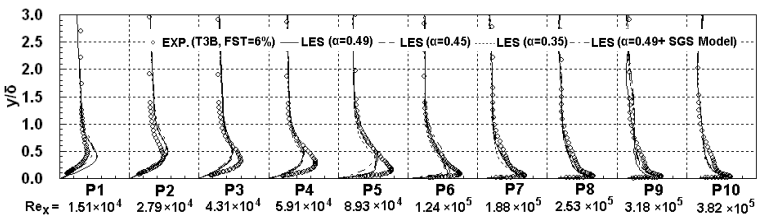


Figure 3: Profiles of streamwise velocity fluctuation u_{rms}/u_∞ at each streamwise position.

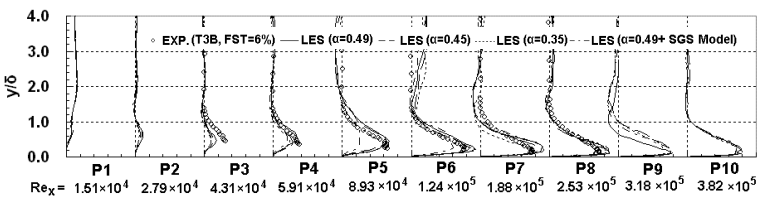
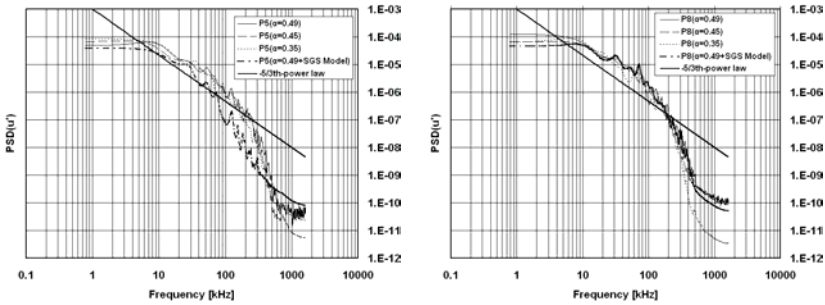


Figure 4: Profiles of Reynolds stress $-\overline{u'v'}/u_\infty^2$ at each streamwise position.



(a) P5 (y/δ=0.162) (b) P8 (y/δ=0.04)

Figure 5: Distributions of power spectrum density of streamwise velocity fluctuation u' at P5 and P8.

Test cases are the calculation with $\alpha_f = 0.49$ for Case A, $\alpha_f = 0.45$ for Case B and $\alpha_f = 0.35$ for Case C when no additional explicit SGS model is used, and $\alpha_f = 0.49$ for Case D when the additional explicit SGS model [10] is used.

Concerning the boundary conditions, laminar boundary layer profile subjected to isotropic free-stream turbulence is imposed at the upstream boundary. The free-stream turbulence is obtained from a LES result of isotropic turbulence. The non-slip adiabatic boundary condition is assumed at the wall boundary. The time increment was set constant at $\Delta t = 1.75 \times 10^{-5} L_x / u_\infty$ where L_x is the streamwise length of the computational domain and u_∞ is the free-stream velocity.

3.2 Results and discussions

The computational results of the friction coefficient C_f compared with the experimental data [11] are shown in fig. 1. The results of Case A, Case B and Case C agree well with the experimental data if the region where transition completes, i.e. P6 is excluded. As α_f is decreased, C_f curves shift downstream due to the artificial dissipation introduced in the calculations. In turbulent region, the predicted C_f agrees well with the experimental data especially when $\alpha_f > 0.45$.

On the other hand, the position of maximum C_f is delayed compared to the experimental data even if α_f is taken to be as high as 0.49. This is likely to originate from the present computational limitation to capture fast vortex breakdown in the early transition process.

Figure 2-4 show streamwise velocity, streamwise velocity fluctuation and Reynolds stress at each streamwise position, respectively.

Although growth of u_{rms} near the wall is underestimated compared to the experimental data at P3-P6 which correspond to transitional region, present results of Case A, Case B and Case C reproduce the growth of disturbances confirmed in the experiment well. Based on the these results, the present numerical method mentioned in Chapter 2 is reasonable to be used in the present study with the grid resolution mentioned in this Chapter and $\alpha_f > 0.45$.

On the other hand, transition in the result of Case D is clearly delayed compared to those of Case A, Case B and Case C as is also confirmed by the distributions of power spectrum density of streamwise velocity fluctuation evaluated at its peak position in fig. 5. This suggests that additional explicit SGS model degrades the accuracy in this computation.

4 Transitional linear turbine cascade

4.1 Computational details

Computational geometry is T106 [12], which is one of the most representative test cases for compressible transitional turbine cascade flows. At its design point, numerical simulation without free-stream turbulence (Case A) and that with about 5% of free-stream turbulence (Case B) are performed. The Mach number at the throat exit is 0.59. The Reynolds number based on the chord length C and the throat exit velocity at the design point is 5.0×10^5.

The grid used in the computations is of H-type topology and generated in a blade passage with 1005, 150 and 40 grid nodes in the streamwise (ξ), pitchwise (η) and spanwise (ζ) directions, respectively. The spanwise length of the grid is 10% of the chord length. Grid resolutions are $\Delta\xi^+<15$, $\Delta\zeta^+<33$ in the streamwise, spanwise directions, respectively near 60%-90% chord length position, and $\Delta\xi^+<10$, $\Delta\zeta^+<20$ near 80% chord length position where critical phenomena like separation or transition are expected to occur. In the pitchwise direction, $\Delta\eta_{min}^+<2.3$ near 60%-90% chord length position, $\Delta\eta_{min}^+<1.0$ near 80% chord length position. The above wall units are based on the local friction velocity. These resolutions are equivalent to those used in Chapter 3. Free-stream turbulence is introduced from the inlet boundary. The number of grid points in the boundary layer is approximately 30.

4.2 Results and discussions

Figure 6 compares time-averaged static pressure distribution around the blade. The computed results agree well with the experimental data [12] for both cases. Figure 7 shows the skin friction coefficients along the suction side of the blade. From fig. 7, a separation bubble is formed near 85% chord length position in Case A while the boundary layer is attached in a time-averaged sense in Case B.

Regarding unsteady characteristics of the cascade flows, divergence of instantaneous velocity field and the iso-surface of the 2nd invariance of velocity gradient tensor are shown in fig. 8. In fig. 9 divergence of instantaneous velocity field and the iso-contour of vorticity magnitude are shown.



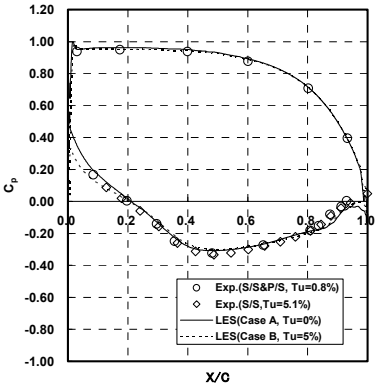


Figure 6: Time-averaged distribution of static pressure on blade's surface.

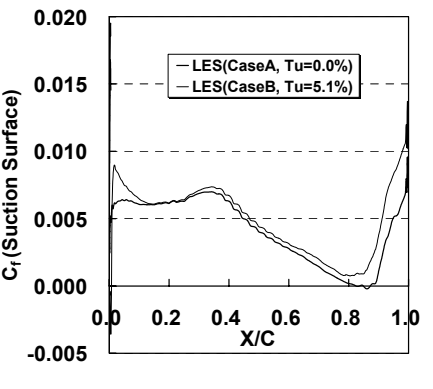
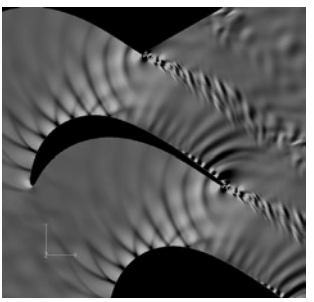
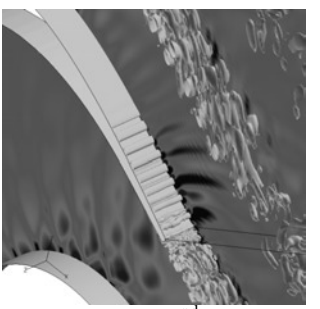


Figure 7: Skin friction coefficients along the suction side of the blade.

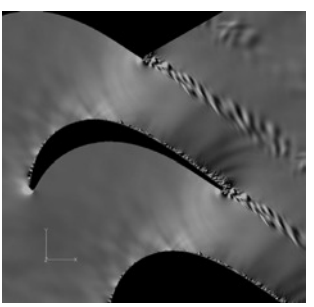


(a) Divergence of instantaneous velocity field

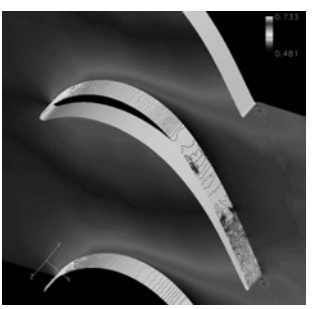


(b) Iso-surface of 2nd invariance

Figure 8: Clean inflow case (Case A).



(a) Divergence of instantaneous velocity field



(b) Iso-contour of vorticity magnitude

Figure 9: Turbulent inflow case (Case B).

In Case A, pressure waves that originate from the unsteady fluctuation in the neighborhood of the trailing-edge propagate in almost entire region of the blade passage. The pressure waves oscillate the separation bubble that is formed near 80% chord length position. Also they reach the suction side of the neighboring blade at its maximum curvature and form a complex pressure field upstream of the blade's throat. In the boundary layer near the trailing-edge, spanwise vorticies are created due to the boundary layer separation and they are convected downstream while maintaining the periodic variation of the wakes near the trailing-edge. To the contrary, no strong periodic pressure waves are generated from the neighborhood of the trailing-edge in Case B. After the generation of turbulent spots, fully three-dimensional turbulent boundary layer convects downstream and the wake consists of minute three-dimensional eddies.

In order to extract dominant unsteady behaviors of the transitional boundary layer, POD Analysis is performed. The method used in the present study is Sirovich's Snapshot POD Method [7]. Figure 10 shows accumulated plots of instantaneous velocity fluctuation profile at X/C=0.95, and instantaneous velocity fluctuation component reconstructed from the dominant POD modes for both Case A and Case B.

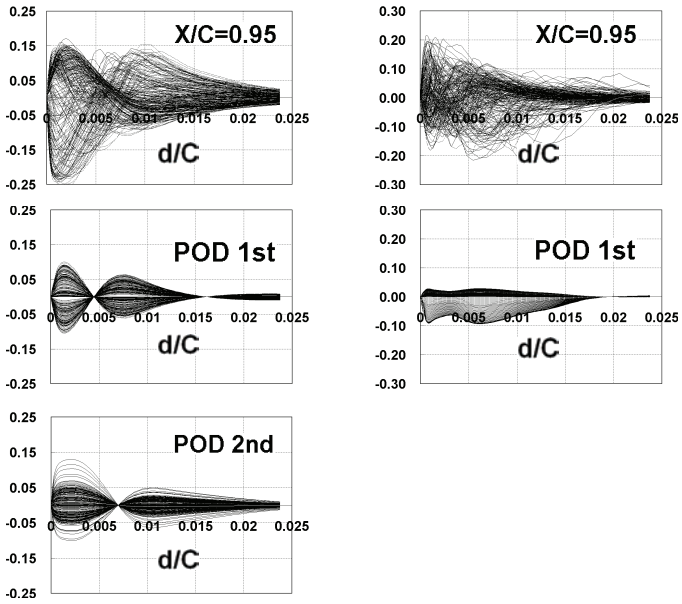
In Case A, the sign of the 2nd mode changes at a point further apart from the wall than the 1st mode. In fig. 8, the vorticies near the trailing-edge are compressed and expanded by the passage of pressure waves as is found in the relationship between the divergence value and the vortices. Therefore, the difference in the position where the sign changes in the 1st mode and the 2nd mode corresponds to the compression and expansion of the vorticies. Furthermore, the region swept by the profiles of the 2nd mode has asymmetry regarding the abscissa. This asymmetry corresponds to the deformation of the spanwise vorticies in the spanwise direction near the trailing-edge as is found in fig. 8. Based on the above discussion, in addition to the passage of the pressure waves, the compression and expansion of the vorticies due to the passage of the pressure waves are the dominant behavior of the boundary layer in the no free-stream turbulence case. Especially at 95% chord length position, the spanwise deformation of vortices is also the dominant unsteady behavior of the transitional boundary layer.

On the other hand, as is found in the similarity of the shape of the region swept by the 1st mode to the turbulence production at X/C=0.95, the dominant behavior of the transitional boundary layer is the turbulence production in Case B. Therefore, the dominant behavior of the transitional boundary layer is intrinsically different in Case A and Case B.

5 Conclusions

Large eddy simulation of compressible transitional flows in a low-pressure turbine cascade is performed by using 6th-order compact difference and 10th-order filtering method. Numerical results without free-stream turbulence and those with approximately of 5% free-stream turbulence are compared. Based on the computed results, differences in the unsteady behaviors of flows in the

cascade, including the propagation of pressure waves and the effect of free-stream turbulence on separated-flows, are clarified. In addition, POD analysis is performed to extract the dominant behaviors of the unsteady boundary layers. From this analysis, the dominant behavior of the transitional boundary layer is shown to intrinsically differ in Case A and Case B.



(a) Case A (b) Case B

Figure 10: Accumulated plots of instantaneous velocity fluctuation profile at X/C=0.95, and instantaneous velocity fluctuation component reconstructed from the dominant POD modes.

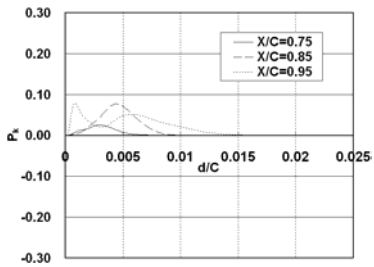


Figure 11: Plot of turbulence production at X/C=75%, 85% and 95% (Case B).

Acknowledgement

This research has been supported by a 21st century COE program "Mechanical System Innovation" of the University of Tokyo.

The authors would also like to thank an IT research program "Frontier Simulation Software for Industrial Science" supported by the Ministry of Education, Culture, Sports, Science and Technology (MEXT), and a collaborative research project with Japan Aerospace Exploration Agency (JAXA) "Simulation of Internal Flows in Rocket Engines," both of which provided computational resources needed to pursue this research.

References

[1] Mayle, R.E., The role of laminar-turbulent transition in gas turbine engines. *Trans. ASME*, *Journal of Turbomachinery*, **113**, pp. 509-537, 1991.

[2] Emmons, H.W., The laminar-turbulent transition in a boundary layer-part I. *Journal of the Aeronautical Sciences*, **18**, pp. 490-498, 1951.

[3] Raverdy, B., Mary, I. & Sagaut, P., High-resolution large-eddy simulation of flow around low-pressure turbine blade. *AIAA Journal*, **41(3)**, pp. 390-397, 2003.

[4] Wu, X. & Durbin, P.A., Evidence of longitudinal vortices evolved from distorted wakes in a turbine passage. *Journal of Fluid Mechanics*, **446**, pp. 199-228, 2001.

[5] Michelassi, V., Wissink, J.G., Fröhlich, J. & Rodi, W., Large-eddy simulation of flow around low-pressure turbine blade with incoming wakes. *AIAA Journal*, **41(11)**, pp. 2143-2156, 2003.

[6] Matsuura, K., Large eddy simulation of compressible transitional cascade flows. *Transactions of the Japan Society of Mechanical Engineers*, **70(700)**, B, pp. 3066-3073, 2004 (in Japanese).

[7] Sirovich, L. & Rodriguez, J.D., Coherent structures and chaos: a model problem. *Physics Letters* A, **120(5)**, pp. 211-214, 1987.

[8] Lele, S.K., Compact finite difference schemes with spectral-like resolution. *Journal of Computational Physics*, **103**, pp. 16-42, 1992.

[9] Gaitonde, D.V. & Visbal, M.R., Padé-type higher-order boundary filters for the Navier-Stokes equations. *AIAA Journal*, **38(11)**, pp. 2103-2112, 2000.

[10] Voke, P., Subgrid-scale modelling at low mesh Reynolds number. *Theoretical and Computational Fluid Dynamics*, **8**, pp. 131-143, (1996).

[11] Pironneau, O., Rodi, W., Ryhming, I.L., Savill, A.M. & Truong, T.V., Numerical simulation of unsteady flows and transition to turbulence. *Proceedings of the ERCOFTAC Workshop held at EPFL 26-28 March 1990 Lausanne, Switzerland*, Cambridge University Press, (1990).

[12] Fottner, L., (ed). Test Cases for Computation of Internal Flows in Aero Engine Components. AR-**275**, AGARD, pp. 112-123, 1990.



CFD modelling of sludge sedimentation in secondary clarifiers

M. Weiss, B. Gy. Plosz, K. Essemiani & J. Meinhold
Anjou Recherche Veolia Water, France

Abstract

We present a CFD model that predicts the sedimentation of activated sludge in a full-scale circular secondary clarifier that is equipped with a suction-lift sludge removal system. The axisymmetric single-phase model is developed using the general-purpose CFD solver FLUENT 6, which uses the finite-volume method. A convection-diffusion equation, which is extended to incorporate the sedimentation of sludge flocs in the field of gravity, governs the mass transfer in the clarifier. The standard k-ε turbulence model is used to compute the turbulent motion, and our CFD model accounts for buoyancy flow and non-Newtonian flow behaviour of the mixed liquor. The activated sludge rheology was measured for varying sludge concentrations and temperatures. These measurements show that at shear rates typical of the flow in secondary clarifiers, the relationship between shear stress and shear rate follows the Casson law. The sludge settling velocity was measured as a function of the concentration, and we have used the double-exponential settling velocity function to describe its dependence on the concentration. The CFD model is validated using measured concentration profiles.
Keywords: computational fluid dynamics, wastewater treatment, activated sludge, secondary clarifiers, sedimentation, rheology, suction-lift sludge removal.

1 Introduction

Secondary clarifiers represent the final stage in the activated sludge wastewater treatment process, separating the treated water from the biologically active sludge (fig. 1). This solid/liquid separation is traditionally achieved by gravity sedimentation. These separation units, which act as clarifier, thickener, and storage tank, are often the major bottlenecks in the activated sludge process. Our



WIT Transactions on Engineering Sciences, Vol 52, © 2006 WIT Press
www.witpress.com, ISSN 1743-3533 (on-line)
doi:10.2495/AFM06050

objective is the development of a modelling tool that may be used in design and optimisation of new and existing secondary clarifiers.

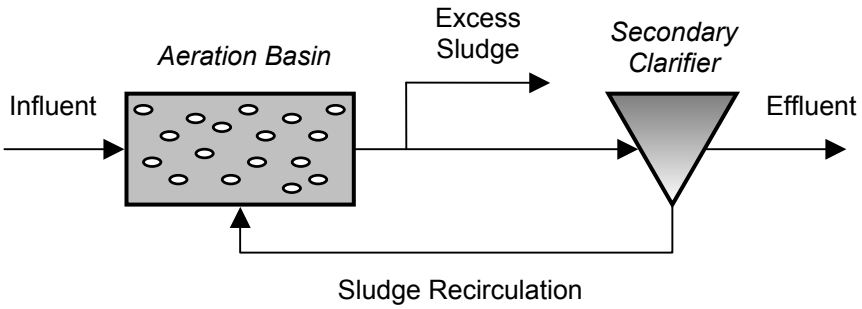


Figure 1: Scheme of an activated sludge wastewater treatment process.

The present study concerns circular clarifiers that are equipped with suction-lift sludge removal systems. In these clarifier systems, which usually have a flat bottom, the sludge is withdrawn through an array of vertical suction pipes from the near-bottom region. This design form may be contrasted with clarifiers that have conical bottoms and where the sludge is removed centrally at the bottom.

We present a computational fluid dynamics (CFD) model of the secondary clarifiers at the wastewater treatment plant of Saint Malo (France), which rests on the numerical model presented by Lakehal *et al*. [1]. Our CFD model differs from that of the aforementioned authors in mainly two ways: (*i*) it employs negative source terms on the governing field equations that represent the sludge removal by suction-lift, and (*ii*) it uses the Casson viscosity law instead of the Bingham law to reflect the non-Newtonian flow behaviour of the activated sludge. We have carried out on-site experiments to determine the rheological flow behaviour and the settling characteristics of the sludge mixture. In addition, the inlet concentration and the flow rates were measured. We have measured concentration profiles within the clarifier to validate the numerical model.

2 Field equations for turbulent flow

The system of Reynolds-averaged flow-governing partial differential equations for two-dimensional, axisymmetric, unsteady, density-stratified, and turbulent mean flow may be given as [1]

$$\frac{\partial u}{\partial x}+\frac{\partial v}{\partial y}+\frac{v}{y}=S_m\,, \tag{1}$$

$$\begin{aligned}\frac{\partial u}{\partial t}+\frac{\partial u^2}{\partial x}+\frac{\partial (uv)}{\partial y}=&-\frac{1}{\rho_w}\frac{\partial p}{\partial x}+\frac{\partial}{\partial x}\left(2(\nu+\nu_t)\frac{\partial u}{\partial x}\right)+\\&+\frac{1}{y}\frac{\partial}{\partial y}\left(y(\nu+\nu_t)\left(\frac{\partial u}{\partial y}+\frac{\partial v}{\partial x}\right)\right)-g\left(\frac{\rho}{\rho_w}-1\right)+S_x\,,\end{aligned} \tag{2}$$

and

$$\frac{\partial v}{\partial t}+\frac{\partial (uv)}{\partial x}+\frac{\partial v^2}{\partial y}=-\frac{1}{\rho_w}\frac{\partial p}{\partial y}+\frac{\partial}{\partial x}\left((\nu+\nu_t)\left(\frac{\partial u}{\partial y}+\frac{\partial v}{\partial x}\right)\right)+ \\ +\frac{1}{y}\frac{\partial}{\partial y}\left(2y(\nu+\nu_t)\frac{\partial u}{\partial y}\right)-\frac{2(\nu+\nu_t)}{y}\frac{v}{y}+S_y. \tag{3}$$

The equation of continuity is given in eqn (1), and eqns (2) and (3) are the x and y momentum conservation equations, respectively. The origin of the coordinate system is placed on the vertical centre line, with the x-axis pointing vertically upwards from the bottom boundary (fig. 2). We note that the field equations are given in terms of averaged flow variables, where u and v are the mean velocity components in the x (axial) and y (radial) directions, respectively, p is the pressure, ρ is the density of the mixed liquor, ρ_w = 998.2 kg m^{-3} is the density of water, g = 9.81 m s^{-2} is the gravitational acceleration constant, ν is the kinematic viscosity of the mixed liquor, and ν_t is the turbulent viscosity.

We have added source terms S_m, S_x, and S_y to eqns (1) to (3) that represent the removal of sludge by suction-lift. These source terms, which are defined as $S_m = -(q_{rec}/V_{rec})$, $S_x = -(q_{rec}/V_{rec})u$, and $S_y = -(q_{rec}/V_{rec})v$, are negative since sludge is removed from the system. They contain the mass flow rate of the recycle stream in [kg s^{-1}], q_{rec}, which is obtained from flow measurements. The volume of the sludge removal zone in the near-bottom region of the clarifier in [m^3], V_{rec}, is defined further down in the paper. The source terms are built into the CFD code using user-defined functions (UDFs) in Fluent.

The governing field equations are formulated using the density of water, and we account for the varying density of the sludge mixture only in the buoyancy terms in the axial momentum equation, eqn (2), and in the equation for the turbulent kinetic energy, eqn (6), which is given further down. We add the buoyancy term to the x momentum equation using a UDF in Fluent. The on-site density measurements of Dahl [2] have shown that the relative density increase at a total suspended solids concentration of 12 kg m^{-3} is only 0.4%. However, the density increases sharply at the sludge blanket, and the buoyancy effect that is caused by this gradient on the flow cannot be neglected.

The density of the mixed liquor, ρ, in the buoyancy term of the x momentum equation may be expressed using an equation of state,

$$\rho = \rho_w + X\left(1-\frac{\rho_w}{\rho_p}\right), \tag{4}$$

where ρ_p = 1600 kg m^{-3} is the density of dry sludge particles [2,3], and X is the sludge concentration, which has the same units as the density.

3 Standard k-ε turbulence model

The turbulent (or eddy) viscosity, $\nu_t = \mu_t/\rho_w$, is determined by the turbulent kinetic energy, k, and also by the rate of dissipation of turbulent kinetic energy, ε, according to [1]

$$\nu_t = C_\mu \frac{k^2}{\varepsilon}, \tag{5}$$

where $C_\mu = 0.09$ is a constant. The semi-empirical model transport equations for k and ε may be given as [1]

$$\frac{\partial k}{\partial t}+\frac{\partial (uk)}{\partial x}+\frac{\partial (vk)}{\partial y}=\frac{\partial }{\partial x}\left(\left(\nu+\frac{\nu_t}{\sigma_k}\right)\frac{\partial k}{\partial x}\right)+\frac{1}{y}\frac{\partial }{\partial y}\left(y\left(\nu+\frac{\nu_t}{\sigma_k}\right)\frac{\partial k}{\partial y}\right)+ \\ +P+G-\varepsilon+S_k, \tag{6}$$

and

$$\frac{\partial \varepsilon}{\partial t}+\frac{\partial (u\varepsilon)}{\partial x}+\frac{\partial (v\varepsilon)}{\partial y}=\frac{\partial }{\partial x}\left(\left(\nu+\frac{\nu_t}{\sigma_\varepsilon}\right)\frac{\partial \varepsilon}{\partial x}\right)+\frac{1}{y}\frac{\partial }{\partial y}\left(y\left(\nu+\frac{\nu_t}{\sigma_\varepsilon}\right)\frac{\partial \varepsilon}{\partial y}\right)+ \\ +C_1\frac{\varepsilon}{k}P-C_2\frac{\varepsilon^2}{k}+S_\varepsilon, \tag{7}$$

respectively, where

$$P=\nu_t\rho_w\left[2\left(\frac{\partial u}{\partial y}\right)^2+2\left(\frac{\partial v}{\partial x}\right)^2+2\left(\frac{u}{r}\right)^2+\left(\frac{\partial u}{\partial x}+\frac{\partial v}{\partial y}\right)^2\right] \tag{8}$$

is the generation of turbulent kinetic energy due to mean velocity gradients (due to shear, that is), and

$$G=-g\frac{\nu_t}{\sigma_t}\frac{\partial \rho}{\partial x} \tag{9}$$

corresponds to the generation of turbulent kinetic energy due to buoyancy, where $\sigma_t = 0.85$ is the turbulent Prandtl number. The sludge density, ρ, in eqn (9) is expressed in terms of the sludge concentration, X, using eqn (4). In eqns (6) and (7), $\sigma_k = 1.0$ and $\sigma_\varepsilon = 1.3$ are the turbulent Prandtl numbers for k and ε, respectively. In eqn (7), $C_1 = 1.44$ and $C_2 = 1.92$ are constants. For stably stratified flow, which prevails in secondary clarifiers and which tends to suppress turbulence ($G < 0$), the effect of buoyancy on the dissipation of turbulent kinetic energy may be neglected [1].

Two source terms, $S_k = -(q_{rec}/V_{rec})k$ and $S_\varepsilon = -(q_{rec}/V_{rec})\varepsilon$, appear in eqns (6) and (7), respectively, which we use to account for the effect of the sludge removal on the turbulence kinetic energy and its dissipation rate. Both S_k and S_ε, and also G, are built into the CFD code using UDFs.

4 Activated sludge rheology

We have used a rotational viscometer to carry out our on-site rheology experiments. These experiments have shown that at low strain rates, typical of the flow in secondary clarifiers, the activated sludge exhibits Casson-type non-Newtonian flow behaviour. At larger strain rates, Bingham-type flow behaviour was observed. Our observations agree well with those made by Dollet [4].

The Casson equation for the dynamic viscosity, μ, may be given as

$$\mu=\nu\rho_w=\left(\frac{K_1}{\dot{\gamma}^{1/2}}+K_2\right)^2, \tag{10}$$

where $\dot{\gamma}$ is the strain rate, K_1 is the Casson yield stress parameter, and K_2 is the Casson viscosity parameter. Our rheology experiments show that K_1 depends quadratically on the concentration,

$$K_1 = C_1 X^2 + C_2 X \,. \tag{11}$$

Our experiments suggest further that K_2 is independent of the concentration for $X \geq X^*$ = 2 kg m^{-3} and equal to the mean value, $\overline{K}_2$. For the water viscosity value, μ_w, to emerge correctly as $X \to 0$, K_2 is assumed to depend linearly on the concentration on the interval $0 < X < X^*$. Thus,

$$K_2 = \begin{cases} \overline{K}_2 & (X \geq X^*) \\ \mu_w^{1/2} + \dfrac{(\overline{K}_2 - \mu_w^{1/2})}{X^*} X & (0 < X < X^*) \end{cases}. \tag{12}$$

The values of the parameters in eqns (11) and (12) are given in table 1 for three different temperatures. During the experiments, which were conducted over three days in April 2005, the concentration was varied between 2.8 and 9.5 kg m^{-3} using dilution and decantation. The sludge samples were taken at the outlet of the aeration basin. We have repeated our rheology measurements in July 2005 and found that the rheological flow behaviour was unchanged. Eqns (10) to (12) are built into the CFD code using a UDF.

Table 1: Viscosity parameters in eqns (11) and (12) for varying temperatures, T. The temperature in the clarifier was 15°C in March and April, and 20°C in July.

T [°C]	$C_1 \left[\dfrac{\mathrm{m}^{11/2}}{\mathrm{kg}^{3/2}\,\mathrm{s}}\right]$	$C_2 \left[\dfrac{\mathrm{m}^{5/2}}{\mathrm{kg}^{1/2}\,\mathrm{s}}\right]$	$\overline{K}_2 \left[\dfrac{\mathrm{kg}^{1/2}}{\mathrm{m}^{1/2}\,\mathrm{s}^{1/2}}\right]$	$\mu_w^{1/2} \left[\dfrac{\mathrm{kg}^{1/2}}{\mathrm{m}^{1/2}\,\mathrm{s}^{1/2}}\right]$
10	0.00307	0.0187	0.0463	0.0362
15	0.00281	0.0176	0.0445	0.0341
20	0.00319	0.0146	0.0436	0.0361

5 Conservation of particulate mass and sludge settling

The concentration field in the clarifier is governed by a convection-diffusion equation, which may be given as [1]

$$\frac{\partial X}{\partial t} + \frac{\partial((u-u_s)X)}{\partial x} + \frac{\partial(vX)}{\partial y} = \frac{\partial}{\partial x}\left(\frac{\nu_t}{\sigma_s}\frac{\partial X}{\partial x}\right) + \frac{1}{y}\frac{\partial}{\partial y}\left(y\frac{\nu_t}{\sigma_s}\frac{\partial X}{\partial y}\right) + S_X \,, \tag{13}$$

where $\sigma_s = 0.7$ is the turbulent Schmidt number, $u_s = u_s(X)$ is the settling velocity function, and $S_X = -(q_{rec}/V_{rec})X$ is the sludge removal source term.

The settling velocity, u_s, is expressed in terms of the concentration, X, using the double-exponential function of Takács *et al.* [5],

$$u_s = u_{s0} \exp[-r_h (X - X_{ns})] - u_{s0} \exp[-r_p (X - X_{ns})] \,. \tag{14}$$

The maximum settling velocity, u_{s0}, and the parameter that describes hindered settling, r_h, were determined from settling experiments. The minimum sludge

concentration, X_{ns}, describes the concentration of non-settleable solids in the effluent, and its value has been measured by decantation. The parameter that describes particulate settling at low sludge concentrations, r_p, is obtained from a fit of eqn (14) to the experimental settling data. It is generally an order of magnitude larger than r_h [6].

From our settling experiments, we found values for u_{s0} that vary between 0.89 and 1.22 mm s^{-1}, and for r_h that vary between 0.225 and 0.284 m^3 kg^{-1}. The value for X_{ns} was found to be 5.2×10^{-3} kg m^{-3}, and we have used a value of 2.5 m^3 kg^{-1} for r_p. The on-site settling experiments were conducted in March and April 2005, and in July 2005. The results of these settling velocity measurements agree well with literature data [6].

We have added eqn (13), including the settling velocity function, eqn (14), the sludge removal source term, S_X, and the turbulent dispersion coefficient, ν_t/σ_s, to the CFD code as a user-defined scalar equation in Fluent using UDFs.

6 Computational domain and sludge removal zone

The clarifier has a depth of 3 m everywhere and a diameter of about 33 m. Settled sludge is removed from the bottom region of the clarifier by means of suction-lift through an array of six suction pipes. These pipes are situated underneath the slowly rotating clarifier bridge and remove sludge locally in the near-bottom region underneath the bridge. The suction-lift sludge withdrawal mechanism thus disturbs the otherwise axisymmetric geometry of the clarifier. To reduce computational efforts, we have abstracted the sludge withdrawal mechanism with a disk-like sludge removal zone in the near-bottom region of the clarifier in our axisymmetric CFD model. In the CFD model, sludge is thus removed everywhere in the near-bottom region of the clarifier.

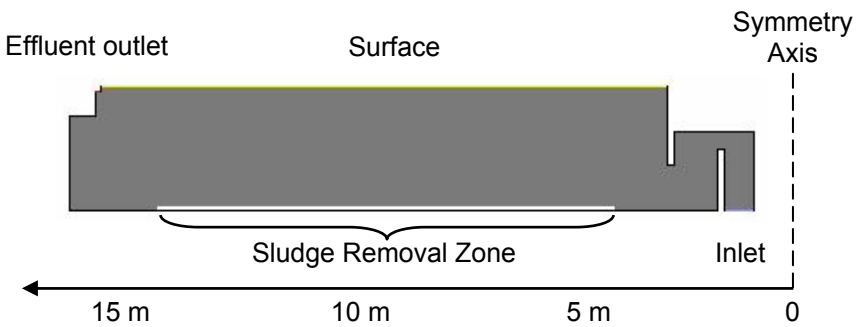


Figure 2: Computational domain and boundaries of the clarifier model.

The computational domain is shown in fig. 2, where the disk-like sludge removal zone in the near-bottom region of the clarifier is indicated (in white). The volume of the sludge removal zone, V_{rec}, can be calculated using

$$V_{rec} = \pi(R_o^2 - R_i^2)h\,. \tag{15}$$

with an inner radius of R_i = 3.7 m, an outer radius of R_o = 14.7 m, and a height of h = 0.15 m from the clarifier bottom, the volume of the sludge removal zone is V_{rec} = 2.86 m^3. The height of the sludge removal zone corresponds to the lower end of the suction pipes, and the distance $R_o - R_i$ = 11.0 m is the length of the array of suction pipes underneath the bridge.

7 Boundary conditions

At the clarifier inlet, we apply the measured inlet concentration, X_{in}, and the inlet velocity components, u_{in} and v_{in}. The axial component of the inlet velocity is determined from the measured flow rate, Q_{in}, and the cross-sectional area,

$$u_{in} = \frac{Q_{in}}{\pi(R_{a,o}^2 - R_{a,i}^2)}, \tag{16}$$

where $R_{a,o}$ and $R_{a,i}$ are the outer and the inner radius of the inlet annulus, respectively, and Q_{in} is the flow rate at the clarifier inlet. The radial component of the inlet velocity is zero, $v_{in} = 0$.

The turbulent kinetic energy at the inlet, k_{in}, is calculated using

$$k_{in} = 1.5 \times (I_u u_{in})^2, \tag{17}$$

where $I_u = 0.05^2$ is the turbulence intensity [1]. Its dissipation rate at the inlet, ε_{in}, is obtained from

$$\varepsilon_{in} = \frac{C_\mu^{3/4} k_{in}^{3/2}}{\kappa L_u}, \tag{18}$$

in which $\kappa = 0.4$ is the von Kármán constant. The turbulence length scale, L_u, is estimated using the recommendations of Lakehal *et al*. [1].

The movement of the free surface is neglected. The axial velocity component is set to zero at the surface, and the radial velocity component is computed assuming full slip. The gradient of the radial velocity and the gradients of all scalar variables normal to the surface are set to zero.

At the effluent outlet boundary, the values of the variables are extrapolated from computed near-outlet values, so that the streamwise gradients are zero.

The no-slip condition must be obeyed at all solid boundaries. The concentration gradients perpendicular to all solid walls are zero. We use logarithmic wall functions to model the turbulent flow in the near-wall region.

8 Computed results and comparison with measurements

The computed velocity field and sludge distribution is shown in figs. 3 and 4, respectively. We note that the steady-state conditions were computed using a time-marching procedure to facilitate convergence. The difference in density between incoming mixed liquor and clear water in the inlet region of the clarifier directs the flow downwards before the sludge mixture spreads out into the clarifier. Fig. 3 shows that the main flow is directed along the upper limit of the sludge blanket before leaving the clarifier through the effluent outlet. The concentration field in fig. 4 shows the layered structure of the sludge blanket.





Figure 3: Velocity field in units of [m s^{-1}] in the clarifier for 7 July 2005 (X_{in} = 4.93 kg m^{-3}, q_{rec} = 100.4 kg s^{-1}, u_{in} = 0.065 m s^{-1}).



Figure 4: Concentration field in units of [kg m^{-3}] in the clarifier for 7 July 2005 (X_{in} = 4.93 kg m^{-3}, q_{rec} = 100.4 kg s^{-1}, u_{in} = 0.065 m s^{-1}).

The comparison of measured and computed concentration profiles in figs. 5 and 6 show that the model predicts the sludge distribution in the inlet region well. At longer radial distances from the centre of the clarifier, the model underpredicts and overpredicts the height of the sludge blanket for the data of March and July, respectively. Unequal sludge withdrawal through the suction pipes or dynamic flow conditions during the measurements may be the cause of these discrepancies. The concentration values that were measured near the clarifier bottom in July are not reproduced by the CFD model (fig. 6). However, the average concentration value in the sludge removal zone computed by the CFD model (9.04 kg m^{-3}) compares very well to the value that was measured in the recycle stream (9.71 kg m^{-3}). The computed effluent concentrations for March and July are nearly equal, at 10.7 and 12.9 g m^{-3}, respectively, which agrees well with our measured effluent concentration values (6 to 16 g m^{-3} for all our measurements).

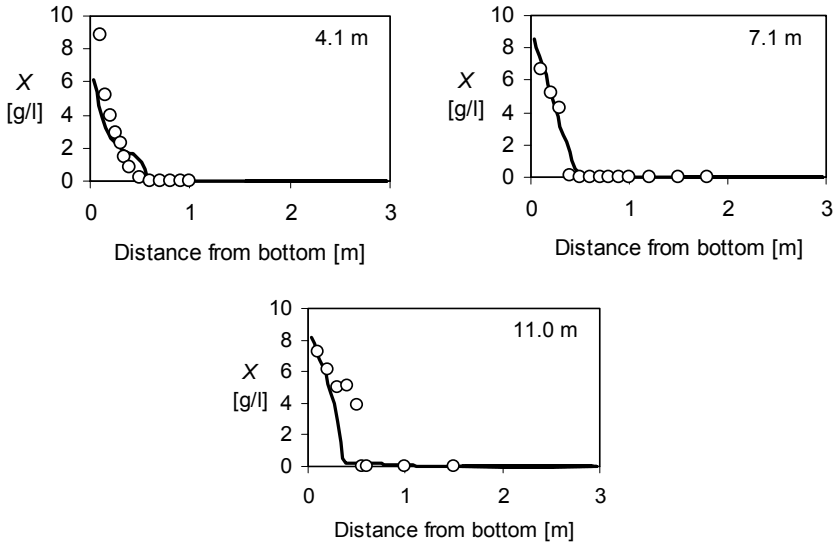


Figure 5: Computed (lines) and measured (symbols) concentration profiles in the clarifier at varying radial distances from the clarifier centre for 31 March 2005 (X_{in} = 3.91 kg m^{-3}, q_{rec} = 75.7 kg s^{-1}, u_{in} = 0.049 m s^{-1}).

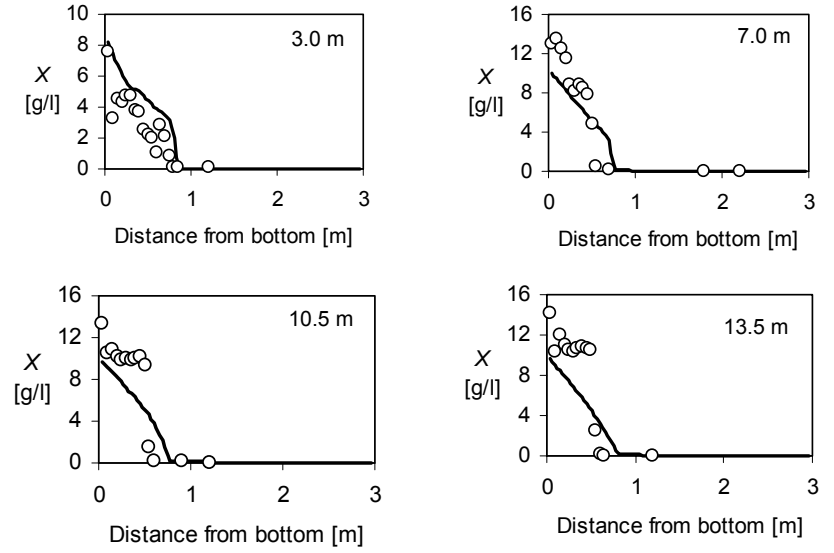


Figure 6: Computed (lines) and measured (symbols) concentration profiles in the clarifier at varying radial distances from the clarifier centre for 7 July 2005 (X_{in} = 4.93 kg m^{-3}, q_{rec} = 100.4 kg s^{-1}, u_{in} = 0.065 m s^{-1}).

9 Conclusions

We have developed an axisymmetric CFD model within the CFD code Fluent 6 that predicts the sedimentation of activated sludge in secondary clarifiers. On-site measurements were carried out at the wastewater treatment plant of Saint Malo (France), where the clarifiers are equipped with suction-lift sludge removal systems. The model employs negative source terms in the governing field equations to simulate this sludge withdrawal mechanism. These source terms remove the sludge within a sludge removal zone adjacent to the clarifier bottom. Sludge rheology measurements showed that the flow behaviour in the clarifier is well described using the Casson viscosity model. Settling experiments provided the parameters for the double-exponential settling velocity function. The computed sludge distribution compares well with measured concentration profiles in the inlet region of the clarifier. At larger distances from the clarifier centre, the prediction of the sludge blanket height is less good, which may be caused by unequal sludge withdrawal and dynamic flow conditions during the measurements. The concentrations in the recirculation stream and in the effluent outlet are well predicted by the CFD model.

Acknowledgement

M. Weiss and B. Gy. Plosz gratefully acknowledge financial support from the European Commission for two industry-host Marie Curie post-doctoral research fellowships.

References

[1] Lakehal, D., Krebs, P., Krijgsman, J. & Rodi, W., Computing Shear Flow and Sludge Blanket in Secondary Clarifiers. *Journal of Hydraulic Engineering*, pp. 253 – 262, March 1999.

[2] Dahl, C., Numerical Modelling of Flow and Settling in Secondary Settling Tanks. *PhD Thesis*, Aalborg University, Denmark, 1993.

[3] Nopens, I., Modelling the Activated Sludge Flocculation Process: A Population Balance Approach. *PhD Thesis*, University of Gent, Belgium, 2005.

[4] Dollet, P., Characterisation of the State of Flocculation of Activated Sludge Using Rheological Measurements (in French), *PhD Thesis*, University of Limoges, France, 2000.

[5] Takács, I., Patry, G.G. & Nolasco, D., A Dynamic Model of the Clarification-Thickening Process. *Water Research*, **25(10)**, pp. 1263 – 1271, 1991.

[6] Ekama, G.A., Barnard, J.L., Günthert, F.W., Krebs, P., McCorquodale, J.A., Parker, D.S. & Wahlberg, E.J., *Secondary Settling Tanks: Theory, Modelling, Design and Operation*. IAWQ: London, 1997.



Hydro-power plant equipped with Pelton turbines: basic experiments relating to the influence of backpressure on the design

A. Arch & D. Mayr
Institute for Hydraulic Engineering and Water Resources Management, Graz University of Technology, Austria

Abstract

Free-jet turbines working under backpressure conditions represent an economical alternative to conventional hydro-electric plant configurations. However, the air introduced into the tailwater generates an air/water mixture. Its reaction to a rising ambient pressure is at present being studied at the above Institute. This report deals with the effect an increase in ambient pressure has on the volume and consistency of the two-phase mixture and the rise velocity of air bubble swarms. In addition, a test set-up is described which was used to study the physical reaction of the water/air mixture to a change in ambient pressure conditions. The results and their effects on the configuration of free-jet turbines working under backpressure are discussed.
Keywords: air/water mixture, Pelton turbines, backpressure, bubble rise velocity.

1 Introduction

Recent developments have shown that multiple-jet Pelton turbines working under backpressure conditions in hydro-electric power plants may be an adequate choice in the case of (1) major tailwater-level oscillations, (2) full turbine operation between 0 and 100% being required without any major efficiency loss, and (3) the need to reduce the difference in turbine and pump levels to minimise construction cost.

Figure 1 is a section through the typical arrangement of a vertical-shaft backpressure Pelton turbine. As the jets emerging from the Pelton bucket hit the water surface in the tailrace channel, air is entrained and carried along into the



WIT Transactions on Engineering Sciences, Vol 52, © 2006 WIT Press
www.witpress.com, ISSN 1743-3533 (on-line)
doi:10.2495/AFM06051

tailwater, which causes an air/water mixture to form directly below the turbine, thus raising the level of the 2-phase mixture. Over the free-flow section which follows, the undissolved air de-trains and the flow depth of the two-phase mixture is reduced to that of single-phase flow. The section between the air entrainment, i.e. the entrance to the tailwater channel, to the point where the air has de-aerated completely, is termed the "de-aeration length". Apart from very small bubbles (d < 0.1mm, micro-bubbles), kept in suspension by turbulence and finally evacuated, no free undissolved air is present in the tailwater downstream of the de-aeration section.

Factors determining the rate of air entrainment are parameters such as the exit velocity at the Pelton bucket, the geometry of the turbine housing, the distance between the buckets and the tailwater level, etc. The air carried along into the tailwater needs replacing as otherwise the turbine runner would suck up an air/water mixture from below, which would involve a loss in turbine efficiency. Therefore, pipelines are provided to introduce air to the runner through openings in the turbine casing. This air has to be taken from the tailrace area, as the turbine housing and the tailrace channel form a closed system. Dissolved air in the water as a result of an increased ambient pressure is evacuated from the system. This air loss must continuously be compensated by the use of compressors.

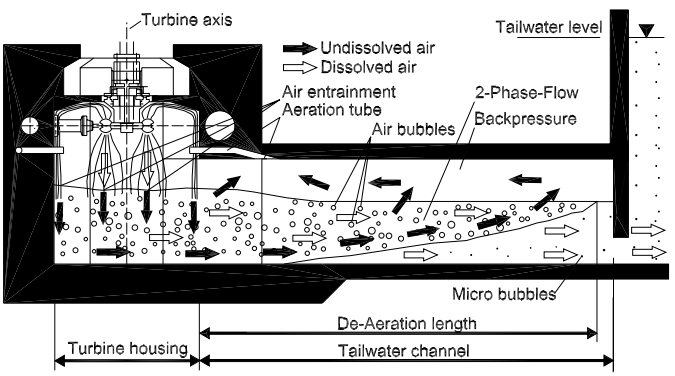


Figure 1: Schematic section through a vertical-shaft backpressure Pelton turbine.

Little is known at present about the influence of overpressure on air/water mixtures produced by a plunging free jet. For this reason, basic experiments have been conducted in a man-sized pressure chamber. The results will be summarised in the following paragraphs.

2 Overview of the relevant literature

Studies relating to the effects of an increase in ambient pressure on the processes of air entrainment and de-aeration in the turbine housing and the tailwater channel of Pelton turbines were conducted on a test rig by Ceravola and Noseda [1] in 1972. They built a turbine housing with runner and tailrace and operated it

under different backpressures. The turbine discharges ranged from 66 to 100 l/s (H ~ 120m). Figure 2 illustrates the flow conditions in the tailrace channel for different backpressures. The turbine housing, not shown, would be to the left of the photos. One can clearly see through the four windows that for a backpressure of $H_c = 11.21$ m, corresponding to 2.1 bar of absolute pressure, the white air/water mixture extends farther into the tailwater than for $H_c = 0.54$ m.

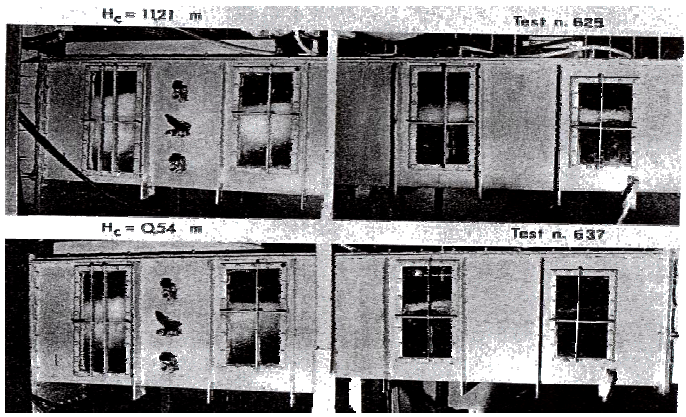


Figure 2: Model set-up by Ceravola / Noseda, tailrace, turbine discharge = approx. 88 l/s, flow direction from left to right.

Based on this and comparable photo studies, the authors concluded that the propagation of the air/water mixture changed substantially as backpressure rose. The solution of air, and the increased air requirements in the turbine chamber involved, was considered to be the reason for the thorough mixing process and, hence, the increased air requirements. The information published did, however, not allow any quantitative conclusions.

Krishna [2] gave a summary of flow processes studied in bubble-column reactors. Air bubble swarms were made to rise vertically through the water fill at different pressure stages. The author found bubbles and bubble swarms to show different rise-velocity behaviours, depending on whether the bubbles were small (d < 17mm) or large (d > 17mm). Krishna concluded that the rise velocity of bubbles smaller than 17 mm were only weakly influenced by the greater air density (resulting from a higher pressure level).

Letzel et al. [3] demonstrated that an increased system pressure influenced the rise velocity of the larger bubbles in bubble column reactors. This is illustrated by the measurements of gas holdup ε depending on superficial velocity U.

$$\varepsilon = \frac{(H - H_0)}{H}[-] \tag{1}$$

$$U = \frac{Q_{Air}}{A}[m/s] \tag{2}$$

where H is the depth of the air/water mixture in the bubble-column reactor and H_0 is the static water head of the static system, Q_{Air} is the air flow introduced at

the bottom, and A is the cross-sectional area of the reactor. Figure 3 demonstrates that for rising system pressures, the increased gradient of the gas holdup ε becomes steeper as the superficial velocity U increases. This suggests that the rise velocity is lower in the case of larger bubbles and thus is a function of the bubble diameter. The lower rise velocity may be explained by the bubble diameter decreasing along with increasing pressure. In physical terms, a higher system pressure may be considered to reduce the stability of the larger bubbles. Based on the Kelvin/Helmholtz stability theory referring to the stability of a gas/liquid interface on the assumption of infinitesimal disturbances of the surface, and on the basis of experiments, Letzel et al. demonstrated that a correction factor DF had to be applied for calculating the rise velocity V_b of large bubbles and gas holdup under pressures above atmospheric in order to allow for the changed air density ρ_G. This is written as

$$DF = \frac{V_B}{V_{B,atm}} = \frac{\varepsilon_{atm}}{\varepsilon} = \sqrt{\frac{\rho_{atm}}{\rho_G}}\ [-] \tag{3}$$

where $V_{B,atm}$ is the bubble-rise velocity, ε_{atm} the gas holdup and ρ_{atm} the air density at atmospheric pressure.

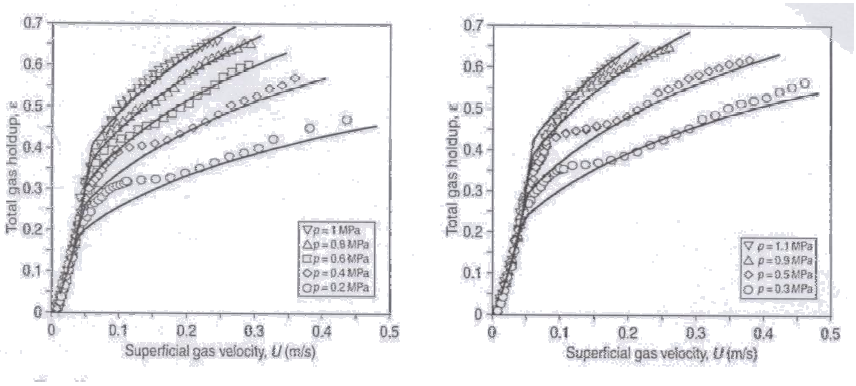


Figure 3: Influence of system pressure on gas holdup ε (taken from [2]).

3 Test set-up and tests

3.1 Test Set-up

The test set-up was built in a man-sized pressure chamber. It consisted of a vertical test cuboid in plexiglass provided with a nozzle at the top, and a feeding pipe equipped with a ball valve, an outlet shaft installed at the bottom of the cuboid, a measuring channel with a calibrated triangular weir, a buffer tank, and a rotary pump with an 8 m-long hose connection to the ball valve. The upright cuboid chamber, 374.4 cm² in horizontal area and 116.5 cm high, was equipped with a measuring screen with a spacing of 5 cm installed at the front. A measuring tape was fixed to the side (Figure 4).

The rotary pump circulated the water at a discharge of up to Q_{Max} = 0.4 l/s, depending on the position of the ball valve. A circular nozzle 5.25 mm in

diameter produced a jet directed vertically downward. The exit velocity of the jet at the nozzle, calculated from the nozzle diameter and from the discharge measured at the triangular weir, was 19.3 m/s at maximum system discharge. The maximum jet impact velocity was 19.6 m/s.

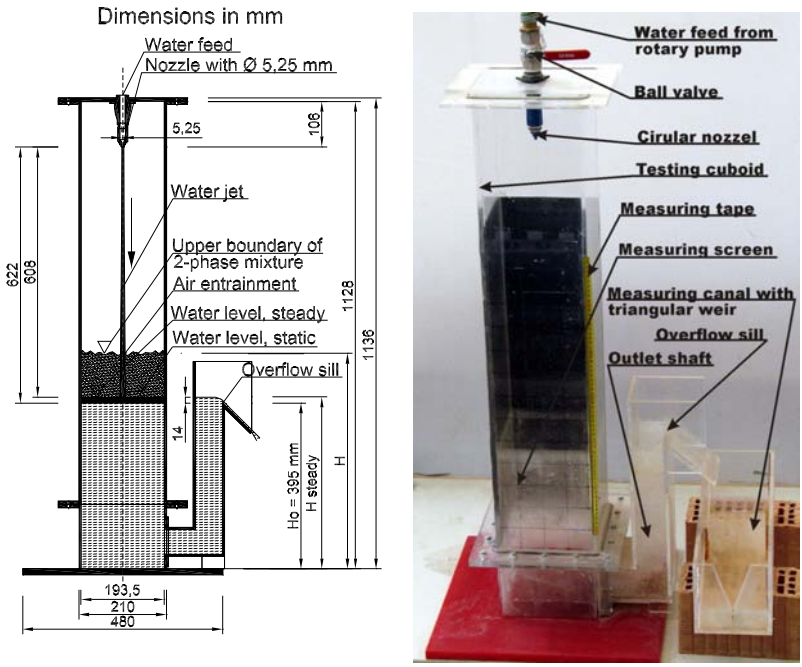


Figure 4: Test set-up.

At first, the cuboid was filled with water to a depth of 395 mm, which was determined by the fixed overflow sill of the outlet shaft. The static water volume in the steady condition was 14.79 litres. The medium used was tap water having a temperature of 20°C.

The steady water-volume condition within the cuboid was reached as a function of the respective discharge from the nozzle, dependent on the overflow characteristic of the overflow sill of the outlet shaft. After leaving the bottom of the chamber, the water climbed vertically through the outlet shaft and dropped over the overflow sill and into the measuring channel with its calibrated triangular weir (cone angle, 40°). The water flowing over the overflow sill was collected in a buffer tank of about 40-litre capacity. From there, the water was sucked in by the rotary pump and conveyed back to the nozzle through an 8 m long hose. The front of the chamber was filmed during the tests, using a video camera having a capability of 25 images per second.

3.2 The tests

Each test series, consisting of 13 tests, was run at constant absolute pressures of 1 bar (corresponding to atmospheric), 2.5 bar, and 4 bar, respectively, and at an

ambient temperature of 20°C throughout. The pressures were raised from one stage to the next within about three minutes. During the pressure increases, an air condition system was used to disperse the compression heat generated in the process, so as to keep the temperature at a constant 20°C.

In order to allow for the potential influence of air dissolving in water, the pump was shut off while the pressure was being raised in the chamber. During this process, the water surface was at rest. This was done to make sure that for each pressure stage, the first test was run with unsaturated water, since saturation is known to be greatly dependent on surface turbulence. Thus it was possible to draw conclusions with regard to the initial saturation and its influence on the behaviour of the air/water mixture.

During decompression from 4 bar to 1 bar, the pump kept working, and the depth of the two-phase mixture in the cuboid was measured for different pressures.

For each pressure level, 13 tests were run at different discharges, the first five tests with the rotary valve completely open, that is, at maximum discharge.

A test run consisted of (1) a phase of steady inflow from the nozzle for some 60 seconds and (2) the unsteady abrupt closing of the ball valve followed by a phase of some 15 seconds, during which the air bubbles raised to the surface and the two-phase mixture disintegrated. Analysis of the digital records allowed the determination of the rise velocity of the lower boundary of the bubble swarms, the gas holdup ε, the sinking velocity of the upper boundary of the air/water mixture, as well as the visual observation bubble size and the behaviour of the mixture.

4 Test results

4.1 Steady conditions

Figure 5 shows the air/water-mixture level under steady conditions and for a maximum system discharge prior to closing the rotary valve, for different ambient pressures.

The video analysis suggested that the water jet penetrating the mixture was slightly extended, the jet appeared to be torn apart to a greater width as the denser air passed through. The penetration depth of the jet was independent of the pressure. The limit ranged around 0.3 litres per second, or around a jet-impact velocity of 14.3 m/s at the static water surface, for each pressure stage. This led to the conclusion that the influence of an increase in ambient pressure on jet turbulence could be ignored. It was seen that, as the pressure increased, the surface of the air/water mixture was higher and more unsteady and that the minimum and maximum air/water mixture levels took longer to reach the steady condition after opening the ball valve. The bubbles of the air/water mixture appeared to be larger around the transition zone between air and mixture. (Our test set-up did not permit exact determination of the bubble diameters).

Figure 6 is a graph showing gas holdup ε, plotted against the jet-impact velocities. In the case under study, with water being fed from above, the steady water level was used as the level H_0 in formula (1) in order to account for the



theoretically larger water volume resulting from water bulking under the overflow at the vertical shaft. (Note: As air bubbles were allowed to escape through the vertical shaft at the higher inflows, this should be considered when interpreting the ε values.)

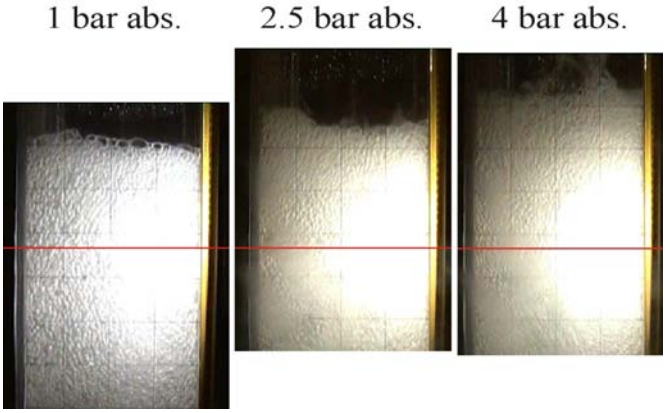


Figure 5: Steady condition, level of the air/water mixture for different pressures, continuous line indicates static water level.

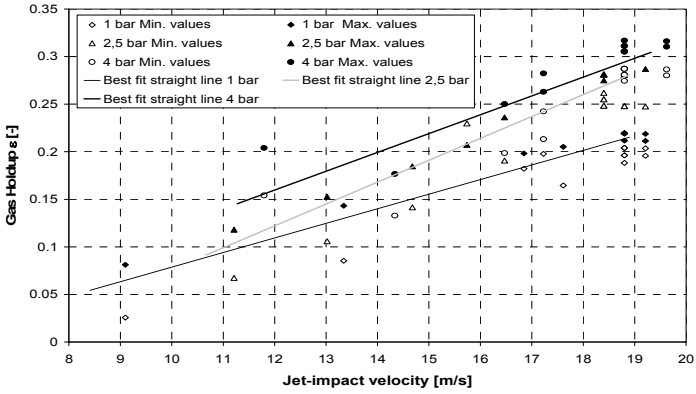


Figure 6: Gas holdup ε, plotted against jet-impact velocity at the steady water surface.

Minimum and maximum values are given in Figure 6 to account for the fact that the surface of the air/water mixture oscillated. In addition, best fit straight lines were entered into the diagram. As can be seen from the figure, gas holdup ε increases along with a rising pressure. The first tests of each series gave no significantly higher or lower air/water mixture levels as compared with the tests that followed. Saturation can, therefore, be assumed to have no influence on hydrodynamic behaviour. Figure 7 shows gas holdup ε plotted against pressure for maximum system discharge. Its value rose from about 0.21 for an absolute

pressure of 1 bar to 0.30 for an absolute pressure of 4 bar. Compression is depicted by the continuous line, decompression is shown by the broken line. During the phase of rapid decompression from 4 bar to 2.5 bar, the formation of micro-bubbles increased as a result of air degassing from the water. The lines for ε were practically identical for both decompression and compression.

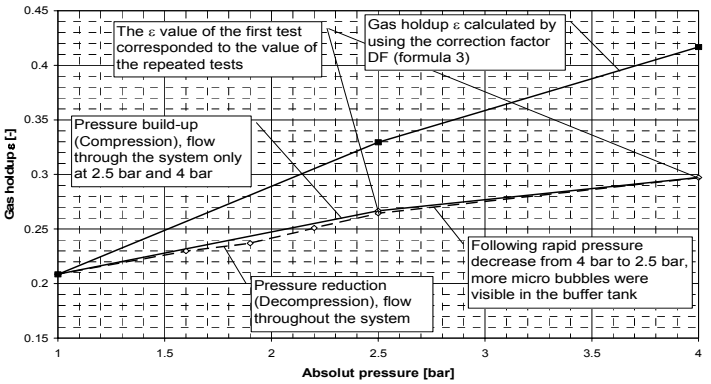


Figure 7: Gas holdup ε, for maximum system discharge, plotted against pressure.

Based on the measured value ε for 1 bar and using the equation for the correction factor DF (formula 3), a theoretical gas holdup for the studied pressure levels has been calculated. Figure 7 shows the line for the calculated ε-values, where a deviation from the measured values with 24 % for 2.5 bar and 40 % for 4 bar was found. Comparing the measured and calculated values for the gas holdup ε a general correlation could be achieved.

4.2 Unsteady conditions

Figure 8 is showing the upper and lower 2-phase boundary of the air/water mixture plotted against time, after system shut-down, for maximum discharge $Q_{Max} = 0.4$ l/s.

This graph demonstrates that for a raised ambient pressure, the upper boundary of the air/water mixture was about 1.4 and 1.62 times higher than at atmospheric pressure. However, the time needed for the air/water mixture to disintegrate remained at a constant 3 seconds, independently of the ambient pressure. The tests run at a low system discharge revealed, however, the ambient pressure to have a great impact on the disintegration time of the air/water mixture. The lower boundary of the air/water mixture, very much like the upper limit, was always higher under an increased ambient pressure than at atmospheric pressure.

The rise velocities of the bubble swarm, calculated from the slope of the lines representing the lower boundaries of the air/water mixture, were all situated within a range of about 10 to 12cm/s for all discharges and for each of the three pressure stages. This suggests that, for the ambient pressures used in the test, the

rise velocity of the swarms of small bubbles is independent of the ambient pressure, while the test results showed the sinking velocity of the upper boundary of the air/water mixture to be a function of discharge and ambient pressure. That means that the sinking velocity rises along with an increase in backpressure and discharge (Figure 9), i.e. a faster disintegration of the 2-phase mixture. Sinking was seen to be initially fast under conditions of maximum discharge. By the time the entrained air had de-aerated completely, the sinking velocity had decreased by about 50%. Further studies have shown the upper air/water mixture boundary to sink fairly evenly under conditions of low discharge (Figure 9).

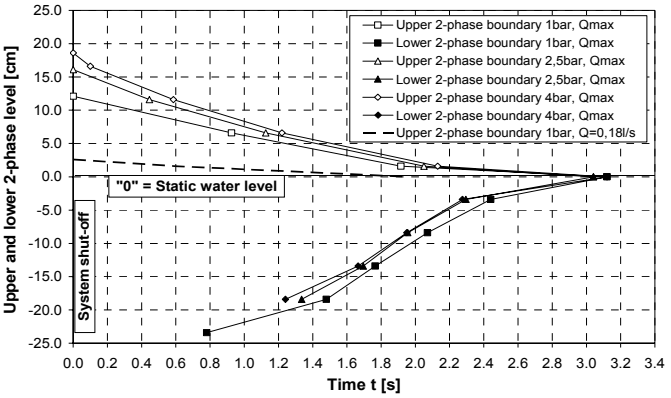


Figure 8: Mean decrease of the upper and lower boundaries of the air/water mixture for maximum system discharge Q = 0.4 l/s (extract from all the test measurements).

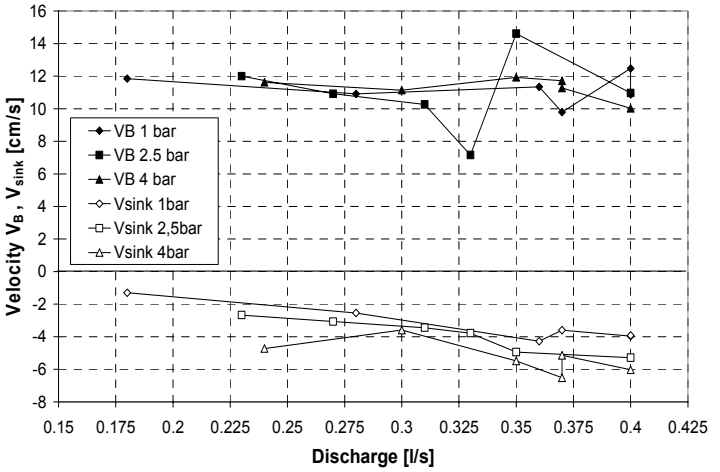


Figure 9: Rise velocity V_B of the bubble swarm and mean sinking velocity V_{sink} of the upper air/water mixture boundary for ambient pressures of 1 bar, 2.5 bar and 4 bar.

5 Summary and conclusion

Basic tests were conducted in a pressure chamber to study the effects of an increase in air pressure on the air/water mixture in the tailwater below Pelton turbines operating in backpressure mode. The results showed a rise in ambient pressure to increase the volume of the air/water mixture generated by a water jet. Gas holdup ε was seen to increase by a maximum of 55 %. For a plant equipped with Pelton turbines operating under backpressure, this may mean that the clearance between the upper boundary of the air/water mixture in the tailrace channel and the runner decreases as the backpressure increases. This would reduce the safety margin allowed for in the design of the turbine clearance. Where the selected clearance is too small, the runner risks sucking the air/water mixture in. The performed tests have supplied no direct quantitative results regarding the increase of the air/water mixture below the Pelton turbine. No difference was found to exist for ε between the initial tests and the remaining tests within each series, representing the conditions of initial saturation and complete saturation. This allows the conclusion that in pumped-storage plants operated under conditions of hydraulic short-circuit, the flow depths of the air/water mixture under backpressure conditions, at maximum discharge, will form independently of the degree of saturation, that is, independently of the load condition.

Analysis of the de-aeration process of the air/water mixture revealed the mean rise velocities of the bubble swarm to range between 10 cm/s and 12 cm/s, independently of the ambient pressure. The time needed for the undissolved air components to de-train and, hence, the de-aeration length, is, therefore, not expected to increase even under changed backpressure conditions. The design and location of the turbine aerators as well as the channel geometry from which the air has to be taken should allow for the increased level of the air/water mixture in the tailwater, as otherwise an air/water mixture might be sucked in instead of pure air.

References

[1] O. Ceravola and G. Noseda, Back pressure operation of Pelton turbines for ternary units in pumped-storage plants, IAHR-Symposium Rome, paper C3, 1972 (including discussion).

[2] R. Krishna, A scale-up strategy for a commercial scale bubble column slurry Reactor for Fischer-Tropsch Synthesis, Oil & Gas Science and Technology, Vol. 55 (2000), No. 4, pp. 359-393.

[3] Letzel et al., Influence of elevated Pressure on the Stability of Bubble Flows, Chem. Eng. Sci., Vol. 52, pp.3733-3739.



Section 11
Turbulence flow

This page intentionally left blank

CFD modelling of wall-particle interactions under turbulent flow conditions

M. Mollagee
Department of Chemical Engineering, University of Johannesburg, South Africa

Abstract

The effects of particle roughness and the impact it has on the development of turbulence in non-Newtonian slurry flow remains difficult to predict. The common analytical tools used take only the viscous characteristics of the slurry into account. Homogenous solid-liquid suspensions are often described using different continuum models. Evidence suggests that these models may be inadequate due to the presence of solid particles sharply influencing velocity gradients. Experimental work was conducted using homogenous non-Newtonian slurries. Comparisons were made of wall-particle interactions experienced for slurries with different representative particle sizes. This was subsequently modeled using the FLUENT Computational Fluid Dynamics software to validate these findings. This paper documents these findings and presents a comparison between the experimental and the computational model.
Keywords: non-Newtonian slurries, experimental versus computational methods, viscous sub-layer, wall turbulence, wall-particle interactions.

1 Introduction

Turbulent flow of non-Newtonian fluids continues to attract the attention of researchers from fields as diverse as physics, hydraulics and engineering. The flow dynamics differs markedly when compared to the behaviour under laminar conditions. Reliable prediction has presented complex theoretical as well as practical problems, both from the point of view of the fundamental physics of the phenomenon as well as in engineering practice. The principle dilemma is whether the turbulent headloss can be predicted from the rheology of the slurry alone, or whether other properties also play a role. In the case of mine tailings where slurries are regarded as stratified flow systems, accurate prediction can be challenging from two perspectives:



WIT Transactions on Engineering Sciences, Vol 52, © 2006 WIT Press
www.witpress.com, ISSN 1743-3533 (on-line)
doi:10.2495/AFM06052

a. The slurry has to be characterised as non-Newtonian, which is often not the case;
b. When operating within the economically profitable transition zone just prior to the onset of turbulence, most modelling tools are of an empirical nature. Treating a slurry as a continuum aggravates the problem.

2 Literature review

2.1 Non-Newtonian turbulence models

There are many different approaches to turbulence modelling for non-Newtonian slurries in pipes. Some of these models are presented below.

Wilson and Thomas [1] developed a model that produced an analysis of turbulent flow based on enhanced micro-scale viscosity effects. The viscous sub-layer is predicted to thicken by an area ratio (A_r). This ratio is defined as the relation between the non-Newtonian and assumed Newtonian rheograms under identical shear conditions. The area ratio is given by:

$$A_r = 2\left[\frac{1+\frac{\tau_y}{\tau_0}}{1+n}\right] \tag{1}$$

The velocity distribution is given by:

$$u^+ = \frac{u}{V_*} = 2.5\ln\left[\frac{\rho V_*}{\mu}\right] + 5.5 + 11.6\left(A_r - 1\right) - 2.5\ln\left(A_r\right) \tag{2}$$

Treating slurries as a continuum works well in the laminar regime where flow is dominated by viscous effects. Slatter [2] proposed a model that accounts for the effects of particle roughness. The model suggests that if the solid particles are of the same order of magnitude as the viscous sub-layer the continuum approximation is compromised in the wall region. A new Reynolds number was developed to predict the onset of turbulence. Schlichting [3] was the first to suggest that a roughness Reynolds number can be used to determine the various regions of turbulent flow in pipes. It is formulated as follows:

$$\mathrm{Re}_r = \frac{8\rho V_*^{\,2}}{\tau_y + K\left[\frac{8V_*}{d_x}\right]^n} \tag{3}$$

If $\mathrm{Re_r} < 3.32$, smooth wall turbulence exists and the mean velocity is given by:

$$\frac{V}{V_*} = 2.5\ln\left(\frac{R}{d_x}\right) + 2.5\ln \mathrm{Re}_r + 1.75 \tag{4}$$

If Rer > 3.32, fully developed rough wall turbulent flow exists and the mean velocity is given by:

$$\frac{V}{V_*} = 2.5 \ln\left(\frac{R}{d_x}\right) + 1.75 \tag{5}$$

Chilton and Stainsby [4] concluded that the friction factor could be directly correlated to the Reynolds number provided that the viscosity at the wall is properly evaluated. Many researchers have supported this conclusion.

2.2 Evidence of particle roughness

Park *et al.* [5] used laser techniques to investigate the turbulent structure of non-Newtonian slurries. Higher intensities were observed in the wall region when compared with that of air. Pokryvalio and Grozberg [6] used electro-diffusion methods to measure the velocity profile of Bentonite clay suspensions and a similar phenomenon had been reported. Mun [7] used fine and coarse ilmenite and coal suspensions and compared this to 24 other correlations in the literature. A variation in turbulence intensity as a function of particle size was found.

2.3 The CFD model

The commercial CFD software package FLUENT 6.1.22 was used for solving the governing set of equations. The discretization equations along with initial boundary conditions were solved using the segregated solver to obtain a numerical solution. Simulating flows in the near-wall region is common in many applications. This is due to the presence of the viscous sub-layer where molecular diffusion and viscous dissipation dominates. The sub-layer has an influence on the overall development of turbulence. Adequate numerical resolution requires a very fine mesh due to the thinness of this layer. The high-Reynolds number (HR) models do not in themselves provide resolution of the viscous sub-layer. The boundary conditions in the case of HR models are represented by wall functions with a limited application. It does however significantly save on computational time. White and Christoph [8] and Huang *et al.* [9] proposed a low-Reynolds (LR) k-ε model to address this problem.

2.3.1 Available models

Turbulent flows in general are significantly affected by the presence of a stationary wall. The mean velocity field is influenced by the no-slip condition that exists at the wall. Viscous damping tends to reduce the tangential velocity fluctuations while kinematic blocking reduces the normal fluctuations. Towards the outer part of the near-wall region the turbulence is rapidly augmented by the production of turbulent kinetic energy due to the large gradients in mean velocity. The solution variables in the wall region have large gradients and momentum and other scalar quantities occur vigorously. Accurate representation of flow in the near-wall region determines successful predictions of wall-bounded turbulent flows. The *k-ε*, *Reynolds Stress*, and *Large Eddy Simulation* models are all primarily valid for turbulent flow in the core of the flow domain under study. The *Spalart-Allmaras* and *k-ω* models are designed for application throughout the boundary layer provided that the wall mesh resolution is sufficient.

2.3.2 The near-wall region

The near-wall region can be sub-divided into three distinctive layers. The "*viscous sub-layer"* is the innermost layer. The molecular viscosity plays a dominant role in momentum and heat or mass transfer. Turbulence dominates in the outer "*fully turbulent layer*". There is an "*interim region*" between the viscous sub-layer and the fully turbulent layer where the effects of molecular viscosity and turbulence are equally important.

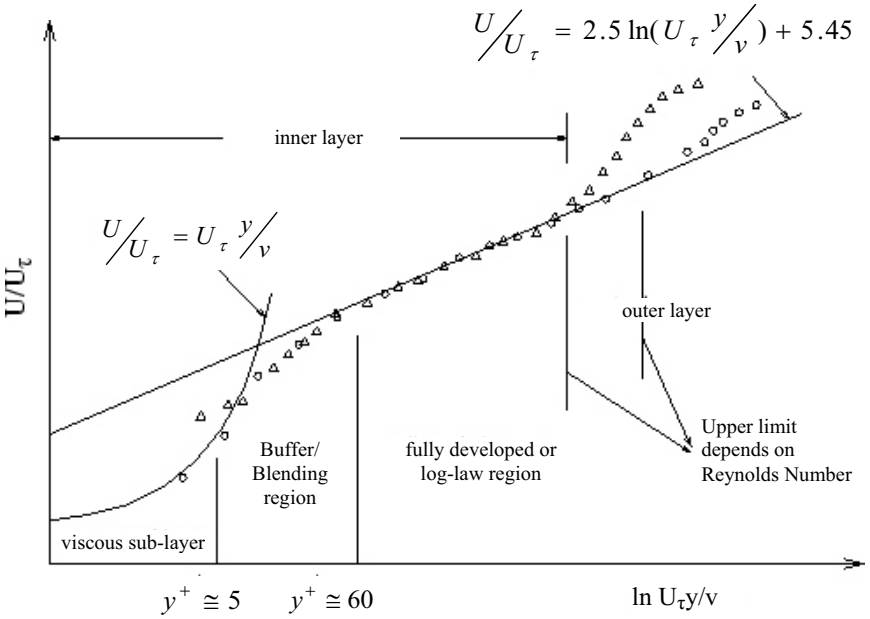


Figure 1: Sub-divisions of the near-wall region.

Traditionally there are two approaches to modelling the near-wall region. In the first approach the viscosity-affected inner region (viscous sub-layer and buffer layer) is not resolved. Semi-empirical formulae (wall functions) are used to bridge the region between the wall and the fully turbulent region. The use of wall functions averts the need to modify the turbulence models to account for the presence of the wall. In HR flows this approach saves computational resources in the near-wall region, where solution variables change rapidly and no resolution is required. It is inadequate in situations where the low-Reynolds-number effects are pervasive and the hypotheses underlying wall functions cease to be valid. Such situations require near-wall models that are valid in the viscosity-affected region and solvable all the way to the wall.

2.3.3 Two-layer model for enhanced wall treatment

A near-wall formulation that can be used with coarse meshes (wall-function meshes) as well as fine meshes (LR meshes) is required. In addition, excessive error should not be incurred for intermediate meshes that are too fine for the

near-wall cell centroid to lie in the fully turbulent region, but also too coarse to properly resolve the sub-layer. In FLUENT the wall region is resolved all the way to the viscous sub-layer. The two-layer approach is an integral part of the enhanced wall treatment and is used to specify both ε and the turbulent viscosity in the near-wall cells. In this approach the whole domain is subdivided into a viscosity-affected region and a fully turbulent region. A wall-distance-based turbulent Reynolds number, Re_y, demarcates the two regions:

$$\mathrm{Re}_y = \frac{\rho y \sqrt{k}}{\mu} \tag{6}$$

where y is the normal distance from the wall at the cell centres.

In the fully developed region the standard k-ε is employed. In the near-wall region the one-equation model of Wolfstein [10] is used. The turbulent viscosity μ_t is re-calculated as follows:

$$\mu_{t,2-layer} = \rho C_\mu \ell_\mu \sqrt{k} \tag{7}$$

The length scale is found from Chen and Patel [11]:

$$\ell_\mu = y c_\ell (1 - e^{-\mathrm{Re}_y / A_\mu}) \tag{8}$$

The two-layer formulation is used as part of the enhanced wall treatment where it is smoothly blended with the HR μ_t definition from the outer region as proposed by Jongen [12]:

$$\mu_{t,enhanced} = \lambda_\varepsilon \mu_t + (1 - \lambda_\varepsilon)\mu_{t,two-layer} \tag{9}$$

μ_t is the HR definition for the k-ε model. A blending function λ_ε is chosen such that it is equal to unity far from the walls and zero close to the wall:

$$\lambda_\varepsilon = \frac{1}{2}\left[1 + \tanh\left(\frac{\mathrm{Re}_y - \mathrm{Re}^*_y}{A}\right)\right] \tag{10}$$

The constant A determines the width of the blending function. A width is defined such that the value of λ_ε will be within 1% of its far-field value:

$$A = \frac{\left|\Delta \mathrm{Re}_y\right|}{\tanh(0.98)} \tag{11}$$

$\Delta\mathrm{Re}_y$ would typically be assigned a value of between 5% and 20% of $\Delta\mathrm{Re}^*_y$. Blending is aimed at preventing the solution convergence from being impeded when the k-ε solution does not match the two-layer solution.

3 Experimental

3.1 Apparatus

The experimental work was conducted as part of the slurry flow research programme at the Cape Peninsula University of Technology (Cape Town, South Africa). A laboratory-scale tube viscometer with pipes of 4 different diameters

was used to generate the experimental data. Mollagee [13] provides more of the construction-related detail.

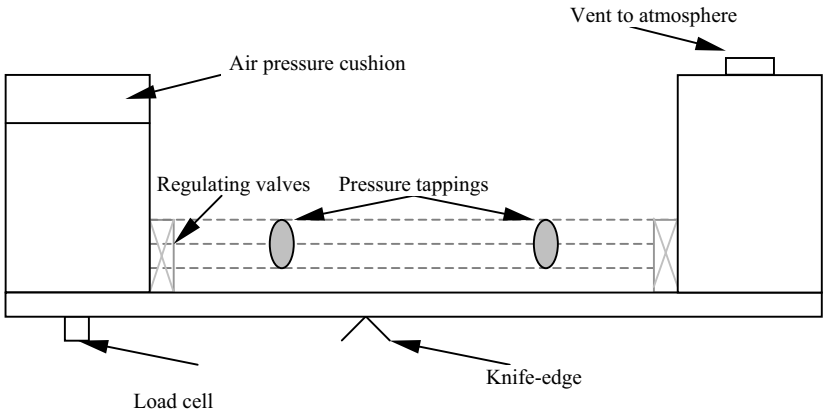


Figure 2: Layout of tube viscometer.

3.2 Mixtures

Sand was introduced into a pure kaolin mixture to gradually increase the particle sizes. Tests were conducted at different relative densities to establish the amount of kaolin required to fully suspend the sand. A volumetric concentration of 6% was used as the baseline test set.

Table 1: Summary of slurry properties.

Test Set	Slurry	Cv (%)	τ_y [Pa]	K	n	ρ_s
K_1	Pure Kaolin	6	5.077	0.0043	0.719	1091.8
K_2	Kaolin/sand	9	7.522	0.014	0.845	1139.1
K_3	Kaolin/sand	12	9.848	0.018	0.831	1200.8
K_4	Kaolin/sand	15	11.55	0.031	0.786	1244.5

3.3 Numerical computation

The differential equations governing turbulent flow in a straight pipe could be written in tensor form in the master Cartesian coordinate system as:
Conservation equation for mass:

$$\nabla.(\rho\vec{u}) = 0 \tag{12}$$

Conservation equation for momentum:

$$\nabla.(\vec{u}\vec{u}) = -\nabla p + \nabla.\left[\mu\left(\nabla\vec{u} + \nabla\vec{u}^{\Gamma}\right)\right] + \rho\vec{g} + \vec{F} \tag{13}$$

The governing equations were solved with a control volume finite element method. The FLUENT/UNS code [14] has been used as the numerical solver.

3.3.1 Grid system

An unstructured non-uniform grid system was used to discretize the governing equations. The convection term in the governing equations was modeled with a bounded first-order upwind scheme. A typical hexahedral element was applied for the three-dimensional grid. The pattern used for this paper consists of 27 nodes, with information stored on the vertex, mid-edge mid-face and center nodes.

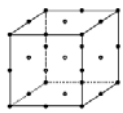


Figure 3: 27-node pattern.

3.3.2 Solution strategy

A second-order upwind discretization scheme was used for the momentum equations while a first-order scheme was used for the turbulent kinetic energy and turbulent dissipation energy. These schemes ensured in general satisfactory accuracy, stability and convergence. Other strategies employed were reduction of under-relaxation factors for momentum, turbulent kinetic energy and turbulent dissipation energy to resolve any non-linearity.

4 Results and discussion

The various turbulent models under review are presented in Table 2, and Figures 4 and 5. The laminar data obtained during the rheological characterisation procedure was obtained through integration across the length of the pipe to furnish the parameters for the Power Law Model. This was found to agree with the literature in that intermediate values for fluid consistency (K) were obtained.

The Yield Pseudoplastic model produced the lowest average percentage error (APE) when compared to the other rheological models. The Wilson and Thomas (W & T) model produced the highest error with the Slatter model performing the best with an APE of 9.84%. The Chilton and Stainsby (C & S) and the CFD model performed similarly. This could partially be attributed to the numerical one-dimensional finite difference model they had used [15]. The CFD model consistently produced APE's in the range of 11.96 (lowest) and 21.00 (highest). The dispersion of particles due to turbulence was predicted using the stochastic tracking model or the particle cloud model. In both models the particles have no direct impact on the generation or dissipation of turbulence in the continuous phase. This was of concern and could be the reason behind the higher APE's. The modelling in the wall region needs to be further investigated.

Figure 4 demonstrates the effect of increasing the concentration and coarse fraction of the slurry by the metered addition of amounts of sand to a pure kaolin mixture. This was done to increase the representative particle size. The effects of increased concentration can be seen when examined in conjunction with the Slatter model.

Table 2: Tabulated average percentage error by rheological model.

Slurry	W & T	Slatter	C & S	CFD
K1_5mm	19.59	8.96	8.08	9.47
K1_13mm	18.82	9.51	10.60	11.96
K1_28mm	10.04	7.19	18.94	16.28
K1_46mm	6.29	11.71	20.25	21.00
K2_5mm	17.00	8.31	3.16	16.89
K2_13mm	19.40	9.65	7.93	15.24
K2_28mm	26.59	19.42	9.36	14.77
K2_46mm	11.87	6.49	6.57	10.55
K3_5mm	20.80	16.39	7.00	13.90
K3_13mm	12.97	8.63	4.92	17.21
K3_28mm	17.77	11.94	7.11	13.84
K3_46mm	10.57	7.23	3.82	8.45
K4_5mm	12.69	11.62	14.02	13.33
K4_13mm	8.68	5.51	8.50	9.66
K4_28mm	13.88	7.28	16.23	14.57
K4_46mm	6.81	7.53	18.90	17.14
AVERAGE	**14.61**	**9.84**	**10.34**	**14.02**

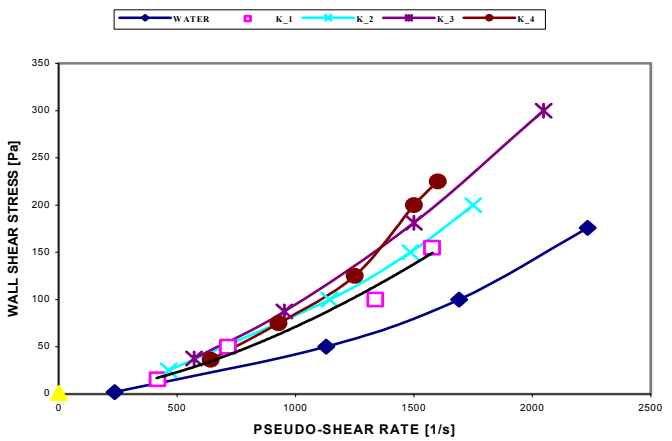


Figure 4: Effect of increasing concentration for 46mm pipe.

Figure 5 gives us a snapshot of the various turbulence models under discussion. The Slatter (APE–9.51%) and C & S models (APE-10.60%) were virtually super-imposable for the 13mm pipe. The FLUENT model over-predicted at low shear rates and under-predicted at higher wall shear stresses.

Although the APE's were only 1% higher (11.96%), this was only due to the net compensating effect across the data spectrum. This erratic scatter can be attributed to modelling inconsistencies in the wall region where particle roughness effects has been proven to exist.

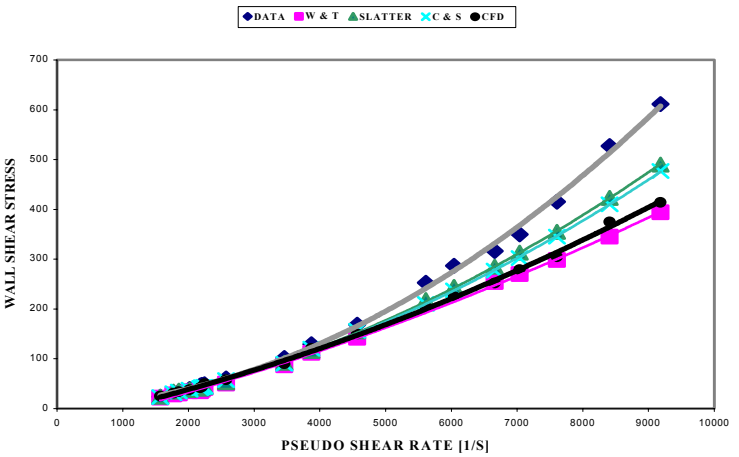


Figure 5: Pseudo shear diagram for K_1 mixture – 13mm pipe.

5 Conclusion

The phenomenon of turbulence for non-Newtonian slurry flow in pipelines was examined in this paper. Computational fluid dynamics software (FLUENT 6.1) was used to perform the numerical calculations. The numerical profile was compared to the particle roughness model of Slatter, the viscous sub-layer model of Wilson and Thomas and the Blasius-type numerical model of Chilton and Stainsby. The agreement between experiment and simulation was found to be within a 15% range of error and can be regarded as satisfactory. The two areas requiring more in-depth investigation are the near-wall region and the particle tracking techniques used in this study.

Acknowledgement

The author wishes to thank the University of Johannesburg for providing the opportunity to proceed with this work.

References

[1] Wilson K C and Thomas A D (1985), A new analysis of the turbulent flow of non-Newtonian fluids, *Can. J. Chem. Eng.,* 63, 539-546.

[2] Slatter P T (1994), Transitional and turbulent flow of non-Newtonian slurries in pipes, *PhD Thesis*, University of Cape Town.

[3] Schlichting H (1960), Chapter XX in *Boundary Layer Theory*, 4th edition, McGraw-Hill, New York.
[4] Chilton R A and Stainsby R (1996), Prediction of pressure losses in turbulent non-Newtonian flows, *Proc. Of 13th International Conference on Slurry Handling and Pipeline Transport* BHR Group HYDROTRANSPORT 13, 21-40.
[5] Park J T, Mannheimer R J, Grimley T A, Morrow T B (1989), Pipeflow measurements of a transparent non-Newtonian slurry, *Journal of Fluids Engineering*, Vol. 111, 331-336.
[6] Pokryvalio N A and Grozberg Y G (1995), Investigation of the structure of turbulent wall flow of clay suspensions in channels with electro-diffusion methods, *Proc. 8th International Conf. On Transport and Sedimentation of Solid Particles*, Prague, Czech Republic.
[7] Mun R (1988), Turbulent pipe flow of yield stress fluids, *M. Eng. Sci. Thesis*, University of Melbourne.
[8] White F and Christoph G, A Simple New Analysis of Compressible Turbulent Skin Friction Under Arbitrary Conditions. *Technical Report* AFFDL-TR-70-133, February 1971.
[9] Huang P, Bradshaw P and Coakley T, Skin Friction and Velocity Profile Family for Compressible Turbulent Boundary Layers, *AIAA Journal*, 31(9), 1600-1604, September 1993.
[10] Wolfstein M, The Velocity and Temperature Distribution of One-Dimensional Flow with Turbulence Augmentation and Pressure Gradient. *Int. J. Heat Mass Transfer*, 12:301-318, 1969.
[11] Chen H C and Patel V C, Near-Wall Turbulence Models for Complex Flows Including Separation. *AIAA Journal*, 26(6), 641-648, 1988.
[12] Jongen T, *Simulation and Modeling of Turbulent Incompressible Flows*. PhD thesis, EPF Lausanne, Lausanne, Switzerland, 1992.
[13] Mollagee M M, *Particle Roughness Turbulence in the Balanced Beam Tube Viscometer*, MTech Thesis, CPUT, Cape Town, South Africa, 1998.
[14] FLUENT 6.1. Users Guide, 2003.
[15] Stainsby R, Chilton R A and Thompson S C, Prediction of Head Losses in non-Newtonian Sludge Pipelines using CFD, *Proc. 2nd CFDS Int. User Conf.*, Pittsburgh, USA, 259-272, 1994.



Exact statistical theory of isotropic turbulence

Z. Ran
Shanghai Institute of Applied Mathematics and Mechanics,
People's Republic of China

Abstract

The starting point for this paper lies in the results obtained by Sedov (1944) for isotropic turbulence with the self-preserving hypothesis. A careful consideration of the mathematical structure of the Karman-Howarth equation leads to an exact analysis of all possible cases and to all admissible solutions of the problem. This kind of appropriate manipulation escaped the attention of a number of scientists who developed the theory of turbulence and processed the experimental data for a long time. This paper revisits this interesting problem from a new point of view. Firstly, a new complete set of solutions are obtained, and Sedov's solution is one special case of this set of solutions. Based on these exact solutions, some physically significant consequences of recent advances in the theory of self-preserved homogenous statistical solution of the Navier-Stokes equations are presented. New results could be obtained for the analysis on turbulence features, such as the scaling behaviour, the energy spectra, and also the large scale dynamics.
Keywords: isotropic turbulence, Karman-Howarth equation, exact solution.

1 Introduction

Homogeneous isotropic turbulence is a kind of idealization for real turbulent motion, under the assumption that the motion is governed by a statistical law invariant for arbitrary translation (homogeneity), rotation or reflection (isotropy) of the coordinate system. This idealization was first introduced by Taylor [29] and used to reduce the formidable complexity of statistical expression of turbulence and thus made the subject feasible for theoretical treatment. Up to now, a large amount of theoretical work has been devoted to this rather restricted kind of turbulence. However, turbulence observed either in nature or in laboratory has much more complicated structure. Although remarkable progress



WIT Transactions on Engineering Sciences, Vol 52, © 2006 WIT Press
www.witpress.com, ISSN 1743-3533 (on-line)
doi:10.2495/AFM06053

has been achieved so far in discovering various characteristics of turbulence, our understanding of the fundamental mechanism of turbulence is still partial and unsatisfactory (Tatsumi [19]).

The assumption of similarity and self-preservation, which permits an analytical determination of the energy decay in isotropic turbulence, has played an important role in the development of turbulence theory for more than half a century. In the traditional approach to search for similarity solutions for turbulence, the existence of a single length and velocity scale has been assumed, and then the conditions for the appearance of such solutions have been examined. Excellent contributions had been made to this direction by von Karman and Howarth [8], who firstly deduced the basic equation and presented a particular set of its solutions for the final decaying turbulence. Later on, two Russian scholars, Loitsiansky [30] and Millionshtchikov [12], separately obtained the solutions for the Karman-Howarth equation after the term related to the effect of the triple velocity correlation has been neglected. Their work was an extension of the "small Reynolds number" solution first given by von Karman and Howarth. Dryden [5] gave a comprehensive review on this subject. Detailed research on the solutions of the Karman-Howarth equation was conducted by Sedov [16], who showed that one could use the separability constraint to obtain the analytical solution of the Karman-Howarth equation. Sedov's solution could be expressed in terms of the confluent hypergeometric function. Batchelor [2] readdressed this problem under the assumption that the Loitsiansky integral is a dynamic invariant, which was a widely accepted assumption, but was later found to be invalid. Batchelor concluded that the only complete self-preserving solution which was intrinsically consistent existed at low turbulence Reynolds number, for which the turbulent kinetic energy is accordant with the final period of turbulent decay. Batchelor [2] also found a self-preserving solution to the Karman-Howarth equation in the limit of infinite Reynolds number, for which the Loitsiansky integral is an invariant. Objections were later raised against using the Loitsiansky integral as a dynamic invariant. In fact, at high Reynolds number this integral can be proved to be a weak function of time (see Proudman and Reid [15] and Batchelor and Proudman [4]). Saffman [15] proposed an alternative dynamic invariant which yielded another power-law decay in the limit of infinite Reynolds number (see Hinze [7]). While the results of Batchelor and Saffman formally constitute complete self-preserving solutions to the inviscid Karman-Howarth equation, it must be kept in mind that they only exhibit partial self-preservation with respect to the full viscous equation. Later on, George [6] revived this issue concerning the existence of complete self-preserving solutions in isotropic turbulence. In an interesting paper he claimed to find a complete self-preserving solution, valid for all Reynolds numbers. George's analysis was based on the dynamic equation for the energy spectrum rather than on the Karman-Howarth equation. Strictly speaking, the solution presented by George was an alternative self-preserving solution to the equations of Karman-Howarth and Batchelor since George relaxed the constraint that the triple longitudinal velocity correlation is self-similar in the classical sense. Speziale and Bernard [17]



reexamined this issue from a basic theoretical and computational standpoint. Several interesting conclusions have been drawn from their analysis.

From the development of turbulence theory, we know that the research on decaying homogeneous isotropic turbulence is one of the most important and extensively explored topics. Despite all the efforts, a general theory describing the decay of turbulence based on the first principles has not yet been developed (Skrbek and Stalp [31]). It seems that the theory of self-preservation in homogeneous turbulence has lots of interesting features which have not yet been fully understood and are worth of further study (see Speziale and Bernard [17] p.665).This paper offers a unified investigation of isotropic turbulence, based on the exact solutions of the Karman-Howarth equation. Firstly, we will point out that new complete solution set may exist if we adopt the Sedov method [16]. Hence, some new results could be obtained for revealing the features of turbulence, such as the scaling behavior, energy spectra, and large-scale dynamics.

2 Self-preservation solution under Sedov's separability constraint

For complete self-preserving isotropic turbulence, the Karman-Howarth equation will have a solution if Reynolds number based on the Taylor microscale is constant as first noticed by Dryden [5]. However, this equation also has solutions where Reynolds number based on the Taylor microscale is time dependents when separability is invoked. The separability condition implies that each side of the equation is equal to zero individually, yielding differential equations from which explicit solution for the correlation functions may be determined depending on the choice of parameters. These solutions were first discovered by Sedov [16] and later compared with experimental data by Korneyev and Sedov [9]. Here, we will discuss the possible new complete solutions under Sedov's separability constraint.

The two-point double longitudinal velocity correlations read as (named Sedov equation)

$$\frac{d^2 f}{d\xi^2}+\left(\frac{4}{\xi}+\frac{a_1}{2}\xi\right)\frac{df}{d\xi}+\frac{a_2}{2}f=0 \tag{1}$$

with boundary conditions $f(0)=1$, $f(\infty)=0$.

In the following analysis, we introduce alternative two parameters denoted by a_1,σ,

here

$$\sigma=\frac{a_2}{2a_1} \tag{2}$$

The complete new set of the solution of the equation (1) with the boundary condition could be given as follows:

The first kind of solution: if $\sigma = \frac{5}{2}$, then

$$f(\xi) = e^{-\frac{a_1}{4}\xi^2} \tag{3}$$

The secondary kind of solution: if $\kappa = \sigma - \frac{5}{4}$, then

$$f(\xi) = e^{-\frac{a_1}{4}\xi^2} F\left(\frac{5}{2} - \sigma, \frac{5}{2}, \frac{a_1}{4}\xi^2\right) \tag{4}$$

The third kind of solution: if $\kappa = \frac{5}{4} - \sigma$, then

$$f(\xi) = e^{-\frac{a_1}{4}\xi^2} F\left(\sigma, \frac{5}{2}, \frac{a_1}{4}\xi^2\right) \tag{5}$$

The fourth kind of solution: if $\sigma = \frac{5}{4}$, then

$$f(\xi) = e^{-\frac{a_1}{4}\xi^2} F\left(\frac{3}{4}, \frac{3}{2}, \frac{a_1}{4}\xi^2\right) \tag{6}$$

where $F(\alpha, \gamma, z)$ is the confluent hypergeometric function and the definition of the existing parameter κ will be given in the Appendix. From the asymptotic expansions and the limiting forms of the confluent hypergeometric function, we could deduce the existence conditions of these solutions:

For all four kind of solutions: $a_1 > 0$,

For the secondary kind of soultions: $\sigma > 0$;

For the third kind of solution: $0 < \sigma < \frac{5}{2}$;

The details could be seen in the Appendix 1. A simple comparison shows that the special solution found by Sedov [16] belongs to one kind of our new set of solutions.

3 Some theoretical results based on the exact solutions

A unified investigation of isotropic turbulence, based on the above exact solutions of Karman-Howarth equation could be given. New results could be obtained for the analysis on turbulence features, such as the scaling behaviour, the spectrum, and also the large scale dynamics, some results could be seen in the following references [22–25] .

Acknowledgements

The work was supported by the National Natural Science Foundation of China (Grant Nos.10272018, 10572083), and also supported by Shanghai Leading

Academic Discipline Project, Project Number: Y0103. The author is grateful to Professor Dai shiqiang for his kind help.

Appendix: Solutions of the correlation coefficients

The ideas of similarity and self-preservation were firstly introduced by von Karman and Howarth [8]. In the light of the methods adopted by Sedov [16,32], the two-point double longitudinal velocity correlations satisfies

$$\frac{d^2 f}{d\xi^2}+\left(\frac{4}{\xi}+\frac{a_1}{2}\xi\right)\frac{df}{d\xi}+\frac{a_2}{2}f=0 \tag{a.1.1}$$

with the boundary conditions

$$f(0)=1$$

$$f(\infty)=0$$

The complete solutions are given in this paper, which are

For $\sigma=\frac{5}{2}$, $f(\xi)=e^{-\frac{a_1}{4}\xi^2}$

For $\kappa=\sigma-\frac{5}{4}$, $f(\xi)=e^{-\frac{a_1}{4}\xi^2}F\left(\frac{5}{2}-\sigma,\frac{5}{2},\frac{a_1}{4}\xi^2\right)$

For $\kappa=\frac{5}{4}-\sigma$, $f(\xi)=e^{-\frac{a_1}{4}\xi^2}F\left(\sigma,\frac{5}{2},\frac{a_1}{4}\xi^2\right)$

For $\sigma=\frac{5}{4}$, $f(\xi)=e^{-\frac{a_1}{4}\xi^2}F\left(\frac{3}{4},\frac{3}{2},\frac{a_1}{4}\xi^2\right)$

The detailed calculation is given as follows:

A lot of useful partial differential equations can be reduced to confluent hypergeometric equations, $P_{\kappa,m}(\varsigma)$ is the solution of the Whittaker equation defined by Whittaker and Waston [26]

$$\frac{d^2W}{d\varsigma^2}+\left[-\frac{1}{4}+\frac{\kappa}{\varsigma}+\frac{1/4-m^2}{\varsigma^2}\right]W=0 \tag{a.1.2}$$

where

$$y(z)=z^{\beta}e^{f(z)}P_{\kappa,m}(h(z)) \tag{a.1.3}$$

After some reduction, the equation of $y(z)$ reads

$$\frac{d^2y}{dz^2}-\left[\frac{h''}{h'}+\frac{2\beta}{z}+2f'(z)\right]\frac{dy}{dz}+g\cdot y(z)=0 \tag{a.1.4}$$

where

$$g=(f')^2-f''+2\beta\frac{f'}{z}+\frac{\beta(\beta+1)}{z^2}+\frac{h''}{h'}\left(\frac{\beta}{z}+f'\right)+g_1$$

$$g_1 = \left(\frac{h'}{h}\right)^2 \left(\frac{1}{4} - m^2 + \kappa h - \frac{h^2}{4}\right)$$

The solutions of above equation could be deduced in terms of the Whittaker function.

We discussed this equation in the following special case:

$$f(z) = az^{\lambda} \tag{a.1.5}$$

$$h(z) = Az^{\lambda} \tag{a.1.6}$$

The equation under this condition reads

$$\frac{d^2y}{dz^2} + \left[\frac{1-\lambda-2\beta}{z} - 2\lambda\alpha z^{\lambda-1}\right]\frac{dy}{dz} + qy(z) = 0 \tag{a.1.7}$$

where

$$q = \lambda^2\left(\alpha^2 - \frac{A^2}{4}\right)z^{2\lambda-2} + \lambda\left(2\alpha\beta + A\kappa\lambda\right)z^{\lambda-2} + \frac{\beta(\beta+\lambda) + \lambda^2\left(1/4 - m^2\right)}{z^2}$$

The solution of this equation is

$$y(z) = z^{\beta}e^{\alpha z^{\lambda}}P_{\kappa,m}\left(Az^{\lambda}\right) \tag{a.1.8}$$

For isotropic turbulence, the corresponding parameters satisfiy

$$1 - \lambda - 2\beta = 4 \tag{a.1.9}$$

$$\lambda - 1 = 1 \tag{a.1.10}$$

$$-2\lambda\alpha = \frac{a_1}{2} \tag{a.1.11}$$

$$\lambda^2\left(\alpha^2 - \frac{A^2}{4}\right) = 0 \tag{a.1.12}$$

$$\beta(\beta+\lambda) + \lambda^2\left(\frac{1}{4} - m^2\right) = 0 \tag{a.1.13}$$

$$\lambda\left(2\alpha\beta + A\kappa\lambda\right) = \frac{a_2}{2} \tag{a.1.14}$$

Hence, we have

$$\lambda = 2 \tag{a.1.15}$$

$$\alpha = -\frac{a_1}{8} \tag{a.1.16}$$

$$\beta = -\frac{5}{2} \tag{a.1.17}$$

$$m = \pm\frac{3}{4} \tag{a.1.18}$$



$$A = \pm\frac{a_1}{4} \tag{a.1.19}$$

$$\kappa = \pm\left\{\frac{a_2}{2a_1} - \frac{5}{4}\right\} \tag{a.1.20}$$

From the above analysis, we can introduce two parameters for classifying turbulence, which are: $a_1, \sigma = \frac{a_2}{2a_1}$.

According to Whittaker and Waston [26], if $2m$ is not an integer, then

$$P_{\kappa,m}(z) = e^{-\frac{z}{2}} z^{\frac{1}{2}+m} F\left(\frac{1}{2} + m - \kappa, 1 + 2m, z\right) \tag{a.1.21}$$

$$P_{\kappa,-m}(z) = e^{-\frac{z}{2}} z^{\frac{1}{2}-m} F\left(\frac{1}{2} - m - \kappa, 1 - 2m, z\right) \tag{a.1.22}$$

For the case $\kappa = 0$, we must use the second Kummer formula,

$$P_{0,m}(z) = z^{\frac{1}{2}+m}\, {}_0F_1\left(1 + m; \frac{z^2}{16}\right) \tag{a.1.23}$$

By making use of the boundary conditions, we could choose the rational parameters for isotropic turbulence. The solution of equation could be rewritten as

$$\begin{aligned} y(z) &= z^{\beta} e^{\alpha z^{\lambda}} P_{\kappa,m}\left(Az^{\lambda}\right) \\ &= z^{\beta} e^{\alpha z^{\lambda}} \cdot e^{-\frac{A}{2}z^2} \left(Az^{\lambda}\right)^{\frac{1}{2}+m} F\left(\frac{1}{2} + m - \kappa, 1 + 2m, Az^{\lambda}\right) \\ &= A^{\frac{1}{2}+m} \cdot e^{\left(\alpha - \frac{A}{2}\right)z^2} z^{\beta+\lambda m+\frac{\lambda}{2}} \cdot F\left(\frac{1}{2} + m - \kappa, 1 + 2m, Az^{\lambda}\right) \end{aligned} \tag{a.1.24}$$

Let $A > 0$, then this results in the definition of exponent.

If we chose $m = -\frac{3}{4}$ in the above solution, the exponent of z is

$$\begin{aligned} &\beta + \lambda m + \frac{\lambda}{2} \\ &= -\frac{5}{2} + 2 \times \left(-\frac{3}{4}\right) + 1 \\ &= -3 < 0 \end{aligned} \tag{a.1.25}$$

The boundary condition $y(0)$ would not be satisfied in this situation. So we only chose

$$m = \frac{3}{4} \tag{a.1.26}$$

Another condition must be satisfied:

$$\alpha + \frac{A}{2} = 0 \tag{a.1.27}$$

The solution is

$$y(z) = A^{\frac{5}{4}} \cdot e^{-Az^2} \cdot F\left(\frac{5}{4} - \kappa, \frac{5}{2}, Az^2\right) \tag{a.1.28}$$

There is an important parameter κ in the above solution, and the multiple values could exist:

As $\kappa = \left\{\frac{a_2}{2a_1} - \frac{5}{4}\right\}$,

$$y(z) = A^{\frac{5}{4}} \cdot e^{-Az^2} \cdot F\left(\frac{5}{2} - \sigma, \frac{5}{2}, Az^2\right) \tag{a.1.29}$$

as $\kappa = -\left\{\frac{a_2}{2a_1} - \frac{5}{4}\right\}$,

$$y(z) = A^{\frac{5}{4}} \cdot e^{-Az^2} \cdot F\left(\sigma, \frac{5}{2}, Az^2\right) \tag{a.1.30}$$

We must treat the other special case $\kappa = 0$, by using the second Kummer formula

$$P_{0,m}(z) = z^{\frac{1}{2}+m}\, {}_0F_1\left(1+m; \frac{z^2}{16}\right) \tag{a.1.31}$$

where

$${}_0F_1\left(1+m; \frac{z^2}{16}\right) = e^{-\frac{z}{2}} F(m, 2m, z)$$

For this case, the solution of equation is

$$y(z) = A^{\frac{5}{4}} \cdot e^{-Az^2} \cdot F\left(\frac{3}{4}, \frac{3}{2}, Az^2\right) \tag{a.1.32}$$

For another reduced case for $\sigma = \frac{5}{2}$, the solution is

$$f(\xi) = e^{-\frac{a_1}{4}\xi^2} \tag{a.1.33}$$

Finally, we have already obtained a complete set solution of isotropic turbulence, depending on two parameters, which are

As $\sigma = \frac{5}{2}$, $f(\xi) = e^{-\frac{a_1}{4}\xi^2}$

As $\kappa = \sigma - \frac{5}{4}$, $f(\xi) = e^{-\frac{a_1}{4}\xi^2} F\left(\frac{5}{2} - \sigma, \frac{5}{2}, \frac{a_1}{4}\xi^2\right)$

As $\kappa = \frac{5}{4} - \sigma$, $f(\xi) = e^{-\frac{a_1}{4}\xi^2} F\left(\sigma, \frac{5}{2}, \frac{a_1}{4}\xi^2\right)$

If $\sigma = \frac{5}{4}$, then $f(\xi) = e^{-\frac{a_1}{4}\xi^2} F\left(\frac{3}{4}, \frac{3}{2}, \frac{a_1}{4}\xi^2\right)$

References

[1] Bareenblatt,G.J.& Garilov,A.A. 1974. Sov. Phys. J. Exp. Theor. Phys. 38,399-402.
[2] Batchelor,G.K. 1948.Q. Appl. Maths. 6,97-116.
[3] Batchelor, G.K. 1953 The Theory of Homogeneous Turbulence Turbulence. Cambrige University Press.
[4] Batchelor,G.K. & Proudman,I. 1956. Phil. Trans. R. Soc. Lond. A.248,369-405.
[5] Dryden,J.L. 1943. Q. Appl. Maths. 1,7-42.
[6] George,W.K. 1992. Phys. Fluids A 4,1492-1509.
[7] Hinze,J.O. 1975 Turbulence. McGraw-Hill.
[8] Karman,T.Von & Howarth,L. 1938. Proc. R. Soc. Lond. A164,192-215.
[9] Korneyev & Sedov, L.I. 1976. Fluid Mechanics-Soviet Research 5,37-48.
[10] Lesieur,M. 1990 Turbulence in Fluids, 2nd Edn. Martinus Nijhoff.
[11] Lin,C.C. 1948. Proc. Natl. Acad. Sci. 34,540-543.
[12] Millionshtchikov, M. 1941. Dokl. Akad. Nauk SSSR 32,615-618.
[13] Monin,A.S. & Yaglom,A.M. 1975 Statistical Fluid Mechanics: Mechanics of Turbulence, vol.2, MIT Press.
[14] Proundman, I. & Reid, W. H. 1954. Philos. Trans. R. Soc. London, A 247,163-189.
[15] Saffman,P.G. 1967. J. Fluid Mech. 27,581-594.
[16] Sedov, L.I. 1944. Dokl.Akad.Nauk SSSR 42,116-119.
[17] Speziale,C.G. & Bernard, P.S. 1992. J. Fluid Mech. 241,645-667.
[18] Skbek,L. & Steven, R.S. 2000. Phys. Fluids 12,1997-2019.
[19] Tatsumi, T. 1980. Advances in Applied Mechanics, 39-133.
[20] Chou Pei-yuan & Tsai Shu-tang. Acta Scientiarum Naturalium Univeritatis Pekinensis,1, 1956:39-49.
[21] J,Qian. Phys. Fluids 2(8), 1983:2098-2104.
[22] Ran zheng, Exact solutions of Karman-Howarth equation. http://www.paper.edu.cn-200510-311
[23] Ran zheng, Scales and their interaction in isotropic turbulence. http://www.paper.edu.cn-200510-205.
[24] Ran zheng, Dynamic of large scales in isotropic turbulence. http://www.paper.edu.cn-200509-230.
[25] Ran zheng, On von Karman's decaying turbulence theory. http://www.paper.edu.cn-200511-233.
[26] Whittaker,E.T. and Waston, G.N., A course of modern analysis. Cambridge University Press, 1935



[27] M.Abramowitz and I.A.Stegun, Handbook of mathematical functions. Dover, New York, 1965
[28] Wang, Z.X. and Guo,D. R., Special functions. The series of advanced physics of Peking University. Peking University Press, 2000 (In Chinese)
[29] Taylor,G.I., 1935 Statistical theory of turbulence. I-IV, Proc. Roy. Soc., A151, No.874, 421-478.
[30] Loitsyansky, L.G., 1939 Some basic laws for isotropic turbulent flow, Trudy Tsentr. Aero.-Giedrodin. Inst., No.440,3-23.
[31] Skbek, L. & S. R.Stalp, S.R. 2000 On the decay of homogeneous isotropic turbulence. Phys. Fluids 12,1997-2019.
[32] Sedov, L.I. 1982 Similarity and dimensional methods in mechanics. Translated from the Russian by V. I. Kisin. Mir Publishers.



The SGS kinetic energy and the viscous dissipation equations as closure relations in LES

F. Gallerano, L. Melilla & E. Pasero
Dipartimento di Ingegneria Idraulica, Trasporti e Strade, Università di Roma "La Sapienza", Italy

Abstract

In this paper the main drawbacks of the large eddy simulation models, present in literature, are analysed and a new LES model is proposed. The closure relation for the generalised SGS turbulent stress tensor: a) complies with the principle of turbulent frame indifference; b) takes into account both the anisotropy of the turbulence velocity scales and turbulence length scales; c) removes any balance assumption between the production and dissipation of SGS turbulent kinetic energy. In the proposed model: a) the closure coefficient which appears in the closure relation for the generalised SGS turbulent stress tensor is theoretically and uniquely determined without adopting Germano's dynamic procedure; b) the generalised SGS turbulent stress tensor is related exclusively to the generalised SGS turbulent kinetic energy (which is calculated by means of its balance equation) and the modified Leonard tensor. In this paper the main drawbacks associated with the calculation of the viscous dissipation by means of an algebraic model are shown. The calculation of the viscous dissipation is carried out by integrating its exact balance equation. The velocity field obtained from the numerical simulation is analysed by using vortex identification methods D, Q and λ_2. The comparative analysis of each identification method is also carried out, highlighting how methods D and Q improperly associate the presence of a vortex to zones of high vorticity while the λ_2 method identifies a vortex only when it coincides with a minimum of pressure.
Keywords: LES, sub grid kinetic energy viscous dissipation, balance equation anisotropy, scale similarity, vortex identification.



WIT Transactions on Engineering Sciences, Vol 52, © 2006 WIT Press
www.witpress.com, ISSN 1743-3533 (on-line)
doi:10.2495/AFM06054

1 Introduction

Among the most common LES models present in literature are the Dynamic Smagorinsky-type SGS Models (*e.g.* Dynamic Smagorinsky Model DSM [2], Dynamic Mixed Model DMM, Lagrangian Dynamic Model LDM [3]), in which the generalised SGS turbulent stress tensor is related to the resolved strain-rate tensor by means of a scalar eddy viscosity. It is assumed in these models that the eddy viscosity is a scalar proportional to the cubic root of the generalised SGS turbulent kinetic energy dissipation and that such dissipation is locally and instantaneously balanced by the production of the generalised SGS turbulent kinetic energy. Consequently, it is evident that the dynamic Smagorinsky-type SGS models are subject to three relevant drawbacks. The first drawback is represented by the scalar definition of the eddy viscosity; the second one is related to the assumption of a local and instantaneous balance between the production and dissipation of the generalised SGS turbulent kinetic energy, whilst the third drawback is related to the dynamic calculation of the coefficient used to model the eddy viscosity (Smagorinsky coefficient).

The scalar definition (first inconsistency) of the eddy viscosity is equivalent to assuming that the principal axes of the generalised SGS turbulent stress tensor, or the unresolved part of it (represented by the cross and Reynolds terms), are aligned with the principal axes of the resolved strain-rate tensor. This assumption has been disproved by many experimental tests and by DNS, which demonstrate that there is no alignment between the generalised SGS turbulent stress tensor, or the unresolved part of it, and the resolved strain-rate tensor. Moreover, as is well known, the eddy viscosity is, in the most general case a symmetric fourth order tensor given by the product of two-second order tensors which represent respectively the turbulence length scale and the turbulence velocity scale. The scalar definition of the eddy viscosity, used in the above-mentioned dynamic Smagorinsky-type SGS models, presupposes the existence of a single turbulence velocity scale and a single turbulence length scale. This is equivalent to assuming that the turbulence is isotropic but, as shown by several authors, even in the dissipation range of the smallest turbulence scales there are high anisotropy levels, even at high Reynolds numbers.

The second inconsistency of the Smagorinsky dynamic models is related to the assumption of a local and instantaneous balance between production and dissipation of the generalised SGS turbulent kinetic energy, formulated in the above-mentioned models to obtain the turbulent viscosity expression. The balance between production and dissipation of the generalised SGS turbulent kinetic energy is confirmed statistically and never instantaneously, and only locally at the scales associated with wave-numbers within the inertial subrange and the latter exists only for isotropic turbulence and at high Reynolds numbers. Moreover, since the dissipation of the generalised SGS turbulent kinetic energy is, by definition, positive, the assumption of local balance implies that the production of generalised SGS turbulent kinetic energy is also positive. This assumption is equivalent to neglect back-scatter i.e. the energy transfer from the smallest unresolved scales to the largest ones.



The third inconsistency concerns the ineffectiveness, in the wall region, of Germano's dynamic procedure for the calculation of the coefficient which appears in the closure relation for the generalised SGS stress tensor. In fact, in the wall region the dimensions of the filters used in the dynamic procedure are larger than those of the largest eddies governing the energy and momentum transfer. Under these conditions the dynamic procedure is not able to fully account for the local subgrid dissipative processes that affect the entire domain.

In this paper a new LES model is proposed which overcomes the above drawbacks. The closure relation for the generalised SGS turbulent stress tensor: a) complies with the principle of turbulent frame indifference [1]; b) takes into account both the anisotropy of the turbulence velocity scales and turbulence length scales; c) removes any balance assumption between the production and dissipation of SGS turbulent kinetic energy. In the proposed model: a) the closure coefficient which appears in the closure relation for the generalised SGS turbulent stress tensor is theoretically and uniquely determined without adopting Germano's dynamic procedure; b) the generalised SGS turbulent stress tensor is related exclusively to the generalised SGS turbulent kinetic energy (which is calculated by means of its balance equation) and the modified Leonard tensor.

The velocity fields obtained by the numerical simulation are analysed by using the so-called D [6], Q [7] e λ_2 [8] methods for the identification of vortices. From the comparative analysis of vortex structures identified by the three different methods mentioned above, the inconsistencies and drawbacks of these methods are shown.

2 A new LES model

In order to remove the assumption of alignment between the unresolved part of the generalised SGS turbulent stress tensor and the resolved strain rate tensor and to take into account the anisotropy of the unresolved scales of turbulence, the generalised SGS turbulent stress tensor is expressed in the following form:

$$\tau_{ij} = L_{ij}{}^{m} - 2\nu_{ijmn}\overline{S}_{mn} \tag{1}$$

in which $\overline{S}_{mn}$ is the resolved strain rate tensor and L_{ij}^{m} is the modified Leonard tensor. The eddy viscosity is expressed in the above-mentioned equation by a fourth-order tensor proportional to the product of a second-order tensor, b_{ij}, which represents the turbulence velocity scales, and a second-order tensor, d_{mn}, which represents the turbulence length scales, according to the following equation:

$$\nu_{ijmn} = Cb_{ij}d_{mn}\ , \text{ where } \quad b_{ij} = b_{ji}\ , \quad d_{mn} = d_{nm}\,. \tag{2}$$

The expression of the eddy viscosity in terms of a fourth-order tensor enables the anisotropic character of the turbulence to be fully represented, since it does not either assume the existence of a single turbulence velocity scale and or a single turbulence length scale, as is found in models in which the viscosity is expressed

as a scalar. The second-order tensor which represents the turbulence velocity scales is defined as follows:

$$b_{ij} = \sqrt{E}\,\frac{L^m_{ij}}{L^m_{ij}} \tag{3}$$

where E is the SGS turbulent kinetic energy. In this manner it is assumed that the anisotropy of the unresolved turbulence velocity scales, expressed by tensor b_{ij}, is equal to the anisotropy of the smallest resolved scales, associated with the modified Leonard tensor. This assumption is based on scale similarity, according to which the scales that are contiguous in the wavenumber space have strict dynamic analogies related to the energy exchange processes which occur between them.

Introducing equation (2) and (3) into (1) gives:

$$\tau_{ij} = (1+r)L^m_{ij} \quad \text{where} \qquad r = -2Cd_{mn}S_{mn}\,\frac{\sqrt{E}}{L^m_{kk}} \tag{4}$$

In order to close the equations governing the turbulent flows, it is necessary to determine the coefficient C which appears in equation in (4.a) or anywhere else, the coefficient r which appears in equation (4.b).

In this paper the coefficient r is determined without Germano's dynamic procedure, the inconsistencies of which are fundamentally linked to the fact that in the wall region the dimensions of the filters used in the dynamic procedure are larger than those of the largest eddies governing the energy and momentum transfer.

The coefficient r is uniquely and theoretically determined by using the relation between the generalised SGS turbulent kinetic energy and the generalised SGS turbulent stress tensor. In fact, by definition, the generalised SGS turbulent kinetic energy is equal to half the trace of the generalised SGS turbulent stress tensor.

$$\tau_{kk} = 2E = (1+r)L^m_{kk}, \quad \text{i.e.} \qquad r = \frac{2E - L^m_{kk}}{L^m_{kk}} \tag{5}$$

introducing (5) into (4) gives:

$$\tau_{ij} = \left(1 + \frac{2E - L^m_{kk}}{L^m_{kk}}\right) L^m_{ij} = \left(\frac{2E}{L^m_{kk}}\right) L^m_{ij} \tag{6}$$

The closure relation (6) is obtained without any assumption of local balance between the production and dissipation of generalised SGS turbulent kinetic energy and may thus be considered applicable to LES with the filter width falling into the range of wave numbers greater than the wave number corresponding to the maximum turbulent kinetic energy.

The closure relation for the generalised SGS turbulent stress tensor (6): a) complies with the principle of turbulent frame indifference given that it relates only objective tensors [1]; b) takes into account both the anisotropy of the turbulence velocity scales and turbulence length scales; c) assumes scale

similarity in the definition of the second-order tensor representing the turbulent velocity scales; d) guarantees an adequate energy drain from the grid scales to the subgrid scales and guarantees backscatter; e) overcomes the inconsistencies linked to the dynamic calculation of the closure coefficient used in the modelling of the generalised SGS turbulent stress tensor.

The generalised SGS turbulent kinetic energy, E, is calculated by solving its balance equation, defined by the following equation:

$$\frac{DE}{Dt} = -\frac{1}{2}\frac{\partial \tau(u_k,u_k,u_m)}{\partial x_m} - \tau_{mk}\frac{\partial \bar{u}_k}{\partial x_m} - \frac{\partial \tau(p,u_m)}{\partial x_m} + \nu\frac{\partial^2 E}{\partial x_m \partial x_m} + \tau\left(F_{Ok},u_k\right) - \nu\tau\left(\frac{\partial u_k}{\partial x_m},\frac{\partial u_k}{\partial x_m}\right) \quad (7)$$

Equation (7) is form-invariant under Euclidean transformations of the frame and frame-indifferent [1]. The last term on the right of (7) is defined viscous dissipation :

$$\varepsilon = \nu\tau\left(\frac{\partial u_i}{\partial x_j},\frac{\partial u_i}{\partial x_j}\right) \quad (8)$$

From a thermodynamic point of view this quantity describes an internal process, *i.e.* the viscous dissipation in the turbulent flow, and therefore can be considered as an internal variable, and its evolution can be described by a transport equation. Some authors [4] model ε with the following expression:

$$\varepsilon = \frac{C^* E^{3/2}}{\bar{\Delta}} \quad (9)$$

and calculate the scalar coefficient C^* which appears in (9) by means of a dynamic procedure based on the following scalar Germano identity:

$$C_* \frac{E^{T3/2}}{\bar{\Delta}^T} - \left\langle C_* \frac{E^{3/2}}{\bar{\Delta}} \right\rangle = \nu\left\langle \frac{\partial \bar{u}_k}{\partial x_m}\frac{\partial \bar{u}_k}{\partial x_m} \right\rangle - \nu\frac{\partial \left\langle \bar{u}_k \right\rangle}{\partial x_m}\frac{\partial \left\langle \bar{u}_k \right\rangle}{\partial x_m} \quad (10)$$

The term on the right of eqn. (10) expresses the viscous dissipation of turbulent kinetic energy which occurs locally in the range of the wavenumbers falling between the two filter dimensions. At high Reynolds numbers the dynamic procedure, expressed in (10) and carried out with grid and test filters of which the dimensions are associated with the wavenumbers lower than those belonging to the inertial subrange, is not applicable because it is subject to three relevant inconsistencies. Equation (10) (first inconsistency) allows the calculation of the closure coefficient C^* only if the dimensions of the test and grid filters are associated with wave numbers belonging to the inertial subrange.

The second inconsistency concerns the calculation of the term on the right of (10), which at high Reynolds numbers is negligible if the dimensions of the filters used in the dynamic procedure are associated with wavenumbers lower than those belonging to the inertial subrange.

The third inconsistency is related to the boundary conditions for ε. As is well known, in wall bounded turbulent flows the viscous dissipation of SGS turbulent kinetic energy, ε, balances the viscous diffusion of E at the wall

$$\varepsilon_W = \nu\frac{\partial^2 E}{\partial x_m \partial x_m} \quad (11)$$

The dissipative processes occurring in the wall region affect the energy cascade process of the entire domain, since in this region the kinetic energy both produced locally and transferred from the rest of the domain is dissipated. Since E is zero at the wall, eqn. (10) implies null values of ε at the wall. This contradicts eqn. (11). In order to remove these drawbacks, and therefore to operate simulations of high Reynolds number flows, in the proposed LES model a further transport equation is introduced for the subgrid viscous dissipation ε. This equation, expressed in terms of the generalised central moments, takes the form

$$\frac{\partial \varepsilon}{\partial t}+\frac{\partial \bar{u}_k \varepsilon}{\partial x_k}-\frac{\partial^2 \varepsilon}{\partial x_k \partial x_k}+\nu \frac{\partial}{\partial x_k}\tau\left(u_k,\frac{\partial u_i}{\partial x_j},\frac{\partial u_i}{\partial x_j}\right)+2\nu\frac{\partial}{\partial x_k}\left(\frac{\partial \bar{u}_i}{\partial x_j}\tau\left(u_k,\frac{\partial u_i}{\partial x_j}\right)\right)+2\nu\frac{\partial}{\partial x_k}\tau\left(\frac{\partial u_k}{\partial x_i},\frac{\partial p}{\partial x_i}\right)-$$

$$2\nu\frac{\partial}{\partial x_k}\left(\frac{\partial \bar{u}_i}{\partial x_j}\frac{\partial \tau_{ik}}{\partial x_j}\right)+2\nu\tau\left(\frac{\partial u_i}{\partial x_k},\frac{\partial u_k}{\partial x_j},\frac{\partial u_i}{\partial x_j}\right)+2\nu\frac{\partial \bar{u}_k}{\partial x_j}\tau\left(\frac{\partial u_i}{\partial x_k},\frac{\partial u_i}{\partial x_j}\right)+2\nu\frac{\partial \bar{u}_i}{\partial x_k}\tau\left(\frac{\partial u_k}{\partial x_j},\frac{\partial u_i}{\partial x_j}\right)+$$

$$2\nu\frac{\partial \bar{u}_i}{\partial x_j}\tau\left(\frac{\partial u_i}{\partial x_k},\frac{\partial u_k}{\partial x_j}\right)+2\nu\frac{\partial \tau_{ik}}{\partial x_j}\frac{\partial^2 \bar{u}_i}{\partial x_j \partial x_k}+2\nu^2\tau\left(\frac{\partial^2 u_i}{\partial x_j \partial x_k},\frac{\partial^2 u_i}{\partial x_j \partial x_k}\right)=0 \qquad (12)$$

The first term on the left-hand side of eqn (12) is the local derivative, the second one expresses the convection term, the third is the viscous diffusion term, the 4th-7th are the turbulent transport terms, the 8th- 12th are the production terms of ε, and the last one expresses its destruction.

The sum of the fourth, fifth and sixth terms on the left of (12) is the divergence of the viscous dissipation turbulent transport vector, $\left(F_\varepsilon\right)_k$, which is modelled according to:

$$\left(F_\varepsilon\right)_k = C_{F\varepsilon}\frac{E}{\varepsilon}\tau_{kl}\frac{\partial \varepsilon}{\partial x_l} \quad \text{which, for (6), is equivalent to} \quad C_{F\varepsilon}\frac{E^2}{\varepsilon}\frac{L^m_{kl}}{L^m_{jj}}\frac{\partial \varepsilon}{\partial x_l} \qquad (13)$$

The scalar coefficient $C_{F\varepsilon}$ in (13) is dynamically calculated by means of a Germano identity applied to the turbulent transport vector of ε.

The sum of the 8th, 9th, 10th and 11th unknown terms of (12) constitutes a production term of ε which is modelled in the following way:

$$P_\varepsilon = C_{P\varepsilon}\frac{\varepsilon\left(-\tau_{ij}\bar{S}_{ij}\right)}{E}, \quad \text{which, for (6), is equivalent to} \quad -C_{P\varepsilon}\frac{\varepsilon L^m_{ij}\bar{S}_{ij}}{L^m_{kk}} \qquad (14)$$

The dynamic calculation of the coefficient $C_{P\varepsilon}$ is carried out by applying a Germano identity to the viscous dissipation production terms. The last term in (12) represents the destruction of ε. This is modelled, according to the closure relation presented in the following way:

$$D_\varepsilon = C_{D\varepsilon}\frac{\varepsilon^2}{E} \qquad (15)$$

The calculation of coefficient $C_{D\varepsilon}$ is carried out dynamically by applying a Germano identity to the viscous dissipation destruction term.

3 Vortex identification

The velocity fields obtained from the numerical simulation are analysed by using vortex identification methods D [6], Q [7] and λ_2 [8].

The first two methods are based on the relations existing between the invariants of the velocity gradient, A_{ij}. The third method identifies a vortical structure from the analysis of the symmetric matrix given by the sum of the square of the strain rate tensor S_{ij} with the square of the anti-symmetric part of the velocity gradient W_{ij}. Both the D method and the Q method formulate hypotheses on the trajectories of the particles in the neighbourhood of a point by analysing the eigenvalues and eigenvectors of the velocity gradient. If there exist two complex and conjugated eigenvalues of the velocity gradient, the path of the particles takes on a spiral shape. The Q method identifies the existence of a vortex if the second invariant, Q, of the velocity gradient is positive:

$$Q = \frac{1}{2} \cdot \left[P^2 - S_{ij} S_{ji} - W_{ij} W_{ji} \right] > 0 \tag{16}$$

where P is the trace of the velocity gradient. The above relation is verified when the enstrophy is greater than local strain intensity. This method fails in the vortex identification, since for negative values of Q, also two complex and conjugated eigenvalues, associated to a vortex, may exist. The D method identifies a vortex when the discriminant of the characteristic polynomial associated with the velocity gradient is positive:

$$D = \left(\frac{Q}{3} \right)^3 + \left(\frac{R}{2} \right)^2 > 0 \quad \text{where} \quad \mathrm{R} = \det(\mathrm{A}) \tag{17}$$

This method cannot identify the vortex core; furthermore, when the second invariant is greater than the third, the method shows the same drawbacks as the Q method. Moreover, when the third invariant is greater than the second one, such a method identifies a vortex where high vorticity exists: therefore the method fails since it identifies a vortex even where it does not exist, as high vorticity is neither a necessary nor a sufficient condition for the presence of a vortex. The λ_2 method [8] identifies a vortex when the symmetric matrix

$$\Lambda_{ij} = S_{ik} S_{kj} + W_{ik} W_{kj} \tag{18}$$

has two negative eigenvalues. By differentiating the Navier-Stokes equation, it holds:

$$\frac{DS_{ij}}{Dt} - \nu \frac{\partial^2 S_{ij}}{\partial x_k \partial x_k} + S_{ik} S_{kj} + W_{ik} W_{kj} = -\frac{1}{\rho} \cdot \frac{\partial^2 P}{\partial x_i \partial x_j} \tag{19}$$

If the first and second terms in equation (19) are negligible, the symmetric matrix Λ_{ij} is proportional to the opposite of the pressure Hessian matrix. When the symmetric matrix Λ_{ij} has two negative eigenvalues, the above mentioned Hessian matrix has two positive eigenvalues. In the plane identified by the eigenvectors associated with the two positive eigenvalues of the Hessian matrix, the quadratic form associated with the two eigenvalues is positive and, consequently, the pressure has a minimum. The criterion, therefore, is

substantially based on the identification of zones corresponding to a minimum pressure. But the existence of a minimum pressure is neither a necessary nor a sufficient condition for a vortex.

4 Numerical set-up and results

The proposed LES model is used for the simulation of a turbulent channel flow (between two flat parallel plates) at Reynolds number $Re^*=u^*\delta/\nu$ =2340, where u^* is the friction velocity, δ is the channel half width and ν is the cinematic viscosity. The dimensions of the computational domain are $2\pi\delta$ in the streamwise direction and 2δ in spanwise direction. The computation is carried out with 128 x 96 x 96 grid points, respectively, in streamwise (x) spanwise (y) and wall-normal (z) directions.

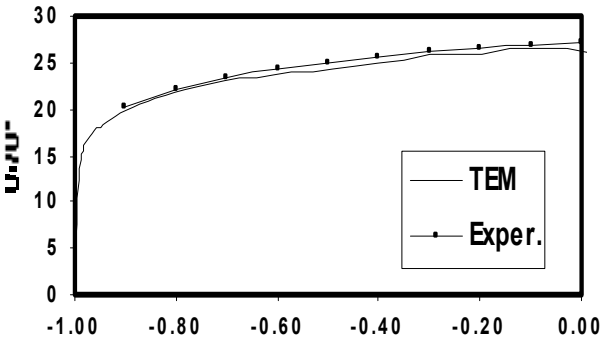


Figure 1: Time averaged streamwise velocity component at Re^*=2340. (Comparison with experimental data).

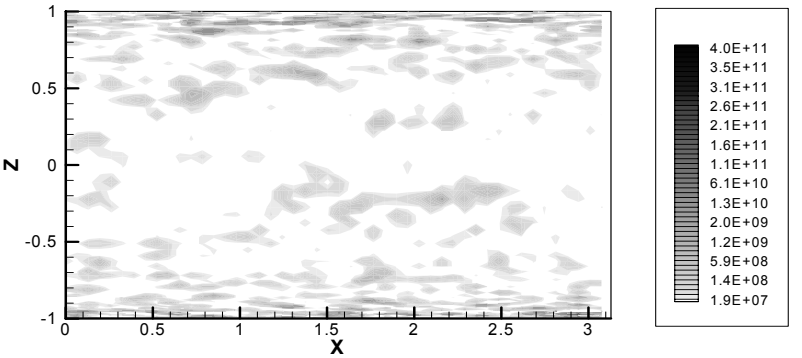


Figure 2: Vortex identification with *D* method, *x-z* plane.

In fig.1 the time-averaged streamwise velocity component is shown. The figure shows that LES and the experimental data agree quite considerably. Figs. 2–4 show the vortex structures, identified by means of the Q, D, λ_2 methods respectively, in the x-z plane (for a better visualisation only a limited part of the domain is shown). As shown by figs. 2 and 3, the D and Q methods improperly associate the presence of a vortex in high vorticity zones *i.e.* at the wall). Moreover, while the first method underestimates the vortex extension, the second one overestimates it. As shown in fig. 4, method λ_2 correctly identifies a vortex.

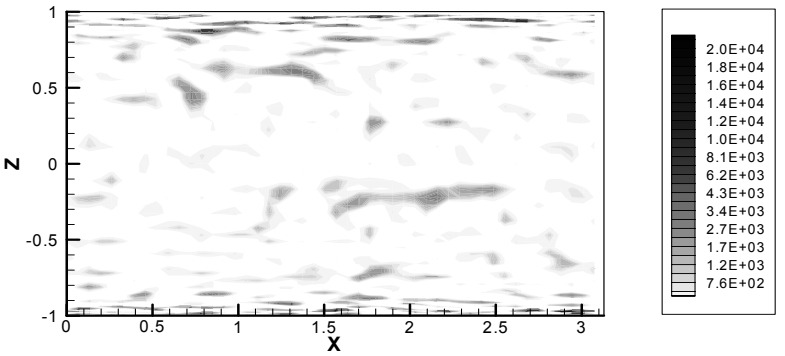


Figure 3: Vortex identification with Q method, x-z plane.

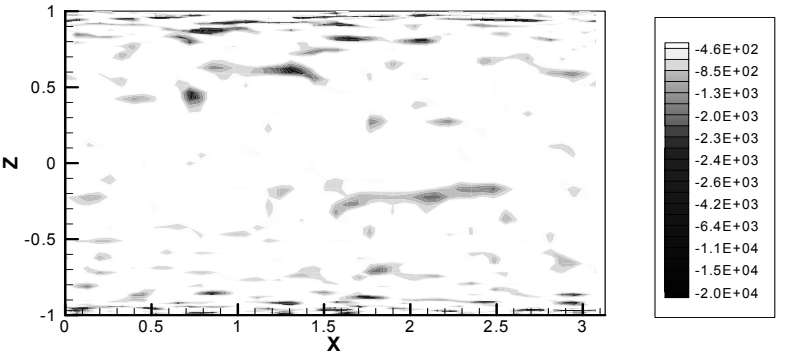


Figure 4: Vortex identification with λ_2 method, x-z plane.

In fig. 4 the near wall vortex structures (inside the turbulent boundary layer) are clearly identified: the dimensions of the spatial discretisation steps allow the optimal simulation of the above mentioned vortex structures that govern the transport, the production and the dissipation of the turbulent kinetic energy.

5 Conclusions

In this paper the main drawbacks of the LES models present in literature are analysed and a new closure relation is proposed for the generalised SGS turbulent stress tensor that: a) complies with the principle of turbulent frame indifference [1]; b) takes into account both the anisotropy of the turbulence velocity scales and turbulence length scales; c) removes any balance assumption between the production and dissipation of SGS turbulent kinetic energy. The figure shows that LES and the experimental data agree considerably well.

References

[1] Hutter, K, Jonk, K, *Coontinum methods of Physical of Modelling*, Springer, 2004.
[2] Germano M, Piomelli U, Moin P, Cabot WH, A dynamic subgrid scale eddy viscosity model. *Phys. Fluids* A3, 1760-1765¸ 1991.
[3] Meneveau C, Lund TS, Cabot WH, A Lagrangian dynamic subgrid-scale model of turbulence, *J. Fluid Mech.* 319, 353-385.
[4] Ghosal S, Lund TS, Moin P, Aksevoll K, A dynamic localisation model for large-eddy simulation of turbulent flows, *J. Fluid Mech.* 286, 229-255, 1995.
[5] Gallerano F., Pasero E., Cannata G., A dynamic two-equation Sub Grid Scale model. *Continuum Mech. Thermodyn*. 17, 101-123, 2005.
[6] Chong, M.S. Perry, A.E. Cantwell, B.J, A general classification of three dimensional flow field, *Phys. Fluids*. A 2, 765, 1990.
[7] Hunt. J.C.R., Vassilicos, J.C. & Kevlahan, N.K.R.,'Turbulence-. A state of nature or a collection of phenomena?', in Branover, H. & Unger, Y. (Eds) Progress in turbulence Research, *7th Beer Sheva Int. Sem. on MHD flows and turbulence*, Beer eb. 1993, Progress in Astronautics Series, AIAA Sheva, Israel, Feb. 1993.
[8] Joeng, J. Hussain, F, On the identification of a vortex, *J. Fluid Mech.* 285, 69-94, 1995.



Deforming mesh with unsteady turbulence model for fluid-structure interaction

J.-T. Yeh
Materials Research Laboratories,
Industrial Technology Research Institute, Taiwan

Abstract

By taking the mesh of the fluid domain as a virtual solid and using the explicit integration scheme to solve the solid dynamics, a deforming mesh method is proposed for the simulation of fluid-structure interaction. The deforming mesh method with an unsteady turbulence model has been implemented into a finite element code derived from slightly compressible flow formulation and an explicit integration scheme. Due to the explicit integration scheme used for the dynamics of both deforming mesh and fluid flow, it is easy to perform parallel computation for a large-scale fluid-structure interaction problem. After the validation of this approach on the flow induced vibration of the flow past a circular cylinder, the unsteady fluid-structure interaction of a heat exchanger-tube row in crossflow is demonstrated.
Keywords: deforming mesh, unsteady turbulence model, fluid-structure interaction.

1 Introduction

The fluid-structure interaction, the unsteady fluid flow making a structure move or deform and the motion of the structure changing the fluid flow, is an important topic in many engineering fields, for example, the flutter of aircraft's wings and the flow induced vibration of tube bundle in heat exchangers. To have a good numerical simulation of the fluid structure interaction, a sufficiently accurate model to solve the unsteady flow field, especially for turbulent flow, and an efficiency method to update the grid/mesh of fluid domain due to the motion of boundaries are of great concern.



WIT Transactions on Engineering Sciences, Vol 52, © 2006 WIT Press
www.witpress.com, ISSN 1743-3533 (on-line)
doi:10.2495/AFM06055

A turbulent flow must be unsteady. To the knowledge of the author, all the major turbulence models, including the large eddy simulation, are not based on the unsteady flow, i.e., once the strain rate exists, the turbulence is computed even though the flow field is steady or without time variation. For example, the unwanted turbulence is computed on the leading edge of flow past an object. In this paper, an unsteady turbulence model where the turbulence is generated from the computed unsteady flow field is presented.

On updating the mesh with moving boundary, re-generation of the mesh with respect to some specified geometric parameters is popularly adopted [1-3]; however, difficulty is encountered when the boundary was not part of a rigid body. A dynamic mesh method [4] with network of artificial springs for the mesh has been developed for the large-scale fluid-structure interactions. However, a large number of linear algebra equations are formed by the implicit time integration scheme of the fluid dynamics or the static analysis of the spring network deformation, and they prove costly when solved using parallel computation. By taking the mesh of the fluid domain as a virtual solid and using the explicit integration scheme to solve the solid dynamics, a deforming mesh method is proposed for the simulation of fluid-structure interaction.

2 Numerical methods

In an unsteady flow such as a flow-induced vibration or noise, the propagation of pressure wave exists and the sound speed or the compressibility of the fluid must be considered. The present numerical method for fluid-structure interaction is based on a slightly compressible flow formulation. The continuity equation can be written, instead of the density, in terms of the pressure as

$$\frac{\partial p}{\partial t} + K u_{i,i} = 0 \tag{1}$$

where p is pressure and u_i represents the velocity vector. $K(=\rho C^2)$ is the bulk modulus of fluid elasticity (ρ and C represent the density and the sound speed of a fluid respectively). For a flow field with low Mach number and small density variation, the bulk modulus can be set as a constant.

By the Arbitrary Lagrangian Eulerian description, the momentum equation of the viscous flow with the moving grid velocity vector $\dot{w}_i$ is

$$\rho \frac{\partial u_i}{\partial t} = (-\delta_{ij} p + \tau_{ij})_{,j} - \rho(u_j - \dot{w}_i) u_{i,j} \tag{2}$$

where $\tau_{ij}(=\nu(u_{i,j} + u_{j,i}))$ is the shear stress and $\nu(=\nu_d + \nu_e)$ represents the total viscosity which is the summation of the dynamic viscosity ν_d and the effective

eddy viscosity $\nu_e (= \rho l^2 \gamma)$ in the unsteady turbulence model. l is the mixing length, the minimum width of the element or grid. γ represents the turbulence strain rate which is generated, dissipated, diffused and convected by

$$\rho \frac{\partial \gamma}{\partial t} = \rho[\left|\dot{\gamma}_{ij}\right| - \frac{\mu + \rho l^2 \gamma}{\rho C l}\left|\gamma_{ij}\right|\gamma + \left|\gamma_{ij}\right| l^2 \gamma_{,kk} - (u_k - \dot{w}_k)\gamma_{,k}]. \quad (3)$$

In the above, $\left|\dot{\gamma}_{ij}\right|$ is the absolute value of the variation rate of the strain rate

$$\gamma_{ij} = (u_{i,j} + u_{j,i})/2 \text{ or } \left|\dot{\gamma}_{ij}\right|\Delta t = \sqrt{2\Delta\gamma_{ij}\Delta\gamma_{ij}}\ .$$

The moving grid is taken as a solid with the same density and bulk modulus of the fluid, and governed by

$$\rho \frac{\partial^2 w_i}{\partial t^2} = \sigma_{ij,j} \quad (4)$$

where the stress σ_{ij} is derived from the displacement field w_i by a constitutive equation.

After dividing the computation domain by finite elements, the field variable, velocity u_i, turbulence strain rate γ and moving grid displacement w_i can be represented by the interpolation of nodal variable $\{U\}$, $\{\Gamma\}$ and $\{W\}$. Based on the weighted residual method, the weak-form of the equilibrium equations derived from eqns. (2)-(4) and boundary conditions with quadrilateral (2D) or hexahedron (3D) element and reduced integration can be written as

$$[M]\{\frac{\partial U}{\partial t}\} = \{R_U\},\ [M]\{\frac{\partial \Gamma}{\partial t}\} = \{R_\Gamma\} \text{ and } [M]\{\frac{\partial^2 W}{\partial t^2}\} = \{R_W\} \quad (5)$$

where $[M]$ is the mass matrix; $\{R_U\}$, $\{R_\Gamma\}$ and $\{R_W\}$ are the corresponding unbalanced or resultant nodal residuals. By using the explicit time integration scheme and the lumped, therefore diagonal, mass matrix, the above equations are efficient to be solved and easy to be implemented into parallel computation for a large scale fluid-structure interaction computation.

It is noticed that the pressure is not a nodal variable but is a derived quantity in an element solved by eqn. (1). Since that the wave propagation distance ($= C\Delta t$) during a time increment is in usual much less than the element width l and numerical divergence is happened by this numerical scheme, a pressure damping ($= \dot{p}(\sqrt{l/C\Delta t} - 1)$) is added in solving the momentum equations. In order to prevent using an element that is too thin, a slipping boundary condition

is used where the nodes are put on one quarter of element thickness away from the wall and the corresponding shear stresses due to viscosity are applied.

3 Examples

Two examples have been carried out to demonstrate the accuracy and versatility of the numerical method for flow induced vibration. One is the typical flow past a single flexible circular cylinder, the other is the tube row in crossflow.

3.1 The flow past a single flexible circular cylinder

Figure 1 shows the computation domain of the flow past a cylinder and the local mesh near the cylinder. The Reynolds number of the flow field is 1.E5 while the density, dynamic viscosity, free stream velocity of the fluid and the diameter (D) of the cylinder are given in a consistent unit as 1, 2.E-8, 1 and 2.E-3, respectively. The upstream (left) boundary and the two sides (top and bottom) are 20 D away from the cylinder center. The downstream boundary is extended to 40 D.

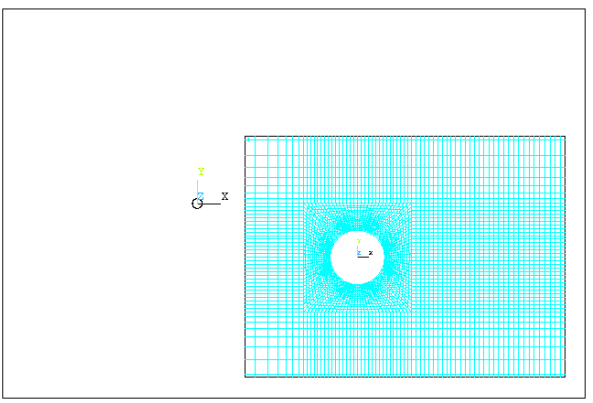


Figure 1: The computation domain and the local mesh near cylinder.

When the cylinder was fixed, the variations of computed drag (X) and lift (Y) forces are plotted in Figure 2. The free stream velocity is risen up during the time from 0. to 0.01 and so the drag force is. From the lift force, the flow field is symmetric for two vortices and the lift is almost vanished at the beginning. It gradually changes to be non-symmetric or shaking vortex street shown in Figure 3 and the lift force comes up before about Time=0.15. After being in vortex shaking, the averaged drag, root mean squared lift and the shaking frequency have a good agreement with experiments [5] and the non-perfect periodic variation shows the chaotic behavior of the turbulent flow. The computed distribution of turbulence strain rate at an instant as displayed in Figure 4 shows quite similar to that taken from shadowgraph in Figure 5 [6].

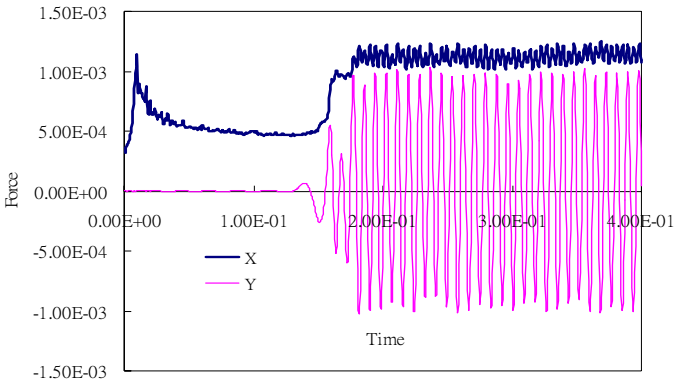


Figure 2: The variations of computed drag (X) and lift (Y) forces.

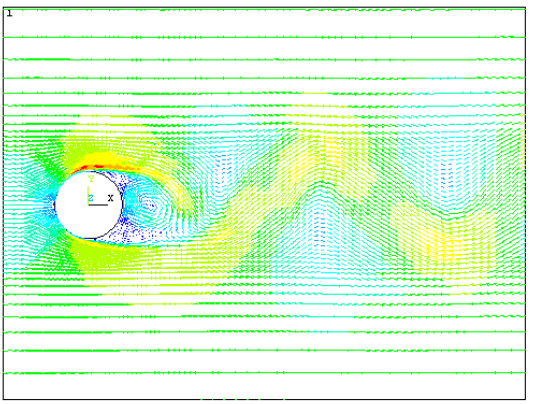


Figure 3: The snapshot of velocity field for the flow past a cylinder.

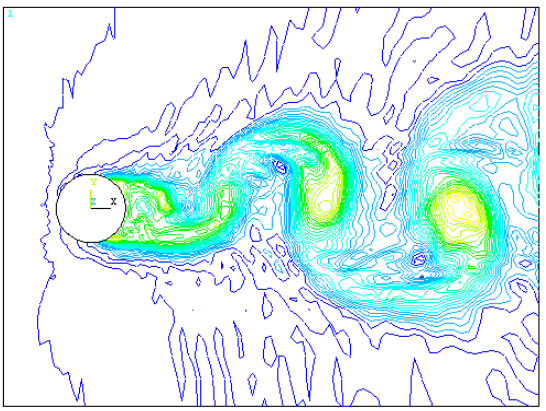


Figure 4: The snapshot of turbulence strain rate.

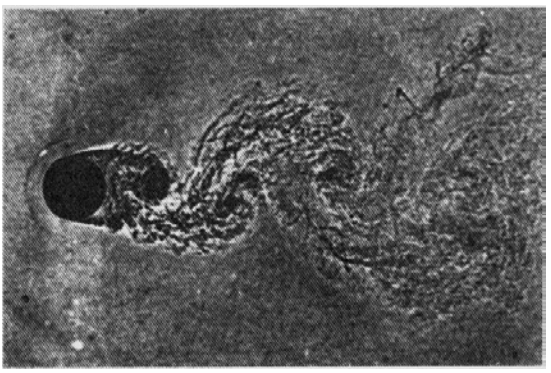


Figure 5: The multiple-spark shadowgraph of turbulence.

When the circular cylinder was flexible, it is supported by a spring and a damper on both X and Y directions in this two-dimensional model. In order to show significant flow induced vibration, the resonance frequency of the cylinder is designed to match the shaking frequency of vortex street. Therefore, the mass of the cylinder (M), the spring constant (K) and a small damping (C) are given in a consistent unit as 7.782e-4, 388.8 and 0.00118, respectively. Figure 6 shows the deformed mesh in significant displacement and the nodal velocity at an instant. It is interesting to find that the nodal velocities of mesh are not all in-phase due to the deforming mesh method being used. As shown in Figure 7, the computed lateral oscillation begins to be amplified as expected due to the resonance after the vortex shaking occurs. The amplifying lateral oscillation makes the averaged drag force slightly increasing as given in Figure 8 which agrees with the observation in experiments [5].

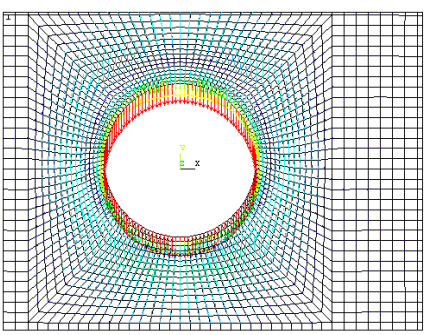


Figure 6: The deformed mesh and the nodal velocities of mesh at an instant.

3.2 The tube row in crossflow

Figure 9 shows the computation domain and the local mesh of the tube row in crossflow [5] considered. The diameter of tube is 0.0159m. The ratio of pitch to

diameter is 1.35. In unit length (m), the mass of tube is 3.861 kg, the equivalent spring constant and damping are given as 103.834 N/m and 57.14 kg/sec, respectively in the two-dimensional model. The density of fluid is 1000 kg/m^3 and its dynamic viscosity is 0.001 N-sec/m^2. A flow rate to have the average velocity 1.5 m/sec in the gaps between the tubes is given.

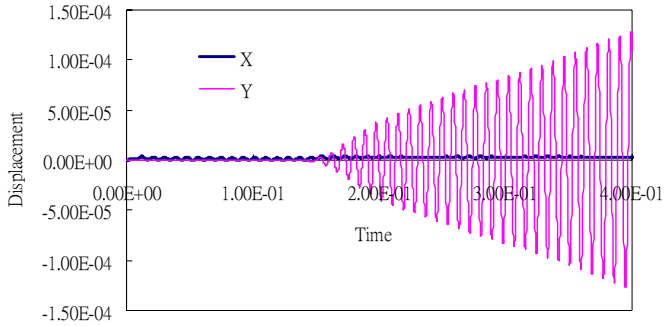


Figure 7: The variations of computed displacements.

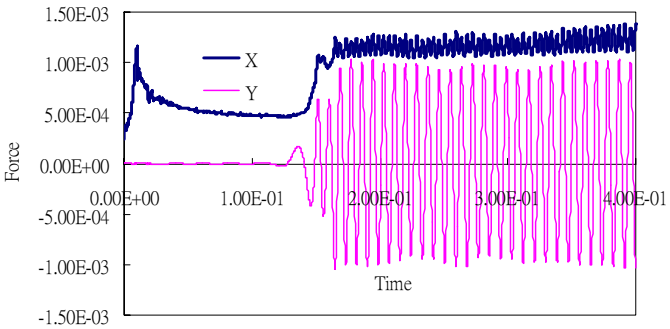


Figure 8: The variations of computed drag (X) and lift (Y) forces.

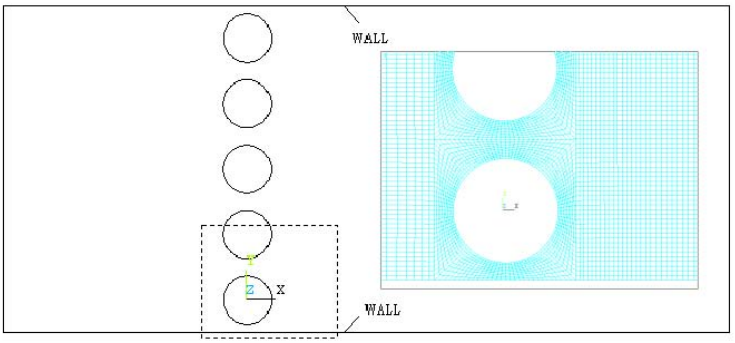


Figure 9: The computation domain of the tube row in crossflow.

Figure 10 and 11 give the snapshots of velocity field and turbulence strain rate for the tube row in crossflow. The unequal spacing between the tubes shows the large displacement of them at that moment. It seems that the jet flow with less turbulence in the gaps penetrates into the fully developed turbulent zone.

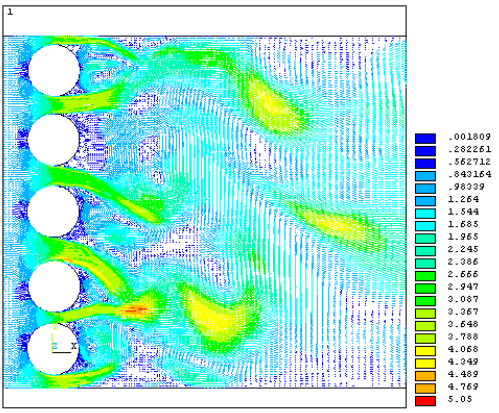


Figure 10: The snapshot of velocity field for the tube row in crossflow.

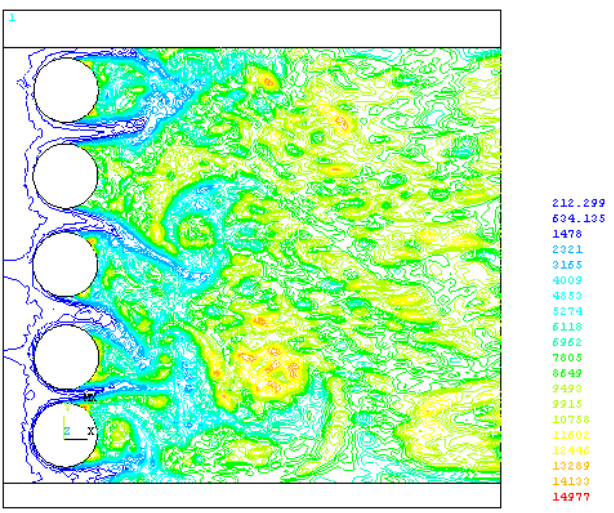


Figure 11: The snapshot of turbulence strain rate for the tube row in crossflow.

Due to a quick start-up of incoming flow from the upstream, all tubes are subjected to an impulsive force and oscillating simultaneously at the beginning as shown in the variation of displacement, Figure 12. The same as the flow past a single cylinder, the symmetry of geometry makes the middle tube (No. 3) show no lateral displacement in the early stage rather than the others. After the vortex

shaking of the middle tube coming up, it seems that there is no significant difference of the oscillation type between all of the tubes. Although the oscillation in the nature frequency of the tube is observed, more significant chaotic fluctuation induced by the turbulence is noticed.

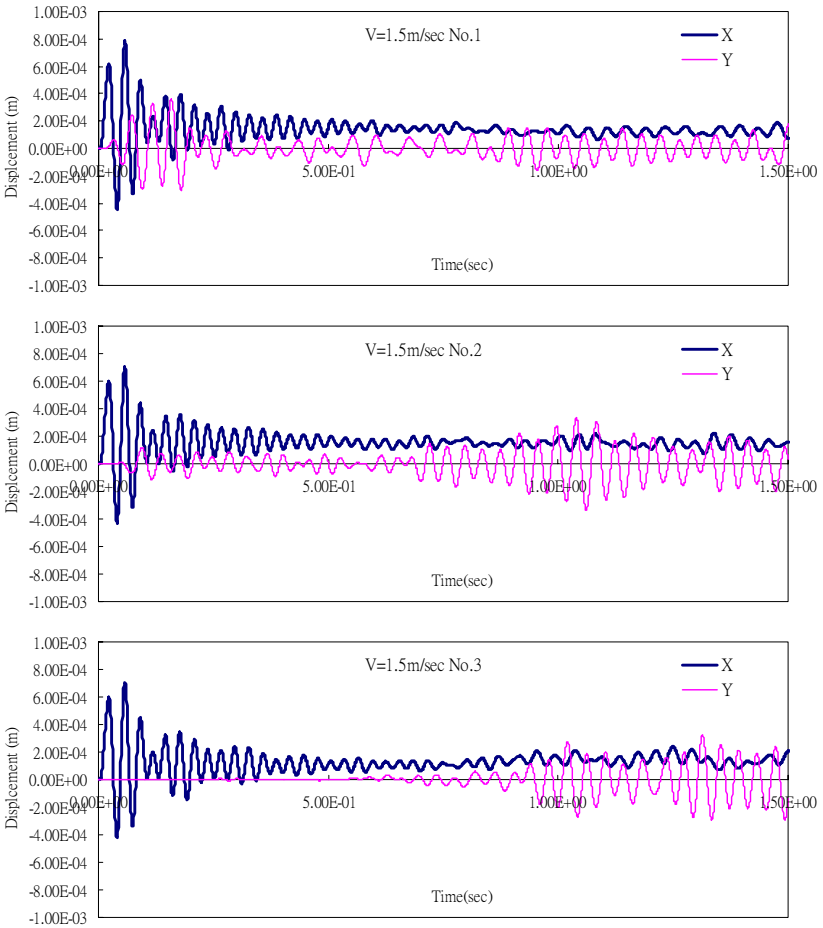


Figure 12: The variations of computed displacements where No. 1 is the tube near the wall, No. 2 is the next and No. 3 is the middle tube.

4 Concluding remarks

The proposed deforming mesh with the unsteady turbulence model shows good results on the fluid-structure interaction of the flow past a cylinder or tube row. The present method has been extended to three-dimensional flow fields and the parallel computation. Further development to free surface flow of material processing, such as the die coating, will be reported in the future.

References

[1] Schroder, K. and Gelbe, H., Two- and Three- Dimensional CFD-Simulation of Flow- Induced Vibration Excitation in Tube Bundles. Chemical Engineering and Processing Vol. 38, pp. 621-629, 1999.
[2] Ichioka, T., etc, Research on Fluid Elastic Vibration of Cylinder Arrays by Computational Fluid Dynamics. JSME International Journal, Series B. Vol. 40, No. 1, pp. 16-24, 1997.
[3] Sadaoka, N., etc, Analysis of Flow- Induced Vibrations in Piping Systems and Circular Cylindrical Structures. JSME International Journal Series B, Vol. 41, No. 1, pp. 221-226, 1998.
[4] Farhat, C., etc, Torsional springs for two-dimensional dynamic unstructured fluid meshes. Computer Methods in Applied Mechanics and Engineering, Vol. 163, No. 1-4, pp. 231-245, 1998.
[5] Chen, S-S. Flow-Induced Vibration of Circular Cylindrical Structures, Hemisphere Pub. Corp., 1987.
[6] Van Dyke, M., An Album of Fluid Motion, The Parabolic Press, 1982.



Dispersion of solid saltating particles in a turbulent boundary layer

H. T. Wang[1], Z. B. Dong[1], X. H. Zhang[2] & M. Ayrault[2]
[1]*Key Laboratory of Desert and Desertification, CAREERI, CAS, Lanzhou Gansu, People's Republic of China*
[2]*Laboratoire de Mécanique des Fluides et d'Acoustique, UMR CNRS Ecully, France*

Abstract

A horizontal saltation layer of glass particles in air is investigated experimentally both on a flat bed and over a two-dimensional ridge. Particle concentrations are measured by Mie scattering diffusion. All the statistical moments of the particle concentration are determined such as mean concentration, rms concentration fluctuations, skewness and flatness coefficients. Measurements of particle concentrations were made at the top of the ridge and in the cavity region. It is confirmed that over a flat bed the mean concentration decreases exponentially with height, the mean dispersion height H being of great meaning. It is shown that the concentration distribution follows quite well a lognormal distribution. At the top of the ridge, the saltation layer is decreased and the concentration increased.
Keywords: particles, saltation, dispersion, turbulent boundary layer.

1 Introduction

Wind erosion is a major cause of soil degradation in arid and semi-arid areas and deserts. It is therefore of great importance to analyze both experimentally and theoretically the motion of wind-blown particles in order to develop effective wind erosion modeling system for controlling the wind erosion of small particles.

Saltation is the primary wind erosion mechanism. Initially aerodynamically lifted off by the wind in short hops and although accelerated by the wind, particles will return to the bed and will impact the ground, rebounding and/or



WIT Transactions on Engineering Sciences, Vol 52, © 2006 WIT Press
www.witpress.com, ISSN 1743-3533 (on-line)
doi:10.2495/AFM06056

ejecting other particles. The impact of saltating sand particles have a severe impact on the natural environment and human activity as for example soil erosion and dust entrainment (Shao et al. 1993).

In the present study, the dispersion of solid glass particles over a flat bed and over a two-dimensional triangular ridge is investigated experimentally by visualizing the wind-blown particles. Detailed measurements of concentration were made over a flat bed, at the hillcrest and in the near wake region. The saltation layer being considered as a continuum and using the Mie scattering diffusion properties, we present the particle concentrations statistics.

2 Experimental set-up

Different experiments were run in the blowing sand wind tunnel in the Key Laboratory of Desert and desertification, the Chinese Academy of Science, PR China (Dong et al. 2002). Particles used are glass particles with a density $\rho_p = 2650\ kgm^{-3}$ and a mean diameter of $208\ \mu m$. The floor of the wind tunnel was covered with particles to a depth of 0.02 m, installed 8 m downstream of the entrance of the test section and over a length of more than 3 m. The measure area was set at 3 m from the upwind edge of the sand bed. The laser tomography visualizations were made in the vertical plane on the longitudinal axis of the wind tunnel.

The two-dimensional symmetrical triangular ridge was set at 3 m from the upwind edge of the sand bed (Figure 1). The height h=24 mm (half the base width B=48 mm) is corresponding to the mean Eulerian dispersion height H of the saltation layer or centroid on a flat bed (Zhang et al., 2004).

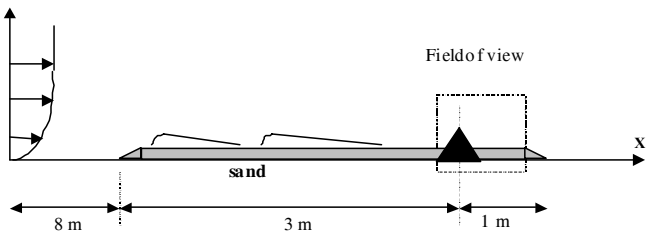


Figure 1: Sketch of the wind tunnel.

Two different experiments were run, over a flat bed for three different external velocities (U_e=6 $ms^{-1,}$ U_e=8 $ms^{-1,}$ and U_e=10 ms^{-1}) and over a steep two-dimensional ridge for U_e=8 ms^{-1}. For the concentration field the saltation layer should be considered as a continuum, camera had a large field of view and the distance between two pixels was Δpix=0.186 mm.

As discussed in detail by Ayrault and Simoens (1995) for the polydispersed incense particles, the grey level of the scattered light is proportional to $\sum d_i^2 N_i$

where N_i is the number density of particles of diameter d_i, and the subscript i denotes the ensembles of different particle diameters in the total sample. This is true provided the absorption of light along the optical path, background illumination, geometrical distortions effects have been account for. Figure 2 represents the instantaneous image over a flat bed and the mean concentration of particles over the ridge image, the mean ensemble average being obtained from a set of 400 instantaneous images.

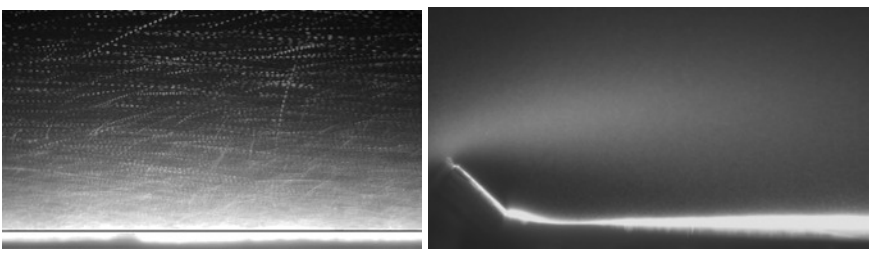


Figure 2: Example of (a) the instantaneous particle image and (b) the mean image concentration of particles over a flat bed and over a triangular ridge for U_e=8 ms^{-1}.

3 Experimental results

3.1 Dispersion over a flat bed

Figure 3 shows the vertical profiles of mean concentration expressed in grey level values for the three external velocity speeds U_e=6, 8, 10 ms^{-1}. The mean concentration profiles agree well with the exponential decay with height, which has been found previously by Nalpanis et al. (1993), Zhou et al. (2001) and Dong et al. (2002). Due to the intense reflection of light on the sand bed as clearly seen in figure 4, we couldn't determine the maximum of concentration at the sand level. Particularly for the U_e=10 ms^{-1} speed of the free stream flow, the very high number of particles ejected causes some absorption of light along the optical paths near the sand bed, this absorption being not negligible. On account of the good agreement with the exponential fit, extrapolation was carried out by using the exponential fit curve and so, the maximum value was estimated and noted $<C(z=0)>_{estimated}=<C>_{\max}$.

Profiles of the normalized mean particle concentration $<C(z)>/<C>_{\max}$ against the normalized height z/H are shown in figure 4. The saltation layer or centroid. Is defined by

$$H=\frac{\int_0^\infty z<C(x,z)>dz}{\int_0^\infty <C(x,z)>dz}$$

When the height is normalized by the mean dispersion height H, all the data collapse together, profiles are similar and are in good agreement with the exponential form, except the near bed region for the U_e=10 ms^{-1} fluid velocity speed. The mean dispersion height should be a characteristic length scale, the mean concentration could be expressed as

$$\frac{<C(z)>}{<C(z=0)>}=\exp\left\{-\frac{z}{H}\right\}$$

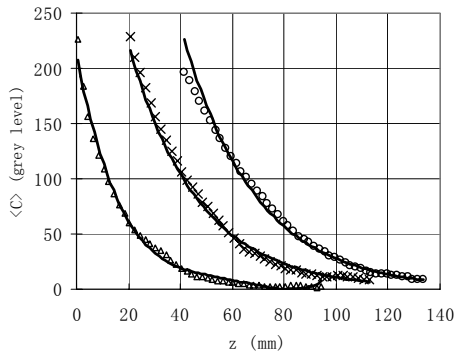


Figure 3: Mean concentration profiles (in grey level values) against vertical distance (in millimeters) for U_e=6, 8, 10 ms^{-1}. Profiles for 8 and 10 ms^{-1} have been translated: for 8 ms^{-1}, (z+20)(mm); for 10 ms^{-1}, (z+40)(mm). Triangles: U_e=6 ms^{-1}; crosses: U_e=8 ms^{-1}; circles: U_e=10 ms^{-1}; Lines: best exponential fit.

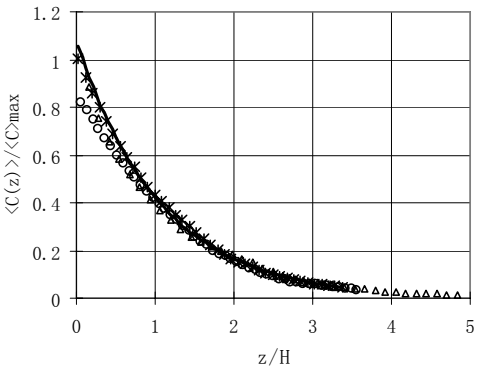


Figure 4: Non dimensionalized mean concentration profiles $<C(z)>/<C>_{max}$ against non dimensionalized height z/H for the three U_e=6, 8, 10 ms^{-1}. Triangles: U_e=6, ms^{-1}; crosses: U_e=8 ms^{-1}; circles: U_e=10 ms^{-1}. Line: best exponential fit for U_e=8 ms^{-1}.

The intensity of concentration $I(z)=\frac{c'(z)}{<C(z)>}$ is shown in figure 5. All the profiles exhibit the same shape but no clear similarity is found. As usual in such semi-bounded flows, the maximum intensity concentration values are obtained at the outer region of the saltation layer, where the mean concentration is small and the intermittency large.

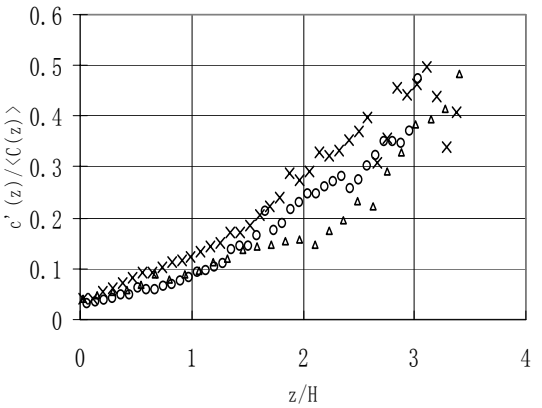


Figure 5: Intensity concentration profiles $I(z)=\frac{c'(z)}{<C(z)>}$ against z/H for U_e=6, 8, 10 ms^{-1}. Triangles: U_e=6 ms^{-1}; crosses: U_e=8 ms^{-1}; circles: U_e=10 ms^{-1}.

The experimental probability density functions at different heights $z=H/2, H, 2H$ inside the saltation layer are plotted in figure 6 for U_e=8 ms^{-1}. The agreement of the experimental values with the theoretical lognormal distribution is quite reasonable. So we could consider that inside the saltation layer and for the three velocity speeds studied, the concentration of saltating sand particles are lognormal distributed.

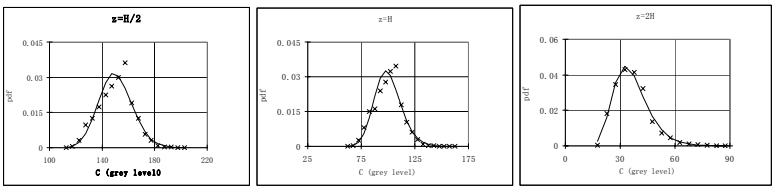


Figure 6: Pdf of concentration at $z=H/2, H, 2H$ for U_e=8 ms^{-1}. Experimental results: symbols; theoretical curve: line.

3.2 Dispersion over a two dimensional ridge

The influence of the ridge on the particle concentration was also investigated. Although the fluid flow is accelerated over the ridge, particles are decelerated due to the effects of the gravity. The mean concentration profiles were measured at six positions along the center line of the wind tunnel: the hill top, the downwind hill foot X=1*h*, X=2*h*, X=4*h*, X=6*h* and X=12*h*. Figure 7 shows the different vertical profiles of mean concentration $<C(z)>$ normalized by the maximum value of the mean concentration at the hill top $<C_{X=0}>_{\max}$. As clearly seen, all these profiles exhibit very different shapes. The theoretical exponential law is quite well verified at the top. As expected, the other profiles in the near wake have different shapes with elevated maxima as profiles for mean and rms concentrations.

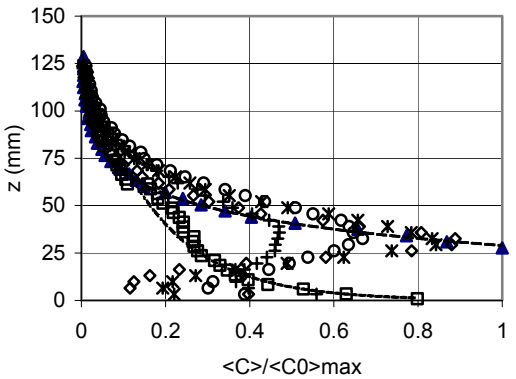


Figure 7: Vertical mean concentration profiles at six downwind positions from the ridge top. Triangles *X*=0h; inclined squares: *X*=1h; crosses: *X*=2h; circles: *X*=4h; plus: *X*=6h; squares: *X*=12h.

The fit line for X=0 represents the theoretical curve $\frac{<C(z)>}{<C(z=0)>}=\exp(-\frac{z}{H})$.

The vertical profiles of the rms of particle concentration exhibit elevated maxima, except for the last section in the wake. The heights of the maxima increase with the hill distance with a relatively high value, more than 15 %. The vertical profiles of the intensity of concentration $I(z)=\frac{c'(z)}{<C(z)>}$ shown in figure 8 exhibit the same shape but no clear similarity is found. As usual in such semi-bounded flows, the maximum intensity concentration values are obtained in the outer region of the saltation layer, where the mean concentration is small and the intermittency large.

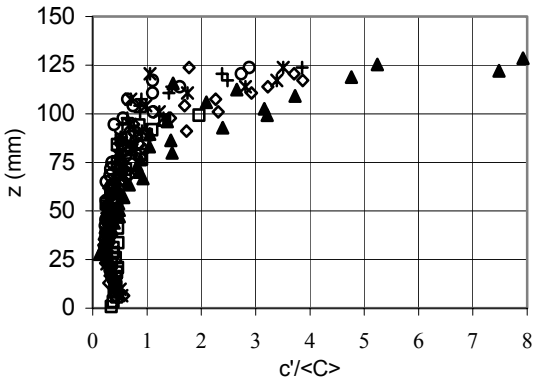


Figure 8: Vertical rms profiles at six downwind positions from the ridge top. Triangles X=0h; inclined squares: X=1h; crosses: X=2h; circles: X=4h plus: X=6h; squares: X=12h.

From the skewness and flatness profiles, it was shown that the concentration distribution is not following a lognormal distribution (Figure 9).

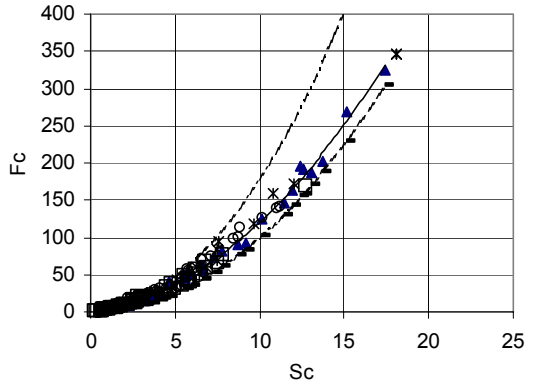


Figure 9: Flatness versus Skewness profiles at four downwind positions downwind the ridge. Triangles $X=0h$; crosses: $X=2h$; circles: $X=4h$; squares: $X=12h$. Dashed line: $K=S^2+1$; dashed line: $K=\frac{16}{9}S^2+3$; line: parabola for $X=4h$.

Hill induced perturbations in the mean concentration were determined from their measured profiles with and without the ridge. The vertical profiles of

fractional concentration-up ratio ΔC, defined by $\Delta C = \frac{<C(z)>}{<C>_{\max}} - \frac{<C_f(z)>}{<C_f>_{\max}}$ where z is the height above the lower surface and $<C_f(z)>$ is the corresponding mean concentration above the flat surface are shown in figure 10. A reduction in concentration with a minimum of -0.25 and -0.5 close to the surface, is observed respectively at the two sections X=2h and X=4h. A positive perturbation persists at heights greater than respectively 10 mm and 15 mm above the sand bed. We note that no negative value is observed for the X=6h section. In the last section, X=12h, only small positive fractional concentration-up values of about 0.2 exist. The particle flow is nearly recovering his behavior without a ridge.

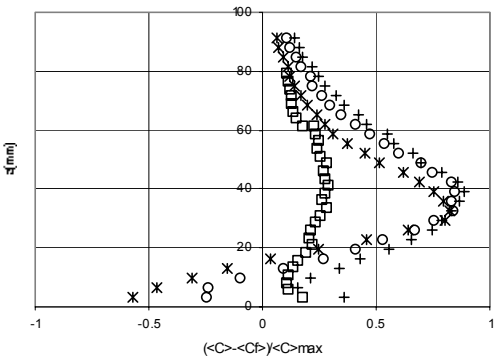


Figure 10: Fractional concentration-up factor at four downwind positions. Crosses: *X=2h*; circles: *X=4h*; plus: *X=6h*; squares: *X=12h.*

4 Conclusion

A horizontal saltation layer of glass particles in air was investigated experimentally. Particle concentrations were measured by Mie scattering diffusion (MSD). All the statistical moments of the particle concentration were determined such as mean and rms concentration, skewness and flatness coefficients, probability density functions.

It was found that the mean concentration over a flat bed is decreasing exponentially with height, the mean dispersion height H being of great meaning. In this framework, the saltation layer could be investigated as composed of two adjacent layers. The inner saltation layer where particles are mainly influenced by the bed effects and the outer saltation layer where this is the external fluid flow which greatly influences particles. It was also shown that the concentration distribution is following quite well a lognormal distribution.

The influence of the ridge on the particle concentration was also investigated. At the hill top, the saltation layer height is smaller than in flat terrain. The

theoretical exponential law is quite well verified at the top and also, for X/h=12, the vertical profile is near this curve. Although the fluid flow is accelerated over the ridge, particles are decelerated due to the effects of the gravity with a minimum speed-up factor of about 0,4 at the hill top. On the lee side, there is a deceleration of the particles and an increase of the velocity fluctuations. As expected, the other profiles have different shapes with elevated maxima as profiles for mean and rms concentrations. From the skewness and flatness profiles, it was shown that the concentration distribution is not following a lognormal distribution.

References

[1] Ayrault M. and Simoens S. 1995, J. Flow Visualization Image Processing 2, 195-208.
[2] Dong Z., Liu X., Li F., Wang H. and Zhao A. 2002, Earth Surface Processes and Landforms 27, 641-658.
[3] Nalpanis, P., Hunt, J.C.R., Barret, C.F., 1993, Saltating particles over flat beds, J. Fluid Mech., vol 251, 661-685.
[4] Dong Z., Wang H., Liu X. Li F. And Zhao A., 2002, Geomorphology 45, 277-289.
[5] Shao Y., Raupach M.R. and Findlater P.A. 1993, J. Geophysical Res., vol. 98, D7, 12719-12726.
[6] Zou, X.Y., Wang, Z.L., Hao, Q.Z., Zhang, C.L., Liu, Y.Z., Dong, G.R., 2001, The distribution of velocity and energy of saltating grains in a wind tunnel, Geomorphology 36, 155-165.



This page intentionally left blank

Section 12
Biofluids

This page intentionally left blank

An exact solution of the Navier-Stokes equations for swirl flow models through porous pipes

N. Vlachakis[1], A. Fatsis[1], A. Panoutsopoulou[2], E. Kioussis[1], M. Kouskouti[1] & V. Vlachakis[3]
[1]*Technological University of Chalkis, Department of Mechanical Engineering, Greece*
[2]*Hellenic Defence Systems, Greece*
[3]*Virginia Polytechnic Institute and State University, Department of Mechanical Engineering, Blacksburg, USA*

Abstract

An exact solution of the Navier-Stokes equations for laminar flow inside porous pipes simulating variable suction and injection of blood flows is proposed in the present article. To solve these equations analytically, it is assumed that the effect of the body force by mass transfer phenomena is the 'porosity' of the porous pipe in which the fluid moves. The resultant of the forces in the pores can be expressed as filtration resistance. The developed solutions are of general application and can be applied to any swirling flow in porous pipes.

The effect of porous boundaries on steady laminar flow as well as on species concentration profiles has been considered for several different shapes and systems. In certain physical and physiological processes filtration and mass transfer occurs as a fluid flows through a permeable tube. The velocity and pressure fields in these situations differ from simple Poiseuille flow in an impermeable tube since the fluid in contact with the wall has a normal velocity component. In the new flow model, a variation of the solutions with Bessel functions based on Terrill's theoretical flow model is adopted.

Keywords: exact solution, Navier-Stokes equations, pipe flow, laminar flow, porous media, blood flow characteristics.



WIT Transactions on Engineering Sciences, Vol 52, © 2006 WIT Press
www.witpress.com, ISSN 1743-3533 (on-line)
doi:10.2495/AFM06057

1 Introduction

Swirl particulate flows can be found in nature and have significant industrial applications including infiltration, blood flow and particle separation. The present study was inspired by the need to model swirl flows in such systems with the goal of developing tools for study, design and improvement of the porous and filtration process in mass fraction systems. Computation of such fields is very challenging being further complicated by each porous character and the possibility of laminar regimes.

One of the approaches to model these porous flows is based on solution of the full Navier-Stokes equations. The effect of porous boundaries on steady laminar flow as well as on species concentration profiles has been considered for several different shapes and systems [1–5]. In certain physical and physiological processes filtration and mass transfer occurs as a fluid flows through a permeable tube [6, 7]. The velocity and pressure fields in these situations differ from simple Poiseuille flow in an impermeable tube since the fluid in contact with the wall has a normal velocity component. Therefore, in processes where a combined free and porous flow occurs under the aforementioned conditions, the flow regime can be naturally modelled by coupling Darcy's law and the Navier-Stokes equations. Moreover, many factors such as the Reynolds number and transport properties of the porous media directly affect the dynamics of the flow. The diversity of underlying phenomena and the complexity of interactions between free and porous flow systems have prevented development of a general theoretical analysis of coupled flow systems. In most cases the Navier-Stokes equations are reduced to ordinary non-linear differential equations of third order for which approximate solutions are obtained by a mixture of analytical and numerical methods [8–10].

In this study, an exact solution of the Navier-Stokes equations is proposed describing the flow in a porous pipe allowing the suction or injection at the wall to vary with axial distance. In the current research work, a new exact solution of Terill proposed phenomenology [11] is presented similar to the model of blood floe through a porous pipe with variable injection and suction at the walls. In the new flows model a variation of the solutions with Bessel functions based on Terrill's theoretical flow models is adopted. This study uses biomechanical procedures to find exact solutions of the Navier-Stokes equations, governing steady porous pipe flows of a viscous incompressible fluid in a three-dimensional case including body force term.

2 Mathematical and physical modelling

The mathematical model simulates the capillary between an arteriole and a venule as a horizontal tube of constant cross-section and inner radius R with a permeable wall of thickness δ.

Assuming the flow of a Newtonian fluid through the pipe, the basic equations that describe the mechanics of blood flow in cardiovascular circulation vessels

are the mass conservation equation and the equations of motion (Navier-Stokes), in a cylindrical system of coordinates (r,θ,z) where the z-axis lies along the centre of the pipe, r is the radial distance and θ is the peripheral angle. A schematic diagram of the model and coordinate system is given in figure 1.

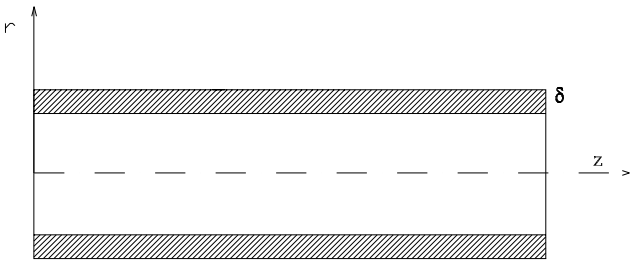


Figure 1: Representation of flow in a tubular membrane with a cylindrical coordinate system.

2.1 The Navier-Stokes equations

Starting from the solutions form suggested by Terrill [11] and taking into account body force phenomena, the following solution is proposed. It is considered that in the porous space of the pipe, mass transfer phenomena appear the body force of that is equivalent to the radial pressure gradient. Moreover, when porous spaces exist a new term is added to the radial pressure gradient which is involved in the first of the wavier-Stokes equations while the following simplified assumptions are made:

a) axial symmetry
b) the fluid is homogeneous and behaves as a Newtonian fluid
c) the pipe is considered of finite length and before the fluid enters the porous pipe its profile has already been developed
d) the permeable membrane is treated as a `fluid medium'.

The continuity equation in c cylindrical system of coordinates is:

$$\frac{1}{r^*}\cdot\frac{\partial}{\partial r}\left(r^* u_r^*\right)+\frac{1}{r^*}\cdot\frac{\partial u_\theta^*}{\partial\theta^*}+\frac{\partial u_z^*}{\partial z^*}=0 \tag{1}$$

The Navier-Stokes equations for the case of the steady axi-symmetric motion of an incompressible fluid in a porous horizontal pipe are:

The r-direction of the momentum equation:

$$\rho\left(u_r^*\frac{\partial u_r^*}{\partial r^*}+\frac{u_\theta^*}{r^*}\cdot\frac{\partial u_r^*}{\partial\theta^*}-\frac{u_\theta^{*2}}{r^*}+u_z^*\frac{\partial u_r^*}{\partial z^*}\right)=$$

$$f_r\rho+\mu\left[\frac{\partial}{\partial r^*}\left(\frac{1}{r^*}-\frac{\partial}{\partial r^*}\left(r^* u_r^*\right)\right)+\frac{1}{r^{*2}}\frac{\partial^2 u_r^*}{\partial\theta^{*2}}-\frac{2}{r^{*2}}\frac{\partial u_\theta^*}{\partial\theta^*}+\frac{\partial^2 u_r^*}{\partial z^{*2}}\right] \tag{2}$$

The θ-direction of the momentum equation:

$$\rho\left(u_r^*\frac{\partial u_\theta^*}{\partial r^*}+\frac{u_\theta^*}{r^*}\cdot\frac{\partial u_\theta^*}{\partial \theta^*}+\frac{u_r^* u_\theta^*}{r^*}+u_z^*\frac{\partial u_\theta^*}{\partial z^*}\right)=-\frac{1}{r^*}\cdot\frac{\partial p^*}{\partial \theta^*}$$

$$+\mu\left[\frac{\partial}{\partial r^*}\left(\frac{1}{r^*}\frac{\partial\left(r^* u_\theta^*\right)}{\partial r^*}\right)+\frac{1}{r^{*2}}\frac{\partial^2 u_\theta^*}{\partial \theta^{*2}}+\frac{2}{r^{*2}}\cdot\frac{\partial u_r^*}{\partial \theta^*}+\frac{\partial^2 u_\theta^*}{\partial z^{*2}}\right] \quad (3)$$

The z-direction of the momentum equation:

$$\rho\left(u_r^*\frac{\partial u_z^*}{\partial r^*}+\frac{u_\theta^*}{r^*}\cdot\frac{\partial u_z^*}{\partial \theta^*}+u_z^*\frac{\partial u_z^*}{\partial z^*}\right)=$$

$$-\frac{\partial p^*}{\partial z^*}+\mu\left[\frac{1}{r^*}\frac{\partial}{\partial r^*}+\left(r^*\frac{\partial u_z^*}{\partial r^*}\right)+\frac{1}{r^{*2}}\cdot\frac{\partial^2 u_z^*}{\partial \theta^{*2}}+\frac{\partial^2 u_z^*}{\partial z^{*2}}\right] \quad (4)$$

2.2 The porous wall equations

Introducing the dimensionless porosity parameter ξ as follows:

$$\xi=\frac{\dot{V}_\delta\cdot k\cdot\rho}{A_\delta\cdot\delta\cdot\mu} \quad (5)$$

where A_δ is the membrane area, k is the permeability coefficient, $\dot{V}_\delta$ is the volumetric flow rate through the porous space and δ is the thickness of the interstitium.

The porous wall is supposed to be homogenous and isotropic in which the main characteristic is intrinsic permeability k. The flow through the porous wall can be simply taken into account as a boundary condition of the flow through the tube at the permeable wall.

At the permeable wall, the wall suction velocity is given by Darcy's law as a 'fluid-tissue' system :

$$u_r=-\frac{k}{\mu}\left(\frac{\partial P}{\partial r}\right) \quad (6)$$

2.3 Dimensionless form of the equations

The above equations are non-dimensionalised by the following transformation:

$$\begin{aligned} r^* &= r \cdot R \\ z^* &= z \cdot R \\ u_r^* &= u_r \cdot U \\ u_z^* &= u_z \cdot U \\ u_\theta^* &= u_\theta \cdot U \\ P^* &= P \cdot \rho \cdot U^2 \end{aligned} \tag{7}$$

Taking into account the above assumptions, the continuity equation is written using the dimensionless quantities as:

$$\frac{u_r}{r} + \frac{\partial u_r}{\partial r} + \frac{\partial u_z}{\partial z} = 0 \tag{8}$$

Defining the Reynolds number as:

$$\mathrm{Re} = \frac{\rho \cdot U \cdot R}{\mu} \tag{9}$$

the system of the Navier-Stokes equations takes the non-dimensional form:

$$\left(u_r \frac{\partial u_r}{\partial r} - \frac{u_\theta^2}{r} + u_z \frac{\partial u_r}{\partial z} \right) = -(\xi + 1)\frac{\partial p}{\partial r} + \frac{1}{\mathrm{Re}}\left[\frac{\partial^2 u_r}{\partial r^2} + \frac{1}{r} \cdot \frac{\partial u_r}{\partial r} - \frac{u_r}{r^2} + \frac{\partial^2 u_r}{\partial z^2} \right] \tag{10}$$

$$u_r \frac{\partial u_\theta}{\partial r} + \frac{u_r \cdot u_\theta}{r} + u_z \frac{\partial u_\theta}{\partial z} = \frac{1}{\mathrm{Re}}\left[\frac{\partial u_\theta^2}{\partial r^2} + \frac{1}{r} \cdot \frac{\partial u_\theta}{\partial r} - \frac{u_\theta}{r^2} + \frac{\partial^2 u_\theta}{\partial z^2} \right] \tag{11}$$

$$\left(u_r \frac{\partial u_z}{\partial r} + u_z \frac{\partial u_z}{\partial z} \right) = -\frac{\partial p}{\partial z} + \frac{1}{\mathrm{Re}}\left[\frac{\partial^2 u_z}{\partial r^2} + \frac{1}{r} \cdot \frac{\partial u_z}{\partial r} + \frac{\partial^2 u_z}{\partial z^2} \right] \tag{12}$$

3 Solution strategy

Extending the procedure of Terrill [11], the axial velocity u_z, the radial velocity u_r and the tangential velocity u_θ, are expressed in terms of two functions:

$$\begin{aligned} u_z &= J_0(rb)e^{-bz} \\ u_r &= J_1(rb)e^{-bz} \\ u_\theta &= \xi \cdot J_1(rb)e^{-bz} \end{aligned} \tag{13}$$

where $J_0(rb)$ and $J_1(rb)$ are the Bessel functions of the First kind and b is the zero of

$$J_0\left(J_0(b)\right)=0 \tag{14}$$

$$J_0(rb)=-b\cdot J_1(rb) \tag{15}$$

and

$$J_1'(rb)=b\cdot J_0(rb)-\frac{J_1(rb)}{r} \tag{16}$$

The functions $J_0(rb)$ and $J_1(rb)$ are shown in figure 2 in terms of $r\cdot b$.

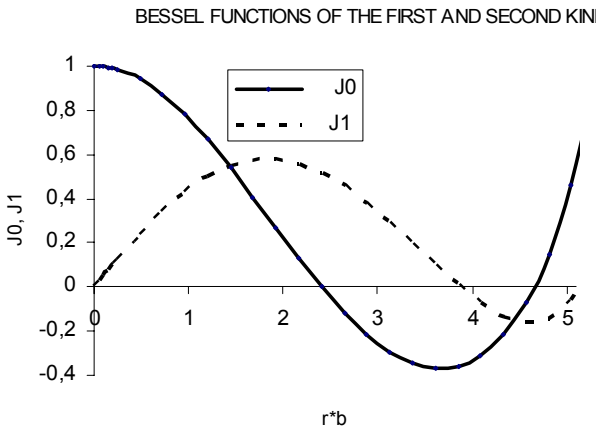


Figure 2: Bessel functions of the first kind.

The following boundary conditions are satisfied:

a. The no-slip condition at the tube wall:

$$u_z=0 \quad \text{at} \quad r=1 \tag{17}$$

b. The suction (b>0) or injection (b<0) condition at the pipe axis:

$$u_r=0 \quad \text{at} \quad r=0 \tag{18}$$

It is assumed that the speed of suction or injection has a finite value at the walls.

c. The swirl condition at the pipe axis:

$$u_\theta=0 \quad \text{at} \quad r=0 \tag{19}$$

Introducing the three velocity components – as expressed in terms of the Bessel functions – in the Navier-Stokes equations, it gives:

$$\frac{\left[J_1(rb)\right]^2 e^{-2bz}}{r} = \frac{\partial P}{\partial r} \tag{20}$$

$$b\left\{\left[J_1(rb)\right]^2 + \left[J_0(rb)\right]^2\right\} e^{-2bz} = \frac{\partial P}{\partial z} \tag{21}$$

Integration of the last equation with respect to z gives:

$$0{,}5\left\{\left[J_1(rb)\right]^2 + \left[J_0(rb)\right]^2\right\} e^{-2bz} = -P(r,z) + \zeta(r) \tag{22}$$

Differentiating the above equation with respect to r and combining the equations (20) and (21) it is finally found:

$$P(r,z) = -0{,}5\left\{\left[J_1(rb)\right]^2 + \left[J_0(rb)\right]^2\right\} e^{-2bz} \tag{23}$$

Thus the required solution of the present model is:

$$\begin{aligned} u_z &= J_0(rb)e^{-bz} \\ u_r &= J_1(rb)e^{-bz} \\ u_\theta &= \xi \cdot J_1(rb)e^{-bz} \end{aligned} \tag{24}$$

$$P(r,z) = -0{,}5\left\{\left[J_1(rb)\right]^2 + \left[J_0(rb)\right]^2\right\} e^{-2bz}$$

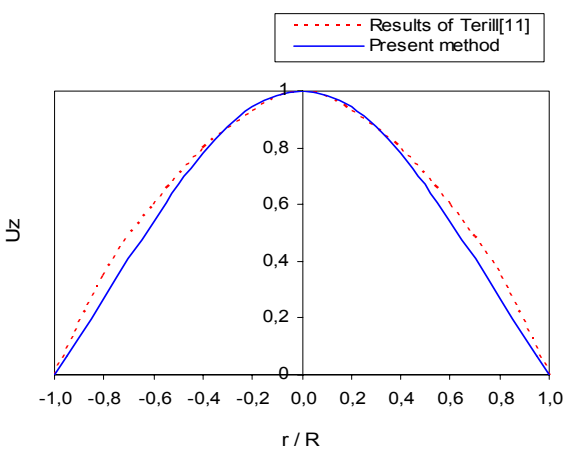


Figure 3: Axial velocity through the pipe at a given axial distance z as a function of the radius of the pipe.

In figure 3 the comparison between the axial velocity predicted by the present model (continuous line) and the couple stress theory of Terill (dashed line) can be seen. A very good comparison overall can be observed.

Figure 4 shows the predicted tangential velocity profiles at a given axial distance with respect to the radius of the pipe. It can be seen that at the center of the pipe the swirl is zero – as imposed by the boundary conditions – and as approaching the wall boundaries it is increasing.

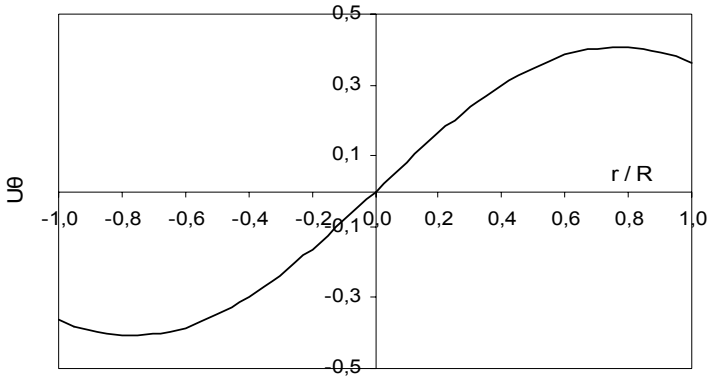


Figure 4: Tangential velocity through the pipe at a given axial distance z as a function of the radius of the pipe.

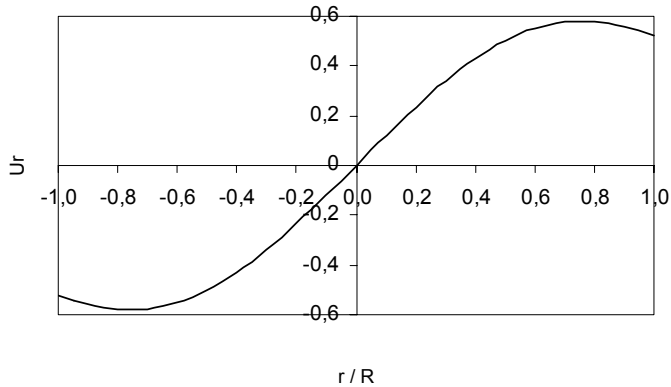


Figure 5: Tangential velocity through the pipe at a given axial distance z as a function of the radius of the pipe.

Figure 5 shows the predicted radial velocity distribution with respect of the pipe radius. At the pipe centre the radial velocity is zero and it increases rapidly up to $r/R = 0.8$. Then the wall porosity causes a deceleration due to the resistance of the fluid through the wall boundary.

4 Conclusions

In this work, a new exact solution of the Navier-Stokes equations is proposed, describing the characteristics of three-dimensional axi-symmetric pipe flows with variable suction and injection at the porous pipe walls. with application to blood flow. In figure 3 the axial velocity distribution across the pipe has been plotted concerning both the theory of Pal et al. [3] and the presented concept of the exact solution blood flow model with porous wall. The pressure and the pressure gradient are dependent on the radial coordinate r in the porous tube. Body force mechanisms in biological membranes are included because of their importance for mass transport. The body force mechanisms which represent here the volume flow rate in the porous space are strongly connected with the angular velocity (twist of the internal particles). The developed solutions are of general application [6, 7] and can be applied to any swirling flow in porous pipes.

References

[1] Bugliarello G., Kapur, C., Hsiao G., *The profile viscosity and other characteristics of blood flow in a Non-uniform Shear Field, Proc.* 4th Intern. Cong. Rheology, New York: Interscience, 1965.

[2] Bugliarello G., *Velocity distribution and other characteristics of steady and pulsating blood flow in Fine Glass Tubes,* Biorheology, **7**, 1970, pp.85-107.

[3] Pal D., Rudraiah N., Devanathan R., *A couple stress model of blood flow in the microcirculation,* Bulletin of mathematical Biology, **4**, 1988, pp.329-344.

[4] Berman A.S., *Laminar flow in channels with porous walls.* Journal of Applied Physics, **24/9**, 1953, 1232-1235.

[5] Yuan, S.W., Finkelstein, A.B., Brooklyn, N.Y., *Laminar pipe flow with injection and suction through a porous wall*, Transactions of the ASME, **78**, (1956), pp.719-724.

[6] Fung Y.C., *Biodynamics – Circulation,* New York, Springer-Verlag, 1984.

[7] McDonald D.A., *Blood Flow in Arteries,* London – Arnold, 1974.

[8] Lu C. *On the asymptotic solution of laminar channel flow with large suction,* Siam J. Math. Anal., **28**, 1997, pp.1113-1134.

[9] Majdalani J., *The oscillatory channel flow with arbitrary wall injection,* Zeitschrift fuer angewandt Mathematik und Physic ZAMP, **52**, 2001, pp.33-61.

[10] Taylor C.L., Banks W.H.H., Zaturska M.B., Drazin P.G., *Three-dimensional flow in a porous channel,* Quart. J. Mech. Appl. Math., **44**, 1991, pp.105-133.

[11] Terril R.M., *Laminar flow in a uniform porous channel with large injection,* Aeronaut. Q. **16**, 1965, pp.323-332.



This page intentionally left blank

Experimental investigation of flow through a bileaflet mechanical heart valve

J. Mejia & P. Oshkai
Department of Mechanical Engineering, University of Victoria, Victoria, BC, Canada

Abstract

Turbulent flow downstream of a bileaflet mechanical heart valve is investigated using digital particle image velocimetry. Evolution of flow structures during the systole and diastole phases of a typical cardiac cycle is characterized by obtaining global flow velocity measurements in multiple cross-sections of the flow field. Instantaneous and time-averaged patterns of flow velocity, vorticity, and streamline topology are used to illustrate the interaction between the unsteady vortices that results in elevation of shear stress levels. This image-based approach can potentially lead to the development of methods for the control of platelet activation and provides insight into the underlying flow physics.
Keywords: bileaflet mechanical heart valves, particle image velocimetry, in-vitro.

1 Introduction

Currently, about 180,000 prosthetic heart valves are implanted each year worldwide, Yoganathan *et al*. [1]. Mechanical Heart Valves (MHVs) are relatively durable but strongly associated with thromboembolisms, which often result in ischemic attacks and stroke, Yin et al. [2]. It is believed that thrombi are caused by flow phenomena not characteristic of physiological conditions, Bluestien *et al*. [3]. The flow phenomena that receive the most attention in this respect include: jet-like flow regions, regions of elevated shear stress, flow separation regions, shed vortices, and turbulence characteristics, Yin *et al*. [2] Despite the recent advances in the field, thromboembolisms occur in



WIT Transactions on Engineering Sciences, Vol 52, © 2006 WIT Press
www.witpress.com, ISSN 1743-3533 (on-line)
doi:10.2495/AFM06058

approximately 3% of all replacement operations involving MHVs, Edmunds *et al*. [4].

On the other hand, biological valves exhibit calcification, and durability problem [1, 5]. However, biological prosthetic heart valves do not require the use of blood thinners to be administered to the patient, making them an attractive alternative to MHVs. A number of experimental and numerical studies have been undertaken in order to address problems with both biological and mechanical heart valves.

1.1 Experimental studies

Significant effort has been devoted to developing realistic laboratory models capable of simulating the fluid mechanic characteristics of the human heart while allowing optical access for the purpose of flow visualization. The complexity of the biological system calls for a compliant setup that not only preserves geometric similarity but also models the pumping cycle. Anatomically correct mock-ups of the aorta have been successfully manufactured and investigated. Scotten and Walker [6] developed a compliant model of the left heart, which allowed the simulation of an arbitrary cardiac cycle and provided optical access to valves in both the aortic and the mitral positions. Several studies have been conducted using this setup, including the development of a new technique to measure the projected dynamic area of prosthetic heart valves, Scotten and Walker [6] Marassi *et al.* [7] developed an artificial heart valve test bench specifically designed to employ particle image velocimetry (PIV). Test benches for digital PIV and stereo PIV were developed. Although slightly different both designs consisted of a valve mounted in a Plexiglas channel. In both cases the channel was surrounded with a Plexiglas chamber in order to minimize optical distortions. His design delivered high versatility in changing and controlling the flow parameters and good optical access for visualization experiments.

It has been suggested that among the many possible causes of thromboembolisms, vortex shedding from the leaflets of MHVs is among the most critical, Yoganathan *et al.* [1]. The shed vortices are associated with regions of high shear stresses in the flow. Blood components (e.g. platelets) can become entrapped in these vortices for relatively long periods of time, increasing their chance of becoming activated.

Several studies have focused on the fundamental fluid dynamics of MHVs in order to provide insight into the flow phenomena. Castellini *et al.* [8] employed PIV techniques to obtain flow velocity measurements upstream and downstream of a bileaflet valve. A symmetric flow pattern including a large separation region behind each leaflet was observed. Furthermore, the authors observed regions of high velocity between the leaflets as well as between each leaflet and the channel walls, which represented the walls of the aorta. Vortex shedding from the trailing edge of each leaflet was also documented.

Bluestien *et al.* [9] performed a study of pulsatile flow through a bileaflet MHV mounted in a non-compliant aorta model. A technique of digital particle image velocimetry (DPIV) was used to characterize the flow. The authors assumed (based on the results of Lamson *et al.* [10]) that no single phase of the



heart cycle (i.e. opening, fully open, closing, or fully closed) contributed significantly more to the formation of thrombi than any other phase. However, a number of other investigations have focused on particular phases of the cardiac cycle. In fact, during the 1970s and 1980s, most of the studies implicitly assumed that blood damage occurs predominantly during forward peak flow through the valve. This assumption is intuitive, as the flow rate is at its maximum when the valve is fully open, but later studies have challenged the validity of this assumption. Manning *et al.* [11] investigated the regurgitant flow field of a bileaflet MHV using PIV under physiological pulsatile flow conditions. The authors found strong jets emerging from the two hinges, and two weaker jets originating from the regions of transition between the tightly sealed central plane and the hinge region. Maximum viscous shear stresses were found to be of the order of 20 N/m^2, which is below the shear stress traditionally associated with the onset of hemolysis. However, other studies have found Reynolds's stresses above the threshold for platelet activation, Meyer [12].

1.2 Numerical studies

Numerical methods play a fundamental role in the research of fluid dynamics. For example, numerical simulations can provide detailed three-dimensional, time-resolved information about a flow. Hence, an integrated approach involving both experimental and numerical techniques is often required to fully characterize a fluid flow problem.

Since platelet activation is closely linked to the occurrence of thromboembolisms, a number of studies have focused on the effect of prosthetic heart valves on platelet activation. If a platelet reaches a certain threshold of cumulative exposure to high shear stress, it becomes activated. The platelet activation state (PAS) was studied for monoleaflet and bileaftlet valves by Yin *et al.* [2]. The authors considered both shear stress magnitude and time of exposure of a given platelet to the elevated shear stress to determine the PAS. In order to determine the amount of activated platelets numerically, tracers were introduced to the calculated flow. The exposure of a tracer to shear stresses over a period of time was then evaluated. Monoleaflet valves were found to cause less PAS compared to bileaflet MHVs. Furthermore, the results showed that virtually no PAS existed in a control case when the valve was removed from the flow field.

Bluestein *et al.* [9] identified vortex shedding as a possible mechanism for the activation of platelets. "The shed vortices also provide the flow conditions that promote the formation of larger platelet aggregates… Following activation, platelets will release their granule constituents and provide positive feedback reactions of coagulation. Platelet aggregates will increase the efficiency of the reaction, eventually resulting in the formation of free emboli."

2 Experimental system and techniques

The experiments for the current study were conducted using a Carbomedics bileaflet mechanical heart valve. The complete flow loop, illustrated in Figure 1,



consisted of a Plexiglas duct, the test section, flexible tubing, a water reservoir, and a pump. A Plexiglas test section was designed to provide optical access to the region downstream of the heart valve. The valve (20.39 mm in diameter) was mounted in the Plexiglas duct. A constant pressure head corresponding to a Reynolds number of 9500 was maintained by a 1/6 hp pump. This Reynolds number corresponds to a net positive average flow speed of approximately 1.35 m/s, corresponding to the peak systolic flow rate of a normal heart with a cardiac output of 5 l/min.

The test section was located 254 mm downstream of the main duct inlet. A honeycomb flow straightener was employed directly downstream of the inlet. To minimize optical distortions, a prismatic acrylic chamber filled with the working fluid surrounding the test section was employed during the experiments. A detailed schematic of the test section is provided in Figure 2.

The coordinate system shown in Figure 3 is used in the analysis presented in later sections. The valve's horizontal axis of symmetry is defined as $z = 0$ and the valve's vertical axis of symmetry is defined as $y = 0$. The $x = 0$ coordinate corresponds to the downstream edge of the valve housing. Flow measurements are not performed within the first 10 mm downstream of the valve housing due to optical inaccessibility.

In order to characterize the three-dimensionality of the flow several parallel planes, positioned along the vertical axis, are used as the data acquisition planes (DAP). The set consisted of three parallel and horizontal planes positioned at 0, 2.6, and 8 mm along the z-axis (DAP A through C), as shown in Figure 3.

Quantitative flow visualization is accomplished by employing DPIV. Titanium dioxide seeding (nominal diameter of 1 μm) serves as tracer particles for the forward flow phase experiments. Images of the particles, which are illuminated by a planar laser sheet, are captured by a high-resolution digital camera. These images are then processed on a computer to yield global instantaneous flow velocity measurements as well as maps of vorticity, streamline topology and time-averaged flow parameters. The displacements of the particles are recorded as a pair of images, each exposed once. The recorded particle displacement field is measured locally across the whole field of view of the images, scaled by the image magnification and then divided by the known laser time delay to obtain flow velocity at each point. The charge-coupled device (CCD) camera is positioned perpendicular to the plane of the light. Depending on the flow velocity and the magnification factor of the camera lens, the time delay between the two pulses is chosen such that adequate displacements of the particle images on the CCD were obtained. From the time delay between the two illuminations and the displacement of the tracers, velocity vectors are calculated.

For the present study, a lens with a focal length of 60 mm is used in conjunction with a 1376 x 1040 pixel CCD camera to provide a physical resolution of the velocity vector field of 4 vectors per square millimeter.

The PIV measurements are acquired at a time interval of 0.204 s, which provided spacing in time appropriate for obtaining random samples for the calculation of averaged turbulence statistics. A total of 1000 images are acquired



and used in the calculation of the following time-averaged parameters: flow velocity $\langle \underline{v} \rangle$, out-of-plane vorticity $\langle \omega_z \rangle$, root-mean-square values of velocity components $\langle u_{rms} \rangle$ and $\langle v_{rms} \rangle$, and Reynolds stress correlation $\langle u'v' \rangle$.

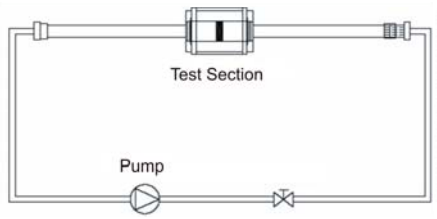


Figure 1: Complete flow loop.

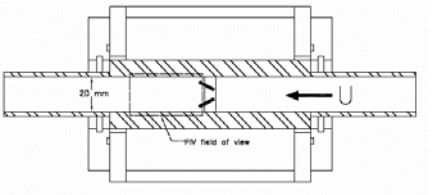


Figure 2: Close-up of the test section.

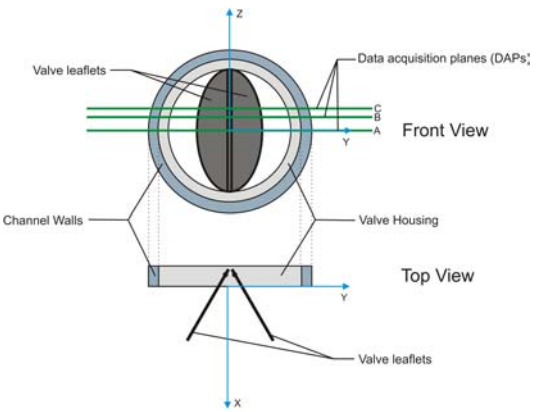


Figure 3: Definition of coordinate system.

3 Results

All results presented here correspond to a steady unidirectional turbulent inflow from right to left. The leaflets of the fully open valve are indicated by the red shaded areas outlined in white. The regions between the leaflets as well as those directly above the upper leaflet do not show velocity vectors due to optical inaccessibility.

3.1 Instantaneous flow patterns

Plots of instantaneous velocity, $\langle \underline{v} \rangle$, and the associated out-of-plane vorticity, $\langle \omega_z \rangle$, corresponding to DAP A are shown in Figure 4.

Generally, the following flow structure is observed downstream of the valve in each of the three horizontal data acquisition planes (DAPs A-C): Shear layers are formed at the tips of both leaflets. The outer shear layers, which form at the trailing edges of the leaflets, roll up into vortices that are shed. It is traditionally

assumed that the inner shear layers, which form at the leading edges of the leaflets, roll into vortices that stay attached to the leaflet surface. Present observations indicate that for the case of unidirectional flow through a fully-open valve, vortex shedding occurs from both the inner and outer tips of the leaflets. The four shear layers define two wake regions, one behind each leaflet. A high velocity jet-like flow region exists between the two wakes. This high-velocity flow will be referred to here as the central jet. The central jet is unsteady in nature. It exhibits a large-scale, low frequency oscillation in the transverse direction. This phenomenon occurs simultaneously with the vortex shedding from the tips of the leaflets. Figures 4(a) through 4(c) illustrate three characteristic phases of this oscillation that correspond to DAP A. These phases are referred to as dominant lower wake regime Figure 4(a), symmetric wake regime Figure 4(b), and dominant upper wake regime Figure 4(c).

Figure 4(a) corresponds to the instant in time when the wake from the lower leaflet dominates the flow field. The velocity vector plot of Figure 4(a) shows that the low velocity region corresponding to the lower wake occupies a significantly larger area compared to the upper wake. In addition, the velocity plot shows a pronounced upward deflection of the central jet.

In comparison, the lower wake exhibits significantly higher levels of vorticity than the upper wake. The vorticity contour plot of Figure 4(a) shows that the outer shear layer of the bottom leaflet contains three well-defined negative vortices that were shed from the trailing edge of the leaflet. The distance between these negative vortices indicates that their shedding frequency is similar to that of the vortices in the inner shear layer. Moreover, the vortices in the outer and inner shear layers of the lower leaflet retain substantial levels of circulation up to 20 mm downstream of the valve.

In contrast to the lower leaflet, the outer and inner shear layers of the upper leaflet are located significantly closer to each other. In particular, the negative vortices of the inner layer develop close to the leaflet surface and interact with the positive vortices of the outer shear layer by forming counter-rotating vortex pairs. As the counter-rotating vortices move downstream the interaction between them results in a rapid decrease of their circulation levels. Rapid dissipation of vorticity due to shear layer interaction results in the early collapse of the upper wake, which extends only 10 mm downstream of the valve. This collapse is accompanied by the upward deflection of the inner shear layer of the lower leaflet.

The next characteristic phase of the flow oscillation cycle is referred to as the symmetric wake regime and is illustrated in Figure 4(b). During this phase, the four shear layers do not exhibit significant transverse deflections. Both the upper and lower wakes contain comparable vorticity levels up to 10 mm downstream of the valve. The symmetric wake regime corresponds to the transition between the dominant lower wake phase of Figure 4(a) and the dominant upper wake phase, which is illustrated in Figure 4(c).

Patterns of instantaneous flow velocity and out-of-plane vorticity shown in Figure 4(c) correspond to the flow oscillation phase that is opposite to the dominant lower wake regime of Figure 4(a). The velocity field of Figure 4(c)



shows that the wake region, which forms behind the upper leaflet, dominates the flow field. Rapid dissipation of positive vorticity in the inner shear layer of the lower leaflet is accompanied by a large-scale downward deflection of the inner shear layer of the upper leaflet and the associated jet-like flow in the middle of the channel.

It is evident that the frequency of the large-scale flow oscillation that is represented by the sequence of images in Figures 4(a) through 4(c) is substantially lower than the frequency of the vortex shedding from the tips of the leaflets. In fact, at least four small-scale vortices are shed from the leaflet tips during a typical large-scale oscillation cycle described above.

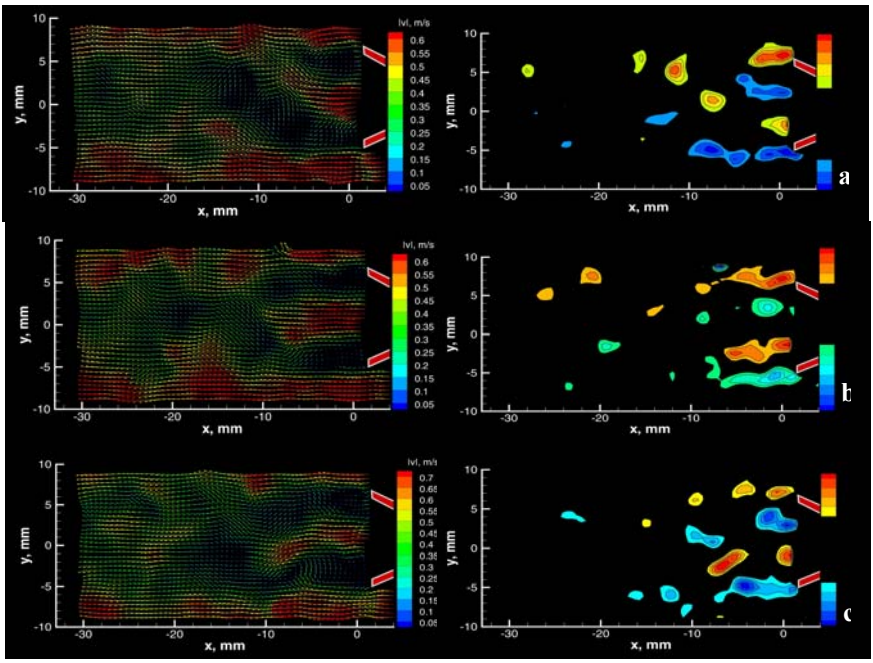


Figure 4: Instantaneous velocity field (left) and out-of-plane vorticity (right) for: (a) the dominant lower wake regime of DAP A (b) the symmetric wake regime of DAP A (c) the dominant upper wake regime of DAP A.

3.2 Time-averaged flow patterns

All images presented in this section are a result of ensemble-averaging of 1000 instantaneous images similar to those presented in the previous section.

The structure of the wake downstream of the bileaflet MHV, corresponding to DAP A, is clearly evident in the plot of time averaged vorticity $\langle\omega_z\rangle$, which is shown in Figure 5(a). The dominant feature of the flow field downstream of the valve is the presence of four separated shear layers that form at the tips of the

leaflets. The outer shear layers form at the trailing tips of the upper and lower leaflet. They are indicated in the plot of out-of-plane vorticity of Figure 5(a) by the regions of high positive and negative time-averaged vorticity respectively. These layers extend approximately 14 mm downstream of the valve. The inner shear layers, which form at the leading tips of the leaflets, exhibit high levels of time-averaged vorticity of the opposite sign, relative to the outer shear layers. Due to the highly unsteady nature of the inner shear layers, the time-averaged vorticity associated with them decreases rapidly with downstream distance. In fact, no significant levels of vorticity exist in the central region of the channel downstream of the valve beyond approximately 8 mm.

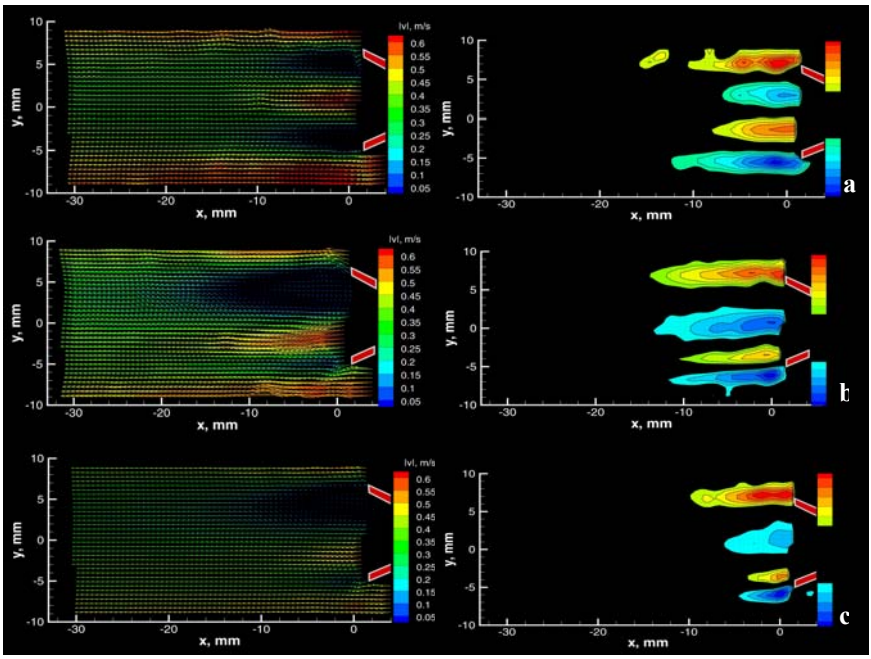


Figure 5: Time-average velocity field (left) and corresponding out-of-plane vorticity (right) for: (a) DAP C (b) DAP B (c) Dap C.

The time-averaged velocity field and the corresponding out-of-plane vorticity plot for DAP B are shown in Figure 5(b). Once again, the dominant feature of the flow field downstream of the valve is the presence of four separated shear layers that originate at the tips of the leaflets. However, the central jet has shifted toward the lower leaflet causing an asymmetry in the flow structure. The inner and outer shear layers that define the relatively large upper wake are formed at the leading and trailing edges of the top leaflet. They are represented, in Figure 5(b), by high levels of out-of-plane vorticity that extend 14 mm downstream of the valve. In contrast, the relatively small lower wake, which is defined by the inner and outer shear layers formed at the leading and

trailing edges of the lower leaflet, contains lower circulation levels that only extend 10 mm downstream of the valve. The shift in the central jet's position reduces the distance between the shear layers that define the lower wake, causing them to interact. This interaction results in reduced levels of circulation in the lower wake as well as higher Reynolds stresses.

DAP C, which corresponds to a further increase in the distance from the centerline of the channel, shows a very similar flow structure as that of DAP B. As can be seen in Figure 5(c), the upper wake dominates the lower wake and the central jet has shifted toward the lower leaflet. In comparison to the results of DAP B, the overall velocity magnitude is lower for DAP C due to the proximity to the channel walls. Consequently, the size of both the upper wake and the lower wake decreases by the same amount.

4 Conclusions

Particle image velocimetry was used to investigate the flow structure downstream of a bileaflet mechanical heart valve (MHV) during peak systole. The data was obtained for three longitudinal cross-sections of the flow field, referred to as data acquisition planes (DAPs) A through C. In all three DAPs, the overall flow structure consisted of four separated shear layers containing vortices shed from the leading and trailing edge of each leaflet. These shear layers define two wakes and a high-velocity jet-like region located in the centre of the channel. Contrary to the traditional assumption of the dominant role of the outer shear layers, it was shown that the large-scale transverse oscillations of the inner shear layers dominate the near-wake of the valve. The large-scale flow oscillation corresponds to transverse undulations of the jet-like flow through the central opening of the valve and to flapping of the associated inner shear layers. These oscillations were characterized in terms of three representative flow regimes. Limited temporal resolution of the DPIV imaging sequence did not allow for accurate estimation of the large-scale oscillation frequency.

The flow directly downstream of the bileaflet MHV was found to be highly three-dimensional. Marked differences were found in the flow structure downstream of the MHV at each DAP. Predominantly, the central jet shifts position along the vertical axis, causing an increase in the size of one wake and a reduction in size of the other. In general, the shift of the central jet causes a significant change in the unsteady flow structures present downstream of the valve. The unsteady flow characteristics, in particular the Reynolds stresses, are of special importance due to their close link to platelet activation. Future investigations will focus on a quantitative characterization of the unsteady flow structures and the mechanisms of their interaction.

References

[1] A .P. Yoganathan, He, Z. and Jones, "Fluid Mechanics of Heart Valves", Annual Review of Biomedical Engineering, Vol. 6, 331-362 2004.



[2] W. Yin, Alemu, Y., Affeld, K., Jesty, J. and Bluestein, D., "Flow-induced platelet activation in bileaflet and monoleaflet mechanical heart valves." Annals of Biomedical Engineering, Vol. 32, 8, 1058-1066, 2004.

[3] D. Bluestien, Yin, W., Affeld, K. and Jesty, J., "Flow- induced Platelet Activation in Mechanical Heart Valves" Journal of Heart Valve Disease, Vol. 13, 501-508, 2004.

[4] L.H. Edmunds, Mckinlay, S., Anderson, J. M., Callahan, T. H., Chesebro, J. H., Geiser, E. A., Makanani, D. M., McIntire, L. V., Meeker, W. Q., Naughton, G. K., Panza, J. A., Schoen, F. J. and Didisheim, P., "Directions for improvement of substitute heart valves: National Heart, Lung, and Blood Institute's Working Group report on heart valves." Journal of Biomedical Material Research, Vol. 38, 3, 263-266, 1997.

[5] Y.-R. Woo, and A. P. Yoganathan, "In-Vitro Fluid Dynamic Characteristics of the Abiomed Trileaflet Heart Valve Prosthesis" ASME, Vol. 105, 338-345, 1983.

[6] L.N. Scotten and Walker, D. K., "New Laboratory Technique Measures Projected Dynamics Area of Prosthetic Heart Valve" Journal of Heart Valve Disease, Vol. 13, 1, 120-133, 2004.

[7] M. Marassi, Castellini P., Pinotti, M., and Scalise, L. "Cardiac valve prosthesis flow performances measured by a 2-D and 3-D-stereo particle image velocimetry" Experiments in Fluids, Vol. 36, 1, 176-186, 2004.

[8] P. Castellini, Pinotti, P., and Scalise, L. "Particle Image Velocimetry for Flow Analysis in Longitudinal Planes across a Mechanical Artificial Heart Valve" Artificial Organs, Vol. 28, 5, 507-513, 2004.

[9] D. Bluestein, Rambod, E. and Gharib, M., "Vortex Shedding as a Mechanism for Free Emboli Formation in Mechanical Heart Valves" Journal of Biomedical Engineering, Vol. 122, 125-134, 2000.

[10] T.C. Lamson, Rosenberg, G., Geselowitz, D. B., Deutsch, S., Stinebring, D. R., Frangos, J. A. and Tarbell, J. M., "Relative Blood Damage in the Three Phases of a Prosthetic Heart Valve Flow Cycle" ASAIO Journal, Vol. 39, 3, M626-M633, 1993.

[11] K.B. Manning, Kini, V., Fontaine, A. A., Deutsch, S. and Tarbell, J., "Regurgitant Flow Field Characteristics of the St. Jude Bileaflet Mechanical Heart Valve under Physiological Pulsatile Flow Using Particle Image Velocimetry" Artificial Organs, Vol. 27, 9, 840-846, 2003.

[12] R.S. Meyer, Deutsch, S., Bachmann, C. B. and Tarbell, J. M., "Laser Doppler Velocimetry and Flow Visualization Studies in the Regurgitant Leakage Flow Region of Three Mechanical Mitral Valves." Artificial Organs, Vol. 25, 4, 292-299, 2001.



Numerical analysis of blood flow in human abdominal aorta

M. Podyma[1], I. Zbicinski[1], J. Walecki[2], M. L. Nowicki[2], P. Andziak[3], P. Makowski[4] & L. Stefanczyk[5]
[1]*Faculty of Process and Environmental Engineering, Technical University of Lodz, Poland*
[2]*Department of Radiology, Postgraduate Medical Center, Poland*
[3]*Surgical Clinic, Central Clinical Hospital MSWiA, Poland*
[4]*Faculty of Electrical and Electronic Engineering, Technical University of Lodz, Poland*
[5]*Department of Radiology and Diagnostic Imaging, Medical University of Lodz, Poland*

Abstract

A CFD model of flow hemodynamics in abdominal aortic aneurysm to estimate the effect of four different flow conditions on velocity and pressure profiles was developed and verified. The reconstruction of blood flow domain geometry was performed on the basis of CT examination. Our own software was used for CT image segmentation and real blood flow domain geometry reconstruction. Data necessary for determination of initial and boundary conditions as well as for verification of developed CFD model were collected from USG-Doppler examinations at 4 characteristic areas of the abdominal aorta. The result of these calculations proved that, irrespective of the applied boundary conditions and flow type, velocity profiles in all of the analysed models were similar. The comparison of theoretical and experimental results showed a significant difference in the absolute values of both velocities and heart-work period length. The reasons for the discrepancies were analyzed indicating both numerical factors and the character and accuracy of the USG examination.
Keywords: numerical simulation, verification of CFD model, hemodynamics, segmentation, CT, USG-Doppler.



WIT Transactions on Engineering Sciences, Vol 52, © 2006 WIT Press
www.witpress.com, ISSN 1743-3533 (on-line)
doi:10.2495/AFM06059

1 Introduction

Human body seen from chemical engineering perspective is a reactor, in which momentum, heat and mass transfer processes accompanied with chemical and biochemical reactions take place. Recent development of experimental techniques and theoretical methods allowed us to observe many distinctive phenomena, particularly in the area of blood flow dynamics. One of developed methods, the CFD technique, enabled analysis of flow hemodynamics in the blood vessel. The CFD models can be used to calculate distributions of tensile stresses expanding the walls of vascular segments and hydraulic resistance. Information on stress distributions, i.e. on hemodynamic forces that accompany blood flow, is very important to indicate areas that are threatened with a vascular wall rupture and helpful in prediction of the rupture time.

There are two simultaneously occurring factors that provoke aneurysm; biochemical ones that cause local lesions of vascular walls, and hemodynamic which lead to dilation of the weakened aorta segment. Hemodynamic factors that have an influence on aneurysm formation include, among the others, disturbance of laminar blood flow, eddies, increased flow rate and first of all raised blood pressure. Hence, attempts of predicting the areas that are specially vulnerable to the above mentioned factors must be based on the real system geometry that reflects anatomic details specific of a given patient, such as local arteriostenosis, presence of clots, etc.

None of the currently applied non-invasive diagnostic methods provides information on shear stress that appears within aortic walls which leads to the aorta rupture. A strategic aim of this project is to develop a mathematical model to determine the growth rate of aortic aneurysm on the basis of flow hemodynamics and mechanical properties of vascular walls.

In literature, there are numerous references on the flow in blood vessels; but there are no papers that refer at the same time to the flow hemodynamics and the behavior of vascular walls. Only such approach can enable specification of the conditions in which aortic aneurysm will form and grow.

The basic target of this work was to construct and verify a CFD model of flow hemodynamics in aortic aneurysm and to assess the effect of initial and boundary conditions on quality of calculations of blood flow related to local narrowing of aorta lumen.

2 Medical data

Patients suffering from aneurysm have been selected and monitored more frequently than in a standard medical procedure. A criterion for including patients into the program was the growth rate of aneurysm diameter. Each patient was subjected to clinical examinations (CT, USG-Doppler, angiography) that enabled determination of hemodynamic parameters of blood vessels (linear dimensions, aneurysm volume increment, the amplitude of vascular wall oscillations, etc.) and development of kinetic equations which control the aneurysm growth rate.



The reconstruction of blood flow domain geometry was performed on the basis of CT examination. Data necessary for determination of initial and boundary conditions as well as for verification of developed CFD model were collected from USG-Doppler examinations at 4 characteristic areas of abdominal aorta: below renal aorta (inlet) – A, aneurysm neck – B, distal part – C, iliac arteries – D1, D2 (see Fig. 1a).

3 Flow geometry

In order to reconstruct the real geometry on the basis of computer tomograms (CT) we used our own software for 2D image processing, extraction of 3D geometry based on the series of cross sections of the reconstructed organ (aorta) and numerical mesh generation.

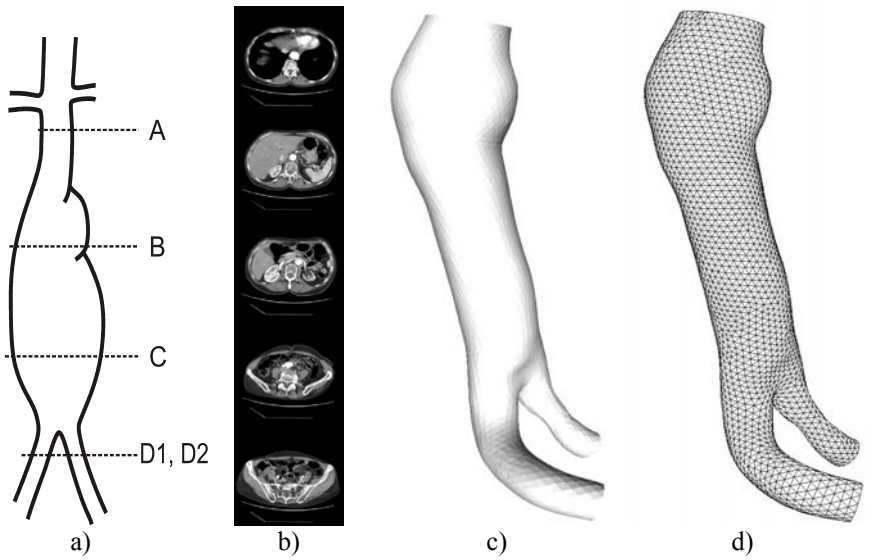


Figure 1: Abdominal artery geometry: a) USG-Doppler measurement points, b) CT scan data, c) 3D geometry of blood flow domain (STL), d) 3D volume mesh (tetrahedral elements).

The expected functionality of the segmentation is a transformation from a series of planar CT images into a 3D structure, representing the lateral surface of blood vessels. The obtained structure indirectly defines the geometrical boundary conditions for CFD simulations. The segmentation method used in this paper has been presented in [1] and modified due to a larger vessel diameter. It allowed us to determine the geometry of the vessel using approximation of the vessel shape by a series of ellipses located in planes perpendicular to the vessel axis.

The method has been initially developed for segmentation of the coronary arteries, significantly smaller in diameter than the aorta with aneurysm described

here. Therefore, the main adaptation, which has been introduced in the frame of this work, was a modification of the assumed shape of the vessel cross-section. Instead of an ellipse with 2 radii [1] we introduced an asymmetrical ellipse with 4 radii. We have also implemented automatic fitting of the ellipse to the image data. In an iterative process we are able to change 7 parameters (position, radii, rotation angle), which results in rigid deformation of the ellipse. The method was efficient for small and middle diameter of the vessel. For large part of the aorta, automatic segmentation often failed and manual adjustment of parameters was required. The main advantage of the segmentation with an approximated, 4-radii elliptical shape is immunity to image artifacts resulting in a smooth surface of the vessel.

Flow geometry obtained in this way was described in a universal STL format (Stereo lithography) and imported into a Gambit 2 numerical preprocessor (Fluent INC). On the basis of STL geometry, a three-dimensional tetrahedral volume mesh of flow domain was generated. Preliminary calculations were performed to get the mesh independent solution (50,000 cells and double density about 100,000 cells). We have found that both meshes delivered results with similar accuracy of calculations, so finally the lower density mesh (50,000 cells) was selected.

4 CFD model

In numerical simulations a commercial CFD package Fluent 6 was used. A numerical grid representing flow geometry was generated on the basis of CT examinations for a selected patient. Calculations were performed in unsteady-state conditions.

4.1 Boundary conditions

Blood flow velocities in selected areas (Fig. 1a) of the abdominal aorta were taken from a USG-Doppler examination. After USG velocity spectrum (Fig. 2) analysis, real transient blood flow velocity profiles were extracted and described by the Fourier series, eqn. (1).

$$u(t) = \frac{a_0}{2} + \sum_{n=1}^{\infty} \left(a_n \cos(n\omega t) + b_n \sin(n\omega t) \right) \tag{1}$$

where a_n and b_n are Fourier coefficients. Twelve Fourier terms were considered to obtain satisfactory approximation of the velocity profile.

Data taken at A position were used to determine transient velocity profile at the inlet to the flow domain (inlet boundary condition). Data from B, C, D1, D2 were used to verify CDF calculation results.

4.2 CFD model parameters

Blood flow in the cardiovascular system caused by cardiac contractions has pulsating character and for big vessels is usually in laminar and transient range. To analyze effect of type of the flow and pressure boundary conditions on

accuracy of calculations four independent hemodynamics models developed for turbulence an laminar flow and constant and transient pressure at the outlet of the aorta. The list of analyzed models is given below.

1. Turbulent flow + constant pressure at the outlet (TCP)
2. Turbulent flow + transient pressure at the outlet (TTP)
3. Laminar flow + constant pressure at the outlet (LCP)
4. Laminar flow + transient pressure at the outlet (LTP)

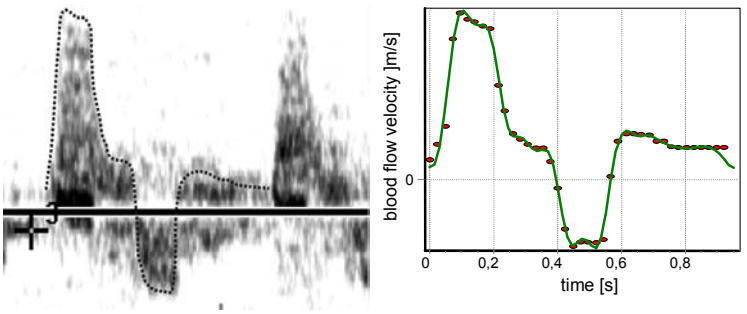


Figure 2: Analysis of USG-Doppler data and Fourier series fit.

In all calculations for turbulent flow Large Eddy Simulation (LES) model was applied [2]. Conceptually, the large eddy simulation (LES) is a compromise between DNS (Direct Numerical Simulation) having large computational cost and the RANS (Reynolds-averaged Navier-Stokes) approach.

Arterial blood pressure in big vessels of a healthy man ranges from about 9.3 kPa (70 mm Hg) to around 16 kPa (120 mm Hg). For both models (laminar and LES), calculations were performed at constant pressure (11.6 kPa) and changing in time pressure profile. A transient profile of outlet pressure was generated on the basis of systolic a diastolic pressures of a selected patient. To describe non-Newtonian properties of blood, Quemada's rheological model was applied [3,4]. Blood density was assumed constant and equal to 1040 kg/m^3 [6].

5 Results

Selected results of the calculations referring to local changes in blood flow velocity and pressure in one heart-work period are shown in Figs. 3 through 5. Figure 3 shows calculated blood velocity profiles in selected cross sections of the aorta (see Fig. 1) for all models.

Analysis of Fig. 3 indicates that irrespective of the applied boundary conditions and flow type, the velocity profiles in all four models are similar and so subsequent comparative analyses concerning blood flow velocities are based on the most complex model (TTP). Setting of the boundary condition at the inlet in the form of blood velocity profile determines its distribution in the whole flow area with the difference between the inlet and outlet pressure being preserved.

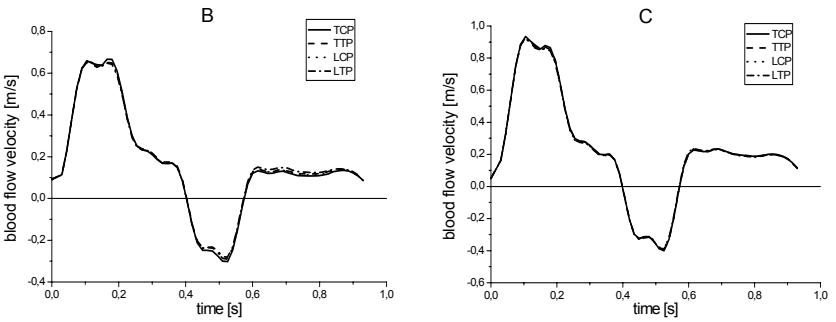


Figure 3: Calculated blood velocity profiles for all models in selected cross sections of the aorta (see Fig. 1).

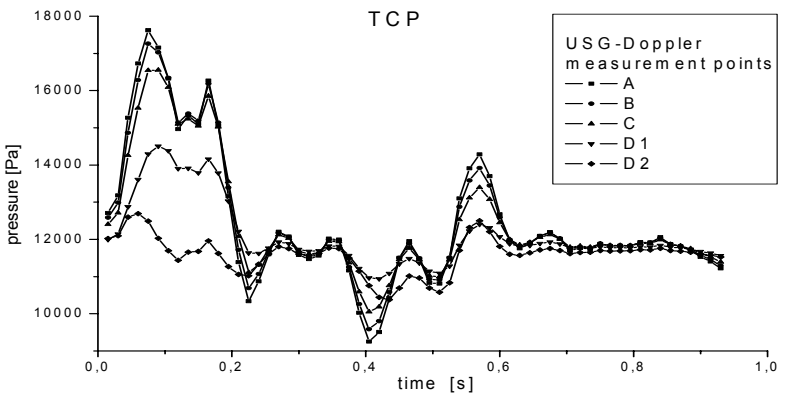


Figure 4: Calculated pressure profiles for models TCP.

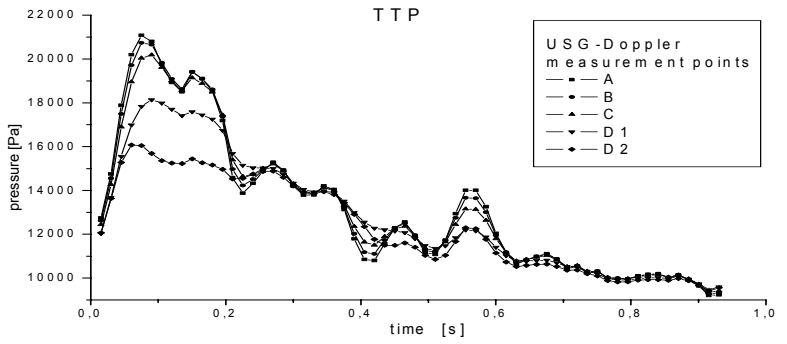


Figure 5: Calculated pressure profiles for models TTP.

A change in the outlet pressure causes only a change in the operation pressure in the artery with constant pressure difference between the analyzed cross section of the aorta (Fig. 4 and 5). In the models with constant outlet pressure, a gradual flattening of the pressure profile until reaching a constant level controlled by the boundary condition, can be observed (Fig. 4). It is worth noting that such a boundary condition may lead to underestimation of pressure in the artery, and as a result to errors in wall stress determination. In view of this, despite correct transient velocity profiles in the models with constant pressure one should apply transient pressure boundary conditions (Fig. 5).

Comparison of the calculations shows also that when the turbulence model (LES) is taken into account in the calculations, this has no effect of blood flow velocity profiles in the aorta which means that real flow in the system is close to laminar one [5, 7].

The main aim of this study, however, was to compare results of theoretical calculations of blood flow velocity profiles with USG experimental data. The USG velocity profiles taken at position A were used as the initial boundary condition for each of four models. Velocity profiles obtained at cross sections B, C, D1, D2 (Fig. 1) were used to verify CDF calculation results.

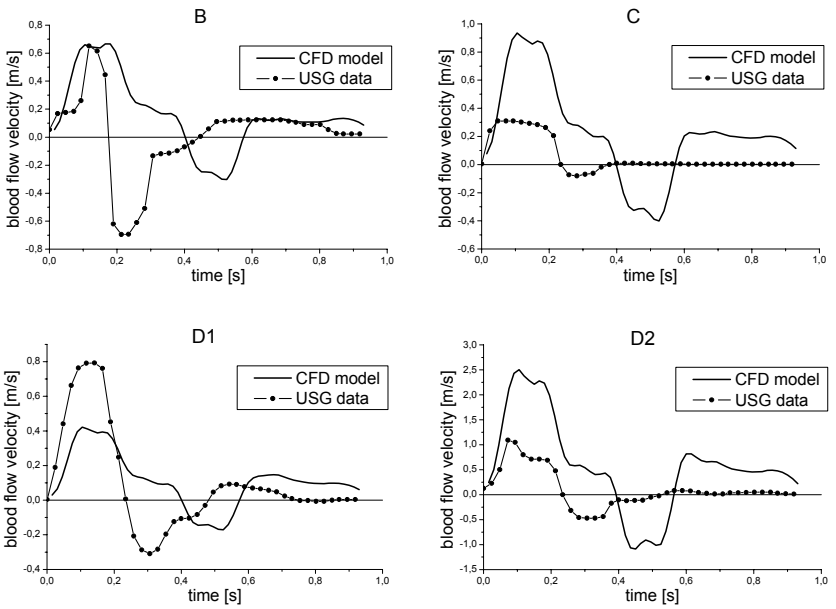


Figure 6: Blood flow velocity profiles at four aorta positions (see Fig. 1) - comparison of calculations results with USG-Doppler data.

Comparison of theoretical and experimental results shows significant difference in the absolute values of both velocities and heart-work period length (see Fig. 6). Reasons of the discrepancies can be both numerical (e.g. the

pulsations of aorta walls are not included into the calculations) and these related to the character and accuracy of USG measurements.

The abdominal aorta is an organ difficult to access which seriously hampers proper USG examinations. A high correction angle (about 60º) causes that even slight deviations (of the order of 3º) result in velocity measuring errors reaching even 30% (we use convex USG probe). From the technical point of view, the USG measurement cannot be considered precise because of difficulties in setting the correction angle, USG probe position and artifacts (noise) arising during the examination.

Additionally, during a USG test lasting for several minutes, a patient's heart rhythm changes due to stress, breathing fluctuations, changes of body position, arrhythmia, etc. These disorders cause that duration of diastolic phase changes [8] which can explain the phase shift shown in the diagrams in Fig. 6.

As it is not possible to fully verify the calculations, results obtained using the CFD models of blood flow in the abdominal aorta have a qualitative rather than quantitative character.

6 Conclusions

1. Despite of correct transient velocity profiles obtained in all models considered, in aortic blood flow calculations the transient pressure boundary conditions should be applied because of a possible underestimation of arterial pressure and as a consequence errors in the determination of wall stress.
2. Due to inaccuracies of USG measurements and possible numerical uncertainties, no full verification of the CFD calculations of blood flow in the aorta was possible. As a result, the CFD modeling of hemodynamics in the abdominal aorta has a more qualitative than quantitative character.

Acknowledgement

Financial support from the State Committee for Scientific Research (Grant No. 3T09C 033 26) is gratefully acknowledged.

References

[1] Makowski P., Ringgaard S., Fruend E. T., Pedersen E. M., A Novel Approach to Segmentation of Coronary Arteries in MR Images for Computational Fluid Dynamics (CFD) Simulations, 2004 ISMRM, Kyoto, Japan.

[2] FLUENT 6.1 Documentation, Fluent INC.

[3] Cokelet G. R., The rheology of human blood. Biomechanics, its fundamentals and objectives, Prentice Hall, Engelwood, Cliffs, New York. 1972, 63.



[4] Quemada D., Rheology of concentrated disperse systems. III. General features of the proposed non-Newtonian model. Comparison with experimental data. Rheol. Acta, 1978, 17, 632.
[5] Leondes C., Biomechanical Systems Techniques and Applications, Vol. IV Biofluid Methods in Vascular and Pulmonary Systems; CRC Press LLC. 2001.
[6] Bebenek B., Flows in cardiovascular system, Cracow. ZGPK (in polish). 1999.
[7] Lieber, B. B., Arterial Macrocirculatory Hemodynamics, The Biomedical Engineering Handbook: Second Edition. Ed. Joseph D. Bronzino. Boca Raton. CRC Press LLC, 2000.
[8] Humes H. D., Kelley's Textbook of Internal Medicine, Lippincott Williams & Wilkins (LWW), 2000.



This page intentionally left blank

Section 13
Permeability problems

This page intentionally left blank

Revising Darcy's law: a necessary step toward progress in fluid mechanics and reservoir engineering

C. Ketata, M. G. Satish & M. R. Islam
Department of Civil Engineering, Dalhousie University, Canada

Abstract

After drilling wells to reach an oil and gas reservoir, its production starts following the fluid flow under surrounding pressure. To characterize an oil and gas reservoir and estimate its production correctly, it is paramount to model its fluid mechanics properly. So far, the main models used to simulate oil and gas flow utilize Darcy's law. However, these run short due to its limited applications and lack of adaptability in oil and gas reservoirs. This paper introduces a novel fluid transport law in porous media that can be used in oil and gas reservoir, as well as in civil, chemical, mechanical, and mineral engineering cases. This comprehensive model describes the oil and gas flow in a reservoir efficiently. It proposes that the pressure gradients in the flow directions depend not only on the fluid velocity but also on a power series and a series of first and higher order partial derivatives of fluid velocities, among other factors. The coefficients in these series are specific to the fluids and rocks representing the reservoir. They portray the fluid-rock interaction. They include rock properties such as composition, porosity, and permeability. Porosity is the ratio of the space taken up by the pores in a rock to its total volume. The pore space determines the amount of space available for storage of fluids. Permeability is the ability of a rock to allow fluids to pass through it. In addition, the flow model is affected by fluid types and properties such as composition, density, and viscosity. Viscosity is the property of a fluid that causes it to resist flowing.
Keywords: fluid flow in porous media, Darcy's law, fluid mechanics, oil and gas engineering, reservoir engineering.



WIT Transactions on Engineering Sciences, Vol 52, © 2006 WIT Press
www.witpress.com, ISSN 1743-3533 (on-line)
doi:10.2495/AFM06060

1 Introduction

Fluid mechanics is the branch of mechanics that deals with the properties of gases and liquids, their motion, and their application in practical engineering such as oil and gas engineering dealing with oil and gas reservoirs. An oil and gas reservoir is a natural chamber in a porous rock where a supply of natural gas and crude oil collects. To solve oil and gas reservoir engineering problems, it is essential to observe, model, simulate, and understand fluid flow motion in porous media. Darcy's law has been used for a long time to describe water and other fluids flow through porous media [1, 2].

Darcy [1] derived an equation that governs the laminar or nonturbulent flow of fluids in homogeneous porous media. In 1855 and 1856, he conducted column experiments that established Darcy's law for flow in sands and therefore the theoretical foundation of groundwater hydrology [1]. Darcy's law is a phenomenological law rather than a fundamental law [3]. Various researchers [4-18] in fluid mechanics and oil and gas engineering accommodated Darcy's law to meet their needs in order to solve complex problems dealing with fluid flow in porous media including oil and gas flow in reservoir rock layers.

To curb the limitations of Darcy's law to comparatively small fluid velocities, Forchheimer's equation and its inertial flow parameter, β, have been used as an extension of Darcy's law beyond the linear flow region [4, 17]. According to Darcy [1], the concept of a constant permeability suggests a linear relationship between flowrate and pressure gradient. However, empirical observations of flowrate at higher differential pressures corroborated that the relationship between flowrate and pressure gradient becomes nonlinear at relatively high velocities [4, 17]. Forchheimer [4] presented an empirical equation that described the observed nonlinear flow behavior. Nevertheless, this new equation has showed limits too [4, 17]. Consequently, it is necessary to develop a fundamental law by revealing a new model.

This paper introduces a novel model of power and partial derivative series describing the fluid flow motion in porous media and considering its dynamic spatial behavior.

2 Darcy's law

Darcy's law [1] expresses fluid motion in porous media. Darcy [1] conducted experiments on water flow through sand beds. He found out that the water velocity in the sand beds was proportional to the pressure gradient as follows:

$$v = k\frac{h_1 - h_2}{L} \tag{1}$$

where v is the water velocity, k the hydraulic conductivity, h_i the hydraulic head, and L the column length. The water velocity equals the water flowrate divided by the sand beds cross area:

$$v = \frac{q}{A} \tag{2}$$

Darcy's law is linear and applies only for incompressible and singlephase fluids following laminar and steady-state flows in homogeneous and isotropic porous media. However, the fluid flow can be laminar or turbulent depending on the porous media composition, porosity, and permeability, among others. In addition, other factors such as distance from the oil and gas wellbore, fluid composition, viscosity, and velocity determine the fluid flow conditions whether they are laminar or turbulent. The fluid flow can follow a steady-state, a pseudo-steady state, or an unsteady-state regime. Moreover, Darcy's law is not a function of the flow direction. Therefore, it is obviously necessary to take into account the flow geometry to correct this flow motion law.

3 Reservoir rock permeability

Permeability is the ability of a rock to transmit fluids. It is influenced by rock properties such as its type, composition, porosity (see Figure 1), and grain shape and size, among others. Furthermore, fluid properties such as its type, composition, and viscosity establish its motion behavior in porous media. Viscosity is the property of a fluid that causes it to resist flowing. Based on lab flow tests, Darcy [1] determined that permeability could be expressed as follows (see Figure 2):

$$k = Q\mu / A(\Delta P / L) \tag{3}$$

where k is the permeability (darcy), Q the volumetric flowrate (cm^3/s), μ the viscosity of flowing medium (cp), A the cross-section of porous medium such as rock (cm^2), ΔP the pressure differential or drop, and L the porous medium length. Figure 3 shows how horizontal and vertical permeabilities are affected by rock grains arrangement, size, shape, and pore structure.

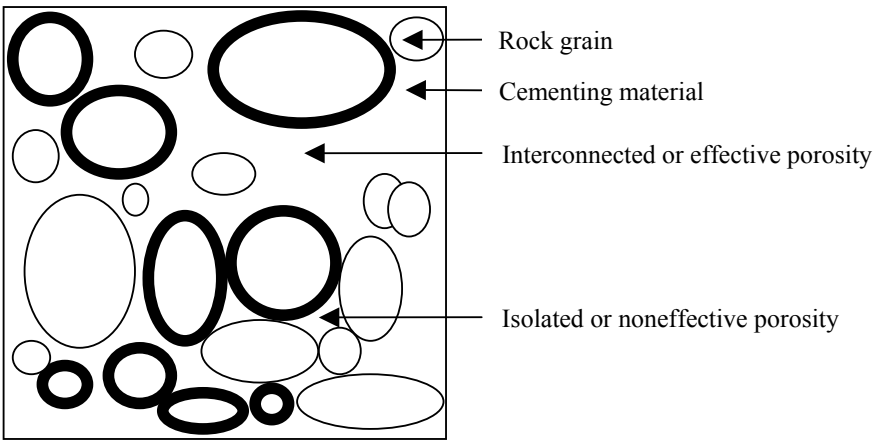


Figure 1: Rock porosity.

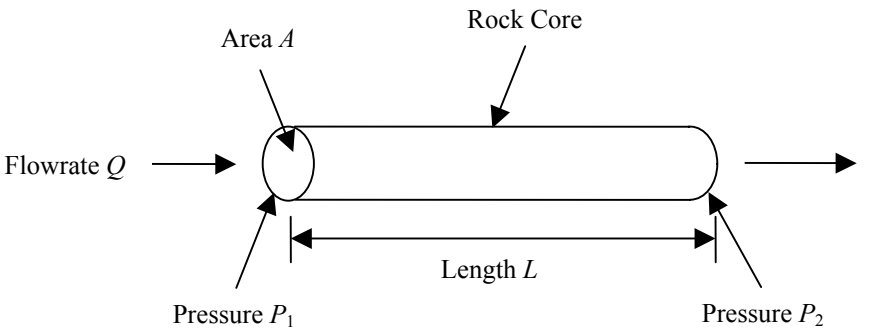


Figure 2: Rock core for permeability assessment.

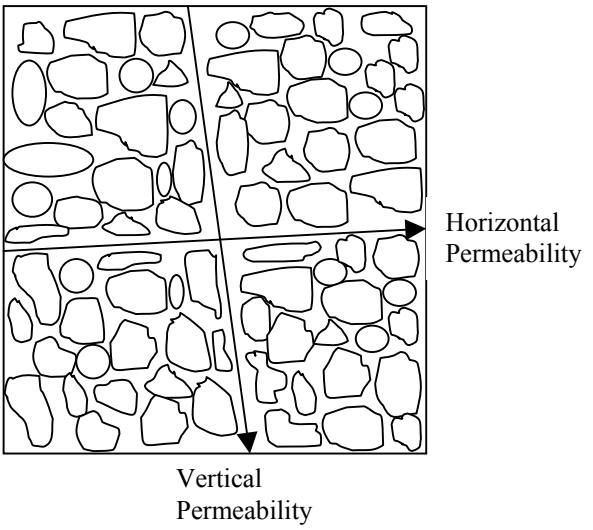


Figure 3: Horizontal and vertical permeabilities.

4 Fluid types

A fluid is a substance whose molecules flow freely, so it has no fixed shape and little resistance to outside stress. Fluids can be liquids or gases. Fluids can be slightly or considerably compressible (see Figures 4 and 5), whereas incompressible fluids do not exist.

5 Flow regimes

The fluid flow can be semisteady-state or unsteady-state as shown in Figure 6. However, since the pressure changes over time, a fluid flow cannot be steady-

state. Furthermore, the fluid flow can be laminar or turbulent. At relatively low fluid velocities, the fluid particles adhere to the streamlines, which results in a laminar flow. At comparatively higher velocities, the fluid flow follows a fluctuating velocity pattern leading to a turbulent flow.

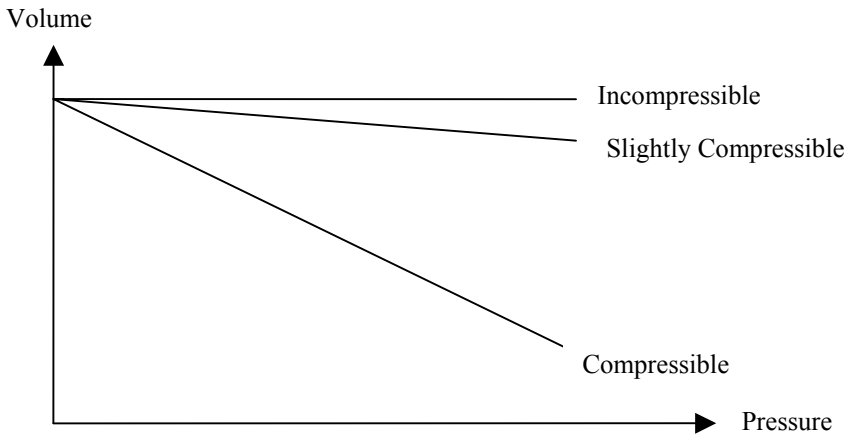


Figure 4: Fluid types depending on volume-pressure relationships.

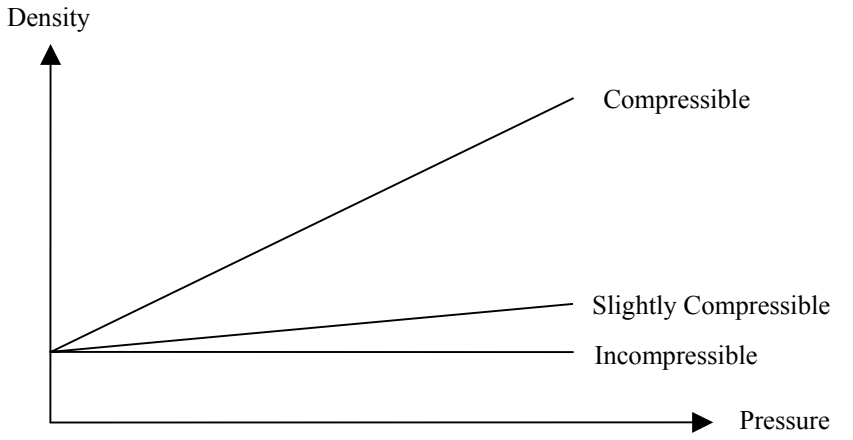


Figure 5: Fluid types depending on density-pressure relationships.

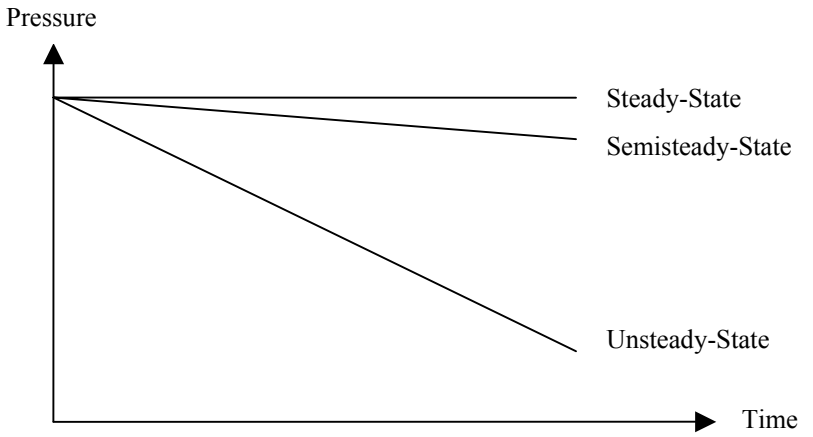


Figure 6: Fluid regimes depending on pressure-time relationships at a reservoir location.

6 Power and Partial Derivative Series (PPDS) model

Fluid flow in porous media is a nonlinear and dynamic process. The pressure differential at time t is a function of fluid velocity variations as follows:

$$\frac{\partial P}{\partial x} = \sum_{i=1}^{m} a_i v^i + \sum_{j=1}^{n} b_j \frac{\partial^j v}{\partial x^j} \tag{4}$$

where the values of m, a_i, n, and b_j depend on the porous medium properties and the fluid characteristics. Every lab or field case of fluid flow motion in porous media is unique. Therefore, these values are case-specific. After observing the flow behavior, the PPDS(m,n) model is calibrated. Next, the defined model is used for further site investigation and case simulations in order to understand, control, and forecast the dynamic flow system.

7 Conclusion

Darcy's law works only for incompressible and singlephase fluids following laminar and steady-state flows in homogeneous and isotropic porous media, which do not exist. Then, it is paramount to develop a new law that takes into account the attributes of a real fluid flow in porous media.

This paper proposes an innovative model for fluid flow motion in porous media considering the porous medium and fluid properties and parameters. This original model corresponds to a power series and a series of first and higher order partial derivatives of fluid velocities at the time of evaluation, which obeys the flow dynamic nonlinear behavior.

Based on lab experiments and field data, the flow model is regulated since every case studied has a unique model. This novel and robust model not only embodies the fluid behavior in an oil and gas reservoir but also enhances the real-time decision making process for its production, which increases the project profitability.

Acknowledgement

The authors would like to thank the Atlantic Canada Opportunities Agency (ACOA) for funding this project under the Atlantic Innovation Fund (AIF).

References

[1] Darcy, H.P.G, *The Public Fountains of the City of Dijon (Appendix)*, Bookseller of the Imperial Corps of Bridges, Highways and Mines, Quay of Augustins, 49, 1856, biosystems.okstate.edu/darcy.

[2] Ahmed, T., *Reservoir Engineering Handbook*, Second Edition, Butterworth-Heinemann: Woburn, 2001.

[3] Hofmann, J.R. & Hofmann, P.A., Darcy's law and structural explanation in Hydrology. *Proceedings of the 1992 Biennial Meeting of the Philosophy of Science Association*, volume 1, eds. D. Hull, M. Forbes & K. Okruhlik, Philosophy of Science Association: East Lansing, 1992.

[4] Forchheimer, P., Wasserbewegung durch Boden. *Zeitschrift des Vereines Deutscher Ingenieure*, 45, pp. 1782-1788, 1901.

[5] Firoozabadi, A. & Katz, D.L., An analysis of high-velocity gas flow through porous media. *Journal of Petroleum Technology*, February, pp. 211-216, 1979.

[6] Thiruvengadam, M. & Pradip Kumar, G.N., Validity of Forchheimer equation in radial flow through coarse granular media. *Journal of Engineering Mechanics*, 123(7), pp. 696-705, 1997.

[7] Andrade, J.S., Costa, U.M., Almeida, M.P., Makse, H.A. & Stanley, H.E., Inertial effects on fluid flow through disordered porous media. *Physical Review Letters*, 82(26), pp. 5249-5252, 1999.

[8] Chen, Z., Qin, G. & Ewing, R.E., Analysis of a compositional model for fluid flow in porous media. *SIAM Journal on Applied Mathematics*, 60(3), pp. 747-777, 2000.

[9] Rose, W., Myths about later-day extensions of Darcy's law. *Journal of Petroleum Science and Engineering*, 26, pp. 187-198, 2000.

[10] Saghir, M.Z., Chaalal, O. & Islam, M.R., Numerical and experimental modeling of viscous fingering during liquid-liquid miscible displacement. *Journal of Petroleum Science and Engineering*, 26, pp. 253-262, 2000.

[11] Layton, W.J., Schieweck, F. & Yotov, I., Coupling fluid flow with porous media flow. *SIAM Journal on Numerical Analysis*, 40(6), pp. 2195-2218, 2003.

[12] Belhaj, H.A., Agha, K.R., Nouri, A.M., Butt, S.D., Vaziri, H.H. & Islam, M.R., Numerical simulation of non-Darcy flow utilizing the new



Forchheimer's diffusivity equation. Paper 81499 presented at the *SPE 13th Middle East Oil Show and Conference* in Bahrain, April 5-8, 2003.

[13] Belhaj, H.A., Agha, K.R., Nouri, A.M., Butt, S.D., Vaziri, H.H. & Islam, M.R., Numerical modeling of Forchheimer's equation to describe Darcy and non-Darcy flow in porous media. Paper 80440 presented at the *SPE Asia Pacific Oil and Gas Conference and Exhibition* in Jakarta, Indonesia, April 15-17, 2003.

[14] Belhaj, H.A., Agha, K.R., Nouri, A.M., Butt, S.D. & Islam, M.R., Numerical and experimental modeling of non-Darcy flow in porous media. Paper 81037 presented at the *SPE Latin American and Caribbean Petroleum Engineering Conference and Exhibition* in Port-of-Spain, Trinidad, West Indies, April 27-30, 2003.

[15] Belhaj, H.A., Agha, K.R., Butt, S.D. & Islam, M.R., A comprehensive numerical simulation model for non-Darcy flow including viscous, inertial and convective contributions. Paper 85678 presented at the *27th Annual SPE International Technical Conference and Exhibition* in Abuja, Nigeria, August 4-6, 2003.

[16] Belhaj, H.A., Agha, K.R., Butt, S.D. & Islam, M.R., Simulation of non-Darcy flow in porous media including viscous, inertial and frictional effects. Paper 84879 presented at the *SPE International Improved Oil Recovery Conference in Asia Pacific* in Kuala Lumpur, Malaysia, October 20-21, 2003.

[17] Barree, R.D. & Conway, M.W., Beyond beta factors: A complete model for Darcy, Forchheimer, and trans-Forchheimer flow in porous media. Paper SPE 89325 presented at the *SPE Annual Technical Conference and Exhibition* in Houston, Texas, September 26-29, 2004.

[18] Miskimins, J.L., Lopez-Hernandez, H.D. & Barree, R.D., Non-Darcy flow in hydraulic fractures: Does it really matter?. Paper SPE 96389 presented at the *SPE Annual Technical Conference and Exhibition* in Dallas, Texas, October 9-12, 2005.



Hydrodynamic permeability prediction for flow through 2D arrays of rectangles

M. Cloete & J. P. du Plessis
Department of Applied Mathematics, University of Stellenbosch, South Africa

Abstract

In the present paper a model to predict the hydrodynamic permeability of viscous flow through an array of squares is generalized to include flow through arrays of rectangles of any aspect ratio. This involves different channel widths in the streamwise and the transverse flow directions. It is shown how, with the necessary care taken during description of the interstitial geometry, a volume averaged approach can be used to obtain results identical to a direct method. Insight into the physical situation is gained during the modelling of the two-dimensional interstitial flow processes and resulting pressure distributions and this may prove valuable when the volume averaging method is applied to more complex three-dimensional cases. The analytical results show close correspondence to numerical calculations except in the higher porosity range for which a more realistic model is needed.
Keywords: porous media, volume averaging, hydrodynamic permeability, rectangles.

1 Introduction

Apart from the spatial dimension of the microstructure, the analytical result involves two parameters, the first of which relates to the extent of staggeredness that a fluid particle experiences on its way downstream. The second parameter introduced is a measure of aspect ratio of the rectangles which will allow us to vary the length of the transverse channels. In this paper the influence of these two parameters on the hydrodynamic permeability will be discussed.

2 Direct analytical modelling

Following Firdaouss and Du Plessis [1], the solid phase and the unit cell are represented by rectangles of the same aspect ratio. This was done to incorporate



WIT Transactions on Engineering Sciences, Vol 52, © 2006 WIT Press
www.witpress.com, ISSN 1743-3533 (on-line)
doi:10.2495/AFM06061

situations where the interstitial velocity in the channels parallel to the streamwise direction differs from that in the transverse channels, while maintaining notational simplicity. The fluid-solid interface parallel to the streamwise direction is denoted by $ds_{\parallel}$ and the perpendicular interface by $ds_{\perp}$. The dimensions of the unit cell are represented by $d_{\parallel}$ and $d_{\perp}$ in the streamwise and the transverse directions respectively, as are shown in Figure 1. The width of the channel wherein the flow is in the streamwise direction is represented by $dc_{\perp}$ and the width of the channel occupied by transversely flowing fluid is represented by $dc_{\parallel}$. Therefore $dc_{\perp} = d_{\perp} - ds_{\perp}$ and $dc_{\parallel} = d_{\parallel} - ds_{\parallel}$.

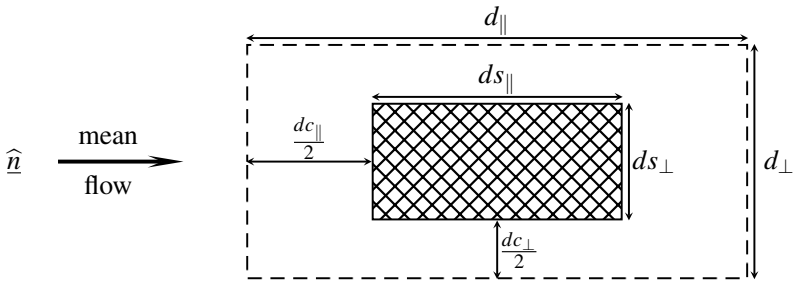


Figure 1: Notation for the unit cell with respect to the streamwise (or mean flow) direction.

The aspect ratio is defined as follows:

$$\alpha \equiv \frac{d_{\perp}}{d_{\parallel}} = \frac{ds_{\perp}}{ds_{\parallel}} = \frac{dc_{\perp}}{dc_{\parallel}}. \tag{1}$$

The porosity of this porous structure is then given by

$$\varepsilon = \frac{d_{\parallel} d_{\perp} - ds_{\parallel} ds_{\perp}}{d_{\parallel} d_{\perp}} = 1 - \left(\frac{ds_{\perp}}{d_{\perp}}\right)^2, \tag{2}$$

yielding the following useful relation for the particular geometry:

$$\frac{ds_{\perp}}{d_{\perp}} = \sqrt{1-\varepsilon}. \tag{3}$$

Two different levels of staggering of the solid phase in the streamwise direction will be studied, namely a regular array and a fully staggered array as shown in Figure 2. We define as follows a parameter ξ which relates to the cross-stream staggeredness of the solid material:

$$\xi \equiv \begin{cases} 0 & \text{Regular array} \\ \frac{1}{2} & \text{Fully staggered array}. \end{cases} \tag{4}$$

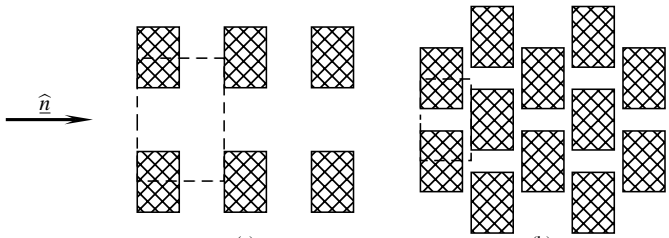


Figure 2: An illustration of the different arrays studied, as well as typical unit cells chosen for the different cases and the streamwise direction $\hat{n}$.

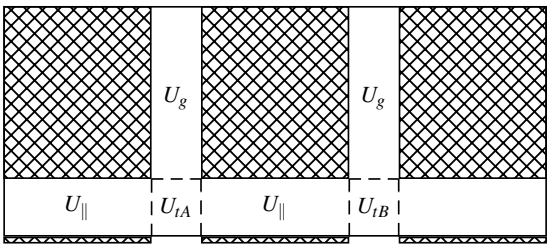


Figure 3: The model considered for a regular configuration where: $p_{U_{tA}} = p + \delta p_{\parallel}$ and $p_{U_{tB}} = p$.

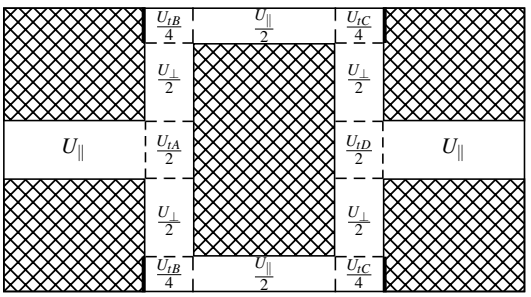


Figure 4: The model considered for a fully staggered configuration where: $p_{U_{tA}} = p + \frac{1}{2}\delta p_{\perp}$, $p_{U_{tB}} = p$, $p_{U_{tC}} = p - \delta p_{\parallel}$ and $p_{U_{tD}} = p - \delta p_{\parallel} - \frac{1}{2}\delta p_{\perp}$.

For the derivations of the permeability, the simplistic models shown in Figures 3 and 4 are considered. That sub-volume of a unit cell occupied by fluid flowing parallel to the net streamwise direction is given by $U_{\parallel}$ and $U_{\perp}$ represents the volume of the transverse channel. In the transfer volume U_t, the wall shear stresses

acting on the fluid-solid interfaces are neglected, thus the pressure drop is assumed zero. It is evident from numerous numerical calculations that the stagnation point with its large pressure causes less shear stress along those parts of S_{of} lying within the transfer volumes U_t.

An analytical model for the determination of the hydrodynamic permeability in the Darcy regime in terms of porosity was developed by Firdaouss and Du Plessis [1]. Unit cells representing different levels of streamwise staggering and different dimensions were examined and a general expression for the dimensionless permeability for these cells was obtained. This analytical model was based on a piece-wise plane Poiseuille flow approximation for interstitial flow between neighbouring particles. In their analytical model, however, the pressure gradient in the transverse channel was taken over the entire $ds_\perp$. In this section an identical analytical method of Firdaouss and Du Plessis [1], is used to obtain an expression for the permeability of the model presented in Figures 3 and 4.

The interstitial flow is assumed to be time independent, incompressible, Newtonian, free of body forces and, since we are interested in hydrodynamic permeability only, creep flow is assumed. The flow is thus governed by the interstitial continuity equation

$$\nabla \cdot \underline{v} = 0 \tag{5}$$

and the interstitial equation for creep flow

$$\nabla p = \nabla \cdot \underline{\underline{\tau}} = \mu \nabla^2 \underline{v}, \tag{6}$$

where $\underline{v}$ is the interstitial velocity defined at each point. In a plane Poiseuille flow approximation, the wall shear stress and corresponding channel-wise pressure gradient are respectively given by

$$\tau_w = \frac{6\mu w}{dc} \quad \text{and} \quad \|-\nabla p\| = \frac{12\mu w}{dc^2}. \tag{7}$$

Here w is the average channel velocity and dc the normal distance between the facing surfaces.

The dimensionless Darcy permeability for the streamwise direction is defined as

$$K \equiv \frac{k}{d_\parallel d_\perp} = \frac{\mu q}{d_\parallel d_\perp \|\nabla p\|} = \frac{\mu q}{d_\perp \delta p}, \tag{8}$$

where $d_\parallel d_\perp$ is the 'volume' of the two dimensional unit cell.

For a streamwise regular array, it follows straightforwardly that the pressure gradient, the total pressure drop and the dimensionless permeability are given by

$$-\nabla_\parallel p = \frac{12\mu w_\parallel}{dc_\perp^2} = \frac{12\mu q}{d_\perp^2 (1-\sqrt{1-\varepsilon})^3}, \tag{9}$$

$$\delta p = \delta p_\parallel = -\nabla_\parallel p \, ds_\parallel \tag{10}$$



and

$$K=\frac{\alpha(1-\sqrt{1-\varepsilon})^3}{12\sqrt{1-\varepsilon}} \tag{11}$$

respectively, as was also obtained by Firdaouss and Du Plessis [1]. Here $\nabla_{\parallel}$ is defined as a scalar operator in the streamwise direction.

2.1 Streamwise staggered array

From flux-conservation it follows for a streamwisely staggered array that

$$w_{\perp}=\xi w_{\parallel}\frac{dc_{\perp}}{dc_{\parallel}}=\xi\alpha w_{\parallel}\,. \tag{12}$$

The total pressure drop over the unit cell consists of the pressure drop in the parallel as well as the transverse channels.

$$\delta p=\delta p_{\parallel}+\xi\delta p_{\perp} \tag{13}$$

The pressure drop in the parallel channel is given by eqn. (10) whereas the pressure drop in the transverse channel is given by

$$\delta p_{\perp}=-\nabla_{\perp}p(2ds_{\perp}-d_{\perp}) \tag{14}$$

where $\nabla_{\perp}$ is a scalar operator. Whence, from eqns. (1), (9) and (12), eqn. (14) reduces to

$$\delta p_{\perp}=-\xi\alpha^4\nabla_{\parallel}p\,ds_{\parallel}\left(2-\frac{1}{\sqrt{1-\varepsilon}}\right). \tag{15}$$

From eqns. (10), (13) and (15) it there-upon follows that

$$\delta p=-\nabla_{\parallel}p\,ds_{\parallel}+\xi\delta p_{\perp}=-\nabla_{\parallel}p\,ds_{\parallel}\left[1+\xi^2\alpha^4\left(2-\frac{1}{\sqrt{1-\varepsilon}}\right)\right]. \tag{16}$$

Substituting eqns. (16) and (9) into eqn. (8) yields the following dimensionless permeability:

$$K=\frac{\mu q}{d_{\perp}\delta p}=\frac{\alpha(1-\sqrt{1-\varepsilon})^3}{12\left[\sqrt{1-\varepsilon}+\xi^2\alpha^4\left(2\sqrt{1-\varepsilon}-1\right)\right]}. \tag{17}$$

This result differs from that of Firdaouss and Du Plessis [1] due to the exclusion of the part of $S_{fs\perp}$ near the stagnation points from the transfer volume U_t, as indicated on Figure 4. In this region there exists a wall shear stress as well as a negative pressure gradient opposite to the interstitial flow direction. There is thus a net force against the flow direction consisting of the positive pressure gradient and the wall shear stress. Firdaouss and Du Plessis [1] neglected the change of the direction of the pressure gradient in their direct model, and thus a much smaller net force against the interstitial flow direction (namely zero) was considered. In the derivation of eqn. (17) the wall shear stress as well as the pressure gradient on that part of $S_{fs\perp}$ was taken as zero.

3 Volume averaging and closure of momentum equations

The results obtained in eqn. (17) may also be obtained more indirectly from the volume averaged transport equation, a method which is also applicable in more general cases of flow in porous media. The actual interstitial flow velocity field $\underline{v}$ can be averaged volumetrically over a Representative Elementary Volume (REV), U_o, yielding the following phase average velocity $\underline{q}$, also known as the superficial velocity and of which the direction is the mean flow (or streamwise) direction used in the previous section,

$$\underline{q} \equiv \frac{1}{U_o} \iiint_{U_f} \underline{v}\, dU\,. \tag{18}$$

Volume averaging of eqns. (5) and (6) over any stationary porous structure, which has a spatially uniform porosity and an average flow which is time independent, yields respectively

$$\nabla \cdot q = 0 \tag{19}$$

and, if $\iint_{S_{fs}} \underline{n} \langle p \rangle_f \, dS$ is assumed to be zero,

$$-\nabla \langle p \rangle_f = \frac{1}{U_f} \iint_{S_{fs}} \underline{n} p \, dS - \frac{1}{U_f} \iint_{S_{fs}} \mu \underline{n} \cdot \nabla \underline{v} \, dS\,. \tag{20}$$

Eqn. (20) may now be 'closed' for a particular porous medium by the introduction of a Rectangular Representative Unit Cell (RRUC) within which the surface integral is evaluated. The notation already established for the unit cell shown in Figure 1 will also be applicable to the RRUC. From eqn. (20) now follows that

$$\begin{aligned} -\nabla \langle p \rangle_f = {} & \underbrace{\frac{1}{U_f} \iint_{S_{fs\parallel}} \underline{n} \overline{p_w} \, dS}_{} + \frac{ds_\parallel}{2 d_\parallel U_f} \iint_{S_{fs\perp AA}} \underline{n} \overline{p_w} \, dS + \frac{dc_\parallel}{d_\parallel U_f} \iint_{S_{fs\perp BB}} \underline{n} \overline{p_w} \, dS \\ & + \frac{ds_\parallel}{2 d_\parallel U_f} \iint_{S_{fs\perp CC}} \underline{n} \overline{p_w} \, dS + \underbrace{\frac{1}{U_f} \iint_{S_{of}} \underline{n} \widetilde{p_w} \, dS}_{} \\ & - \frac{1}{U_f} \iint_{S_{fs\parallel}} \mu \underline{n} \cdot \nabla \underline{v} \, dS - \underbrace{\frac{dc_\parallel}{d_\parallel U_f} \iint_{S_{fs\perp BB}} \mu \underline{n} \cdot \nabla \underline{v} \, dS}_{} \end{aligned}$$

$$-\frac{ds_{\parallel}}{2d_{\parallel}U_f}\iint_{S_{fs\perp AA}}\mu\underline{n}\cdot\nabla\underline{v}\,dS-\frac{ds_{\parallel}}{2d_{\parallel}U_f}\iint_{S_{fs\perp CC}}\mu\underline{n}\cdot\nabla\underline{v}\,dS. \tag{21}$$

The pressure term was split into the average wall channel pressure and a wall pressure deviation. The latter term is zero, because, according to the definition of deviation, the positive and the negative parts of the deviation will cancel out on each fluid-solid interface. The integral of the average wall channel pressure is then split into an integral over the fluid-solid interface in the fluid channels parallel to the streamwise direction and one over the fluid-solid interface in the transverse fluid channels. The integral over the parallel channel will be zero, since the average wall channel pressures on the upper and the lower surfaces will be equal and thus cancel vectorially. The integral over the transverse channels is then split into three integrals which are weighed according to their relative frequency of occurrence if the RRUC is shifted in the streamwise direction. The $S_{fs\perp BB}$ term corresponds to the instances when the boundaries of the RRUC are situated in the transverse fluid channels. The $S_{fs\perp AA}$ term and the $S_{fs\perp CC}$ term correspond to the instances when the transverse boundaries of the RRUC intercept the second half of the solid phase and the first half of the solid phase, respectively. These different RRUC orientations are shown in Figure 5.

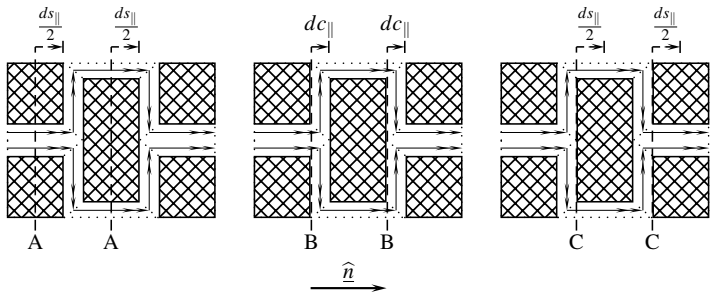


Figure 5: The shifting method of the RRUC for a fully-staggered configuration.

The shear stress integral is split in a similar manner as the pressure term. The magnitude of the wall shear stress on each fluid-solid interface in the transverse channels is equal. The $S_{fs\perp AA}$, $S_{fs\perp BB}$ and $S_{fs\perp CC}$ terms should thus be zero since the wall shear stresses on their two surfaces will cancel vectorially. If the solid phase was not fully staggered in the streamwise direction and the length of the transverse channel, where the interstitial flow direction is $\underline{\check{n}}$, differs from the length of the transverse channel wherein the flow is in the $-\underline{\check{n}}$ direction, (with $\underline{\check{n}}\times\underline{\hat{n}}=\underline{0}$) the integrals over $S_{fs\perp AA}$ and $S_{fs\perp CC}$ will not be zero respectively. If an REV is considered, there should only exist a pressure drop in the mean streamwise direction $\underline{\hat{n}}$, and the net pressure drop in the direction perpendicular to $\underline{\hat{n}}$ should

be zero. The net force acting on the fluid in a particular channel is zero if piecewise straight streamlines (as illustrated in Figure 5) are assumed. The magnitude of the wall shear stress times the surface area it is acting on should be equal to the magnitude of the pressure drop in that channel times its cross-sectional area. Since the net pressure drop in the transverse direction is zero, the net wall shear stress on the surfaces of those channels should also be zero. The RRUC should be a representative unit cell and therefore it is expected that, in eqn. (20), the part of the integral of the shear stress term which is taken over $S_{fs\perp}$ should be zero. Since $S_{fs\perp BB}$ is zero for all levels of streamwise staggering, the net effect of the integrals taken over $S_{fs\perp AA}$ and $S_{fs\perp CC}$ should also be zero. The wall shear stresses on the surfaces of $S_{fs\perp AA}$ will cancel vectorially with the wall shear stresses on the surfaces of $S_{fs\perp CC}$, if the two terms are weighed equally.

The underlined terms in eqn. (21) is zero. This equation thus reduces to

$$-\nabla\langle p\rangle_f = \frac{ds_\parallel}{2d_\parallel U_f}\iint_{S_{fs\perp AA}} \underline{n\overline{p_w}}\,dS + \frac{dc_\parallel}{d_\parallel U_f}\iint_{S_{fs\perp BB}} \underline{n\overline{p_w}}\,dS + \frac{ds_\parallel}{2d_\parallel U_f}\iint_{S_{fs\perp CC}} \underline{n\overline{p_w}}\,dS - \frac{1}{U_f}\iint_{S_{fs\parallel}} \mu\underline{n}\cdot\nabla\underline{\widetilde{v}}\,dS$$

and substitutions according to the geometric assumptions yield:

$$-\nabla\langle p\rangle_f = \xi\delta p_\perp\left[\frac{dc_\parallel d_\perp + ds_\parallel dc_\perp}{d_\parallel U_f}\right] + \delta p_\parallel\left[\frac{ds_\perp dc_\parallel}{d_\parallel U_f}\right] + \frac{\tau_\parallel S_\parallel}{U_f} \tag{22}$$

$$= \left[\frac{\xi\delta p_\perp + \delta p_\parallel}{d_\parallel}\right], \tag{23}$$

which exactly corresponds with eqn. (13), used in the derivation of the dimensionless permeability with the direct method. The gradient of the intrinsic phase average of the pressure can also be written in terms of the shear stresses in the parallel and the transverse channels. It then follows from eqn. (22) that

$$-\nabla\langle p\rangle_f = \frac{1}{d_\parallel dc_\perp}\left[\tau_\parallel S_\parallel + \alpha\xi\tau_\perp S_\perp\right]\widehat{n}, \tag{24}$$

where $\tau_\perp S_\perp = \delta p_\perp dc_\parallel$ and $S_\perp = 2(ds_\perp - dc_\perp)$.

It is assumed that plane Poiseuille flow is a good approximation for the interstitial flow in the channels between the solid particles for this two dimensional case study. We thus have the following expressions for the shear forces in the transverse and the streamwise channels respectively:

$$\tau_\perp S_\perp = \frac{6\mu w_\perp}{dc_\parallel}(4ds_\perp - 2d_\perp) \qquad \text{and} \qquad \tau_\parallel S_\parallel = \frac{6\mu w_\parallel}{dc_\perp}(2ds_\parallel). \tag{25}$$

The interstitial velocity relation is given by

$$\frac{w_\perp}{w_\parallel} = \xi\alpha. \tag{26}$$

From eqn. (24) it then follows that

$$-\nabla \langle p \rangle_f = \frac{12\mu q d_\perp}{dc_\perp^3 d_\parallel} \left[ds_\parallel + \alpha^4\xi^2(2ds_\parallel - d_\parallel)\right] \underline{\hat{n}}. \tag{27}$$

From the definition of the dimensionless Darcy permeability for the streamwise direction it there-upon follows that

$$K \equiv \frac{\mu q}{U_o \left\| \nabla \langle p \rangle_f \right\|} \frac{dc_\perp^3 d_\parallel}{12 d_\perp^2 d_\parallel \left[ds_\parallel + \alpha^4\xi^2(2ds_\parallel - d_\parallel)\right]}. \tag{28}$$

After substitutions, this expression, obtained by means of volume averaging, is identical to expression (17) where the permeability was obtained directly without involving volume averaging.

4 Discussion

Eqn. (24) corresponds to the following equation obtained by Lloyd *et al.* [3] (their equation (15)),

$$-\nabla \langle p \rangle_o = \frac{U_f}{U_\parallel + U_t} \cdot \frac{\tau_\parallel S_\parallel + \xi\tau_\perp S_\perp}{U_o}, \tag{29}$$

where squares rather than rectangles were considered and the aspect ratio, α, was thus set equal to 1. Note that $S_\perp$ in eqn. (29) is $2dc_\perp$ larger than $S_\perp$ in eqn. (24) due to the assumption of the present model.

In a staggered configuration the dimensionless permeability obtained is defined only for porosities up to the point $ds_\perp = dc_\perp$ where subsequent rectangles cease to overlap. Note that the denominator of eqn. (17) is zero or negative if

$$\varepsilon \geq \frac{(3\alpha^4\xi^2 + 1)(\alpha^4\xi^2 + 1)}{(2\alpha^4\xi^2 + 1)^2}, \tag{30}$$

where the lower bound of the RHS of eqn. (30) is 0.75 when α tends to infinity.

In the following example expression (17) is compared with the numerical results obtained by Firdaouss and Du Plessis [1] as well as their analytical results (which is identical to the analytical results obtained by Lloyd *et al.* [3] if $\alpha = 1$). In this example, the aspect ratio is 4 and thus the tortuosity in the streamwise direction is

$$\chi = \frac{L_e}{L} = 1 + \xi\alpha\sqrt{1-\varepsilon} = 1 + 2\sqrt{1-\varepsilon}. \tag{31}$$



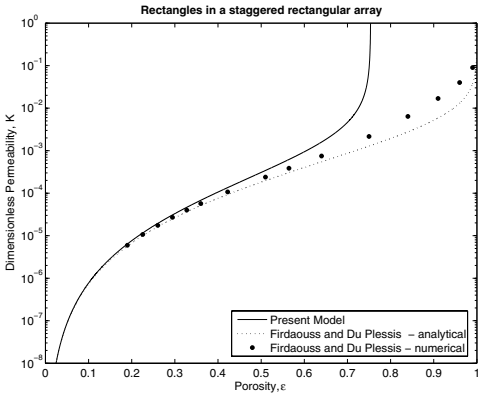


Figure 6: Streamwise staggered array with $\alpha = 4$.

5 Conclusions

A new pore-scale model was introduced to predict the hydrodynamic permeability of low porosity configurations of rectangles. The results closely correlate with numerical computations reported in literature. Important outcomes of this study are the identical results obtained by the direct approach and by the volumetric averaging coupled with closure by a pore-scale model, even in the case of high aspect ratio solid parts and high tortuosities.

References

[1] Firdaouss, M. & Du Plessis, J.P., On the prediction of Darcy permeability in non-isotropic periodic two-dimensional porous media, *Journal of Porous Media*, **7(2)**, pp. 119-131, 2004.

[2] Lloyd, C.A., Hydrodynamic permeability of staggered and non-staggered regular arrays of squares, MSc Thesis, University of Stellenbosch, South Africa, 2003.

[3] Lloyd, C.A., Du Plessis, J.P. & Halvorsen, B.M., On closure modelling of volume averaged equations for flow through two-dimensional arrays of squares, Advances in Fluid Mechanics, vol. V, A. Mendes, M. Rahman & C.A. Brebbia (Eds), Proc. of the International Conference on Advances in Fluid Mechanics AFM2004, Lisbon, Portugal, May 2004, pp. 85-93.

[4] Whitaker, S., The Method of Volume Averaging, *Theory and Applications of Transport in Porous Media*, **13**, Kluwer Academic Publishers, 1999.



Analytical approach predicting water bidirectional transfers: application to micro and furrow irrigation

D. Crevoisier
Irrigation Research Unit, Cemagref Montpellier, France

Abstract

This paper presents an analytical or semi analytical method capable of predicting water bidirectional transfers in a soil under different irrigation systems, and specifically for micro and furrow irrigation systems. The method developed in this article uses the Green's function to solve Richards' equation. Some assumptions are made that allow the equation to be linearized and thus solved. The Green's function is a well-known method used to solve the partial differential equation (PDE) with constant coefficients in simple geometries and general boundary conditions. The singularity of the method lies in its approach to Richards' equation in real irrigation contexts as it superposes simple solutions which can be treated by Green's function method. This work has two main aims: to propose analytical and explicit forms of water content in the soil, and to treat irrigation scenarios (unspecified furrow shapes in the case of furrow irrigation, heterogeneous initial conditions, which take into account precipitation events and plant uptakes, etc.) in a simple and operational manner. It also allows the evaluation of the coefficients of the solute transfers equation which depend on soil water content. This equation can then be solved with the same approach developed for water transfers. We present here the main principles of the model, the first results and improvements that could be made in the future.
Keywords: furrow irrigation, analytical method, Green's function, water and solute transfers, bidirectional.

1 Introduction

Inadequate irrigation and fertilization practices can have important environmental impacts: waste of water, nitrate pollution. Furrow irrigation is one



WIT Transactions on Engineering Sciences, Vol 52, © 2006 WIT Press
www.witpress.com, ISSN 1743-3533 (on-line)
doi:10.2495/AFM06062

of the most commonly used irrigation system in the world and micro irrigation systems installations are on the increase. A better understanding of water and nitrate transfers specific to these irrigation systems and fertilization practices could reduce water drainage and nitrate leaching.

Unidirectional models combining water and solute transfers, soil chemical and plant uptake exist and are able to simulate changes occurring in the soil and plant state along a whole crop season [2, 6]. The main fertilization practices concentrate nitrate in the top layers of the ridge in the context of furrow irrigation. Experiments shows that the nitrate distribution in the soil highly depends on irrigation practices: impact of the water application depth [7], use of an alternative furrow practice, which consists in irrigating every second furrows and applying fertilizer in dry furrows [9]. Here, lateral transfers increase due to the initial distribution of nitrate and unidirectional modelling isn't useful when predicting the fate of water and nitrate in the soil profile. This observation is all the more relevant under environmental contexts where water and nitrate application is adjusted to plants' needs.

Some numerical models can be used to predict water and solute bidirectional dynamics [12, 14], but require a large set of parameters and significant computing time. General analytical solutions concerning water transfers have been developed [1, 8], models specialized in drip irrigation have been adapted from general methods [3, 15] and other models concerning furrow irrigation allow the simulation of cumulative infiltration for a given opportunity time [11, 16]. But in the context of furrow irrigation, the prediction of nitrate leaching requires a better understanding of water and solutes bidirectional transfers' mechanisms.

The model developed in this work, predicts soil water transfers, analytically or semi analytically, under different irrigation scenarios. In the case of furrow irrigation, the resolution of the Richards' equation poses 4 major problems: the significant non-linearity of the Richards' equation, the complexity of the geometry, the mixed boundary conditions on the soil surface and the processing of heterogeneous initial conditions. This work proposes methods to solve each of these problems. The first section of this article deals with the linearization of the equation and its resolution in some theoretical cases. The second section explains how these simple solutions are superposed to recompose the initial complex problem solution. Lastly, improvements of the model and its adaptation to solute transfers, plant uptakes and atmospheric conditions are presented.

2 Resolution of the transfer equation in theoretical cases

The theoretical cases treated in this section concern sloped-plot submitted to simple initial and boundary conditions. To simplify the further calculations, the plot is considered to be horizontal and the gravity force sloped with regard to the vertical axis. The domain of resolution is then semi infinite on the vertical direction and infinite in the horizontal direction. After the resolution of equations, a rotation of the medium produces solutions to the initial theoretical problem (see Figure 1).



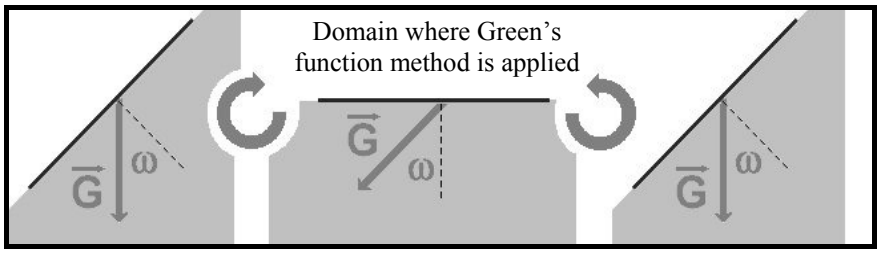


Figure 1: Studied domain transformations.

2.1 The Richards' equation

Water transfers are submitted to Richards' equation [10]. Considering the previous transformation and ω the angle between gravity force and vertical axis, this equation can be written

$$\nabla\left[k\nabla\left(h-\sin(\omega)x-\cos(\omega)z\right)\right]=\partial_t\theta+S \tag{1}$$

where k is the hydraulic conductivity (cm.h^{-1}), h the pressure head (cm), θ the water content (cm^3.cm^{-3}), z the vertical coordinate taken positive downward (cm) and S a sink or source term, usually the plant uptake (h^{-1}).

This equation is highly non-linear and it's writing has to be simplified to allow its resolution using Green's function. The following three equations allow the linearization of Richards' equation by applying the Kirchhoff transformation defined in eqn. (2) and by choosing θ and k relationships suited to the problem, respectively linear soil model defined in eqn. (3) and used by Warrick [15] and Gardner model [4] defined in eqn. (4).

$$\phi(h)=\int_{-\infty}^{h}k(h)dh \tag{2}$$

$$\theta(h)=\theta_R+\frac{k(h)}{\kappa}\ \text{ there }\ \kappa=\frac{k_S}{(\theta_S-\theta_R)} \tag{3}$$

$$k(h)=k_S e^{\alpha h} \tag{4}$$

where k_S is the saturated hydraulic conductivity (cm.h^{-1}), α the inverse of the capillary length (cm^{-1}), θ_R and θ_S, the retention and saturated water content (cm^3.cm^{-3}). ϕ is the flux potential (cm^2.h^{-1}). The resulted linear PDE is then submitted to two transformations. First, dimensionless variables are introduced and a function change is used. The Richards' equation become

$$\partial_T\Psi=\Delta\Psi \tag{5}$$

with the following dimensionless variables

$$\frac{X}{x}=\frac{Z}{z}=\frac{\alpha}{2};\quad \frac{T}{t}=\frac{\alpha\kappa}{4};\quad \frac{\Phi}{\phi}=\frac{\alpha}{K_s} \tag{6}$$

and the following function change

$$\Psi = e^{(-X\sin\omega - Z\cos\omega + T)}\Phi \tag{7}$$

the initial condition is

$$\left[\Psi\right]_{T=0} = e^{(-X\sin\omega - Z\cos\omega)}\Phi_i \tag{8}$$

In the context of soil water transfers in irrigation, two types of boundary conditions are considered. They are also affected by the introduction of dimensionless variables and function change. Considering Φ_0 and q_0 the dimensionless charge and flux on the surface, the Dirichlet and Cauchy boundary conditions respectively become

$$\left[\Psi\right]_{Z=0} = e^{(-X\sin\omega + T)}\Phi_0 \tag{9}$$

$$\left[\partial_Z\Psi - (2-\cos\omega)\Psi\right]_{Z=0} = e^{(-X\sin\omega + T)}q_0 \tag{10}$$

2.2 The Green's function method

Green's function method gives analytical solutions to PDE with complex boundary conditions. It involves multiplying the initial PDE by the Green's function G and integrating the result. The use of Green's function is fully developed by Greenberg [5]. This function G (X_S, Z_S, T_S) is the solution to the initial PDE submitted to an infinite pulse at the point (X_S, Z_S) and time T_S as the initial condition. Green's function depends on the type of boundary conditions considered in the PDE but is, in both cases, the linear combination of functions G_{1D} (X, X_S, T, T_S) G_{1D} (Z, Z_S, T, T_S) defined in eqn. (11).

$$G_{1D}(U,U_S,T,T_S) = \frac{1}{\sqrt{4\pi(T-T_S)}}e^{-\frac{(U-U_S)^2}{4(T-T_S)}} \tag{11}$$

Thanks to the Green's function, the solution of the PDE considered in the eqn. (5) can be analytically written

$$\begin{aligned}\Psi = &\int_0^\infty\int_{-\infty}^{\infty}\left[G\Psi\right]_{T_S=0}dX_S\,dZ_S \\ &+\int_0^T\int_{-\infty}^{\infty}\left[\Psi\partial_{Z_S}G - G\partial_{Z_S}\Psi\right]_{Z_S=0}dX_S\,dT_S\end{aligned} \tag{12}$$

where the first integral accounts for the initial condition and the second for the boundary condition at the soil surface.

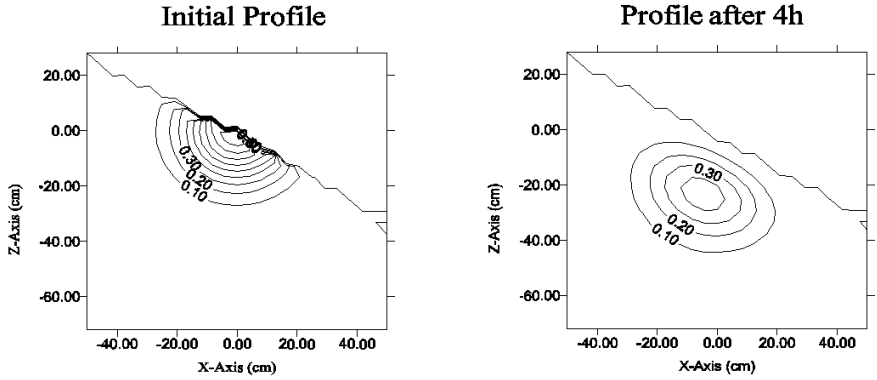


Figure 2: Dimensionless flux potential after 4h simulation with a Gaussian initial condition.

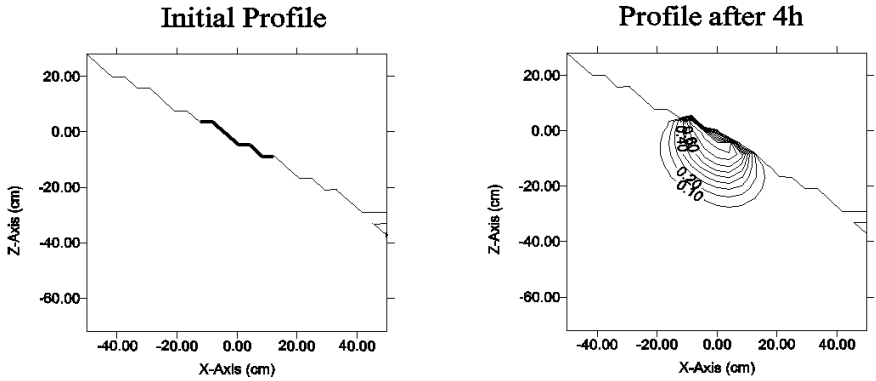


Figure 3: Dimensionless flux potential after 4h simulation with a constant pressure head.

2.3 Some results for theoretical cases

Green's function allows the analytical writing of the solution. But explicit evaluation of eqn. (12) is only possible in particular configurations. This paragraph describes some of these configurations and gives their solutions.

Four kinds of elementary solutions are analysed in this section. The first case studied is a semi infinite medium with an initial condition Φ_i (X, Z), where Φ_i (X, Z) is a Gaussian distribution. The boundary condition considered at the surface is either no pressure head, or no flux. The initial Gaussian condition is well adapted when using Green's function; the evaluation of the eqn. (12) is explicit in the case of Dirichlet boundary conditions and easy to obtain, semi analytically, in the case of Cauchy boundary conditions. The second case we analysed is a semi infinite medium with a zero initial condition and a constant pressure head or flux at the soil surface. The two following plots show the evaluations of the eqn. (12) in the case of Dirichlet boundary condition. In Figure 3, the bold line represents the segment of the surface which is submitted to a

constant pressure head. The same type of results can be obtained in the case of Cauchy boundary conditions.

These elementary problems can be considered as parts of more complex global problem just like analytic element method described by Strack [13]. The next section gives explanations to link these elementary bricks together in order to obtain the global solution of the more complex initial problem.

3 Recomposition of the complete solution

3.1 Theory

The previous section explains how to solve the Richards' equation in simple theoretical cases. Using these results, this section explains how to recompose the solution of a more complex problem. Let's consider the following flow problem illustrated on the left side of Figure 4.

Figure 4 represents a furrow irrigation event with a given initial water content and a given water height in the furrow. In this case, no time variable water height is considered. The geometry considered is a half furrow (due to the symmetry of the system, a half furrow vertically limited by no lateral flux boundary conditions is sufficient to represent the event). The boundary conditions on furrow surface depend on the position of the water level. Under this position, the boundary conditions are considered as variable pressure head boundary conditions, on the other part of the soil surface, the boundary conditions are considered to be no flux boundary conditions. The vertical no lateral flux boundary conditions are simulated by reproducing the symmetry of the system.

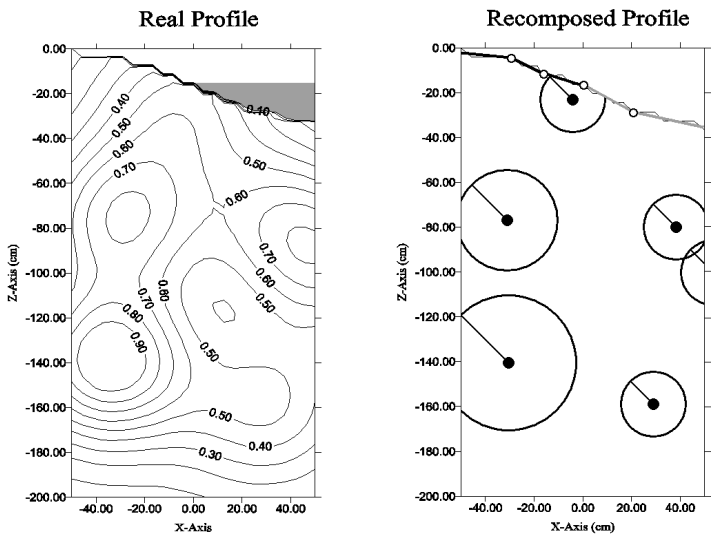


Figure 4: Recomposed initial profile to the model a complex event.

To solve this problem, the shape of the furrow is discretized in segments with specified constant boundary conditions and the initial conditions are composed of several Gaussians (represented on the right side of Figure 14 by circles of different radius standing for different Gaussians amplitudes). The solutions to each of these elementary problems are known thanks to the study previously explained in this paper. The analytical form of the PDE solution from eqn. (12) is rewritten as a sum of these elementary problems.

$$\Psi = \sum_i \int_0^{\infty} \int_{-\infty}^{\infty} \left[G\Psi_i \right]_{T_S=0} dX_S dZ_S + \sum_j \int_0^{T} \int_{\Gamma_j} \left[\Psi \partial_{\vec{n}_j} G - G \partial_{\vec{n}_j} \Psi \right]_{\Gamma_j} d\Gamma_S dT_S \tag{13}$$

Where Ψ_i are the different Gaussian distributions which make up the initial conditions and Γ_j and n_j are respectively the different segments composing the surface boundary and their normal vectors.

3.2 The case of micro irrigation

A first model validation concerns the case of micro irrigation practice. Modelling has been done in 2D context, but the transition to axisymmetric or tridirectional coordinates can be treated by Green's function with few modifications. Geometry is rectangular and boundary conditions are only Cauchy type: constant flux on a segment of the surface and no flux on the other part of the surface. The validation has been led by comparison with the numerical model Hydrus-2D [12] on an initial homogeneous wet Clay Loam soil ($\Delta\theta = \theta_S - \theta_I = 0.05$ cm^3.cm^{-3}) for 4h irrigation. Results are illustrated in Figure 5. Simulation performed gives satisfying results.

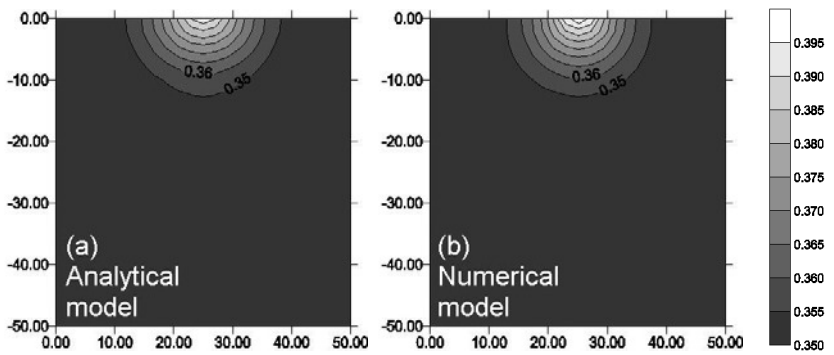


Figure 5: Comparison between analytical and numerical modelling of water content profile under micro irrigation.

3.3 The case of furrow irrigation

Furrow irrigation modelling is more complex than the previous case and the reliability of the model is questionable. Validation is also carried out by comparing it with the Hydrus-2D numerical model using the same soil characteristics as employed previously. Analytical model discretizes the furrow as described in the previous section. Simulation performed concerns a 4h furrow irrigation event on the homogeneous dryer soil ($\Delta\theta$ = 0.14 $cm^3.cm^{-3}$). Figure 6 gives the results of this comparison. Due to the linear soil assumption, the wetting front decreases from saturated water content to initial water content is lower in the simulation performed using the analytical model. The numerical modelling takes into account the relationship between soil characteristics and moisture conditions, and the wetting front is also governed by this relationship.

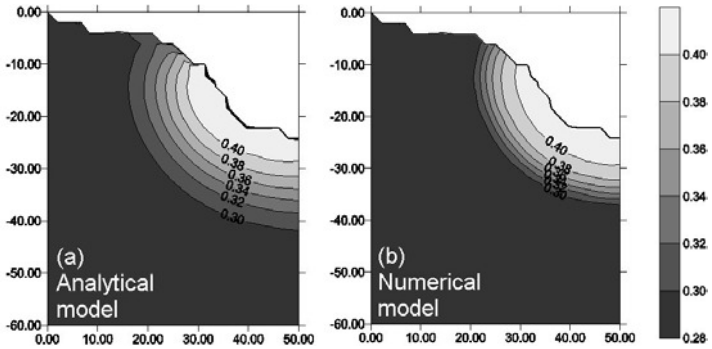


Figure 6: Comparison between analytical and numerical modelling of water content profile under furrow irrigation.

4 Discussion and complements

The Green's function method has been used to provide analytical solutions to the Richards' equation. Some theoretical cases provided an explicit or semi implicit evaluation of these analytical solutions and these elementary solutions can be linked together to build solutions for a more complex global problem. The advantage of this semi analytical model with regards to other analytical models is its adaptability. It's able to simulate heterogeneous initial conditions and takes into account complex boundary conditions and geometries. Concerning the numerical models, it is more operative and reduces the computing time. No notion of CFL (Courant Friedrichs Lewy) condition is introduced (imposed relationship between time and space steps for the stability of the numerical scheme), the initial conditions are easier to build for given experimental data and the number of elementary problems to solve is less than the number of cells using in numerical models.

However, this work is based on some assumptions that permit the linearization of the equations and the application of Green's function. Some of

these assumptions, especially those of linear soil conditions, defined by the eqn. (3) can lead to difficulties in representing real water transfers in soil. In micro irrigation contexts, soil water content is generally maintained close to field capacity and its variation is low. In that case, the linear soil assumption is acceptable and its impact on results is low (see Figure 5). In the furrow irrigation context, soil moisture variations are higher. This form of irrigation often results in higher water application depth, but the irrigations events are less frequent. Consequently, the impact of the linear soil assumption is greater as shown in Figure 6.

On the way of reducing these impacts is proposed by means of an iterative process: a run of the analytical model provides an approximation of soil characteristics, based on an evaluation of PDE coefficients for a next model iteration. Another more mathematical approach to improve the linearization of water content model was proposed by Basha [1]. He introduced a perturbation solution in the original nonlinear problem.

The methods applied in this work can therefore be completed by the modelling of other phenomena that occur during a cropping season. For instance, the approach developed in this article gives the soil water content profile which is necessary for the evaluation of the nitrate transfers equation coefficients. This equation can be solved using the same principles as those used for the resolution of the Richards' equation.

References

[1] Basha, H.A., Multidimensional nonsteady infiltration with prescribed boundary conditions at the soil surface. Water resources research, 1999. **35**: p. 75-84.

[2] Brisson, N., et al., STICS: a generic model for the simulation of crops and their water and nitrogen balances. I. Theory and parameterization applied to wheat and corn. Agronomie, 1998. **18**(5-6): p. 311-346.

[3] Coelho, F.E. and D. Or, Applicability of analytical solutions for flow from point sources to drip irrigation management. Soil Sci. Soc. Am. J., 1997. **61**: p. 1331-1341.

[4] Gardner, W.R. and M.S. Mayhugh, Solution and tests of the diffusion equation for the movement of water in soil. Soil Science Society of Am. Proc., 1958. **22**: p. 197-201.

[5] Greenberg, M.D., Application of Green's functions in science and engineering. 1971, Englewood Cliffs, N.J.: Prentice-Hall.

[6] Jones, C.A. and J.R. Kinity, CERES-MAIZE, a Simulation Model of Maize Growth and Development. 1986: Texas A.M. University Press.

[7] Mailhol, J.-C., P. Ruelle, and I. Nemeth, Impact of fertilisation practices on nitrogen leaching under irrigation. Irrigation Science, 2001. **20**: p. 139-147.

[8] Philip, J.R., Linearized unsteady multidimensional infiltration. Water resources research, 1986. **22**(12): p. 1717-1727.



[9] Popova, Z., et al. Lysimeter study on ground water degradation due to different fertilisation and irrigation management. in ICID-ICWRM in the 21st Century. 2000. Budapest, Hungary.
[10] Richards, L.A., Capillary condiction of liquids through porous medium. Physics, 1931. **1**: p. 318-333.
[11] Schmitz, G.H., Transient infiltration from cavities - I : theory. Journal of irrigation and drainage engineering, 1993. **119**(3): p. 443-457.
[12] Simunek, J., M. Sejna, and M.T. Van Genuchten, The HYDRUS-1D and HYDRUS-2D codes for estimating unsaturated soil hydraulic and solutes transport parameters. Agron. Abstr., 1999. **357**.
[13] Strack, O.D.L., Groundwater Mechanics. 1989, Englewood Cliffs, N.J.: Prentice-Hall.
[14] Van Genuchten, M.T., A numerical model for water and solute movement in and below the root zone. Research Report. 1987, U.S. Salinity laboratory, USDA, ARS,: Riverside, California.
[15] Warrick, A.W., Time-depend linearized infiltration. I. Point sources. Soil science society of Am. Proc., 1974. **38**(12): p. 383-386.
[16] Wöhling, T., G.H. Schmitz, and J.-C. Mailhol, Modelling 2D-infiltration from irrigation furrow. Analysis of analytical and numerical approaches. Journal of Irrigation and Drainage Engineering, 2004. **130**(4): p. 296-303.



The meniscus depression of a porous spherical particle at the three phase contact line

P. Basařová[1], D. Horn[1] & A. Capriotti[2]
[1]*Department of Chemical Engineering,*
Prague Institute of Chemical Technology, Czech Republic
[2]*Department of Chemical Engineering,*
Mining and Environmental Technologies, University of Bologna, Italy

Abstract

The description of the processes at the three phase contact line is very important for the study of elementary steps in flotation. When a hydrophobic particle is attached to a gas-liquid interface, it is influenced by a number of forces, including surface tension, capillary and buoyancy forces on one hand and the particle weight on the other. In the case of porous particles, capillary forces acting in the porous surface must also be considered. The meniscus depression at the three-phase contact line is determined by the resultant force. The meniscus depression of the floating particle was studied using the image analysis method. The depression was studied for spherical polystyrene particles of diameters from 0.5 to 3mm. We compared the experimental values of meniscus depression with the data calculated using theoretical and semi-empirical models. The theoretical description of forces acting on the floating spherical porous particle is also given. We found that the existence of pores and surface inequalities has a significant influence on particle behaviour on the phase interface.
Keywords: floating particle, meniscus depression, porous surface, capillarity.

1 Introduction

The analysis of forces on the particle attached to the bubble surface has been the focus of the study of flotation processes since the early days of its industrial utilization. When a hydrophobic particle is attached to a gas-liquid interface, it is influenced by a number of forces, including the surface tension and buoyancy forces on the one hand and the particle weight on the other [1,2]. It is customary



WIT Transactions on Engineering Sciences, Vol 52, © 2006 WIT Press
www.witpress.com, ISSN 1743-3533 (on-line)
doi:10.2495/AFM06063

to sum the forces, which are a function of the position of the three-phase contact and to describe them jointly as the adhesive forces. The other forces, which are independent of the position of the three-phase contact, such as the particle weight less its buoyancy and the inertial forces, are jointly termed the detaching force.

One of the most important forces is the capillary force F_c. Due to the rotational symmetry along the vertical axis, the horizontal component of this force vanishes and only the vertical component remains.

$$F_c = 2\pi r_p \sigma \sin \alpha \sin(\theta - \alpha) \tag{1}$$

The next force, which supports the particle suspension at the interface, is the buoyancy F_b of the particle immersed in the liquid phase. This force can be described by the following equation

$$F_b = \frac{\pi r_p^3 \rho_l g}{3}(2 + 3\cos\alpha - \cos^3\alpha) \tag{2}$$

The pressure force F_p, which stabilizes the particle suspension, results from the hydrostatic pressure, which acts over an effective area πr_{tpc}^2 enclosed by the three-phase contact line.

$$F_p = \pi r_p^2 H \rho_l g \sin^2 \alpha \tag{3}$$

Another important force acting on the particle is the particle weight F_g, which tends to pull the attached particle into the liquid phase.

$$F_g = -\frac{4\pi r_p^3 \rho_p g}{3} \tag{4}$$

Here H is the meniscus depression at the three-phase contact, r_p is the particle radius, r_{tcp} is the radius of the three phase contact line, σ is the surface tension, g is the acceleration due to gravity, and ρ_p, ρ_l and ρ_g are the densities of the particle, liquid and gas, respectively. θ is the contact angle and α is the central angle. The model behaviour of a solid particle is depicted on figure 1.

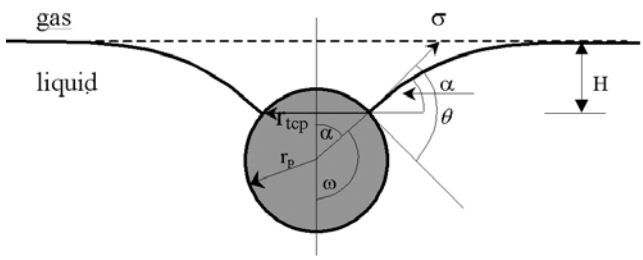


Figure 1: A model of solid spherical particle attached to planar gas-liquid surface.

In summary, there are four static forces acting on the smooth and spherical non-porous particle attached to a free water surface [1,2,3]. Equilibrium is attained if

$$F_c + F_b + F_p + F_w = 0 \tag{5}$$

and consequently

$$\left\{\frac{H}{r_p}\sin^2\alpha + \frac{2+3\cos\alpha-\cos^3\alpha}{3}\right\}(\rho_l-\rho_g)g\pi r_p^3 + 2\pi r_p\sigma\sin\alpha\sin(\theta-\alpha) - g(\rho_p-\rho_g)4\pi r_p^3/3 = 0 \quad (6)$$

Let's consider about a slightly porous particle. The capillary force for one pore [4] is given as

$$F_c = 2\pi R_p\sigma\sin\gamma \quad (7)$$

Here R_p is the pore radius and γ is the contact angle inside the pore. When we consider the capillary force for all pores around the three-phase contact line and the force equilibrium, it is possible to re-write equation 5:

$$F_c + F_b + F_p + F_w + \sum_i 2\pi R_{pi}\sigma\sin\gamma_i = 0 \quad (8)$$

This equation should be a general relationship to express the meniscus depression for a slightly porous particle.

In a flotation process, empirical equations are used often also. For three-phase contact line with small radius, the fundamental equation (6) can be solved by employing the method of matched asymptotic perturbation [5]. The final result for the meniscus depression is described by the Derjaguin equation:

$$H = r_{tpc}\sin\beta\left(\ln\frac{4L/r_{tpc}}{1+\cos\beta} - \gamma\right), \quad (9)$$

where $\gamma = 0.577$ and it is the Euler constant, r_{tpc} is the radius of three-phase contact line and due geometric symmetry $\beta = \theta - \alpha$ [2]. The capillary length L is defined by the following equation

$$L = \sqrt{\frac{\sigma}{(\rho_l-\rho_g)g}}. \quad (10)$$

Comparison of this equation to the numerical results of the Young-Laplace equation[2] indicates, that the Derjaguin equation is accurate for $r_{tcp}/L \le 0.2$. For three-phase contact with large radius the approximate solution of the equation (6) can be derived also. For the meniscus depression the modification yields

$$\frac{H}{L} = \sin(\beta/2)\frac{2}{\sqrt{1+(L/r_{tpc})}} \quad (11)$$

This simple equation derived in the limit of the large radius compares with the numerical results surprisingly well, down to $r_{tcp}/L \ge 2$. For three-phase contacts with the radius in the range of $2.0 \ge r_{tcp}/L \ge 0.2$ no analytical solutions for the meniscus depression are available. The explicit dependence of the meniscus depression on the three-phase contact radius and the meniscus angular inclination can be obtained only empirically. Nguyen [3] describes this solution based on the asymptotic analytical results and the numerical

computational results of solution to the Young-Laplace equation. According to this method one can obtain

$$\frac{H}{L} = a \sin\left(b\beta\right), \tag{12}$$

where a and b are empirical parameters. It is assumed, that b is independent of β and is a function of r_{tcp} / L only. It has two asymptotes, b = 0.5 and 1 for very small and very large values of r_{tcp} / L, respectively. For the range of $2 \geq r_{tcp} / L \geq 0.1$, fitting to the exact numerical data gives:

$$b = 0.5 + 0.332 \exp\left(-2.122\, r_{tpc} / L\right) \quad \text{and} \quad a = \frac{2.186}{1 + 0.649\left(L / r_{tpc}\right)} \tag{13}$$

The aim of this research was the experimental study of the meniscus depression at the three-phase contact of the floating plastic particle using image analysis method. Plastic materials are characteristic for their polymeric structure with long chains. Therefore for these compounds it is possible to assume the occurrence of surface inequality from a microscopic point of view and also the appearance of pores. The depression was studied for polystyrene particles of different diameters (0.1 – 3mm). All experiments were performed in a small apparatus monitored by a high-speed CCD camera with a macro-objective. The obtained data were processed using an image analysis software LUCIA. The experimental data were compared with the theoretical models.

2 Experimental materials and methods

The model spherical particles of expandable polystyrene EPS (originating from Kaucuk Kralupy, Czech. Rep.) were used for the experiments. We used 70 particles with diameters from 0.5 mm to 2.6 mm and the density of these balls was 1.03 $g.cm^{-3}$. The value of the contact angle for this type of polystyrene in distilled water was $79{,}2^0$ [6]. The contact angles were measured by direct method, monitoring the drop profile on smooth flat surface, represented by a foil made from polystyrene balls. For all the measurements the distilled and de-ionised water was used. Here, pH was 6.13 and conductivity 1,6 μS/cm.

For interpretation of obtained data the program LUCIA was used. LUCIA is a software program evaluated for capturing, analysing and saving images. This program works with an A/D converter on the graphical chip in computer, the graphical chip converts the analogue signal to the digital signal. The program uses dimensional analysis and with a calibrated picture it is possible to obtain the precise size of particles. The program enables automatic detection of boundaries, measurement of angles and automatic calculation of the count of objects with help of attributes of objects. The system of image analysis consists of three parts: a microscope, CCD camera and PC with LUCIA software for analysis of captured images. Resulting images from the experiment are adjusted by the software (brightness, contrast and detection of objects) and mathematically evaluated.

3 Results and discussions

For polymeric compounds it is possible to assume the occurrence of surface inequality from a microscopic point of view and also the appearance of pores. As an experimental material we used expandable polystyrene, which contains pentane as an expanding component. This gas vanishes after a short time, but in the interior structure small bubbles or holes remain. Their diameter is 6 μm and this value was measured using the electronic microscope. If the bubble is in the near vicinity of the surface, it can happen that the smooth structure is damaged and a pore is originated. On the figure 2 are illustrated details of the surface with a big enlargement. Here some pores and surface inequalities are visible. From the image analysis we know that the pore radii lie between 6 to 15μm. Unfortunately, it was not possible to measure pore diameters for all particles separately. According to our measurements we expect that the number of pores could not exceed the value of 5 pores per 1 mm on the contact line.



Figure 2: The detail of a surface.

The images of floating particles were the basis of all experimental data. The software LUCIA uses dimensional analysis and using calibrated images the particle diameters were determined with an accuracy 0,001 mm. The obtained data (r_p) were utilized for the assessment of the radius of the three-phase contact r_{tpc} and meniscus depression H. On the figure 3 (left) is an original image of a floating particle. The scanned image was processed using the software LUCIA On a figure 3 (right) is plotted a spherical particle shape and results of a size analysis are also marked.

All used experimental particles have the same density and the value of a contact angle. Therefore, it is possible to presume, that the radius of three-phase contact r_{tpc} should be proportional to the particle radius r_p. This dependence was confirmed and the results are depicted on the figure 4. We found, that the radius of three-phase contact can be calculated for the polystyrene balls using the equation

$$r_{tpc} = 0,8835\ r_p \tag{14}$$

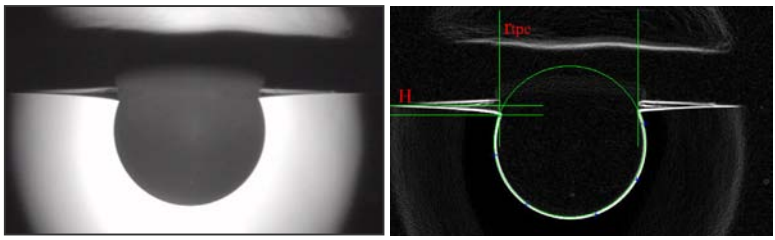


Figure 3: Detail of the floating particle (left) and the image analysis using the software LUCIA (right).

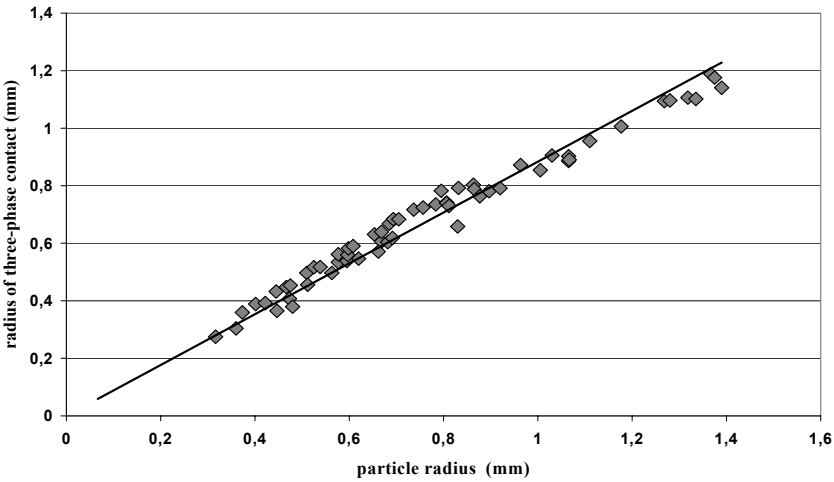


Figure 4: The dependence of the radius of the three-phase contact r_{tpc} on the particle radius r_p.

The angle α was measured experimentally and the angle β (see Fig.1) was calculated according to the relation $\beta = \theta - \alpha$ [2]. For the calculation of meniscus depression H three equations were used. In the literature [2,3], it is recommended to calculate meniscus depression with regard to the value of r_{tcp} / L. For three-phase contact with small radius ($r_{tcp} / L \leq 0.2$) the Derjaguin equation (9) is suggested. The data, calculated using this equation, are denoted as H_{small}. For three-phase contacts with the radius in the range of $2.0 \geq r_{tcp} / L \geq 0.2$ the semi-theoretical equations (12-13) were used. The calculated values are denoted as $H_{middle.}$ Finally the fundamental theoretical equation (6) was applied. The calculated data are denoted as H_{theor}. On figure 5 are demonstrated experimental data and calculated dependences of meniscus depression on the radius of three-phase contact.

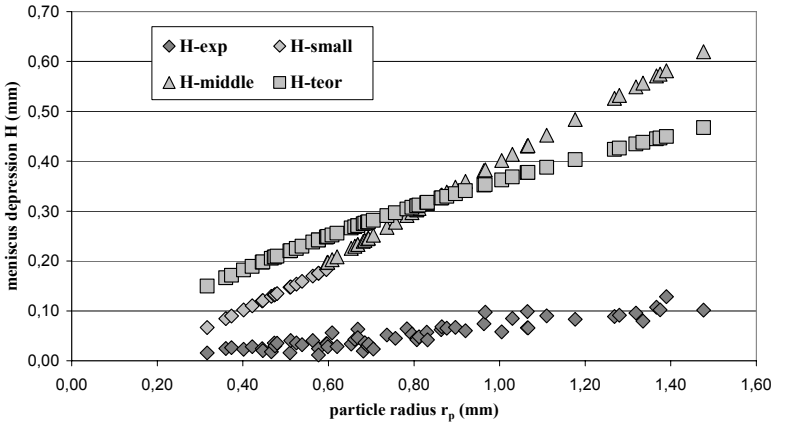


Figure 5: The dependence of the meniscus depression on the radius of three-phase contact line – experimental and calculated data.

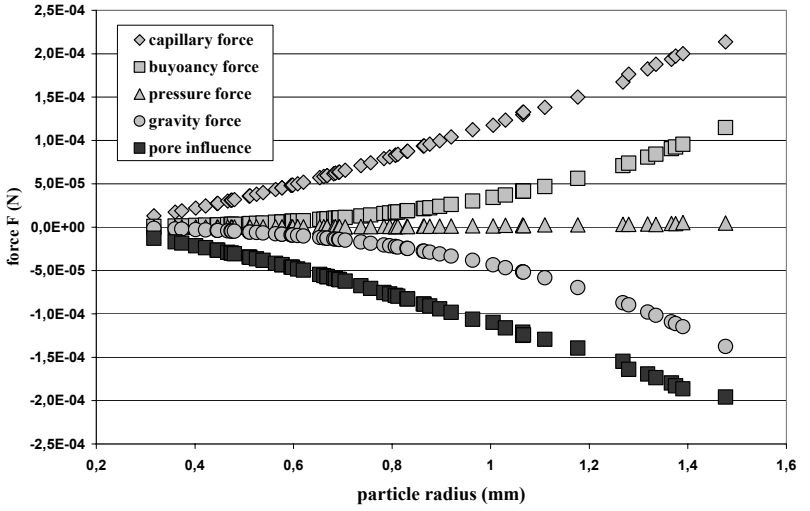


Figure 6: The calculated values of capillary force F_c, buoyancy F_b, pressure force F_p, particle weight F_g and capillary force of pores F_c' and their dependence on the particle radius.

A substantial inconsistency of experimental and calculated data is obvious from these results. All used theoretical relationships (equations 6, 9 and 12 – 13) were derived for smooth and non-porous spherical particles and therefore do not reflect the pore existence. It is obvious from experimental measurements that the influence of surface roughness and pores is remarkable. The value of meniscus depression is even several times lower. Thus for even slightly porous particles

the usage of theoretical relationships is not suitable for calculations in flotation, e.g. for the estimation of maximum size of a floating particle.

On figure 6 are plotted the calculated values of capillary force F_c, buoyancy F_b, pressure force F_p and particle weight F_g as a dependence on the particle radius. Also the force reflecting the pore influence was calculated according to eqn. (8). Here the force balance at equilibrium should be equal to zero. The most significant forces are the capillary force acting on the whole particle and the force influenced by the pore existence. This result is not surprising if we consider all aspects of the law of capillary rise [4]. On figure 7 is given one example of the estimation of pore number. Here the pore radius 15μm was used and the calculation was done for several values of the contact angle. We could expect that the contact angles in pores have the same or lower value than the contact angles on a flat surface.

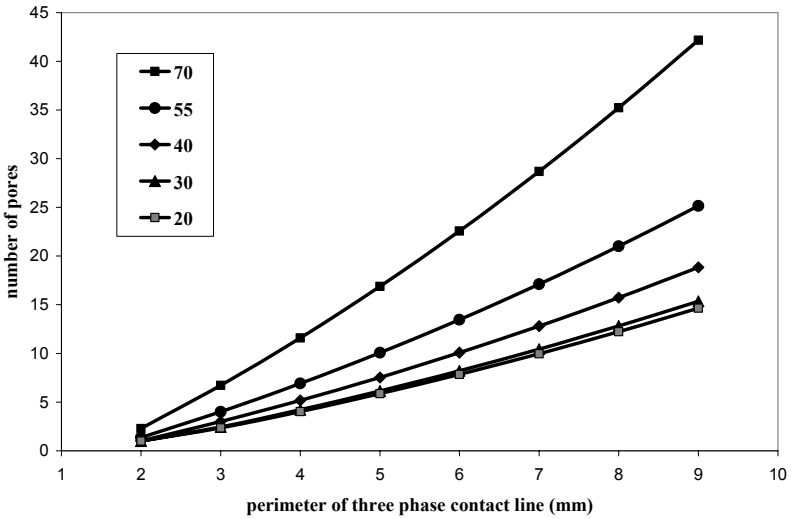


Figure 7: The estimated number of pores as a dependence on the perimeter of the three phase contact line for contact angles from 20° to 70° and pore radius 15μm.

4 Conclusions

The meniscus depression H at the three-phase contact line of the floating slightly porous particle was studied using the image analysis method (software LUCIA). We compared the experimental values of meniscus depression with the data calculated using theoretical and semi-empirical models derived for the non-porous particles. We found out a big difference between experimental and theoretical values. It is obvious from experimental measurements that the influence of surface roughness and pores is remarkable. The value of meniscus

depression is even several times lower. Thus for even slightly porous particles the usage of theoretical relationships is not suitable for calculations in flotation, e.g. for the estimation of maximum size of a floating particle. The existence of pores and surface inequalities has a really significant influence on the particle behavior on the phase interface.

Acknowledgements

This work has been supported by the Grant no. 104/05/2566 from the Grant Agency of Czech Rep. and by the Grant Research Project MSM60446137306 of the Czech Ministry of Education.

5 References

[1] Schulze, H.J., *Physico-chemical Elementary Processes in Flotation*, Elsevier: Amsterdam, Oxford, New York and Tokyo, pp.182-196, 1984.

[2] Nguyen, A. V. & Schulze, H .J., *Colloidal Science of Flotation*, Surfactant Science Series, Marcel Dekker: New York and Basel, pp.527-558, 2004.

[3] Nguyen, A.V., Empirical equations for meniscus depression by particle attachment. *J. Colloid Interface Sci*. **249**, pp. 147-151, 2002.

[4] De Gennes, P.G., Quere, D., Brochard-Wyart, F. & Reisinger, A., *Capillarity and Wetting Phenomena: Drops, Bubbles, Pearls, Waves,* Springer-Verlag: New York, pp. 51-53, 2004.

[5] Derjaguin, B., Theory of meniscus depression in liquids due to immersed small objects and its utilization for the measurements of border contact angles for thin threads and fibres. *Dokl. Akad. Nauk SSSR* 51(7), pp. 517-520, 1946.

[6] Basařová, P. & Horn, D., Study of the hydrodynamics in the plastics flotation, *Proc. of 50th Conf. of Chem. and Proc. Engineering – CHISA 2003*, eds. J. Novosad, Praha, pp.1-7, 2003.



This page intentionally left blank

Author Index

Abu-Nada E. 371
Afsharpoya B. 287
Aguilar D. A. 317
Akbari G. 389
Al-Sarkhi A. 371
Amadou H. 133
Amano R. S. 153
Andreeva T. 143
Andziak P. 603
Arch A. 519
Ayrault M. 571

Barrera P. 297, 327
Basařová P. 643
Batayneh M. 371
Beck C. 133
Bizzarri G. 399
Bourisli R. I. 13
Brugarino T. 297, 327

Calin C. D. 351
Campbell L. J. 457
Capriotti A. 643
Carapau F. 409
Castellani I. 341
Chai A. 381
Chang H.-C. 223
Charpin J. P. F. 421
Chu P. C. 123
Cintoli S. 399
Cloete M. 623
Cooper-White J. J. 69
Crevoisier D. 633

D'Alessio S. J. D. 175, 445
Davidson M. R. 69
Dayan Y. 165
de Weerd A. 255
Derksen R. W. 59
Deshpande A. P. 101
Di Federico V. 399
Diego I. 113
Dimokritou F. K. 479
Dobrovska J. 91
Dong Z. B. 571
du Plessis J. P. 3, 623
Dumas G. 245
Durgin W. 143

Essemiani K. 509

Fatsis A. 49, 479, 489, 583
Filios A. E. 479

Gallerano F. 551
Gill L. 361

Hadadin A. N. 193
Halvorsen B. M. 3
Harvie D. J. E. 69
Heger J. 91
Ho J. 381
Horn D. 643
Hossain M. M. 255
Hriberšek M. 267
Hua J. 79

Inoue T. 277
Islam M. R. 615

Kaminski D. A. 13
Kato C. 499
Kavicka F. 91
Ketata C. 615
Kinsey T. 245
Kioussis E. 583
Kouskouti M. 583

Labadin J. 381
Layrenti F. 49
Lebrun M. 307
Lou J. 79

Makowski P. 603
Martín E. 213
Martins A. M. 469

Matsuura K. 499
Mavrommatis S. 49, 489
Mayr D. 519
Mehemed Abughalia M. A. 39
Meinhold J. 509
Mejia J. 593
Melilla L. 551
Mendes A. C. 469
Mollagee M. 531
Moodie T. B. 175, 445
Mosselman E. 255
Mousavizadegan S. H. 435
Myers T. G. 421

Neves A. C. V. 203
Nowicki M. L. 603

Oshkai P. 593

Panoutsopoulou A. 49, 489, 583
Papadopoulos P. 235
Pascal J. P. 175, 445
Pasero E. 551
Patel T. 361
Pinto F. T. 203
Plosz B. Gy. 509
Podyma M. 603
Poulet J.-B. 133
Pushpavanam S. 101

Rahman M. 435
Ran Z. 541
Ravnik J. 267
Ray G. 123
Rigit A. 381
Rimmer J. 59
Rodríguez R. 113

Sadowski A.-G. 133
Santhanagopalan S. 101
Satish M. G. 615
Sekanina B. 91
Sengupta S. 21
Sequeira A. 409
Shahidullah Md. 255
Shirvani M. 351
Sinhamahapatra K. P. 21
Škerget L. 267
Staff Ø. 31
Stefanczyk L. 603
Stetina J. 91
Subrahmanyam P. 235
Subramanian C. S. 307
Sutherland B. R. 317
Suzuki Y. 277
Swaters G. E. 185

Toraño J. 113
Touati D. 165
Tshehla M. S. 421

van Roessel H. J. 351
van Wielink P. 255
Vega J. M. 213
Vlachakis N. 489, 583
Vlachakis V. 489, 583
Vrachopoulos M. Gr. . 49, 479, 489

Walecki J. 603
Wang H. T. 571
Wang L.-P. 287
Weiss M. 509
Wille S. Ø. 31
Woudberg S. 3

Xiao Y. M. 153

Yeh J.-T. 561
Yeo L. Y. 223

Zahidul Islam Md. 255
Zbicinski I. 603
Zhang X. H. 571



WITPRESS

Monitoring, Simulation, Prevention and Remediation of Dense and Debris Flows

Edited by: G. LORENZINI, University of Bologna, Italy, C. A. BREBBIA, Wessex Institute of Technology, UK, D. EMMANOULOUDIS, Technical Educational Institute of Kavala, Greece

Debris flows, such as the other dense and hyper-concentrated flows, are among the most frequent and destructive of all geomorphic processes and the damage they cause is often devastating. This book, featuring papers from the First International Conference on Monitoring, Simulation, Prevention and Remediation of Dense and Debris Flows, considers these issues. Topics of interest include: Mass Wasting and Solid Transport; Slope Failure and Landslides; Sediment, Slurry and Granular flows; Solid Transport within a Streamflow; Hyper-concentrated Flows; Debris-flow Phenomenology and Rheology; Debris-flow Triggering and Mobilisation Mechanisms; Debris Flow Modeling; Debris Flow Disaster Mitigation (structural and non structural measures); Case Studies; Computer Models; Rock Falling Problems; Mechanics of Solid-Liquid-Flows.

ISBN: 1-84564-169-8 2006 apx 300pp apx £110.00/US$195.00/€165.00

We are now able to supply you with details of new WIT Press titles via E-Mail. To subscribe to this free service, or for information on any of our titles, please contact the Marketing Department, WIT Press, Ashurst Lodge, Ashurst, Southampton, SO40 7AA, UK
Tel: +44 (0) 238 029 3223
Fax: +44 (0) 238 029 2853
E-mail: marketing@witpress.com

Atmosphere Ocean Interactions

Volume 2

Edited by: W. PERRIE, Bedford Institute of Oceanography, Canada

In recent years intense scientific research has been devoted to the understanding of atmosphere-ocean interactions.
This volume continues and expands on some of the topics covered in Volume 1 (ISBN: 1-85312-892-9). The contributors consider hurricanes and severe marine storms within the context of atmosphere-ocean interactions. Factors related to storm intensity and evolution are mentioned, while impacts of storms on the upper ocean and related atmospheric variables are described. Relationships between climate time-scales and storms and the impacts of storms on climate-related factors such as air-sea gas transfer are also considered.
Series: Advances in Fluid Mechanics Vol 39

ISBN: 1-85312-929-1 2006 apx 300pp apx £89.00/US$142.00/€133.50

WIT eLibrary

Home of the Transactions of the Wessex Institute, the WIT electronic-library provides the international scientific community with immediate and permanent access to individual papers presented at WIT conferences. Visitors to the WIT eLibrary can freely browse and search abstracts of all papers in the collection before progressing to download their full text.

Visit the WIT eLibrary at
http://library.witpress.com



WITPRESS

Solitary Waves in Fluids

Edited by: R. H. J. GRIMSHAW, Loughborough University, UK

After the initial observation by John Scott Russell of a solitary wave in a canal, and the subsequent theoretical work of Boussinesq, Rayleigh and Korteweg and de Vries, interest in solitary waves in fluids lapsed until the mid 1960's with the seminal paper of Zabusky and Kruskal describing the discovery of the soliton. This book describes the role that soliton theory plays in fluids in several contexts. After an historical introduction, the book covers the basic theory of the Korteweg-de Vries equation, and the consequent application to free-surface solitary waves in water to internal solitary waves in the coastal ocean and the atmospheric boundary layer, solitary waves in rotating flows, and to planetary solitary waves with applications to the ocean and atmosphere. The theory and application of envelope solitary waves and the nonlinear Schrodinger equation to water waves are then examined.

Series: Advances in Fluid Mechanics Vol 45

ISBN: 1-84564-157-4 2006 apx 250pp apx £89.00/US$157.00/€133.50

Transport of Organic Liquids

G. LATINI, Universita Politecnica delle Marche, Italy, R. COCCI GRIFONI, Universita delle Marche, Italy, G. PASSERINI, Universita Politecnica delle Marche, Italy

The liquid state is possibly the most difficult and intriguing state of matter to model. Organic liquids are required, mainly as working fluids, in almost all industrial activities and in most appliances (e.g. in air conditioning). Transport properties (namely dynamic viscosity and thermal conductivity) are possibly the most important properties for the design of devices and appliances. Most theoretical studies on the liquid state date back to the Fifties however huge advances in experimental studies and applied research on heat and mass transfer in liquids have been achieved during past decades. Most of the models cannot rely on theory alone and are empirical, while for most organic liquids, only a few experimental points and empirical correlations are available in literature.

The aim of this book is to present both theoretical approaches and the latest experimental advances on the issue, and to merge them into a wider approach. The book is organised into five chapters. The first chapter presents our theoretical knowledge of the liquid state. The second presents the tentative models for the evaluation of the thermal conductivity of organic liquids and confronts their results with the experimental data available in literature. The third presents the tentative models for the evaluation of the dynamic viscosity of organic liquids and confronts their results with the experimental data available in literature. The fourth presents a deeper review of the choice methods for thermal conductivity and their applications to mixtures of organic liquids and the fifth chapter presents a deeper review of the choice methods for dynamic viscosity and their applications to mixtures of organic liquids.

ISBN: 1-84564-053-5 2006 apx 200pp apx £72.00/US$130.00/€108.00

Find us at
http://www.witpress.com

Save 10% when you order from our encrypted ordering service on the web using your credit card.



WITPRESS

Computational Methods in Multiphase Flow III

Edited by: C. A. BREBBIA, Wessex Institute of Technology, UK, A. A. MAMMOLI, The University of New Mexico, USA

New advanced numerical methods and computer architectures have greatly improved our ability to solve complex multiphase flow problems. In this volume modellers, computational scientists and experimentalists share their experiences, successes, and new methodologies in order to further progress this important area of fluid mechanics.

Originally presented at the Third International Conference on Computational Methods in Multiphase Flow, the papers included cover topics such as: BASIC SCIENCE - Creeping Flow; Turbulent Flow; Linear and Nonlinear Fluids; Cavitation. DNS AND OTHER SIMULATION TOOLS - Finite Elements; Boundary Elements; Finite Volumes; Stokesian Dynamics; Large Eddy Simulation; Interface Tracking Methods. MEASUREMENT AND EXPERIMENTS - Laser Doppler Velocimetry; Nuclear Magnetic Resonance; X-Ray; Ultrasound. APPLICATIONS - Combustors; Injectors, Nozzles; Injection Moulding; Casting.

WIT Transactions on Engineering Sciences Volume 50

ISBN: 1-84564-030-6 2005 384pp apx £125.00/US$235.00/€187.50

All prices correct at time of going to press but subject to change.
WIT Press books are available through your bookseller or direct from the publisher.

Flow-Induced Vibrations in Engineering Practice

Editor: P. ANAGNOSTOPOULOS, Aristotle University, Thessaloniki, Greece

"The articles, all well written in engineering style, are mainly intended to give an engineer working in this field an overview on the latest developments of the subject, but are also well suited to serve as an introduction for readers who want to get in contact and get acquainted with this fascinating field."

ZENTRALBLATT FÜR MATHEMATIK

Many of the papers presented in journals or at conferences regarding flow-induced vibrations are too complex for background reading or design purposes. This text provides a compilation of the salient points of various flow-induced vibration mechanisms.

Partial Contents: Vibrations Induced by Vortex Shedding; Mathematical Models for Vortex-Induced Vibrations of Beams; Galloping of Slender Bodies.

Series: Advances in Fluid Mechanics, Vol 31

ISBN: 1-85312-644-6 2002 400pp £132.00/US$199.00/•198.00

WIT Press is a major publisher of engineering research. The company prides itself on producing books by leading researchers and scientists at the cutting edge of their specialities, thus enabling readers to remain at the forefront of scientific developments. Our list presently includes monographs, edited volumes, books on disk, and software in areas such as: Acoustics, Advanced Computing, Architecture and Structures, Biomedicine, Boundary Elements, Earthquake Engineering, Environmental Engineering, Fluid Mechanics, Fracture Mechanics, Heat Transfer, Marine and Offshore Engineering and Transport Engineering.



WIT*PRESS*

Numerical Models in Fluid-Structure Interaction

Edited by: S. K. CHAKRABARTI, Offshore Structure Analysis Inc., USA

This book covers a wide range of numerical computation techniques within the specialized area of fluid mechanics. Numerical computation methods on the effects of fluid on structures are described, with particular emphasis on the offshore application.
The book emphasizes the latest international research in the area for the advancement of the interaction problem and new applications of the development to the real world problems. The basic mathematical formulations of fluid structure interaction and their numerical modeling are discussed with reference to the physical modeling of the interaction problems.
The state-of-the-art on numerical methods in fluid-structure interaction is included, with emphasis on detailed numerical methods. Examples of the numerical methods and their validations and accuracy check are given, stressing the practical application of the problem. Some interesting results on numerical procedure are cited showing the limiting criteria of the numerical methods and typical execution time.
Series: Advances in Fluid Mechanics Vol 42
ISBN: 1-85312-837-6 2005 448pp
£150.00/US$240.00/€225.00

WIT*Press*
Ashurst Lodge, Ashurst, Southampton, SO40 7AA, UK.
Tel: 44 (0) 238 029 3223
Fax: 44 (0) 238 029 2853
E-Mail: marketing@witpress.com



Instability of Flows

Edited by: M. RAHMAN, DalTech, Dalhousie University, Canada

A state-of-the art analysis of studies in the field of instability of flows, this book contains chapters by leading experts in fluid mechanics. The text brings together many important aspects of flow instabilities and one of the primary aims of the contributors is to determine fruitful directions for future advanced studies and research.
Contents: Preface; Contact-Line Instabilities of Driven Liquid Films; Numerical Simulation of Three-Dimensional Bubble Oscillations; Stratified Shear Flow - Instability and Wave Radiation; Instability of Flows; Stability, Transition and Turbulence in Rotating Cavities; A Comprehensive Investigation of Hydrodynamic Instability.
Series: Advances in Fluid Mechanics Vol 41
ISBN: 1-85312-785-X 2005 248pp
£89.00/US$142.00/€133.50

Vorticity and Turbulence Effects in Fluid Structure Interaction

F. TRIVELLATO, University of Trento, Italy

This book contains a collection of 11 research and review papers which have been contributed by each research unit joining the MIUR funded project: "Influence of vorticity and turbulence in interactions of water bodies with their boundary elements and effects on hydraulic design". The book features state-of-the-art Italian research devoted to the topic of fluid-structure interaction.

ISBN: 1-84564-052-7 2006 apx 330pp
apx £115.00/US$195.00/€172.50

This page intentionally left blank

This page intentionally left blank

This page intentionally left blank

This page intentionally left blank

This page intentionally left blank

This page intentionally left blank